Habilitationsschrift

Wireless Communications Over Time-Variant Channels

ausgeführt zum Zwecke der Erlangung der Lehrbefugnis für das Fach

Mobilkommunikation
(Mobile Communications)

eingereicht an der
Technischen Universität Wien
Fakultät für Elektrotechnik und Informationstechnik

von

Dipl.-Ing. Dr.techn. Thomas Zemen

Wien, Juni 2012

TU WIEN

Acknowledgement

This thesis collects my research results obtained throughout the last eight years at FTW Telecommunications Research Center Vienna. During this time I had the pleasure to work with and advice a group of talented researchers that pursuit their PhD degree within my different research projects at FTW. I want to thank, in chronological order, Florian Kaltenberger, Nicolai Czink, Charlotte Dumard, Laura Bernadó, and Paolo Castiglione for the fruitful collaboration. I would also like to thank Alexander Paier and Sebastian Caban for the joint work during their time at Vienna University of Technology as well as Christian Vogel for many helpful discussions on writing a habilitation thesis.

I am grateful to Prof. Christoph Mecklenbräuker, Prof. Andreas Molisch, Prof. Gottfried Magerl and Prof. Christoph Überhuber for their support, encouragement and help during the preparation of this thesis.

Finally, I would like to thank Dada for constantly being the sun in my life and our two children, Sophia and Theo, that made sure that my mind got enough distraction by experiencing the adventure of raising children.

Abstract

This habilitation thesis is based on a collection of articles dealing with wireless communications over time-variant channels. The wireless communication scenario is characterized by a high relative velocity between transmitter and receiver, fast changes of environment conditions for wave propagation, bursty frame based data transmission and by low-latency demands. This thesis addresses open problems in four closely connected research fields relevant for wireless communications over time-variant channels, which are:

Characterization and Modeling of Wireless Communications Channels - We discuss the acquisition of empirical vehicular channel measurement data in two campaigns conducted in Lund, Sweden, in 2007 and 2009. We found that the wireless vehicular communication channel is characterized by a non-stationary fading process. We analyze in detail the extent of the region in time and frequency for which the fading process can be approximated as stationary. Furthermore, we assess the time-variant coherence-time and coherence-bandwidth, as well as the Rician K-factor variation in time, frequency and space. These results provide the foundation for a realistic vehicular geometry based stochastic channel model (GSCM). We develop a method for complexity reduction of a GSCM utilizing a small dimensional subspace spanned by discrete prolate spheroidal (DPS) sequences. Finally, we provide an algorithm to obtain a probability density function describing the placement of scattering objects from channel measurements to directly parametrize a GSCM.

Estimation and Prediction of Channel State Information - For robust subspace-based channel estimation and prediction we provide the theoretical foundation by generalizing DPS sequences to band-limits consisting of disjoint intervals. The subspace spanned by generalized DPS sequences enables minimum-energy band-limited prediction. A finite set of pre-calculated subspaces is defined, and the subspace with the smallest reconstruction error is selected and used for prediction. The algorithm is validated with vehicular channel measurement data and its robustness is proven. Furthermore, we use the generalized DPS sequences to define a tight two dimensional subspace for iterative time-variant channel estimation for IEEE 802.11p.

Low Complexity Multi-User Detection - An iterative multi-user detection and interference cancellation structure in user-space is designed for time-variant channels. This structure enables the low complexity implementation of the linear minimum mean square error (MMSE) multi-user filter using the Krylov subspace method. In a

next step we develop a low-complexity modification of the sphere decoding algorithm exploiting the reduced rank description of the time-variant channel utilizing DPS sequences. A variant of this algorithm is also able to provide soft-output. Both, the Krylov subspace and the sphere decoding based multi-user detector, are shown to reduce the numerical complexity by more than one order of magnitude if compared with a linear MMSE based multi-user detector in chip space.

Utilization of Cooperation and Selection Diversity - Utilizing diversity in time-variant channels is important to obtain a dependable communication link. For cooperative diversity in vehicular scenarios we investigate coded cooperation and analyze its performance in terms of the velocity of the users and the quality of the inter mobile-station link. To exploit selection diversity we use multiple antennas but only a single receive chain that is connected to the best antenna through an antenna switch. Minimum-energy band-limited prediction is used to decide which antenna to choose for reception in a time-variant channel.

The scientific results discussed in this thesis enable reliable frame-based wireless communications with low-latency in vehicular scenario that are characterized by a high relative velocity between transmitter and receiver and fast changes of environment conditions. The low numerical complexity of the algorithms enable an increased battery runtime.

Kurzfassung

Diese Habilitationsschrift basiert auf einer Sammlung von Originalarbeiten die offene Forschungsfragen der drahtlosen Kommunikation in zeitveränderlichen Kanälen adressieren. Hohe Relativgeschwindigkeiten zwischen Sender und Empfänger, eine schnelle Veränderung der Umgebungsbedingungen für die Wellenausbreitung, blockbasierte Datenübertragung und hohe Anforderungen an die Latenz charakterisieren diese Kommunikationssysteme. In dieser Habilitationsschrift werden vier eng miteinander verknüpfte Forschungsgebiete adressiert:

Charakterisierung und Modellierung des Funkkommunikationskanals - Wir beschreiben zwei neuartige Fahrzeugkanalmesskampagnen in Lund, Schweden im Jahr 2007 und 2009. Die Messkampagnen zeigen, dass der Fahrzeugkanal durch einen nicht stationären Schwundprozess gekennzeichnet ist. Wir analysieren die Ausdehnung der Stationaritätsregion in Zeit und Frequenz für welche der Schwundprozess noch als stationär angenähert werden kann. Weiter beschreiben wir Methoden um die zeitveränderliche Kohärenzzeit und Kohärenzbandbreite, als auch den zeitveränderlichen K-Faktor zu bestimmen. Dies dient zur Gewinnung der Grundlagen für die Entwicklung eines geometriebasierten stochastischen Kanalmodells (geometry based stochastic channel model, GSCM). Wir stellen ein Verfahren zur Komplexitätsreduktion von GSCMs vor, das eine Projektion auf einen Unterraum – aufgespannt von diskreten abgeflachten spheroidalen (discrete prolate spheroidal, DPS) Basisfunktionen – nützt. Schlussendlich entwickeln wir einen Algorithmus um die Wahrscheinlichkeitsdichtefunktion der Streuobjekte direkt aus Kanalmessungen zu bestimmen und damit ein GSCM zu parametrisieren.

Schätzung und Prädiktion der Kanalimpulsantwort - Wir verallgemeinern die DPS Sequenzen auf Bandbegrenzungen bestehend aus disjunkten Intervallen. Der Unterraum der durch die verallgemeinerten DPS Sequenzen aufgespannt wird ermöglicht bandlimitierte minimale Energie Kanalprädiktion. Aus einer endlichen Anzahl an vorberechneten Unterräumen wird der Unterraum mit dem kleinsten Rekonstruktionsfehler ausgewählt und für die Prädiktion verwendet. Die Validierung mit Fahrzeugkanalmessungen beweist die Robustheit dieses Algorithmus. Weiters verwenden wir die verallgemeinerten DPS Sequenzen um einen zweidimensionalen Unterraum für die iterative Kanalschätzung für IEEE 802.11p zu definieren.

Mehrbenutzerdetektion mit geringer Komplexität - Wir entwickeln einen iterativen Mehrbenutzerdetektor für zeitvariante Kanäle. Unsere Struktur erlaubt eine kom-

plexitätsreduzierte Implementierung des Wienerfilters für die Mehrbenutzerdetektion mittels der Krylov Unterraummethode. In einem weiteren Schritt beschreiben wir einen Sphere-Dekoder der die rangreduzierte Darstellung des zeitveränderlichen Kanals mittels DPS Sequenzen ausnützt. Beide Methoden ermöglichen eine Reduktion der numerischen Komplexität um mehr als eine Zehnerpotenz im Vergleich zur klassischen Mehrbenutzerdetektion mittels Wienerfilter.

Nutzung von Kooperations- und Selektionsdiversität - Durch die Nutzung von Diversität in zeitveränderlichen Kommunikationskanälen kann die Verlässlichkeit der Datenübertragung erhöht werden. Wir untersuchen Kooperationsdiversität in der Form von kodierter Kooperation und analysieren ihre Bitfehlerrate in Abhängigkeit von der Fahrzeuggeschwindigkeit und der Qualität des Kanals zwischen den beiden kooperierenden Mobilteilen. Zur Nutzung der Selektionsdiversität verwenden wir Mehrfachantennen von denen jeweils immer nur eine über einen Antennenschalter mit dem Empfänger verbunden ist. Mittels bandlimitierter minimaler Energie Prädiktion kann die beste Antenne in zeitveränderlichen Kanälen ausgewählt werden.

Die Forschungsergebnisse dieser Habilitation ermöglichen eine zuverlässige blockbasierte drahtlose Kommunikation bei hohen Relativgeschwindigkeiten zwischen Sender und Empfänger. Wir können damit schnelle Veränderung der Wellenausbreitungsbedingungen beherrschen, kurze Latenzzeiten garantieren als auch die Batterielaufzeiten durch geringe numerische Komplexität verlängern.

Contents

1 Introduction

Wireless broadband communications for mobile users provides an important cornerstone for our society. In this thesis we focus on wireless communications where the transmitter, the receiver, or both, move at vehicular velocities. We will address open scientific questions for the reliable operation of such communication systems with reduced computational complexity.

In cellular scenarios one side of the communication link is mobile while the base station is mounted fixed. With the introduction of systems like UMTS LTE [3] data rates of up to a maximum bit rate of 100 Mbit/s are already commercially available for nomadic mobility. However, with increasing velocity of the user the achievable data rates are strongly reduced [116] indicating the need for appropriate time-variant channel estimation, equalization and prediction methods as well as transceiver algorithms. These algorithms shall demand low-complexity to ensure sustained battery life of mobile handsets.

In the last years vehicular communication systems for intelligent transportation systems are being developed. In these systems the wireless communication link is different from cellular communication systems as depicted in Fig. 1.1. Both sides of the communication link are mobile, leading to higher relative velocities. Furthermore the antennas are mounted at a height of about 1.5 meter above ground, and many metallic objects in the form of other vehicles are in close vicinity of the transmitter and receiver. The wireless communication link in intelligent transportation systems is used for safety-relevant services [40] like collision avoidance at street crossing or in traffic jams. Hence aspects like reliability, low-latency and strict packet delay bounds become important. We will refer to these characteristics jointly by the term *dependability* [84].

1.1 Characterization and Modeling of Wireless Communication Channels

The performance of any wireless communications system is to a large extent determined by the properties of the wireless communication channel. The radio waves interact with dielectric and conducting objects by reflection, transmission, scattering and diffraction. Multiple scatterers like buildings, vehicles, hills, etc., cause radio

(a) Cellular *(b)* Vehicular
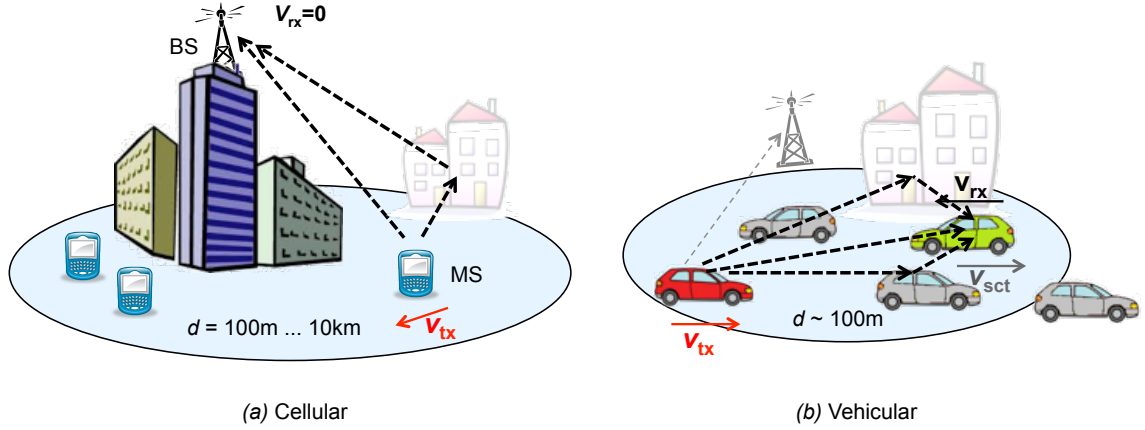
Figure 1.1: Comparison of the scenario for *(a)* cellular and *(b)* vehicular communications.

wave propagation along several paths. At the receive antenna multiple attenuated and delayed copies of the transmitted signal add up.

Such a wireless channel can be well approximated by a linear time-variant system that is defined by a time-variant impulse response[1] $h(t, \tau)$ incorporating multi-path propagation and mobility

$$r(t) = \int_0^\infty h(t, \tau)s(t - \tau)\mathrm{d}\tau \,, \tag{1.1}$$

where t denotes time and τ time delay, $s(t)$ denotes the transmitted signal and $r(t)$ the received signal, respectively. The channel impulse response taking into account P distinct propagation paths can be given in the form

$$h(t, \tau) = h_{\mathrm{RX}}(\tau) * \left(\sum_{p=1}^P h_p \delta(t - \tau_p)\mathrm{e}^{\mathrm{j}2\pi\nu_p t} \right) * h_{\mathrm{TX}}(\tau) \,, \tag{1.2}$$

where p denotes the path index, h_p the complex attenuation factor, τ_p the time delay, ν_p the Doppler frequency, $h_{\mathrm{TX}}(\tau)$ the transmit filter, $h_{\mathrm{RX}}(\tau)$ the receive filter, and $*$ the convolution operator, respectively

Bello [13] generalized (1.2) to a continuum of scatterers by means of the delay-Doppler spreading function $S(\tau, \nu)$ as

$$r(t) = h_{\mathrm{RX}}(\tau) * \int_{-\infty}^\infty \int_{-\infty}^\infty S(\tau, \nu)(h_{\mathrm{TX}}(\tau) * s(t - \tau_p))\mathrm{e}^{\mathrm{j}2\pi\nu_p t}\mathrm{d}\tau \, \mathrm{d}\nu \,, \tag{1.3}$$

---

[1]In this thesis we generally employ the equivalent baseband notation abstracting from the specific carrier frequency f_{C}.

see also [50, 89, 102]. The delay-Doppler spreading function represents the dispersion of the transmitted signal in delay and Doppler-shift.

Often a characterization of the wireless propagation channels for a wide variety of operating conditions is sought for. This motivates a stochastic characterizations where the linear time-variant impulse response is treated as a random process. The autocorrelation of the time-variant frequency response

$$H(t, f) = \int_{-\infty}^{\infty} h(t, \tau) \mathrm{e}^{-\mathrm{j}2\pi f\tau} \mathrm{d}\tau \qquad (1.4)$$

depends on four variables:

$$R_H(t, t', f, f') = \mathbb{E}\{H(t, f)H^*(t', f')\} \,. \qquad (1.5)$$

This description can be simplified if the second order statistic does not change in time, hence the fading process is wide sense stationary (WSS). In this case the correlation just depends on the time difference $\Delta t = t - t'$. This property is fulfilled if signal components with different Doppler shift are uncorrelated.

If the second order statistic does not change with frequency we call the fading process uncorrelated scattering (US). In this case the correlation depends on the frequency difference $\Delta f = f - f'$ and the signal components with different delays are uncorrelated.

In case the fading process exhibits both properties we can combine them in the WSSUS assumption [13] allowing the definition of a simplified time and frequency correlation function

$$R_H(t, t', f, f') = R_H(\Delta t, \Delta f) \,. \qquad (1.6)$$

The two dimensional Fourier transform of $R_H(\Delta t, \Delta f)$ gives the scattering function $C(\tau, \nu) \geq 0$ [89] indicating the mean energy distribution in the delay-Doppler plane:

$$C(\tau, \nu) = \int_{-\infty}^{+\infty} \int_{-\infty}^{+\infty} R_H(\Delta t, \Delta f) \mathrm{e}^{-\mathrm{j}2\pi(\nu\Delta t - \tau\Delta f)} \mathrm{d}\Delta t \, \mathrm{d}\Delta f \,. \qquad (1.7)$$

The WSSUS assumption is commonly made for the definition of wireless channel models and for channel characterization. This assumption is a valid approximation for users at low velocities in cellular communication systems. However, the WSSUS assumption does not hold for mobile users [96, 126] at vehicular speed. In Fig. 1.2 *(b)* we depict an exemplary time-variant power delay profile obtained from vehicular measurements. The measurement scenario is shown by the aerial picture in Fig. 1.2 *(a)*.

In this measurement the line-of-sight is partly obstructed by surrounding buildings. The signal obtained from the line-of-sight component is the first and strongest signal component that is visible from second 4 to second 9. The time-delay of the

(a) Scenario   *(b)* Time-variant power delay profile
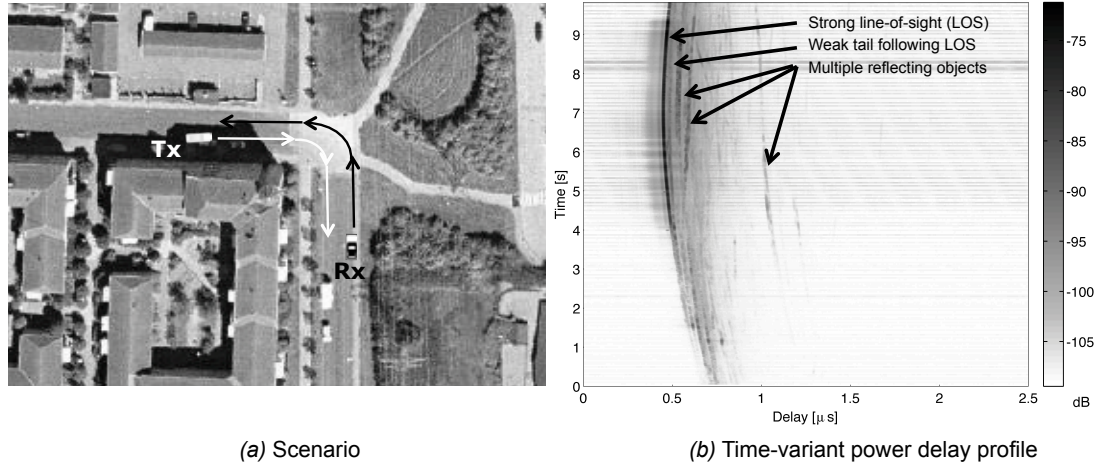
Figure 1.2: Vehicle-to-vehicle communication link in a partly obstructed line-of-sight (LOS) scenario with surrounding buildings: *(a)* Aerial scenario picture, *(b)* time-variant power delay profile.

line-of-sight components varies due to the moving vehicles. After the line-of-sight component we can see a diffuse tail and other line structures that each represent a dedicated reflecting object in the vicinity of the communication link.

Obviously, the fading process in Fig. 1.2 *(b)* is non-stationary. Hence, the WSSUS assumption will be at most valid for a limited region in time and frequency. For the description of such a non-stationary channel the scattering function (1.7) must be replaced by a *local* scattering function (LSF) that is associated with a locally defined stationarity region [79, 80] [50, Chapter 1]:

$$C(t, f; \tau, \nu) = \int_{-\infty}^{+\infty} \int_{-\infty}^{+\infty} R_H(t, f; \Delta t, \Delta f) e^{-j2\pi(\nu\Delta t - \tau\Delta f)} d\Delta t \, d\Delta f \qquad (1.8)$$

with

$$R_H(t, f; \Delta t, \Delta f) = \mathbb{E}\{H(t, f + \Delta f)H^*(t - \Delta t, f)\}. \qquad (1.9)$$

For non-stationary vehicular channels (1.2) will be only valid for a limited time period $t_0 < t < t_1$ where $t_1 - t_0$ indicates the extent of the stationary region in time.

To obtain a detailed characterization of the non-stationary vehicular channel by means of the LSF, empirical channel measurements must be gathered in a carefully designed experimental setup.

Channel Sounding   The channel impulse response can be estimated with a channel sounder [78, 89]. Thereto, a known signal $s(t)$ is transmitted, and the received signal

$$y(t) = \int_0^\infty h(t, \tau) s(t - \tau) \mathrm{d}\tau + n(t)$$

is used to obtain an estimate of the channel impulse response $h(t, \tau)$, where $n(t)$ denotes noise.

For the practical implementation of a wideband channel sounder either the correlation principal [6, 20, 98], i.e., using time domain measurements, or the multi-tone principle [121] using frequency domain measurements are applied [14, 63]. The multitone principle is closely related to the principle of orthogonal frequency division multiplexing (OFDM) [127, 130]. This type of channel sounders directly obtains a sampled time-variant frequency response

$$H[m, q] := H(T_\mathrm{S} m, F_\mathrm{S} q) \tag{1.10}$$

for a finite region in time and frequency. We represent by $m \in \{0, \ldots, M - 1\}$ the discrete time index at rate $1/T_\mathrm{S}$, and by $q \in \{0, \ldots, N - 1\}$ the discrete frequency index. The total number of snapshots is denoted by M, and the number of measured frequency bins by N. The measurement bandwidth is denoted by B resulting in a frequency resolution $F_\mathrm{S} = B/N$.

To measure spatial wave propagation properties of mobile users, which are important for multiple-input multiple-output (MIMO) systems, two different approaches can be used. One can connect multiple parallel radio frequency (RF) chains to all antenna elements at the transmitter and receiver side. This allows to transmit and receive test signals simultaneously. The transmit signals are differentiated, e.g., using specific pseudo noise sequences [78, 100]. The drawback of this principle is the high effort for multiple RF chains, their calibration [97, 98] and sufficient co-channel interference suppression.

For the switched-array principle only a single RF chain is used. The different antenna elements at the transmitter and receiver side are sequentially connected to the RF chain using switches [121]. For vehicular scenarios one has to take into account that this principle needs more time to acquire a channel snapshot by sounding the individual channels between all transmit and receive antenna elements consecutively. The switched-array principle is the most common way to sound radio channels nowadays due to its robustness, the need to calibrate only one RF chain and reduced cost.

For the non-stationary vehicular channel the design and practical execution of channel measurements is a complex task. Measurements are scarce but urgently needed to obtain reliable channel models. Measurements exclusively on the vehicle-to-vehicle channel with vehicles driving in the same direction are reported in [5–7,

21, 77, 82, 103] for either the 2.4 GHz or the 5 GHz band. Channel measurements where the vehicles are traveling in the same and in opposite directions at a carrier frequency of 3.5 GHz are presented in [38]. See [84, 87] for an overview and further references.

Channel Models   After empirical data has been gathered, one has to *(i)* decide on the structure of the model and *(ii)* parameterize the model utilizing the measured channel impulse responses. The model can then be applied for numeric link level simulation or for channel emulation to test specific transmitter and receiver hardware in a clearly determined and repeatable setting.

Channel models can be grouped into three different categories [14, 89]:

- *Geometry based channel models*: The time-variant impulse response can in principle be obtained by solving the Maxwell equations for a specific environment. However, the properties of every physical object must be known in details. By ray tracing [9, 27, 44, 76] an approximate solution can be obtained applying the fundamental geometric principles of reflection, diffraction, and scattering. The channel impulse response is represented by a (large) sum of propagation paths requiring high computational complexity especially for time-variant scenarios. For the modeling of vehicular communication channels, ray tracing was applied by Maurer et al. [81–83].

  Ray tracing is a valuable tool for characterizing a cite specific environment. However, it cannot be used for describing general scenarios.

- *Stochastic channel models* do no assume an underlying geometry. The channel impulse responses are generated such that they fulfill given statistical properties in terms of first and second order moments. Most often employed is the so called tap delay line model where the impulse response consists of a finite number of delay taps with fixed spacing [89]. The tap delay line model can capture basic statistical properties like the power delay profile, the Doppler power spectral density or spatial correlation [115, 129, 132] for general scenarios.

  This modeling approach was adopted by standardization bodies as reference channel model for GSM [41], and UMTS [55] . Due to its design, assuming a fixed second order statistic, a tap delay line model is not able to capture non-stationary properties of the fading process in vehicular scenarios.

- *Geometry based stochastic channel models (GSCMs)* provide a good compromise between complexity and accuracy [51, 64, 69, 90] [23, Chapter 6.8] when compared to the previous two models. Here important point scatterers are randomly placed according to a given distribution. This allows to capture

non-stationary properties of the propagation channel as well as spatial and temporal correlations. For LTE a GSCM was specified by 3GPP [69]. Reducing the computational complexity of such channel models while maintaining their accuracy is another important thread of research. So far complexity reduction was only treated for narrowband models [22, 58, 135, 139].

Scientific Contributions

In the journal paper *Characterization of vehicle-to-vehicle radio channels from measurements at 5.2 GHz* [Article 1] we address scenarios most relevant for future intelligent transportation systems with highly dynamic propagation conditions. In the year 2007 in Lund Sweden, we conducted a pioneering channel sounding campaign [94, 95] in collaboration with Vienna University of Technology and Lund University. We measured vehicle-to-vehicle and vehicle-to-infrastructure links with high temporal sampling rate and a bandwidth of 240 MHz. Key parameters like path loss, power-delay-profile and the delay-Doppler spectrum are evaluated.

We found that in vehicular scenarios the statistical channel properties show only local stationarity. Hence, the second order statistics of the fading process are constant for just a finite region in time and frequency. In the conference paper *Non-WSSUS vehicular channel characterization in highway and urban scenarios at 5.2 GHz using the local scattering function* [Article 2] these stationary regions are characterized using the concept of the LSF [80]. The LSF calculation is implemented by means of a multi-taper power spectral density estimator [79, 101, 122]. This estimator relies on the knowledge of a minimum stationarity region with dimension $M' \times N'$ in time and frequency as depicted in Fig. 1.3. In [Article 2] we introduce the collinearity measure to obtain an estimate of the extent of the stationarity region from channel measurements.

In the conference paper *Non-WSSUS vehicular channel characterization at 5.2 GHz - spectral divergence and time-variant coherence parameters* [Article 3] we analyze the time-variant coherence time of vehicular channels in drive by scenarios building on the LSF estimates from [Article 3] .

In 2009 we carried out a second improved measurement campaign, again in Lund Sweden. Now, VW Touran passenger cars were used and the vehicle-to-vehicle channel in safety critical scenarios relevant for intelligent traffic systems was measured. The international consortium was extended by Volkswagen, Delphi Fuba and the University of Southern California. Overview articles summarizing the Lund 2009 measurement campaign and the related research activities have appeared in [84, 133]. Utilizing the measurement data from the Lund 2009 campaign, we provided in a conference paper a *Multi-dimensional K-factor analysis for V2V radio channels in open sub-urban street crossings* [Article 4] linking the K-factor variation of the channel
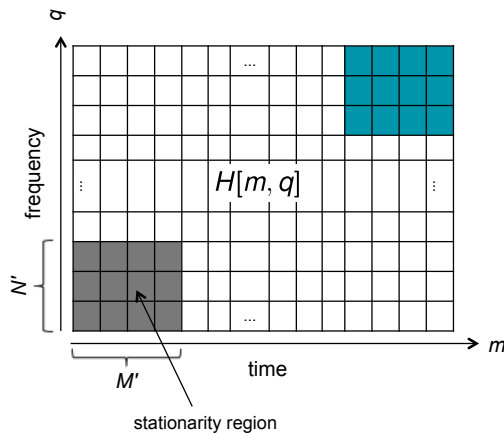
Figure 1.3: Stationarity region with extension $M' \times N'$ in the time-frequency plane defined by the sampled time-variant frequency response $H[m, q]$.

to the physical properties of the environment.

The above vehicular channel characterization work is an important foundation to obtain realistic geometry based stochastic channel models (GSCMs) [64]. They allow to model a wide range of propagation scenarios including non-stationary vehicular channels by superposing multiple propagation paths P as defined in (1.2). The accuracy of a GSCM increases with the number of paths and so does its numerical complexity. In the journal paper *Low-complexity geometry based MIMO channel emulation* [Article 5] we present an algorithm to reduce the complexity of a general wideband GSCM utilizing a multi dimensional subspace spanned by discrete prolate spheroidal (DPS) sequences. This algorithm enables the projection of each path on the DPS subspace in $\mathcal{O}(1)$ operations. In [25] we applied this technique to reduce the complexity of the non-stationary vehicular channel model of Karedal et al. [64].

In the journal paper *A time-variant MIMO channel model directly parametrised from measurements* [Article 6] multi-path components, extracted by means of a high resolution method [43] from indoor measurement data, are grouped according to clusters that can be linked to physical objects [45, 106]. The statistical cluster properties and their temporal evolution are used to obtain a probability density function characterizing a specific environment. Using this probability density function, new random time-variant channel realizations can be drawn for realistic numerical simulations or equipment testing. Effectively, we create a GSCM that can be automatically parametrized directly from measurements.

Publications

[Article 1] A. Paier, J. Karedal, N. Czink, C. Dumard, T. Zemen, F. Tufvesson, A. F. Molisch, and C. F. Mecklenbräucker, "Characterization of vehicle-to-vehicle radio channels from measurements at 5.2 GHz," *Wireless Personal Communications*, vol. 50, no.1, July 2009 pp. 19-32, doi:10.1007/s11277-008-9546-6.

[Article 2] A. Paier, T. Zemen, L. Bernadó, G. Matz, J. Karedal, N. Czink, C. Dumard, F. Tufvesson, A. F. Molisch, and C. F. Mecklenbräuker, "Non-WSSUS vehicular channel characterization in highway and urban scenarios at 5.2 GHz using the local scattering function," in *Workshop on Smart Antennas (WSA)*, Darmstadt, Germany, Feb. 26-27, 2008.

[Article 3] L. Bernadó, T. Zemen, A. Paier, G. Matz, J. Karedal, N. Czink, C. Dumard, F. Tufvesson, M. Hagenauer, A. F. Molisch, C. F. Mecklenbräuker, "Non-WSSUS vehicular channel characterization at 5.2 GHz - spectral divergence and time-variant coherence parameters," in *XXIX General Assembly of the International Union of Radio Science (URSI)*, Chicago, Illinois, USA, August 7-16, 2008, invited.

[Article 4] L. Bernadó, T. Zemen, J. Karedal, A. Paier, A. Thiel, O. Klemp, N. Czink, F Tufvesson, A. F. Molisch and C. F. Mecklenbräuker, "Multi-dimensional K-factor analysis for V2V radio channels in open sub-urban street crossings," in *21st Annual IEEE International Symposium on Personal, Indoor and Mobile Radio Communications (PIMRC)*, Istanbul, Turkey, September 26-30, 2010.

[Article 5] F. Kaltenberger, T. Zemen, and C. Ueberhuber, "Low-complexity geometry based MIMO channel emulation," *EURASIP Journal on Advances in Signal Processing*, vol. 2007, Article ID 95281, 17 pages, 2007. doi:10.1155/2007/95281.

[Article 6] N. Czink, T. Zemen, J. Nuutinen, J. Ylitalo, and E. Bonek, "A time-variant MIMO channel model directly parametrised from measurements," *EURASIP Journal on Wireless Communications and Networking (special issue on "Advances in Propagation Modelling for Wireless Systems")*, vol. 2009, doi:10.1155/2009/627238.

1.2 Estimation and Prediction of Channel State Information

A main challenge for vehicular communications are the rapidly changing radio propagation conditions that strongly differ from cellular wireless networks. In vehicular communications, both, the transmitter and the receiver are potentially mobile, and

the scattering environment changes rapidly. Even more, the channel statistics are non-stationary as discussed in Section 1.1.

Intelligent transportation systems demand dependable communication links with a strict upper bound on the packet delay for safety relevant applications. The short stationarity time of the channel together with short latency demands have as consequence that most processing at the receiver side shall be done based on only a *single* received (short) frame.

We consider OFDM systems [130], transmitting coded data-blocks in frames over a time-variant frequency-selective channel. Pilot symbols are interleaved with data symbols in the time-frequency plane [1, 2, 4, 31, 46, 84]. Hence, the sampled time-variant and frequency-selective channel $H[m, q]$, $(m, q) \in \{0, \ldots, M - 1\} \times \{0, \ldots, N - 1\}$ can be observed for a certain region in time and frequency during the transmission of a single frame.

Channel state information at the receiver side is an important prerequisite for coherent detection algorithms. At the transmitter side channel state information is required additionally for spatial multiplexing in multiple-input multiple-output (MIMO) systems [99, 119, 120], for interference management in multi-user systems [48, 56] as well as for coordinated multipoint transmission (CoMP) [108]. In order to acquire channel state information at the transmitter side one can rely on channel reciprocity in time-division duplex (TDD) systems. For frequency division duplexing (FDD) a dedicated channel state information transfer is required. For both, FDD and TDD, channel prediction must be employed to compensate for the time delay between channel estimation and data transmission.

Channel Estimation   Second order statistics are required for pilot based channel estimation using a classical MMSE filter [93, 110]. It is hard to obtain such statistics for a fading process with short stationarity time using bursty frame based data transmission. Consequently, robust channel estimation is important in such an environment.

A robust Wiener filter is employed in [61, 62] for time-variant channel estimation utilizing knowledge on the maximum Doppler bandwidth and the maximum support of the power-delay-profile. A delay-Doppler scattering function prototype [13] with flat spectrum is used to calculate the filter coefficients. Such a robust Wiener filter design is clearly mismatched to the actual shape of the scattering function. However, its performance in terms of mean square error shows only a minor degradation for a wide parameter range compared to the matched Wiener filter [61].

To reduce the complexity of the robust Wiener filter one can exploit the fact that the time-variant frequency-selective impulse response of the channel is restricted to

a low-dimensional subspace, i.e.,

$$H[m,q] \approx \sum_{i=0}^{D-1} \sum_{k=0}^{D'-1} u_i[m] u_k'[q] \psi_{i,k}$$

with $u_i[m]$ and $u_k'[q]$ being orthonormal basis functions and $D \ll M$ as well as $D' \ll N$. The estimation of $\psi_{i,k}$ leads to a reduced-rank Wiener filter [30, 111].

Zemen and Mecklenbräuker [135] developed a fundamentally new approach for robust time-variant channel estimation, exploiting the correlation in time. In [135] the low-dimensional subspace spanned by DPS sequences [117] is used for the first time to model the time evolution of the fading process. These, estimator is robust because the subspace is designed according to only two parameters: *(i)* the given maximum Doppler bandwidth and *(ii)* the observation period in time, i.e., the frame length. In [135] Zemen and Mecklenbräuker show analytically that the square channel estimation bias obtained with the DPS basis expansion is more than a magnitude smaller compared to the Fourier basis expansion (i.e., a truncated discrete Fourier transform) [71, 109].

A large number of different basis expansion models is discussed in literature. A good overview of different basis expansion models with their pros and cons is given in [50, Section 1.6]. To exploit the correlation in the frequency domain a truncated Fourier transform was used in [110], which is only optimal for sample-spaced path delays. For more realistic real-valued path delays Edfors et al. [37] exploited the correlation in the frequency domain by using the singular value decomposition of the channels covariance matrix which is assumed to be known. In [32] the singular value decomposition was calculated in an adaptive manner using an estimate of the covariance matrix. In [134] two successive DPS subspace projections in the time and frequency domain are used for time-variant frequency-selective channel estimation. Iterative time-variant channel estimation using soft-symbol feedback from a soft-input soft-output BCJR decoder [11] is discussed in [136] for a multi-user system. A joint projection on a two dimensional DPS subspace is further explored in [104].

Channel Prediction   In mobile communication systems channel state information at the transmitter side proves to be beneficial for increasing the system capacity. Channel state information can be obtained by exploiting channel reciprocity or explicit feedback. However for users at vehicular speed the channel state information gets outdated rapidly. Thus, appropriate channel prediction is necessary to compensate for the delay. The second order statistic of the fading process is exploited in [111], [65, Sec. 12.7] for channel prediction, while in [10, 16, 18, 39, 112] the channel impulse response is modeled as the superposition of multiple plane waves representing distinct propagation paths. Each path is characterized by its distinct complex

weight and Doppler shift. The estimation error of the path wise model increases drastically if the Doppler frequency difference between two paths becomes small [43]. Hence, this type of algorithm shows good performance in simulations but reduced performance with measured channel data [16, 17].

Prediction of continuous-time channels based on minimum-energy band-limited prediction utilizing prolate spheroidal functions is treated in [73–75, 118]. Minimum-energy band-limited prediction for multi-dimensional energy-concentrated signals with an a-priori known band-limiting region is presented in [28]. The noiseless discrete case is treated in [57].

Scientific Contributions

Our contribution focuses on robust time-variant channel prediction and estimation algorithms for non-stationary channels, where *robust* means insensitive to mismatches in the second order statistics of the fading process. In the journal paper *Minimum-energy band-limited predictor with dynamic subspace selection for time-variant flat-fading channels* [Article 7] we develop a low-complexity prediction algorithm based on noisy channel observations that are obtained while receiving a *single* frame of coded data symbols. We generalize DPS sequences to band-limits consisting of disjoint intervals. The subspace spanned by generalized DPS sequences enables minimum-energy band-limited prediction. We establish the relation of minimum-energy band-limited prediction to reduced-rank Wiener prediction. A finite set of pre-calculated subspaces is defined, representing different hypothesis on the disjoint band-limiting region of the fading process. The subspace with the smallest reconstruction error is selected and utilized for channel prediction using a probabilistic bound on the reconstruction error [12].

In a conference paper, the *Validation of minimum-energy band-limited prediction using vehicular channel measurements* [Article 8] is presented. The robustness of the algorithm is proven, no outlier removal or other preprocessing is necessary for consistent performance on a large number of measured vehicular channel samples for line-of-sight and non line-of-sight scenarios.

Building on our first results on channel estimation in vehicular communications systems [84] we developed an *Iterative time-variant channel estimation for IEEE 802.11p using generalized discrete prolate spheroidal sequences* [Article 9] . In this journal paper we invesigate a subspace based channel estimator. The two dimensional subspace uses generalized DPS sequences that were introduced in [Article 7] . Due to the generalized bandlimit of the generalized DPS sequences we are able to design a tighter subspace as the one used in [104]. Tight is meant in the sense that the support of the power spectral density represented by the subspace basis functions is closely matched to the support of the delay-Doppler scattering function

of the channel. This allows to reduce the error of the iterative channel estimator. The time-variant channel estimator is validated with a GSCM [64].

Due to the tight subspace design, near-optimal channel estimation can be obtained iteratively in an IEEE 802.11p compliant system, despite the pilot pattern of IEEE 802.11p that is not adapted to time-variant propagation conditions. Additionally, a backward-compatible extension to the IEEE 802.11p standard is proposed in [Article 9] by adding an OFDM pilot symbol to the end of the frame (an international patent application is pending [26]). These standard extension allows a threefold complexity reduction for channel estimation.

The channel estimator described in [Article 9] has been extended to vehicle-to-vehicle communication links by Zemen and Molisch in [137]. In [137] the subspace selection algorithm from [Article 7] is extended to two dimensional time- and frequency-selective channel observations allowing to adapt the channel estimation filter to the wide velocity range in drive by scenarios.

Publications

[Article 7]   T. Zemen, C. F. Mecklenbräuker, F. Kaltenberger, and B. H. Fleury, "Minimum-energy band-limited predictor with dynamic subspace selection for time-variant flat-fading channels," *IEEE Transactions on Signal Processing*, vol. 55, no. 9, pp. 4534–4548, September 2007.

[Article 8]   T. Zemen, S. Caban, N. Czink, and M. Rupp, "Validation of minimum-energy band-limited prediction using vehicular channel measurements," in *17th European Signal Processing Conference (EUSIPCO)*, Glasgow, Scotland, August 2009.

[Article 9]   T. Zemen, L. Bernadó, N. Czink, and A. F. Molisch, "Iterative time-variant channel estimation for 802.11p using generalized discrete prolate spheroidal sequences," in *IEEE Transactions on Vehicular Technology*, vol. 61, no. 3, pp. 1222–1233, March 2012.

1.3 Low Complexity Multi-User Detection

In a wireless multi-user communication system the access of users to a given shared frequency band must be controlled. *Orthogonal* multiple-access methods utilize independent resources, e.g., in time and frequency, known as time-division multiple access (TDMA) or frequency-division multiple access (FDMA), respectively. This concept is used in cellular communication systems like GSM or LTE. Due to the orthogonality of the resources simple user separation at the base station is possible.

Non-orthogonal multiple-access methods are, e.g., code-division multiple access (CDMA), where linear spreading sequences are used to distinguish different users, or space-division multiple access, where beam-forming is applied. In case of CDMA the linear spreading sequences and the effect of the time- and frequency-selective channel can not be distinguished at the receiver side. This leads to non-orthogonal *effective* spreading sequences even if the spreading sequences used at the transmitter side are selected from an orthogonal set. However, the use of non-orthogonal (random) spreading sequences allows to operate the communication system with a higher number of users leading to a higher system capacity [125]. The price one needs to pay for this advantages is the effort for separating the individual users, known as multi-user detection.

In current third generation cellular communication systems like UMTS and CDMA2000 a linear spreading sequence is applied in the time-domain, which is termed direct-sequences (DS) CDMA [128]. In an OFDM based communication system the spreading sequences can be applied in the frequency domain. This concept is called multi-carrier (MC) CDMA [61]. In the reminder of this section we will focus specifically on MC-CDMA, although the developed algorithms are also applicable to other communication systems.

For MC-CDMA the joint received signal vector $\boldsymbol{y}[m] \in \mathbb{C}^N$ at time m can be represented as [136]

$$\boldsymbol{y}[m] = (\boldsymbol{G}[m] \odot \boldsymbol{S}) \, \boldsymbol{d}[m] + \boldsymbol{z}[m] \,, \tag{1.11}$$

where the k-th column of matrix $\boldsymbol{S} \in \mathbb{C}^{N \times K}$ contains the spreading sequences $\boldsymbol{s}_k$ of user $k \in \{1, \ldots, K\}$, matrix $\boldsymbol{G}[m] \in \mathbb{C}^{N \times K}$ collects all time-varying frequency-reponses $\boldsymbol{g}_k[m] = [H_k[m, 0], \ldots, H_k[m, N-1]]^{\mathrm{T}}$, N denotes the number of OFDM subcarriers, K the number of users, and $\odot$ the element wise product, respectively. Vector $\boldsymbol{z}[m] \in \mathbb{C}^N$ denotes additive white symmetric Gaussian noise, and $\boldsymbol{d}[m] \in \mathbb{C}^K$ collects the coded data symbols $\boldsymbol{b}[m]$ of all K users as well as pilot information.

As already mentioned, the effect of the spreading sequence and the time- and frequency-selective channel cannot be separated for multi-user detection. Therefore, the linear system can be written in compact notation using the *effective time-variant* spreading sequence $\tilde{\boldsymbol{S}}[m] = \boldsymbol{G}[m] \odot \boldsymbol{S}$:

$$\boldsymbol{y}[m] = \tilde{\boldsymbol{S}}[m]\boldsymbol{d}[m] + \boldsymbol{z}[m] \,. \tag{1.12}$$

Equation (1.12) demonstrates the importance of time-variant channel estimation for multi-user detection. The channel estimates are needed to calculate the effective spreading sequences matrix $\tilde{\boldsymbol{S}}[m]$ which is central for any following multi-user detection algorithm.

The sequence maximum a-posteriori (MAP) detector [68] is known to provide the optimum solution for (1.12), however its computational complexity is prohibitive
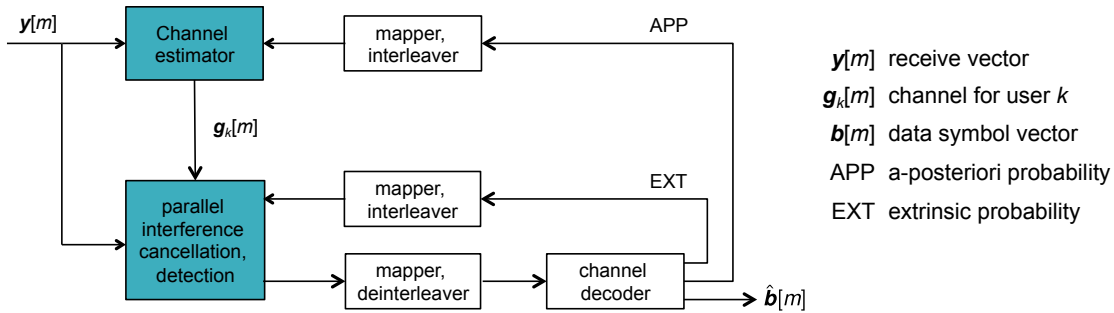
Figure 1.4: Iterative multi-user detection.

for practical applications with a realistic number of users [33, 34]. The MAP detector can be approximated using an iterative structure. A schematic overview of the approximated MAP receiver is given in Fig. 1.4.

As a first step, pilots interleaved with data symbols are used to obtain channel estimates for all K users. In the second step, linear MMSE filtering and parallel interference cancelation [52, 85, 136] is applied neglecting the code constraints. In the third step, code constraints are taken into account by a soft-input soft-output decoder, implemented by the BCJR algorithm [11]. This decoder supplies extrinsic probabilities (EXT) and a-posteriori probabilities (APP) on the code symbols. This APP and EXT information is fed back for enhanced channel estimation and multi-user detection, respectively [85, 136]. While the iterative procedure has traditionally been viewed as ad hoc, recent theoretical justification based on divergence minimization was given in [53].

It has been demonstrated by Zemen et al. [136] that the receiver structure described above allows to reach a load $\beta = K/N = 1$ for velocities up to 150km/h. For time-variant channel estimation a robust reduced-rank subspace estimator utilizing DPS sequences is used as discussed in Section 1.2.

Due to the rapid time-variation of the channel the computational complexity of the multi-user receiver increases since the joint detection filter to solve (1.12) needs to be re-calculated for each time instant m individually. One way to mitigate the complexity problem is to compute the linear MMSE filter approximately, e.g., using the Krylov subspace method [60, 92, 105, 124] that allows to solve a linear system with low complexity by trading accuracy for efficiency [29, 35]. Another approach is based on random matrix theory [36], allowing to compute universal filter weights exploiting the self-averaging properties of random matrices modeling the propagation channel [24].

However, the complexity reduction obtained by the Krylov subspace method or the random matrix approach are lost if simply combined with parallel interference cancellation. This is due to the interference term that varies from user to user.

Scientific Contributions

In the journal paper *Low-complexity MIMO multiuser receiver: A joint antenna detection scheme for time-varying channels* [Article 10] we address the numerical complexity problem of MIMO multi-user detection in time-variant channels. The numerical complexity increases with the number of users, the number of receive antennas and with the time-variability of the communication channel. We are able to reduce the numerical complexity substantially by developing a detection and interference cancellation structure in *user-space*. Hence, multi-user detection is performed using

$$\boldsymbol{x}[m] = \tilde{\boldsymbol{S}}[m]^{\mathrm{H}}\boldsymbol{y}[m]\,, \tag{1.13}$$

i.e., after the correlation of the received signal vector $\boldsymbol{y}[m]$ with the effective spreading matrix $\tilde{\boldsymbol{S}}[m]$. This user-space approach enables a low complexity implementation of the linear MMSE filter using the Krylov subspace method jointly for all receive antennas.

Alternative to linear MMSE multi-user detection and interference cancellation one can also combine the sphere decoding algorithm [15, 42] with interference cancellation. In the conference paper *Subspace-based sphere decoder for MC-CDMA in time-varying MIMO channels* [Article 11] we show that the robust DPS subspace representation of the time-variant channel [135], as discussed in Section 1.2, allows for a complexity reduction of the sphere decoder. The QR decomposition, one step in the sphere decoding algorithm, needs to be computed only once for the DPS subspace channel representation. In a conventional sphere decoder, the QR decomposition must be calculated for each symbol individually if the channel is time-variant.

In the conference paper *Soft sphere decoder for an iterative receiver in time-varying MIMO channels* [Article 12] we extend the method from [Article 11] to sphere decoders with soft-output which is important for soft-input soft-output decoding with the BCJR algorithm [11] in iterative receiver structures.

The algorithms of [Article 10] and [Article 12] allow for a complexity reduction of more than one order of magnitude if compared to multi-user detection in chip-space [34, 136].

Publications

[Article 10]   C. Dumard and T. Zemen, "Low-complexity MIMO multiuser receiver: A joint antenna detection scheme for time-varying channels," *IEEE Transactions on Signal Processing*, vol. 56, no. 7, pp. 2931-2940, July 2008.

[Article 11]   C. Dumard and T. Zemen, "Subspace-based sphere decoder for MC-CDMA in time-varying MIMO channels," in *18th IEEE International Symposium*

on Personal, Indoor and Mobile Radio Communications (PIMRC), Athens, Greece, Sept. 3-7, 2007.

[Article 12]   C. Dumard, J. Jalden and T. Zemen, "Soft sphere decoder for an iterative receiver in time-varying MIMO channels," in *16th European Signal Processing Conference (EUSIPCO)*, Lausanne, Switzerland, Aug. 25-29, 2008, invited.

1.4 Utilization of Cooperation and Selection Diversity

The communication link in vehicular scenarios on the road experiences severe variations due to time- and frequency-selective fading. To increase the dependability of the communication link spatial redundancy can be exploited by means of MIMO systems [99] to reduce the variation of the users data rate. Hence, the information is sent in a redundant fashion via multiple spatial propagation paths [8].

Cooperative communication [70,113,114] allows to utilize spatial diversity in networks of single antenna terminals through redundant transmissions from multiple mobile stations. Coded cooperation [54] integrates user cooperation with channel coding to utilize spatial diversity. An analysis of coded cooperation for block fading channels is given in [72] and first results for time-variant channels are presented in [123].

Multiple antennas at the receiver side is another option to exploit spatial diversity, but hardware costs and power consumption of multiple receive chains are a limiting factor. Antenna selection [86,91,107] chooses one of multiple antenna elements and requires only a single radio-frequency receive chain. It allows the same diversity gain as can be obtained with multiple receive chains and coherent combining [49]. The diversity-multiplexing tradeoff for antenna selection was studied in [19,47,59,88,131]. Pilot-based training for antenna selection is treated in [138] and first results on antenna selection for time-variant channels are provided in [66,67].

Scientific Contributions

In the conference paper *Cooperative regions for coded cooperation over time-varying fading channels* [Article 13] we provide an analytic framework to analyze the performance of coded cooperation as a function of the time-bandwidth product, i.e., the Doppler bandwidth of the time-variant channel times the codeword duration. We define a cooperative region in terms of the vehicle velocity and the block error probability of the inter mobile-station link. The cooperative region defines where cooperation is advantageous compared to non-cooperative transmission. The scheduler at the base-station may use this result in order two decide whether two mobile-stations should engage in coded cooperation to reduce the bit error rate of the transmission.

In the journal paper *Receive antenna selection for time-varying channels using discrete prolate spheroidal sequences* [Article 14] we assume that detailed channel covariance knowledge is not available due to bursty transmission and short stationarity time of the fading process. We apply minimum-energy band-limited prediction from [Article 7] to obtain reliable channel state information for antenna selection at the receiver. Closed-form expressions are provided for the channel prediction and estimation error as well as for the symbol error probability with receive antenna selection.

Publications

[Article 13]   P. Castiglione, M. Nicoli, S. Savazzi and T. Zemen, "Cooperative regions for coded cooperation over time-varying fading channels," in *International ITG/IEEE Workshop on Smart Antennas (WSA)*, Berlin, Germany, February 16-19, 2009.

[Article 14]   H. A. Saleh, A. F. Molisch, T. Zemen, S. D. Blostein, and N. B. Mehta, "Receive antenna selection for time-varying channels using discrete prolate spheroidal sequences," in *IEEE Transaction on Wireless Communications*, vol. 11, pp. 2616–2627, July 2012.

1.5 Conclusions

For wireless communications over time-variant channels the acquisition of empirical channel measurement data allows to obtain key insights in the non-stationary fading process. Based on this data one can define channel models reflecting most of the properties of vehicular communication channels. Differently from cellular communications systems, channel properties must be obtained for clearly defined safety relevant scenarios such as street crossings, merging lanes, traffic jams, etc.

The non-stationary channel characterization results provide the foundation for the design of channel estimation and prediction methods. The channels frequency response is rapidly time- and frequency-selective but spans a subspace of small dimensionality. This small dimensional subspace is also spanned by generalized discrete prolate spheroidal sequences in time and frequency allowing for the definition of low-complexity channel estimation and prediction algorithms. Another insight obtained is that the support of the scattering function has a strong impact on the estimation and prediction error, while the detailed shape of the scattering function is of less importance.

For multi-user detection the small-dimensional subspace spanned by the time- and frequency-selective fading process is a key factor for obtaining reliable channel

estimates. Which in turn enable multi-user detection. For linear multi-user detection the Krylov subspace method allows to exploit a small dimensional subspace for solving the linear system approximately with low complexity. To obtain a maximum likelihood solution with the sphere decoding algorithm we can again utilize a small dimensional subspace spanned by discrete prolate spheroidal sequences to obtain a low complexity solution.

As already mentioned, vehicular communication channels are characterized by rapid time- and frequency-selective fading. In order to obtain a dependable communication system the utilization of spatial diversity provides strong advantages. Coded-cooperation over time-variant channels shows a substantially different behavior as over block fading channels. The inter-mobile station link quality as well as the product of Doppler bandwidth and frame length are the key influence factors here. We saw that selection diversity in time-variant channels can be exploited by low-complexity channel prediction algorithms to choose the antenna element with the best channel conditions for the duration of the data frame.

In this thesis we have successfully addressed a selection of fundamental open issues for wireless communications over time-variant channels. These results enable reliable frame-based wireless communications with low-latency. They also allow for increased battery runtime due to the low numerical complexity of the algorithms. With the imminent deployment of intelligent transportation systems many open questions such as, e.g., vehicular relay channel characterization and modeling as well as relay channel transceiver algorithms remain. Similarly, high bit rate cellular communication systems for vehicular users pose challenging research question such as interference management as well as scheduling algorithms that are closely linked to the properties of the time-variant channel.

2 Characterization and Modeling of the Wireless Communication Channel

[Article 1]   A. Paier, J. Karedal, N. Czink, C. Dumard, T. Zemen, F. Tufvesson, A. F. Molisch, and C. F. Mecklenbräucker, "Characterization of vehicle-to-vehicle radio channels from measurements at 5.2 GHz," *Wireless Personal Communications*, vol. 50, no.1, July 2009 pp. 19-32, doi:10.1007/s11277-008-9546-6.

[Article 2]   A. Paier, T. Zemen, L. Bernadó, G. Matz, J. Karedal, N. Czink, C. Dumard, F. Tufvesson, A. F. Molisch, and C. F. Mecklenbräuker, "Non-WSSUS vehicular channel characterization in highway and urban scenarios at 5.2 GHz using the local scattering function," in *Workshop on Smart Antennas (WSA)*, Darmstadt, Germany, Feb. 26-27, 2008.

[Article 3]   L. Bernadó, T. Zemen, A. Paier, G. Matz, J. Karedal, N. Czink, C. Dumard, F. Tufvesson, M. Hagenauer, A. F. Molisch, C. F. Mecklenbräuker, "Non-WSSUS vehicular channel characterization at 5.2 GHz - spectral divergence and time-variant coherence parameters," in *XXIX General Assembly of the International Union of Radio Science (URSI)*, Chicago, Illinois, USA, August 7-16, 2008, invited.

[Article 4]   L. Bernadó, T. Zemen, J. Karedal, A. Paier, A. Thiel, O. Klemp, N. Czink, F Tufvesson, A. F. Molisch and C. F. Mecklenbräuker, "Multi-dimensional K-factor analysis for V2V radio channels in open sub-urban street crossings," in *21st Annual IEEE International Symposium on Personal, Indoor and Mobile Radio Communications (PIMRC)*, Istanbul, Turkey, September 26-30, 2010.

[Article 5]   F. Kaltenberger, T. Zemen, and C. Ueberhuber, "Low-complexity geometry-based MIMO channel emulation," *EURASIP Journal on Advances in Signal Processing*, vol. 2007, Article ID 95281, 17 pages, 2007. doi:10.1155/2007/95281.

[Article 6]   N. Czink, T. Zemen, J. Nuutinen, J. Ylitalo, and E. Bonek, "A time-variant MIMO channel model directly parametrised from measurements,"

EURASIP Journal on Wireless Communications and Networking (special issue on "Advances in Propagation Modelling for Wireless Systems"), vol. 2009, doi:10.1155/2009/627238.

Characterization of Vehicle-to-Vehicle Radio Channels from Measurements at 5.2 GHz

**Alexander Paier · Johan Karedal · Nicolai Czink · Charlotte Dumard ·
Thomas Zemen · Fredrik Tufvesson · Andreas F. Molisch ·
Christoph F. Mecklenbräuker**

Abstract   The development of efficient vehicle-to-vehicle (V2V) communications systems requires an understanding of the underlying propagation channels. In this paper, we present results on pathloss, power-delay profiles (PDPs), and delay-Doppler spectra from a high speed measurement campaign on a highway in Lund, Sweden. Measurements were performed at a

---

A. Paier ( ) · C. F. Mecklenbräuker
Institut für Nachrichtentechnik und Hochfrequenztechnik, Technische Universität Wien, Vienna, Austria
e-mail: apaier@nt.tuwien.ac.at

C. F. Mecklenbräuker
e-mail: cfm@nt.tuwien.ac.at

J. Karedal · F. Tufvesson · A. F. Molisch
Department of Electrical and Information Technology, Lund University, Lund, Sweden
e-mail: Johan.Karedal@eit.lth.se

F. Tufvesson
e-mail: Fredrik.Tufvesson@eit.lth.se

A. F. Molisch
e-mail: Andreas.Molish@ieee.org

N. Czink · C. Dumard · T. Zemen
Forschungszentrum Telekommunikation Wien (ftw.), Vienna, Austria
e-mail: czink@ftw.at

C. Dumard
e-mail: dumard@ftw.at

T. Zemen
e-mail: thomas.zemen@ftw.at

N. Czink
Smart Antennas Research Group, Information Systems Lab, Standford University,
Stanford, CA 94305, USA

A. F. Molisch
Mitsubishi Electric Research Labs, Cambridge, USA

✠ Springer

A. Paier et al.

carrier frequency of 5.2 GHz with the communicating vehicles traveling on the highway in opposite directions. A pathloss coefficient of 1.8 shows the best fit in the mean square sense with our measurement. The average root mean square (RMS) delay spread is between 263 ns and 376 ns, depending on the noise threshold. We investigate and describe selected paths in the delay-Doppler domain, where we observe Doppler shifts of more than 1,000 Hz.

Keywords Channel measurements · High mobility channel · MIMO measurements · Radio channel characterization · Power-delay profile · Delay-Doppler spectrum

1 Introduction

V2V communications systems have recently drawn great attention, because they have the potential to reduce traffic jams and accident rates. The simulation and performance evaluation of existing systems like IEEE 802.11p [2], as well as the design of future, improved systems, requires a deep understanding of the underlying propagation channels. However, the time-frequency selective fading nature of such V2V channels is significantly different from the well-explored cellular (base-station to mobile) channel, and thus requires distinct measurement campaigns and models. In contrast to cellular systems there exist only a few measurements for V2V communications systems.

Earlier measurements report exclusively on the V2V case with vehicles driving in the *same* direction [3–8], where in [3,4] the radio channel is investigated at 2.4 GHz and in [5–8] in the 5 GHz band. Channel measurements where the vehicles are traveling in the same *and* in opposite directions at a carrier frequency of 3.5 GHz are presented in [9]. Reference [10] reports on V2V measurements in the 900 MHz band between parked vehicles and in [11] the fading statistics of the received signal strength indicator (RSSI) are investigated.

In order to alleviate the current lack of measurements, we recently carried out an extensive measurement campaign in the 5 GHz band in Lund, Sweden. One of the great advantages of these measurements is the high Doppler sampling and the high measurement bandwidth of 240 MHz. This campaign encompassed measurements of vehicle-to-infrastructure (V2I) and V2V scenarios on highways, rural, and urban streets. The current paper concentrates on the evaluation of pathloss, PDP, and delay-Doppler spectrum in a particularly interesting highway V2V measurement run, where the vehicles were traveling in opposite directions. A detailed description of the measurement setup as well as measurement results for V2I and V2V radio channels in other environments can be found in [1,12,13]. In [14] a novel geometry-based stochastic multiple-input multiple-output (MIMO) channel model is presented.

This paper is an extended and enhanced version of [1] and is organized as follows: Section 2 describes the measurement equipment and measurement scenario. Section 3 provides results, including pathloss, PDP, and delay-Doppler spectrum. Section 4 summarizes the paper and presents conclusions.

2 Measurements

2.1 Measurement Equipment

As measurement vehicles, we used two VW LT35 transporters (similar to pickup trucks), which are depicted in Fig. 1a. The measurements that were carried out were MIMO measurements with four antennas at the transmit and receive side, respectively. The MIMO setup impacted the resolvable Doppler frequency because the employed channel sounder,

Fig. 1 (**a**) Photo of the highway from the passenger compartment, (**b**) satellite photo of the highway E22 in the east of Lund (source [16])

Table 1 Measurement parameters

Center frequency, f	5.2 GHz
Measurement bandwidth, BW	240 MHz
Delay resolution, $\Delta\tau = 1/BW$	4.17 ns
Transmit power, P_{Tx}	27 dBm
Test signal length, $\tau_{\max}$	3.2 μs
Number of Tx antenna elements, N_{Tx}	4
Number of Rx antenna elements, N_{Rx}	4
Snapshot time, t_{snap}	102.4 μs
Snapshot repetition rate, t_{rep}	307.2 μs
Number of snapshots, N	32,500
Recording time, t_{rec}	10 s
File size, FS	1 GB
Tx antenna height, h_{Tx}	2.4 m
Rx antenna height, h_{Rx}	2.4 m

RUSK-LUND, is based on the "switched-array" principle [15]. The measurement setup of the RUSK-LUND channel sounder is summarized in Table 1. The snapshot repetition rate was $t_{\text{rep}} = 307.2\,\mu\text{s}$, leading to a maximum resolvable Doppler shift of 1.6 kHz corresponding to a maximum speed of 338 km/h. From the channel transfer functions acquired by the channel sounder, we obtain the complex channel impulse responses (IRs) by an inverse Fourier transform using the Hanning window, giving $h(nt_{\text{rep}}, k\Delta\tau, p)$, where $\Delta\tau$ denotes the delay resolution and p denotes the number of the antenna-to-antenna channels out of the 4×4 MIMO configuration. A more detailed description of the measurement equipment and practice can be found in [12].

2.2 Measurement Scenario

In this paper, we present detailed evaluation results from one especially selected measurement run. It is a highway scenario with medium traffic (approximately 1 vehicle per second), where the vehicles traveled in opposite directions. Figure 1a shows the receiver (Rx) vehicle traveling on the opposite lane just before the vehicles were passing. The satellite photo of the highway scenario indicates that the transmitter (Tx) vehicle was heading in southwest direction while the Rx vehicle headed northeast. The Tx and Rx of the channel sounder were equipped with Global Positioning System (GPS) receivers. With these GPS receivers, we recorded the locations and speeds of both measurement vehicles. The speeds agree well with
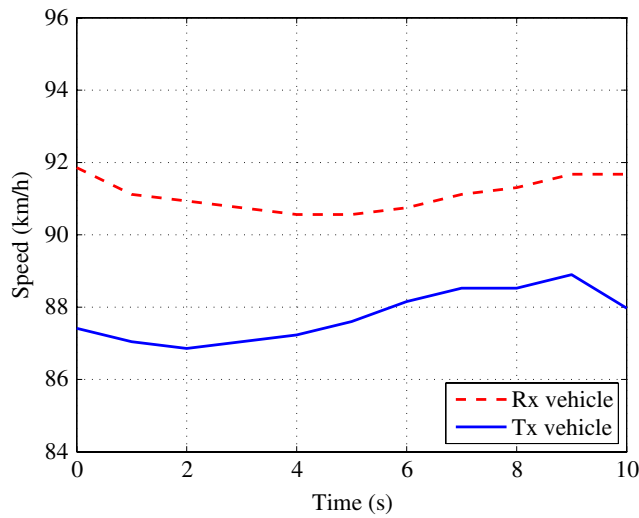
Fig. 2 Speed over time of the two measurement vehicles

those observed on the speedometers (90 km/h) of the vehicles during the measurement run (see Fig. 2). The relative speed between the two vehicles, which is in this case the sum of the speeds of the individual vehicles, is approximately 180 km/h.

3 Evaluation Results

3.1 Pathloss

For calculating the pathloss, the received power was calculated by averaging the magnitude squared of the channel coefficients over 20 wavelengths, in order to average over the small scale fading, and taking the sum over all $K = 769$ delay bins and all $P = 16$ antenna-to-antenna channels, i.e.,

$$P_{Rx}(it_{av}) = \frac{1}{L} \sum_{n=iL}^{(i+1)L-1} \sum_{k=0}^{K-1} \sum_{p=1}^{P} |h(nt_{rep}, k\Delta\tau, p)|^2. \tag{1}$$

Twenty wavelengths are equal to 1.2 m and thus yield at a relative speed of 180 km/h an averaging time interval of $t_{av} = 23$ ms, i.e., $L = 75$ snapshots. By investigations of the stationarity time in [13], it was found that in this particular scenario, the channel can be considered stationary during a time interval of 23 ms. After calculating the received power and investigating the noise level, we used a noise threshold of -102.7 dBm. In the following, we show that a noise threshold does not have a large effect on the calculation of the pathloss, but does affect the calculation of the mean excess delay and RMS delay spread (see Sect. 3.2). All values below the noise threshold are considered as noise and therefore set to zero. The pathloss was calculated by taking the difference of the transmitted power of 27 dBm and the received power in logarithmic scale

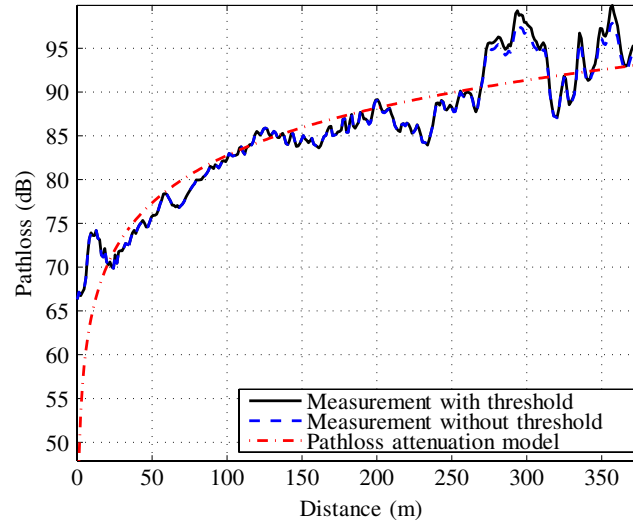$$PL|_{dB} = P_{Tx}|_{dBm} - P_{Rx}|_{dBm}. \tag{2}$$

Fig. 3 Comparison between measured pathloss (with and without noise threshold) and a pathloss model with attenuation coefficient 1.8

Figure 3 presents the pathloss *PL* (with and without noise threshold). We fitted the measured pathloss to the standard model [17, Chap. 4]

$$PL_{\text{model}}|_{\text{dB}} = -20 \cdot \log_{10}\left(\frac{c_0}{4\pi f}\right) + n_{\text{att}} \cdot 10 \cdot \log_{10}(d), \tag{3}$$

where c_0 is the speed of light, f is the carrier frequency, d is the distance between Tx and Rx, and n_{att} is the attenuation coefficient. An attenuation coefficient of 1.8 yields the lowest RMS error of 3.3 dB considering the noise threshold and 3.1 dB without considering the noise threshold. The measurement results are taken from the first 7.5 s of our measurement run, where the two vehicles were approaching each other. In Fig. 3, we observe that the pathloss curves calculated with and without considering the noise threshold are strongly overlapping. In our measurement small differences only occur at distances greater than 250 m (see Fig. 3). This is because large pathlosses mean small Rx power and in this case the noise power affects the result. We conclude that the inclusion of a noise threshold has no significant impact on the pathloss.

3.2 Power-Delay Profile

Similar to the calculation of the received power, we calculated the short-time average PDP by averaging the magnitude squared IRs over 20 wavelengths, $L = 75$ snapshots, and taking the sum over all $P = 16$ antenna-to-antenna channels

$$P_{\text{PDP}}(it_{\text{av}}, k\Delta\tau) = \frac{1}{L} \sum_{n=iL}^{(i+1)L-1} \sum_{p=1}^{P} |h(nt_{\text{rep}}, k\Delta\tau, p)|^2. \tag{4}$$

Using this calculation, we obtained 433 averaged PDPs ($i = 1, \ldots, 433$) for the 10 s measurement run. Figure 4a shows the strong LOS path with delay decreasing until 7.5 s (vehicles passing) and increasing delay afterwards. There are also several paths that are approximately parallel to the LOS path. These paths result from reflections from vehicles that are traveling
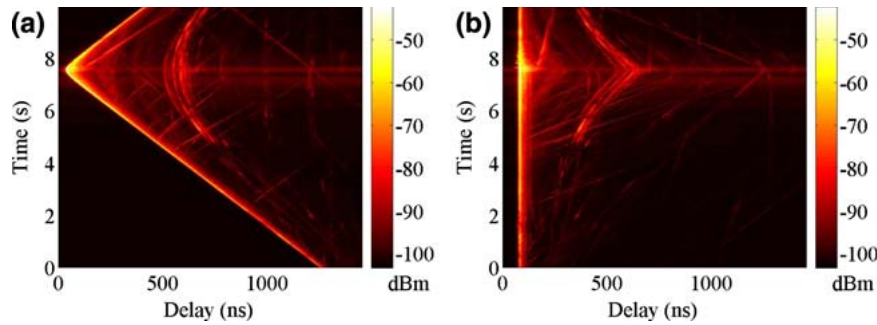
Fig. 4 (**a**) Average PDP, (**b**) average PDP with shifted LOS paths to delay 83 ns

with approximately the same speed as our measurement vehicles. Such a path is exactly parallel to the LOS path if the speed of the reflecting vehicle and the measurement vehicle are equal. Further, there is a group of paths from approximately 5–10 s, whose delays are slightly decreasing from a delay of about 700 ns to 600 ns until a time of 7.5 s and increasing afterwards. These paths are much stronger than most of the paths, reflected from vehicles. The most likely explanation for this group of paths is scattering at factory buildings in the southeast of the highway, see Fig. 1b. Note that such paths should show a Doppler shift that is less than the Doppler shift of the LOS path, because the angle between driving direction and wave propagation direction is larger than zero. We will show this in Sect. 3.3.

In Fig. 4b, the maximum of the LOS path is shifted to a constant delay of 83 ns. These shifted paths are used for all further calculations of the PDPs and delay-Doppler spectra in this paper, except for the calculation of the mean excess delay, because there we need a shift to the constant delay of zero. The delay of 83 ns is chosen arbitrarily in order to see also the increasing part of the LOS path before its maximum.

In the following, we calculate the mean excess delay and RMS delay spread with and without considering a noise threshold, in order to show the impact of such a threshold. The mean excess delay of discrete PDPs can be computed as [17, Chap. 6.5]

$$\bar{\tau}(it_{\mathrm{av}}) = \sum_{k=0}^{K-1} k\Delta\tau \, P_{\mathrm{PDP}}(it_{\mathrm{av}}, k\Delta\tau) \Big/ P_{\mathrm{Rx}}(it_{\mathrm{av}}). \tag{5}$$

The RMS delay spread is the square root of the second central moment of the PDP [17, Chap. 6.5]

$$\tau_{\mathrm{rms}}(it_{\mathrm{av}}) = \sqrt{\sum_{k=0}^{K-1} (k\Delta\tau - \bar{\tau}(it_{\mathrm{av}}))^2 \, P_{\mathrm{PDP}}(it_{\mathrm{av}}, k\Delta\tau) \Big/ P_{\mathrm{Rx}}(it_{\mathrm{av}})}. \tag{6}$$

Figure 5 shows the RMS delay spread over time with and without a noise threshold. Similar to the comparison of pathlosses in Fig. 3, we observe differences only at small received powers at $t < 4$ s. The differences are so large that they influence also the mean RMS spread over 10 s. In the vicinity, where the vehicles are passing, the received power is higher, and therefore the threshold does not affect the RMS delay spread results. In order to get one average mean
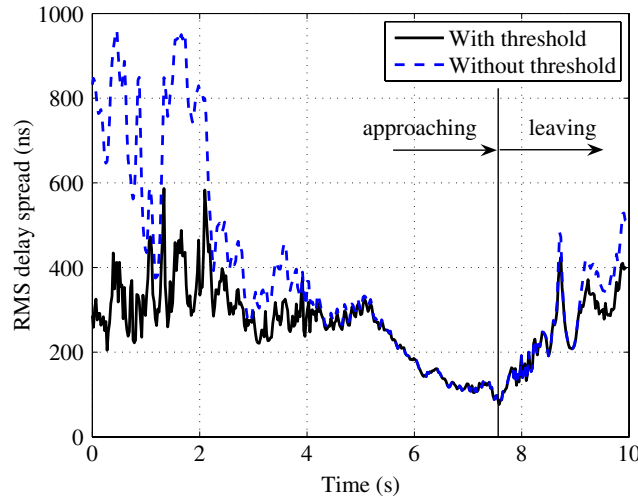
Fig. 5 RMS delay spread with and without noise threshold

Table 2 Average mean excess delay and average RMS delay spread with and without noise threshold

	Av. mean excess delay $\bar{\tau}_{av}$	Av. RMS delay spread $\tau_{rms,av}$
With noise threshold	58 ns	263 ns
Without noise threshold	129 ns	376 ns

excess delay, $\bar{\tau}_{av}$, and one average RMS delay spread, $\tau_{rms,av}$, for the 10 s measurement run, we average over all 433 values

$$\bar{\tau}_{av} = \frac{1}{433} \sum_{i=1}^{433} \bar{\tau}(i t_{av}), \tag{7}$$

$$\tau_{rms,av} = \frac{1}{433} \sum_{i=1}^{433} \tau_{rms}(i t_{av}). \tag{8}$$

Table 2 summarizes these results calculated with and without a noise threshold. Considering a noise threshold implies a much higher impact on these calculations than on the calculations of the pathloss in the previous section. This is because for the calculation of the mean excess delay and RMS delay spread, the discrete PDPs at each delay bin are weighted with the delay $k \Delta \tau$. Therefore the noise, which occurs at larger delays has more impact because of the larger weighting factors. This is not the case for the pathloss calculation, where we just sum up over all PDPs. These results show us that it is important to set a well-selected noise threshold for the calculation of the mean excess delay and the RMS delay spread. The influence of different noise thresholds on the RMS delay spread is described in more detail in [18].

Six short-time PDPs, each over a duration of 23 ms, from 5 s to 5.5 s are depicted in Fig. 6. There are some changes of the short-time PDP over this time period. At a delay of 83 ns, the LOS path is constant over the 0.5 s period, which is a consequence of shifting this path to this delay. Shortly after the LOS path, we observe a small peak with increasing delay. The second
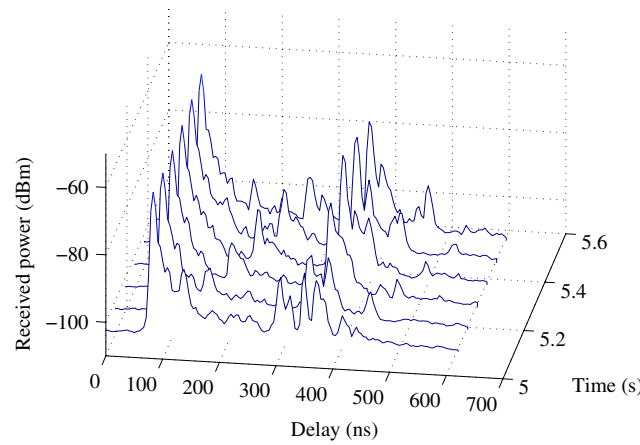
Fig. 6 Short-time average PDPs from 5 s to 5.5 s

strongest peak in this figure, at a delay of approximately 370 ns, comes from scattering at the factory buildings, described above. This path is changing from three smaller peaks in the first PDP to more or less one larger peak in the last PDP. This demonstrates the non-stationarity of the radio channel over the time period of 0.5 s.

3.3 Delay-Doppler Spectrum

In order to validate our measurement, we compared the measured LOS Doppler shift to the theoretical value

$$\nu(t) = -\frac{v}{\lambda}\cos(\gamma(t)). \tag{9}$$

In this equation, $v = 180$ km/h is the relative speed between the two vehicles, $\lambda = 58$ mm is the wavelength, and $\gamma(t)$ is the angle between driving direction and LOS path direction. Figure 7 shows the range between the two vehicles in the upper figure and the calculated and measured Doppler shift in the figure below. The measured Doppler shift (crosses) and the calculated Doppler shift (curve) fit very well.

We estimated the delay-Doppler spectrum

$$P_{\text{DD}}(r\Delta\nu, k\Delta\tau) = \sum_{p=1}^{P} |f_{\text{fft}}(h(nt_{\text{rep}}, k\Delta\tau, p))|^2, \tag{10}$$

using the fast-Fourier transform (FFT) from the time domain indexed by n to the Doppler domain indexed by r. Subsequently we took the sum of the magnitude squared of these terms over all 16 channels. For the short-time delay-Doppler spectrum, we perform the FFT over 75 snapshots, which results in a Doppler resolution of $\Delta\nu = 43$ Hz for $-37 \leq r \leq 37$. Figure 8 shows the short-time delay-Doppler spectrum normalized to its maximum after a time of 5 s of the measurement run. In the following, we describe peaks with their maxima at (i) 83 ns/868 Hz, (ii) 371 ns/543 Hz, and (iii) 304 ns/$-$1107 Hz. Peak (i) is the LOS path with a Doppler shift of 868 Hz, corresponding to a relative speed of 180 km/h between Tx and Rx, which agrees exactly with the intended speed. Positive Doppler frequencies indicate that the vehicles are approaching. Peak (ii) represents the path scattered at the factory buildings with a Doppler shift of 543 Hz (see Fig. 9). Note that this Doppler shift, lying between zero and
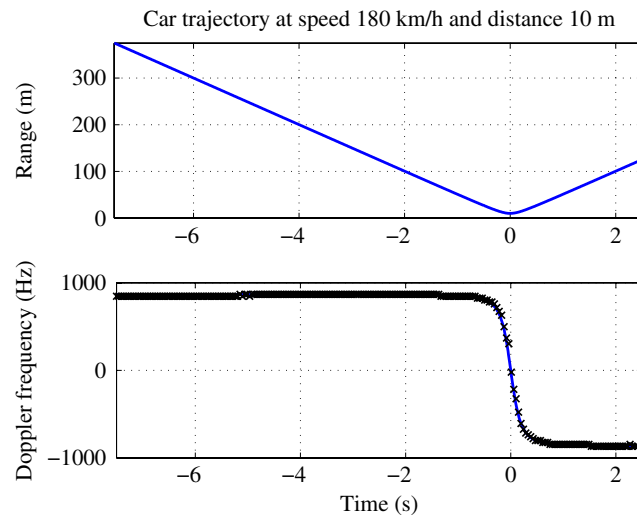
Fig. 7 Comparison of measured and calculated Doppler shifts of the LOS path
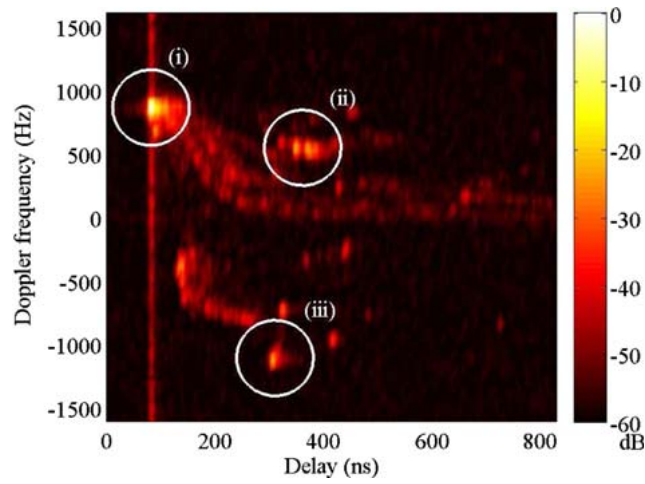

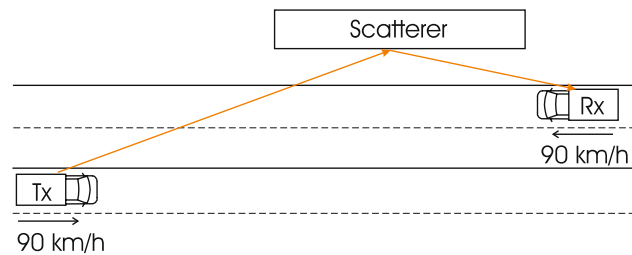**Fig. 8** Short-time delay-Doppler spectrum in logarithmic scale at 5 s

Fig. 9 Doppler shift scenario (ii), leading to a shift of 543 Hz
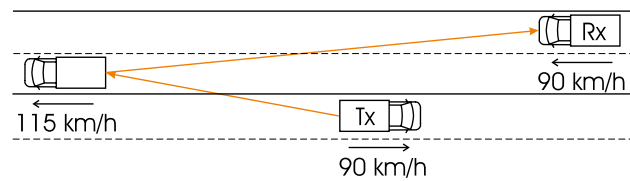
A. Paier et al.

Fig. 10 Doppler shift scenario (iii), leading to a shift of -1107 Hz

the LOS Doppler shift, is congruent with our deductions in Sect. 3.2. Considering the delay of peak (iii), we can find in Fig. 4 that it is approximately parallel to the LOS path delay. With a Doppler shift of -1107 Hz this path is reflected at a vehicle with a speed of 115 km/h which is thus 25 km/h faster than the measurement vehicles. Figure 10 depicts this scenario.

4 Conclusions

In this paper, we presented results from a V2V measurement campaign at 5.2 GHz in a typical highway scenario. The RMS delay spread ranges from 263 ns to 376 ns, and the average mean excess delay is between 58 ns and 129 ns. It is noteworthy that the delay-Doppler spectrum *cannot* be described by the standard model, i.e., a product of exponentially-decaying PDPs and Jakes Doppler spectrum. Rather, we found multiple clusters in the delay domain, each with distinct Doppler spectra. More detailed modeling considerations will be discussed in [14]. Beside a strong LOS path, we observed several paths approximately parallel to the LOS path, which were reflected at other vehicles on the highway. Other strong paths were found, scattering at factory buildings next to the highway. These paths have a Doppler shift less than the Doppler shift of the LOS path, which is in accordance with the theory.

References

1. Paier, A., Karedal, J., Czink, N., Hofstetter, H., Dumard, C., Zemen, T., Tufvesson, F., Molisch, A. F., & Mecklenbräuker, C. F. (2007). Car-to-car radio channel measurements at 5 GHz: Pathloss, power-delay profile, and delay-Doppler spectrum. In *IEEE International Symposium on Wireless Communication Systems (ISWCS 2007)*, 17–19 October 2007, pp. 224–228.
2. 802.11p. (2006). Draft amendment to wireless LAN medium access control (MAC) and physical layer (PHY) specifications: Wireless access in vehicular environments. IEEE P802.11p/D0.26, January 2006.
3. Acosta, G., Tokuda, K., & Ingram, M. A. (2004). Measured joint Doppler-delay power profiles for vehicle-to-vehicle communications at 2.4 GHz. In *Global Telecommunications Conference 2004*, Vol. 6, 29 November–3 December 2004, pp. 3813–3817.
4. Acosta, G., & Ingram, M. A. (2006). Model development for the wideband expressway vehicle-to-vehicle 2.4 GHz channel. In *IEEE Wireless Communications and Networking Conference (WCNC) 2006*, Vol. 3, 3–6 April 2006, pp. 1283–1288.
5. Acosta-Marum, G., & Ingram, M. A. (2006). Doubly selective vehicle-to-vehicle channel measurements and modeling at 5.9 GHz. In *Wireless Personal Multimedia Communications (WPMC) 2006*, 17–20 September 2006.

6. Maurer, J., Fügen, T., & Wiesbeck, W. (2002). Narrow-band measurement and analysis of the inter-vehicle transmission channel at 5.2 GHz. In *Vehicular Technology Conference (VTC) 2002*, Vol. 3, 6–9 May 2002, pp. 1274–1278.
7. Matolak, D. W., Sen, I., Xiong, W., & Yaskoff, N. T. (2005). 5 GHz wireless channel characterization for vehicle to vehicle communications. In *IEEE Military Communications Conference (MILCOM 2005)*, Vol. 5, 17–20 October 2005, pp. 3016–3022.
8. Cheng, L., Henty, B. E., Stancil, D. D., Bai, F., & Mudalige, P. (2007). Mobile vehicle-to-vehicle narrow-band channel measurement and characterization of the 5.9 GHz dedicated short range communication (DSRC) frequency band. *IEEE Journal on Selected Areas in Communications, 25*(8), 1501–1516.
9. Eggers, P. C. F., Brown, T. W. C., Olesen, K., & Pedersen, G. F. (2007). Assessment of capacity support and scattering in experimental high speed vehicle to vehicle MIMO links. In *65th IEEE Vehicular Technology Conference (VTC2007-Spring)*, 22–25 April 2007, pp. 466–470.
10. Davis, J. S., & Linnartz, J. P. M. G. (1994). Vehicle to vehicle RF propagation measurements. In *Conference Record of the Twenty-Eighth Asilomar Conference on Signals, Systems and Computers, 1994*, Vol. 1, 31 October–2 November 1994, pp. 470–474.
11. Yin, J., Holland, G., ElBatt, T., Bai, F., & Krishnan, H. (2006). DSRC channel fading analysis from empirical measurement. In *First International Conference on Communications and Networking in China (ChinaCom '06)*, 25–27 October 2006, pp. 1–5.
12. Paier, A., Karedal, J., Czink, N., Hofstetter, H., Dumard, C., Zemen, T., Tufvesson, F., Mecklenbräuker, C. F., & Molisch, A. F. (2007). First results from car-to-car and car-to-infrastructure radio channel measurements at 5.2 GHz. In *International Symposium on Personal, Indoor and Mobile Radio Communications (PIMRC 2007)*, 3–7 September 2007, pp. 1–5.
13. Paier, A., Zemen, T., Bernadó, L., Matz, G., Karedal, J., Czink, N., Dumard, C., Tufvesson, F., Molisch, A. F., & Mecklenbräuker, C. F. (2008). Non-WSSUS vehicular channel characterization in highway and urban scenarios at 5.2 GHz using the local scattering function. In *International Workshop on Smart Antennas (WSA 2008)*, 26–27 February 2008, pp. 9–15.
14. Karedal, J., Tufvesson, F., Czink, N., Paier, A., Dumard, C., Zemen, T., Mecklenbräuker, C. F., & Molisch, A. F. (2008). A geometry-based stochastic MIMO model for vehicle-to-vehicle communications. *IEEE Transactions on Wireless Communications*, 2008, to be submitted.
15. Thomä, R., Hampicke, D., Richter, A., Sommerkorn, G., Schneider, A., Trautwein, U., & Wirnitzer, W. (2000). Identification of time-variant directional mobile radio channels. *IEEE Transactions on Instrumentation and Measurement, 49*, 357–364.
16. http://hitta.se, January, 2008.
17. Molisch, A. F. (2005). *Wireless Communications*. IEEE-Press, Wiley.
18. Rossi, J.-P. (1999). Influence of measurement conditions on the evaluation of some radio channel parameters. *IEEE Transactions on Vehicular Technology, 48*, 1304–1316.

Author Biographies

Alexander Paier was born in Bruck/Mur, Austria. From 1999 to 2006 he studied electrical engineering with special subject communications and information technology at the Vienna University of Technology, where he received his Dipl.-Ing. (MSc) degree in 2006. Since July 2006 he is working as research assistant on his doctoral thesis at the Institute of Communications and Radio-Frequency Engineering also at the Vienna University of Technology. He participates in the COST Action 2100 "Pervasive Mobile and Ambient Wireless Communications". His current research interests focus on channel sounding and modeling for vehicular communication networks.

Johan Karedal received the M.S. degree in engineering physics in 2002 from Lund University in Sweden. In 2003, he started working towards the Ph.D. degree at the Department of Electroscience, Lund University, where his research interests are on channel measurement and modeling for MIMO and UWB systems. Johan has participated in the European research initiative "MAGNET".

Nicolai Czink was born in Vienna, Austria, in 1979. He received the Dipl.-Ing. (MSc) degree in 2004 and Dr.techn. (PhD) degree in 2008, both with distinction from Technische Universität Wien, Vienna, Austria. In 2008, he received an Erwin Schrödinger Fellowship award from the Austrian Science Fund (FWF) to join Stanford University as postdoctoral scholar. He is also Senior Researcher at the Forschungszentrum Telekommunikation Wien (ftw.) in the area of wireless communications. His main research focus is radio channel modeling and parameter estimation, as well as cooperative wireless communications.

Charlotte Dumard was born in Paris, France. She received a double Master of Science Degree from the Royal Institue of Technology (KTH) in Stockholm, Sweden and the École Supérieure d'Électricité (Supélec) in Gif-sur-Yvette, France, both 2002. Since September 2004 Charlotte Dumard is with the Telecommunications Research Center Vienna (ftw.), working as a Junior Researcher in the projects "Future Mobile Communications Systems—Mathematical Modeling, Analysis, and Algorithms for Multi Antenna Systems" and later on "Cooperative Communications in Traffic Telematics", both funded by the Vienna Science and Technology Fund (Wiener Wissenschafts-, Forschungs- und Technologiefonds, WWTF). Since February 2006 she is a Ph.D. Student at the Vienna University of Technology. Her research interest are low-complexity transceiver design for time-varying MIMO channels as well as distributed signal processing.

Thomas Zemen (S'03–M'05) was born in Mödling, Austria. He received the Dipl.-Ing. degree (with distinction) in electrical engineering from Vienna University of Technology in 1998 and the doctoral degree (with distinction) in 2004. He joined Siemens Austria in 1998 where he worked as hardware engineer and project manager for the radio communication devices department. He engaged in the development of a vehicular GSM telephone system for a German car manufacturer. Since October 2003 Thomas Zemen has been with the Telecommunications Research Center Vienna. His research interests include orthogonal frequency division multiplexing (OFDM), multi-user detection, time-variant channel estimation, iterative MIMO receiver structures, cooperative communication systems, software defined radio concepts, vehicle-to-vehicle channel measurements and modeling. Since 2008 Thomas Zemen works as key researcher in the area of mobile communications and coordinates the research activities in the sector intelligent transportation. He leads the project "Cooperative Communications for Traffic Telematics" which is funded by the Vienna Science and Technology Fund (Wiener Wissenschafts-, Forschungs- und Technologiefonds, WWTF). He is the speaker of the national research network for "Signal and Information Processing in Science and Engineering" funded by the Austrian Science Fund (FWF). Dr. Zemen teaches "MIMO Communications" as external lecturer at Vienna University of Technology.

Fredrik Tufvesson was born in Lund, Sweden in 1970. He received the M.S. degree in Electrical Engineering in 1994, the Licentiate Degree in 1998 and his Ph.D. in 2000, all from Lund University in Sweden. After two years at a startup company developing mesh network technologies, Fredrik is now associate professor in Radio systems at the department of Electrical and Information Technology, Lund University. His main research interests are channel measurements and modeling for wireless communication, including channels for both MIMO and UWB systems. Beside this, he also works with channel estimation and synchronization problems, OFDM system design and UWB transceiver design.

Andreas F. Molisch received the Dipl.-Ing., Dr. techn., and habilitation degrees from the Technical University Vienna (Austria) in 1990, 1994, and 1999, respectively. From 1991 to 2000, he was with the TU Vienna, becoming an associate professor there in 1999. From 2000 to 2002, he was with the Wireless Systems Research Department at AT&T (Bell) Laboratories Research in Middletown, NJ. Since then, he has been with Mitsubishi Electric Research Labs, Cambridge, MA, where he is now a Distinguished Member of Technical Staff and Chief Wireless Standards Architect. He is also professor and chairholder for radio systems at Lund University, Sweden. Dr. Molisch has done research in the areas of SAW filters, radiative transfer in atomic vapors, atomic line filters, smart antennas, and wideband systems. His current research interests are measurement and modeling of mobile radio channels, UWB, cooperative communications, and MIMO systems. Dr. Molisch has authored, co-authored or edited four books (among them the recent textbook Wireless Communications, Wiley-IEEE Press), eleven book chapters, some 100 journal papers, and numerous conference contributions. Dr. Molisch is an editor of the IEEE Trans. Wireless Comm., co-editor of recent or upcoming special issues in J. Wireless Comm. Mob. Comp., IEEE-JSAC, and the Proceedings of the IEEE. He has been member of numerous TPCs, vice chair of the TPC of VTC 2005 spring, general chair of ICUWB 2006, TPC co-chair of the wireless symposium of Globecomm 2007, and TPC chair of Chinacom2007. He

A. Paier et al.

has participated in the European research initiatives "COST 231", "COST 259", and "COST 273", where he was chairman of the MIMO channel working group, he was chairman of the IEEE 802.15.4a channel model standardization group, and is also chairman of Commission C (signals and systems) of URSI (International Union of Radio Scientists). Dr. Molisch is a Fellow of the IEEE, a Fellow of the IET, an IEEE Distinguished Lecturer, and recipient of several awards.

Christoph F. Mecklenbräuker received the Dipl.-Ing. degree in Electrical Engineering from Vienna University of Technology in 1992 and the Dr.-Ing. degree from Ruhr-University of Bochum in 1998, respectively. His doctoral thesis was awarded with the Gert Massenberg Prize 1998. During 1997–2000, he worked for the Mobile Networks Radio department of Siemens AG Austria where he participated in the European Project "Future Radio Wideband Multiple Access Systems (FRAMES)". He was a delegate to the Third Generation Partnership Project (3GPP) and engaged in the standardisation of the radio access network for UMTS. From June 2000 on, he was a senior researcher at the Telecommunications Research Center Vienna (ftw.) in the field of mobile communications, key researcher since November 2002, and proxy since July 2003. Since beginning 2006, he coordinates the project "Multiple-Access Space-Time Coding Testbed" (MASCOT) within the Sixth Framework Programme (FP6) of the European Union. He participates in the COST Action 2100 "Pervasive Mobile and Ambient Wireless Communications". In October 2006, he joined the Institute of Communications and Radio Frequency Engineering at Vienna University of Technology as a full professor. His current research interests include vehicular networks, ultra-wideband radio (UWB), and MIMO-OFDM based transceiver algorithms.

NON-WSSUS VEHICULAR CHANNEL CHARACTERIZATION IN HIGHWAY AND URBAN SCENARIOS AT 5.2 GHZ USING THE LOCAL SCATTERING FUNCTION

Alexander Paier[1], Thomas Zemen[3], Laura Bernadó[3], Gerald Matz[1], Johan Karedal[2],
Nicolai Czink[1,3], Charlotte Dumard[3], Fredrik Tufvesson[2], Andreas F. Molisch[2,4], Christoph F.
Mecklenbräuker[1]

[1]Institut für Nachrichtentechnik und Hochfrequenztechnik, Technische Universität Wien, Vienna, Austria
[2]Department of Electrical and Information Technology, Lund University, Lund, Sweden
[3]Forschungszentrum Telekommunikation Wien (ftw.), Vienna, Austria
[4]Mitsubishi Electric Research Labs, Cambridge, USA
Contact: apaier@nt.tuwien.ac.at

ABSTRACT

The fading process in high speed vehicular traffic telematic applications at 5 GHz is expected to fulfill the wide-sense stationarity uncorrelated scattering (WSSUS) assumption for very short time-intervals only. In order to test this assumption we apply the concept of a *local* time– and frequency–variant scattering function, which we estimate from measurements of vehicle-to-vehicle wave propagation channels by means of a multi-window spectrogram. The obtained temporal sequence of local scattering functions (LSF) is used to calculate a collinearity measure. We define the *stationarity time* as the support of the region where the collinearity exceeds a certain threshold. The stationarity time is the maximum time duration over which the WSSUS assumption is valid. Measurements from an highway with vehicles driving in opposite directions show stationarity times as small as 23 ms whereas vehicles driving in the same direction show stationarity times of 1479 ms.

1. INTRODUCTION

Reliable delivery of traffic telematic services via IEEE 802.11p is required in a large range of different road traffic scenarios. The wide-sense stationary uncorrelated scattering (WSSUS) assumption [1, 2] is very popular for the simplified description of random linear time-varying channels. Since practical channels never exactly satisfy the WSSUS assumption we consider a *local scattering function* (LSF) which is defined for non-WSSUS channels in [3, 4]. The LSF extends the scattering function [5] of WSSUS channels. Especially for high speed vehicular radio channels the WSSUS assumption is not valid. Due to the high vehicle velocities the wave propagation conditions change rapidly, leading to non stationary channel properties.

Contributions of the paper

- We present estimates of the temporal LSF sequence of a vehicular channel using the concepts from [3, 4]. The vehicular channels were measured in highway and urban environments in Lund, Sweden, during a recent MIMO measurement campaign [6, 7].

- We evaluate the collinearity of this LSF sequence which allows to quantify the time-interval over which the vehicular channel can be approximated as WSSUS. Our method generalizes the approach proposed in [8].

2. MEASUREMENTS

Measurement Equipment

The measurements were carried out with the RUSK LUND channel sounder at a center frequency of 5.2 GHz and with a measurement bandwidth of 240 MHz. As measurement vehicles we used two similar VW LT35 transporters. In Fig. 1 a photograph of the receiver (Rx) vehicle during the measurements is shown. The most important measurement parameters are listed in Tab. 1. A detailed description of the measurement equipment is presented in [6].

Measurement Scenario

For the estimation of the LSF and its correlation function in this paper we consider measurements in three scenarios in Lund, Sweden, and in the surrounding area of Lund. In Scenario 1 the two measurement vehicles were traveling on the highway in opposite directions with a speed of 25 m/s (90 km/h). Fig. 1 presents a photograph of the highway, where we see the receiver vehicle traveling on the lane in opposite direction. Scenario 2 also considers measurement vehicles traveling on the highway with a speed of 25 m/s, but with both vehicles driving in the same direction. In Scenario 3 the two vehicles were traveling in the same direction in an urban environment with a speed of 8.3 m/s (30 km/h). Fig. 2

9

Table 1. Measurement configuration parameters.

Center frequency, f_c	5.2 GHz
Measurement bandwidth, BW	240 MHz
Delay resolution, $\Delta\tau = 1/BW$	4.17 ns
Transmit power, P_{Tx}	27 dBm
Test signal length, τ_{max}	3.2 µs
Number of Tx antenna elements, N_{Tx}	4
Number of Rx antenna elements, N_{Rx}	4
Snapshot time, t_{snap}	102.4 µs
Snapshot repetition rate, t_{rep}	307.2 µs
Number of snapshots in time, S'	32500
Number of sample in frequency domain, N'	769
Recording time, t_{rec}	10 s
File size, FS	1 GB
Tx antenna height, h_{Tx}	2.4 m
Rx antenna height, h_{Rx}	2.4 m

Fig. 1. Photograph of the highway from Scenario 1 and 2.

depicts a photograph of Scenario 3. A further description of the measurement scenarios as well as satellite photographs can be found in [6]. A summary of the measurement scenario properties is shown in Tab. 2.

Table 2. Measurement scenario properties.

Scenario	Environment	Driving direction	Velocity
1	Highway	Opposite direction	25 m/s (90 km/h)
2	Highway	Same direction	25 m/s (90 km/h)
3	Urban	Same direction	8.3 m/s (30 km/h)

Measurement Evaluation

The sampled channel transfer function of a linear time-variant channel **H**

$$L_{\mathbf{H}}[m,q] = L_{\mathbf{H}}(mt_{rep}, q/(N\Delta\tau)) \qquad (1)$$

is measured by the channel sounder and stored over a duration of $t_{rec} = 10$ s, with time index $m \in \{0 \dots S'-1\}$ and frequency index $q \in \{-(N'-1)/2 \dots (N'-1)/2\}$. We obtain the complex sampled channel impulse response

$$h[m,n] = h(mt_{rep}, n\Delta\tau) \qquad (2)$$

Fig. 2. Photograph of the Scenario 3.

by means of an inverse Fourier transform using a Hanning windowing function. No significant signal components were measured for delays larger than $1\,\mu s$, hence we consider only the first $N = 256$ delay samples, $n \in \{0, \dots, N-1\}$. The time index m was limited to a segment with time duration of $t_{seg} = 2$ s for all three scenarios, $m \in \{0, \dots, S-1\}$ with $S = 6500 = S' t_{seg}/t_{rec}$.

We performed measurements with 4 antenna elements at the transmitter (Tx) side and 4 antenna elements at the receiver side. For the estimation of the LSF and its correlation function in this paper we consider only a single antenna link out of this set of 16 individual channels. In the case of Scenario 1 we investigate the channel between the antenna elements whose main lobes are facing towards each other, when the vehicles are approaching. In the other two Scenarios 2 and 3 we consider also a channel where the elements are facing towards each other during the whole time duration of 2 s, see [6, Fig. 1].

Fig. 3 (a) - (c) present the power-delay profiles (PDPs) over time for each of the three scenarios. The PDP at a specific time instant is based on the impulse repsonses over a time duration of 20 ms. In Fig. 3 (a) we observe a strong line of sight (LOS) path with decreasing delay until approximately 0.5 s and increasing delay afterwards, and some paths with larger delays resulting from scattering, e.g. a group of scattered paths at a delay of approximately 600 ns. From the characteristic of the LOS path in this figure we observe the passing time of the two vehicles at approximately 0.5 s. In Scenario 2 and 3, Fig. 3 (b) and (c), the vehicles were driving in the same direction, therefore the delay of the LOS path is staying approximately constant over the considered time of 2 s. In Scenario 2, the highway environment, we measured only one path beside the LOS path, also with constant delay over time, occurring approximately 50 ns after the LOS path. In Fig. 3 (c), the urban environment, we observe some discrete paths with time varying delays and also contributions from diffuse scattering. This means that in the urban environment there are much more significant scatterers[1] than in the

---

[1]When speaking of "scatterers", we mean any objects that redirect elec-

considered highway environment.

3. LOCAL SCATTERING FUNCTION

The WSSUS assumption is a very popular assumption allowing for a simplified description of random linear time-varying channels. Especially for high speed vehicular radio channels the WSSUS assumption is not valid. In this paper we use the concept of a LSF which is defined for non-WSSUS channels in [3] for continuous time as

$$\mathcal{C}_{\mathbf{H}}(t, f; \tau, \nu) = \int_{-\infty}^{\infty} \int_{-\infty}^{\infty} R_h(t, \tau; \Delta t, \Delta \tau) \\ \times e^{-j2\pi(\nu \Delta t + f \Delta \tau)} d\Delta t\, d\Delta \tau, \quad (3)$$

where

$$R_h(t, \tau; \Delta t, \Delta \tau) = \mathsf{E}\{h(t, \tau + \Delta \tau)h^*(t - \Delta t, \tau)\} \quad (4)$$

is the 4-D covariance function and $\mathsf{E}\{\cdot\}$ denotes mathematical expectation, i.e., ensemble averaging.

Local Scattering Function Estimator

As explained in [3] the LSF is not guaranteed to be positive and furthermore depends on the whole correlation function $R_h(t, \tau; \Delta t, \Delta \tau)$. Therefore, [3] additionally defines a generalized LSF based on K linear time-variant prototype systems $\boldsymbol{G}_k$ whose transfer function $L_{\boldsymbol{G}_k}(t, f)$ is smooth and localized about the origin of the time-frequency plane. This means $\boldsymbol{G}_k$ amounts to a temporally localized low-pass filter.

The generalized LSF is defined as

$$\mathcal{C}_{\mathbf{H}}^{(\Phi)}(t, f; \tau, \nu) = \mathsf{E}\left\{ \sum_{k=0}^{K-1} \gamma_k \left| \mathcal{H}^{(\boldsymbol{G}_k)}(t, f; \tau, \nu) \right|^2 \right\}, \quad (5)$$

where

$$\mathcal{H}^{(\boldsymbol{G}_k)}(t, f; \tau, \nu) = e^{j2\pi f\tau} \int_{-\infty}^{\infty} \int_{-\infty}^{\infty} L_{\mathbf{H}}(t', f') \\ \times L_{\boldsymbol{G}_k}^*(t' - t, f' - f)e^{-j2\pi(\nu t' - \tau f')} dt'\, df' \quad (6)$$

and the coefficients γ_k need to fulfill the condition

$$\sum_{k=0}^{K-1} \gamma_k = 1. \quad (7)$$

From (6) it becomes clear that the generalized LSF can be interpreted as an expected multi-window spectrogram [9, 10] of $\mathbf{H}$. This interpretation allows to obtain a practical estimation method [4] which we will use for our vehicular channel

---

tromagnetic radiation into a different direction, including specular reflectors and diffracting edges. A more precise formulation would be "interacting objects".
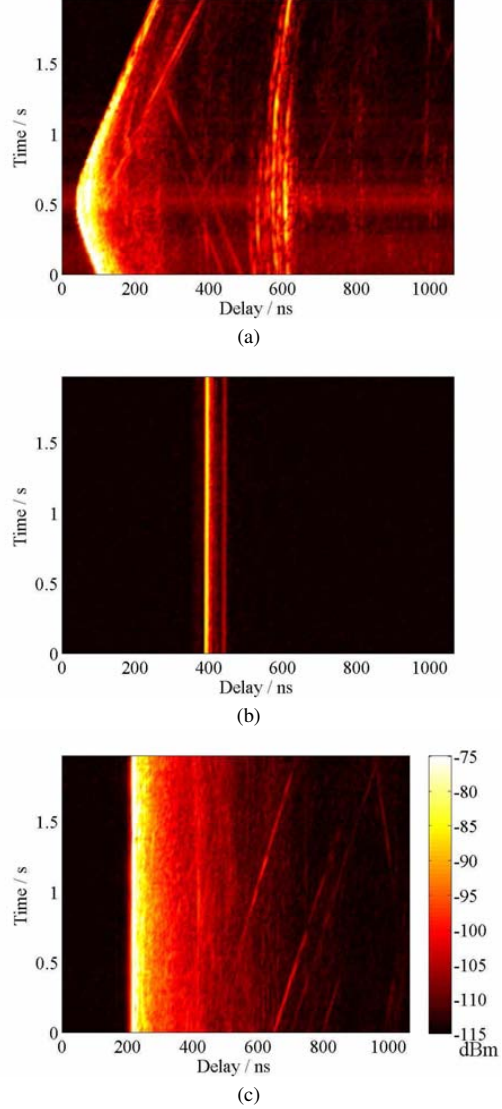

Fig. 3. Average PDPs of (a) Scenario 1, (b) Scenario 2, and (c) Scenario 3.

measurements. From now on we will omit the explicit dependence of $\mathcal{C}_{\mathbf{H}}$ on f considering the dependence of the LSF on t only.

We use a discrete time implementation of the scattering function estimator described in [4]. The temporally localized low-pass filters $\boldsymbol{G}_k$ are represented by the sampled transfer function

$$L_{\boldsymbol{G}_k}[m,q] = L_{\boldsymbol{G}_k}(mt_{\text{rep}}, \frac{q}{N\Delta\tau}) \qquad (8)$$

for $q \in \{-N/2 \dots N/2 - 1\}$. We apply the discrete time equivalent of the separable transfer function used in [4]:

$$L_{\boldsymbol{G}_k}[m,q] = u_i[m+M/2]\tilde{u}_j[q+N/2], \qquad (9)$$

where $k = iJ+j$, $i \in \{0 \dots I-1\}$, and $j \in \{0 \dots J-1\}$. The sequences $u_i[m]$ are the discrete prolate spheroidal (DPS) sequences with concentration in the interval $\mathcal{I}_M = \{0 \dots M - 1\}$ and bandlimited to $[-I/M, I/M]$, defined as [11]

$$\sum_{\ell=0}^{M-1} \frac{\sin(2\pi I/M(\ell-m))}{\pi(\ell-m)} u_i[\ell] = \lambda_i u_i[m]. \qquad (10)$$

The sequences $\tilde{u}_j[q]$ are defined similarly with concentration in the interval $\mathcal{I}_N$ and bandlimited to $[-J/N, J/N]$.

The multi-window spectrogram is computed according to

$$\mathcal{C}_{\mathbf{H}}^{(\Phi)}[m;n,p] = \frac{1}{IJMN} \sum_{k=0}^{K-1} \left| \mathcal{H}^{(\boldsymbol{G}_k)}[m;n,p] \right|^2 \qquad (11)$$

with $n \in \{0, \dots, N-1\}$ and $p \in \{-M/2, \dots M/2 - 1\}$ where

$$\mathcal{H}^{(\boldsymbol{G}_k)}[m;n,p] = \sum_{m'=-M/2}^{M/2-1} \sum_{q'=-N/2}^{N/2-1} L_{\mathbf{H}}[m',q']$$
$$\times L_{\boldsymbol{G}_k}[m'-m,q']\mathrm{e}^{-\mathrm{j}2\pi(pm'-nq')}. \qquad (12)$$

Note that $L_{\mathbf{H}}[m,q] = L_{\mathbf{H}}(mt_{\text{rep}}, \frac{q}{N\Delta\tau})$ and $\mathcal{C}_{\mathbf{H}}^{(\Phi)}[m;n,p] = \mathcal{C}_{\mathbf{H}}^{(\Phi)}(mt_{\text{rep}}; n\Delta\tau, \frac{p}{Mt_{\text{rep}}})$.

4. MEASUREMENT RESULTS FOR THE LOCAL SCATTERING FUNCTION

We estimate the LSF from noisy measurements using (11). As temporal windows we use $I = 5$ DPS sequences with energy concentration in an interval with length $M = 64$ assuming a lower bound of the *stationarity time* of $T_S > Mt_{\text{rep}} = 19.2$ ms. In the frequency domain we used $J = 1$ DPS sequence with concentration in the interval with length $N = 256$ assuming a *stationarity bandwidth* of $F_S > 240$ MHz. This assumption can be justified by the fact that 240 MHz corresponds to less than 5% relative bandwidth and the antenna voltage standing wave ratio (VSWR) varies by less than 1 dB over the measurement bandwidth. With these assumptions
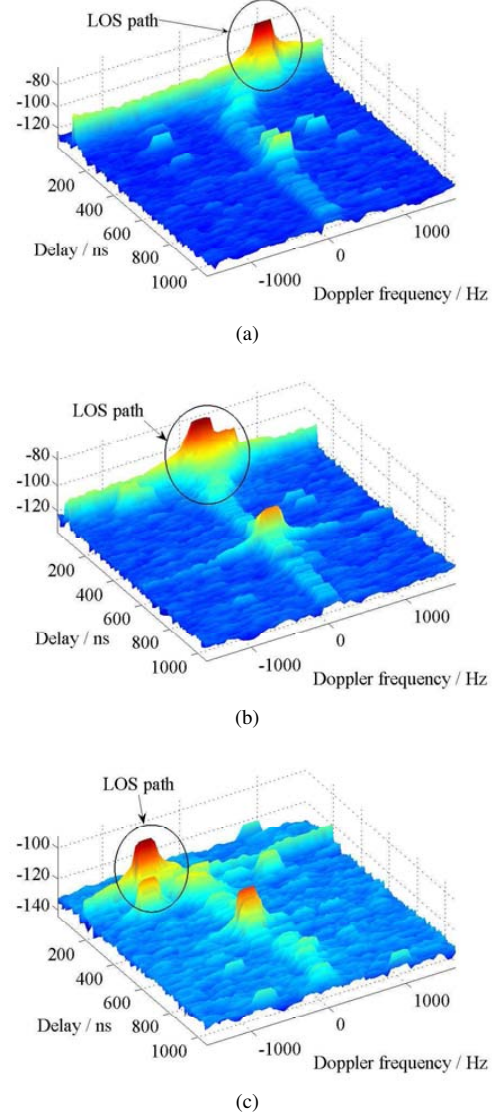
(a)

(b)

(c)

Fig. 4. Estimated generalized LSF for different time snapshots in Scenario 1: (a) $t = 0$ s, (b) $t = 0.5$ s, and (c) $t = 1.5$ s

we achieve a Doppler resolution of 51 Hz for the generalized LSF.

The estimated generalized LSF can directly be related to the propagation scenario. In the following we describe the estimated generalized LSF by means of the measurement in Scenario 1. Figure 4 presents the estimated generalized LSF from Scenario 1 for three different time snapshots: (a) $t = 0$ s — vehicles are approaching, (b) $t = 0.5$ s — vehicles are passing and (c) $t = 1.5$ s — vehicles are leaving.

We can explain the time variance of the generalized LSF by focusing on the LOS path. In Figure 4 (a) the LOS path has a delay of approximately 110 ns and a Doppler of frequency of approximately 865 Hz. This Doppler frequency agrees exactly with our intended speed of 50 m/s, 25 m/s for each of the two vehicles. Figure 4 (b) shows a LOS path with reduced delay (approximately 60 ns) — vehicles are now closer together — and a Doppler of frequency near to 0 Hz. In this passing scenario the LOS path wave propagation is perpendicular to the driving direction. We can observe an increased delay of approximately 190 ns in Figure 4 (c) and a Doppler frequency of approximately -815 Hz. In this case the relative speed between the two vehicles is a little bit lower than the intended speed of 50 m/s. The negative Doppler frequency confirms that the vehicles are leaving at this time.

Beside this strong LOS path in Fig. 4 we can also observe smaller paths with variant delays and Doppler frequencies, which also indicate the time variance of the generalized LSF, and therefore a non-stationary channel.

5. COLLINEARITY OF THE GENERALIZED LOCAL SCATTERING FUNCTION SEQUENCE

The collinearity of the generalized LSF sequence between two time instances allows to quantify the dimension of the stationarity region in time, i.e. the stationarity time T_s of the non-WSSUS fading process. For the duration of the stationarity time simplified WSSUS models can be applied. Note that the stationarity time will be itself time-variant $T_s[m]$ since it depend on the changing wave propagation environment.

In [8] the PDP is used to obtain an estimate of the stationarity time of the fading process. We extend this approach by using the generalized LSF which incorporates dispersion in delay and Doppler.

To obtain estimates for the time-variant stationarity time $T_s[m]$ we proceed in two steps. First we compute collinearity of the generalized LSF sequence. Secondly we set a threshold for the collinearity. Similar to [8] we define the *stationarity time* as the support of the region where the collinearity exceeds a certain threshold. Furthermore we need to validate that the lower bound $T_s > 19.4$ ms is a valid choice.

We stack all MN elements of the generalized LSF $\mathcal{C}_{\mathbf{H}}^{(\Phi)}$ in the vector $\boldsymbol{c}_{\mathbf{H}}[m]$ computing the collinearity of the general-ized LSF

$$R_{\mathcal{C}_{\mathbf{H}}}[m_1, m_2] = \frac{\boldsymbol{c}_{\mathbf{H}}[m_1]^{\mathrm{T}} \boldsymbol{c}_{\mathbf{H}}[m_2]}{\|\boldsymbol{c}_{\mathbf{H}}[m_1]\| \|\boldsymbol{c}_{\mathbf{H}}[m_2]\|} \tag{13}$$

for two time instances m_1 and m_2, i.e. a distance measure in Hilbert space.

We calculate $R_{\mathcal{C}_{\mathbf{H}}}[m_1, m_2]$ using a step size of $\Delta m = 10$, $m_1 = \Delta m m_1'$ and $m_2 = \Delta m m_2'$ for $m_1', m_2' \in \{0 \ldots S/\Delta m - 1\}$ to limit the computational complexity

6. STATIONARITY TIME ESTIMATES

Fig. 5 (a) - (c) present the collinearity of the generalized LSF between two time instances m_1 and m_2 for each of the three scenarios in logarithmic scale. In Fig. 5 (a) we observe a strong decrease of the collinearity away from the main diagonal. This means that two generalized LSF at different time snapshots show a high correlation only for a very small time difference between the generalized LSFs. Fig. 5 (b) and (c) present a much higher correlation over longer time differences. Special attention should be paid to the different logarithmic scale for the color maps of the three scenarios. In Scenario 1 the collinearity decreases much faster than in the other two scenarios. Remember that in Scenario 1 the vehicles are going in opposite directions and in Scenario 2 and 3 the vehicles are going in the same direction.

As mentioned above the 2D plot of the collinearity of Scenario 2 and 3 both show higher correlation in time. The collinearity matrix of Scenario 2 can be described as more or less homogeneous over the 2 s time duration, whereas the collinearity matrix of Scenario 3 has a time-variant structure. This can be explained by the existence of much more scatterers in Scenario 3 than in Scenario 2, as described in Sec. 2. A comparison of Fig. 5 (b), (c) and Fig. 3 (b), (c) shows this difference in the number of scatterers too.

In order to estimate the *stationarity time* we have to set a threshold for the collinearity. Similar to [8] we define the *stationarity time* as the support of the region where the collinearity exceeds a certain threshold.

We define the indicator function

$$\gamma[m', \tilde{m}] = \begin{cases} 1 & : & R_{\mathcal{C}_{\mathbf{H}}}[m', m' + \tilde{m}] > c_{\mathrm{thres}} \\ 0 & : & \text{otherwise} \end{cases} \tag{14}$$

to calculate the (time-variant) *stationarity-time* as

$$T_s[m'] = \Delta m t_{\mathrm{rep}} \sum_{\tilde{m}=-S/\Delta m - 1}^{S/\Delta m - 1} \gamma[m', \tilde{m}] \tag{15}$$

In contrast to the spatial distance expression in [8] we specify a *stationarity time*. Spatial distances are difficult to compare if both, transmitter and receiver, are moving. For the estimation of the stationarity time we assume a threshold of $c_{\mathrm{thres}} = 0.9$ $(10 \log(0.9) = -0.46)$.

(a)

(b)

(c)
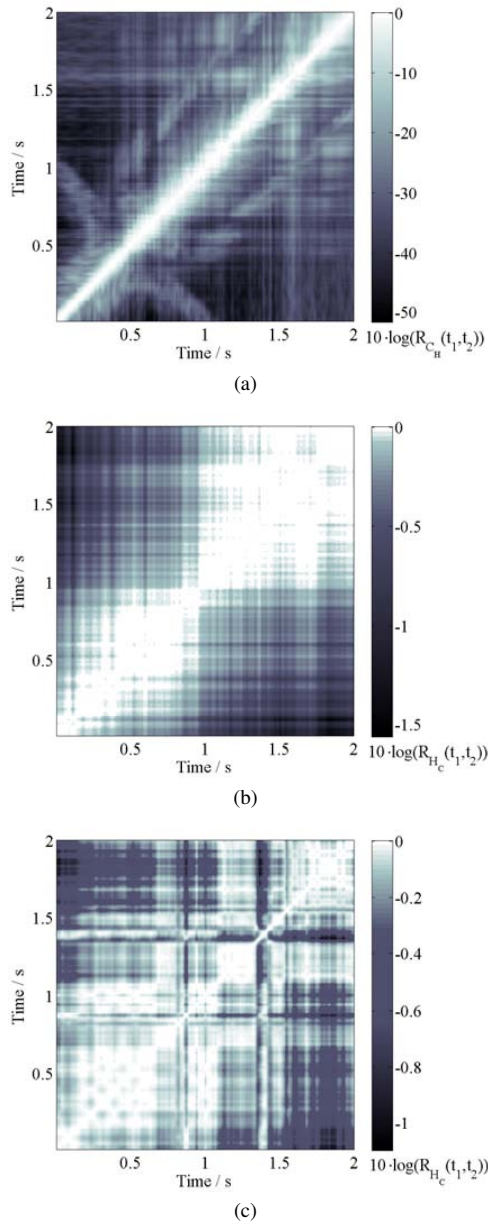
Fig. 5. Estimated collinearity of the generalized LSF of (a) Scenario 1, (b) Scenario 2, and (c) Scenario 3 (note the different color scales).
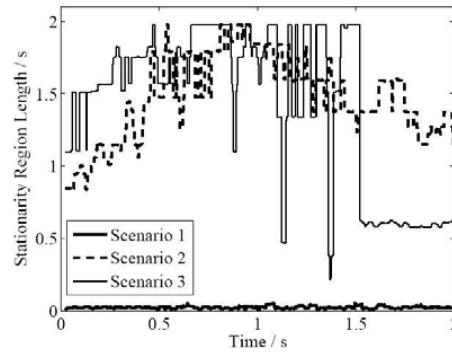
Fig. 6. LRS of all three scenarios

Fig. 6 shows the time-variant stationarity time for each of the three scenarios over the duration of 2 s. We observe a very short stationarity time with a mean of 23 ms for Scenario 1. Scenario 2 shows a mean stationarity time of 1479 ms and Scenario 3 a mean time of 1412 ms.

In the case of Scenario 1, where the vehicles are traveling in opposite directions we achieve a very short stationarity time. Scenario 2 and 3, where both vehicles are traveling in the same direction, show a longer stationarity time. It is interesting that the stationarity times of these two scenarios are in a similar range, because the number of scatterers in these scenarios is very different — only a few scatterers in Scenario 2 and a lot of scatterers in Scenario 3. In this case we also have to consider the different speed of the vehicles in the two scenarios — 25 m/s in Scenario 2 and 8.3 m/s in Scenario 3. This means that the vehicles in Scenario 2 cover a larger distance as in Scenario 3.

7. CONCLUSIONS

We applied the concept of a *local* scattering function (LSF) to characterize real-world vehicular channels from measurements in high-speed scenarios. We observed rapid variations of the line of sight path in the delay-Doppler domain. In order to estimate the stationarity time, we estimated the collinearity of the temporal LSF sequence. We found a very short mean stationarity time of 23 ms for a highway scenario, where the vehicles were traveling in opposite directions. In the same environment, but with both vehicles driving in the same direction, we got a much higher mean stationarity time of 1479 ms. For an urban scenario, also with both vehicles driving in the same direction, but with a speed of one third compared with the speed on the highway, we estimated a mean stationarity time of 1412 ms which is in the same range as on the highway. We conclude that there is a large difference in the time

of stationarity if the vehicles are going in same or in opposite directions. It is also noteworthy that the popular tapped-delay channel models assume the validity of WSSUS, and can therefore only be used within a stationarity time. A more general modeling approach that is not restricted by these concerns will be given in [12].

8. ACKNOWLEDGMENTS

9. REFERENCES

[1] P. A. Bello, "Characterization of randomly time-variant linear channels," *IEEE Transactions on Communications*, vol. 11, pp. 360–393, 1963.

[2] R. Kattenbach, "Charakterisierung zeitvarianter Indoor-Funkkanäle anhand ihrer System- und Korrelationsfunktionen," Ph.D. dissertation, Universitätsgesamthochschule Kassel, 1997.

[3] G. Matz, "On non-WSSUS wireless fading channels," *IEEE Transactions on Wireless Communications*, vol. 4, pp. 2465–2478, September 2005.

[4] ——, "Doubly underspread non-WSSUS channels: Analysis and estimation of channel statistics," in *Proc. IEEE Int. Workshop Signal Processing Advance Wireless Communications (SPAWC)*, Rome, Italy, June 2003, pp. 190–194.

[5] A. F. Molisch, *Wireless Communications*. IEEE-Press - Wiley and Sons, 2005.

[6] A. Paier, J. Karedal, N. Czink, H. Hofstetter, C. Dumard, T. Zemen, F. Tufvesson, C. F. Mecklenbräuker, and A. F. Molisch, "First results from car-to-car and car-to-infrastructure radio channel measurements at 5.2 GHz," in *International Symposium on Personal, Indoor and Mobile Radio Communications (PIMRC) 2007*, September 2007, pp. 1–5.

[7] A. Paier, J. Karedal, N. Czink, H. Hofstetter, C. Dumard, T. Zemen, F. Tufvesson, A. F. Molisch, and C. F. Mecklenbräuker, "Car-to-car radio channel measurements at 5 GHz: Pathloss, power-delay profile, and delay-Doppler spectrum," in *IEEE International Symposium on Wireless Communication Systems (ISWCS)*, October 2007, pp. 224–228.

[8] A. Gehring, M. Steinbauer, I. Gaspard, and M. Grigat, "Empirical channel stationarity in urban environments," in *Proc. Eur. Personal Mobile Communications Conf. (EPMCC)*, Vienna, Austria, February 2001.

[9] D. J. Thomson, "Spectrum estiamtion and harmonic analysis," vol. 70, no. 9, pp. 1055–1096, September 1982.

[10] D. B. Percival and A. T. Walden, *Spectral Analysis for Physical Applications*. Cambridge University Press, 1963.

[11] D. Slepian, "Prolate spheroidal wave functions, Fourier analysis, and uncertainty - V: The discrete case," *The Bell System Technical Journal*, vol. 57, no. 5, pp. 1371–1430, May-June 1978.

[12] J. Karedal, F. Tufvesson, A. F. Molisch, N. Czink, A. Paier, C. F. Mecklenbräuker, C. Dumard, and T. Zemen, "A geometry-based stochastic MIMO model for vehicle-to-vehicle communications," *IEEE Transactions on Wireless Communications*, 2008, to be submitted.

Non-WSSUS Vehicular Channel Characterization at 5.2 GHz - Spectral Divergence and Time-Variant Coherence Parameters

Laura Bernadó[1], *Thomas Zemen*[1], *Alexander Paier*[2], *Gerald Matz*[2], *Johan Karedal*[3], *Nicolai Czink*[1], *Charlotte Dumard*[1], *Fredrik Tufvesson*[3], *Martin Hagenauer, Andreas F. Molisch*[3,4], *Christoph F. Mecklenbräuker*[2]

[1]Forschungszentrum Telekommunikation Wien (ftw.), Vienna, Austria
[2]Institut für Nachrichtentechnik und Hochfrequenztechnik, Technische Universität Wien, Vienna, Austria
[3]Department of Electrical and Information Technology, Lund University, Lund, Sweden
[4]Mitsubishi Electric Research Labs, Cambridge, MA, USA
Contact: bernado@ftw.at

Abstract

The scattering environment in vehicle-to-vehicle communication channels at 5.2 GHz changes rapidly. Hence the wide-sense stationary (WSS) uncorrelated scattering (US) assumption for the fading process is valid for short time intervals only. We characterize the spectral divergence of the local scattering function (LSF) sequence in order to assess the non-WSSUS characteristics in different scenarios. We find that the vehicle-to-vehicle channels violate the wide-sense stationarity much stronger than the US assumption. Additionally, we use the LSF to quantify the time dependence of the channel coherence time and bandwidth. Both parameters vary strongly over time depending on the chosen scenario. Furthermore the effect of the antenna radiation pattern on the fading process is quantified, which can cause the strength of a multipath component to change by more than 40 dB in drive-by experiments.

1 Introduction

The wide-sense stationary (WSS) uncorrelated scattering (US) assumption is not valid for the fading process describing a high speed vehicular-to-vehicular radio communication channel. The two constraints that define the WSSUS assumption may be violated. On the one hand, the second order statistic of the fading process changes over time (non-WSS) and, on the other hand, the contributions at different delays can be correlated (non-US) due to reflections on large objects, e.g. a guardrail on the road side. This leads us to characterize the non-WSSUS properties of vehicle-to-vehicle communication channels by means of the local scattering function (LSF) [1].

Contribution of the paper: We reformulate the LSF estimator from [1, 2] in a discrete-time setting suitable for our measurements. Based on the LSF we analyze the spectral divergence in time and frequency to assess the non-WSSUS assumption. Furthermore, an analysis of the time-variant coherence parameters of vehicle-to-vehicle links is provided and the inter-vehicle calibration function is quantified.

Organization of the paper: In Section 2 the LSF estimator is described and in Section 3 the spectral divergence is evaluated in time and frequency. The time-variant coherence parameters are calculated in Section 4 and the influence of the antenna radiation pattern is quantified in Section 5. We conclude this paper in Section 6.

2 Local Scattering Function

A doubly underspread non-WSSUS channel [2] can be seen as an extension of the WSSUS case in the way that the dependency on time and frequency is added to the stochastic analysis. In this paper we use a discrete-time representation of the LSF estimator presented in [1, 2]. The equivalent continuous-time description can be found in [1].

We characterize the wireless communication channel by means of the time-varying transfer function $H(t, f)$ using measurements from the sounding campaign in April 2007 in Lund, Sweden [3]. The channel sounder provides sampled $H[m', q'] = H(m't_{\text{rep}}, q'B/Q)$, where $t_{\text{rep}} = 307.2\,\mu$s is the repetition time of the channel sounder, $B = 240$ MHz denotes the measurement bandwidth and $Q = 256$ the frequency bins considered in this paper. The samples in the frequency domain are indexed by $q' \in \{0, \ldots, Q-1\}$ and the discrete time-index $m' \in \{0, \ldots, S-1\}$, where $S = 32500$ for an overall measurement period of 10 s.

Note that the LSF $\hat{\mathcal{C}}[m, q; n, p]$ is a sampled version of the continuous time LSF $\hat{\mathcal{C}}(t, f; \tau, \nu)$ in the sense $\hat{\mathcal{C}}[m, q; n, p] = \hat{\mathcal{C}}(mt_{\text{rep}}, qB/Q; n/B, p/(Mt_{\text{rep}}))$. Hence the variables $[m, q; n, p]$ correspond to $[t, f; \tau, \nu]$, respectively.

We compute an estimate of the discrete LSF [2, 4]

$$\hat{\mathcal{C}}[m, q; n, p] = \frac{1}{IJMN} \sum_{k=0}^{K-1} \left| \mathcal{H}^{(\boldsymbol{G}_k)}[m, q; n, p] \right|^2 \tag{1}$$

with $n \in \{0, \ldots, N-1\}$ and $p \in \{-M/2, \ldots M/2 - 1\}$ where

$$\mathcal{H}^{(\boldsymbol{G}_k)}[m, q; n, p] = \sum_{m''=-M/2}^{M/2-1} \sum_{q''=-N/2}^{N/2-1} H[m'' - m, q'' - q] \boldsymbol{G}_k[m'', q''] e^{-j2\pi(pm'' - nq'')} \tag{2}$$

using the temporal analysis window length $M = 64$ and the window bandwidth $N = 128$.

The window functions $\boldsymbol{G}_k[m'', q'']$ are well localized within the support region $[-M/2, M/2-1] \times [-N/2, N/2-1]$. Owing to the use of sliding windows, the time and frequency indices m and q for the LSF correspond to the centered sample value of the evaluated window, hence $m \in \{M/2 \ldots S - M/2\}$ and $q \in \{N/2 \ldots Q - N/2\}$. We apply the discrete time equivalent of the separable transfer function used in [2], $\boldsymbol{G}_k[m'', q''] = u_i[m'' + M/2] \tilde{u}_j[q'' + N/2]$ where $k = iJ + j$, $i \in \{0 \ldots I - 1\}$, and $j \in \{0 \ldots J - 1\}$. The sequences $u_i[m'']$ are chosen as the discrete prolate spheroidal sequences [5] with concentration in the interval $\mathcal{I}_M = \{0 \ldots M - 1\}$ and bandlimited to $[-I/M, I/M]$, defined as $\sum_{\ell=0}^{M-1} \sin(2\pi I/M(\ell - m''))/(\pi(\ell - m'')) u_i[\ell] = \lambda_i u_i[m'']$. The sequences $\tilde{u}_j[q'']$ are defined similarly with concentration in the interval $\mathcal{I}_N$ and bandlimited to $[-J/N, J/N]$.

3 Spectral Divergence

In [4] we use the collinearity measure to assess the similarity of LSF snapshots at different time instants. However the strict positivity of the LSF is not taken into account by such a distance measure. In [6] the spectral divergence measure is introduced as a measure to compare power spectral densities and its usage for fading channels is proposed in [7]. We define the spectral divergence

$$\gamma_t[m_1, m_2] = \log \left(\frac{1}{(MN)^2} \sum_n \sum_p \frac{\hat{\mathcal{C}}^{(t)}[m_1; p, n]}{\hat{\mathcal{C}}^{(t)}[m_2; p, n]} \sum_n \sum_p \frac{\hat{\mathcal{C}}^{(t)}[m_2; p, n]}{\hat{\mathcal{C}}^{(t)}[m_1; p, n]} \right) \tag{3}$$

between two time instants m_1 and m_2, where $\hat{\mathcal{C}}^{(t)}[m; p, n] = \sum_q \hat{\mathcal{C}}[m, q; p, n]$. The spectral divergence in frequency $\gamma_f[q_1, q_2]$ is defined similarly with $\hat{\mathcal{C}}^{(f)}[q; p, n] = \sum_m \hat{\mathcal{C}}[m, q; p, n]$. Note that $\hat{\mathcal{C}}[m, q; n, p]$ is a time-frequency-varying power spectrum and that $\gamma_t[m_1, m_2] \geq 0$ with equality iff $\hat{\mathcal{C}}^{(t)}[m_1; n, p] = \hat{\mathcal{C}}^{(t)}[m_2; n, p]$, which is fulfilled for a WSS fading process. And similarly $\gamma_f \geq 0$ with equality iff $\hat{\mathcal{C}}^{(f)}[q_1; n, p] = \hat{\mathcal{C}}^{(f)}[q_2; n, p]$, which is valid for US.
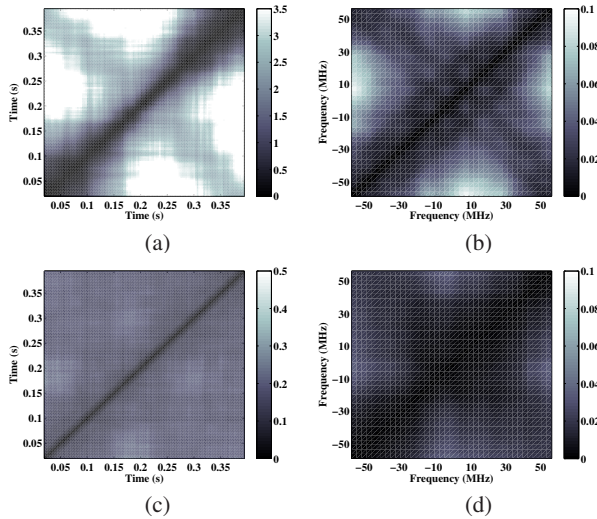
We selected the following two scenarios: Highway scenario — two cars driving on the highway in opposite direction at 30.6 m/s (110 km/h). Urban scenario — two cars driving in an urban scenario in the same direction at 13.9 m/s (50 km/h). The normalized power delay profile for both scenarios is shown in Fig. 2.

Figure 1 (a) and (c) show the LSF divergence in time for the highway scenario and the urban scenario, respectively. We zoom into the most extreme conditions for the highway scenario, where the two cars are passing, with length 0.4 s. The divergence is larger in the highway scenario compared to the urban scenario. Please note that the line of sight (LOS) remains almost at a constant delay in the urban scenario (see Fig. 2 (b)). The cross-diagonal in Fig. 1 (a) is due to the geometric symmetry of the scenario (see Fig. 2 (a)). Hence two LSFs have the same delay of the LOS component when $|m_1 - m_p| = |m_2 - m_p|$ where the two cars are crossing at m_p.

Figure 1: (a) γ_t highway scenario, (b) γ_f highway scenario, (c) γ_t urban scenario, (d) γ_f urban scenario.

Furthermore, the spectral divergence depending on frequency is shown in Fig. 1 (b) and (d). In that case, we observe that the divergence over frequency is rather small, even though we consider two scenarios with strongly different propagation conditions. Taking into account that the divergence range in frequency is much smaller than in time, we can state that the channels presented in this paper violate the wide-sense stationarity much stronger than the US assumption.
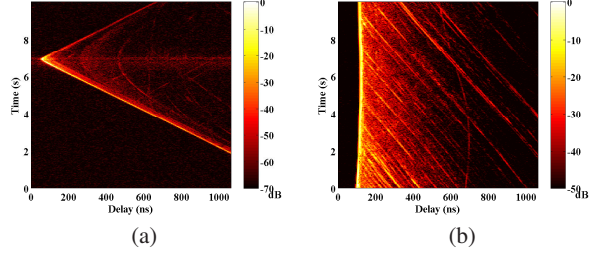

Figure 2: Normalized power delay profile: (a) highway scenario, (b) urban scenario.

4 Coherence Parameters

In the non-WSSUS case the coherence bandwidth F_c and the coherence time T_c are time variant. In that sense, we define $F_c[m] = 1/\sqrt{\tau^2[m]}$ and $T_c[m] = 1/\sqrt{\nu^2[m]}$ with the delay spread [1]

$$\tau^2[m] \triangleq \frac{\sum_q \sum_n \sum_p (\frac{n}{B})^2 \hat{\mathcal{C}}[m,q;n,p]}{\sum_q \sum_n \sum_p \hat{\mathcal{C}}[m,q;n,p]} - \left(\frac{\sum_q \sum_n \sum_p \frac{n}{B} \hat{\mathcal{C}}[m,q;n,p]}{\sum_q \sum_n \sum_p \hat{\mathcal{C}}[m,q;n,p]} \right)^2 \tag{4}$$

for time instant m and similarly the instantaneous Doppler spread is given by

$$\nu^2[m] \triangleq \frac{\sum_q \sum_n \sum_p (\frac{n}{Mt_{\text{rep}}})^2 \hat{\mathcal{C}}[m,q;n,p]}{\sum_q \sum_n \sum_p \hat{\mathcal{C}}[m,q;n,p]} - \left(\frac{\sum_q \sum_n \sum_p \frac{n}{Mt_{\text{rep}}} \hat{\mathcal{C}}[m,q;n,p]}{\sum_q \sum_n \sum_p \hat{\mathcal{C}}[m,q;n,p]} \right)^2 . \tag{5}$$

In order to cover the 10 s duration of the measurement, we calculate the LSF with a spacing of 250 samples.

The results in Fig. 3 make clear that the LOS component influences the coherence parameters strongly. In the highway scenario (see Fig. 2 (a)) the LOS component is strong when the two antennas of the considered link, described in Section 5, are facing each other. The coherence bandwidth decreases dramatically after seven seconds, when the two cars are passing each other (see Fig. 3 (a)). From this point on, the two antennas are not facing each other and the LOS component experiences a fast decay of its power. This fast-fading process also decreases the coherence time. In Fig. 3 (b) for the highway scenario, the coherence time decreases strongly after seven seconds, exactly when the antenna link has no direct connection. It is important to notice in Fig. 3 (b) for the highway scenario that the coherence time is largest when the two cars are closest, between six and seven seconds. From zero to two seconds no analysis is possible because the LOS component is outside the maximum delay range of 1000 ns considered in this analysis.

In the urban scenario the strength of the LOS component remains constant over time (see Fig. 2 (b)). Its coherence parameters remain also approximately constant (see Fig. 3 (a) and (b)). The fluctuations occurring throughout the 10s measurement duration correspond to the variation of the reflections produced by the scatterers.

Figure 3: (a) Coherence bandwidth, (b) Coherence time.

5 Influence of the Antenna Pattern

In these measurement data, the LOS component exhibits large dynamics in power level when both vehicles are passing close by. For the investigations in this paper we consider only the single antenna element No. 3 at both sides

---

[1]Note that these measures of the coherence time are only approximate; as a matter of fact the coherence bandwidth is related to the delay spread via an uncertainty relationship [8], and similarly for the coherence time / Doppler spread [9].

of the radio link. A short description of the employed antennas is given in [3]. Fig. 4 (a) presents the azimuthal antenna radiation pattern at elevation $0°$ of element No. 3 for the highway scenario. We choose the same antenna element at the Tx and Rx sides because the main lobes are facing towards each other when the vehicles are approaching. Since the antenna is not omnidirectional it will influence the observed Rx power of multipath components strongly. In order to consider this influence we calculated an inter-vehicle calibration function, which includes the impact of *both* antenna radiation patterns (Rx and Tx).

Figure 4 (b) presents this calibration function over time (solid line) as well as the unequalized Rx power (dotted line) and the pathloss-equalized Rx power (dashed line) of the LOS component. This power includes the pathloss calculated with the standard exponential model, considering an attenuation exponent of 1.8, found in [10]. The vehicles are passing after approximately seven seconds. When the vehicles are approaching, the calibration function stays almost constant because there are only small variations in the main lobe. We observe large fluctuations of the calibration function when the vehicles are driving away from each other. This is because of the nulls of the antenna radiation pattern in this angle area (see Fig. 4 (a)). We can see in Fig. 4 (b) that the computed Rx power without the pathloss (dotted line) approximately matches with the calibration function (solid line).
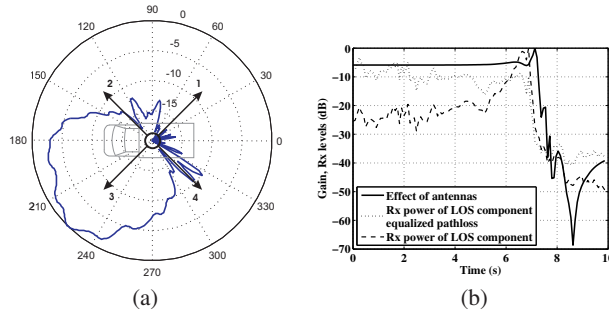

(a) (b)

Figure 4: (a) Antenna radiation pattern for antenna element No. 3, (b) inter-vehicle calibration function

6 Conclusions

We presented a local scattering function (LSF) estimator in time and frequency. Using the spectral divergence of the LSF sequence in time and frequency we showed that the vehicle-to-vehicle channels violate the wide-sense stationarity much stronger than the US assumption. Using the LSF we quantified the time dependence of the channel coherence time and coherence bandwidth. Both parameters vary strongly over time in a drive-by-scenario. Furthermore we showed that the strong variation of the LOS power by more than $40\,\mathrm{dB}$ is caused by the antenna radiation pattern. We quantified the inter-vehicle calibration function which fits very well with our measurement results.

References

[1] G. Matz, "On non-WSSUS wireless fading channels," *IEEE Trans. Wireless Commun.*, vol. 4, no. 5, pp. 2465–2478, September 2005.

[2] ——, "Doubly underspread non-WSSUS channels: Analysis and estimation of channel statistics," in *Proc. IEEE Int. Workshop on Signal Processing Advance Wireless Communications (SPAWC)*, Rome, Italy, June 2003, pp. 190–194.

[3] A. Paier, J. Karedal, N. Czink, H. Hofstetter, C. Dumard, T. Zemen, F. Tufvesson, C. F. Mecklenbräuker, and A. F. Molisch, "First results from car-to-car and car-to-infrastructure radio channel measurements at 5.2 GHz," in *International Symposium on Personal, Indoor and Mobile Radio Communications (PIMRC 2007)*, September 2007, pp. 1–5.

[4] A. Paier, T. Zemen, L. Bernadó, G. Matz, J. Karedal, N. Czink, C. Dumard, F. Tufvesson, A. F. Molisch, and C. F. Mecklenbräuker, "Non-WSSUS vehicular channel characterization in highway and urban scenarios at 5.2 GHz using the local scattering function," in *Workshop on Smart Antennas (WSA)*, Darmstadt, Germany, February 2008.

[5] D. Slepian, "Prolate spheroidal wave functions, Fourier analysis, and uncertainty - V: The discrete case," *The Bell System Technical Journal*, vol. 57, no. 5, pp. 1371–1430, May-June 1978.

[6] T. T. Georgiou, "Distances and Riemannian metrics for spectral density functions," *IEEE Trans. Signal Processing*, vol. 55, no. 8, pp. 3995–4003, August 2007.

[7] G. Matz, "Characterization and analysis of doubly dispersive MIMO channels," in *Fortieth Annual Asilomar Conference on Signals, Systems, and Computers*, Pacific Grove, CA, USA, October 2006.

[8] B. Fleury, "An uncertainty relation for WSS processes and its application to WSSUS systems," *Communications, IEEE Transactions on*, vol. 44, no. 12, pp. 1632–1634, December 1996.

[9] M. Molisch, A.F.and Steinbauer, "Condensed parameters for characterizing wideband mobile radio channels," *International Journal of Wireless Information Networks*, vol. 6, pp. 133–154, July 1999.

[10] A. Paier, J. Karedal, N. Czink, H. Hofstetter, C. Dumard, T. Zemen, F. Tufvesson, A. F. Molisch, and C. F. Mecklenbräuker, "Car-to-car radio channel measurements at 5 GHz: Pathloss, power-delay profile, and delay-Doppler spectrum," in *IEEE International Symposium on Wireless Communication Systems (ISWCS 2007)*, October 2007, pp. 224–228.

Multi-Dimensional K-Factor Analysis for V2V Radio Channels in Open Sub-urban Street Crossings

Laura Bernadó[1], Thomas Zemen[1], Johan Karedal[2], Alexander Paier[3], Andreas Thiel[4],
Oliver Klemp[4], Nicolai Czink[1], Fredrik Tufvesson[2], Andreas F. Molisch[5], Christoph F. Mecklenbräuker[3]

[1]Forschungszentrum Telekommunikation Wien (FTW), Vienna, Austria
[2]Department of Electrical and Information Technology, Lund University, Lund, Sweden
[3]Institut für Nachrichtentechnik und Hochfrequenztechnik, Technische Universität Wien, Vienna, Austria
[4]Delphi Delco Electronics Europe GmbH, Bad Salzdetfurth, Germany
[5]Department of Electrical Engineering, University of Southern California, Los Angeles, CA, USA
Contact: bernado@ftw.at

Abstract—**In this paper we analyze the Ricean K-factor for vehicle-to-vehicle (V2V) communications in a typical open sub-urban street crossing. The channel conditions vary from non line-of sight (NLOS) to line-of-sight (LOS). The antenna arrays used for recording the radio channels consist of 4 elements with directional radiation patterns. We measured 16 individual single-input single-output channels, with a bandwidth of $240\,$MHz for a duration of $20\,$s. We performed two kind of evaluations. For the first analysis we partitioned the $240\,$MHz bandwidth into 24 sub-bands with $10\,$MHz each, according to 802.11p. The small-scale fading of the first delay bin is Ricean distributed with a time-varying K-factor. The later delay bins are mostly Rayleigh distributed. We observe that the large/small K-factor values are not necessarily correlated with the received power. We show that the K-factor can not be assumed to be constant in time, frequency, and space. The antenna radiation patterns, and the illuminated objects by them at different time instances are the cause of these variations. The second evaluation considers the $240\,$MHz bandwidth, and the narrow-band K-factor is calculated for each frequency bin, with $\Delta f = 312\,$kHz. We corroborate the need to consider the frequency variation of the K-factor. We conclude that a multi-dimensional varying K-factor models the large-scale statistical behaviour more accurately than a constant K-factor.**

I. Introduction

In wireless communication systems, small-scale fading statistics have a large impact on the performance of a communication link. The received signal consists of a deterministic component, and random components. The K-factor is defined as the ratio of the energy of the deterministic and the random part of the signal, and it is an indicator of the severity of the fading. A K-factor value close to 0 indicates strong fading (Rayleigh distributed), and a large K-factor value is related to less variations (Ricean distributed). It is a common approach in wireless communication systems to describe the distribution of the amplitude of the channel coefficient with the K-factor of a Ricean distribution.

For testing and simulation purposes the assumption of a constant K-factor is widely used. However, in mobile communications there are several factors that could introduce variability to the K-factor. Therefore, we propose to extend the small-scale fading model by a time-/frequency-/space-varying K-factor to make the model comply with large-scale statistics.

There are few investigations regarding those variations [1], [2]. The authors in [1] develop an empirical model for time-varying Ricean fading. The model is based on measurements taken at $1.9\,$GHz with a bandwidth of $1.23\,$MHz. A dense urban environment with a cellular setting scenario is considered. In [2] a cellular setting is also considered. The same carrier frequency is used but with a bandwidth of $9\,$MHz. This allowed the authors to analyze time and frequency variability of the K-factor. It was found that the K-factor remains more or less constant over frequency.

Investigations on the small-scale fading statistics have also been carried out for vehicular communications at the $5\,$GHz frequency band [3], [4], [5], [6], [7]. It is a general finding that the amplitude of the first delay bin follows a Ricean distribution. In [3], [7], vehicle-to-vehicle (V2V) communications are considered for a highway scenario. Urban scenario results are presented in [4], [5], [6] but always considering two cars driving one after the other. None of these contributions describes the variability of the K-factor.

II. Measurement Data Description

In this section we describe the parameters of the data. The parameters relate to the instrumentation settings and the scenario where the measurement was performed.

A. Collected Measurement Data

The data used in this paper was collected during a measurement campaign named DRIVEWAY'09 [8] conducted in Lund, Sweden, in June 2009. For this investigation, we consider the 4×4 multiple-input multiple-output (MIMO) measurement setting. The selected carrier frequency is $5.6\,$GHz, close enough to the one dedicated for IEEE 802.11p deployment. The measured bandwidth covers a total of $240\,$MHz in 769 frequency bins with a frequency separation $\Delta f = 312\,$kHz.

A measurement run consists of $S = 65535$ snapshots at a repetition time of $t_{rep} = 307.2\,\mu\mathrm{s}$ resulting in a total measured time of $20\,\mathrm{s}$.

The 802.11p standard dedicated to vehicular communications defines a carrier frequency of $5.9\,\mathrm{GHz}$ in a $10\,\mathrm{MHz}$ bandwidth OFDM modulation scheme. In order to obtain meaningful results for V2V systems, we split our measurement data. We consider $L = 16$ individual single-input single-output (SISO) channels and $Q = 24$ frequency sub-bands of $10\,\mathrm{MHz}$ bandwidth each. Table I summarizes the measurement parameters and the chosen parameters for estimation of the small-scale fading statistics.
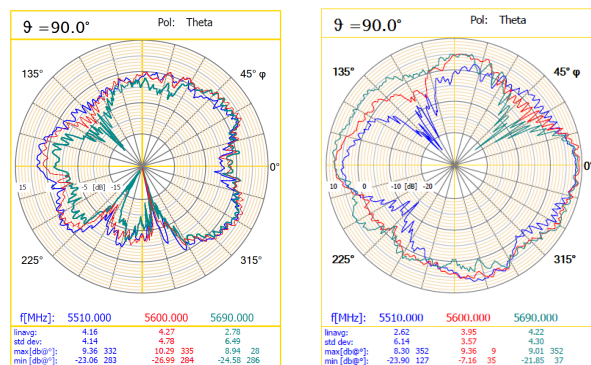
TABLE I
PARAMETERS FOR MEASUREMENT AND FOR K-FACTOR ANALYSIS.

Parameters	Measurement	Analysis
Channels:	4×4 MIMO	16 SISO
Carrier frequency:	$5.6\,\mathrm{GHz}$	$5.6\,\mathrm{GHz}$
Measurement bandwidth:	$240\,\mathrm{MHz}$	$24 \times 10\,\mathrm{MHz}$
Snapshot repetition time:	$307.2\,\mu\mathrm{s}$	$307.2\,\mu\mathrm{s}$
Recording time:	$20\,\mathrm{s}$	$20\,\mathrm{s}$

The transmitter (Tx) and receiver (Rx) parts of the channel sounder are mounted into two cars. Each car is equipped with 4 circular patch antennas mounted in a linear array perpendicular to the driving direction. The antennas have a main lobe that covers the 4 main propagation directions, respectively, to the front, to the back, and to both sides of the car [9].

The selected parameters for investigation provide K-factor results for 16 different channels, each channel contains 24 different $10\,\mathrm{MHz}$ frequency sub-bands. Each sub-band is measured for a time duration of $20\,\mathrm{s}$. With these available data we can conduct space-frequency-time K-factor analysis.

The time and frequency analysis in Section IV is focused mainly on link 10, Tx element 3 to Rx element 3, the radiation pattern of the corresponding antenna elements 3 are shown in Fig. 1. Figure 2 shows an schematic view of the orientation of the radiation patterns for the Tx and the Rx, and Tab. II shows the mapping between the links and the antenna elements.

(a) Radiation pattern Tx antenna 3. (b) Radiation pattern Rx antenna 3.

Fig. 1. Radiation pattern of antenna element 3, 0° shows the driving direction.

TABLE II
LINKS AND CORRESPONDING TX-RX ANTENNA PAIRS.

link	Tx ant.	Rx ant.	link	Tx ant.	Rx ant.
1	1	4	9	3	4
2	1	3	10	3	3
3	1	2	11	3	2
4	1	1	12	3	1
5	2	4	13	4	4
6	2	3	14	4	3
7	2	2	15	4	2
8	2	1	16	4	1
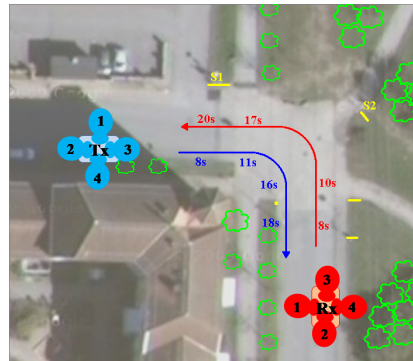
Fig. 2. Scenario layout. Position of trees, traffic signs and car trajectories.

B. Measurement Scenario

The selected scenario for this investigation is depicted in Fig. 2. The Tx and the Rx cars approach a sub-urban open crossing. There are only buildings in one of the quadrants of the intersection, which causes a non line-of-sight (NLOS) communication between Tx and Rx when the cars are far away from each other. During the measurement run there is a transition between NLOS and LOS situation. In the other 3 quadrants there are trees and other far buildings. The measurements were taken with light wind.

The two cars describe a parallel trajectory, they approach the crossing and turn right/left respectively, as indicated in Fig. 2 in blue for the Tx and red for the Rx. They are in LOS situation when they both are right at the crossing, between 11 and 16 s. The drivers are able to establish visual contact with the other car at $8\,\mathrm{s}$. The Tx leaves the crossing at $18\,\mathrm{s}$, the Rx does it at $20\,\mathrm{s}$. The colored numbers in Fig. 2 show the position at which the Tx (blue) and the Rx (red) are at the time given by the number.

III. K-FACTOR ESTIMATION

In order to perform the small-scale fading analysis of the measured data, we need to conduct some pre-processing. This pre-processing consists of searching for the delay bins corresponding to the first strong path in the impulse response (IR), and shift it to the origin. This is done on a per link, per frequency sub-band, and per time instance basis. The delay resolution of each IR is $0.1\,\mu\mathrm{s}$.

We first have a look at the per-delay-bin small-scale fading distribution. To do that, we select a link, a frequency sub-band and a time instance. We estimate the K-factor by using

(a) t=6.5 s   (b) t=11.5 s   (c) t=17.5 s
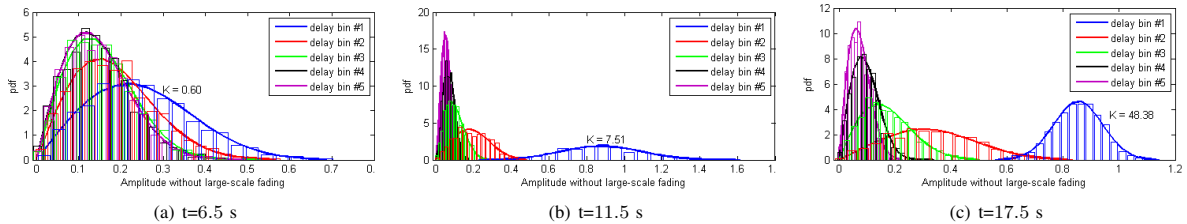
Fig. 3. Fitted pdf and histogram for 1-5 delay bins for link 10 and frequency sub-band 1 at three different time instances using a sample size of 1500 samples.

Fig. 4. Bias^2 and variance of the K-factor estimator for three K-factor variation velocities.

Fig. 5. CDF for 1-5 delay bins for link 10 and sub-band 1 at 17.5 s using a sample size of 1500 samples.

the method of moments (MoM) [10] that provides us with a first guess. Then we apply a least squares (LS) fit of the Rice distribution curve to the data histogram so that the mean-square-error (MSE) between the empirical and the analytical cumulative density function (CDF) is minimized. The MoM estimator fits the first and second order moments of the data in order to derive the K-factor, with the LS fit estimator, the shape of the Ricean distribution is fitted to the actual data [11]. We have tried out several sample lengths and corroborated that MoM and LS fit estimators deliver very similar results when considering an assemble larger than 1000 samples.

In order to select the sample size used for estimation, we have to take several aspects into account. First, the observation period can not exceed the stationarity length of the process. Second, a large number of samples has to be used in order to obtain meaningful statistical results.

In that sense we analyzed the performance of the estimator for different sample sizes in terms of variance and bias. We generate Ricean distributed channels analytically with a K-factor of 10, and add white Gaussian noise with a signal-to-noise ratio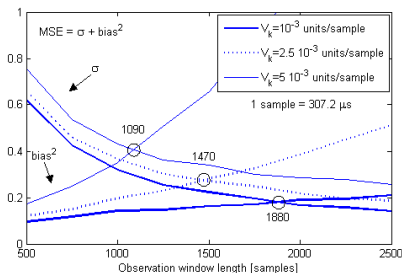 of 25 dB, which is the one observed in measurements. Since we assume that the K-factor changes in time, we test the estimator for three different K-variation speeds: 10^{-3}, $2.5 \cdot 10^{-3}$, and $5 \cdot 10^{-3}$ units/sample, which correspond to 3.25, 8.14, and 16.28 units/second respectively.

Figure 4 shows the bias^2 and the variance of the estimator for the different speeds. The intersection between the bias^2 and the variance curves sets the point at which the MSE is minimum, which is highlighted with a circle for the three cases.

In Fig. 4 we can observe the effects of the two important aspects we commented before. The observation window length achieving the minimum MSE decreases as the velocity
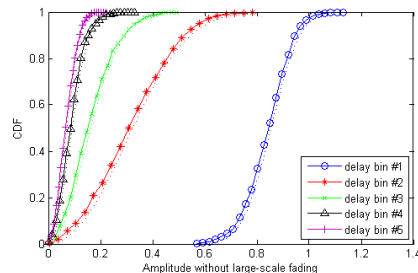
increases. This also corroborates that the stationarity time is strongly dependent on the K-factor changes. Further, we observe that the minimum MSE increases when short window lengths are considered, i.e. the number of used samples for estimation is not sufficient to obtain a trustfully estimate.

Based on these conclusions, we select a sample size of 1500 snapshots. The samples are surrounding the selected time instance. With that, we assume that the process remains stationary within 0.46 s. In section IV-A we cross-check this result by calculating the mode of the velocity of change in the K-factor in the measurements, which results to be $2.32 \cdot 10^{-3}$ units/sample.

Figure 3 (a), (b), and (c) show the probability density function (pdf) of the first five delay bins of link 10, frequency sub-band 1 at time instances 6.5 s, 11.5 s, and 17.5 s respectively. At 6.5 s the two cars are approaching the crossing, they are in NLOS situation. At 11.5 s both are entering the crossing and they leave it at 17.5 s.

We can observe that delay bins 3-5 follow a Rayleigh distribution throughout the time instances. The second delay bin evolves from a Rayleigh to a Ricean distribution. On the other hand, the first delay bin appears to be clearly Ricean distributed with a varying K-factor for the three different time instances, $K_{t=6.5} = 0.60$, $K_{t=11.5} = 7.51$, and $K_{t=17.5} = 48.38$.

Both CDFs are depicted in Fig. 5 for link 10, frequency sub-band 1 at 17.5 s. The solid line corresponds to the CDF of the data and the dotted line to the empirical one calculated with the estimated K-factor, and they show a very good match.

IV. SPACE-TIME-FREQUENCY VARYING ANALYSIS FOR THE FIRST DELAY BIN

We want to investigate the temporal, spatial (link-wise), and frequency dependency of the small-scale fading. We focus

(a) Time-frequency (per sub-band) dependent K-factor.

(b) Time-frequency (per sub-band) dependent power.
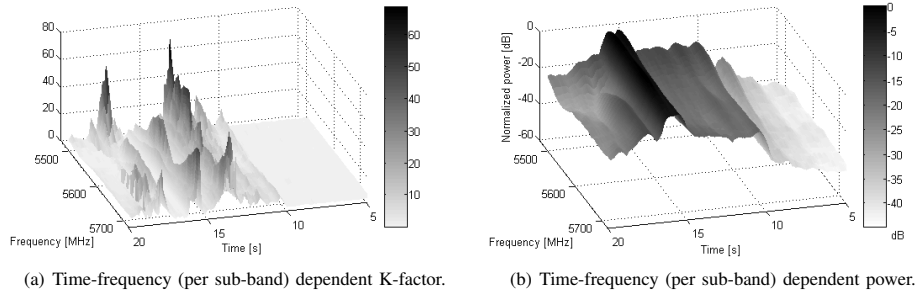
Fig. 6.   Time-frequency dependent results for tap 1 of link 10.

on the first delay bin. Figure 6 shows a 3D representation of the K-factor for the first delay bin of link 10 next to its corresponding time-frequency power. We observe an evolution of the K-factor and the normalized power in both domains, frequency and time.

There is not necessarily a correspondence between received power and K-factor. Large K-factors are observed between 13 and 18 s. However, the estimated K-factor is small from 6 to 13 s, although the received power is not negligible. In that case, there is almost no deterministic part in the received signal and thus it is described by a Rayleigh distribution. On what follows, we discuss time, frequency, and space variability of the K-factor of the first delay bin independently.

A. Time-varying K-factor

We show the time evolution of the K-factor and received power for three different frequency sub-bands in Fig. 7. Although the K-factors do not present the same value, they show the same tendency.
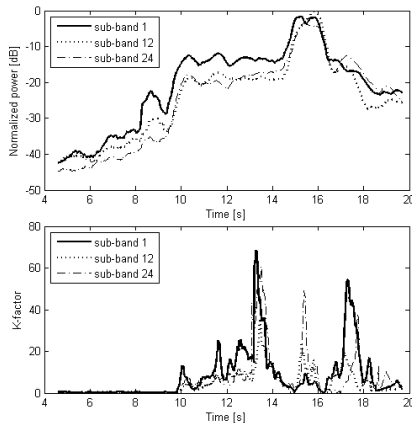
Fig. 7.   Time-varying K-factor and power for link 10 and three different frequency sub-bands for a sample size of 1500.

At around 13.5 s the K-factor experiences an increase, in contrast to the received power which remains constant. To explain the variations in the received power we look at the radiation pattern of the antennas. The antennas do not have omni-directional radiation patterns and present a lower gain

between 120° and 150°, and between 180° and 210° with respect to the driving direction, with lower gain within the first sector (120° - 150°), see Fig. 1. At 13.5 s, the first low-gain cones at 135° are aligned and the cars are very close to each other with no objects in between. At that point, the radiated power is not enough to reach further objects that could produce scattering, and the direct connection Tx-Rx predominates resulting in a large K-factor. At 17.5 s, the second low-gain sectors at 195° are aligned. At that point there is a tree and a street light relatively close to the straight line joining Tx and Rx, which can contribute with scattering and thus increasing the effect of the random components in the received signal.

B. Frequency-varying K-factor

We analyze now the frequency-varying behaviour of the K-factor. For that, we select three different time instances for link 10 and plot their K-factor as a function of the 24 frequency sub-bands in Fig. 8. We cannot necessarily assume the same small fading statistics characteristics throughout a range of 240 MHz.
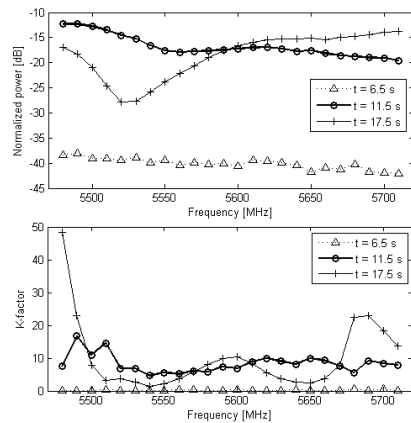
Fig. 8.   Frequency-varying per sub-band K-factor and power of the first delay tap for link 10 and three different time instances.

This might be due to small reflecting elements contributing at different frequencies, such as foliage from the trees surrounding the road, or due to frequency dependent antenna

pattern that could especially influence the power of the dominating component. We observe different small-scale fading statistics throughout the 24 different frequency sub-bands.

Another cause of the frequency variation of the K-factor is the frequency dependent antenna pattern gains throughout the 240 MHz measurement bandwidth. As it can be observed in Fig. 1, the radiation pattern of elements Tx3 and Rx3 changes significantly at the lower, central, and upper band. This effect is mainly observed for Tx element 3, where the gain experiences an increase/decrease of 10 dB at the bandwidth edges with respect to the carrier frequency. Even though they do not lose the directionality, there are certain regions where deep dips appear, such as at $50°$, and $280°$ for the Tx element 3. For the Rx element 3, the variations in frequency of the radiation pattern are not as severe as for the Tx element.

It is normally expected that the large-scale behaviour of the K-factor does not change within a narrow-band frequency bandwidth. In our case, the relative bandwidth of two consecutive frequency sub-bands, i.e. 20 MHz, is less than 10%. Therefore it is noteworthy the strong frequency variation of the K-factor already from sub-band to sub-band.

C. Space-varying K-factor

The K-factor is also different depending on the selected link between Tx and Rx antennas because we used directional antennas. We consider 4 of the 16 measured SISO channels, links 1, 7, 10, 16. Link 1 corresponds to a bad communication situation, where the antennas of the Tx and the Rx are facing towards the quadrants where there are no objects. Therefore, a sufficiently strong received signal may be obtained only very close to the crossing, almost when the two cars already see each other. On the other hand, link 10 consists of the Tx and Rx antennas with the radiation pattern oriented to the front. In that case it is more likely to have a sufficient signal strength before arriving to the crossing since we basically need diffraction. The additional reflection will not help getting the signal to reach the Rx before we have LOS. The complementary Tx-Rx antenna combination is given in link 7, where the antennas radiate towards the back side of the car. The last case we analyze here is link 16, which considers the two antennas of Tx and Rx having a radiation pattern oriented to the side of the road that has buildings.

Figure 9 shows the time-frequency dependent K-factor for the four described links.

Due to the orientation of the antenna radiation patterns and the position of trees and traffic signs (see Fig. 2), the time-frequency variation of the K-factor is different depending on the considered link. There is a big traffic sign (S1) parallel to the road at which the Rx antenna 4 is facing at 17 s. The K-factor for link 1 appears to be large at this time instance.

The effect of another traffic sign (S2) can be appreciated in link 7, when the two cars are leaving the crossing. The K-factor at that time is large due to a reflection of the signal on S2.

The Tx antenna 4 faces the inner part of the corner during the whole measurement run. On this side of the street there are

(a) link 1

(b) link 7

(c) link 10
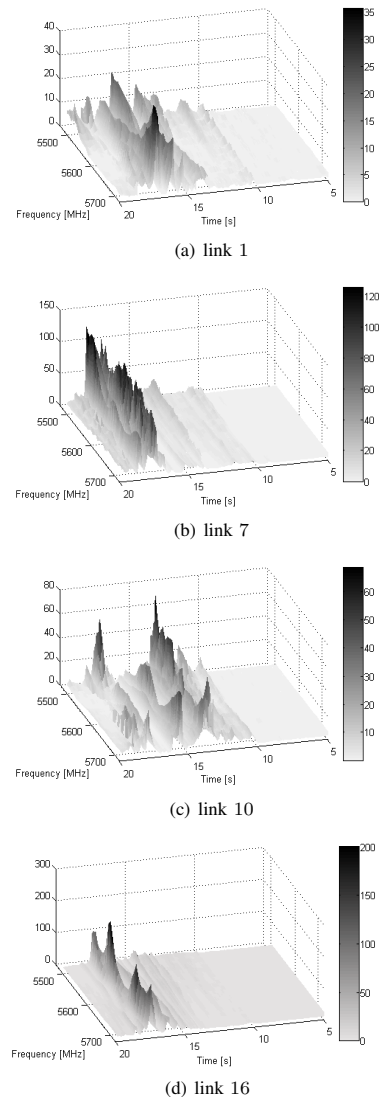
(d) link 16

Fig. 9. Time-frequency dependent K-factor for four different links.

trees. When we look at link 16, the Rx antenna is also facing the same part of the street. Therefore, the largest K-factor is observed at about 17.5 s, when the Rx car benefits from the influence of the large street sign, present on the other side of the road.

For these 3 links (1, 7, and 16), the frequency variation is not as severe as for link 10, where the influence of the trees seems to be more important.

V. NARROW-BAND K-FACTOR

We observed a strong frequency dependability of the K-factor in the analysis performed in Sec. IV-B. Since the IEEE 802.11p standard is OFDM based, this frequency variability will have an influence on the communication system per-

formance. Therefore, we look now into the time-frequency variation of the narrow-band K-factor.

We proceed with the estimation of the K-factor in the frequency domain instead of in the delay domain, as it was done in the previous section. In that case, we do not separate the frequencies in sub-bands. The K-factor is estimated per frequency bin for the whole bandwidth of $240\,\mathrm{MHz}$ with a frequency resolution of $\Delta f = 312\,\mathrm{kHz}$ and using a sample size of 1500 snapshots.

The upper plot in Fig. 10 shows a 2D representation of the time-frequency dependence of the K-factor for link 10. The explanation of the variation in time is similar to the one given in Sec. IV-A. The increase and decrease of the K-factor depends on the interacting objects, and orientation of the cars, and the antenna patterns.
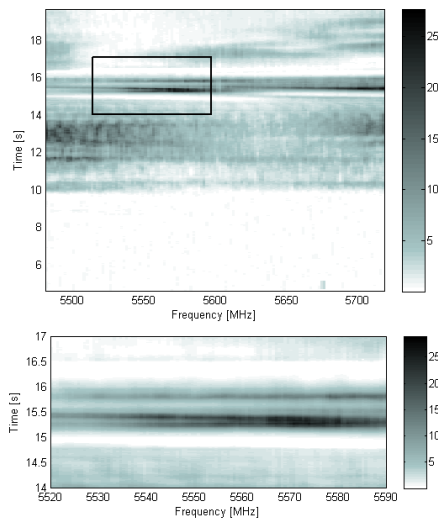
Fig. 10.   Narrowband K-factor for link 10.

In the narrowband analysis we can also appreciate the frequency variation of the K-factor. From an OFDM system point of view, the fading affecting the different sub-carriers is different. On the bottom of Fig. 10 we see an enlarged portion of the upper plot, namely the one surrounded by a black square. The bandwidth in the 802.11p standard is $10\,\mathrm{MHz}$, then we see 7 consecutive sub-bands. The frequency variation is also observed already within one sub-band.

VI. Conclusions and Outlook

We analyzed the per-delay-bin narrow-band small-scale fading statistics for vehicle-to-vehicle communication radio channels. We analyzed a set of measurement data where a single run consists of $20\,\mathrm{s}$ of measurement time, 24 frequency sub-bands each of $10\,\mathrm{MHz}$ bandwidth, and 16 different links. For each sub-band we found that the first delay bin is Ricean distributed with a varying K-factor, and the following delay bins are mostly Rayleigh distributed. We investigated the

variability of the K-factor in the time, frequency (per sub-band), and spatial domain, and found that it is necessary to account for these variations. Since the communication system for vehicular communications is OFDM based, we also analyzed the K-factor on a per-frequency-bin basis. The narrow-band results show a different fading behaviour per sub-carrier, thus also supportting the results obtained in the delay domain. The K-factor changes dramatically depending on several factors: (*i*) Number of illuminated scatterers due to the antenna radiation pattern and objects in between Tx and Rx, (*ii*) the antenna radiation pattern changes over frequency, (*iii*) presence of good reflecting objects near the cars (traffic signs). The effect of the radiation pattern of a realistic vehicular antenna is important, since its characteristics will influence the K-factor a receiver will be able to estimate. Given these observations, a stochastic approach could be followed to model the multi-dimensional variability of the K-factor for such communication scenarios. Such a model is crucial for realistic link-level testing of future vehicular communication systems.

References

[1] G. G. Messier and J. A. Hartwell, "An Empirical Model for Nonstationary Ricean Fading," *Vehicular Technology, IEEE Transactions on*, vol. 58, no. 1, pp. 14–20, January 2009.

[2] L. J. Greenstein, S. Ghassemzadeh, V. Erceg, and D. G. Michelson, "Ricean K-Factors in Narrow-Band Fixed Wireless Channels: Theory, Experiments, and Statistical Models," *Vehicular Technology, IEEE Transactions on*, vol. 58, no. 8, pp. 4000–4012, October 2009.

[3] J. Karedal, F. Tufvesson, N. Czink, A. Paier, C. Dumard, T. Zemen, C. Mecklenbräuker, and A. Molisch, "A Geometry-Based Stochastic MIMO Model for Vehicle-to-Vehicle Communications," *Wireless Communications, IEEE Transactions on*, vol. 8, no. 7, pp. 3646–3657, July 2009.

[4] G. Acosta-Marum and M. A. Ingram, "Six Time- and Frequency-Selective Empirical Channel Models for Vehicular Wireless LANs," *IEEE Vehicular Technology Magazin*, pp. 4–11, December 2007.

[5] J. Maurer, T. Fügen, and W. Wiesbeck, "Narrow-Band Measurement and Analysis of the Inter-Vehicle Transmission Channel at 5.2 GHz," in *IEEE 55th Vehicular Technology Conference*, Birmingham, Alabama, USA, May 2002.

[6] L. Cheng, B. E. Henty, D. D. Stancil, F. Bai, and P. Mudalige, "Mobile Vehicle-to-Vehicle Narrow-Band Channel Measurements and Characterization of the 5.9 GHz Dedicated Short Range Communication (DSRC) Frequency Band," *Journal on Selected Areas in Communications, IEEE Transactions on*, vol. 25, no. 8, pp. 1501–1516, October 2007.

[7] O. Renaudin, V.-M. Kolmonen, P. Vainikainen, and C. Oestges, "Wideband MIMO Car-to-Car Radio Channel Measurements at 5.3 GHz," in *IEEE 68th Vehicular Technology Conference*, Calgary, Alberta, Canada, September 2008.

[8] A. Paier, L. Bernadó, J. Karedal, O. Klemp, and A. Kwoczek, "Overview of Vehicle-to-Vehicle Radio Channel Measurements for Collision Avoidance Applications," in *IEEE 71st Vehicular Technology Conference, to be presented*, Taipei, Taiwan, May 2010.

[9] O. Klemp, A. Thiel, A. Paier, L. Bernadó, J. Karedal, and A. Kwoczek, "In-situ vehicular antenna integration and design aspects for vehicle-to-vehicle communications," in *The 4th European Conference on Antennas and Propagation (Eucap 2010), to be presented*, Barcelona, Spain, April 2010.

[10] L. J. Greenstein, S. Michelson, D. G., and V. Erceg, "Moment-method estimation of the Ricean K-factor," vol. 3, no. 6, June 1999, pp. 175–176.

[11] C. Oestges, N. Czink, B. Bandemer, P. Castiglione, F. Kaltenberger, and A. J. Paulraj, "Experimental characterization and modeling of outdoor-to-indoor and indoor-to-indoor distributed channels," *Vehicular Technology, IEEE Transactions on*, vol. 59, no. 5, pp. 2253 –2265, jun 2010.

Research Article

Low-Complexity Geometry-Based MIMO Channel Simulation

Florian Kaltenberger,[1] Thomas Zemen,[2] and Christoph W. Ueberhuber[3]

[1] *Austrian Research Centers GmbH (ARC), Donau-City-Strasse 1, 1220 Vienna, Austria*
[2] *ftw. Forschungszentrum Telekommunikation Wien, Donau-City-Strasse 1, 1220 Vienna, Austria*
[3] *Institute for Analysis and Scientific Computing, Vienna University of Technology,*
  Wiedner Hauptstrasse 8-10/101, 1040 Vienna, Austria

Recommended by Marc Moonen

The simulation of electromagnetic wave propagation in time-variant wideband multiple-input multiple-output mobile radio channels using a geometry-based channel model (GCM) is computationally expensive. Due to multipath propagation, a large number of complex exponentials must be evaluated and summed up. We present a low-complexity algorithm for the implementation of a GCM on a hardware channel simulator. Our algorithm takes advantage of the limited numerical precision of the channel simulator by using a truncated subspace representation of the channel transfer function based on multidimensional discrete prolate spheroidal (DPS) sequences. The DPS subspace representation offers two advantages. Firstly, only a small subspace dimension is required to achieve the numerical accuracy of the hardware channel simulator. Secondly, the computational complexity of the subspace representation is *independent* of the number of multipath components (MPCs). Moreover, we present an algorithm for the projection of each MPC onto the DPS subspace in $\mathcal{O}(1)$ operations. Thus the computational complexity of the DPS subspace algorithm compared to a conventional implementation is reduced by more than one order of magnitude on a hardware channel simulator with 14-bit precision.

1. INTRODUCTION

In mobile radio channels, electromagnetic waves propagate from the transmitter to the receiver via multiple paths. A geometry-based channel model (GCM) assumes that every multipath component (MPC) can be modeled as a plane wave, mathematically represented by a complex exponential function. The computer simulation of time-variant wideband multiple-input multiple-output (MIMO) channels based on a GCM is computationally expensive, since a large number of complex exponential functions must be evaluated and summed up.

This paper presents a novel low-complexity algorithm for the computation of a GCM on hardware channel simulators. Hardware channel simulators [1–5] allow one to simulate mobile radio channels in real time. They consist of a powerful baseband signal processing unit and radio frequency frontends for input and output. In the baseband processing unit, two basic operations are performed. Firstly, the channel impulse response is calculated according to the GCM. Secondly, the transmit signal is convolved with the channel impulse response. The processing power of the baseband unit limits the number of MPCs that can be calculated and hence the model accuracy. We note that the accuracy of the channel simulator is limited by the arithmetic precision of the baseband unit as well as the resolution of the analog/digital converters. On the ARC SmartSim channel simulator [2], for example, the baseband processing hardware uses 16-bit fixed-point processors and an analog/digital converter with 14-bit precision. This corresponds to a maximum achievable accuracy of $E_{\max} = 2^{-13}$.

The new simulation algorithm presented in this paper takes advantage of the limited numerical accuracy of hardware channel simulators by using a truncated basis expansion of the channel transfer function. The basis expansion is based on the fact that wireless fading channels are highly oversampled. Index-limited snapshots of the sampled fading process span a subspace of small dimension. The same subspace is also spanned by index-limited discrete prolate spheroidal (DPS) sequences [6]. In this paper, we show that the projection of the channel transfer function onto the DPS subspace can be calculated approximately but very efficiently

in $\mathcal{O}(1)$ operations from the MPC parameters given by the model. Furthermore, the subspace representation is independent of the number of MPCs. Thus, in the hardware simulation of wireless communication channels, the number of paths can be increased and more realistic models can be computed. By adjusting the dimension of the subspace, the approximation error can be made smaller than the numerical precision given by the hardware, allowing one to trade accuracy for efficiency. Using multidimensional DPS sequences, the DPS subspace representation can also be extended to simulate time-variant wideband MIMO channel models.

One particular application of the new algorithm is the simulation of Rayleigh fading processes using Clarke's [7] channel model. Clarke's model for time-variant frequency-flat single-input single-output (SISO) channels assumes that the angles of arrival (AoAs) of the MPCs are uniformly distributed. Jakes [8] proposed a simplified version of this model by assuming that the number of MPCs is a multiple of four and that the AoAs are spaced equidistantly. Jakes' model reduces the computational complexity of Clarke's model by a factor of four by exploiting the symmetry of the AoA distribution. However, the second-order statistics of Jakes' simplification do not match the ones of Clarke's model [9] and Jakes' model is not wide-sense stationary [10]. Attempts to improve the second-order statistics while keeping the reduced complexity of Jakes' model are reported in [6, 9–14]. However, due to the equidistant spacing of the AoAs, none of these models achieves all the desirable statistical properties of Clarke's reference model [15]. Our new approach presented in this paper allows us to reduce the complexity of Clarke's original model by more than an order of magnitude without imposing any restrictions on the AoAs.

Contributions of the paper

(i) We apply the DPS subspace representation to derive a low-complexity algorithm for the computation of the GCM.

(ii) We introduce approximate DPS wave functions to calculate the projection onto the subspace in $\mathcal{O}(1)$ operations.

(iii) We provide a detailed error and complexity analysis that allows us to trade efficiency for accuracy.

(iv) We extend the DPS subspace projection to multiple dimensions and describe a novel way to calculate multidimensional DPS sequences using the Kronecker product formalism.

Notation. Let $\mathbb{Z}$, $\mathbb{R}$, and $\mathbb{C}$ denote the set of integers, real and complex numbers, respectively. Vectors are denoted by **v** and matrices by **V**. Their elements are denoted by v_i and $V_{i,l}$, respectively. Transposition of a vector or a matrix is indicated by $\cdot^T$ and conjugate transposition by $\cdot^H$. The Euclidean (ℓ^2) norm of the vector **a** is denoted by $\|\mathbf{a}\|$. The Kronecker product and the Khatri-Rao product (columnwise Kronecker product) are denoted by $\otimes$ and $\diamond$, respectively. The inner product of two vectors of length N is defined as $\langle \mathbf{x}, \mathbf{y} \rangle = \sum_{i=0}^{N-1} x_i y_i^*$, where $\cdot^*$ denotes complex conjugation. If X is a discrete index set, $|X|$ denotes the number of el-
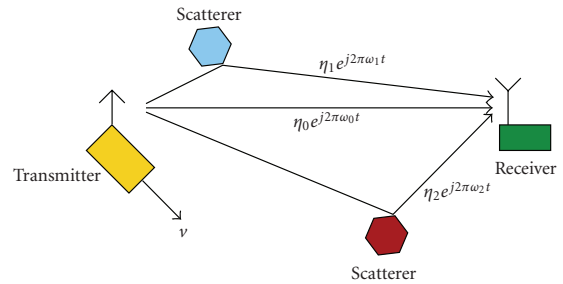
FIGURE 1: GCM for a time-variant frequency-flat SISO channel. Signals sent from the transmitter, moving at speed v, arrive at the receiver via different paths. Each MPC p has complex weight η_p and Doppler shift ω_p [16].

ements of X. If X is a continuous region, $|X|$ denotes the Lebesgue measure of X. An N-dimensional sequence $v_\mathbf{m}$ is a function from $\mathbf{m} \in \mathbb{Z}^N$ onto $\mathbb{C}$. For an N-dimensional, finite index set $I \subset \mathbb{Z}^N$, the elements of the sequence $v_\mathbf{m}$, $\mathbf{m} \in I$, may be collected in a vector **v**. For a parameterizable function f, $\{f\}$ denotes the family of functions over the whole parameter space. The absolute value, the phase, the real part, and the imaginary part of a complex variable a are denoted by $|a|$, $\Phi(a)$, $\Re a$, and $\Im a$, respectively. $\mathcal{E}\{\cdot\}$ denotes the expectation operator.

Organization of the paper

In Section 2, a subspace representation of time-variant frequency-flat SISO channels based on one-dimensional DPS sequences is derived. The main result of the paper, that is, the low-complexity calculation of the basis coefficients of the DPS subspace representation, is given in Section 3. Section 4 extends the DPS subspace representation to higher dimensions, enabling the computer simulation of wideband MIMO channels. A summary and conclusions are given in Section 5. Appendix A proposes a novel way to calculate the multidimensional DPS sequences utilizing the Kronecker product. Appendix B gives a detailed proof of a central theorem. A list of symbols is defined in Appendix C.

2. THE DPS SUBSPACE REPRESENTATION

2.1. Time-variant frequency-flat SISO geometry-based channel model

We start deriving the DPS subspace representation for the generic GCM for time-variant frequency-flat SISO channels depicted in Figure 1. The GCM assumes that the channel transfer function $h(t)$ can be written as a superposition of P MPCs:

$$h(t) = \sum_{p=0}^{P-1} \eta_p e^{2\pi j \omega_p t}, \tag{1}$$

where each MPC is characterized by its complex weight η_p, which embodies the gain and the phase shift, as well as its
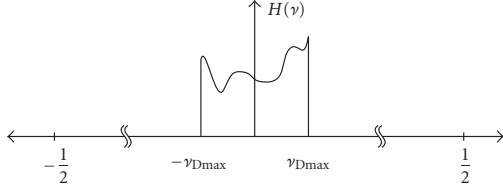
Figure 2: Doppler spectrum $H(\nu)$ of the sampled time-variant channel transfer function h_m. The maximum normalized Doppler bandwidth $2\nu_{\text{Dmax}}$ is much smaller than the available normalized channel bandwidth.

Doppler shift ω_p. With $1/T_S$ denoting the sampling rate of the system, the sampled channel transfer function can be written as

$$h_m = h(mT_S) = \sum_{p=0}^{P-1} \eta_p e^{2\pi j \nu_p m}, \qquad (2)$$

where $\nu_p = \omega_p T_S$ is the normalized Doppler shift of the pth MPC. We refer to (2) as the sum of complex exponentials (SoCE) algorithm for computing the channel transfer function h_m.

We assume that the normalized Doppler shifts ν_p are bounded by the maximum (one-sided) normalized Doppler bandwidth ν_{Dmax}, which is given by the maximum speed ν_{max} of the transmitter, the carrier frequency f_C, the speed of light c, and the sampling rate $1/T_S$,

$$|\nu_p| \leq \nu_{\text{Dmax}} = \frac{\nu_{\text{max}} f_C}{c} T_S. \qquad (3)$$

In typical wireless communication systems, the maximum normalized Doppler bandwidth $2\nu_{\text{Dmax}}$ is much smaller than the available normalized channel bandwidth (see Figure 2):

$$\nu_{\text{Dmax}} \ll \frac{1}{2}. \qquad (4)$$

Thus, the channel transfer function (1) is highly oversampled.

Clarke's model [17] is a special case of (2) and assumes that the AoAs ψ_p of the impinging MPCs are distributed uniformly on the interval $[-\pi, \pi)$ and that $\mathcal{E}\{|\eta_p|^2\} = 1/P$. The normalized Doppler shift ν_p of the pth MPC is related to the AoA ψ_p by $\nu_p = \nu_{\text{Dmax}} \cos(\psi_p)$. Jakes' model [8] and its variants [9–14] assume that the AoAs ψ_p are spaced equidistantly with some (random) offset ϑ:

$$\psi_p = \frac{2\pi p + \vartheta}{P}, \quad p = 0, \dots, P-1. \qquad (5)$$

If P is a multiple of four, symmetries can be utilized and only $P/4$ sinusoids have to be evaluated [8]. However, the second-order statistics of such models do not match the ones of Clarke's original model [9].

In this paper, a truncated subspace representation is used to reduce the complexity of the GCM (2). The subspace representation does *not* require special assumptions on the AoAs ψ_p. It is based on DPS sequences, which are introduced in the following section.

2.2. DPS sequences

In this section, one-dimensional DPS sequences are reviewed. They were introduced in 1978 by Slepian [17]. Their applications include spectrum estimation [18], approximation, and prediction of band-limited signals [15, 17] as well as channel estimation in wireless communication systems [6]. DPS sequences can be generalized to multiple dimensions [19]. Multidimensional DPS sequences are reviewed in Section 4.2, where they are used for wideband MIMO channel simulation.

Definition 1. The one-dimensional discrete prolate spheroidal (DPS) sequences $v_m^{(d)}(W, I)$ with band-limit $W = [-\nu_{\text{Dmax}}, \nu_{\text{Dmax}}]$ and concentration region $I = \{M_0, \dots, M_0 + M - 1\}$ are defined as the real solutions of

$$\sum_{n=M_0}^{M_0+M-1} \frac{\sin(2\pi\nu_{\text{Dmax}}(m-n))}{\pi(n-m)} v_n^{(d)}(W, I)$$

$$= \lambda_d(W, I) v_m^{(d)}(W, I). \qquad (6)$$

They are sorted such that their eigenvalues $\lambda_d(W, I)$ are in descending order:

$$\lambda_0(W, I) > \lambda_1(W, I) > \dots > \lambda_{M-1}(W, I). \qquad (7)$$

To ease notation, we drop the explicit dependence of $v_m^{(d)}(W, I)$ on W and I when it is clear from the context. Further, we define the DPS vector $\mathbf{v}^{(d)}(W, I) \in \mathbb{C}^M$ as the DPS sequence $v_m^{(d)}(W, I)$ index-limited to I.

The DPS vectors $\mathbf{v}^{(d)}(W, I)$ are also eigenvectors of the $M \times M$ matrix $\mathbf{K}$ with elements $K_{m,n} = \sin(2\pi\nu_{\text{Dmax}}(m-n))/\pi(n-m)$. The eigenvalues of this matrix decay exponentially and thus render numerical calculation difficult. Fortunately, there exists a tridiagonal matrix commuting with $\mathbf{K}$, which enables fast and numerically stable calculation of DPS sequences [17, 20]. Figures 3 and 4 illustrate one-dimensional DPS sequences and their eigenvalues, respectively.

Some properties of DPS sequences are summarized in the following theorem.

Theorem 1. (1) *The sequences $v_m^{(d)}(W, I)$ are band-limited to W.*

(2) *The eigenvalue $\lambda_d(W, I)$ of the DPS sequence $v_m^{(d)}(W, I)$ denotes the energy concentration of the sequence within I:*

$$\lambda_d(W, I) = \frac{\sum_{m \in I} |v_m^{(d)}(W, I)|^2}{\sum_{m \in \mathbb{Z}} |v_m^{(d)}(W, I)|^2}. \qquad (8)$$

(3) *The eigenvalues $\lambda_d(W, I)$ satisfy $1 < \lambda_i(W, I) < 0$. They are clustered around 1 for $d \leq D' - 1$, and decay exponentially for $d \geq D'$, where $D' = \lceil |W||I| \rceil + 1$.*

(4) *The DPS sequences $v_m^{(d)}(W, I)$ are orthogonal on the index set I and on $\mathbb{Z}$.*

(5) *Every band-limited sequence h_m can be decomposed uniquely as $h_m = h'_m + g_m$, where h'_m is a linear combination of DPS sequences $v_m^{(d)}(W, I)$ for some I and $g_m = 0$ for all $m \in I$.*
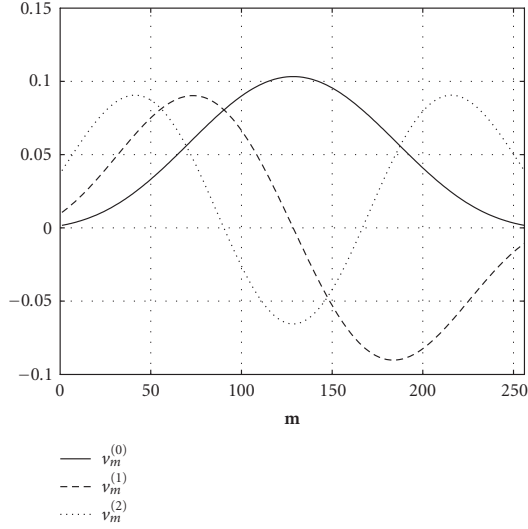
FIGURE 3: The first three one-dimensional DPS sequences $v_m^{(0)}$, $v_m^{(1)}$, and $v_m^{(2)}$ for $M_0 = 0$, $M = 256$, and $M\nu_{\text{Dmax}} = 2$.
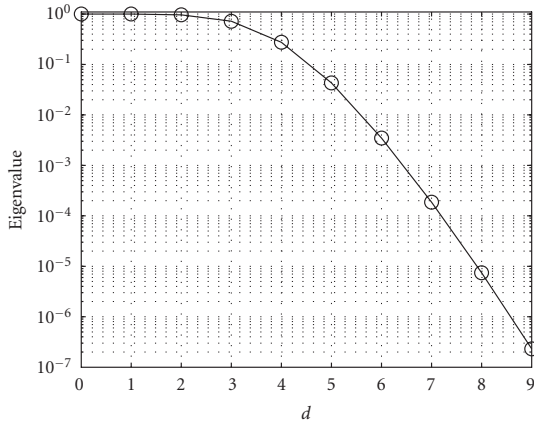
FIGURE 4: The first ten eigenvalues λ_d, $d = 0,\ldots,9$, of the one-dimensional DPS sequences for $M_0 = 0$, $M = 256$, and $M\nu_{\text{Dmax}} = 2$. The eigenvalues are clustered around 1 for $d \leq D' - 1$, and decay exponentially for $d \geq D'$, where the essential dimension of the signal subspace $D' = \lceil 2\nu_{\text{Dmax}}M \rceil + 1 = 5$.

Proof. See Slepian [17]. □

2.3. DPS subspace representation

The time-variant fading process $\{h_m\}$ given by the model in (2) is band-limited to the region $W = [-\nu_{\text{Dmax}}, \nu_{\text{Dmax}}]$. Let $I = \{M_0,\ldots,M_0 + M - 1\}$ denote a finite index set on which we want to calculate h_m. Due to property (5) of Theorem 1, h_m can be decomposed into $h_m = h'_m + g_m$, where h'_m is a linear

combination of the DPS sequences $v_m^{(d)}(W,I)$ and $h_m = h'_m$ for all $m \in I$. Therefore, the vectors

$$\mathbf{h} = [h_{M_0}, h_{M_0+1},\ldots,h_{M_0+M-1}]^T \in \mathbb{C}^M \qquad (9)$$

obtained by index limiting h_m to I can be represented as a linear combination of the DPS vectors

$$\mathbf{v}^{(d)}(W,I)$$
$$= \left[v_{M_0}^{(d)}(W,I), v_{M_0+1}^{(d)}(W,I),\ldots,v_{M_0+M-1}^{(d)}(W,I)\right]^T \in \mathbb{C}^M. \qquad (10)$$

Properties (2) and (3) of Theorem 1 show that the first $D' = \lceil 2\nu_{\text{Dmax}}M \rceil + 1$ DPS sequences contain almost all of their energy in the index-set I. Therefore, the vectors $\{\mathbf{h}\}$ span a subspace with essential dimension [6]

$$D' = \lceil 2M\nu_{\text{Dmax}} \rceil + 1. \qquad (11)$$

Due to (4), the time-variant fading process is highly oversampled. Thus the maximum number of subspace dimensions M is reduced by $2\nu_{\text{Dmax}} \ll 1$. In typical wireless communication systems, the essential subspace dimension D' is in the order of two to five only. This fact is exploited in the following definition.

Definition 2. Let $\mathbf{h}$ be a vector obtained by index limiting a band-limited process with band-limit W to the index set I. Further, collect the first D DPS vectors $\mathbf{v}^{(d)}(W,I)$ in the matrix

$$\mathbf{V} = \left[\mathbf{v}^{(0)}(W,I),\ldots,\mathbf{v}^{(D-1)}(W,I)\right]. \qquad (12)$$

The *DPS subspace representation* of $\mathbf{h}$ with dimension D is defined as

$$\hat{\mathbf{h}}^D = \mathbf{V}\boldsymbol{\alpha}, \qquad (13)$$

where $\boldsymbol{\alpha}$ is the projection of the vector $\mathbf{h}$ onto the columns of $\mathbf{V}$:

$$\boldsymbol{\alpha} = \mathbf{V}^H\mathbf{h}. \qquad (14)$$

For the purpose of channel simulation, it is possible to use $D > D'$ DPS vectors in order to increase the numerical accuracy of the subspace representation. The subspace dimension D has to be chosen such that the bias of the subspace representation is small compared to the machine precision of the underlying simulation hardware. This is illustrated in Section 3.2 by numerical examples.

In terms of complexity, the problem of computing the series (2) was reformulated into the problem of computing the basis coefficients $\boldsymbol{\alpha}$ of the subspace representation (13). If they were computed directly using (14), the complexity of the problem would not be reduced. In the following section, we derive a novel low-complexity method to calculate the basis coefficients $\boldsymbol{\alpha}$ approximately.

3. MAIN RESULT

3.1. Approximate calculation of the basis coefficients

In this section, an approximate method to calculate the basis coefficients $\boldsymbol{\alpha}$ in (13) with low complexity is presented. Until now we have only considered the time domain of the channel and assumed that the band limiting region W is symmetric around the origin. To make the methods in this section also applicable to the frequency domain and the spatial domains (cf. Section 4), we make the more general assumption that

$$W = [W_0 - W_{\max}, W_0 + W_{\max}]. \tag{15}$$

The projection of a single complex exponential vector $\mathbf{e}_p = [e^{2\pi j\nu_p M_0}, \ldots, e^{2\pi j\nu_p (M_0+M-1)}]^T$ onto the basis functions $\mathbf{v}^{(d)}(W,I)$ can be written as a function of the Doppler shift ν_p, the band-limit region W, and the index set I,

$$\gamma_d(\nu_p; W, I) = \sum_{m=M_0}^{M_0+M-1} \nu_m^{(d)}(W,I) e^{2\pi jm\nu_p}. \tag{16}$$

Since $\mathbf{h}$ can be written as

$$\mathbf{h} = \sum_{p=0}^{P-1} \eta_p \mathbf{e}_p, \tag{17}$$

the basis coefficients $\boldsymbol{\alpha}$ (14) can be calculated by

$$\boldsymbol{\alpha} = \sum_{p=0}^{P-1} \eta_p \mathbf{V}^H \mathbf{e}_p = \sum_{p=0}^{P-1} \eta_p \boldsymbol{\gamma}_p, \tag{18}$$

where $\boldsymbol{\gamma}_p = [\gamma_0(\nu_p; W, I), \ldots, \gamma_{D-1}(\nu_p; W, I)]^T$ denote the basis coefficients for a single MPC.

To calculate the basis coefficients $\gamma_d(\nu_p; W, I)$, we take advantage of the DPS wave functions $U_d(f; W, I)$. For the special case $W_0 = 0$ and $M_0 = 0$ the DPS wave functions are defined in [17]. For the more general case, the DPS wave functions are defined as the eigenfunctions of

$$\int_W \frac{\sin(M\pi(\nu - \nu'))}{\sin(\pi(\nu - \nu'))} U_d(\nu'; W, I) d\nu \tag{19}$$
$$= \lambda_d(W, I) U_d(\nu; W, I), \quad \nu \in W.$$

They are normalized such that

$$\int_W |U_d(\nu; W, I)|^2 d\nu = 1,$$
$$U_d(W_0; W, I) \ge 0, \quad \left.\frac{dU_d(\nu; W, I)}{df}\right|_{\nu=W_0} \ge 0, \tag{20}$$
$$d = 0, \ldots, D-1.$$

The DPS wave functions are closely related to the DPS sequences. It can be shown that the amplitude spectrum of a DPS sequence limited to $m \in I$ is a scaled version of the

associated DPS wave function (cf. [17, equation (26)])

$$U_d(\nu; W, I) = \epsilon_d \sum_{m=M_0}^{M_0+M-1} \nu_m^{(d)}(W, I) e^{-j\pi(2M_0+M-1-2m)\nu}, \tag{21}$$

where $\epsilon_d = 1$ if d is even, and $\epsilon_d = j$ if d is odd.

Comparing (16) with (21) shows that the basis coefficients can be calculated according to

$$\gamma_d(\nu_p; W, I) = \frac{1}{\epsilon_d} e^{j\pi(2M_0+M-1)\nu_p} U_d(\nu_p; W, I). \tag{22}$$

The following definition and theorem show that $U_d(\nu_p; W, I)$ can be approximately calculated from $\nu_m^{(d)}(W, I)$ by a simple scaling and shifting operation [21].

Definition 3. Let $\nu_m^{(d)}(W, I)$ be the DPS sequences with band-limit region $W = [W_0 - W_{\max}, W_0 + W_{\max}]$ and index set $I = \{M_0, \ldots, M_0 + M - 1\}$. Further denote by $\lambda_d(W, I)$ the corresponding eigenvalues. For $\nu_p \in W$ define the index m_p by

$$m_p = \left\lfloor \left(1 + \frac{\nu_p - W_0}{W_{\max}}\right) \frac{M}{2} \right\rfloor. \tag{23}$$

Approximate DPS wave functions are defined as

$$\tilde{U}_d(\nu_p; W, I) := \pm e^{2\pi j(M_0+M-1+m_p)W_0} \sqrt{\frac{\lambda_d M}{2W_{\max}}} \nu_{m_p}^{(d)}(W, I), \tag{24}$$

where the sign is taken such that the following normalization holds:

$$\tilde{U}_d(W_0; W, I) \ge 0, \quad \left.\frac{d\tilde{U}_d(\nu_p; W, I)}{d\nu_p}\right|_{\nu_p=W_0} \ge 0, \tag{25}$$
$$d = 0, \ldots, D-1.$$

Theorem 2. *Let $\psi_d(c, f)$ be the prolate spheroidal wave functions [22]. Let $c > 0$ be given and set*

$$M = \left\lfloor \frac{c}{\pi W_{\max}} \right\rfloor. \tag{26}$$

If $W_{\max} \to 0$,

$$\sqrt{W_{\max}} \tilde{U}_d(W_{\max} \nu_p; W, I) \sim \psi_d(c, \nu_p),$$
$$\sqrt{W_{\max}} U_d(W_{\max} \nu_p; W, I) \sim \psi_d(c, \nu_p). \tag{27}$$

In other words, both the approximate DPS wave functions as well as the DPS wave functions themselves converge to the prolate spheroidal wave functions.

Proof. For $W_0 = 0$ and $M_0 = 0$, that is, $W' = [-W_{\max}, W_{\max}]$ and $I' = \{0, \ldots, M-1\}$ the proof is given in [17, Section 2.6]. The general case follows by using the two identities

$$\nu_m^{(d)}(W, I) = e^{2\pi j(m+M_0)W_0} \nu_{m+M_0}^{(d)}(W', I'),$$
$$U_d(\nu, W, I) = e^{\pi j(2M_0+M-1)(\nu-W_0)} U_d(\nu - W_0; W', I'). \tag{28}$$

$\square$

Theorem 2 suggests that the approximate DPS wave functions can be used as an approximation to the DPS wave functions. Therefore, the basis coefficients (22) can be calculated approximately by

$$\tilde{\gamma}_d(\nu_p; W, I) := \frac{1}{\epsilon_d} e^{j\pi(2M_0 + M - 1)\nu_p} \tilde{U}_d(\nu_p; W, I). \quad (29)$$

The theorem does not indicate the quality of the approximation. It can only be deduced that the approximation improves as the bandwidth $W_{\max}$ decreases, while the number of samples $M = \lfloor c/\pi W_{\max} \rfloor$ increases. This fact is exploited in the following definition.

Definition 4. Let **h** be a vector obtained by index limiting a band-limited process of the form (2) with band-limit $W = [W_0 - W_{\max}, W_0 + W_{\max}]$ to the index set $I = \{M_0, \dots, M_0 + M - 1\}$. For a positive integer r—*the resolution factor*—define

$$I_r = \{M_0, M_0 + 1, \dots, M_0 + rM - 1\},$$
$$W_r = \left[W_0 - \frac{W_{\max}}{r}, W_0 + \frac{W_{\max}}{r} \right]. \quad (30)$$

The *approximate DPS subspace representation* with dimension D and resolution factor r is given by

$$\tilde{\mathbf{h}}^{D,r} = \mathbf{V}\tilde{\boldsymbol{\alpha}}^r \quad (31)$$

whose *approximate basis coefficients* are

$$\tilde{\alpha}_d^r = \sum_{p=0}^{P-1} \eta_p \tilde{\gamma}_d\left(\frac{\nu_p}{r}, W_r, I_r\right). \quad (32)$$

Note that the DPS sequences are required in a higher resolution only for the calculation of the approximate basis coefficients. The resulting $\tilde{\mathbf{h}}^{D,r}$ has the same sample rate for any choice of r.

3.2. Bias of the subspace representation

In this subsection, the square bias of the subspace representation

$$\text{bias}_{\hat{\mathbf{h}}^D}^2 = \mathcal{E}\left\{ \frac{1}{M} ||\mathbf{h} - \hat{\mathbf{h}}^D||^2 \right\} \quad (33)$$

and the square bias of the approximate subspace representation

$$\text{bias}_{\tilde{\mathbf{h}}^{D,r}}^2 = \mathcal{E}\left\{ \frac{1}{M} ||\mathbf{h} - \tilde{\mathbf{h}}^{D,r}||^2 \right\} \quad (34)$$

are analyzed.

For ease of notation, we assume again that $W = [-\nu_{\text{Dmax}}, \nu_{\text{Dmax}}]$, that is, we set $W_0 = 0$ and $W_{\max} = \nu_{\text{Dmax}}$. However, the results also hold for the general case (15). If the Doppler shifts ν_p, $p = 0, \dots, P - 1$, are distributed independently and uniformly on W, the DPS subspace representation $\hat{\mathbf{h}}$ coincides with the Karhunen-Loève transform of **h** [23] and it can be shown that

$$\text{bias}_{\hat{\mathbf{h}}^D}^2 = \frac{1}{M\nu_{\text{Dmax}}} \sum_{d=D}^{M-1} \lambda_d(W, I). \quad (35)$$

Table 1: Simulation parameters for the numerical experiments in the time domain. The carrier frequency and the sample rate resemble those of a UMTS system [24]. The block length is chosen to be as long as a UMTS frame.

Parameter	Value
Carrier frequency f_c	2 GHz
Sample rate $1/T_S$	3.84 MHz
Block length M	2560 samples
Mobile velocity $v_{\max}$	100 km/h
Maximum norm. Doppler ν_{Dmax}	4.82×10^{-5}

If the Doppler shifts ν_p, $p = 0, \dots, P - 1$, are not distributed uniformly, (35) can still be used as an approximation for the square bias [21].

For the square bias of the approximate DPS subspace representation $\tilde{\mathbf{h}}^{D,r}$, no analytical results are available. However, for the minimum achievable square bias, we conjecture that

$$\text{bias}_{\min,r}^2 = \min_D \text{bias}_{\tilde{\mathbf{h}}^{D,r}}^2 \approx \left(\frac{2\nu_{\text{Dmax}}}{r} \right)^2. \quad (36)$$

This conjecture is substantiated by numerical Monte-Carlo simulations using the parameters from Table 1. The Doppler shifts ν_p, $p = 0, \dots, P - 1$, are distributed independently and uniformly on W. The results are illustrated in Figure 5. It can be seen that the square bias of the subspace representation $\text{bias}_{\hat{\mathbf{h}}^D}^2$ decays with the subspace dimension. For $D \geq \lceil 2M\nu_{\text{Dmax}} \rceil + 1 = 2$ this decay is even exponential. These two properties can also be seen directly from (35) and the exponential decay of the eigenvalues $\lambda_d(W, I)$. The square bias $\text{bias}_{\tilde{\mathbf{h}}^{D,r}}^2$ of the approximate subspace representation is similar to $\text{bias}_{\hat{\mathbf{h}}^D}^2$ up to a certain subspace dimension. Thereafter, the square bias of the approximate subspace representation levels out at $\text{bias}_{\min,r}^2 \approx (2\nu_{\text{Dmax}}/r)^2$. Increasing the resolution factor pushes the levels further down.

Let the maximal allowable square error of the simulation be denoted by $E_{\max}^2$. Then, the approximate subspace representation can be used without loss of accuracy if D and r are chosen such that

$$\text{bias}_{\tilde{\mathbf{h}}^{D,r}}^2 \stackrel{!}{\leq} E_{\max}^2. \quad (37)$$

Good approximations for D and r can be found by

$$D = \operatorname*{argmin}_D \text{bias}_{\hat{\mathbf{h}}^D}^2 \leq E_{\max}^2, \qquad r = \operatorname*{argmin}_r \text{bias}_{\min,r}^2 \leq E_{\max}^2. \quad (38)$$

The first expression can be computed using (35). Using conjecture (36), the latter evaluates to

$$r = \left\lfloor \frac{2\nu_{\text{Dmax}}}{E_{\max}} \right\rfloor. \quad (39)$$

Using a 14-bit fixed-point processor, the maximum achievable accuracy is $E_{\max}^2 = (2^{-13})^2 \approx 1.5 \times 10^{-8}$. For the example of Figure 5, where the maximum Doppler shift $\nu_{\text{Dmax}} = 4.82 \times 10^{-5}$ and the number of samples $M = 2560$, the choice $D = 4$ and $r = 2$ makes the simulation as accurate as possible on this hardware. Depending on the application, a lower accuracy might also be sufficient.
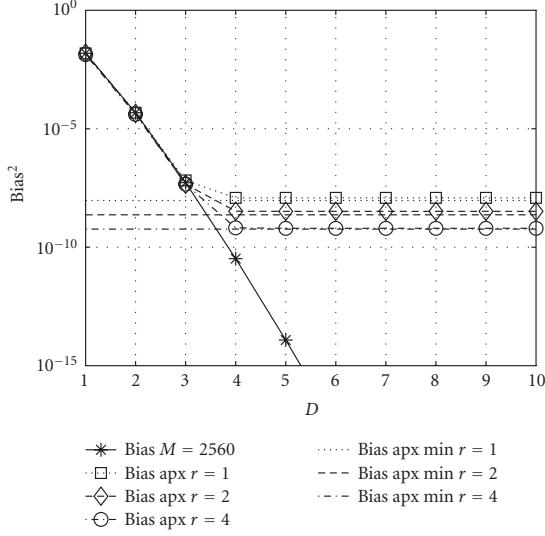
FIGURE 5: $\mathrm{bias}^2_{\tilde{\mathbf{h}}^D}$ (denoted by "bias"), $\mathrm{bias}^2_{\tilde{\mathbf{h}}^{D,r}}$ (denoted by "bias apx"), and $\mathrm{bias}^2_{\min,r}$ (denoted by "bias apx min") for $\nu_{\mathrm{Dmax}} = 4.82 \times 10^{-5}$ and $M = 2560$. The factor r denotes the resolution factor.

FIGURE 6: Complexity in terms of number of arithmetic operations (left abscissa) and memory access operations (right abscissa) versus the number of MPCs P. We show results for the sum of complex exponentials algorithm (denoted by "SoCE") and the approximate subspace representation (denoted by "DPSS") using $M = 2560$, $\nu_{\mathrm{Dmax}} = 4.82 \times 10^{-5}$, and $D = 4$.

3.3. Complexity and memory requirements

In this subsection, the computational complexity of the approximate subspace representation (31) is compared to the SoCE algorithm (2). The complexity is expressed in number of complex multiplications (CM) and evaluations of the complex exponential (CE). Additionally, we compare the number of memory access (MA) operations, which gives a better complexity comparison than the actual memory requirements.

We assume that all complex numbers are represented using their real and imaginary part. A CM thus requires four multiplication and two addition operations. As a reference for a CE we use a table look-up implementation with linear interpolation for values between table elements [2]. This implementation needs six addition, four multiplication, and two memory access operations.

Let the number of operations that are needed to evaluate $\mathbf{h}$ and $\tilde{\mathbf{h}}$ be denoted by $C_{\mathbf{h}}$ and $C_{\tilde{\mathbf{h}}}$, respectively. Using the SoCE algorithm, for every $m \in I = \{M_0, \ldots, M_0 + M - 1\}$ and every $p = 0, \ldots, P - 1$, a CE and a CM have to be evaluated, that is,

$$C_{\mathbf{h}} = MP\,\mathrm{CE} + MP\,\mathrm{CM}. \tag{40}$$

For the approximate DPS subspace representation with dimension D, first the approximate basis coefficients $\tilde{\boldsymbol{\alpha}}$ have to be evaluated, requiring

$$C_{\tilde{\boldsymbol{\alpha}}} = DP(\mathrm{CE} + 2\,\mathrm{CM} + \mathrm{MA}) + DP\,\mathrm{CM} \tag{41}$$

operations where the first term accounts for (29) and the second term for (32). In total, for the evaluation of the approximate subspace representation (31),

$$C_{\tilde{\mathbf{h}}} = MD(\mathrm{CM} + \mathrm{MA}) + C_{\tilde{\boldsymbol{\alpha}}} \tag{42}$$

operations are required. For large P, the approximate DPS subspace representation reduces the number of arithmetic operations compared to the SoCE algorithm by

$$\frac{C_{\mathbf{h}}}{C_{\tilde{\mathbf{h}}}} \longrightarrow \frac{M(\mathrm{CE} + \mathrm{CM})}{D(\mathrm{CE} + 3\,\mathrm{CM})}. \tag{43}$$

The memory requirements of the DPS subspace representation are determined by the block length M, the subspace dimension D and the resolution factor r. If the DPS sequences are stored with 16-bit precision,

$$\mathrm{Mem}_{\tilde{\mathbf{h}}} = 2rMD \text{ byte} \tag{44}$$

are needed.

In Figure 6, $C_{\mathbf{h}}$ and $C_{\tilde{\mathbf{h}}}$ are plotted over the number of paths P for the parameters given in Table 1. Multiplications and additions are counted as one operation. Memory access operations are counted separately. The subspace dimension is chosen to be $D = 4$ according to the observations of the last subsection. The memory requirements for the DPS subspace representation are $\mathrm{Mem}_{\tilde{\mathbf{h}}} = 80$ kbyte.

It can be seen that the complexity of the approximate DPS subspace representation in terms of number of arithmetic operations as well as memory access operations increases with slope D, while the complexity of the SoCE algorithm increases with slope M. Since in the given example
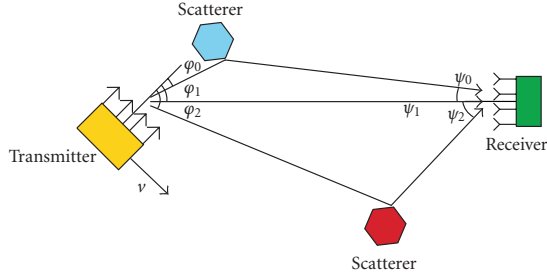
Figure 7: Multipath propagation model for a time-variant wideband MIMO radio channel. The signals sent from the transmitter, moving at speed v, arrive at the receiver. Each path p has complex weight η_p, time delay τ_p, Doppler shift ω_p, angle of departure φ_p, and angle of arrival ψ_p.

$D \ll M$, the approximate DPS subspace representation already enables a complexity reduction by more than one order of magnitude compared to the SoCE algorithm for $P = 30$ paths. Asymptotically, the number of arithmetic operations can be reduced by a factor of $C_{\mathbf{h}}/C_{\tilde{\mathbf{h}}} \rightarrow 465$.

4. WIDEBAND MIMO CHANNEL SIMULATION

4.1. The wideband MIMO geometry-based channel model

The time-variant GCM described in Section 2.1 can be extended to describe time-variant wideband MIMO channels. For simplicity we assume uniform linear arrays (ULA) with omnidirectional antennas. Then the channel can be described by the time-variant wideband MIMO channel transfer function $h(t, f, x, y)$, where t denotes time, f denotes frequency, x the position of the transmit antenna on the ULA, y the position of the receive antenna on the ULA [25].

The GCM assumes that $h(t, f, x, y)$ can be written as a superposition of P MPCs,

$$h(t, f, x, y) = \sum_{p=0}^{P-1} \eta_p e^{2\pi j \omega_p t} e^{-2\pi j \tau_p f} e^{2\pi j/\lambda \sin \varphi_p x} e^{-2\pi j/\lambda \sin \psi_p y},$$
(45)

where every MPC is characterized by its complex weight η_p, its Doppler shift ω_p, its delay τ_p, its angle of departure (AoD) φ_p, and its AoA ψ_p (see Figure 7) and λ is the wavelength. More sophisticated models may also include parameters such as elevation angle, antenna patterns, and polarization.

There exist many models for how to obtain the parameters of the MPCs. They can be categorized as *deterministic*, *geometry-based stochastic*, and *nongeometrical stochastic* models [26]. The number of MPCs required depends on the scenario modeled, the system bandwidth, and the number of antennas used. In this paper, we choose the number of MPCs such that the channel is Rayleigh fading, except for the line-of-sight component.

For narrowband frequency-flat systems, approximately $P_0 = 40$ MPCs are needed to achieve a Rayleigh fading statis-

tics [13]. If the channel bandwidth is increased, the number of resolvable MPCs increases also. The ITU channel models [27], which are used for bandwidths up to 5 MHz in UMTS systems, specify a power delay profile with up to six delay bins. The I-METRA channel models for the IEEE 802.11n wireless LAN standard [28] are valid for up to 40 MHz and specify a power delay profile with up to 18 delay bins. This requires a total number of MPCs of up to $P_1 = 18 P_0 = 720$. Diffuse scattering can also be modeled using a GCM by increasing the number of MPCs. In theory, diffuse scattering results from the superposition of an infinite number of MPCs [29]. However, good approximations can be achieved by using a large but finite number of MPCs [30, 31]. In MIMO channels, the number of MPCs multiplies by $N_{Tx} N_{Rx}$, since every antenna sees every scatterer from a different AoA and AoD, respectively. For a 4×4 system, the total number of MPCs can thus reach up to $P = 16 P_1 = 1.2 \times 10^4$.

We now show that the sampled time-variant wideband MIMO channel transfer function is band-limited in time, frequency, and space. Let F_S denote the width of a frequency bin and D_S the distance between antennas. The sampled channel transfer function can be described as a four-dimensional sequence $h_{m,q,r,s} = h(mT_S, qF_S, rD_S, sD_S)$, where m denotes discrete time, q denotes discrete frequency, s denotes the index of the transmit antenna, and r denotes the index of the receive antenna.[1] Further, let $\nu_p = \omega_p T_S$ denote the normalized Doppler shift, $\theta_p = \tau_p F_S$ the normalized delay, $\zeta_p = \sin(\varphi_p) D_S/\lambda$ and $\xi_p = \sin(\psi_p) D_S/\lambda$ the normalized angles of departure and arrival, respectively. If all these indices are collected in the vectors

$$\mathbf{m} = [m, q, s, r]^T,$$
$$\mathbf{f}_p = [\nu_p, -\theta_p, \zeta_p, -\xi_p]^T,$$
(46)

$h_{\mathbf{m}}$ can be written as

$$h_{\mathbf{m}} = \sum_{p=0}^{P-1} \eta_p e^{j2\pi \langle \mathbf{f}_p, \mathbf{m} \rangle},$$
(47)

that is, the multidimensional form of (2).

The band-limitation of $h_{\mathbf{m}}$ in time, frequency, and space is defined by the following physical parameters of the channel.

(1) The maximum normalized Doppler shift of the channel ν_{Dmax} defines the band-limitation in the time domain. It is determined by the maximum speed of the user v_{max}, the carrier frequency f_C, the speed of light c, and the sampling rate $1/T_S$, that is,

$$\nu_{Dmax} = \frac{v_{max} f_C}{c} T_S.$$
(48)

---

[1] In the literature, the time-variant wideband MIMO channel is often represented by the matrix $\mathbf{H}(m, q)$, whose elements are related to the sampled time-variant wideband MIMO channel transfer function $h_{m,q,r,s}$ by $H_{r,s}(m, q) = h_{m,q,r,s}$.

(2) The maximum normalized delay of the scenario $\theta_{\max}$ defines the band-limitation in the frequency domain. It is determined by the maximum delay $\tau_{\max}$ and the sample rate $1/F_S$ in frequency

$$\theta_{\max} = \tau_{\max} F_S. \tag{49}$$

(3) The minimum and maximum normalized AoA, $\xi_{\min}$ and $\xi_{\max}$ define the band-limitation in the spatial domain at the receiver. They are given by the minimum and maximum AoA, $\psi_{\min}$ and $\psi_{\max}$, the spatial sampling distance D_S and the wavelength λ:

$$\xi_{\min} = \sin{(\psi_{\min})}\frac{D_S}{\lambda}, \qquad \xi_{\max} = \sin{(\psi_{\max})}\frac{D_S}{\lambda}. \tag{50}$$

The band-limitation at the transmitter is given similarly by the normalized minimum and maximum normalized AoD, $\zeta_{\min}$ and $\zeta_{\max}$.

In summary it can be seen that $h_{\mathbf{m}}$ is band-limited to

$$W = [-\nu_{\mathrm{Dmax}}, \nu_{\mathrm{Dmax}}] \times [0, \theta_{\max}] \\ \times [\zeta_{\min}, \zeta_{\max}] \times [\xi_{\min}, \xi_{\max}]. \tag{51}$$

Thus the discrete time Fourier transform (DTFT)

$$H(\mathbf{f}) = \sum_{\mathbf{m} \in \mathbb{Z}^N} h_{\mathbf{m}} e^{-2\pi j \langle \mathbf{f}, \mathbf{m} \rangle}, \quad \mathbf{f} \in \mathbb{C}^N, \tag{52}$$

vanishes outside the region W, that is,

$$H(\mathbf{f}) = 0, \quad \mathbf{f} \notin W. \tag{53}$$

4.2. Multidimensional DPS sequences

The fact that $h_{\mathbf{m}}$ is band-limited allows one to extend the concepts of the DPS subspace representation also to time-variant wideband MIMO channels. Therefore, a generalization of the one-dimensional DPS sequences to multiple dimensions is required.

Definition 5. Let $I \subset \mathbb{Z}^N$ be an N-dimensional finite index set with $L = |I|$ elements, and $W \subset (-1/2, 1/2)^N$ an N-dimensional band-limiting region. *Multidimensional discrete prolate spheroidal (DPS) sequences* $v_{\mathbf{m}}^{(d)}(W, I)$ are defined as the solutions of the eigenvalue problem

$$\sum_{\mathbf{m}' \in I} v_{\mathbf{m}'}^{(d)}(W, I) K^{(W)}(\mathbf{m}' - \mathbf{m}) = \lambda_d(W, I) v_{\mathbf{m}}^{(d)}(W, I),$$
$$\mathbf{m} \in \mathbb{Z}^N, \tag{54}$$

where

$$K^{(W)}(\mathbf{m}' - \mathbf{m}) = \int_W e^{2\pi j \langle \mathbf{f}'', \mathbf{m}' - \mathbf{m} \rangle} d\mathbf{f}''. \tag{55}$$

They are sorted such that their eigenvalues $\lambda_d(W, I)$ are in descending order

$$\lambda_0(W, I) > \lambda_1(W, I) > \cdots > \lambda_{L-1}(W, I). \tag{56}$$

To ease notation, we drop the explicit dependence of $v_{\mathbf{m}}^{(d)}(W, I)$ on W and I when it is clear from the context. Further, we define the multidimensional DPS vector $\mathbf{v}^{(d)}(W, I) \in \mathbb{C}^L$ as the multidimensional DPS sequence $v_{\mathbf{m}}^{(d)}(W, I)$ index-limited to I. In particular, if every element $\mathbf{m} \in I$ is indexed lexicographically, such that $I = \{\mathbf{m}_l, l = 0, 1, \ldots, L-1\}$, then

$$\mathbf{v}^{(d)}(W, I) = [v_{\mathbf{m}_0}^{(d)}(W, I), \ldots, v_{\mathbf{m}_{L-1}}^{(d)}(W, I)]^T. \tag{57}$$

All the properties of Theorem 1 also apply to multidimensional DPS sequences [19]. The only difference is that m has to be replaced with $\mathbf{m}$ and $\mathbb{Z}$ with $\mathbb{Z}^N$.

Example 1. In the two-dimensional case $N = 2$ with band-limiting region W and index set I given by

$$W = [-\nu_{\mathrm{Dmax}}, \nu_{\mathrm{Dmax}}] \times [0, \theta_{\max}],$$
$$I = \{0, \ldots, M-1\} \times \left\{-\left\lfloor\frac{Q}{2}\right\rfloor, \ldots, \left\lfloor\frac{Q}{2}\right\rfloor - 1\right\}. \tag{58}$$

Equation (54) reduces to

$$\sum_{n=0}^{M-1} \sum_{p=-\lfloor Q/2 \rfloor}^{\lfloor Q/2 \rfloor - 1} \frac{\sin{(2\pi \nu_{\mathrm{Dmax}}(m-n))}}{\pi(n-m)} \frac{e^{2\pi i (p-q)\theta_{\max}} - 1}{2\pi i (p-q)} v_{n,p}^{(d)}$$
$$= \lambda_d v_{m,q}^{(d)}. \tag{59}$$

Note that due to the nonsymmetric band-limiting region W, the solutions of (59) can take complex values. Examples of two-dimensional DPS sequences and their eigenvalues are given in Figures 8 and 9, respectively. They have been calculated using the methods described in Appendix A.

4.3. Multidimensional DPS subspace representation

We assume that for hardware implementation, $h_{\mathbf{m}}$ is calculated blockwise for M samples in time, Q bins in frequency, N_{Tx} transmit antennas, and N_{Rx} receive antennas. Accordingly, the index set is defined by

$$I = \{0, \ldots, M-1\} \times \left\{-\left\lfloor\frac{Q}{2}\right\rfloor, \ldots, \left\lfloor\frac{Q}{2}\right\rfloor - 1\right\} \\ \times \{0, \ldots, N_{\mathrm{Tx}} - 1\} \times \{0, \ldots, N_{\mathrm{Rx}} - 1\}. \tag{60}$$

The DPS subspace representation can easily be extended to multiple dimensions. Let $\mathbf{h}$ be the vector obtained by index limiting the sequence $h_{\mathbf{m}}$ (47) to the index set I (60) and sorting the elements lexicographically. In analogy to the one-dimensional case, the subspace spanned by $\{\mathbf{h}\}$ is also spanned by the multidimensional DPS vectors $\mathbf{v}^{(d)}(W, I)$ defined in Section 4.2. Due to the common notation of one- and multidimensional sequences and vectors, the *multidimensional DPS subspace representation* of $\mathbf{h}$ can be defined similarly to Definition 2.

(a)

(b)

(c)

(d)
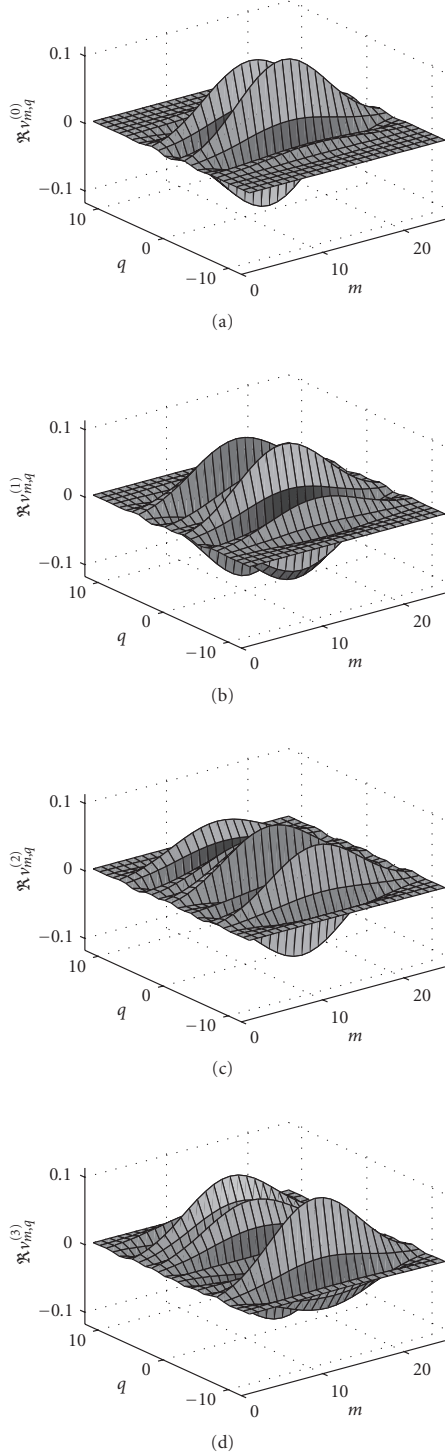
FIGURE 8: The real part of the first four two-dimensional DPS sequences $v_{m,q}^{(d)}$, $d = 0,\dots,3$ for $M = Q = 25$, $M\nu_{Dmax} = 2$, and $Q\theta_{max} = 5$.
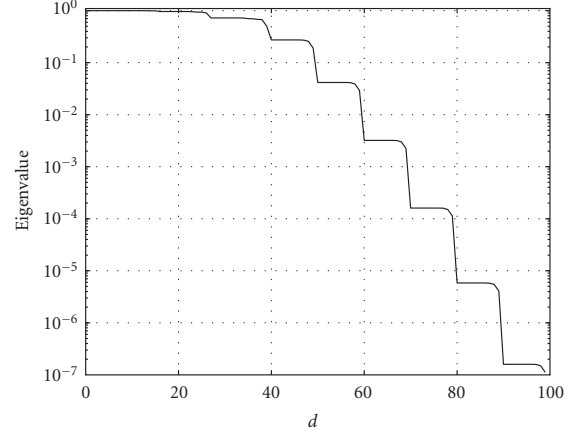
FIGURE 9: First 100 eigenvalues λ_d, $d = 0,\dots,99$, of two-dimensional DPS sequences for $M = Q = 25$, $M\nu_{Dmax} = 2$, and $Q\theta_{max} = 5$. The eigenvalues are clustered around 1 for $d \leq D' - 1$, and decay exponentially for $d \geq D'$, where the essential dimension of the signal subspace $D' = \lceil |W||I| \rceil + 1 = 41$.

Definition 6. Let $\mathbf{h}$ be a vector obtained by index limiting a multidimensional band-limited process of the form (47) with band-limit W to the index set I. Let $\mathbf{v}^{(d)}(W,I)$ be the multidimensional DPS vectors for the multidimensional band-limit region W and the multidimensional index set I. Further, collect the first D DPS vectors $\mathbf{v}^{(d)}(W,I)$ in the matrix

$$\mathbf{V} = \left[\mathbf{v}^{(0)}(W,I),\dots,\mathbf{v}^{(D-1)}(W,I)\right]. \quad (61)$$

The *multidimensional DPS subspace representation* of $\mathbf{h}$ with subspace dimension D is defined as

$$\hat{\mathbf{h}}^D = \mathbf{V}\boldsymbol{\alpha}, \quad (62)$$

where $\boldsymbol{\alpha}$ is the projection of the vector $\mathbf{h}$ onto the columns of $\mathbf{V}$:

$$\boldsymbol{\alpha} = \mathbf{V}^H\mathbf{h}. \quad (63)$$

The subspace dimension D has to be chosen such that the bias of the subspace representation is small compared to the machine precision of the underlying simulation hardware. The following theorem shows how the multidimensional projection (63) can be reduced to a series of one-dimensional projections.

Theorem 3. *Let $\hat{\mathbf{h}}^D$ be the N-dimensional DPS subspace representation of $\mathbf{h}$ with subspace dimension D, band-limiting region W, and index set I. If W and I can be written as Cartesian products*

$$W = W_0 \times \cdots \times W_{N-1}, \quad (64)$$
$$I = I_0 \times \cdots \times I_{N-1}, \quad (65)$$

where $W_i = [W_{0,i} - W_{\max,i}, W_{0,i} + W_{\max,i}]$, *and* $I_i = \{M_{0,i}, \ldots, M_{0,i} + M_i - 1\}$, *then for every* $d = 0, \ldots, D - 1$, *there exist* $d_0, \ldots, d_{N-1}$ *such that the N-dimensional DPS basis vectors* $\mathbf{v}^{(d)}(W, I)$ *can be written as*

$$\mathbf{v}^{(d)}(W, I) = \mathbf{v}^{(d_0)}(W_0, I_0) \otimes \cdots \otimes \mathbf{v}^{(d_{N-1})}(W_{N-1}, I_{N-1}). \tag{66}$$

Further, the basis coefficients of the approximate DPS subspace representation

$$\widetilde{\mathbf{h}}^D = \mathbf{V}\widetilde{\boldsymbol{\alpha}} \tag{67}$$

are given by

$$\widetilde{\boldsymbol{\alpha}} = \sum_{p=0}^{P-1} \eta_p \left(\widetilde{\boldsymbol{\gamma}}_p^{(0)} \otimes \cdots \otimes \widetilde{\boldsymbol{\gamma}}_p^{(N-1)} \right), \tag{68}$$

where $\widetilde{\gamma}_{p,d}^{(i)} = \widetilde{\gamma}_{d_i}(f_{p,i}, W_i, I_i)$ *are the one-dimensional approximate basis coefficients defined in* (29). *Additionally, resolution factors* r_i *can be used to improve the approximation.*

Proof. See Appendix B □

The band-limiting region W (51) and the index set I (60) of the channel model (47) fulfill the prerequisites of Theorem 3 with

$$W_{0,0} = 0, \qquad W_{\max,0} = \nu_{\mathrm{Dmax}}, \qquad M_{0,0} = 0, \qquad M_0 = M,$$

$$W_{0,1} = W_{\max,1} = \frac{\theta_{\max}}{2}, \qquad M_{0,1} = -\left\lfloor \frac{Q}{2} \right\rfloor, \qquad M_1 = Q,$$

$$W_{0,2} = \frac{\zeta_{\max} + \zeta_{\min}}{2}, \qquad W_{\max,2} = \frac{\zeta_{\max} - \zeta_{\min}}{2},$$

$$M_{0,2} = 0, \qquad M_2 = N_{\mathrm{Tx}},$$

$$W_{0,3} = \frac{\xi_{\max} + \xi_{\min}}{2}, \qquad W_{\max,3} = \frac{\xi_{\max} - \xi_{\min}}{2},$$

$$M_{0,3} = 0, \qquad M_3 = N_{\mathrm{Rx}}. \tag{69}$$

Thus, Theorem 3 allows us to use the methods of Section 3.1 to calculate the basis coefficients of the multidimensional DPS subspace representation approximately with low complexity. The resolution factors r_i, $i = 0, \ldots, N - 1$, have to be chosen such that the bias of the subspace representation is small compared to the machine precision $E_{\max}$ of the underlying simulation hardware. A necessary but not sufficient condition for this is to use the methods of Section 3.2 for each dimension independently, that is, to choose $r_i = 2W_{\max,i}/E_{\max}$. However, it has to be verified numerically that the multidimensional DPS subspace representation achieves the required numerical accuracy.

4.4. Complexity and memory requirements

In this subsection, we evaluate the complexity and memory requirements of the N-dimensional SoCE algorithm and the N-dimensional approximate DPS subspace representation,

given by Theorem 3. These results are a generalization of the results of Section 3.3. We assume that the one-dimensional DPS sequences $\mathbf{v}^{(d_i)}(W_i, I_i)$, $i = 0, \ldots, N - 1$, have been precalculated. Further, we assume that $D = D_0 \cdots D_{N-1}$, where $D_i = \max d_i$ is the maximum number of one-dimensional DPS vectors in dimension i needed to construct the N-dimensional vectors $\mathbf{v}^{(d)}(W, I)$, $d = 0, \ldots, D - 1$.

Let the number of operations that are needed to evaluate $\mathbf{h}$ (47) and $\widetilde{\mathbf{h}}^D$ (67) be denoted by $C_{\mathbf{h}}$ and $C_{\widetilde{\mathbf{h}}^D}$, respectively. For the SoCE algorithm,

$$C_{\mathbf{h}} = |I|P(\mathrm{CE} + \mathrm{CM}). \tag{70}$$

For the approximate DPS subspace representation with dimension D, firstly the N-dimensional DPS basis vectors need to be calculated from the one-dimensional DPS vectors (cf. (66)), requiring

$$C_{\mathbf{V}} = (N - 1)|I|D\ \mathrm{CM}. \tag{71}$$

Secondly, the approximate basis coefficients $\widetilde{\boldsymbol{\alpha}}$ have to be evaluated according to (68), requiring

$$C_{\widetilde{\boldsymbol{\alpha}}} = \left(\sum_{i=0}^{N-1} |D_i|(\mathrm{CE} + \mathrm{CM} + \mathrm{MA}) + ND\ \mathrm{CM} \right)P. \tag{72}$$

In total, for the evaluation of the approximate subspace representation (67),

$$C_{\widetilde{\mathbf{h}}^D} = |I|D(\mathrm{CM} + \mathrm{MA}) + C_{\mathbf{V}} + C_{\widetilde{\boldsymbol{\alpha}}} \tag{73}$$

operations are required.

Asymptotically for $P \to \infty$, the N-dimensional DPS subspace representation reduces the number of arithmetic operations compared to the SoCE algorithm by the factor

$$\frac{C_{\mathbf{h}}}{C_{\widetilde{\mathbf{h}}}} \longrightarrow \frac{|I|(\mathrm{CE} + \mathrm{CM})}{\sum_{i=0}^{N-1} D_i(\mathrm{CE} + \mathrm{CM}) + ND\ \mathrm{CM}}. \tag{74}$$

The memory requirements of the DPS subspace representation are determined by the size of the index set I, the number of DPS vectors D_i, and the resolution factors r_i. If the DPS sequences are stored with 16-bit precision,

$$\mathrm{Mem}_{\widetilde{\mathbf{h}}} = \sum_{i=0}^{N-1} 2r_i |I_i| D_i\ \mathrm{byte} \tag{75}$$

are needed.

4.5. Numerical examples

Section 3 demonstrated that an application of the approximate DPS subspace representation to the time-domain of wireless channels may save more than an order of magnitude in complexity. In this subsection, the multidimensional approximate DPS subspace representation is applied to an example of a time-variant frequency-selective channel as well as an example of a time-variant frequency-selective MIMO channel. A comparison of the arithmetic complexity is given. We assume a 14-bit fixed-point hardware architecture, that is, a maximum allowable square error of $E_{\max}^2 = (2^{-13})^2 \approx 1.5 \times 10^{-8}$.

TABLE 2: Simulation parameters for the numerical experiments in the frequency domain.

Parameter	Value
Width of frequency bin F_S	15 kHz
Number of frequency bins Q	256
Maximum delay τ_{max}	3.7 μs
Maximum norm. delay θ_{max}	$\approx 1/18$

4.5.1. Time and frequency domain

Table 2 contains the simulation parameters of the numerical experiments in the frequency domain. The parameters in the time domain are chosen according to Table 1. We assume a typical urban environment with a maximum delay spread of $\tau_{max} = 3.7$ milliseconds given by the ITU Pedestrian B channel model [27].

By omitting the spatial domains **x** and **y** in (47), we obtain a time-variant frequency-selective GCM

$$h_{\mathbf{m}'} = \sum_{p=0}^{P-1} \eta_p e^{j2\pi\langle \mathbf{f}_p', \mathbf{m}'\rangle}, \qquad (76)$$

where $\mathbf{m}' = [m, q]^T$ and $\mathbf{f}_p' = [\nu_p, \theta_p]^T$. Since (76) is band-limited to

$$W' = \left[-\nu_{Dmax}, \nu_{Dmax}\right] \times \left[0, \theta_{max}\right] \qquad (77)$$

and we wish to calculate (76) in the index set

$$I' = \{0, \dots, M-1\} \times \left\{ -\left\lfloor \frac{Q}{2} \right\rfloor, \dots, \left\lfloor \frac{Q}{2} \right\rfloor - 1\right\}, \qquad (78)$$

we can apply a two-dimensional DPS subspace representation (Definition 6) to (76). Further, we can use Theorem 3 to calculate the basis coefficients $\boldsymbol{\alpha}$ of the subspace representation.

For a given maximum allowable square bias $E_{max}^2 = (2^{-13})^2$, the estimated values of the resolution factors in the time and frequency domain are $r_0 = 2\nu_{Dmax}/E_{max} \approx 2$ and $r_1 = \theta_{max}/E_{max} \approx 512$ (rounded to the next power of two). The square bias

$$\text{bias}_{\tilde{\mathbf{h}}^D}^2 = \mathcal{E}\left\{ \frac{1}{MQ}\|\tilde{\mathbf{h}}^D - \mathbf{h}^D\|^2\right\} \qquad (79)$$

of the two-dimensional exact and the approximate DPS subspace representation is plotted in Figure 10 against the subspace dimension D. It can be seen that $\text{bias}_{\tilde{\mathbf{h}}^D}^2 \approx E_{max}^2$ at a subspace dimension of approximately $D = 80$. The maximum number of one-dimensional DPS vectors is $D_0 = 4$ and $D_1 = 23$.

4.5.2. Time, frequency, and spatial domain

Table 3 contains the simulation parameters of the numerical experiments in the spatial domain. The remaining parameters are chosen according to Tables 1 and 2. We assume uniform linear arrays at the transmitter and the receiver with
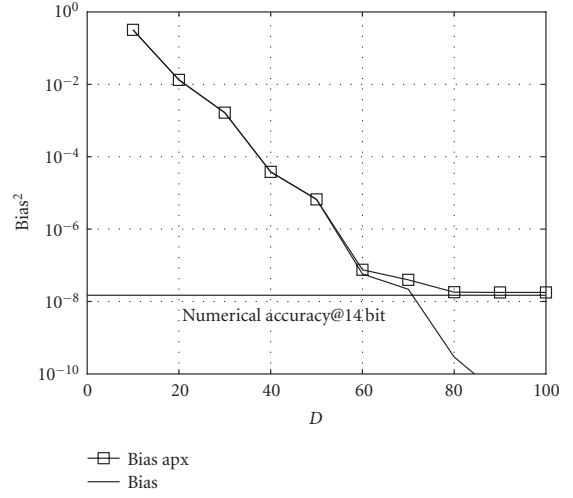
FIGURE 10: $\text{bias}_{\tilde{\mathbf{h}}^D}^2$ for the subspace representation in the time and frequency domain with $\nu_{Dmax} = 4.82 \times 10^{-5}$, $M = 2560$, $\theta_{max} = 0.056$, and $Q = 256$. The resolution factors are fixed to $r_0 = 2$ and $r_1 = 512$. The thin horizontal line denotes the numerical accuracy of a fixed-point 14-bit processor.

TABLE 3: Simulation parameters for the numerical experiments in the spatial domains.

Parameter	Value
Spacing between antennas D_S	$\lambda/2$ m
Number of Tx antennas N_{Tx}	8
Number of Rx antennas N_{Rx}	8
AoD interval $[\varphi_{min}, \varphi_{max}]$	$[-5°, 5°]$
AoA interval $[\psi_{min}, \psi_{max}]$	$[-5°, 5°]$
Normalized AoD bandwidth $\zeta_{max} - \zeta_{min}$	0.087
Normalized AoA bandwidth $\xi_{max} - \xi_{min}$	0.087

spacing $D_S = \lambda/2$ and $N_{Tx} = N_{Rx} = 8$ antennas each. Further we assume that there is only one cluster of scatterers in the scenario which is not in the vicinity of the transmitter or receiver (see Figure 11) and we assume no line-of-sight component. The AoD and AoA are assumed to be limited by $[\varphi_{min}, \varphi_{max}] = [\psi_{min}, \psi_{max}] = [-5°, 5°]$, which has been observed in measurements [32].

A four-dimensional DPS subspace representation is applied to the channel transfer function (47) with W and I defined in (51) and (60). Following the same procedure as in the previous subsection, for a numerical accuracy of 14 bits the estimated values of the resolution factors and the number of one-dimensional DPS vectors in the spatial domains are $r_2 = (\zeta_{max} - \zeta_{min})/E_{max} \approx 512$, $r_3 = (\xi_{max} - \xi_{min})/E_{max} \approx 512$ (rounded to the next power of 2), and $D_2 = D_3 = 5$.

4.5.3. Hybrid DPS subspace representation

Last but not least, we propose a hybrid DPS subspace representation that applies a DPS subspace representation in time
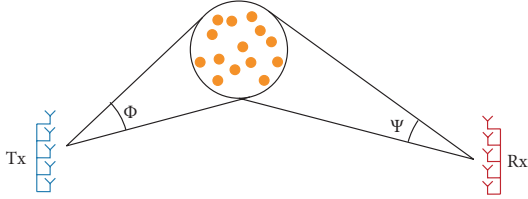
FIGURE 11: Scenario of a mobile radio channel with one cluster of scatterers. The AoD and the AoA are limited within the intervals $\Phi = [\varphi_{\min}, \varphi_{\max}]$ and $\Psi = [\psi_{\min}, \psi_{\max}]$, respectively.

and frequency domains, and computes the complex exponentials in the spatial domain directly. Therefore, the four-dimensional channel transfer function $h_{\mathbf{m}}$ (47) is split into $N_{\text{Tx}}N_{\text{Rx}}$ two-dimensional transfer functions $h_{\mathbf{m}'}^{s,r}$ describing the transfer function between transmit antenna s and receiver antenna r;

$$h_{\mathbf{m}'}^{s,r} := h_{\mathbf{m}',s,r} = \sum_{p=0}^{P-1} \underbrace{\eta_p e^{-j2\pi\zeta_p s} e^{j2\pi\xi_p r}}_{\eta_p^{k,l}} e^{j2\pi\langle\mathbf{f}_p', \mathbf{m}'\rangle} \quad (80)$$

$$\text{for } \mathbf{m}' \in I', \mathbf{f}_p' \in W',$$

where the band-limit region W' and the index set I' are the same as in the two-dimensional case (cf. (77) and (78)). Then, the two-dimensional DPS subspace representation can be applied to each $h_{\mathbf{m}'}^{s,r}, s = 0, \ldots, N_{\text{Tx}} - 1, r = 0, \ldots, N_{\text{Rx}} - 1,$ independently.

4.5.4. Results and discussion

A complexity comparison of the SoCE algorithm and the approximate DPS subspace representation for one, two, and four dimensions is given in **Figure 12**. It was evaluated using (70) and (73). Also shown is the complexity of the four-dimensional hybrid DPS subspace representation. It can be seen that for time-variant frequency-flat SISO channels, the one-dimensional DPS subspace representation requires fewer arithmetic operations for $P > 2$ MPCs. The more MPCs are used in the GCM, the more complexity is saved. Asymptotically, the number of arithmetic operations is reduced by $C_{\mathbf{h}}/C_{\tilde{\mathbf{h}}} \to 465$.

For time-variant frequency-selective SISO channels, the two-dimensional DPS subspace representation requires fewer arithmetic operations for $P > 30$ MPCs. However, as noted in **Section 4.1**, channel models for systems with the given parameters require $P = 400$ paths or more. For such a scenario, the DPS subspace representation saves two orders of magnitude in complexity. Asymptotically, the number of arithmetic operations is reduced by a factor of $C_{\mathbf{h}}/C_{\tilde{\mathbf{h}}} \to 6.8 \times 10^3$ (cf. (74)). The memory requirements are $\text{Mem}_{\tilde{\mathbf{h}}} = 5.83$ Mbyte (cf. (75)).

For time-variant frequency-selective MIMO channels, the four-dimensional DPS subspace representation requires fewer arithmetic operations for $P > 2 \times 10^3$ MPCs. Since MIMO channels require the simulation of up to 10^4 MPCs
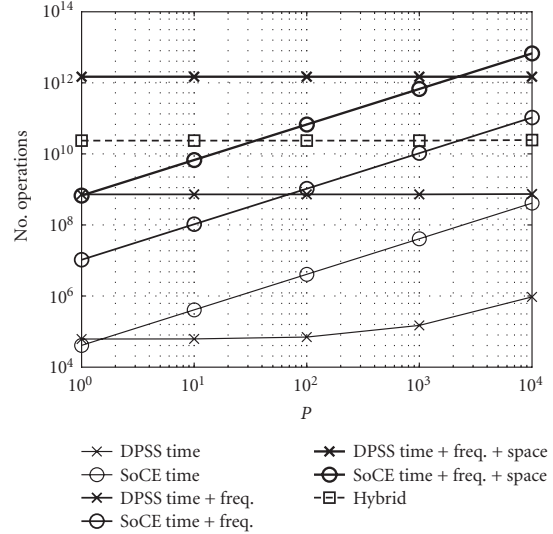
FIGURE 12: Complexity in terms of number of arithmetic operations versus the number of MPCs P. We show results for the SoCE algorithm (denoted by "SoCE") and the approximate DPS subspace representation (denoted by "DPSS") for one, two, and four dimensions. Also shown is the complexity of the four-dimensional hybrid DPS subspace representation (denoted by "Hybrid").

(cf. Section 4.1), complexity savings are still possible. The asymptotic complexity savings are $C_{\mathbf{h}}/C_{\tilde{\mathbf{h}}} \to 1.9 \times 10^4$. However, in the region $P < 2 \times 10^3$ MPCs, the four-dimensional DPS subspace representation requires more complex operations than the corresponding SoCE algorithm. Thus, even though we choose a "best case" scenario with only one cluster, a small angular spread and a low numerical accuracy, there is hardly any additional complexity reduction if the DPS subspace representation is applied in the spatial domain.

The hybrid DPS subspace representation on the other hand exploits the savings of the DPS subspace representation in the time and frequency domain only. From **Figure 12** it can be seen that it has fewer arithmetic operations than the four-dimensional DPS subspace representation and the four-dimensional SoCE algorithm for $60 < P < 2 \times 10^3$ MPCs. Thus the hybrid method is preferable for channel simulations in this region. Further, this method also allows for an efficient parallelization on hardware channel simulators [33].

5. CONCLUSIONS

We have presented a low-complexity algorithm for the computer simulation of geometry-based MIMO channel models. The algorithm exploits the low-dimensional subspace spanned by multidimensional DPS sequences. By adjusting the dimension of the subspace, it is possible to trade computational complexity for accuracy. Thus the algorithm is ideally suited for fixed-point hardware architectures with limited precision.

We demonstrated that the complexity reduction depends mainly on the normalized bandwidth of the underlying fading process in time, frequency, and space. If the bandwidth is very small compared to the sampling rate, the essential subspace dimension of the process is small and the complexity can be reduced substantially. In the time domain, the maximum Doppler bandwidth of the fading process is much smaller than the system sampling rate. Compared with the SoCE algorithm, our new algorithm reduces the complexity by more than one order of magnitude on 14-bit hardware.

The bandwidth of a frequency-selective fading process is given by the maximum delay in the channel, which is a factor of five to ten smaller than the sampling rate in frequency. Therefore, the DPS subspace representation also reduces the computational complexity when applied in the frequency domain. To achieve a satisfactory numerical accuracy, the resolution factor in the approximation of the basis coefficients needs to be large, resulting in high memory requirements. On the other hand, it was shown that the number of memory access operations is small. Since this figure has more influence on the run-time of the algorithm, the approximate DPS subspace representation is preferable over the SoCE algorithm for a frequency-selective fading-process.

The bandwidth of the fading process in the spatial domain is determined by the angular spread of the channel, which is almost as large as the spatial sampling rate for most scenarios in wireless communications. Therefore, applying the DPS subspace representation in the spatial domain does not achieve any additional complexity reduction for the scenarios of interest. As a consequence, for the purpose of wideband MIMO channel simulation, we propose to use a hybrid method which computes the complex exponentials in the spatial domain directly and applies the subspace representation to the time and frequency domain only. This method also allows for an efficient parallelization on hardware channel simulators.

APPENDICES

A. CALCULATION OF MULTIDIMENSIONAL DPS SEQUENCES

In the one-dimensional case ($N = 1$), where $W = [W_0 - W_{max}, W_0 + W_{max}]$ and $I = \{M_0, \ldots, M_0 + M - 1\}$, the DPS sequences can be calculated efficiently [17, 20]. The efficient and numerically stable calculation of multidimensional DPS sequences with arbitrary W and I is not trivial and has not been treated satisfactorily in the literature. In this section a new way of calculating multidimensional DPS sequences is derived if their passband region can be written as a Cartesian product of one-dimensional intervals.

Indexing every element $\mathbf{m} \in I$ lexicographically, such that $I = \{\mathbf{m}_l, l = 0, 1, \ldots, L - 1\}$, we define the matrix $\mathbf{K}^{(W)}$ by

$$K_{k,l}^{(W)} = K^{(W)}(\mathbf{m}_k - \mathbf{m}_l), \quad k, l = 0, \ldots, L - 1, \quad \text{(A.1)}$$

where the kernel $K^{(W)}$ is given by (55). Let $\mathbf{v}^{(d)}(W, I)$ and $\lambda_d(W, I)$, $d = 0, \ldots, L - 1$, denote the eigenvectors and eigenvalues of $\mathbf{K}^{(W)}$:

$$\mathbf{K}^{(W)} \mathbf{v}^{(d)}(W, I) = \lambda_d(W, I) \mathbf{v}^{(d)}(W, I), \quad \text{(A.2)}$$

where

$$\lambda_0(W, I) \geq \lambda_1(W, I) \geq \cdots \geq \lambda_{L-1}(W, I). \quad \text{(A.3)}$$

It can be shown that the eigenvectors $\mathbf{v}^{(d)}(W, I)$ and the eigenvalues $\lambda_d(W, I)$ are exactly the multidimensional DPS vectors defined in (57) and their corresponding eigenvalues. If the DPS sequences are required for $\mathbf{m} \notin I$, they can be extended using (54).

The multidimensional DPS vectors can theoretically be calculated for an arbitrary passband region W directly from the eigenproblem (A.2). However, since the matrix $\mathbf{K}^{(W)}$ has an exponentially decaying eigenvalue distribution, this method is numerically unstable.

If W can be written as a Cartesian product of one-dimensional intervals (i.e., W is a hyper-cube),

$$W = W_0 \times \cdots \times W_{N-1}, \quad \text{(A.4)}$$

where $W_i = [W_{0,i} - W_{max,i}, W_{0,i} + W_{max,i}]$, and the index-set I is written as

$$I = I_0 \times \cdots \times I_{N-1}, \quad \text{(A.5)}$$

where $I_i = \{M_{0,i}, \ldots, M_{0,i} + M_i - 1\}$, the defining kernel $K^{(W)}$ for the multidimensional DPS vectors evaluates to

$$\begin{aligned} K^{(W)}(\mathbf{u}) &= \int_{W_{0,i} - W_{max,i}}^{W_{0,i} + W_{max,i}} \cdots \int_{W_{0,N-1} - W_{max,N-1}}^{W_{0,N-1} + W_{max,N-1}} e^{2\pi j f_0'' u_0} \\ &\quad \cdots e^{2\pi j f_{N-1}'' u_{N-1}} df_0'' \cdots df_{N-1}'' \\ &= \prod_{i=0}^{N-1} K^{(W_i)}(u_i), \end{aligned} \quad \text{(A.6)}$$

where $\mathbf{u} = [u_0, \ldots, u_{N-1}]^T \in I$. This means that the kernel $K^{(W)}$ is separable and thus the matrix $\mathbf{K}^{(W)}$ can be written as a Kronecker product

$$\mathbf{K}^{(W)} = \mathbf{K}^{(W_0)} \otimes \cdots \otimes \mathbf{K}^{(W_{N-1})}, \quad \text{(A.7)}$$

where $\mathbf{K}^{(W_i)}$, $i = 0, \ldots, N - 1$, are the kernel matrices corresponding to the one-dimensional DPS vectors. Now let $\lambda_{d_i}(W_i, I_i)$ and $\mathbf{v}^{(d_i)}(W_i, I_i)$, $d_i = 0, \ldots, M_i - 1$, denote the eigenvalues and the eigenvectors of $\mathbf{K}^{(W_i)}$, $i = 0, \ldots, N - 1$, respectively. Then the eigenvalues of $\mathbf{K}^{(W)}$ are given by [34, Chapter 9]

$$\begin{aligned} \lambda_{\mathbf{d}}(W, I) &= \lambda_{d_0}(W_0, I_0) \cdots \lambda_{d_{N-1}}(W_{N-1}, I_{N-1}), \\ &\quad d_i = 0, \ldots, M_i - 1, \ i = 0, \ldots, N - 1 \end{aligned} \quad \text{(A.8)}$$

and the corresponding eigenvectors are given by

$$\mathbf{v}^{(\mathbf{d})}(W, I) = \mathbf{v}^{(d_0)}(W_0, I_0) \otimes \cdots \otimes \mathbf{v}^{(d_{N-1})}(W_{N-1}, I_{N-1}),$$

$$d_i = 0, \ldots, M_i - 1, \; i = 0, \ldots, N - 1. \quad \text{(A.9)}$$

The eigenvalues $\lambda_{\mathbf{d}}(W, I)$ and the eigenvectors $\mathbf{v}^{(\mathbf{d})}(W, I)$ are index by $\mathbf{d} = [d_0, \ldots, d_{N-1}]^T \in I$. The multidimensional DPS vectors $\mathbf{v}^{(d)}(W, I)$ are obtained by reordering the eigenvectors $\mathbf{v}^{(\mathbf{d})}(W, I)$ and eigenvalues $\lambda_{\mathbf{d}}(W, I)$ according to (A.3). Therefore, we define the mapping $d = \sigma(\mathbf{d})$, such that $\lambda_d(W, I) = \lambda_{\sigma(\mathbf{d})}(W, I)$ is the dth largest eigenvalue. Further define the inverse mapping $\mathbf{d} = \delta(d) = \sigma^{-1}(d)$, such that for a given order d of the multidimensional DPS vector $\mathbf{v}^{(d)}(W, I)$, the corresponding one-dimensional DPS vectors can be found. When a certain multidimensional DPS sequence of a given order d is needed, the eigenvalues λ_d, $d = 0, \ldots, L - 1$, have to be calculated and sorted first. Then the one-dimensional DPS sequences corresponding to $\mathbf{d} = \delta(d)$ can be selected.

B. PROOF OF THEOREM 3

For I given by (65), $\mathbf{h}$ can be written as

$$\mathbf{h} = \sum_{p=0}^{P-1} \eta_p \left(\mathbf{e}_p^{(0)} \otimes \cdots \otimes \mathbf{e}_p^{(N-1)} \right), \quad \text{(B.1)}$$

where $\mathbf{e}_p^{(i)} = [e^{2\pi j f_{p,i} M_{0,i}}, \ldots, e^{2\pi j f_{p,i}(M_{0,i}+M_i-1)}]^T$. Further, since W is given by (64), the results of Appendix A can be used and $\mathbf{V}$ can be written as

$$\mathbf{V} = \mathbf{V}_0 \diamond \cdots \diamond \mathbf{V}_{N-1}, \quad \text{(B.2)}$$

where every $M_i \times D_i$ matrix $\mathbf{V}_i$ contains the one-dimensional DPS vectors $\mathbf{v}^d(W_i, I_i)$ in its columns.

Using the identity

$$(\mathbf{A}_0 \diamond \cdots \diamond \mathbf{A}_{N-1})(\mathbf{b}_0 \otimes \cdots \otimes \mathbf{b}_{N-1})$$
$$= \mathbf{A}_0 \mathbf{b}_0 \otimes \cdots \otimes \mathbf{A}_{N-1} \mathbf{b}_{N-1}, \quad \text{(B.3)}$$

the basis coefficients $\boldsymbol{\alpha}$ can be calculated by

$$\boldsymbol{\alpha} = \mathbf{V}^H \mathbf{h} = \sum_{p=0}^{P-1} \eta_p \left(\mathbf{V}_0^H \diamond \cdots \diamond \mathbf{V}_{N-1}^H \right) \left(\mathbf{e}_p^{(0)} \otimes \cdots \otimes \mathbf{e}_p^{(N-1)} \right)$$

$$= \sum_{p=0}^{P-1} \eta_p \left(\underbrace{\mathbf{V}_0^H \mathbf{e}_p^{(0)}}_{=:\boldsymbol{\gamma}_p^{(0)}} \otimes \cdots \otimes \underbrace{\mathbf{V}_{N-1}^H \mathbf{e}_p^{(N-1)}}_{=:\boldsymbol{\gamma}_p^{(N-1)}} \right). \quad \text{(B.4)}$$

C. LIST OF SYMBOLS

t, f, x, y:	Time, frequency, antenna location at transmitter, and antenna location at receiver
$h(t, f, x, y)$:	Channel transfer function
T_S, F_S, D_S:	Duration of a sample, width of a frequency bin, and spacing between antennas
m, q, s, r:	Discrete time index, frequency index, antenna index at transmitter, antenna index at receiver
$h_{m,q,r,s}$:	Sampled channel transfer function
M, Q:	Number of samples in time and frequency
$N_{\text{Tx}}, N_{\text{Rx}}$:	Number of transmit antennas, number of receive antennas
$\mathbf{h}$:	Vector of index-limited transfer function
P:	Number of MPCs
η_p:	Complex path weight
ω_p, ν_p:	Doppler shift and normalized Doppler shift of the pth MPC
$\omega_{\text{Dmax}}, \nu_{\text{Dmax}}$:	Maximum Doppler shift, maximum normalized Doppler shift
τ_p, θ_p:	Delay and normalized delay of the pth MPC
$\tau_{\text{max}}, \theta_{\text{max}}$:	Maximum delay, maximum normalized delay
φ_p, ζ_p:	AoD and normalized AoD of the pth MPC
$\varphi_{\text{max}}, \varphi_{\text{min}}$:	Maximum and minimum AoD
$\zeta_{\text{max}}, \zeta_{\text{min}}$:	Maximum and minimum normalized AoD
ψ_p, ξ_p:	AoA and normalized AoA of the pth MPC
$\psi_{\text{max}}, \psi_{\text{min}}$:	Maximum and minimum AoD
$\xi_{\text{max}}, \xi_{\text{min}}$:	Maximum and minimum normalized AoD
f_C, c:	Carrier frequency, speed of light
ν_{max}:	Maximum velocity of user
W:	Band-limiting region
I:	Index set
$\nu_m^{(d)}(W, I)$:	dth one-dimensional DPS sequence
$\nu_{\mathbf{m}}^{(d)}(W, I)$:	dth multidimensional DPS sequence
$\mathbf{v}(d)(W, I)$:	One-dimensional or multidimensional DPS vector
$\lambda_d(W, I)$:	Eigenvalue of dth DPS sequence
D, D':	Subspace dimension and essential subspace dimension
$U_d(\nu), \widetilde{U}_d(\nu)$:	DPS wave function and approximate DPS wave function
$\alpha_d, \tilde{\alpha}_d$:	dth basis coefficient and approximate basis coefficient of DPS subspace representation of $\mathbf{h}$

$\gamma_{p,d}, \widetilde{\gamma}_{p,d}$: dth basis coefficient and approximate basis coefficient of DPS subspace representation of the pth MPC

r_i, D_i: Resolution factor and maximum number of one-dimensional DPS vectors in time ($i = 0$), frequency ($i = 1$), space at the transmitter ($i = 2$), and space at the receiver ($i = 3$)

$E_{\max}^2$: Maximum squared accuracy of hardware

$\text{bias}_{\hat{\mathbf{h}}^D}^2$: Squared bias of the D-dimensional subspace representation of $\mathbf{h}$

$C_{\hat{\mathbf{h}}^D}$: Computational complexity of the D-dimensional subspace representation of $\mathbf{h}$

ACKNOWLEDGMENTS

REFERENCES

[1] L. M. Correia, Ed., *Mobile Broadband Multimedia Networks Techniques, Models and Tools for 4G*, Elsevier, New York, NY, USA, 2006.

[2] F. Kaltenberger, G. Steinböck, R. Kloibhofer, R. Lieger, and G. Humer, "A multi-band development platform for rapid prototyping of MIMO systems," in *Proceedings of ITG Workshop on Smart Antennas*, pp. 1–8, Duisburg, Germany, April 2005.

[3] J. Kolu and T. Jamsa, "A real-time simulator for MIMO radio channels," in *Proceedings of the 5th International Symposium on Wireless Personal Multimedia Communications (WPMC '02)*, vol. 2, pp. 568–572, Honolulu, Hawaii, USA, October 2002.

[4] Azimuth Systems Inc., "ACE 400NB MIMO channel emulator," Product Brief, 2006, http://www.azimuthsystems.com/files/public/PB_Ace400nb_final.pdf.

[5] Spirent Communications Inc., "SR5500 wireless channel emulator," Data Sheet, 2006, http://www.spirentcom.com/documents/4247.pdf.

[6] T. Zemen and C. F. Mecklenbräuker, "Time-variant channel estimation using discrete prolate spheroidal sequences," *IEEE Transactions on Signal Processing*, vol. 53, no. 9, pp. 3597–3607, 2005.

[7] R. Clarke, "A statistical theory of mobile-radio reception," *The Bell System Technical Journal*, vol. 47, no. 6, pp. 957–1000, 1968.

[8] W. Jakes, *Microwave Mobile Communications*, John Wiley & Sons, New York, NY, USA, 1974.

[9] M. Pätzold and F. Laue, "Statistical properties of Jakes' fading channel simulator," in *Proceedings of the 48th IEEE Vehicular Technology Conference (VTC '98)*, vol. 2, pp. 712–718, Ottawa, Canada, May 1998.

[10] M. F. Pop and N. C. Beaulieu, "Limitations of sum-of-sinusoids fading channel simulators," *IEEE Transactions on Communications*, vol. 49, no. 4, pp. 699–708, 2001.

[11] P. Dent, G. E. Bottomley, and T. Croft, "Jakes fading model revisited," *Electronics Letters*, vol. 29, no. 13, pp. 1162–1163, 1993.

[12] Y. Li and X. Huang, "The simulation of independent Rayleigh faders," *IEEE Transactions on Communications*, vol. 50, no. 9, pp. 1503–1514, 2002.

[13] Y. R. Zheng and C. Xiao, "Simulation models with correct statistical properties for Rayleigh fading channels," *IEEE Transactions on Communications*, vol. 51, no. 6, pp. 920–928, 2003.

[14] A. G. Zajić and G. L. Stüber, "Efficient simulation of Rayleigh fading with enhanced de-correlation properties," *IEEE Transactions on Wireless Communications*, vol. 5, no. 7, pp. 1866–1875, 2006.

[15] T. Zemen, C. Mecklenbräuker, F. Kaltenberger, and B. H. Fleury, "Minimum-energy band-limited predictor with dynamic subspace selection for time-variant flat-fading channels," to appear in *IEEE Transactions on Signal Processing*.

[16] T. Zemen, "OFDM multi-user communication over time-variant channels," Ph.D. dissertation, Vienna University of Technology, Vienna, Austria, July 2004.

[17] D. Slepian, "Prolate spheroidal wave functions, Fourier analysis, and uncertainty—V: the discrete case," *The Bell System Technical Journal*, vol. 57, no. 5, pp. 1371–1430, 1978.

[18] D. J. Thomson, "Spectrum estimation and harmonic analysis," *Proceedings of the IEEE*, vol. 70, no. 9, pp. 1055–1096, 1982.

[19] S. Dharanipragada and K. S. Arun, "Bandlimited extrapolation using time-bandwidth dimension," *IEEE Transactions on Signal Processing*, vol. 45, no. 12, pp. 2951–2966, 1997.

[20] D. B. Percival and A. T. Walden, *Spectral Analysis for Physical Applications*, Cambridge University Press, Cambridge, UK, 1963.

[21] F. Kaltenberger, T. Zemen, and C. W. Ueberhuber, "Low complexity simulation of wireless channels using discrete prolate spheroidal sequences," in *Proceedings of the 5th Vienna International Conference on Mathematical Modelling (MATHMOD '06)*, Vienna, Austria, February 2006.

[22] D. Slepian and H. O. Pollak, "Prolate spheroidal wave functions, Fourier analysis and uncertainty—I," *The Bell System Technical Journal*, vol. 40, no. 1, pp. 43–64, 1961.

[23] A. Papoulis, *Probability, Random Variables and Stochastic Processes*, McGraw-Hill, New York, NY, USA, 3rd edition, 1991.

[24] H. Holma and A. Tskala, Eds., *WCDMA for UMTS*, John Wiley & Sons, New York, NY, USA, 2nd edition, 2002.

[25] M. Steinbauer, A. F. Molisch, and E. Bonek, "The double-directional radio channel," *IEEE Antennas and Propagation Magazine*, vol. 43, no. 4, pp. 51–63, 2001.

[26] P. Almers, E. Bonek, A. Burr, et al., "Survey of channel and radio propagation models for wireless MIMO systems," *EURASIP Journal on Wireless Communications and Networking*, vol. 2007, Article ID 19070, 19 pages, 2007.

[27] Members of 3GPP, "Technical specification group radio access network; User Equipment (UE) radio transmission and reception (FDD)," Tech. Rep. 3GPP TS 25.101 version 6.4.0, 3GPP, Valbonne, France, March 2004.

[28] V. Erceg, L. Schumacher, P. Kyritsi, et al., "TGn channel models," Tech. Rep. IEEE P802.11, Wireless LANs, Garden Grove, Calif, USA, May 2004.

[29] V. Degli-Esposti, F. Fuschini, E. M. Vitucci, and G. Falciasecca, "Measurement and modelling of scattering from buildings," *IEEE Transactions on Antennas and Propagation*, vol. 55, no. 1, pp. 143–153, 2007.

[30] T. Pedersen and B. H. Fleury, "A realistic radio channel model based on stochastic propagation graphs," in *Proceedings of the 5th Vienna International Conference on Mathematical Modelling (MATHMOD '06)*, Vienna, Austria, February 2006.

[31] O. Norklit and J. B. Andersen, "Diffuse channel model and experimental results for array antennas in mobile environments," *IEEE Transactions on Antennas and Propagation*, vol. 46, no. 6, pp. 834–840, 1998.

[32] N. Czink, E. Bonek, X. Yin, and B. Fleury, "Cluster angular spreads in a MIMO indoor propagation environment," in *Proceedings of the 16th International Symposium on Personal, Indoor and Mobile Radio Communications (PIMRC '05)*, vol. 1, pp. 664–668, Berlin, Germany, September 2005.

[33] F. Kaltenberger, G. Steinböck, G. Humer, and T. Zemen, "Low-complexity geometry based MIMO channel emulation," in *Proceedings of European Conference on Antennas and Propagation (EuCAP '06)*, Nice, France, November 2006.

[34] T. K. Moon and W. Stirling, *Mathematical Methods and Algorithms*, Prentice-Hall, Upper Saddle River, NJ, USA, 2000.

Florian Kaltenberger was born in Vienna, Austria, in 1978. He received his Diploma (Dipl.-Ing. degree) and his Ph.D. degree both in technical mathematics from the Vienna University of Technology in 2002 and 2007, respectively. During the summer of 2001, he held an internship position with British Telecom, BT Exact Technologies in Ipswich, UK, where he was working on mobile video conferencing applications. After his studies, he started as a Research Assistant at the Vienna University of Technology, Institute for Advanced Scientific Computing, working on distributed signal processing algorithms. In 2003, he joined the wireless communications group at the Austrian Research Centers GmbH, where he is currently working on the development of low-complexity smart antenna and MIMO algorithms as well as on the ARC SmartSim real-time hardware channel simulator. His research interests include signal processing for wireless communications, MIMO communication systems, receiver design and implementation, MIMO channel modeling and simulation, and hardware implementation issues.

Thomas Zemen was born in Mödling, Austria, in 1970. He received the Dipl.-Ing. degree (with distinction) in electrical engineering from Vienna University of Technology in 1998 and the Ph.D. degree (with distinction) in 2004. He joined Siemens Austria in 1998, where he worked as Hardware Engineer and Project Manager for the radio communication devices department. He was engaged in the development of a vehicular GSM telephone system for a German car manufacturer. From October 2001 to September 2003, Mr. Zemen was delegated by Siemens Austria as a Researcher to the mobile communications group at the Telecommunications Research Center Vienna (ftw.).

Since October 2003, Thomas Zemen has been with the Telecommunications Research Center, Vienna, working as a Researcher in the strategic I0 project. His research interests include orthogonal frequency division multiplexing (OFDM), multiuser detection, time-variant channel estimation, iterative MIMO receiver structures, and distributed signal processing. Since May 2005, Thomas Zemen leads the project "Future Mobile Communications Systems-Mathematical Modeling, Analysis, and Algorithms for Multi Antenna Systems" which is funded by the Vienna Science and Technology Fund (Wiener Wissenschafts-, Forschungs- und Technologiefonds—WWTF). Dr. Zemen teaches "MIMO Communications" as external lecturer at Vienna University of Technology.

Christoph W. Ueberhuber received the Dipl.-Ing. and Ph.D. degrees in technical mathematics and the Venia Docendi Habilitation degree in numerical mathematics from the Vienna University of Technology, Vienna, Austria, in 1973, 1976, and 1979, respectively. He has been with the Vienna University of Technology since 1973 and is currently a Professor of numerical mathematics. He has published 15 books and more than 100 papers in journals, books, and conference proceedings. His research interests include numerical analysis, high-performance numerical computing, and advanced scientific computing.

Research Article

A Time-Variant MIMO Channel Model Directly Parametrised from Measurements

Nicolai Czink,[1,2] Thomas Zemen,[1] Jukka-Pekka Nuutinen,[3] Juha Ylitalo,[3] and Ernst Bonek[4]

[1] *Telecommunications Research Center Vienna (FTW), 1220 Vienna, Austria*

[2] *Smart Antennas Research Group, Stanford University, Stanford, CA 94305, USA*

[3] *Elektrobit Ltd., 90570 Oulu, Finland*

[4] *Institute of Communications and Radio Frequency Engineering, Vienna University of Technology, 1040 Vienna, Austria*

Correspondence should be addressed to Nicolai Czink, czink@ftw.at

This paper presents the Random-Cluster Model (RCM), a stochastic time-variant, frequency-selective, propagation-based MIMO channel model that is directly parametrised from measurements. Using a fully automated algorithm, multipath clusters are identified from measurement data without user intervention. The cluster parameters are then used to define the propagation environment in the RCM. In this way, the RCM provides a direct link between MIMO channel measurements and MIMO channel modelling. For validation, we take state-of-the-art MIMO measurements, and parametrise the RCM exemplarily. Using three different validation metrics, namely, mutual information, channel diversity, and the novel Environment Characterisation Metric, we find that the RCM is able to reflect the measured environment remarkably well.

1. Introduction

Multiple-input multiple-output technology (MIMO) [1] made its way in the recent years from an information-theoretic shooting star [2] to actual products on the mass market [3, 4]. Currently the 3GPP [5] is standardising MIMO for the next generation's mobile communications, what is called Long Term Evolution (LTE) as well as IEEE is standardising MIMO for WiMAX [6]. Already information theory told that the promise of increased spectral efficiency of MIMO systems is *only* available when the radio channel permits, but this seems to have faded out of people's memory.

Despite this fact, numerous algorithms were developed, mostly considering ideal uncorrelated i.i.d. Rayleigh fading channels between the transmit and receive antennas, which is only true in rich-scattering environments with sufficiently large antenna spacings at both transmitter and receiver. Otherwise, the performance of the algorithms deteriorates. To reach the goal of gigabit transmissions over the wireless link, one needs to include the knowledge of the actual channel into the algorithms. Thus, an accurate model of the propagation channel is paramount.

One can distinguish between three different types of MIMO channel models: (i) channel models for developing signal-processing algorithms, for example, [7, 8]. These models describe the radio channel by the *correlations between the different links*, established between individual antenna elements. This makes the model mathematically tractable, yet inaccurate when it comes to reflecting real-world propagation conditions, because current correlation-based models always base on the Rayleigh-fading (or, to some extent, Ricean fading) assumption. While the so-called "Kronecker" model [7] is favoured by many people because it can be treated by random-matrix theory [9], the Weichselberger Model [8] shows a much better fit to measurement data [10, 11]. (ii) channel models for MIMO deployment in a given environment, for example, ray-tracing [12, 13]. These models try to predict MIMO conditions given a map (or floor plan) for optimal positioning of MIMO-enabled base stations, which comes with high demands on computational power and accuracy of environment data bases; (iii) channel models for testing of algorithms and systems, for example, [14–16, Chapter 6.8]. These models typically represent a certain kind of propagation scenario (like indoor offices,

or outdoor picocells), without considering a specific propagation environment. This is achieved by modelling the *propagation environment* in a *stochastic* way. Such models usually have a medium complexity and represent realistic channels very well, however a closed-form expression of the channel model, as in the first case, does not exist. The major difference between these models is their ability to describe time variation.

A time-variant channel is an essential feature of *mobile* communications. The 3GPP Spatial Channel Model (SCM) [14] is well suited for simulating random-access communications. It models the channel in blocks (so-called "drops"), during which the channel only undergoes Doppler fading, but after a drop, the channel changes completely. This assumption makes it impossible to test signal processing algorithms that track the channel parameters between different snapshots. Additionally, the abrupt changes between the drops are challenging for hardware testing using channel simulators, since the device under test and the channel model need to be synchronized. A major improvement is the WINNER II geometry-based stochastic channel model [15], which includes a smooth transition between drops. This smooth transition is only provided by the full implementation of the WINNER II model. The popular downscaled version "clustered-delay line" does not provide the basis to track the channel! The COST 273 MIMO channel model [16, Chapter 6.8] does not use the concept of drops, but intrinsically models the channel in a smooth way. While the user is moving through a randomly-generated map, he is illuminated via groups of different propagation paths depending on his location on this map. When the receiver moves out of a certain region "visibility region", a particular group of paths fades out, and vice versa. Unfortunately, the COST 273 model is not yet completely parametrised, nor fully implemented.

1.1. Contribution. In this paper, we present the novel Random-Cluster Model (RCM), a geometry-based stochastic MIMO channel model for time-variant frequency-selective channels. The application of the RCM focuses on algorithm and system testing, yet it is parametrised directly from measurements.

The Random-Cluster Model uses multipath clusters to model the radio channel. Generally, multipath clusters can be seen as groups of propagation paths having similar parameters. We concisely define a cluster by its mathematical description provided in Section 2.2. Clusters allow to characterise the propagation environment in a compact way using much less parameters than characterisation by individual multipath components (MPCs). This data reduction is the primary purpose for using clusters in radio channel models. Clusters were first only observed in delay domain by Saleh and Valenzuela [17]. Their concept was extended to the joint angle-of-arrival/delay domain in [18]. Recently [19] developed a test to prove the existence or non-existence of clusters in propagation path estimates from channel measurements, showing that clusters indeed exist independent of the authors' view. We were able to match clusters to real-world scattering objects [20].

Several innovations were necessary to construct the RCM, some of which have been introduced in conference papers. First, to accurately parametrise the RCM, *automatic clustering techniques* are necessary. The first semiautomatic approach for clustering MIMO channel data was introduced in [21]. We gradually extended these ideas by a meaningful *joint* clustering approach [22], a power-weighted clustering algorithm [23], a criterion to decide on the number of clusters, a reasonable initial guess, and the ability to track clusters over multiple time-variant snapshots [24]. The mere fact that clusters *can* be tracked demonstrates that clustering makes sense showing that they obviously stem from scattering objects. The automatic parametrisation by identifying clusters *without user intervention* turned out to be essential to process a large amount of multiantenna measurement data.

Regarding the ability to describe time-variant channels, the RCM is capable to model random-access channels, and, in addition, to cover continuous transmission in a time-variant environment as well by creating smoothly time-variant channel realisations. A major innovation of the RCM is the concept of *linearly moving clusters*. In this article, we will use the RCM to model smoothly time-variant channels. (A first description of the RCM, modelling random-access channels only was provided in [25], and [26] briefly outlines the ideas of using clusters for time-variant channel modelling.)

The RCM is a *stochastic* MIMO channel model, yet it is parametrised directly from measurements. By double-directional MIMO channel measurements in a specific environment, a single multivariate pdf of the cluster parameters is created, which is representative for the electromagnetic wave propagation in this environment. The parameters of a single realisation are drawn from this distribution. In this way, the RCM is a stochastic channel model, deriving its parameters directly from measurements.

The complexity of the RCM should be divided into (i) the parametrisation complexity and (ii) the execution complexity. Regarding the parametrisation complexity, the RCM is parametrised automatically from measurements, even if the number of parameters appears to be high. The execution complexity of the RCM is governed by the calculation of the channel matrix, as in all other prominent physical channel models [27]. It adds up to $22 \cdot LN_{Tx}N_{Rx}B$ real operations, where L denotes the number of MPCs, N_{Tx} and N_{Rx} denote the number of transmit and receive antennas, respectively, and B denotes the number of frequency samples, for which the channel matrix is calculated.

The ultimate challenge for any channel model is its comparison to measurements. We will describe the extensive validation of the RCM against measurements using three different validation metrics: (i) mutual information [2], (ii) channel diversity [28], and (iii) the novel Environment Characterisation Metric [29]. We find that the RCM is able to reflect the measured time-variant environment noticeably well. Additionally, we will demonstrate why the popular mutual information "capacity" is a poor validation metric for *time variant* MIMO channel models.

1.2. Organisation. This article is organised as follows. Section 2 provides a first overview of the features of the Random Cluster Model. Section 2.1 outlines the structure of the RCM, Section 2.2 details the description of the environment by multipath clusters. The initialisation of the model is provided in Section 2.3, and details on the implementation of the time variance are given in Section 2.4. Section 3 describes the model validation by first outlining the validation framework. We then introduce the validation metrics used in Section 3.2, followed by the validation results in Section 3.3. Finally, Section 4 concludes the article. In Appendix A, we provide an overview of the measurements used for parametrisation and validation.

2. The Random-Cluster Model

The RCM is based on the concept of multipath clusters. The most significant feature of the RCM is that it is parametrised directly from *channel measurements* by an *automatic* procedure. In this way, the RCM is *specific to the environment*; it closes the gap between channel measurements and channel modelling. Nonetheless it is a stochastic model as we will clarify shortly.

The novel approach of the RCM is to describe the time-variant geometry of the channel *completely* by *statistical cluster parameters*. Clusters provide a compact way of describing the underlying propagation environment. To accurately parametrise the clusters, we extract their parameters from measurements. An important feature of the MIMO channel also reflected by the model is the coupling between propagation paths in space and time, also known as the double-directional MIMO channel model [30]. To enable time-variance, *clusters* may move, relative to the Tx or Rx. By this, the RCM creates correlated snapshots in time of the propagation environment.

Summarising, the model has the following properties. It is

  (i) cluster-based,
 (ii) propagation-based, but stochastic,
(iii) double-directional,
 (iv) time-variant.

What the RCM Provides. The main focus of the RCM is link-level simulation, for both algorithm testing and device testing. It is well suited to reflect time-variant scenarios that are similar, but not equal to the ones measured before. A major feature is that the parametrisation of the RCM, directly derived from measurements, is achieved automatically. In this way it perfectly fills the gap between channel *sounding* and channel *simulation*. Typical applications include testing in specifically challenging channel situations, or in specific application scenarios.

In contrast to "playback simulations" [31] where previously recorded impulse response data from a channel sounder are used to directly model the environment, the RCM is neither fixed in bandwidth, antenna array parameters, or simulation duration.

What the RCM Does Not Provide. By the way it is parametrised, the RCM is very specific in reflecting a certain type of environment. Being rooted in the COST 273 model [16, Chapter 6.8], one might think that the RCM is an all-purpose model. The model user will be warned that it does not perform like this. Many aspects that make a model very general have been intentionally omitted in the RCM in order to reduce complexity, for example, a dedicated path loss calculation, or a description of general environments.

For scenarios close to the measured ones, the RCM will still perform better than other (even standardised) models available, but proper parametrisation is always necessary.

The RCM is definitely not intended for supporting MIMO *deployment*. Since the model does not include any geometry, it is not suited for predicting the properties of the electromagnetic field in specific locations on a map, particularly not in environments that were not measured before.

2.1. General Model Structure. In the following we describe the RCM by its flow diagram shown in Figure 1. The RCM consists of two major parts: the *initialisation*, and the implementation of *smooth time variation*:

(1) During initialisation, a first snapshot of the scenario is generated from the environment parameter function.

(2) The implementation of the smooth time variation is split in two parts: (i) moving the clusters introduces small-scale changes to the environment and generates the Doppler-induced fading; (ii) the birth/death-process accounts for shadowing and large-scale changes.

Both of these parts rely on an accurate parametrisation of the environment. In the next paragraphs we will first detail how the environment is described. Subsequently we will explain the model flow step by step.

2.2. Environment Description—Multipath Clusters. Multipath clusters are the basis for the RCM. Each cluster is described by a number of parameters (Table 1), which are stacked into the cluster parameter vector Θ_c. We distinguish between the *cluster location parameters* (mean delay, azimuth and elevation positions), *cluster spread parameters* (delay spread, angular spreads), *cluster power parameters* (power of the cluster and power of the snapshot in which the cluster exists), *cluster number parameters* (number of paths within the cluster, average number of coexisting clusters in the same snapshot), and *cluster movement parameters* (change rates of the cluster location and power parameters, and cluster lifetime).

A time-variant environment may contain transitions between different *propagation conditions*, for example, from LOS to NLOS and back. Clusters in these propagation conditions have quite different properties. Different propagation conditions are mainly reflected by two simple parameters: the snapshot power and the number of clusters. These two parameters are included in the set of cluster parameters,

FIGURE 1: Flow diagram of the Random-cluster model.

TABLE 1: Cluster parameters of a single cluster, contained in $\mathbf{\Theta_c}$.

Symbol	Cluster parameter
$\overline{\tau}$	Cluster mean delay
$\overline{\varphi}_{Tx}$	Azimuth cluster position at Tx
$\overline{\varphi}_{Rx}$	Azimuth cluster position at Rx
$\overline{\theta}_{Tx}$	Elevation cluster position at Tx
$\overline{\theta}_{Rx}$	Elevation cluster position at Rx
σ_{τ}	Cluster delay spread
$\sigma_{\varphi_{Tx}}$	Cluster azimuth spreads seen from Tx
$\sigma_{\varphi_{Rx}}$	Cluster azimuth spreads seen from Rx
$\sigma_{\theta_{Tx}}$	Cluster elevation spreads seen from Tx
$\sigma_{\theta_{Rx}}$	Cluster elevation spreads seen from Rx
σ_{γ}^2	Cluster mean power
ρ	Total snapshot power, in which the cluster occurs
N_c	Number of clusters coexisting in the snapshot
N_p	Number of paths within a cluster
$\Delta\sigma_{\gamma}^2$	Change rate of cluster power per travelled wavelength in dB
$\Delta\overline{\tau}$	Change rate of cluster mean delay per travelled wavelength
$\Delta\overline{\varphi}_{Rx}$	Change rate of cluster mean AOA per travelled wavelength
$\Delta\overline{\varphi}_{Tx}$	Change rate of cluster mean AOD per travelled wavelength
$\Delta\overline{\theta}_{Rx}$	Change rate of cluster mean EOA per travelled wavelength
$\Delta\overline{\theta}_{Tx}$	Change rate of cluster mean EOD per travelled wavelength
Λ	Cluster lifetime

receiver having a certain power, a certain direction of departure, direction of arrival, and delay. Extending the concept of a single MPC, a cluster shows a certain spread in its parameters, describing the size of the cluster in space.

This leads to a significant reduction in the number of parameters. One cluster describing a manifold of multipath components showing similar propagation parameters is described by only 21 parameters (see Table 1), while a single MPC already needs 12 parameters (such seemingly large numbers of parameters are necessary for a *time-variant* description of clusters and propagation paths).

When we look at a cluster that stems from multiple bounces of an electromagnetic wave on its way from Tx to Rx, Figure 2 shows how a cluster appears when perceived from Tx and Rx separately. The cluster splits up in two parts. For single-bounce scattering, these two parts of a cluster overlap physically. For a direct path (line-of-sight), the cluster contains only a strong, single path. From the cluster parameters, one cannot deduct whether the cluster stems from single or from multiple-bounces scattering. From a modelling perspective concentrating on clusters, however, this knowledge is redundant (the same applies to MIMO modelling by multipath components). Note that we are using

being *cluster selection parameters*. They label clusters for specific propagation conditions in a statistical way.

2.2.1. Geometrical Interpretation. A straight-forward extension of a MIMO channel description by single, discrete MPCs, is the usage of multipath clusters.

Clusters are able to describe a double-directional wave-propagation environment in the same way as multipath components do. Figure 2 illustrates this concept. A cluster represents a unique link between the transmitter and the

FIGURE 2: Geometrical interpretation of the RCM, demonstrated for a single cluster.

multiple clusters to describe the multipath structure of the radio channel, but Figure 2 shows just one cluster.

2.2.2. Environment pdf. In a measured environment, different kinds of clusters occur. We regard the parameters of these clusters as an ensemble of a multivariate distribution, which we call the *environment pdf*, (we use the established statistical notation, where $\boldsymbol{\theta}_c$ is the argument of the pdf of the random vector $\boldsymbol{\Theta}_c$),

$$\boldsymbol{\Theta}_{\text{env}} \doteq f_{\boldsymbol{\Theta}_c}(\boldsymbol{\theta}_c). \tag{1}$$

The environment pdf characterises the multipath structure in a *specific measured environment*. In this way, the environment is completely parametrised by a description that is purely statistical. In some cases, this multivariate distribution may be multimodal and does not necessarily follow a simple closed-form distribution.

2.2.3. Parametrisation. The parameters of the RCM are characterized by the environment pdf, which can conveniently be estimated from MIMO channel measurements in a straightforward way.

(1) *MIMO channel measurements* provide multiple impulse responses of the scenario. While the channel sounder continuously 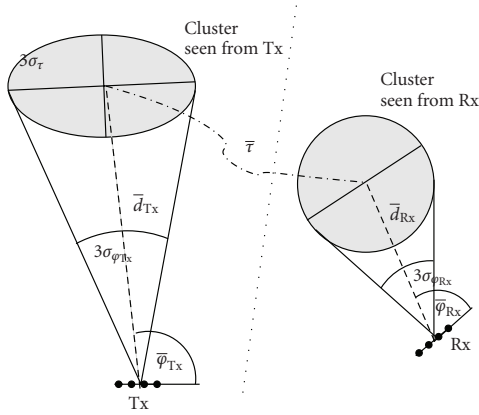records frequency-selective MIMO channel matrices at each time instant "*snapshots*", the transmitter is moved to capture the time-variant properties of the scenario.

(2) *Propagation paths are estimated* from each snapshot of the channel measurements using a high-resolution parameter estimation. For this purpose we used the Initialization-and-Search-Improved SAGE (ISIS) estimator [32] to estimate 100 paths from every measured snapshot.

(3) We *identify and track clusters* in these propagation paths using the fully automatic framework presented in [24]. This framework has the following key features.

(a) The initial guess algorithm identifies the cluster locations by separating clusters as far as possible in the parameter space while taking already existing clusters from previous snapshots into account. The number of clusters is estimated by a power-threshold criterion.

(b) The clustering is optimized using the KPowerMeans algorithm [23], which makes clusters as compact as possible. This is achieved by including the concept of path power into the classic KMeans algorithm and by enabling joint clustering by appropriate scaling of the input data.

(c) Clusters are tracked using a Kalman filter between snapshots, where a probabilistic cluster fitting criterion decides whether a cluster has actually moved or has to be regarded as new.

As a result we obtain the parameters of all clusters in the measured environment, as described in Table 1. The change-rate parameters and cluster lifetimes are determined by the tracking of the clusters. Typical examples of the change-rate parameters and more discussion about their physical interpretation are provided in [33].

(1) We *estimate the environment pdf* from all identified clusters using a kernel density estimator (KDE) [34].

The KDE approximates the underlying distribution by a sum of kernels. In this way, even multimodal distributions can be described easily. As result, the environment pdf can be written as

$$\boldsymbol{\Theta}_{\text{env}} = f_{\boldsymbol{\Theta}_c}(\boldsymbol{\theta}_c) = \frac{1}{N_K} \sum_{i=1}^{N_K} K\left(\boldsymbol{\theta}_c, \boldsymbol{\mu}_{\boldsymbol{\Theta}_i}, \mathbf{C}_{\boldsymbol{\Theta}_i}\right), \tag{2}$$

where $\boldsymbol{\mu}_{\boldsymbol{\Theta}_i}$ and $\mathbf{C}_{\boldsymbol{\Theta}_i}$ denote the mean and covariance of the ith kernel, and N_K denotes the number of kernels used.

To parametrise the environment pdf for the RCM, we use Gaussian kernels, hence a Gaussian mixture pdf, such that

$$K\left(\boldsymbol{\theta}_c, \boldsymbol{\mu}_{\boldsymbol{\Theta}_i}, \mathbf{C}_{\boldsymbol{\Theta}_i}\right) = \frac{1}{(2\pi)^{D/2} |\mathbf{C}_{\boldsymbol{\Theta}_i}|^{1/2}}$$
$$\times exp\left(-\frac{1}{2}\left(\boldsymbol{\theta}_c - \boldsymbol{\mu}_{\boldsymbol{\Theta}_i}\right)^{\text{T}} \mathbf{C}_{\boldsymbol{\Theta}_i}^{-1}\left(\boldsymbol{\theta}_c - \boldsymbol{\mu}_{\boldsymbol{\Theta}_i}\right)\right), \tag{3}$$

where $D = 21$ denotes the dimension of the cluster parameter vector. We used Gaussian kernels for their low complexity and analytical tractability. Furthermore, Gaussian kernels manage to describe all kinds of (continuous) pdfs with low error [35].

The kernel parameters $\boldsymbol{\mu}_{\boldsymbol{\Theta}_i}$ and $\mathbf{C}_{\boldsymbol{\Theta}_i}$ need to be estimated. The input data for this estimation are the identified clusters from a measurement route.

A straight-forward way to find the kernel parameters is to choose the N_K equal to the total number of identified clusters. Each individual identified cluster is used as (mean) parameter for an individual kernel. The variances of the

kernel can then be estimated using the minimum average mean integrated squared error (AMISE) criterion [35]. This parametrisation approach is the most accurate one, although the number of kernels may become quite large.

Of course, the obtained environment pdf is very specific to the measured environment since it is directly parametrised from measurements.

Figure 3 shows four different two-dimensional cuts of the same environment pdf, which was evaluated from a measurement run at 2.55 GHz in the office environment, described in the appendix. These two-dimensional pdfs are colour coded from black (low probability) to white (high probability).

It becomes obvious that the environment pdf is indeed a multimodal distribution, strongly depending on which parameters are observed. For example, Figure 3(a) demonstrates that clusters with large mean delay usually have weaker power, which was to be expected. Additionally, Figure 3(b) details from which Rx directions clusters with stronger power appear. Some of the cluster parameters are even intrinsically correlated. For instance, Figures 3(c)-3(d) show that there is a correlation between the cluster azimuth spreads. Additional values of the environment pdf can be found in [33, 36, Chapter 7.4].

2.3. RCM Initialisation. The initialisation procedure generates the first snapshot of the model.

2.3.1. Drawing Initial Cluster Parameters. The environment pdf Θ_{env} provides a description for all kinds of clusters that were identified in the environment. To actually generate a snapshot, the momentary propagation condition of the environment must be selected. This is done by determining the intended snapshot power and the number of clusters (which are the cluster selection parameters). Their joint distribution function is contained in the environment pdf.

Thus, we draw cluster parameters in a stepwise procedure.

(i) First, we obtain the pdf of the number of clusters, $f(N_c)$, by marginalizing the environment pdf to the number of clusters, which is done by integrating the environment pdf over the other dimensions. Then the actual number of clusters for the first snapshot, $\widetilde{N}_c$, is determined by drawing a random sample from this pdf. Since the number of clusters must be an integer number, the ceiling of the drawn value is assigned to $\widetilde{N}_c$.

(ii) Then, we obtain the pdf of the snapshot power (given the number of clusters) by conditioning the environment pdf on the chosen number of clusters $\widetilde{N}_c$, and marginalising it to the snapshot power. From this marginal distribution $f(\rho \mid \widetilde{N}_c)$, the *intended* snapshot power, $\widetilde{\rho}$, is determined by drawing a random sample from this pdf. This intended snapshot is only used as a selection criterion for the clusters to be drawn in the next steps. In general, the sum power of the clusters will not exactly match the intended snapshot power.

(iii) Finally, to select a specific type of clusters, the environment pdf is conditioned on both the number of clusters and on the intended snapshot power, $f(\Theta_c \mid \widetilde{N}_c, \widetilde{\rho})$. From this final distribution, we draw $\widetilde{N}_c$ cluster parameter sets $\widetilde{\Theta}_c$.

These parameters are drawn from a multivariate sum-of-Gaussian distribution, which sometimes leads to invalid parameters because of the Gaussian tails. For this reason, the drawn spread parameters and the mean delay are lower-bounded by zero, the number of paths within a cluster is rounded to the next larger integer and lower bounded by one, and the drawn cluster lifetime is rounded to the closest integer value larger or equal to one. In this way, we can retain the low-complexity kernel density estimation but still create valid cluster parameters for the model.

These (post-processed) cluster parameters specify the multipath structure of the initial snapshot.

2.3.2. Placing Multipath Components within the Clusters.

(1) In every cluster c, the corresponding number of paths (which is an initial cluster parameter drawn before), $\widetilde{N}_{p,c}$, is placed as follows. Every path is described by the *path* parameters: complex amplitude (γ), total delay (τ), and the azimuth and elevation of arrival and departure, respectively, ($\varphi_{\mathrm{Tx/Rx}}, \theta_{\mathrm{Tx/Rx}}$).

The delay is drawn from a Gaussian distribution with its mean and variance given in the cluster parameters. Similarly, the angular parameters are drawn from a *wrapped* Gaussian distribution [37] (in the wrapped Gaussian distribution, all realisations are mapped to their principal value in $[-\pi, \pi)$), where the mean and variance are again determined in the cluster parameters (Table 1). All paths within a cluster show the same amplitude, $|\gamma_{p,c}| = \sqrt{\rho_c/\widetilde{N}_{p,c}}$, determined by the total cluster power and the number of paths within a cluster, and have a random phase, which is drawn from a uniform distribution $\mathcal{U}(-\pi, \pi)$.

After having placed paths in all clusters, the propagation environment of the initial snapshot is completely specified by its *multipath structure*.

2.3.3. Generating the MIMO Channel Matrix "System Model". To calculate the MIMO channel matrix, we use the common approach of a bandwidth filter and antenna filters [38].

The time-dependent MIMO channel transfer matrix is calculated from the multipath structure as

$$
\mathbf{H}(t, \Delta f) = \sum_{c=1}^{\widetilde{N}_c} \sum_{p=1}^{\widetilde{N}_{p,c}} \gamma_{p,c}(t)
$$
$$
\cdot \mathbf{a}_{\mathrm{Rx}}\left(\varphi_{\mathrm{Rx},p,c}(t), \theta_{\mathrm{Rx},p,c}(t)\right) \qquad (4)
$$
$$
\cdot \mathbf{a}_{\mathrm{Tx}}^{\mathrm{T}}\left(\varphi_{\mathrm{Tx},p,c}(t), \theta_{\mathrm{Tx},p,c}(t)\right)
$$
$$
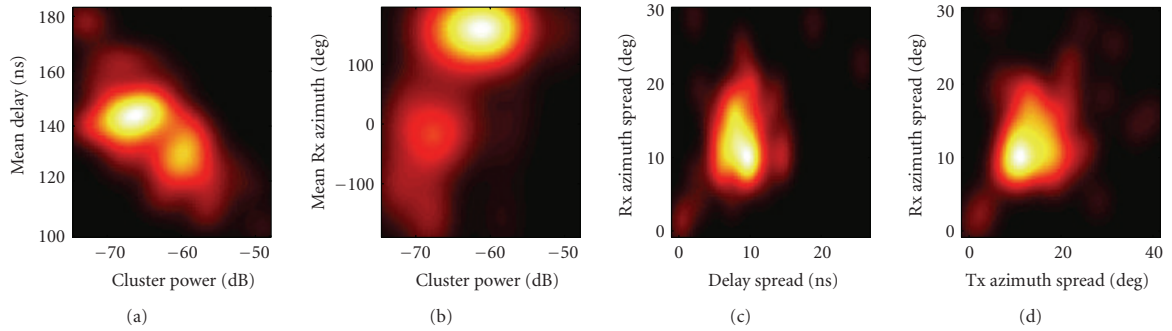\cdot \mathrm{e}^{-j2\pi\Delta f \tau_{p,c}(t)},
$$

FIGURE 3: Exemplary marginal distributions of the environment pdf.

at a certain frequency bin Δf equidistantly spaced on a limited bandwidth between $[f_0 - B/2, f_0 + B/2]$, where f_0 denotes the carrier frequency and B the simulated bandwidth. The antenna array patterns are described in $\mathbf{a}_{\text{Tx/Rx}}(\varphi_{\text{Tx/Rx}}, \theta_{\text{Tx/Rx}})$, and the subset p, c denotes the pth path in cluster c. This calculation dominates the computational complexity of the model (a low-complexity implementation of this equation is also available in [39]).

For the exemplary implementation of the RCM that we validated (see Section 3), we imply an 8×8 MIMO configuration with uniform linear arrays at both link ends, a bandwidth of 20 MHz, and 32 frequency bins. The centre frequency was set to either 2.55 GHz or to 5.25 GHz matching the measurement. An 8×8 configuration provides a much tougher test whether a model renders the spatial environment properties correctly than the 4×4 or 2×2 configurations envisaged for LTE. By including the actual antenna array pattern, the RCM can easily be extended to arbitrary array configurations other than ULAs.

2.4. Implementation of the Time Variation. After the generation of the initial snapshot, the RCM generates channels correlated in time. The implementation of the time variation, based on the novel idea of *linearly moving clusters*, is an integral part of the model. In this way, both stationary and nonstationary time-variant channels can be modelled.

2.4.1. Time Bases. We distinguish between small-scale and large-scale time variations. Small-scale variations, which introduce fading, take place every sampling instant. Large-scale variations, reflecting changes in the propagation structure, occur in less frequent intervals.

For this reason, the RCM distinguishes between two time bases: the *sampling time interval*, Δt_s, and the *cluster-lifetime interval*, Δt_Λ, where $\Delta t_\Lambda = N_\Lambda \cdot \Delta t_s$. Cluster lifetimes, Λ_c, are multiples of Δt_Λ (see Table 1).

2.4.2. Large-Scale Variation—Cluster Birth/Death Process. In time-variant scenarios, where at least one of the transceivers is moving, the propagation conditions can change

significantly. To introduce these large-scale changes into the model, we included a cluster birth/death process.

This birth/death process is motivated from observations in measurements, where clusters smoothly show up, exist over a period of time, and eventually fade away. We reflect this behaviour in our model by three parameters: (i) the cluster lifetime, responsible for the cluster death, (ii) a cluster birth pdf, and (iii) a fade-in/fade-out coefficient.

The lifetime of each cluster is already intrinsically defined in the cluster parameters (see Table 1), which was drawn from the environment pdf when the cluster was created. Cluster death is implemented by decreasing the lifetime of each cluster in every cluster lifetime interval, Δt_Λ. Dying clusters are fading out during the next cluster lifetime interval.

An additional probability mass function (pmf), describing the *number of cluster births per cluster lifetime interval*, is also extracted from the measurements. The extraction method and examples of extracted parameters are provided in [33]. According to this pmf, a number of new clusters are drawn every cluster lifetime interval. After drawing the number of new clusters, the actual parameters of these new clusters are drawn in the same way as described in the initialisation procedure in Section 2.3.1. New-born clusters fade in during the next cluster lifetime interval.

The appearance or disappearance of clusters is done exponentially in the small-scale updates, controlled by the cluster fade-in/fade-out coefficient $|\sigma_{\text{in/out}}|_{\text{dB}}$. Empirical evaluations showed that a maximum cluster attenuation of 10 dB provides best results, hence $|\sigma_{\text{in/out}}|_{\text{dB}} = 10/N_\Lambda$.

Note that our approach is different from using "visibility regions" [40], which cannot be used since we do not consider the actual geometry of the environment.

2.4.3. Small-Scale Variation—Cluster Movement. The RCM models small-scale changes by the movement of the clusters in parameter space. In every sampling time interval, the parameters of the paths within a cluster are linearly incremented. These increments are provided in the cluster parameters $\mathbf{\Theta}_c$ of the respective cluster (see Table 1).

The update equations of the pth path in the cth cluster for a moving station with speed v (in wavelengths per second) are given as

$$\tau_{p,c}(t + \Delta t_s) = \tau_{p,c}(t) + \Delta\overline{\tau}_c \cdot v\Delta t_s,$$

$$\varphi_{\text{Tx},p,c}(t + \Delta t_s) = \varphi_{\text{Tx},p,c}(t) + \Delta\overline{\varphi}_{\text{Tx},c} \cdot v\Delta t_s,$$

$$\varphi_{\text{Rx},p,c}(t + \Delta t_s) = \varphi_{\text{Rx},p,c}(t) + \Delta\overline{\varphi}_{\text{Rx},c} \cdot v\Delta t_s,$$

$$\theta_{\text{Tx},p,c}(t + \Delta t_s) = \theta_{\text{Tx},p,c}(t) + \Delta\overline{\theta}_{\text{Tx},c} \cdot v\Delta t_s, \quad (5)$$

$$\theta_{\text{Rx},p,c}(t + \Delta t_s) = \theta_{\text{Rx},p,c}(t) + \Delta\overline{\theta}_{\text{Rx},c} \cdot v\Delta t_s,$$

$$\left|\gamma_{p,c}(t + \Delta t_s)\right|_{\text{dB}} = \left|\gamma_{p,c}(t)\right|_{\text{dB}} + \Delta\sigma^2_{\gamma,c} \cdot v\Delta t_s.$$

In this way, clusters are moving in delay (causing Doppler shifts) and in angles, and they smoothly change their power. The speed v is a scalar defining how fast clusters move. The "direction" of movement is defined by the cluster movement parameters.

These small-scale changes intrinsically introduce correlated fading. This repeated update inherently creates a Doppler spectrum, where each individual path contributes with its Doppler shift $v_{p,c} = -f_0 \cdot v \cdot \Delta\overline{\tau}_c$ (equal for all paths within a cluster). Of course, linear movement is just a first-order approximation of the true movement of clusters, a more complex method can be found in [41]. However, the model validation will show that modelling movements linearly is sufficient to accurately reflecting the time-variant propagation environment.

Whenever a cluster is fading in or fading out due to the birth/death process, the path weights, $\gamma_{p,c}$, are additionally updated over the course of one cluster-lifetime interval by

$$\left|\gamma_{p,c}(t + \Delta t_s)\right|_{\text{dB}} = \left|\gamma_{p,c}(t + \Delta t_s)\right|_{\text{dB}} \pm |\sigma_{\text{in/out}}|_{\text{dB}}. \quad (6)$$

3. Model Validation

Validation is paramount, it scrutinises whether a model reflects important properties of the propagation channel. Particularly for MIMO channels, models need to reflect the *spatial structure* of the channel correctly.

We validated the RCM against MIMO channel measurements carried out with an Elektrobit Propsound CS wideband channel sounder at two centre frequencies of 2.55 GHz and 5.25 GHz. Details about the measurements and the validated scenarios are presented in Appendix A. For validation we will use three different validation metrics reflecting the spatial structure of the channels.

3.1. Validation Framework. We use the following procedure to validate the RCM (Figure 4).

(1) Perform radio channel measurements in representative scenarios and estimate propagation paths [32] from the measurements for every snapshot of the channel.

(2) Parametrise the RCM (see Section 2.2.3).
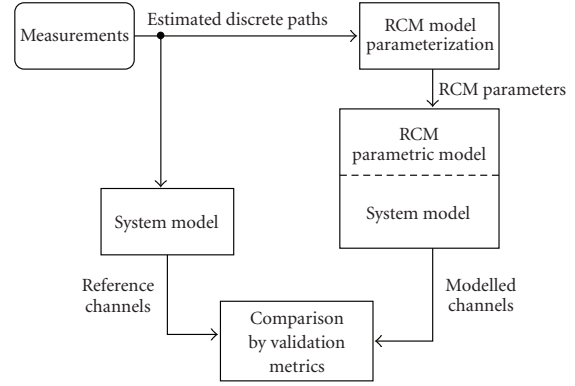
FIGURE 4: Validation framework.

(3) Generate *reference channels* by applying the system model (see Section 2.3.3) to the estimated paths parameters.

(4) Generate *smoothly time-variant modelled channels* by invoking the RCM.

(5) Compare the modelled channels with the reference channels according to the cdf of different validation metrics.

3.2. Validation Metrics. Before detailing the validation results, we present the different validation metrics. We concentrate on the validation of the *spatial properties* of the modelled channels.

3.2.1. Mutual Information. For the purpose of comparison with literature we take mutual information (MI) for model validation [42, 43]. (Quite frequently the term "capacity" is misused for mutual information.) However, we will show later in this section that MI has an intrinsic disadvantage, which disqualifies it as a good metric *for validating the double-directional multipath structure* of a time-varying channel.

We use the *narrowband MI* at frequency Δf and time t, which is defined as

$$I(t, \Delta f) = \log_2 \det\left[\mathbf{I} + \frac{\text{SNR}}{N_t}\mathbf{H}_n(t, \Delta f)\mathbf{H}_n^{\text{H}}(t, \Delta f)\right], \quad (7)$$

where $\mathbf{H}_n(t, \Delta f)$ denotes the *normalised* channel matrix, hence $\mathbf{H}_n = \text{const} \cdot \mathbf{H}$. We use the normalisation to keep the receive SNR constant, which corresponds to perfect power control at the Tx. In this case, the channel transfer matrix at every time instant is normalized separately as

$$\mathbf{H}_n(t, \Delta f) = \frac{1}{(1/M)\sum_{\Delta f}\|\mathbf{H}(t, \Delta f)\|_{\text{F}}^2}\mathbf{H}(t, \Delta f), \quad (8)$$

where M denotes the number of frequencies. Then, the validation metric reflects the spatial structure of the channel best. We chose an SNR of 10 dB for the following validation

evaluations. For creating a cdf, we use all time realisations and frequencies as our ensemble of samples.

The deficiencies of MI as a validation metric will now be demonstrated by a meaningful example. This example will also highlight the difference between *average MI* and *ergodic capacity*.

In Figure 5(a) we consider a *single snapshot* measured in the cafeteria environment (see Appendix A.2). This snapshot is described by a number of propagation paths with their parameters power, AoA, AoD, and delay. We now calculate the channel matrix of this scenario using the system model (4). Then, we create further channel realisations by just *changing the phases of the paths randomly*, but do not alter any other parameter. This method was introduced in [44] to generate multiple MIMO fading realisations from *a single measurement*. Note that this does not change the spatial structure of the channel at all. Finally, we calculate the MI for all these realisations according to (8).

Figure 5(b) shows the cdf of the so-computed MI. The *MI varies considerably*, even though the *spatial structure of the channel remains the same*. The reason for this effect is the fading created by randomly changing the phases of the paths. One can see that *mutual information fails to reflect the spatial structure* of a *single realisation* of an environment. A validation metric reflecting the *spatial structure* should provide one unique result, and not a widespread distribution. For this reason, MI is not suited to assess whether a channel model provides a correct spatial representation of the scenario or not.

As the spatial structure determines which gains the channel offers, the RCM strives to reflect the spatial structure as accurately as possible. Thus, also the validation metric should be specific to the spatial structure. Nevertheless, as MI is frequently used for validating MIMO channel models, we will also use MI in this paper, for reasons of comparison, but point out its deficiencies in the results.

3.2.2. Environment Characterisation Metric. The Environment Characterisation Metric (ECM) [29] is directly applied to the *path parameters* rather than to the channel matrix. This section shortly describes the significance of the ECM. For better readability, we will (i) enumerate all paths in each time instant from $l(t') = 1, \ldots, L(t')$, disregarding cluster structures for the time being, and (ii) skip the time index t' in the following derivations whenever it is redundant.

The metric copes with path parameters in different units (angles and delay). For every path l, the *angular data* is transformed into its coordinates on the unit sphere for both Rx and Tx. For angles of arrival the transformation is given as

$$\left[x_{\text{Rx},l} \quad y_{\text{Rx},l} \quad z_{\text{Rx},l} \right]$$
$$= \frac{1}{2} \left[\sin(\varphi_{\text{Rx},l}) \cdot \sin(\theta_{\text{Rx},l}) \quad \sin(\varphi_{\text{Rx},l}) \cdot \cos(\theta_{\text{Rx},l}) \quad \cos(\theta_{\text{Rx},l}) \right], \tag{9}$$

for angles at the Tx it reads similarly. The *delays* are scaled by the maximum expected delay that occurs in the considered

snapshots [45], hence $\tilde{\tau}_l = \tau_l/(\tau_l^{(\max)})$. So, every path is now described by seven *dimensionless* parameters collected in

$$\boldsymbol{\pi}_l = \left[x_{\text{Rx},l} \quad y_{\text{Rx},l} \quad z_{\text{Rx},l} \quad x_{\text{Tx},l} \quad y_{\text{Tx},l} \quad z_{\text{Tx},l} \quad \tilde{\tau}_l \right]^{\text{T}}, \tag{10}$$

and by its power $|\gamma_l|^2$. When considering only azimuthal propagation, the z-direction must be excluded. (Since the elevation estimation from our data was not trustworthy, we excluded elevation in the validation.)

The *environment characterization metric* (ECM) is defined as the empirical covariance matrix of the path parameter vector $\boldsymbol{\pi}$,

$$\mathbf{C}_\pi = \frac{\sum_{l=1}^{L} |\gamma_l|^2 (\boldsymbol{\pi}_l - \overline{\boldsymbol{\pi}})(\boldsymbol{\pi}_l - \overline{\boldsymbol{\pi}})^T}{\sum_{l=1}^{L} |\gamma_l|^2}, \tag{11}$$

with the mean parameter vector given as $\overline{\boldsymbol{\pi}} = (\sum_{l=1}^{L} |\gamma_l|^2 \boldsymbol{\pi}_l)/ (\sum_{l=1}^{L} |\gamma_l|^2)$.

The ECM has the following properties [29].

(i) The metric is *system independent* as it is calculated from the propagation paths directly. Additionally, the metric is independent of the phases of the propagation paths.

(ii) The main diagonal contains the directional spreads (comparable to the azimuth and elevation spreads) at Rx and Tx, and the (normalized) rms delay spread. In this way, the ECM jointly represents the *spatial structure, and wideband properties* of the channel.

(iii) The trace $\text{tr}\{\mathbf{C}_\pi\}$ is the sum of the directional spreads [46] at Rx and Tx plus the (normalized) delay spread.

(iv) The determinant $\det\{\mathbf{C}_\pi\}$ describes the volume spanned in the parameter space.

We use the ECM for the following two purposes.

(1) Validating the spatio-temporal multipath structure: the *singular values of the ECM* (SV-ECM) can be interpreted as the *fingerprint* of the scenario, by which one can judge the compactness of the paths in the channel. Assuming that the parameters of all paths span a multidimensional ellipsoid, the SVs describe the lengths of the main axes of this ellipsoid. In this way, it transforms the traditional view of individual parameter spread values into a joint-spread approach. These properties make the SV-ECM genuinely suited for comparing channels. Calculating the SV-ECM for the example shown in Figure 5(a), the snapshot would result in the *same values* of the SV-ECM, no matter which phases the paths have. This demonstrates that the SV-ECM is a consistent metric, reflecting the multipath structure of the channel.

(2) Validating the time-variance: the rate of change of the ECM shows how strongly the parametric channel changes between two neighbouring time instants. To quantify the rate of change between two ECM
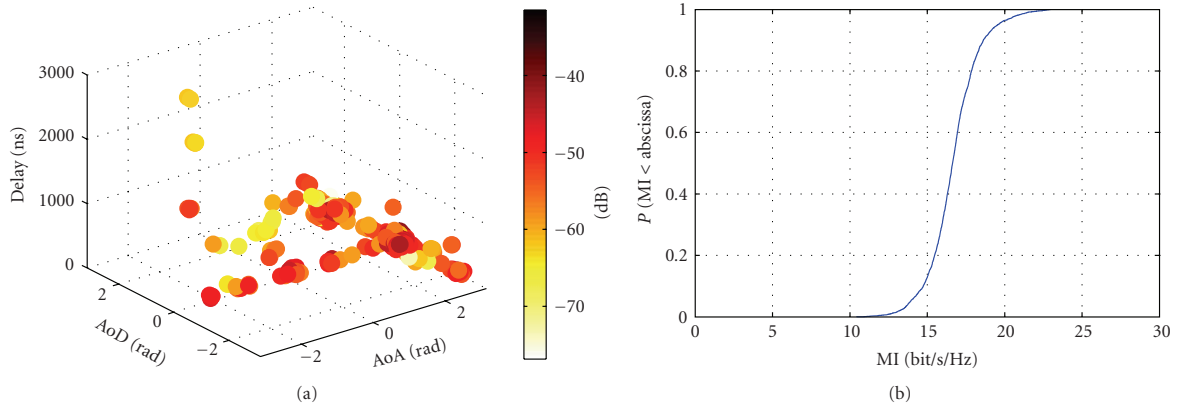
FIGURE 5: Why mutual information (MI) is no good validation metric: (a) multipath structure of an environment; each MPC is represented by a color-coded dot. (b) MI cdf computed from environment (a) by adding random phases to the paths, but not changing them otherwise.

matrices of adjacent snapshots, we use the Frobenius inner matrix product [47] as

$$
\xi(\mathbf{C}_\pi(t'), \mathbf{C}_\pi(t' + \Delta t_s))
$$

$$
= \frac{\mathrm{tr}\left\{\mathbf{C}_\pi(t')^T \mathbf{C}_\pi(t' + \Delta t_s)\right\}}{\|\mathbf{C}_\pi(t')\|_\mathrm{F}\|\mathbf{C}_\pi(t' + \Delta t_s)\|_\mathrm{F}}, \tag{12}
$$

where tr$\{\cdot\}$ denotes the matrix trace operator, and $\|\cdot\|_\mathrm{F}$ denotes the Frobenius matrix norm. The Frobenius inner product quantifies how similar the eigenvectors of the two matrix arguments are. For collinear matrices, we have $\xi = 1$, while for orthogonal matrices, $\xi = 0$.

3.2.3. Diversity Measure. Spatial diversity describes the number of independent fading links between the Tx and Rx antenna arrays. In a full-diversity system, where all links between the Tx and Rx arrays are independent, one observes a spatial diversity of $N_{\mathrm{Tx}}N_{\mathrm{Rx}}$ [48]. This diversity is directly linked with the uncoded bit-error ratio (BER) performance of MIMO systems [1].

Channel correlation reduces this diversity significantly. Ivrlac and Nossek provided the *Diversity Measure* [28], a way to quantify the available diversity directly from the MIMO channels without taking the detour via BER simulations. We will use this measure to quantify the diversity in both the measured and the modelled channels, and subsequently compare the results.

The Diversity Measure $D(\mathbf{R})$ of a MIMO system described by a channel matrix $\mathbf{H}$ with channel correlation matrix $\mathbf{R} = \mathrm{E}\{\mathrm{vec}(\mathbf{H})\mathrm{vec}(\mathbf{H})^\mathrm{H}\}$ is given by

$$
D(\mathbf{R}) = \left(\frac{\mathrm{tr}(\mathbf{R})}{\|\mathbf{R}\|_\mathrm{F}}\right)^2. \tag{13}
$$

Invoking the channel *correlation* matrix implicitly assumes the channel to be stationary over the time period of a sliding window. We want to bring to attention that the *channel*

correlation matrix used here is entirely different from the *path covariance matrix* used as ECM in (11). To estimate samples of the channel correlation matrix, we chose a sliding window over $W = 8$ snapshots and all frequencies, that is,

$$
\mathbf{R}(t) = \frac{1}{MW} \sum_{\Delta f} \sum_{t=t'}^{t'+W\Delta t_s} \mathrm{vec}\{\mathbf{H}(t, \Delta f)\}\mathrm{vec}\{\mathbf{H}(t, \Delta f)\}^\mathrm{H}, \tag{14}
$$

with $\mathbf{H}(t, \Delta f)$ defined in (4). These estimated correlation matrices for all time instants are taken as ensemble to obtain the cdf of (13).

3.3. Validation Results. This paper presents validation results for two particularly interesting scenarios, (i) a measurement route in an office scenario, *without* line of sight between transmitter and receiver, and (ii) a route within a cafeteria (large room) mostly with LOS between transmitter and receiver (see Figure 11 in Appendix A.2). The Tx was moved through the rooms while the Rx was placed at a fixed position. The cafeteria scenario is a particularly challenging one, difficult to represent by any MIMO channel model, as it is a combination of two totally different propagation environments, depending on whether the LOS between Rx and Tx is blocked or not. For validation we generated *smoothly-time varying channels* using the RCM and used the three validation metrics described in the previous paragraphs. The validation of more scenarios can be found in [36, Chapter 4].

First, we use the ECM to *validate the spatiotemporal multipath structure.* Figure 6 compares the SV-ECM of the modelled paths with those identified directly from measurements "reference channels", both at 2.55 GHz and at 5.25 GHz, neglecting elevation. The ECM offers five SVs, shown as dashed lines (RCM) and solid lines (measurements). We observe that, judging from the ECM, the multipath structure is quite similar at the two carrier frequencies in both scenarios. The NLOS office scenario is much better matched at 2.55 GHz than at 5.25 GHz. At 5.25 GHz, the third and
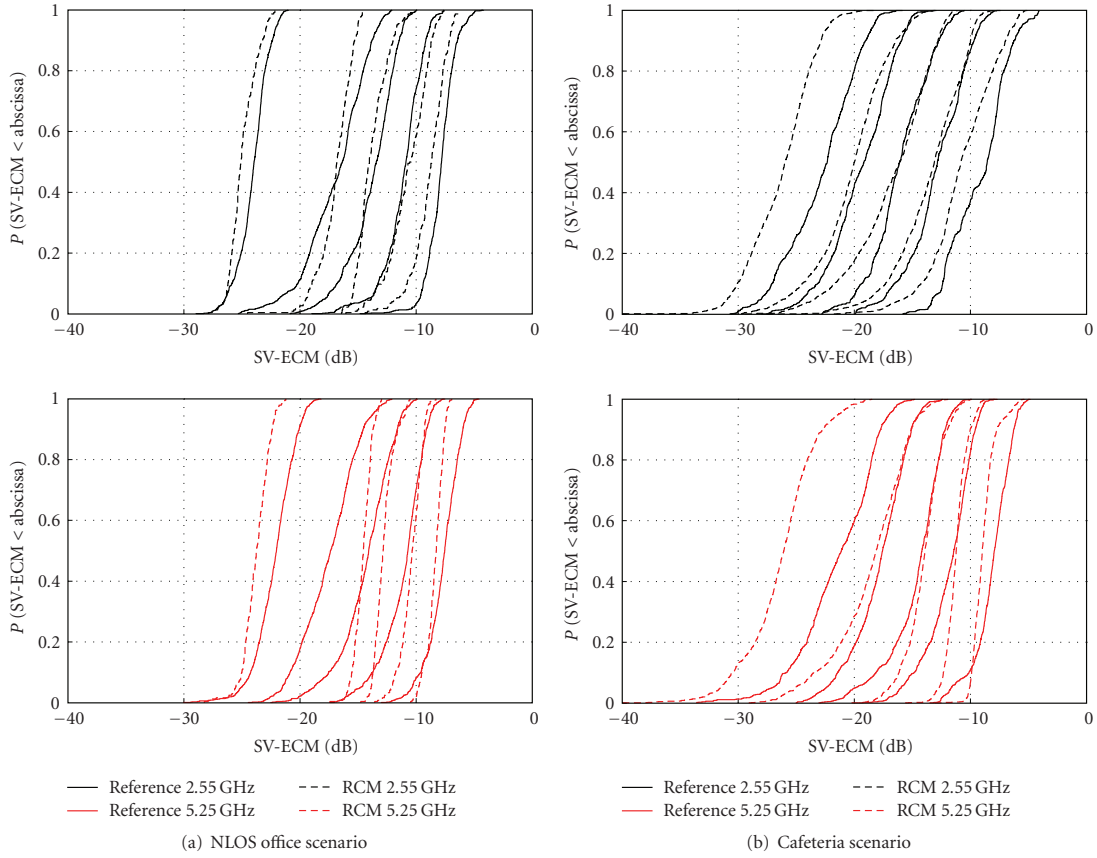
FIGURE 6: Model validation using the Environment Characterisation Metric. Shown are the distributions of the five singular values of the ECM.
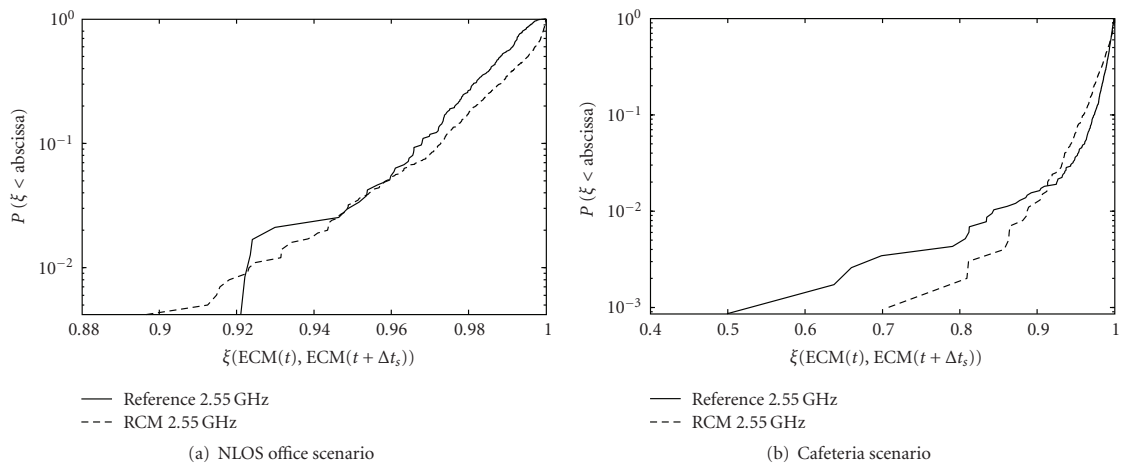
FIGURE 7: Time-variant validation using the Environment Characterisation Metric: CDF of collinearity between snapshots adjacent in time ($\Delta t = 0.22$ seconds).

(a) Office scenario   (b) Cafeteria scenario
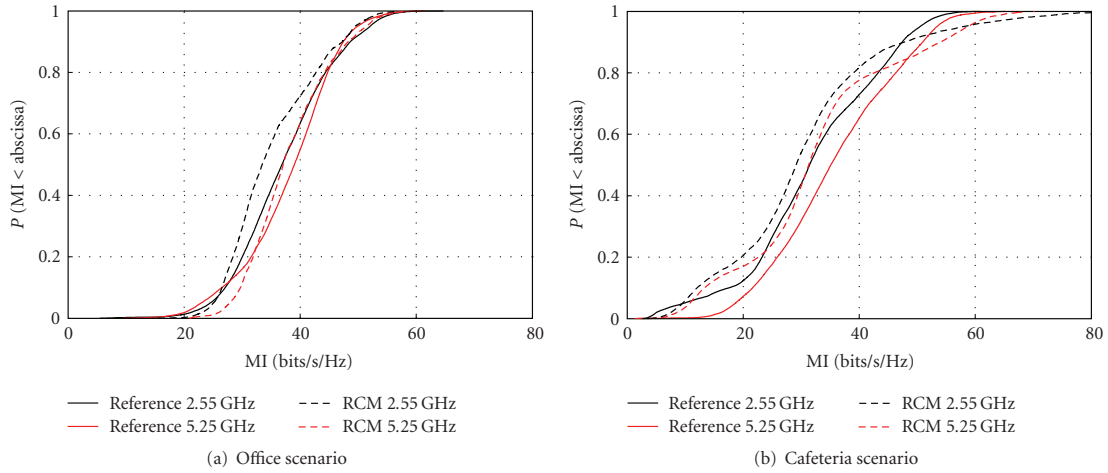
FIGURE 8: Model validation using mutual information.

(a) Office scenario   (b) Cafeteria scenario
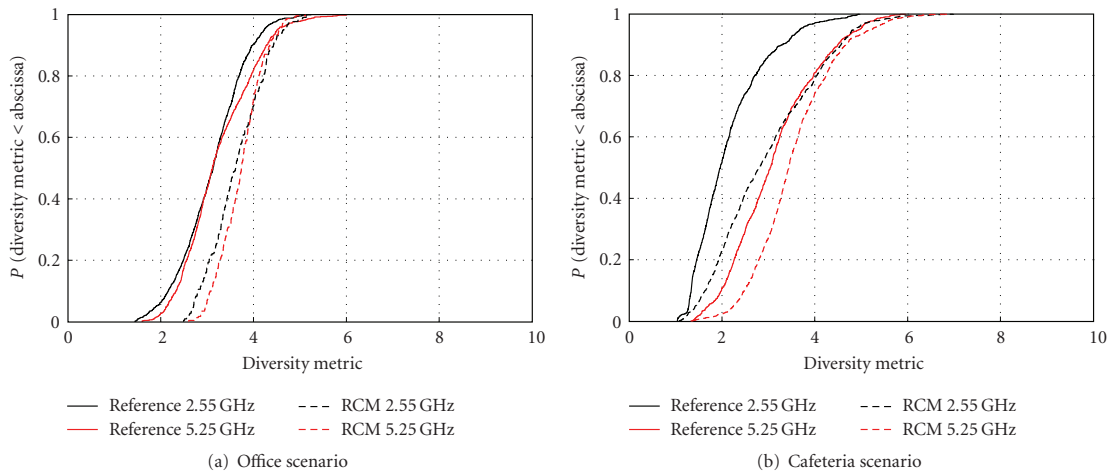
FIGURE 9: Model validation using the diversity measure.

fourth SV-ECM of the modelled channels obviously have a positive bias. The reason for this poor match is an environment pdf that has little variation, particularly in the cluster receive azimuth position domain. This leads to reduced randomness when drawing the parameters of the scenarios, resulting in steeper SV-ECM cdfs. Considering the cafeteria scenario, there is much stronger variability, but still the environment is represented quite well. In both scenarios, the smallest SV-ECM of the modelled channels has a significant negative bias. We found the reason for this to be outlier paths that were estimated from the measurement, but these are not modelled by the RCM.

In a second step, we use the collinearity between two ECM matrices to *validate the time variance*. Figure 7 quantifies how strongly the channels change from snapshot to snapshot. In detail, the figure shows the cdfs of the ECM

distances evaluated between all two adjacent time instants for both the modelled channels and the reference channels. A value of $\xi = 1$ indicates that the channels did not change, while smaller numbers indicate changes in the multipath structure.

In the NLOS office scenario, where the SNR of the measurement was only average, we observe that the model has a slightly lower number of small changes than the reference channels (rightmost part of Figure 7(a)). This is due to the path parameter estimation algorithm, which always estimates a number of outlier paths that appear at random in any single time snapshot. In the cafeteria scenario, we observe much stronger changes than in the office scenario due to the changes in the LOS part of the environment. The measurement SNR was high, so random outliers were no problem, as the rightmost part of the curves show. Between

the outage probabilities of 10^{-2} and 1, the model fits the measurement very well, which is the statistically relevant part. The few much larger changes that are observed in the measurements occur during the abrupt transition from LOS to NLOS.

Next, we present the validation using *mutual information*. Figure 8 shows the cdf of the evaluated mutual information for both modelled and reference channels at both carrier frequencies. We observe that the MI of the modelled channels have a negative bias in both scenarios. This could be already expected from the ECM validation, where the spreading of the paths (strongest SV-ECM) was also slightly too low. We discourage the use of MI for validating the spatial structure of the radio channel, since *MI is influenced by both spatial structure and fading*.

Finally, Figure 9 compares the Diversity Measure values of the modelled channels with the reference channels. In both scenarios, diversity is slightly overmodelled. While this is also a common effect of analytical channel models, there is no connection here. It may also happen that the RCM undermodels diversity. This result could also have been expected from the MI cdfs, where the cdf of the modelled channels showed a sligtly steeper slope than the cdf of the reference channels.

4. Conclusions

The presented Random-Cluster Model is well able to reflect the spatial properties of measured time-variant MIMO channels, even if the properties of the environment are varying between LOS and NLOS. By its direct parametrisation from measurement data, the RCM is specific to the measured environment. Since the RCM is propagation-based, the RCM is also scalable in carrier frequency, in bandwidth, and in its antenna array configuration. Still, it is a stochastic model. The propagation environment is described using a multivariate pdf of the cluster parameters. Depending on the accuracy of the estimation of this pdf from measurements, the parametrisation complexity is scalable. Time variance is implemented by linear cluster movement. Using the recommended clustering algorithm in combination with a Kernel Density Estimator, the RCM is parametrised automatically without user interaction.

Validation showed a close fit between the channels modelled by the RCM, and reference channels obtained from the measurements. Even though the RCM was only successfully validated against indoor measurements, the model structure is also well suited to represent outdoor radio channels, when adapting the parameters, respectively. This renders the RCM to be ideally suited to model particularly interesting propagation conditions that were measured before.

Appendix

A. Channel Measurements

This appendix describes the channel measurement equipment and the investigated scenarios.

TABLE 2: Parameter settings for the PropSound Channel Sounder[CS].

Parameter	2.55 GHz	5.25 GHz
Transmit power [dBm]	26	26
Bandwidth [MHz]	200	200
Chip frequency [MHz]	100	100
Number of TX antennas	56	50
Number of RX antennas	8	32
Code length [μs]	2.55	2.55
Channel sampling rate [Hz]	92.6	59.4
Cycle duration [μs]	1542.24	8415.00
TX antenna height [m]	1.53	1.53
RX antenna height [m]	1.05	0.82

A.1. Equipment

We employed a wideband radio channel sounder, EB Propsound CS [49], which utilizes periodic pseudorandom binary signals. The sounder is described in more detail in [50]. In sounding, M-sequences with adjustable code lengths are transmitted and multiplexed by switching the transmit and receive antennas. The spread spectrum signal has 100 Mchip/s chip rate and switches through all the antennas with the cycle rates presented in Table 2. Thus, sequential radio channel measurement between all possible TX and RX antenna pairs is achieved. The number of antenna elements used is inversely proportional to the cycle rate. The sounder was operated in burst-mode, that is, after four measuring cycles there was a break to allow real-time data transfer to the hard disk unit. During the measurements, a real-time display of the received impulse responses (IRs) could be monitored from the control laptop computer. In addition to basic data handling features, the post-processing tools include the ISIS (Initialization and Search Improved SAGE) software to identify individual MPCs by a super-resolution SAGE algorithm employing maximum likelihood techniques for parameter estimation [51].

The selected antenna arrays (Figure 10) are able to capture largely the spatial characteristics of the radio channel at *both* link-ends. The 2.55 GHz array (Figure 10(a)) used at the TX consists of 28 dual-polarized patch elements. The elements are positioned in a way that allows channel probing in the *full* azimuth domain. The upper ring of antenna elements in the ODA was not operative on one link end, so elevation information was not extracted from the measurements. Figure 10(b) shows the uniform circular array with 7 + 1 monopoles used at the RX end at 2.55 GHz. It supports full azimuth direction probing but not the elevation. At 5.25 GHz both TX and RX had 25 element patch arrays shown in Figure 10(c). Their properties are similar to the 2.55 GHz patch array. Table 3 shows the azimuth and elevation coverage of the antennas.

All antennas had been calibrated in an anechoic chamber. The signal model on which SAGE is based is using the measured array pattern data for calculating the angles of impinging or outgoing waves. In the calibration process, the antenna pattern of each single element was measured in

(a) 3 × 8 ODA, 2.55 GHz

(b) 7 + 1 UCA, 2.55 GHz

(c) 2 × 9 ODA, 5.25 GHz
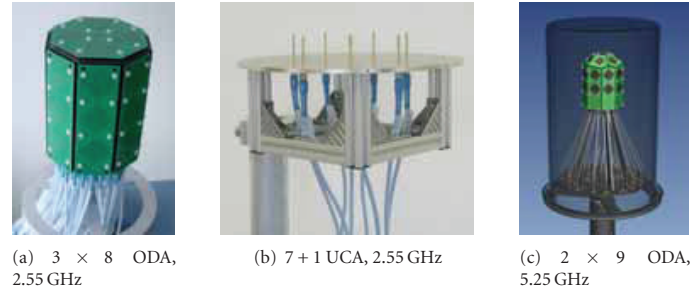
FIGURE 10: Antenna arrays. (a) 2.55 GHz omni-directional patch array (ODA), (b) 2.55 GHz circular monopole array (UCA), (c) 5.25 GHz ODA.

(a) Office environment

(b) Cafeteria
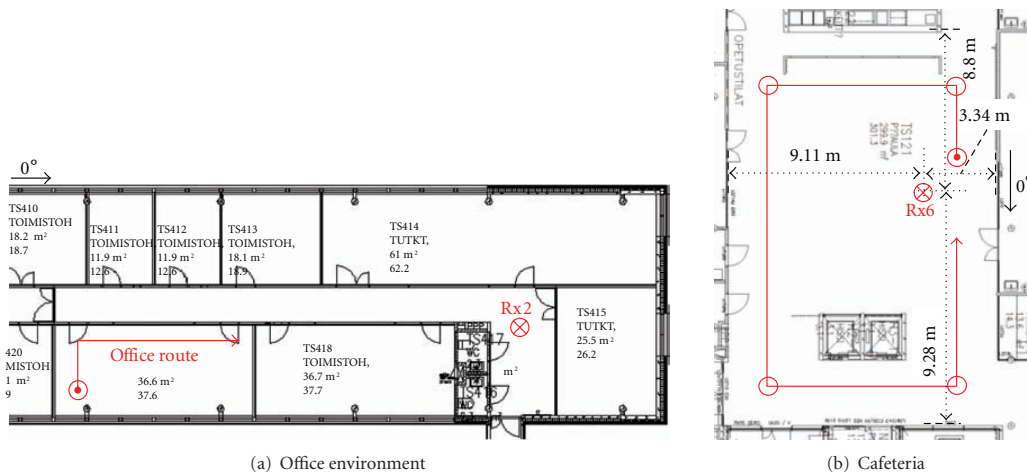
FIGURE 11: Measured scenarios.

TABLE 3: Antenna parameters.

Antenna	Azimuth coverage	Elevation coverage
3 × 8 ODA 2.55 GHz	−180° · · · 180°	−55° · · · 90°
7 + 1 UCA 2.55 GHz	−180° · · · 180°	0° · · · 60°
2 × 9 ODA 5.25 GHz	−180° · · · 180°	−55° · · · 90°

amplitude and phase over azimuth and elevation, resulting in an azimuth/elevation matrix. This measurement was done for both horizontal and vertical polarisation. To minimize the interference of WLAN and Bluetooth, one center frequency for the measurements was chosen to be 2.55 GHz. Still, there seems to have been (spurious) radiation from these devices above 2.45 GHz, so we had to expect an enhanced noise floor in the IRs. The ensuing smaller dynamic range resulted in a smaller number of paths that ISIS could extract from the measurement. At the other center frequency of 5.25 GHz we did not observe any interference.

A.2. Scenarios

We took measurements on 28 different routes [36], of which we analyse two particularly interesting ones in this paper. The outer walls of the building were reinforced concrete or brick-stone walls, while inside walls were mostly of plasterboard with internal metal mounts.

The first measurement, NLOS throughout, was done in an office environment, where the receiver was fixed in the corridor and the transmitter was moved along a route in an office (Figure 11(a)).

The second measurement, predominantly LOS, was recorded in a cafeteria with metal tables and chairs. The receiver was fixed on a table, and the transmitter was moved along a route in the room. The Tx-Rx distance variation was large, and the LOS between transmitter and receiver was sometimes shadowed by an elevator (Figure 11(b)). People were moving randomly in the environment.

measurement campaign. The Telecommunications Research Center Vienna (ftw.) is supported by the Austrian Government and the City of Vienna within the competence centre programme COMET.

References

[1] A. J. Paulraj, D. A. Gore, R. U. Nabar, and H. Bölcskei, "An overview of MIMO communications—a key to gigabit wireless," *Proceedings of the IEEE*, vol. 92, no. 2, pp. 198–218, 2004.

[2] I. E. Telatar, "Capacity of multi-antenna Gaussian channels," Tech. Rep. BL0112170-950615-07TM, AT&T Bell Laboratories, Murray Hill, NJ, USA, 1995.

[3] http://www.beceem.com.

[4] http://www.linksys.com.

[5] "3GPP—The 3rd Generation Partnership Project," 2008, http://www.3gpp.org.

[6] "IEEE 802.16 working group on broadband wireless access standards," 2008, http://wirelessman.org.

[7] D.-S. Shiu, G. J. Foschini, M. J. Gans, and J. M. Kahn, "Fading correlation and its effect on the capacity of multielement antenna systems," *IEEE Transactions on Communications*, vol. 48, no. 3, pp. 502–513, 2000.

[8] W. Weichselberger, M. Herdin, H. Özcelik, and E. Bonek, "A stochastic MIMO channel model with joint correlation of both link ends," *IEEE Transactions on Wireless Communications*, vol. 5, no. 1, pp. 90–100, 2006.

[9] A. Edelman and N. R. Rao, "Random matrix theory," *Acta Numerica*, vol. 14, pp. 233–297, 2005.

[10] L. C. Wood and W. S. Hodgkiss, "MIMO channel models and performance metrics," in *Proceedings of IEEE Global Telecommunications Conference (GLOBECOM '07)*, pp. 3740–3744, Washington, DC, USA, November 2007.

[11] S. Wyne, A. F. Molisch, P. Almers, G. Eriksson, J. Karedal, and F. Tufvesson, "Outdoor-to-indoor office MIMO measurements and analysis at 5.2 GHz," *IEEE Transactions on Vehicular Technology*, vol. 57, no. 3, pp. 1374–1386, 2008.

[12] T. Fügen, J. Maurer, C. Kuhnert, and W. Wiesbeck, "A modelling approach for multiuser MIMO systems including spatially-colored interference," in *Proceedings of IEEE Global Telecommunications Conference (GLOBECOM '04)*, vol. 2, pp. 938–942, Dallas, Tex, USA, November-December 2004.

[13] V. Degli-Esposti, D. Guiducci, A. de'Marsi, P. Azzi, and F. Fuschini, "An advanced field prediction model including diffuse scattering," *IEEE Transactions on Antennas and Propagation*, vol. 52, no. 7, pp. 1717–1728, 2004.

[14] "Spatial channel model for Multiple Input Multiple Output (MIMO) simulations," Tech. Rep. TR 25.996 V6.1.0, 3GPP, Valbonne, France, September 2003.

[15] P. Kyösti, J. Meinilä, L. Hentilä, et al., "WINNER II channel models (d1.1.2v1.1)," November 2007, http://www.ist-winner.org.

[16] L. Correia, Ed., *Mobile Broadband Multimedia Networks*, Academic Press, San Diego, Calif, USA, 2006.

[17] A. Saleh and R. Valenzuela, "A statistical model for indoor multipath propagation," *IEEE Journal on Selected Areas in Communications*, vol. 5, no. 2, pp. 128–137, 1987.

[18] Q. H. Spencer, B. D. Jeffs, M. A. Jensen, and A. L. Swindlehurst, "Modeling the statistical time and angle of arrival characteristics of an indoor multipath channel," *IEEE Journal on Selected Areas in Communications*, vol. 18, no. 3, pp. 347–360, 2000.

[19] H. Xiao, A. G. Burr, L. Hentilä, and P. Kyösti, "Statistical technique to identify clusters from multi-dimensional measurement data," in *Proceedings of the 2nd European Conference on Antennas and Propagation (EuCAP '07)*, pp. 1–7, Edinburgh, UK, November 2007.

[20] G. D. Galdo, N. Czink, and M. Haardt, "Cluster spatial localization from high-resolution parameter estimation," in *Proceedings of IEEE/ITG Workshop on Smart Antennas (WSA '06)*, pp. 1–7, Ulm, Germany, March 2006.

[21] J. Salo, J. Salmi, N. Czink, and P. Vainikainen, "Automatic clustering of nonstationary MIMO channel parameter estimates," in *Proceedings of the 2nd International Conference on Telecommunications (ICT '05)*, Cape Town, South Africa, May 2005.

[22] N. Czink, P. Cera, J. Salo, E. Bonek, J-.P. Nuutinen, and J. Ylitalo, "Improving clustering performance using multipath component distance," *Electronics Letters*, vol. 42, no. 1, pp. 33–35, 2006.

[23] N. Czink, P. Cera, J. Salo, E. Bonek, J.-P. Nuutinen, and J. Ylitalo, "A framework for automatic clustering of parametric MIMO channel data including path powers," in *Proceedings of IEEE Vehicular Technology Conference (VTC '06)*, pp. 114–118, Montreal, Canada, September 2006.

[24] N. Czink, R. Tian, S. Wyne, et al., "Tracking time-variant cluster parameters in MIMO channel measurements," in *Proceedings of the 2nd International Conference on Communications and Networking in China (ChinaCom '07)*, pp. 1147–1151, Shanghai, China, August 2007.

[25] N. Czink, E. Bonek, L. Hentilä, J.-P. Nuutinen, and J. Ylitalo, "A measurement-based random-cluster MIMO channel model," in *Proceedings of IEEE Antennas and Propagation International Symposium*, pp. 5363–5366, Honolulu, Hawaii, USA, June 2007.

[26] N. Czink, E. Bonek, J. Ylitalo, and T. Zemen, "Measurement-based time-variant MIMO channel modelling using clusters," in *Proceedings of the 29th General Assembly of the International Union of Radio Science (URSI '08)*, Chicago, Ill, USA, August 2008.

[27] P. Kyösti and T. Jämsä, "Complexity comparison of MIMO channel modelling methods," in *Proceedings of the 4th IEEE Internatilonal Symposium on Wireless Communication Systems (ISWCS '07)*, pp. 219–223, Trondheim, Norway, October 2007.

[28] M. T. Ivrlac and J. A. Nossek, "Quantifying diversity and correlation in Rayleigh fading MIMO communication systems," in *Proceedings of the 3rd IEEE International Symposium on Signal Processing and Information Technology (ISSPIT '03)*, pp. 158–161, Darmstadt, Germany, December 2003.

[29] N. Czink, G. D. Galdo, X. Yin, E. Bonek, and J. Ylitalo, "A novel environment characterizationmetric for clustered MIMO channels: used to validate a SAGE parameter estimator," *Wireless Personal Communications*, vol. 46, no. 1, pp. 83–98, 2008.

[30] M. Steinbauer, A. F. Molisch, and E. Bonek, "The double-directional radio channel," *IEEE Antennas and Propagation Magazine*, vol. 43, no. 4, pp. 51–63, 2001.

[31] J. Kolu, J.-P. Nuutinen, T. Jämsä, J. Ylitalo, and P. KyÖsti, "Playback simulations of measured MIMO radio channels," COST 273, TD(04)110, COST, Gothenburg, Sweden, June 2004.

[32] B. H. Fleury, M. Tschudin, R. Heddergott, D. Dahlhaus, and K. I. Pedersen, "Channel parameter estimation in mobile radio environments using the SAGE algorithm," *IEEE Journal on Selected Areas in Communications*, vol. 17, no. 3, pp. 434–450, 1999.

EURASIP Journal on Wireless Communications and Networking

[33] N. Czink, R. Tian, S. Wyne, et al., "Cluster parameters for time-variant MIMO channel models," in *Proceedings of the 2nd European Conference on Antennas and Propagation (EuCAP '07)*, pp. 1–8, Edinburgh, UK, November 2007.

[34] A. Ihler, "Kernel Density Estimation Toolbox for MATLAB (R13)," July 2007, http://ttic.uchicago.edu/~ihler/code.

[35] D. W. Scott, *Multivariate Density Estimation*, John Wiley & Sons, New York, NY, USA, 1992.

[36] N. Czink, *The random-cluster model—a stochastic MIMO channel model for broadband wireless communication systems of the 3rd generation and beyond*, Ph.D. dissertation, Technische Universität Wien, Vienna, Austria, FTW Dissertation Series, December 2007.

[37] K. V. Mardia and P. E. Jupp, *Directional Statistics*, John Wiley & Sons, New York, NY, USA, 2000.

[38] P. Almers, E. Bonek, A. Burr, et al., "Survey of channel and radio propagation models for wireless MIMO systems," *EURASIP Journal on Wireless Communications and Networking*, vol. 2007, Article ID 19070, 19 pages, 2007.

[39] F. Kaltenberger, T. Zemen, and C. W. Üeberhuber, "Low-complexity geometry-based MIMO channel simulation," *EURASIP Journal on Advances in Signal Processing*, vol. 2007, Article ID 95281, 17 pages, 2007.

[40] H. Asplund, A. A. Glazunov, A. F. Molisch, K. I. Pedersen, and M. Steinbauer, "The COST 259 directional channel model—part II: macrocells," *IEEE Transactions on Wireless Communications*, vol. 5, no. 12, pp. 3434–3450, 2006.

[41] J. W. Wallace and M. A. Jensen, "Time-varying MIMO channels: measurement, analysis, and modeling," *IEEE Transactions on Antennas and Propagation*, vol. 54, no. 11, pp. 3265–3273, 2006.

[42] V. Erceg, L. Schumacher, P. Kyritsi, et al., "TGn channel models," Tech. Rep., IEEE P802.11, Geneva, Switzerland, 2004, http://grouper.ieee.org/groups/802/11/.

[43] P. Kyösti, D. Laselva, L. Hentilä, and T. Jämsä, "Validating IST-WINNER indoor MIMO radio channel model," in *IST Mobile and Wireless Summit*, Mykonos, Greece, June 2006.

[44] A. F. Molisch, M. Steinbauer, M. Toeltsch, E. Bonek, and R. S. Thomä, "Capacity of MIMO systems based on measured wireless channels," *IEEE Journal on Selected Areas in Communications*, vol. 20, no. 3, pp. 561–569, 2002.

[45] M. Steinbauer, H. Özcelik, H. Hofstetter, C. F. Mecklenbräuker, and E. Bonek, "How to quantify multipath separation," *IEICE Transactions on Electronics*, vol. E85-C, no. 3, pp. 552–557, 2002.

[46] B. H. Fleury, "First- and second-order characterization of direction dispersion and space selectivity in the radio channel," *IEEE Transactions on Information Theory*, vol. 46, no. 6, pp. 2027–2044, 2000.

[47] G. Golub and C. van Loan, *Matrix Computations*, The Johns Hopkins University Press, London, UK, 3rd edition, 1996.

[48] C. Oestges and B. Clerckx, *MIMO Wireless Communications*, Academic Press, London, UK, 2007.

[49] Elektrobit EB Propsim, 2008, http://www.propsim.com.

[50] L. Hentilä, P. Kyösti, J. Ylitalo, X. Zhao, J. Meinilä, and J.-P. Nuutinen, "Experimental characterization of multi-dimensional parameters at 2.45 and 5.25 GHz indoor channels," in *Proceedings of the Wireless Personal Multimedia Communications (WPMC '05)*, pp. 254–258, Aalborg, Denmark, September 2005.

[51] B. H. Fleury, P. Jourdan, and A. Stucki, "High-resolution channel parameter estimation for MIMO applicationsusing the SAGE algorithm," in *Proceedings of the International Zurich Seminar on Broadband Communications*, pp. 1–9, Zurich, Switzerland, February 2002.

3 Estimation and Prediction of Channel State Information

[Article 7] T. Zemen, C. F. Mecklenbräuker, F. Kaltenberger, and B. H. Fleury, "Minimum-energy band-limited predictor with dynamic subspace selection for time-variant flat-fading channels," *IEEE Transactions on Signal Processing*, vol. 55, no. 9, pp. 4534–4548, September 2007.

[Article 8] T. Zemen, S. Caban, N. Czink, and M. Rupp, "Validation of minimum-energy band-limited prediction using vehicular channel measurements," in *17th European Signal Processing Conference (EUSIPCO)*, Glasgow, Scotland, August 2009.

[Article 9] T. Zemen, L. Bernadó, N. Czink, and A. F. Molisch, "Iterative time-variant channel estimation for 802.11p using generalized discrete prolate spheroidal sequences," in *IEEE Transactions on Vehicular Technology*, vol. 61, no. 3, pp. 1222–1233, March 2012.

Minimum-Energy Band-Limited Predictor With Dynamic Subspace Selection for Time-Variant Flat-Fading Channels

Thomas Zemen, Christoph F. Mecklenbräuker, *Member, IEEE*, Florian Kaltenberger, and
Bernard H. Fleury, *Senior Member, IEEE*

Abstract—In this paper, we develop and analyze the basic methodology for minimum-energy (ME) band-limited prediction of sampled time-variant flat-fading channels. This predictor is based on a subspace spanned by time-concentrated and band-limited sequences. The time-concentration of these sequences is matched to the length of the observation interval and the band-limitation is determined by the support of the Doppler power spectral density of the fading process. Slepian showed that discrete prolate spheroidal (DPS) sequences can be used to calculate the ME band-limited continuation of a finite sequence. We utilize this property to perform channel prediction. We generalize the concept of time-concentrated and band-limited sequences to a band-limiting region consisting of disjoint intervals. For a fading process with constant spectrum over its possibly discontiguous support we prove that the ME band-limited predictor is identical to a reduced-rank maximum-likelihood predictor which is a close approximation of a Wiener predictor. In current cellular communication systems the time-selective fading process is highly oversampled. The essential dimension of the subspace spanned by time-concentrated and band-limited sequences is in the order of two to five only. The prediction error mainly depends on the support of the Doppler spectrum. We exploit this fact to propose low-complexity time-variant flat-fading channel predictors using dynamically selected predefined subspaces. The subspace selection is based on a probabilistic bound on the reconstruction error. We compare the performance of the ME band-limited predictor with a predictor based on complex exponentials. For a prediction horizon of one eights of a wavelength the numerical simulation results show that the ME band-limited predictor with dynamic subspace selection performs better than, or similar to, a predictor based on complex exponentials with perfectly known frequencies. For a prediction horizons of three eights of a wavelength the performance of the ME band-limited predictor approaches that of a Wiener predictor with perfectly known Doppler bandwidth.

Index Terms—Discrete prolate spheroidal sequences, minimum-energy band-limited predictor, time-variant channel prediction.

I. INTRODUCTION

IN mobile communication systems channel state information at the transmitter proves to be beneficial for increasing the system capacity. In a time-division duplex (TDD) system, channel state information can be obtained by exploiting channel reciprocity: While a data block is received, channel state information is obtained. This information can be utilized in the following transmission period. However, for moving users at vehicular speed the channel state information gets outdated rapidly. Thus, appropriate channel prediction is necessary.

Existing linear prediction algorithms for time-variant channels can be categorized into two groups. The first group of algorithms exploits the long-term correlation property of the fading process without considering a physical wave propagation model [1]. Thus, second-order statistics must be known in detail. In wireless communication systems, detailed second-order statistics are difficult to acquire due to the short time-interval over which the channel can be assumed to be stationary (in the wide sense) [2], [3]. Furthermore, bursty data transmission in multiuser systems pose another problem for obtaining channel observations over a sufficiently long time-interval.

The second group of algorithms take physical wave propagation models into account. The time-variant flat-fading channel is represented as the superposition of P propagation paths. Each path is characterized by its distinct complex weight and Doppler shift. A finite number of noisy channel observations is used to identify the parameters of all P paths.

1) The Doppler shift of each path is identified [4]–[8].
2) The complex weight of each path is estimated in the minimum mean square error (MMSE) sense.
3) Future channel values are predicted based on the above estimates.

The Doppler shift estimation for each individual path requires high computational complexity. Another drawback of the specular path models is rooted in the fact that the estimation error

for the complex weight increases drastically if the Doppler frequency difference between two paths becomes small [9]. In [6] a prediction algorithm assuming few discrete scatterers is analyzed. The results in [6] show good performance in simulations but reduced performance with measured channel data.

In this paper, we deal with the prediction of time-variant flat-fading channels in a single-input single-output wireless mobile communication system. We are concerned with low-complexity prediction of a fading process from noisy channel observations that are obtained while receiving a *single* data block. We consider a data block length such that the time-selective fading process is observed at most for one or two wavelength at the maximum user velocity.

The symbol rate, or equivalently the sampling rate of the fading process, in wireless communication systems is much higher than the Doppler bandwidth. Thus, time-limited snapshots of the sampled fading process span a subspace with small dimension [10]. The essential subspace dimension D' depends on the Doppler bandwidth B_{D} the sampling rate $1/T_{\mathrm{S}}$ and the number of observed samples M

$$D' = \lceil 2MB_{\mathrm{D}}T_{\mathrm{S}} \rceil + 1. \tag{1}$$

The number of maximal possible subspace dimensions M gets reduced by the factor $2B_{\mathrm{D}}T_{\mathrm{S}}$. In practical wireless communication systems D' is in the order of two to five only.

The same subspace is also spanned by index-limited discrete prolate spheroidal (DPS) sequences [11]. The band-limitation of the DPS sequences is chosen according to the support of the power spectral density of the time-selective fading process. The energy of the DPS sequences is most concentrated in an interval equal to the length of the observed data block. Thus, the DPS sequences allow to calculate the minimum-energy (ME) band-limited continuation of a finite sequence [10], hence, *predict* future samples.

Prediction of continuous-time channels is treated in [12]–[14]. In the present paper, we deal with discrete-time, i.e., sampled channels which are important for practical implementations using digital signal processing hardware. ME band-limited prediction for multidimensional energy-concentrated signals with *a priori known* band-limiting region is presented in [15].

Contributions of the Paper:
- We prove that ME band-limited prediction is equivalent to a reduced-rank approximation [16] of the Wiener predictor [17, Sec. 12.7] for a fading process with constant Doppler spectrum. A first result in the same direction but for the noiseless case is given in [18].
- Using analytic performance results we show for Clarke's fading model that the prediction error of a reduced-rank predictor is strongly dependent on the support of the Doppler power spectral density, while the actual shape of the Doppler spectrum is of minor importance [19].
- In mobile communication channels, fading processes frequently arise whose spectral support is the union of disjoint intervals. Examples for such short-time Doppler spectra are reported in [20], [21]. We generalize the concept of ME band-limited prediction to processes whose band-limit is defined by a region consisting of disjoint intervals.

- In practical systems, detailed information about the Doppler spectrum or its band-limiting region is not available. Instead, we exploit the small subspace dimension and define a finite set of precalculated subspaces. Each subspace represents a hypothesis about the disjoint band-limiting region of the fading process. We obtain probabilistic bounds on the reconstruction error of each predefined subspace using the method from [22] for the current data block. The subspace with the smallest reconstruction error is selected and utilized for channel prediction [23].

Notation: We denote a column vector by $\boldsymbol{a}$ and its ith element with $a[i]$. Similarly, we denote a matrix by $\boldsymbol{A}$ and its (i, ℓ)th element by $[\boldsymbol{A}]_{i,\ell}$. The transpose of $\boldsymbol{A}$ is given by $\boldsymbol{A}^{\mathrm{T}}$ and its conjugate transpose by $\boldsymbol{A}^{\mathrm{H}}$. A diagonal matrix with elements $a[i]$ is written as $\mathrm{diag}(\boldsymbol{a})$ and the $Q \times Q$ identity matrix as $\boldsymbol{I}_Q$. The absolute value of a is denoted by $|a|$ and its complex conjugate by a^*. The largest (smallest) integer that is lower (greater) or equal than $a \in \mathbb{R}$ is denoted by $\lfloor a \rfloor$ ($\lceil a \rceil$). We denote the set of all integers by $\mathbb{Z}$, the set of real numbers by $\mathbb{R}$ and the set of complex numbers by $\mathbb{C}$.

Organization of the Paper: The signal model for time-variant flat-fading channels is presented in Section II. In Section III, we explain the ME band-limited prediction method. The tight relation between the ME band-limited predictor and the Wiener predictor is highlighted in Section IV. In Section V, analytic expressions for the prediction error of the ME band-limited predictor are presented and an analytic performance comparison with the Wiener predictor is conducted in Section VI. In Section VII, a dynamic subspace selection scheme for the ME band-limited predictor is introduced and its computational complexity is assessed in Section VIII. An enhancement for discontiguous Doppler spectra is shown in Section IX. We provide Monte Carlo simulation results in Section X and draw conclusions in Section XI.

II. SIGNAL MODEL FOR TIME-VARIANT FLAT-FADING CHANNELS

We consider a TDD communication system transmitting data in blocks of length M over a time-variant channel. The symbol duration T_{S} is much longer than the delay spread T_{D} of the channel, i.e., $T_{\mathrm{S}} \gg T_{\mathrm{D}}$. Hence, we assume the channel as frequency-flat. Discrete time at rate $R_{\mathrm{S}} = 1/T_{\mathrm{S}}$ is denoted by m. The channel incorporates the transmit filter, the transmit antenna, the physical channel, the receive antenna, and the receive matched filter. The data symbols $b[m]$ are randomly and evenly drawn from a symbol alphabet with constant modulus. Without loss of generality $|b[m]| = 1$. The discrete-time signal at the matched filter output

$$h[m]b[m] + n'[m] \tag{2}$$

is the superposition of the data symbol multiplied by the sampled time-variant channel weight $h[m]$ and complex white Gaussian noise $n'[m]$ with variance σ_n^2. Without loss of generality $\{h[m]\}$ is a zero-mean, circularly symmetric, unit-variance (due to power control) process.

We assume an error-free decision feedback structure [24], [25]. Thus, we are able to obtain noisy channel observations [11] using the error-free data symbol estimates $\hat{b}[m] = b[m]$

$$
\begin{aligned}
y[m] &= (h[m]b[m] + n'[m])\hat{b}[m]^* \\
&= h[m] + n'[m]\hat{b}[m]^* = h[m] + n[m].
\end{aligned} \tag{3}
$$

Note that $n[m]$ has the same statistical properties as $n'[m]$. The signal-to-noise ratio (SNR) is $\mathrm{SNR} = 1/\sigma_n^2$.

The transmission is block oriented. A data block spans the time interval $\mathcal{I}_M = \{0, \ldots, M-1\}$. The noisy channel observations $y[m]$, $m \in \mathcal{I}_M$ obtained during a single data block are used to predict the channel weight up to N symbols into the future.

The electromagnetic field at the receiver is the superposition of the contribution of the individual fields of P impinging wave fronts. Each wave front is conceived as originating from a specific scatterer. For a user moving with velocity v the time-variant fading process $\{h[m]\}$ is band-limited by the one-sided normalized Doppler bandwidth

$$
\nu_{\mathrm{D}} = \frac{v f_{\mathrm{C}}}{c_0} T_{\mathrm{S}} \ll \frac{1}{2} \tag{4}
$$

where f_{C} is the carrier frequency and c_0 stands for the speed of light. As indicated with the inequality in (4) the sampling rate $1/T_{\mathrm{S}}$ is much higher than the Nyquist sampling rate.

We assume a time-variant block-fading channel model. Hence, the fading process $\{h[m]\}$ is wide-sense stationary over the limited time interval $\mathcal{I}_{M+N}$ (cf. Section X-A) with covariance function

$$
R_h[k] = \mathsf{E}\{h^*[m]h[m+k]\}. \tag{5}
$$

III. MINIMUM-ENERGY BAND-LIMITED PREDICTION

The samples of the channel weights in a single block $\mathcal{I}_M$ are collected in the vector

$$
\boldsymbol{h} = [h[0], h[1], \ldots, h[M-1]]^{\mathrm{T}}. \tag{6}
$$

The covariance matrix of $\boldsymbol{h}$ is defined as $\boldsymbol{\Sigma_h} = \mathsf{E}\{\boldsymbol{h}\boldsymbol{h}^{\mathrm{H}}\}$ with elements $[\boldsymbol{\Sigma_h}]_{\ell,m} = R_h[\ell-m]$ for $\ell, m \in \mathcal{I}_M$. The noisy observation vector $\boldsymbol{y} = [y[0], y[1], \ldots, y[M-1]]^{\mathrm{T}}$ is used for channel prediction. Its covariance matrix reads

$$
\boldsymbol{\Sigma_y} = \boldsymbol{\Sigma_h} + \sigma_n^2 \boldsymbol{I}_M. \tag{7}
$$

A. Reduced-Rank Channel Estimation

We consider a subspace-based approximation which expands the vector $\boldsymbol{h}$ in terms of D orthonormal basis vectors $\boldsymbol{u}_i = [u_i[0], u_i[1], \ldots, u_i[M-1]]^{\mathrm{T}}$, $i \in \{0, \ldots, D-1\}$

$$
\boldsymbol{h} \approx \boldsymbol{U}\boldsymbol{\gamma} = \sum_{i=0}^{D-1} \gamma_i \boldsymbol{u}_i. \tag{8}
$$

In this expression

$$
\boldsymbol{U} = [\boldsymbol{u}_0, \ldots, \boldsymbol{u}_{D-1}] \tag{9}
$$

contains the orthonormal basis vectors and $\boldsymbol{\gamma} = [\gamma_0, \ldots, \gamma_{D-1}]^{\mathrm{T}}$ collects the basis expansion coefficients. The least square estimate of $\boldsymbol{\gamma}$ simplifies to

$$
\hat{\boldsymbol{\gamma}} = \boldsymbol{U}^{\mathrm{H}}\boldsymbol{y} \tag{10}
$$

due to the orthogonality of the basis functions. The reconstruction error per data block is defined as

$$
z = \frac{1}{M}\|\boldsymbol{h} - \hat{\boldsymbol{h}}\|^2 = \frac{1}{M}\|\boldsymbol{U}^{\mathrm{H}}\boldsymbol{n}\|^2 + \frac{1}{M}\|\boldsymbol{V}^{\mathrm{H}}\boldsymbol{h}\|^2 \tag{11}
$$

where

$$
\hat{\boldsymbol{h}} = \boldsymbol{U}\hat{\boldsymbol{\gamma}} \tag{12}
$$

and $\boldsymbol{V} = [\boldsymbol{u}_D, \ldots, \boldsymbol{u}_{M-1}]$ contains the basis vectors spanning the subspace orthogonal to the signal subspace spanned by the columns of $\boldsymbol{U}$. The noise samples are collected in the vector $\boldsymbol{n} = [n[0], \ldots, n[M-1]]^{\mathrm{T}}$.

We define the mean square reconstruction error per sample

$$
\mathrm{MSE}[m] = \mathsf{E}\left\{\left|h[m] - \hat{h}[m]\right|^2\right\}. \tag{13}
$$

and the mean square reconstruction error per data block

$$
\mathrm{MSE} = \mathsf{E}\{z\} = \frac{1}{M}\sum_{m=0}^{M-1}\mathrm{MSE}[m] \tag{14}
$$

$$
= \frac{D}{M}\sigma_n^2 + \frac{1}{M}\mathsf{E}\left\{\|\boldsymbol{V}^{\mathrm{H}}\boldsymbol{h}\|^2\right\}. \tag{15}
$$

In the sequel, we seek basis vectors $\boldsymbol{u}_0, \ldots, \boldsymbol{u}_{D-1}$ and the subspace dimension D which minimize the reconstruction error per data block.

B. Time-Concentrated and Band-Limited Sequences

Slepian analyzed discrete prolate spheroidal (DPS) sequences $\{u_i[m]\}$ in [10]. DPS sequences time-limited to $\mathcal{I}_M$ form a set of orthogonal basis vectors $\boldsymbol{u}_i$. This set of basis vectors is used in [11] for the estimation of fading processes with symmetric spectral support $\mathcal{W} = (-\nu_{\mathrm{D}}, \nu_{\mathrm{D}})$ with $\nu_{\mathrm{D}} < 1/2$.

In mobile radio communication channels, the most significant part of the power in the estimated Doppler spectrum of the fading process is usually localized on the union of disjoint intervals in the frequency range $(-1/2, +1/2)$ as depicted in Fig. 1. Examples for such estimated (short-time) Doppler spectra are reported in [20] and [21]. In the sequel, we generalize the concept of time-concentrated and band-limited sequences from a symmetric band-limiting interval to the union of multiple disjoint intervals using results presented in [26].

Fig. 1 depicts a region $\mathcal{W} \subseteq (-1/2, 1/2)$ consisting of I disjoint intervals. Each interval is defined as $\mathcal{B}_i = (\nu_{i1}, \nu_{i2})$, $i \in \{1, \ldots, I\}$ and

$$
\mathcal{W} = \bigcup_{i=1}^{I} \mathcal{B}_i = \mathcal{B}_1 \cup \mathcal{B}_2 \cup \ldots \cup \mathcal{B}_I \tag{16}
$$
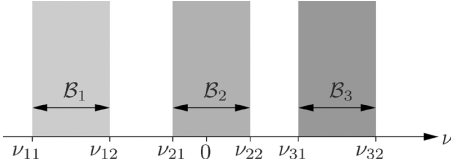
Fig. 1.   Band-limiting region $\mathcal{W}$ (16) consisting of $I = 3$ disjoint intervals.

with $\nu_{11} \leq \nu_{12} \leq \ldots \leq \nu_{I1} \leq \nu_{I2}$. The Lebesgue measure of $\mathcal{W}$ reads

$$|\mathcal{W}| = \sum_{i=1}^{I} (\nu_{i2} - \nu_{i1}). \tag{17}$$

Definition 1: A sequence $\{u[m, \mathcal{W}]\}$ is band-limited to the region $\mathcal{W} \subseteq (-1/2, 1/2)$, if its spectrum

$$U(\nu, \mathcal{W}) = \sum_{m=-\infty}^{\infty} u[m, \mathcal{W}] \mathrm{e}^{-\mathrm{j}2\pi m\nu}, \quad |\nu| \leq \frac{1}{2} \tag{18}$$

vanishes outside $\mathcal{W}$. Thus,

$$u[m, \mathcal{W}] = \int_{\mathcal{W}} U(\nu, \mathcal{W}) \mathrm{e}^{\mathrm{j}2\pi m\nu} \mathrm{d}\nu, \quad m \in \mathbb{Z}. \tag{19}$$

Definition 2: The energy-concentration of a sequence $\{u[m, \mathcal{W}]\}$ in the interval $\mathcal{I}_M$ is defined as

$$\rho(\mathcal{W}) = \frac{\sum_{m=0}^{M-1} |u[m, \mathcal{W}]|^2}{\sum_{m=-\infty}^{\infty} |u[m, \mathcal{W}]|^2}. \tag{20}$$

Theorem 1: The sequences $\{u_i[m, \mathcal{W}]\}$, $i \in \{0, \ldots, M-1\}$ band-limited to the region $\mathcal{W}$ and with *most concentrated* energy in the interval $\mathcal{I}_M$ are the solutions to

$$\sum_{\ell=0}^{M-1} C[\ell - m, \mathcal{W}] u_i[\ell, \mathcal{W}] = \lambda_i(\mathcal{W}) u_i[m, \mathcal{W}], \quad m \in \mathbb{Z} \tag{21}$$

where

$$C[k, \mathcal{W}] = \int_{\mathcal{W}} \mathrm{e}^{\mathrm{j}2\pi k\nu} \mathrm{d}\nu. \tag{22}$$

Note that $C[k, \mathcal{W}]$ is proportional to the covariance function of a process exhibiting a constant spectrum with support $\mathcal{W}$. More details are given in Section III-C.

Equation (22) evaluates to

$$C[k, \mathcal{W}] = \frac{1}{\mathrm{j}2\pi k} \sum_{i=1}^{I} \left(\mathrm{e}^{\mathrm{j}2\pi k\nu_{i2}} - \mathrm{e}^{\mathrm{j}2\pi k\nu_{i1}} \right) \tag{23}$$

if the band-limiting region $\mathcal{W}$ consists of I disjoint intervals as defined in (16) and depicted in Fig. 1.

The actual energy-concentration of the sequence $\{u_i[m, \mathcal{W}]\}$ is given by

$$\rho_i(\mathcal{W}) = \frac{\sum_{m=0}^{M-1} |u_i[m, \mathcal{W}]|^2}{\sum_{m=-\infty}^{\infty} |u_i[m, \mathcal{W}]|^2} = \lambda_i(\mathcal{W}). \tag{24}$$

Proof: See Appendix II.   □

Theorem 1 shows, that the eigenvalue $\lambda_i(\mathcal{W})$ is a direct measure of the energy-concentration of the sequence $\{u_i[m, \mathcal{W}]\}$ in the interval $\mathcal{I}_M$. The sequences $\{u_i[m, \mathcal{W}]\}$ and the eigenvalues $\lambda_i(\mathcal{W})$ depend on the region $\mathcal{W}$ and the interval length M. In the sequel, we omit the dependence on the block length M since this parameter is kept fixed throughout the paper.

Both, the sequences $\{u_i[m, \mathcal{W}]\}$ and their restrictions on $\mathcal{I}_M$ form orthogonal sets [27]. The eigenvalues $\lambda_i(\mathcal{W})$ decay exponentially for $i \geq D'(\mathcal{W})$ [26]. The essential subspace dimension is defined as

$$D'(\mathcal{W}) = \lceil |\mathcal{W}| M \rceil + 1. \tag{25}$$

Let us define the vectors $\boldsymbol{u}_i(\mathcal{W}) = [u_i[0, \mathcal{W}], \ldots, u_i[M-1, \mathcal{W}]]^{\mathrm{T}}$ and the matrix $[\boldsymbol{C}(\mathcal{W})]_{\ell,m} = C[\ell - m, \mathcal{W}]$ for $\ell, m \in \mathcal{I}_M$. It follows from (21) that

$$\boldsymbol{C}(\mathcal{W}) \boldsymbol{u}_i(\mathcal{W}) = \lambda_i(\mathcal{W}) \boldsymbol{u}_i(\mathcal{W}) \tag{26}$$

i.e., the vectors $\boldsymbol{u}_i(\mathcal{W})$ are the eigenvectors of $\boldsymbol{C}(\mathcal{W})$ and $\lambda_i(\mathcal{W})$ are their corresponding eigenvalues.

C. Relation to the Karhunen-Loève Identity

Identity (26) coincides with the Karhunen-Loève identity [28] in the case where the fading process $\{h[m]\}$ has a constant spectrum with support $\mathcal{W}$ given in (16)

$$S_h(\nu, \mathcal{W}) = \begin{cases} \frac{1}{|\mathcal{W}|} & \nu \in \mathcal{W}; \\ 0 & \text{otherwise.} \end{cases} \tag{27}$$

The covariance function of $\{h[m]\}$ reads in this case

$$R_h[k, \mathcal{W}] = \frac{1}{\mathrm{j}2\pi k |\mathcal{W}|} \sum_{i=1}^{I} \left(\mathrm{e}^{\mathrm{j}2\pi k\nu_{i2}} - \mathrm{e}^{\mathrm{j}2\pi k\nu_{i1}} \right). \tag{28}$$

Comparing (28) and (23) yields

$$R_h[k, \mathcal{W}] = \frac{1}{|\mathcal{W}|} C[k, \mathcal{W}]. \tag{29}$$

The restriction of the process $\{h[m]\}$ to the interval $\mathcal{I}_M$ has a covariance matrix proportional to $\boldsymbol{C}(\mathcal{W})$

$$\boldsymbol{\Sigma}_h(\mathcal{W}) = \frac{1}{|\mathcal{W}|} \boldsymbol{C}(\mathcal{W}) \tag{30}$$

The Karhunen-Loève identity writes in this case

$$\boldsymbol{\Sigma}_{\boldsymbol{h}}(\mathcal{W}) \boldsymbol{u}_i(\mathcal{W}) = \frac{\lambda_i(\mathcal{W})}{|\mathcal{W}|} \boldsymbol{u}_i(\mathcal{W}). \tag{31}$$

From the Karhunen-Loève identity it follows that the basis vectors $\boldsymbol{u}_i(\mathcal{W})$ minimize the mean square reconstruction error (14) for a fading process with constant Doppler spectrum $S_h(\nu, \mathcal{W})$ with support $\mathcal{W}$. The subspace dimension minimizing the MSE per observation interval for a given SNR is found to be [29]

$$D(\mathcal{W}) = \underset{\mathcal{D} \in \{1,...,M\}}{\arg\min} \left(\frac{1}{|\mathcal{W}|M} \sum_{i=\mathcal{D}}^{M-1} \lambda_i(\mathcal{W}) + \frac{\mathcal{D}}{M}\sigma_n^2 \right). \quad (32)$$

We implicitly assume here that the eigenvalues are ranked $\lambda_0(\mathcal{W}) \geq \lambda_1(\mathcal{W}) \geq \ldots \geq \lambda_{M-1}(\mathcal{W})$. Moreover, the term in the parentheses results immediately from (15) for the particular choice of $\boldsymbol{U}$. By optimizing $D(\mathcal{W})$ we perform a square bias-variance tradeoff, see also Section V.

D. Channel Prediction

So far we considered the channel estimation problem for a channel observed over a time interval $\mathcal{I}_M$. We used orthogonal basis vectors that result from time-limiting infinite sequences to the interval $\mathcal{I}_M$.

However, the main interest of this paper lies on channel prediction. Slepian points out [10, Sec. 3.1.4] that given the channel samples $h[m], m \in \mathcal{I}_M$ there are infinitely many ways to choose the channel samples $h[m], m \in \mathbb{Z} \setminus \mathcal{I}_M$ such that the infinite sequence $\{h[m]\}$ is band-limited. However, there exists only one way to extend a band-limited sequence in the sense of a ME continuation. This is achieved by using the time-concentrated and band-limited sequences $\{u_i[m, \mathcal{W}]\}$ because the sequences $\{u_i[m, \mathcal{W}]\}$ are most energy-concentrated in the interval $\mathcal{I}_M$.

Evaluating (26) we obtain $\boldsymbol{u}_i(\mathcal{W})$, i.e., we know $u_i[m, \mathcal{W}]$ for $m \in \mathcal{I}_M$. The sequences $\{u_i[m, \mathcal{W}]\}$ can be continued over $\mathbb{Z}$ in the ME band-limited sense by evaluating (21). Finally, we can express the ME band-limited prediction of a time-variant channel for any $m \in \mathbb{Z}$ as

$$\hat{h}[m] = \boldsymbol{f}[m, \mathcal{W}]^{\mathrm{T}}\hat{\boldsymbol{\gamma}} = \sum_{i=0}^{D(\mathcal{W})-1} \hat{\gamma}_i u_i[m, \mathcal{W}] \quad (33)$$

where

$$\boldsymbol{f}[m, \mathcal{W}] = [u_0[m, \mathcal{W}], \ldots, u_{D(\mathcal{W})-1}[m, \mathcal{W}]]^{\mathrm{T}}. \quad (34)$$

In the next section we explain the relation between ME band-limited prediction and the Wiener predictor. The main benefit of ME band-limited prediction will become clear in Section VII. There we utilize the insights into the subspace structure of linear prediction, gained in this section, to design a new *low complexity* prediction scheme based on a *finite* set of hypothesis about the actual Doppler spectrum of the fading process. Each hypothesis is represented by a *precalculated* subspace spanned by the time-concentrated and band-limited sequences defined in this section.

IV. RELATION TO THE WIENER PREDICTOR

In [17, Sec. 12.7] a solution to the prediction problem is presented using a Wiener (linear minimum MSE) predictor. The Wiener predictor can be closely approximated by a reduced-

rank predictor where the subspace dimensions with small eigenvalues are truncated [16]. Both, the Wiener predictor and its reduced rank approximation are defined for a process with general Doppler spectrum and the related covariance matrix $\boldsymbol{\Sigma}_h$.

A process $\{h[m]\}$ exhibiting a constant Doppler spectrum $S_h(\nu, \mathcal{W})$ with support $\mathcal{W}$ given in (27) (see Fig. 1) has the covariance function $R_h[k, \mathcal{W}]$ (28). The restriction of $\{h[m]\}$ on the interval $\mathcal{I}_M$ is described by the covariance matrix $\boldsymbol{\Sigma}_h(\mathcal{W})$ given in (30). For this class of processes we show that the reduced-rank maximum-likelihood (ML) predictor coincides with a ME band-limited predictor [19].

A. Wiener Predictor

With the definition

$$\boldsymbol{r}_h[m] = [R_h[m], R_h[m-1], \ldots, R_h[m-(M-1)]]^{\mathrm{T}} \quad (35)$$

for $m > M - 1$ the ℓ-step Wiener predictor, $\ell = m - (M-1)$, is of the form

$$\hat{h}'[m] = \boldsymbol{r}_h[m]^{\mathrm{H}}\boldsymbol{\Sigma}_{\boldsymbol{y}}^{-1}\boldsymbol{y}. \quad (36)$$

B. Reduced-Rank Maximum-Likelihood Predictor

Similar to the reduced-rank ML *estimator* [16], [30] we are able to define a reduced-rank ML *predictor*. The reduced-rank ML channel estimation described in Section III-A uses a deterministic signal model: The channel weight vector $\boldsymbol{h}$ depends deterministically on $\boldsymbol{\gamma}$ given the matrix $\boldsymbol{U}$. However, as is pointed out in [16, Sec. 1] we implicitly exploit the long-term correlation properties: Matrix $\boldsymbol{U}$ (9) is comprised of the first D essential eigenvectors defined by the eigenvalue identity $\boldsymbol{\Sigma}_h\boldsymbol{u}_i = \lambda_i\boldsymbol{u}_i$. The optimum dimension D is chosen according to

$$D = \underset{\mathcal{D} \in \{1,...,M\}}{\arg\min} \left(\frac{1}{M} \sum_{i=\mathcal{D}}^{M-1} \lambda_i + \frac{\mathcal{D}}{M}\sigma_n^2 \right). \quad (37)$$

Note that D depends on the noise variance.

The reduced-rank ML *predictor* closely approximates (36) using a subspace of $\boldsymbol{\Sigma}_h$ with the optimum subspace dimension D:

$$\hat{h}[m] = \underbrace{\boldsymbol{r}_h[m]^{\mathrm{H}}\boldsymbol{U}\boldsymbol{\Lambda}^{-1}}_{\boldsymbol{f}[m]}\underbrace{\boldsymbol{U}^{\mathrm{H}}\boldsymbol{y}}_{\hat{\boldsymbol{\gamma}}} = \sum_{i=0}^{D-1} u_i[m]\hat{\gamma}_i \quad (38)$$

where $\boldsymbol{\Lambda} = \mathrm{diag}([\lambda_0, \ldots, \lambda_{D-1}])$ and $\boldsymbol{f}[m] = [u_0[m], \ldots, u_{D-1}[m]]^{\mathrm{T}}$. The sequences $\{u_i[m]\}$ are defined as

$$\sum_{\ell=0}^{M-1} R_h[\ell-m]u_i[\ell] = \lambda_i u_i[m], \quad m \in \mathbb{Z} \quad (39)$$

generalizing (21). Again, the sequences $\{u_i[m]\}$ and the restrictions of these sequences on $\mathcal{I}_M$ form orthogonal sets. Note that $\boldsymbol{u}_i = [u_i[0], \ldots, u_i[M-1]]^{\mathrm{T}}$.

For reduced-rank ML prediction the situation is similar to reduced-rank ML channel estimation. The predicted channel

weights depend deterministically on $\boldsymbol{\gamma}$. However, again the deterministic sequences $\{u_i[m]\}$ are obtained by assuming a specific channel covariance matrix.

C. ME Band-Limited Prediction

For a fading process with constant Doppler spectrum $S_h(\nu, \mathcal{W})$ with support $\mathcal{W}$ we can show the similarity between the reduced-rank ML predictor (38) and the ME band-limited predictor (33). We recast (21) as

$$u_i[m, \mathcal{W}] = \frac{|\mathcal{W}|}{\lambda_i(\mathcal{W})} \sum_{\ell=0}^{M-1} R_h[m - \ell, \mathcal{W}]^* u_i[\ell, \mathcal{W}] \quad (40)$$

$$= \frac{|\mathcal{W}|}{\lambda_i(\mathcal{W})} \boldsymbol{r}_h[m, \mathcal{W}]^{\mathrm{H}} \boldsymbol{u}_i(\mathcal{W}) \quad (41)$$

where we use the fact that $R_h[k, \mathcal{W}] = R_h[-k, \mathcal{W}]^*$ and $C[k, \mathcal{W}] = |\mathcal{W}| R_h[k, \mathcal{W}]$. Moreover, inserting (40) in (34) yields

$$\boldsymbol{f}[m, \mathcal{W}]^{\mathrm{T}} = \boldsymbol{r}_h[m, \mathcal{W}]^{\mathrm{H}} \boldsymbol{U}(\mathcal{W}) \boldsymbol{\Lambda}^{-1}(\mathcal{W}) \quad (42)$$

where $\boldsymbol{r}_h[m, \mathcal{W}] = [R_h[m, \mathcal{W}], \dots, R_h[m - (M-1), \mathcal{W}]]^{\mathrm{T}}$, $\boldsymbol{\Lambda}(\mathcal{W}) = 1/|\mathcal{W}| \mathrm{diag}([\lambda_0(\mathcal{W}), \dots, \lambda_{D-1}(\mathcal{W})])$, and $\boldsymbol{U}(\mathcal{W}) = [\boldsymbol{u}_0(\mathcal{W}), \dots, \boldsymbol{u}_{D-1}(\mathcal{W})]$.

Inserting (42) into the ME band-limited predictor (33) we obtain

$$\hat{h}[m] = \boldsymbol{f}[m, \mathcal{W}]^{\mathrm{T}} \hat{\boldsymbol{\gamma}} \quad (43)$$

$$= \boldsymbol{r}_h[m, \mathcal{W}]^{\mathrm{H}} \boldsymbol{U}(\mathcal{W}) \boldsymbol{\Lambda}^{-1}(\mathcal{W}) \boldsymbol{U}(\mathcal{W})^{\mathrm{H}} \boldsymbol{y} \quad (44)$$

which is identical to the reduced-rank ML predictor (38) for fading processes with constant Doppler spectrum $S_h(\nu, \mathcal{W})$. Hence, both predictors use a subspace spanned by time-concentrated and band-limited sequences.

V. ANALYTICAL EXPRESSIONS FOR THE PREDICTION ERROR

A. Wiener Predictor

The minimum MSE per sample, which is achieved with the Wiener predictor is given by [17, Sec. 12.7]

$$\mathrm{MSE}[m] = 1 - \boldsymbol{r}_h[m]^{\mathrm{H}} \boldsymbol{\Sigma}_{\boldsymbol{y}}^{-1} \boldsymbol{r}_h[m]. \quad (45)$$

Specializing to constant Doppler spectra $S_h(\nu, \mathcal{W})$ we can express the $\mathrm{MSE}[m]$ of the Wiener predictor in terms of time-concentrated and band-limited sequences $\{u_i[m, \mathcal{W}]\}$ and their eigenvalues $\lambda_i(\mathcal{W})$. Utilizing (42) we obtain

$$\mathrm{MSE}[m, \mathcal{W}] = 1 - \sum_{i=0}^{M-1} \frac{\lambda_i(\mathcal{W})^2/|\mathcal{W}|}{|\mathcal{W}|\sigma_n^2 + \lambda_i(\mathcal{W})} |u_i[m, \mathcal{W}]|^2. \quad (46)$$

For constant Doppler spectra $S_h(\nu, \mathcal{W})$ we can conclude that the prediction horizon of linear prediction methods is inherently limited because the energy of $\{u_i[m, \mathcal{W}]\}$ is most concentrated in the interval $\mathcal{I}_M$ and $\lim_{m\to\infty} u_i[m, \mathcal{W}] = 0$. This conclusion is a direct consequence of (46). Indeed, $\mathrm{MSE}[m, \mathcal{W}]$ directly depends on the absolute value of the time-concentrated and band-limited sequences $\{u_i[m, \mathcal{W}]\}$. Since the energy of

these sequences is most concentrated in the interval $\mathcal{I}_M$ the absolute value of $u_i[m, \mathcal{W}]$ decays outside $\mathcal{I}_M$ and the MSE per sample $\mathrm{MSE}[m, \mathcal{W}]$ increases at the same time. A similar conclusion can be drawn from (45) and the decay of the covariance function $R_h[k]$.

B. Reduced-Rank ML Predictor

The MSE per sample of the reduced-rank ML predictor can be described as the sum of a square bias and a variance term

$$\mathrm{MSE}[m] = \mathrm{bias}^2[m] + \mathrm{var}[m]. \quad (47)$$

The expression for square bias and variance developed in [31, Sec. 6] and [11] can be extended for reduced-rank ML prediction [19]. Note that in all equations in this section $m \in \mathbb{Z}$.

The following (48)–(51) are valid for any Doppler power spectral density $S_h'(\nu)$ of the actual fading process $\{h[m]\}$. Thus, we can evaluate the prediction error for the mismatched case too. This mean, the predictor design is based on the assumed Doppler spectrum $S_h(\nu)$ but the actual fading process has Doppler spectrum $S_h'(\nu)$.

We define the instantaneous frequency response of the reduced-rank ML predictor according to

$$G[m, \nu] = \boldsymbol{f}^T[m] \sum_{\ell=0}^{M-1} \boldsymbol{f}^*[\ell] \mathrm{e}^{-\mathrm{j}2\pi\nu(m-\ell)} \quad (48)$$

where $|\nu| < 1/2$ and $\boldsymbol{f}[m]^{\mathrm{T}} = \boldsymbol{r}_h[m]^{\mathrm{H}} \boldsymbol{U} \boldsymbol{\Lambda}^{-1}$. In (48), the sum $\sum_{\ell=0}^{M-1} \boldsymbol{f}^*[\ell] \mathrm{e}^{-\mathrm{j}2\pi\nu(m-\ell)}$ projects the complex exponential onto the basis function, i.e., we calculate the inner product with every basis function. Then, the realization at time instant m is calculated by left multiplying with $\boldsymbol{f}^{\mathrm{T}}[m]$.

The complex exponential in (48) is shifted by m, thus, $|G[m, \nu]|$ is the instantaneous amplitude response of the reduced-rank ML predictor at time instant m. The design goal for the predictor is to have no amplitude error and no phase error. Therefore, the instantaneous error characteristic of the reduced rank Wiener predictor is defined as [31, Sec. 6.1.4]

$$E[m, \nu] = |1 - G[m, \nu]|^2. \quad (49)$$

The square bias per sample $\mathrm{bias}^2[m]$ of the reduced-rank ML predictor can be computed from the instantaneous error characteristic $E[m, \nu]$ and the power spectral density of $\{h[m]\}$ according to

$$\mathrm{bias}^2[m] = \int_{-\frac{1}{2}}^{\frac{1}{2}} E[m, \nu] S_h'(\nu) \mathrm{d}\nu. \quad (50)$$

The variance of reduced-rank ML prediction can be approximated according to

$$\mathrm{var}[m] \approx \sigma_n^2 \boldsymbol{f}^H[m] \boldsymbol{f}[m]. \quad (51)$$

C. ME Band-Limited Prediction

The MSE per sample

$$\mathrm{MSE}[m, \mathcal{W}] = \mathrm{bias}^2[m, \mathcal{W}] + \mathrm{var}[m, \mathcal{W}] \qquad (52)$$

for ME band-limited prediction can be obtained by specializing the equations from the previous section by setting $\boldsymbol{f}[m] = \boldsymbol{f}[m, \mathcal{W}]$ (34).

VI. ANALYTIC PERFORMANCE COMPARISON

In this section, we show analytic performance results for the Wiener predictor (36) and the reduced-rank ML predictor (38) using full covariance information. These results are compared with the performance of ME band-limited prediction (33) where the knowledge of the support of the Doppler power spectral density is utilized only.

A. Channel Model and System Assumption

The time-variant flat-fading channel $\{h[m]\}$ is assumed to conform to Clarke's model [32]. The covariance function of $h[m]$ is $R_h[k] = \mathrm{J}_0(2\pi\nu_{\mathrm{D}}k)$ where $\mathrm{J}_0(\cdot)$ is the zeroth-order Bessel function of the first kind. The spectrum of $\{h[m]\}$ reads

$$S_h(\nu) = \frac{1}{\pi\nu_{\mathrm{D}}\sqrt{1 - \left(\frac{\nu}{\nu_{\mathrm{D}}}\right)^2}} \qquad (53)$$

for $|\nu| < \nu_{\mathrm{D}}$ and is zero elsewhere.

The symbol duration $T_{\mathrm{S}} = 20.57 \ \mu s$ is chosen according to the system parameters considered in [11]. The speed of the user varies in the range $0 \leq v \leq v_{\max} = 100 \ \mathrm{km/h} = 27.8 \ \mathrm{m/s}$. The carrier frequency is $f_{\mathrm{C}} = 2$ GHz. This results in a Doppler bandwidth range $0 \leq B_{\mathrm{D}} \leq 180$ Hz. Thus, the normalized Doppler bandwidth, $\nu_{\mathrm{D}} = B_{\mathrm{D}}T_{\mathrm{S}}$, ranges in $0 \leq \nu_{\mathrm{D}} \leq \nu_{\mathrm{D}\,\max} = 3.8 \times 10^{-3}$. The channel is observed over $M = 256$ symbols. During the observation, interval the user travels a distance of at most one wavelength $0 < \nu_{\mathrm{D}}M < 1$. We are interested in the prediction error at a prediction horizon $\ell = m - M + 1 \in \{32, 64, 128\}$ symbols. At speed $v_{\max}$ the prediction horizon $\ell \in \{32, 64, 128\}$ corresponds to a distance of $\{\lambda/8, \lambda/4, \lambda/2\}$ where $\lambda = c_0/f_{\mathrm{C}}$ denotes the wavelength. For all simulations the SNR is 10 dB.

B. Analytic Results

In Fig. 2, we use the MSE of the Wiener predictor (denoted Wiener predictor) as lower bound and plot $\mathrm{MSE}[M - 1 + \ell]$ given by (45) for $\ell \in \{32, 64, 128\}$.

Second, we plot the MSE of the reduced-rank ML predictor (47) calculating the integral (50) numerically (denoted RR ML predictor). The reduced-rank ML predictor uses the exact Doppler spectrum of the fading process, $S_h'(\nu) = S_h(\nu)$. The steps in the curve corresponds to the transitions when the dimension of the (approximation) subspace is increased, see (37).

Third, we show the results for the ME band-limited predictor (denoted ME band-limited) given by $\mathrm{MSE}[M - 1 + \ell, \mathcal{W}(\nu_{\mathrm{D}})]$ in (52). For this predictor, we assume no knowledge about the detailed shape of the Doppler spectrum and assume exact
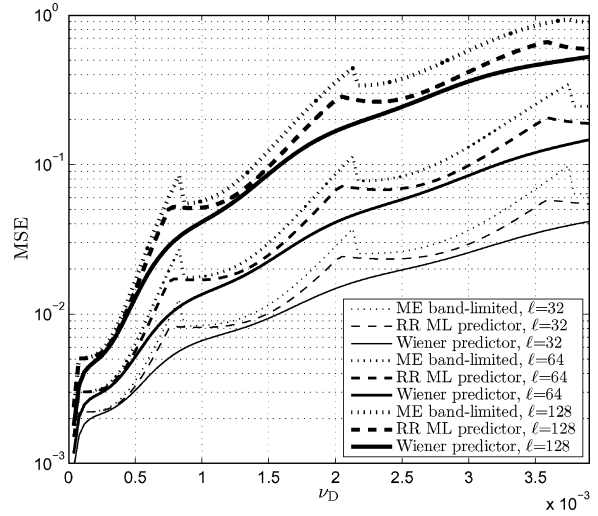
Fig. 2. Mean square prediction error $\mathrm{MSE}[M - 1 + \ell]$ at prediction horizon $\ell \in \{32, 64, 128\}$ versus the normalized Doppler bandwidth ν_{D}. The normalized Doppler bandwidth $\nu_{\mathrm{D}} = 0 \ldots 3.8 \times 10^{-3}$ is induced by a receiver moving with $v = 0 \ldots 27.8 \ \mathrm{m/s}$. The block length $M = 256$. The measurement period relates to a distance traveled by the user in the range of $\nu_{\mathrm{D}}M = 0 \ldots 1$ wavelengths. The SNR equals 10 dB. We compare a Wiener predictor (Wiener predictor) with a reduced-rank ML predictor (RR ML predictor) and the ME band-limited predictor (ME band-limited).

knowledge of the Doppler bandwidth only represented by the band-limiting region $\mathcal{W}(\nu_{\mathrm{D}}) = (-\nu_{\mathrm{D}}, \nu_{\mathrm{D}})$. This assumption leads to a subspace spanned by DPS sequences. The dimension switching points obtained by (32) for this case are slightly suboptimal.

We can see that the MSE for the reduced-rank ML predictor is larger than the MSE achieved with the Wiener predictor. If we assume knowledge of the Doppler bandwidth only the MSE is increased again. However, the MSE changes by several orders of magnitude with increasing Doppler bandwidth. Thus, for a practical implementation the ME band-limited predictor based on DPS sequences achieves close to optimum results while needing information about the Doppler-bandwidth only. The reason for the small loss incurred by utilizing the Doppler bandwidth information only is rooted in the extremely small dimension of the time-concentrated and band-limited channel subspace.

VII. DYNAMIC SUBSPACE SELECTION

In practical systems, information about the Doppler bandwidth must be obtained from channel observations. In [33], a ME band-limited predictor is presented that utilizes the Doppler-bandwidth estimator from [34]. The estimator in [34] assumes a Doppler spectrum according to Clarke's model. Measured Doppler spectra deviate substantially from Clarke's model [20], [21]. Thus, specular Rice components lead to biased Doppler-bandwidth estimates as well as channels with a small number of specular propagation paths. The Doppler-bandwidth estimator proposed in [35] is less sensitive to deviations from Clarke's model, however it requires large observation intervals and an SNR larger than 30 dB.
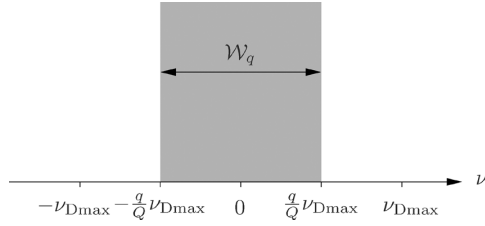
Fig. 3. Symmetric band-limiting region $\mathcal{W}_q = (-q/Q\nu_{\mathrm{D\,max}}, +q/Q\nu_{\mathrm{D\,max}})$ for $q \in \{1, \ldots, Q\}$ used to define a set of Q subspaces.

We are interested in a low complexity implementation of the channel predictor. To this end we develop a dynamic subspace selection scheme for ME band-limited prediction that does not need an explicit Doppler-bandwidth estimate [23]:

- First, we define a finite number of hypotheses about the actual Doppler bandwidth in Section VII-A. Utilizing the theoretical results from Section III we represent each hypothesis by a subspace spanned by time-concentrated and band-limited sequences. The orthogonal basis vectors spanning each subspace are calculated once and then stored.

- Second, we propose a subspace selection method based on a probabilistic bound on the reconstruction error z (11) in Section VII-B. The subspace with the smallest reconstruction error is selected based on the observation of a single data block. This subspace is used for ME band-limited prediction.

A. Subspace Definition

We define the maximum Doppler bandwidth

$$\nu_{\mathrm{D\,max}} = \frac{v_{\max} f_C T_S}{c_0} \tag{54}$$

as system parameter given by the maximum (supported) user velocity $v_{\max}$. Furthermore, we define a set of Q subspaces with spectral support

$$\mathcal{W}_q = \left(-\frac{q}{Q}\nu_{\mathrm{D\,max}}, +\frac{q}{Q}\nu_{\mathrm{D\,max}}\right) \tag{55}$$

for $q \in \{1, \ldots, Q\}$ as shown in Fig. 3. The selection of Q for a specific simulation scenario is treated in Section X-B. The time-concentrated and band-limited sequences $\{u_i[m, \mathcal{W}_q]\}$ corresponding to the band-limiting region $\mathcal{W}_q$ are calculated according to (21). We define the subspace $\boldsymbol{U}_q = [\boldsymbol{u}_0(\mathcal{W}_q), \ldots, \boldsymbol{u}_{D_q-1}(\mathcal{W}_q)]$ for $q \in \{1, \ldots, Q\}$. The subspace dimension $D_q = D(\mathcal{W}_q)$ is chosen according to (32). The dimension of the subspace spanned by $\boldsymbol{U}_q$ grows with increasing $q \in \{1, \ldots, Q\}$ due to the increasing spectral support $\mathcal{W}_q$ with Lebesgue measure $|\mathcal{W}_q| = 2q/Q\nu_{\mathrm{D\,max}}$ [cf. (32)]. The subspace orthogonal to $\boldsymbol{U}_q$ is spanned by $\boldsymbol{V}_q = [\boldsymbol{u}_{D_q}(\mathcal{W}_q), \ldots, \boldsymbol{u}_{M-1}(\mathcal{W}_q)]$.

B. Subspace Selection

In [22], an information theoretic subspace selection scheme is proposed. This method uses the observable data error

$$x_q = \frac{1}{M}\|\boldsymbol{y} - \hat{\boldsymbol{h}}_q\|^2 \tag{56}$$

where

$$\hat{\boldsymbol{h}}_q = \boldsymbol{U}_q \boldsymbol{U}_q^{\mathrm{H}} \boldsymbol{y} \tag{57}$$

to obtain an estimate on the reconstruction error

$$z_q = \frac{1}{M}\|\boldsymbol{h} - \hat{\boldsymbol{h}}_q\|^2 \tag{58}$$

which cannot be observed directly. For the subspace selection, $\boldsymbol{h}$ is considered deterministic. The results in [22] are derived for real valued signals. They are adapted here for complex valued signals and noise.

a) Distribution of the Reconstruction Error: The reconstruction error z_q is a sample of a random variable Z_q which is distributed as [22, Lemma 1]

$$\frac{2M}{\sigma_n^2}\left(Z_q - \frac{1}{M}\left\|\boldsymbol{V}_q^{\mathrm{H}}\boldsymbol{h}\right\|^2\right) \sim \chi_{2D_q}^2 \tag{59}$$

where $\chi_{2D_q}^2$ is a Chi-square random variable of order $2D_q$. Therefore, Z_q has expected value

$$\mathsf{E}\{Z_q\} = \frac{D_q}{M}\sigma_n^2 + \frac{1}{M}\|\boldsymbol{V}_q\boldsymbol{h}\|^2 \tag{60}$$

and variance

$$\mathrm{var}(Z_q) = \frac{D_q}{M^2}\left(\sigma_n^2\right)^2. \tag{61}$$

b) Distribution of the Data Error: The data error x_q is a sample of a random variable X_q which is distributed as [22, Lemma 2]

$$\frac{2M}{\sigma_n^2}X_q \sim \chi_{2(M-D_q)}^2. \tag{62}$$

Therefore, X_q has expected value

$$\mathsf{E}\{X_q\} = \left(\frac{1}{2} - \frac{D_q}{M}\right)\sigma_n^2 + \frac{1}{M}\|\boldsymbol{V}_q\boldsymbol{h}\|^2 \tag{63}$$

and variance

$$\mathrm{var}(X_q) = \frac{1}{M}\left(\frac{1}{2} - \frac{D_q}{M}\right)\left(\sigma_n^2\right)^2 + \frac{2\sigma_n^2}{M^2}\|\boldsymbol{V}_q\boldsymbol{h}\|^2. \tag{64}$$

c) Probabilistic Lower Bound On The Reconstruction Error: First, assuming $(1/M)\|\boldsymbol{V}_q^{\mathrm{H}}\boldsymbol{h}\|^2$ is known, the reconstruction error z_q is bounded with probability p_1 according to [22, Sec. III.C.]

$$\underline{z_q'}(p_1) \leq z_q \leq \overline{z_q'}(p_1), \tag{65}$$

where

$$\underline{z_q'}(p_1) = \frac{D_q}{M}\sigma_n^2 + \frac{1}{M}\|\boldsymbol{V}_q^{\mathrm{H}}\boldsymbol{h}\|^2 - G_q(p_1, \sigma_n, 2D_q) \tag{66}$$

and

$$\overline{z_q'}(p_1) = \frac{D_q}{M}\sigma_n^2 + \frac{1}{M}\|\boldsymbol{V}_q^{\mathrm{H}}\boldsymbol{h}\|^2 + G_q(p_1, \sigma_n, 2D_q). \tag{67}$$

The term $G_q(p_1, \sigma_n, 2D_q)$ is calculated by solving

$$p_1 = F\left(2D_q + 2G_q\frac{M}{\sigma_n^2}, 2D_q\right) - F\left(2D_q - 2G_q\frac{M}{\sigma_n^2}, 2D_q\right) \tag{68}$$

numerically for G_q. In (68) $F(x, n)$ denotes the Chi-square cumulative distribution function with n degrees of freedom. Note that G_q is actually independent of the current channel realization [36] which will be important for a practical low complexity implementation as discussed in Section VIII.

Second, we utilize x_q to obtain a probabilistic bound on $(1/M)\|\boldsymbol{V}_q^{\mathrm{H}}\boldsymbol{h}\|^2$. Because $2(M - D_q)$ is large we can invoke the Central Limit Theorem to approximate X_q with a Gaussian random variable. The term $(1/M)\|\boldsymbol{V}_q^{\mathrm{H}}\boldsymbol{h}\|^2$ is bounded with probability p_2 according to [22, Theorem 1]

$$\underline{B_q}(x_q, p_2) \le \frac{1}{M}\|\boldsymbol{V}_q^{\mathrm{H}}\boldsymbol{h}\|^2 \le \overline{B_q}(x_q, p_2). \qquad (69)$$

The lower bound $\underline{B_q}$ is zero if $(m_q - \alpha\sqrt{v_q}) \le x_q \le (m_q + \alpha\sqrt{v_q})$, where the probability p_2 is considered in the form $p_2 = \int_{-\alpha}^{\alpha}(1/\sqrt{2\pi})e^{-x^2/2}\mathrm{d}x$, $m_q = (1/2 - D_q/M)\sigma_n^2$ and $v_q = 1/M(1/2 - D_q/M)\sigma_n^4$. Otherwise, the lower bound is

$$\underline{B_q}(x_q, p_2) = x_q - m_q + \frac{\alpha^2\sigma_n^2}{M} - K_q(\alpha) \qquad (70)$$

where

$$K_q(\alpha) = 2\alpha\frac{\sigma_n}{\sqrt{2M}}\sqrt{\frac{\alpha^2\sigma_n^2}{2M} + x_q - \frac{1}{2}m_q}. \qquad (71)$$

The upper bound is

$$\overline{B_q}(x_q, p_2) = x_q - m_q + \frac{\alpha^2\sigma_n^2}{M} + K_q(\alpha). \qquad (72)$$

Finally, we use the upper bound $\overline{z_q}(x_q, p_1, p_2) \ge \overline{z_q'}(p_1)$,

$$\overline{z_q}(x_q, p_1, p_2) = \frac{D_q}{M}\sigma_n^2 + \overline{B_q}(x_q, p_2) + G_q(p_1, \sigma_n, 2D_q) \quad (73)$$

on the reconstruction error to select the appropriate subspace q spanned by the columns of $\boldsymbol{U}_q$

$$\hat{q} = \arg\min_q \overline{z_q}(x_q, p_1, p_2). \qquad (74)$$

The chosen subspace $\boldsymbol{U}_{\hat{q}}$ and the associated sequences $\{u_i[m, \mathcal{W}_q]\}$ are used for ME band-limited prediction. The probability p_1 is chosen as $p_1 = Q(\alpha)|_{\alpha=1}$ with $Q(\alpha) = \int_{-\alpha}^{\alpha}(1/\sqrt{2\pi})e^{-x^2/2}\mathrm{d}x$. The probability $p_2 = Q(8) \approx 1 - 10^{-15}$.

VIII. COMPLEXITY

We assume the following known system parameters for the predictor: The block length M, the maximum velocity of the user $v_{\max}$, the maximum Doppler bandwidth $\nu_{\mathrm{D\,max}}$, the number of precalculated subspaces Q, and the operating range of the SNR $\in (\mathrm{SNR}_{\min}, \mathrm{SNR}_{\max})$. The noise variance σ_n^2 is represented by N discrete values over the operating range of the predictor.
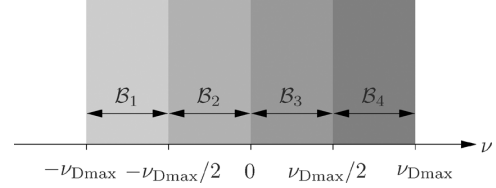
Fig. 4. Asymmetric band-limiting region. Example for $Q' = 4$.

The complexity of the proposed ME band-limited predictor with dynamic subspace selection is mainly determined by the complexity of projecting the observation vector $\boldsymbol{y}$ on all Q subspaces $\boldsymbol{U}_q$ in (57). This operation requires $2(\sum_{q=1}^{Q} D_q)M$ complex multiply accumulate instructions. The storage of all precalculated basis functions needs memory for $QD_q(M+N)$ values.

The computational effort needed to calculate the upper bound on the reconstruction error for each single subspace $\boldsymbol{U}_q, q \in \{1, \ldots, Q\}$ in (73) can be neglected since it involves the simple calculation of three terms (p_1, p_2 and α fixed): The first term in (73), $\sigma_n^2 D_q/M$, can be precalculated and needs storage of NQ values. The second term, $\overline{B_q}(x_q, p_2)$, depends directly on the data error x_q. For the calculation of the individual terms of $\overline{B_q}$ we need storage for $5NQ$ precalculated values and the calculation of Q square roots for $K_q(\alpha)$. The third term, $G_q(p_1, \sigma_n, 2D_q)$, can be precalculated needing storage of NQ values.

A predictor based on complex exponentials needs Doppler shift estimates for all P paths. Most methods for Doppler shift estimation rely on an eigenvalue decomposition of the channel's sample covariance matrix [37]. The complexity of the eigenvalue decomposition grows with PM^2. Hence, the complexity the ME band-limited predictor with dynamic subspace selection is much smaller then the complexity of complex-exponential-based predictors if $PM > 2(\sum_{q=1}^{Q} D_q)$. For the simulation parameters used in Section X this relation is fulfilled.

IX. ADAPTION TO DISJOINT DOPPLER SPECTRA

In mobile communication channels, fading processes frequently arise whose spectral support is the union of disjoint intervals. Such short-time Doppler spectra are caused by a nonuniform scatterer distribution or by a small number of specular propagation paths, as reported in [20] and [21]. For such fading processes the set of subspaces defined based on symmetric constant Doppler spectra (55) are suboptimal.

If the number of specular propagation paths is small it is likely that all paths, for example, have either a positive or a negative Doppler shift only. The band-limiting region $\mathcal{W}_q$ defining the subspace $\boldsymbol{U}_q$ in Fig. 3 is symmetric to the origin, hence in this case the support of the band-limiting region is larger than necessary leading to a reduced prediction horizon, see the Monte Carlo simulation results in Section X.

Based on the above explanations we propose to partition the region $(-\nu_{\mathrm{D\,max}}, \nu_{\mathrm{D\,max}})$ into Q' spectral bins with equal length as depicted in Fig. 4. The spectral bin $i \in \{1, \ldots, Q'\}$ spans the interval

$$\mathcal{B}_i = \left[-\nu_{\mathrm{D\,max}} + (i-1)\frac{\nu_{\mathrm{D\,max}}}{Q'}, -\nu_{\mathrm{D\,max}} + i\frac{\nu_{\mathrm{D\,max}}}{Q'}\right].$$
$$(75)$$

99

Using all possible binary combinations of $\mathcal{B}_i$ we can define $2^{Q'} - 1$ band-limiting regions $\mathcal{W}'_{q'}$, $q' \in \{1, \ldots, 2^{Q'} - 1\}$

$$\mathcal{W}'_1 = \mathcal{B}_1 \tag{76}$$

$$\mathcal{W}'_2 = \mathcal{B}_2, \tag{77}$$

$$\mathcal{W}'_3 = \mathcal{B}_1 \cup \mathcal{B}_2 \tag{78}$$

$$\vdots$$

$$\mathcal{W}'_{(2^{Q'}-1)} = \mathcal{B}_1 \cup \ldots \cup \mathcal{B}_{Q'} = (\nu_{\mathrm{D\,max}}, \nu_{\mathrm{D\,max}}). \tag{79}$$

Based on the band-limiting regions $\mathcal{W}'_{q'}$ we can define $\boldsymbol{U}'_{q'}$, $\boldsymbol{V}'_{q'}$ and $D'_{q'}$ similar to the definition in Section VII-A.

X. MONTE CARLO SIMULATIONS

In this section, we present performance results for ME band-limited prediction using the dynamic subspace selection scheme derived in the previous section. We provide comparisons to a Wiener predictor that utilized the long-term Doppler spectrum and to a classic predictor based on complex exponentials. The predictor using complex exponentials is described in Appendix I.

A. Physical Wave Propagation Channel Model

We simulate the fading process $\{h[m]\}$ using physical wave propagation principles [32], [38]. The electromagnetic field at the receiving antenna is the superposition of the contribution of the individual fields of P impinging plane waves. Each plane wave is conceived as propagating along a specific path. Under these assumptions the channel weight is of the form

$$h[m] = \sum_{p=0}^{P-1} a_p \mathrm{e}^{\mathrm{j}2\pi f_p T_{\mathrm{S}} m} = \sum_{p=0}^{P-1} a_p \mathrm{e}^{\mathrm{j}2\pi \nu_p m}. \tag{80}$$

Here f_p is the Doppler shift of wave p. For easier notation we define the normalized Doppler frequency as $\nu_p = f_p T_{\mathrm{S}}$. Note that $|\nu_p| \leq \nu_{\mathrm{D}} < 1/2$. The gain and phase shift of path p are embodied in the complex weight $a_p \in \mathbb{C}$. We model the random parameter sets a_p and ν_p, $p \in \{0, \ldots, P-1\}$ as independent. The random variables in each set are independent and identically distributed. The path angles α_p are uniformly distributed over $[-\pi, \pi]$. The normalized Doppler shift per path is $\nu_p = \nu_{\mathrm{D}} \cos \alpha_p$. The path weights are defined as $a_p = (1/\sqrt{P})\mathrm{e}^{\mathrm{j}\psi_p}$ where ψ_p is uniformly distributed over $[-\pi, \pi]$. Under the above assumptions, the covariance function of $\{h[m]\}$ converges to $R_h[k] = \mathrm{J}_0(2\pi\nu_{\mathrm{D}}k)$, for $P \to \infty$, where J_0 is the zeroth-order Bessel function of the first kind [32].

We assume a time-variant block-fading channel model comprised of P paths. Hence, the random path parameters a_p and ν_p are assumed to be constant over a block of $M + N$ symbols. However, the path parameters a_p and ν_p change independently from block to block, therefore, the short-time spectrum changes as well [2].

We note that the overidealized simulation models from Jakes [39] or Zheng [40] are *not* suitable for the evaluation of channel prediction algorithms. This is because a symmetric distribution of the scatterers with equidistant spacing is assumed in [39],
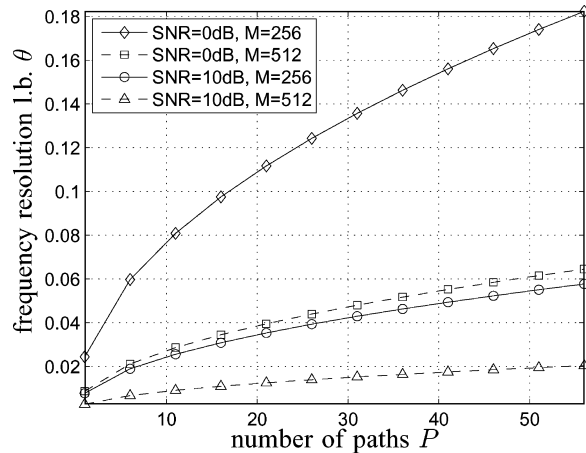
Fig. 5. Lower bound on the frequency resolution (82) versus number of propagation paths P. The $\mathrm{SNR} \in \{0, 10\}$ dB and the block length $M \in \{256, 512\}$.

[40]. However real-world channels will not exhibit equidistantly spaced scatterers. Prediction algorithms assuming a finite number of specular paths [41] show optimistically biased performance due to this overidealized scatterer distribution.

B. Choice of the Number of Subspaces Q

The lower bound for the frequency estimation error of a single complex exponential in white Gaussian noise is given by the Cramér-Rao lower bound (CRLB) [17, Sec. 15.10],

$$\sqrt{\mathrm{var}(\hat{\nu})} \geq \sqrt{\frac{6\sigma_n^2}{(2\pi)^2 M(M^2 - 1)}}. \tag{81}$$

This bound applies to the problem of Doppler frequency estimation for $P = 1$ propagation path, too. With increasing number of paths P the estimation error for the Doppler frequency per path increases due to reduced energy per propagation path. The higher likelihood of closely spaced frequencies increases the CRLB additionally [9]. We conjecture that the CRLB for frequency estimation is a lower bound for the problem of Doppler bandwidth estimation for a fading process with $P > 1$ propagation paths.

We are interested to define a finite number of Q hypothesis about the Doppler bandwidth of the fading process (see Fig. 3). To this end we quantize the range $0 \leq \nu_{\mathrm{D}} \leq \nu_{\mathrm{D\,max}}$ into Q sub-intervals. We define the relative frequency resolution as

$$\theta = \frac{1}{\nu_{\mathrm{D\,max}}} \sqrt{\frac{6P\sigma_n^2}{(2\pi)^2 M(M^2 - 1)}} \tag{82}$$

and use its inverse to get an upper bound on the number of subspaces $Q \leq 1/\theta$. In Fig. 5 we plot θ versus the number of paths P for an $\mathrm{SNR} \in \{0, 10\}$ dB. Fig. 5 documents that the lower bound on the frequency resolution is in the order of $0.03\nu_{\mathrm{D\,max}}$ to $0.11\nu_{\mathrm{D\,max}}$ for $P = 20$ propagation paths and block length $M = 256$. Since frequencies can only be estimated with 10% accuracy, 10 hypothesis (subspaces) are sufficient to estimate the Doppler bandwidth. We partition the range $0 \leq \nu_{\mathrm{D}} \leq \nu_{\mathrm{D\,max}}$ into $Q = 10$ intervals, see (55).

C. Simulation Setup and Results

We use the simulation parameters from Section VI-A. For all simulations the SNR is 10 dB. Monte Carlo simulations have been performed to contrast the performance of the three following predictors:

- The Wiener predictor (denoted Wiener predictor) is defined in (36) and utilizes knowledge of the long-term model covariance function $R_h[k] = J_0(2\pi\nu_D k)$. This predictor is a sensible choice for large number of propagation paths $P = 30$. However, for $P = 2$ paths this predictor will be suboptimal.
- The predictor based on complex exponential functions (denoted compl. exponential) which is derived based on the specular-path model (80) knows the number of paths P and the Doppler frequencies of each path perfectly. Only the complex path weights are estimated, see Appendix I. This allows us to obtain a lower bound on the performance of the predictor based on complex exponentials.
- The new ME band-limited predictor is presented in two configurations.
  1) We show simulation results (denoted ME band-limited sym.) using the set of symmetric subspaces U_q, $q \in \{1, \ldots, Q\}$ with $Q = 10$ defined according to Fig. 3 in Section VII-A.
  2) We combine the set of symmetric subspaces U_q with the set of asymmetric subspaces $U'_{q'}$, $q' \in \{1, \ldots, 2^{Q'} - 1\}$ with $Q' = 4$ defined according to Fig. 4 in Section IX. Both sets contain two identical band-limiting regions, which are $\mathcal{W}_5 = \mathcal{W}'_5 = \mathcal{B}_2 \cup \mathcal{B}_3$ and $\mathcal{W}_{10} = (-\nu_{D\,\max}, \nu_{D\,\max}) = \mathcal{W}'_{15} = \mathcal{B}_1 \cup \mathcal{B}_2 \cup \mathcal{B}_3 \cup \mathcal{B}_4$. Thus, U'_6 and U'_{15} are not used. The subspace selection method from Section VII is applied on the combined set of subspaces. The simulation results are denoted ME band-limited sym.+asym.

The MSE of all three predictors are reported in Figs. 6–10 versus the normalized Doppler frequency ν_D. We present results for the prediction horizons $\ell = m - M + 1 \in \{32, 96\}$ and considering a channel model with $P \in \{2, 30\}$ propagation paths. At speed $v_{\max}$ the prediction horizon $\ell \in \{32, 96\}$ corresponds to a distance of $\{\lambda/8, 3\lambda/8,\}$ where $\lambda = c_0/f_C$ denotes the wavelength.

All MSE results in the paper are given in terms of the sample mean $\widehat{\text{MSE}}[m] = 1/B \sum_{b=0}^{B-1} |h_b[m] - \hat{h}_b[m]|^2$ where the index b denotes the block number. We average over $B = 1000$ independent channel realizations. We do *not* perform any further normalization or outlier removal as in [5], [6].

D. Discussion of Simulation Results

We can observe that the Wiener predictor performance is independent of the number of propagation paths P. In Fig. 6, we show the results for the ME band-limited predictor with dynamic subspace selection. This predictor shows slightly higher MSE than the Wiener predictor. Note that the Wiener predictor knows the model covariance function exactly while the ME band-limited predictor selects the best subspace based on the observation of a single data block. The results in Fig. 6 agree
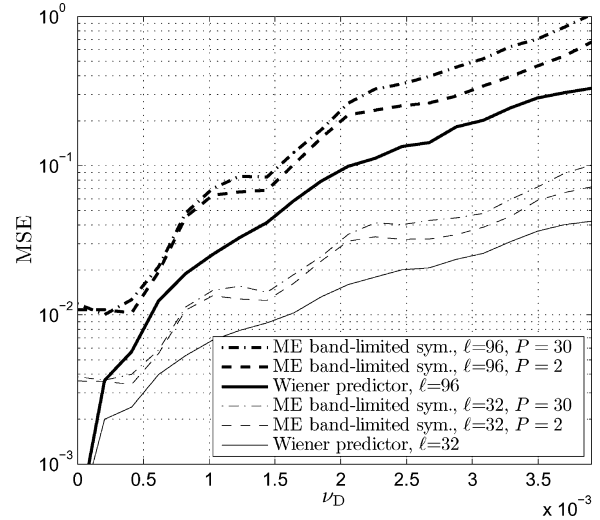
Fig. 6. Mean square prediction error $\text{MSE}[M - 1 + \ell]$ at prediction horizon $\ell \in \{32, 96\}$ versus the normalized Doppler bandwidth ν_D. The normalized Doppler bandwidth $\nu_D = 0 \ldots 3.8 \times 10^{-3}$ is induced by a receiver moving with $v = 0 \ldots 27.8$ m/s. The block length $M = 256$. The measurement period relates to a distance traveled by the user in the range of $\nu_D M = 0 \ldots 1$ wavelengths. The SNR equals 10 dB. We compare a Wiener predictor (Wiener predictor) with a ME band-limited predictor with dynamic subspace selection (ME band-limited sym.).

qualitatively with the analytic results presented in Fig. 2 which where obtained with perfect Doppler bandwidth knowledge.

By combining the set of symmetric and the set of asymmetric subspaces in Figs. 7 and 8 we are able to enhance the performance for small number of paths $P \leq 4$ and large Doppler bandwidth. The dynamic subspace selection has now added freedom to exclude empty regions from the signal subspace. Each spectral bin $\mathcal{B}_1 \ldots \mathcal{B}_4$ in Fig. 4 can be switched on or off individually leading to enhanced prediction performance.

Additionally, we show the performance of the predictor based on complex exponentials. This predictor performs poorly if the Doppler bandwidth ν_D is small, see Figs. 7 and 8. This is because the estimation error for the complex weight of each individual path increases if the Doppler shift difference between two paths becomes small. A detailed analysis of the Cramér-Rao lower bound (CRLB) for the situation of two paths is presented in [9]. For less than four paths and for large Doppler spread the predictor based on complex exponentials performs better than the Wiener predictor (see Figs. 7 and 8). We emphasize that we assumed perfect knowledge of the number of paths P and the Doppler shift of each path ν_p, $p \in \{1, \ldots, P\}$, which leads to highly optimistic performance for the predictor based on complex exponentials. We stick to this assumption to obtain a lower bound on the complex exponential predictor performance.

In Fig. 9, we plot the lower bound for a Wiener predictor by using the exact Doppler power spectral density of the current data block (denoted Wiener pred. inst. spectrum). In this case, the Doppler power spectral density is given as the sum of Dirac pulses at the Doppler shift of each path $S_h(\nu) = \sum_{p=0}^{P-1} E\{|a_p|^2\} \delta(\nu - \nu_p)$. Additionally, we plot the result for the most simple predictor that assumes a band-limiting
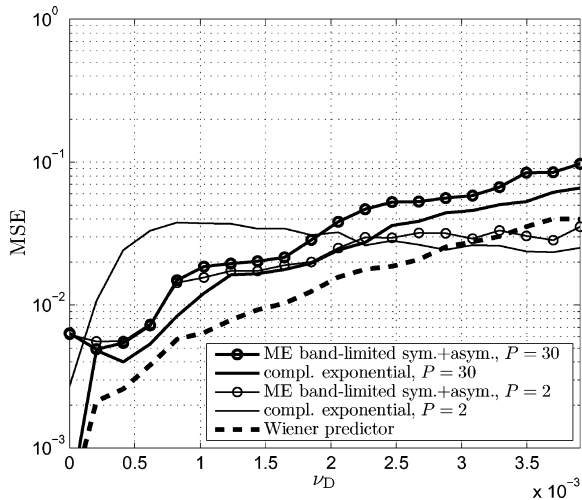
Fig. 7. Mean square prediction error $\mathrm{MSE}[M - 1 + \ell]$ versus Doppler bandwidth ν_D at prediction horizon $\ell = 32$ for a channel with $P \in \{2, 30\}$ propagation paths. We compare a predictor using complex exponential basis functions (compl. exponential) with perfectly known frequencies, the Wiener predictor (Wiener predictor) and the ME band-limited predictor with dynamically selected symmetric and asymmetric subspaces (ME band-limited sym.+asym.). The $\mathrm{SNR} = 10$ dB and the observation block length $M = 256$.

Fig. 9. Mean square prediction error $\mathrm{MSE}[M - 1 + \ell]$ versus Doppler bandwidth ν_D at prediction horizon $\ell = 96$ for a channel with $P \in \{2, 4, 30\}$ propagation paths. We compare the ME band-limited predictor with dynamically selected subspaces with a predictor that uses a fixed subspace according to the maximum Doppler spread (ME band-limited $\nu_\mathrm{D\,max}$). As lower bound we show results for a Wiener predictor that knows the instantaneous Doppler frequencies perfectly (Wiener pred. inst. spectrum). The $\mathrm{SNR} = 10$ dB and the observation block length $M = 256$.

Fig. 8. Mean square prediction error $\mathrm{MSE}[M - 1 + \ell]$ versus Doppler bandwidth ν_D at prediction horizon $\ell = 96$ for a channel with $P \in \{2, 30\}$ propagation paths. The $\mathrm{SNR} = 10$ dB and the observation block length $M = 256$.
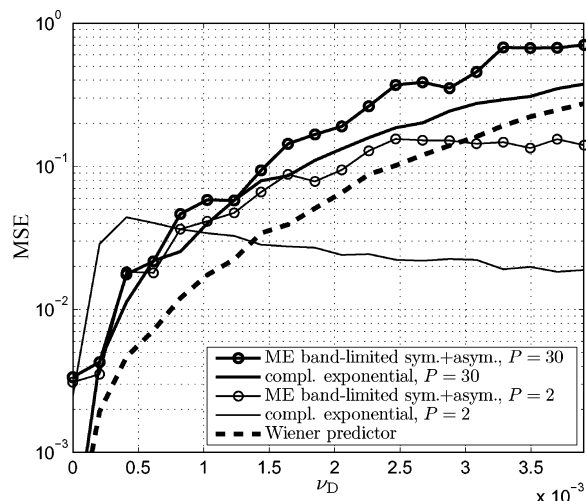
Fig. 10. Mean square prediction error $\mathrm{MSE}[M - 1 + \ell]$ versus Doppler bandwidth ν_D at prediction horizon $\ell = 96$ for a channel with $P \in \{2, 30\}$ propagation paths. The $\mathrm{SNR} = 10$ dB and the observation block length $M = 512$.

region $\mathcal{W} = \left(-\nu_\mathrm{D\,max}, +\nu_\mathrm{D\,max}\right)$ according to the maximum velocity v_max (denoted ME band-limited $\nu_\mathrm{D\,max}$), see (54). For large Doppler bandwidth, the dynamic subspace selection scheme performs slightly worse than the predictor with the fixed bandlimiting region. This is due to the fact that the subspace selection scheme decides to use the wrong subspace sometimes.

In Fig. 10, we show results for a data block length of $M = 512$. By doubling the observation interval the prediction performance of the Wiener predictor and the predictor based on complex exponentials changes only slightly. However, the subspace

selection scheme benefits from the enlarged observation period because the probabilistic estimate of the upper bound on the reconstruction error (73) shows reduced variance.

XI. CONCLUSION

In this paper, we presented a new ME band-limited prediction method for a time-variant process with arbitrary power spectral density. The predictor is based on time-concentrated and band-

limited sequences. We obtain time-concentrated and band-limited sequences for a band-limiting region consisting of disjoint intervals by generalizing results from Slepian [10].

We showed that ME band-limited prediction is identical to reduced-rank ML prediction for fading processes with constant Doppler spectrum. For a fading process with constant Doppler spectrum, this equivalence allows the conclusion that the subspace underlying the linear prediction problem is energy-concentrated. This fact inherently limits the prediction horizon of linear prediction methods. A similar conclusion can be drawn from the decay of the covariance function $R_h(k)$.

We provided a performance analysis for reduced-rank ML prediction using full information about the channel covariance function and for ME band-limited prediction using information about the Doppler bandwidth only. Numeric evaluation of the prediction error shows that knowledge of the detailed power spectral density is not crucial. We conclude that the predictor performance primarily depends on the Doppler bandwidth, but is almost indifferent to other features of the Doppler spectrum.

We exploit these observations to design a set of subspaces spanned by sequences with fixed time-concentration but growing Doppler bandwidth. The sequences in each subspace exhibit a fixed time-concentration and a subspace-specific bandwidth. Each subspace is matched to the support of a certain Doppler power spectral density. The dimensions of the predefined subspaces are in the range from one to five for practical communication systems. The subspace applied for ME prediction is selected based on a probabilistic bound on the reconstruction error. For a prediction horizon of one eights of a wavelength the numerical simulation results show that the ME band-limited predictor with dynamic subspace selection performs better than or similar to a predictor based on complex exponentials with perfectly known frequencies. For a prediction horizons of three eights of a wavelength the performance of the ME band-limited predictor approaches that of a Wiener predictor with perfectly known Doppler bandwidth.

APPENDIX I
CHANNEL PREDICTION BASED ON COMPLEX EXPONENTIAL BASIS FUNCTIONS

The ME band-limited predictor described in Section III uses time-concentrated and band-limited sequences to span the channel subspace. Classical channel prediction algorithms describe the channel subspace using complex exponential basis functions. In the method proposed in [4] and [5] the path parameters a_p and ν_p in (80) are estimated to enable channel prediction. We review here shortly the method, so that we are able to compare it with our ME band-limited predictor.

For a limited observation interval $\mathcal{I}_M$, we can rewrite (80) in vector matrix notation according to

$$\boldsymbol{h} = \begin{bmatrix} 1 & 1 & \ldots & 1 \\ w_0 & w_1 & \ldots & w_{P-1} \\ \vdots & \vdots & & \vdots \\ w_0^{M-1} & w_1^{M-1} & \ldots & w_{P-1}^{M-1} \end{bmatrix} \begin{bmatrix} a_0 \\ a_1 \\ \vdots \\ a_{P-1} \end{bmatrix} = \boldsymbol{Wa} \tag{83}$$

where $w_p = \mathrm{e}^{\mathrm{j}2\pi\nu_p}$. In [4] ESPRIT [42] is used to estimate the Doppler shift ν_p of each single propagation path. ESPRIT requires $P \leq M$. The number of paths P is known as well.

The complex weight vector $\boldsymbol{a} = [a_1, \ldots, a_P]^{\mathrm{T}}$ is estimated according to

$$\hat{\boldsymbol{a}} = \left(\hat{\boldsymbol{W}}^{\mathrm{H}} \hat{\boldsymbol{W}} + \sigma_n^2 \boldsymbol{I}_P \right)^{-1} \hat{\boldsymbol{W}}^{\mathrm{H}} \boldsymbol{y} \tag{84}$$

where $\hat{\boldsymbol{W}}$ results by inserting the Doppler estimates in $\boldsymbol{W}$. Finally, the time-variant channel is predicted via

$$\hat{h}[m] = \sum_{p=0}^{P-1} \hat{a}_p \mathrm{e}^{\mathrm{j}2\pi\nu_p m} \tag{85}$$

for $m \in \{M, \ldots, M+N-1\}$. In this paper we assume that all ν_p, $p \in \{0, \ldots, P-1\}$ are known exactly which allows us to obtain a lower bound on the performance of the predictor based on complex exponentials.

APPENDIX II
PROOF OF THEOREM 1

Consider square-summable sequences $u[m] \in \ell^2(\mathbb{Z})$, which are band-limited to a region $\mathcal{W} \subseteq (-1/2, 1/2)$, i.e., whose Fourier transform $U(\nu)$ vanishes outside $\mathcal{W}$, see (18) and (19). Furthermore, the energy-concentration on an arbitrary but fixed index set $\mathcal{I} \subset \mathbb{Z}$ should be maximal, i.e.,

$$\rho = \frac{\sum_{m\in\mathcal{I}} |u[m]|^2}{\sum_{m=-\infty}^{\infty} |u[m]|^2} \to \max. \tag{86}$$

Using Parseval's theorem ρ can be recast as

$$\rho = \frac{\int_{\mathcal{W}} \int_{\mathcal{W}} \sum_{m\in\mathcal{I}} e^{\mathrm{j}2\pi(\nu-\nu')m} U(\nu)U^*(\nu')\mathrm{d}\nu\mathrm{d}\nu'}{\int_{\mathcal{W}} |U(\nu)|^2 \mathrm{d}\nu}. \tag{87}$$

It can be seen, that ρ is maximum if, and only if, $U(\nu)$ satisfies the integral equation

$$\int_{\mathcal{W}} K(\nu,\nu')U(\nu)\mathrm{d}\nu = \gamma U(\nu') \tag{88}$$

with the Hermitian kernel $K(\nu,\nu')$ defined as

$$K(\nu,\nu') = \sum_{m\in\mathcal{I}} e^{\mathrm{j}2\pi(\nu-\nu')m}. \tag{89}$$

Notice that inserting (88) into (87) yields

$$\gamma = \rho. \tag{90}$$

Since the kernel K is degenerate and has the specific form (89), the solutions of (88) are finite and can be found by writing the left-hand side (LHS) of (88) as [43]

$$\int_{\mathcal{W}} K(\nu,\nu')U_i(\nu)\mathrm{d}\nu = \sum_{\ell\in\mathcal{I}} u_i[\ell]e^{-\mathrm{j}2\pi\nu'\ell}. \tag{91}$$

103

In the above expression, i is an indexing of the solutions. Substituting in (88) and replacing ν' by ν results in

$$\sum_{\ell \in \mathcal{I}} u_i[\ell] e^{-\mathrm{j}2\pi\nu\ell} = \rho_i U_i(\nu). \tag{92}$$

Multiplying both sides with $e^{\mathrm{j}2\pi\nu m}$ and integrating with respect to ν over the region $\mathcal{W}$ yields

$$\sum_{\ell \in \mathcal{I}} u_i[\ell] \int_{\mathcal{W}} e^{\mathrm{j}2\pi\nu(m-\ell)} \mathrm{d}\nu = \rho_i u_i[m], \quad m \in \mathbb{Z}. \tag{93}$$

This identity is exactly the defining (21) of the band-limited and time-concentrated sequences in Theorem 1.

Note that in [27], identity (90) is derived assuming that the defining (21) is already known. The present proof yields all results by maximizing the energy-concentration of the sought sequence in the interval $\mathcal{I}$ only. In [10], identity (90) is proven for a symmetric band-limiting region $\mathcal{W} = (-\nu_{\mathrm{D}}, \nu_{\mathrm{D}})$.

The proof presented here is valid for any Lebesgue-measurable subset of $(-1/2, +1/2)$ and in particular when $\mathcal{W}$ is the union of disjoint intervals as considered in Section III-B. Moreover, throughout the paper we consider the special case $\mathcal{I} = \mathcal{I}_M$.

REFERENCES

[1] L. L. Scharf, *Statistical Signal Processing: Detection, Estimation, and Time Series Analysis*. Reading, MA: Addison-Wesley, 1991.
[2] I. Viering, *Analysis of Second Order Statistics for Improved Channel Estimation in Wireless Communications*, ser. Fortschritts-Berichte VDI Reihe. Düsseldorf, Germany: VDI Verlag GmbH, 2003, no. 733.
[3] G. Matz, "On non-WSSUS wireless fading channels," *IEEE Trans. Wireless Commun.*, vol. 4, no. 5, pp. 2465–2478, Sep. 2005.
[4] J. B. Andersen, J. Jensen, S. H. Jensen, and F. Frederiksen, "Prediction of future fading based on past measurements," in *Proc. 50th IEEE Veh. Technol. Conf. (VTC)—Fall*, Sep. 19–22, 1999, vol. 1, pp. 151–155.
[5] M. Chen, M. Viberg, and T. Ekman, "Two new approaches to channel prediction based on sinusoidal modelling," presented at the 13th Workshop on Statistical Signal Processing (SSP), Bordeaux, France, Jul. 17–20, 2005.
[6] M. Chen, T. Ekman, and M. Viberg, "New approaches for channel prediction based on sinusoidal modelling," *EURASIP J. Appl. Signal Process.*, 2006, to be published.
[7] T. Ekman, "Prediction of mobile radio channels—modeling and design," Ph.D. dissertation, Uppsala Univ., Uppsala, Sweden, 2002.
[8] S. Semmelrodt, "Methoden zur prädiktiven Kanalschätzung für adaptive Übertragunstechniken im mobilfunk," Ph.D. dissertation, Kassel Univ., Kassel, Germany, 2003.
[9] B. H. Fleury, M. Tschdin, R. Heddergott, D. Dalhaus, and K. I. Pedersen, "Channel parameter estimation in mobile radio environments using the SAGE algorithm," *IEEE J. Sel. Areas Commun.*, vol. 17, no. 3, pp. 434–450, Mar. 1999.
[10] D. Slepian, "Prolate spheroidal wave functions, Fourier analysis, and uncertainty—V: The discrete case," *The Bell Syst. Tech. J.*, vol. 57, no. 5, pp. 1371–1430, May–Jun. 1978.
[11] T. Zemen and C. F. Mecklenbräuker, "Time-variant channel estimation using discrete prolate spheroidal sequences," *IEEE Trans. Signal Process.*, vol. 53, no. 9, pp. 3597–3607, Sep. 2005.
[12] R. J. Lyman, W. W. Edmonson, S. McCullough, and M. Rao, "The predictability of continuous-time, bandlimited processes," *IEEE Trans. Signal Process.*, vol. 48, no. 2, pp. 311–316, Feb. 2000.

[13] R. J. Lyman and W. W. Edmonson, "The prediction of bandlimited processes with flat spectral densities," *IEEE Trans. Signal Process.*, vol. 49, no. 7, pp. 1564–1569, Jul. 2001.
[14] R. J. Lyman, "Optimal mean-square prediction of the mobile-radio fading envelope," *IEEE Trans. Signal Process.*, vol. 51, no. 3, pp. 819–824, Mar. 2003.
[15] S. Dharanipragada and K. S. Arun, "Bandlimited extrapolation using time-bandwidth dimension," *IEEE Trans. Signal Process.*, vol. 45, no. 12, pp. 2951–2966, Dec. 1997.
[16] F. A. Dietrich and W. Utschik, "Pilot-assisted channel estimation based on second-order statistics," *IEEE Trans. Signal Process.*, vol. 53, no. 3, pp. 1178–1193, Mar. 2005.
[17] S. Kay, *Fundamentals of Statistical Signal Processing: Estimation Theory*. Upper Saddle River, NJ: Prentice-Hall, 1993.
[18] A. K. Jain and S. Ranganath, "Extrapolation algorithms for discrete signals with application in spectral estimation," *IEEE Trans. Acoust., Speech, Signal Process.*, vol. ASSP-29, no. 4, pp. 830–845, Aug. 1981.
[19] T. Zemen, C. F. Mecklenbräuker, and B. H. Fleury, "Time-variant channel prediction using time-concentrated and band-limited sequences—Analytic results," in *5th Vienna Symp. Math. Model. (MATHMOD)*, Vienna, Austria, Feb. 8–10, 2006, (Invited Paper).
[20] G. Acosta and M. A. Ingram, "Model development for the wideband vehicle-to-vehicle 2.4 GHz channel," presented at the IEEE Wireless Commun. Netw. Conf. (WCNC), Las Vegas, NV, Apr. 3–6, 2006.
[21] X. Zhao, J. Kivinen, P. Vainikainen, and K. Skog, "Characterization of Doppler spectra for mobile communications at 5.3 GHz," *IEEE Trans. Veh. Technol.*, vol. 52, no. 1, pp. 14–23, Jan. 2003.
[22] S. Beheshti and M. A. Dahleh, "A new information-theoretic approach to signal denoising and best basis selection," *IEEE Trans. Signal Process.*, vol. 53, no. 10, pp. 3613–3624, Oct. 2005.
[23] T. Zemen, C. F. Mecklenbräuker, and B. H. Fleury, "Minimum-energy bandlimited time-variant channel prediction with dynamic subspace selection," presented at the Proc. 14th Eur. Signal Process. Conf. (EUSIPCO), Florence, Italy, Sep. 4–8, 2006, (Invited Paper).
[24] T. Zemen, C. F. Mecklenbräuker, J. Wehinger, and R. R. Müller, "Iterative joint time-variant channel estimation and multi-user detection for MC-CDMA," *IEEE Trans. Wireless Commun.*, vol. 5, no. 6, pp. 1469–1478, Jun. 2006.
[25] T. Zemen, C. F. Mecklenbräuker, J. Wehinger, and R. R. Müller, "Iterative multi-user decoding with time-variant channel estimation for MC-CDMA," in *Proc. 5th Int. Conf. 3G Mobile Commun. Technol.*, London, U.K., Oct. 18–20, 2004, pp. 88–92, (Invited Paper).
[26] H. J. Landau and H. Widom, "Eigenvalue distribution of time and frequency limiting," *J. Math. Anal. Applicat.*, vol. 77, pp. 469–481, 1980.
[27] S. Dharanipragada, "Time-bandwidth dimension and its application to signal reconstruction," Master's thesis, Univ. Illinois at Urbana-Champaign, Urbana-Champaign, 1991.
[28] A. Papoulis, *Probability, Random Variables and Stochastic Processes*, Singapore: McGraw-Hill, 1991.
[29] L. L. Scharf and D. W. Tufts, "Rank reduction for modeling stationary signals," *IEEE Trans. Acoust., Speech, Signal Process.*, vol. ASSP-35, no. 3, pp. 350–355, Mar. 1987.
[30] M. Nicoli, O. Simenone, and U. Spagnolini, "Multislot estimation of fast-varying space-time communication channels," *IEEE Trans. Signal Process.*, vol. 51, no. 5, pp. 1184–1195, May 2003.
[31] M. Niedzwiecki, *Identification of Time-Varying Processes*. New York: Wiley, 2000.
[32] R. H. Clarke, "A statistical theory of mobile-radio reception," *Bell Syst. Tech. J.*, p. 957, Jul.–Aug. 1968.
[33] T. Zemen, C. F. Mecklenbräuker, and B. H. Fleury, "Time-variant channel prediction using time-concentrated and band-limited sequences," in *Proc. IEEE Int. Conf. Commun. (ICC)*, Istanbul, Turkey, May 2006, pp. 5660–5665.
[34] J. Holtzmann and A. Sampath, "Adaptive averaging methodology for handoffs in cellular systems," *IEEE Trans. Veh. Technol.*, vol. 44, no. 1, pp. 59–66, Feb. 1995.
[35] K. E. Baddour and N. C. Beaulieu, "Robust Doppler spread estimation in nonisotropic fading channels," *IEEE Trans. Wireless Commun.*, vol. 4, no. 6, pp. 2677–2682, Nov. 2005.
[36] S. Beheshti, 2006, private communication.
[37] T. K. Moon and W. C. Stirling, *Mathematical Methods and Algorithms for Signal Processing*. Upper Saddle River, NJ: Prentice-Hall, 2000.
[38] H. Hofstetter and G. Steinböck, "A geometry based stochastic channel model for MIMO systems," presented at the ITG Workshop Smart Antennas, Munich, Germany, Jan. 2004.
[39] W. Jakes, *Microwave Mobile Communications*. New York: Wiley, 1974.

[40] Y. R. Zheng and C. Xiao, "Simulation models with correct statistical properties for Rayleigh fading channels," *IEEE Trans. Commun.*, vol. 51, no. 6, pp. 920–928, Jun. 2003.

[41] I. C. Wong and B. L. Evans, "Joint channel estimation and prediction for OFDM systems," in *Proc. IEEE Global Telecommun. Conf. (IEEE GLOBECOM)*, St. Louis, MO, Nov. 2005, vol. 4, pp. 2255–2259.

[42] R. Roy and T. Kailath, "ESPRIT—Estimation of signal parameters by rotational invariance techniques," *IEEE Trans. Acoust., Speech, Signal Process.*, vol. 37, no. 7, pp. 984–995, Jul. 1989.

[43] D. Porter and D. S. G. Stirling, *Integral Equations*. Cambridge, U.K.: Cambridge Univ. Press, 1990.

Thomas Zemen was born in Mödling, Austria, in 1970. He received the Dipl.-Ing. degree (with distinction) in electrical engineering and the doctoral degree (with distinction) both from Vienna University of Technology, Vienna, Austria, in 1998 and 2004, respectively.

He joined Siemens, Austria, in 1998 where he worked as hardware engineer and project manager for the Radio Communication Devices Department. From October 2001 to September 2003, he was delegated by Siemens Austria as a researcher to the mobile communications group at the Telecommunications Research Center Vienna (ftw.). Since October 2003, he has been with the Telecommunications Research Center Vienna, working as researcher in the strategic I0 project. His research interests include orthogonal frequency division multiplexing (OFDM), multiuser detection, time-variant channel estimation, iterative MIMO receiver structures, and distributed signal processing. Since May 2005, he has led the project "Future Mobile Communications Systems—Mathematical Modeling, Analysis, and Algorithms for Multi Antenna Systems," which is funded by the Vienna Science and Technology Fund (Wiener Wissenschafts-, Forschungs- und Technologiefonds, WWTF). He also teaches MIMO Communications as external lecturer at the Vienna University of Technology.

Christoph F. Mecklenbräuker (S'88–M'97) was born in Darmstadt, Germany, in 1967. He received the Dipl.-Ing. degree in electrical engineering from Technische Universität Wien, Austria, in 1992 and the Dr.-Ing. degree from Ruhr-Universität Bochum, Germany, in 1998, both with distinction.

He was with Siemens, Vienna, from 1997 to 2000, where he participated in the European framework of ACTS 90 Future Radio Wideband Multiple Access System (FRAMES). He was a delegate to the Third Generation Partnership Project (3GPP) and engaged in the standardization of the radio access network for the Universal Mobile Telecommunications System (UMTS). From 2000 to 2006, he has held a senior research position with the Forschungszentrum Telekommunikation Wien (ftw.), Wien, Austria, in the field of mobile communications. In 2006, he joined the Faculty of Electrical Engineering and Information Technology as a Full Professor with the Technische Universität Wien, Austria. He has authored approximately 80 papers in international journals and conferences, for which he has also served as a reviewer, and holds eight patents in the field of mobile cellular networks. His current research interests include antenna array and MIMO-signal processing for wireless systems, and ultrawideband radio.

Dr. Mecklenbräuker is a member of the IEEE Signal Processing, Antennas and Propagation, and Vehicular Technology Societies, and EURASIP. His doctoral dissertation on matched field processing received the Gert-Massenberg Prize in 1998.

Florian Kaltenberger was born in Vienna, Austria, in 1978. He received the Diploma degree (Dipl.-Ing.) and the Ph.D. degree, both in technical mathematics, from the Vienna University of Technology, Vienna, Austria, in 2002 and 2007, respectively.

During summer 2001, he held an internship position with British Telecom, BT Exact Technologies, Ipswich, U.K., where he was working on mobile video conferencing applications. After his studies, he started as a Research Assistant with the Vienna University of Technology, Institute for Advanced Scientific Computing, working on distributed signal processing algorithms. In 2003, he joined the Wireless Communications Group, Austrian Research Centers GmbH, where he is currently working on the development of low-complexity smart antenna and MIMO algorithms, as well as on the ARC SmartSim real-time hardware channel emulator.

Bernard H. Fleury (SM'99) received the Diploma degree in electrical engineering and mathematics in 1978 and 1990, respectively, and the doctoral degree in electrical engineering in 1990, all from the Swiss Federal Institute of Technology Zurich (ETHZ), Switzerland.

From 1978 to 1985 and 1988 to 1992, he was a Teaching Assistant and Research Assistant, respectively, at the Communication Technology Laboratory and at the Statistical Seminar at ETHZ. In 1992, he joined again the former laboratory as Senior Research Associate. Since 1997, he has been with the Department of Communication Technology, Aalborg University, Denmark, where he is currently Professor in digital communications. He has also been affiliated with the Telecommunication Research Center, Vienna (ftw.) since April 2006. He is presently Chairman of Department 2 Radio Channel Modelling for Design Optimisation and Performance Assessment of Next Generation Communication Systems of the ongoing FP6 network of excellence NEWCOM (Network of Excellence in Communications). His general fields of interest cover numerous aspects within communication theory and signal processing mainly for wireless communications. His current areas of research include stochastic modelling and estimation of the radio channel, characterization of multiple-input multiple-output (MIMO) channels, and iterative (turbo) techniques for joint channel estimation and data detection/decoding in multiuser communication systems.

105

VALIDATION OF MINIMUM-ENERGY BAND-LIMITED PREDICTION USING VEHICULAR CHANNEL MEASUREMENTS

Thomas Zemen[1], Sebastian Caban[2], Nicolai Czink[1,3] and Markus Rupp[2]

[1]ftw. Forschungszentrum Telekom-
munikation Wien
Donau-City-Straße 1, 1220 Vienna,
Austria
email: thomas.zemen@ftw.at
http://userver.ftw.at/ zemen/

[2]Institute of Communications and
Radio-Frequency Engineering,
Vienna University of Technology
Gusshausstr. 25/389, 1010 Vienna,
Austria

[3]Smart Antennas Research Group,
Information Systems Lab, Stanford
University
Packard 215, Stanford, CA 94305,
USA

ABSTRACT

We demonstrate that minimum-energy (ME) band-limited prediction shows the same robust performance for vehicular channel measurements as well as for the numeric Clarke channel model. By contrast, channel prediction based on sinusoidal modelling presented by Chen et al., 2007, shows poor performance for a small percentage of measured channel realizations. This increases the mean square error dramatically, hence *outlier removal is required*. The ME band-limited predictor introduced by Zemen et al., 2007, is based on a subspace spanned by time-concentrated and band-limited sequences. The time-concentration of these sequences is matched to the length of the observation interval and the band-limitation is determined by the support of the Doppler power spectral density of the fading process. The low-complexity time-variant flat-fading channel predictor dynamically selects a predefined subspace from a small set such that the prediction error is minimized. We validate the ME band-limited predictor using channel measurements from an alpine region. The predictor performance with measured channels is comparable to the one obtained with Clarke's channel model for non line-of-sight situations. For line-of-sight situations the performance is better than for Clarke's model. We present results in terms of mean square error averaged over *all* measured snapshots.

1. INTRODUCTION

In mobile communication systems channel state information at the transmitter proves to be beneficial for increasing the system capacity. In a time-division duplex (TDD) system channel state information can be obtained by exploiting channel reciprocity: While a data block is received, channel state information is obtained. This information can be utilized in the following transmission period. However, for moving users at vehicular speed the channel state information gets outdated rapidly. Thus, appropriate channel prediction is necessary.

In [1] Zemen et al. present a new minimum-energy (ME) band-limited prediction algorithm. This algorithm allows for low-complexity prediction of a fading process from noisy channel observations that are obtained while receiving a *single* data block. The symbol rate, or equivalently the sampling rate of the fading process, in wireless communication systems is much higher than the Doppler bandwidth. Thus, time-limited snapshots of the sampled fading process span a subspace with small dimension [2].

In [1] it is shown that a time-concentrated and band-limited sequence can be defined for generalized band-limits consisting of disjoint intervals matching the support of the Doppler power spectral density of the time-selective fading process. The energy of these sequences is most concentrated in an interval equal to the length of the observed data block. Thus, they allow to calculate the ME band-limited continuation of a finite sequence [2], hence *predict* future samples. In [1] the algorithm is validated by the numeric Clarke model, only.

In [3] a prediction algorithm based on sinusoidal modeling is presented by Chen et al. It is shown that channel prediction based on sinusoidal modelling performs poor for a small number of *measured* channel realizations [3, Sect. 6]. This increases the mean square error (MSE) dramatically. Hence, [3] performs outlier removal and results are presented in terms of MSE with a given level of confidence. An enhanced approach utilizing multicomponent polynomial phase signals is presented in [4], however outlier removal is still required.

Contribution of this paper: In this paper the ME band-limited prediction algorithm with dynamic subspace selection is validated with vehicular channel measurements. We demonstrate the robustness of our algorithm. No outlier removal or other preprocessing is necessary for consistent performance on a large number of measured vehicular channel samples for line-of-sight (LOS) and non-LOS scenarios.

Organization of the paper: In Section 2 we introduce the signal model for time-variant flat-fading channels. The ME band-limited prediction algorithm [1] is shortly reviewed in Section 3 and the dynamic subspace selection in Section 4, respectively. Section 5 decribes the vehicular measurement scenario and the post-processing is discussed in Section 6. We present the simulation results in Section 7 and draw conclusions in Section 8.

Notation: We denote a column vector by $\boldsymbol{a}$ and its i-th element with $a[i]$. Similarly, we denote a matrix by $\boldsymbol{A}$ and its (i, ℓ)-th element by $[\boldsymbol{A}]_{i,\ell}$. The transpose of $\boldsymbol{A}$ is given by $\boldsymbol{A}^{\mathrm{T}}$ and its conjugate transpose by $\boldsymbol{A}^{\mathrm{H}}$. The absolute value of a is denoted by $|a|$ and its complex conjugate by a^*. The largest (smallest) integer that is lower (greater) or equal than $a \in \mathbb{R}$ is denoted by $\lfloor a \rfloor$ ($\lceil a \rceil$). We denote the set of all integers by $\mathbb{Z}$, the set of real numbers by $\mathbb{R}$ and the set of complex numbers by $\mathbb{C}$.

2. SIGNAL MODEL FOR TIME-VARIANT FLAT-FADING CHANNELS

We consider a time division duplex (TDD) communication system transmitting data in blocks of length M over a time-variant channel. The symbol duration T_S is much longer than the delay spread T_D of the channel, i.e., $T_S \gg T_D$. Hence we assume the channel as frequency-flat. Discrete time at rate $R_S = 1/T_S$ is denoted by m. The channel incorporates the transmit filter, the transmit antenna, the physical channel, the receive antenna, and the receive matched filter. The data symbols $b[m]$ are randomly and evenly drawn from a symbol alphabet with constant modulus. Without loss of generality $|b[m]| = 1$. The discrete-time signal at the matched filter output $h[m]b[m] + n'[m]$ is the superposition of the data symbol multiplied by the sampled time-variant channel weight $h[m]$ and complex white Gaussian noise $n'[m]$ with variance σ_n^2. Without loss of generality $\{h[m]\}$ is a circularly symmetric, unit-variance (due to power control) process.

We assume an error-free decision feedback structure [5]. Thus, we are able to obtain noisy channel observations [6] using the error-free data symbol estimates $\hat{b}[m] = b[m]$:

$$y[m] = h[m] + n[m] . \tag{1}$$

Note that $n[m]$ has the same statistical properties as $n'[m]$. The signal-to-noise ratio (SNR) is $\mathrm{SNR} = 1/\sigma_n^2$.

The transmission is block oriented. A data block spans the time interval $\mathscr{I}_M = \{0, \ldots, M-1\}$. The noisy channel observations $y[m]$, $m \in \mathscr{I}_M$ obtained during a single data block are used to predict the channel weight up to N symbols into the future.

For a user moving with velocity v the time-variant fading process $\{h[m]\}$ is band-limited by the one-sided normalized Doppler bandwidth

$$\nu_D = \frac{v f_C}{c_0} T_S \ll \frac{1}{2} \tag{2}$$

where f_C is the carrier frequency and c_0 stands for the speed of light. As indicated with the inequality in (2) the sampling rate $1/T_S$ is much higher than the Nyquist sampling rate.

We assume a time-variant block-fading channel model. Hence the fading process $\{h[m]\}$ is wide-sense stationary over the limited time interval $\mathscr{I}_{M+N}$ with covariance function

$$R_h[k] = \mathsf{E}\{h^*[m]h[m+k]\} . \tag{3}$$

3. MINIMUM-ENERGY (ME) BAND-LIMITED PREDICTION

The samples of the channel weights in a single block $\mathscr{I}_M$ are collected in the vector

$$\boldsymbol{h} = [h[0], h[1], \ldots, h[M-1]]^{\mathrm{T}} . \tag{4}$$

We consider a subspace-based approximation which expands the vector $\boldsymbol{h}$ in terms of D orthonormal basis vectors $\boldsymbol{u}_i = [u_i[0], u_i[1], \ldots, u_i[M-1]]^{\mathrm{T}}, i \in \{0, \ldots, D-1\}$:

$$\boldsymbol{h} \approx \boldsymbol{U}\boldsymbol{\gamma} = \sum_{i=0}^{D-1} \gamma_i \boldsymbol{u}_i . \tag{5}$$

In this expression $\boldsymbol{U} = [\boldsymbol{u}_0, \ldots, \boldsymbol{u}_{D-1}]$ contains the orthonormal basis vectors and $\boldsymbol{\gamma} = [\gamma_0, \ldots, \gamma_{D-1}]^{\mathrm{T}}$ collects the basis

expansion coefficients. The least square estimate of $\boldsymbol{\gamma}$ simplifies to

$$\hat{\boldsymbol{\gamma}} = \boldsymbol{U}^{\mathrm{H}}\boldsymbol{y} \tag{6}$$

due to the orthogonality of the basis functions. The reconstruction error per data block is defined as

$$z = \frac{1}{M}\|\boldsymbol{h} - \boldsymbol{U}\hat{\boldsymbol{\gamma}}\|^2 . \tag{7}$$

We define the mean square reconstruction error per sample

$$\mathrm{MSE}[m] = \mathsf{E}\left\{|h[m] - \hat{h}[m]|^2\right\} , \tag{8}$$

and the mean square reconstruction error per data block,

$$\mathrm{MSE} = \frac{D}{M}\sigma_n^2 + \frac{1}{M}\mathsf{E}\{\|\boldsymbol{V}^{\mathrm{H}}\boldsymbol{h}\|^2\} , \tag{9}$$

where $\boldsymbol{V} = [\boldsymbol{u}_D, \ldots, \boldsymbol{u}_{M-1}]$ contains the basis vectors spanning the subspace orthogonal to the signal subspace spanned by the columns of $\boldsymbol{U}$. The noise samples are collected in the vector $\boldsymbol{n} = [n[0], \ldots, n[M-1]]^{\mathrm{T}}$. We seek basis vectors $\boldsymbol{u}_0, \ldots, \boldsymbol{u}_{D-1}$ and the subspace dimension D which minimize the reconstruction error per data block.

In mobile radio-communication channels, the most significant part of the power in the estimated Doppler spectrum of the fading process is usually localized on the union of disjoint intervals in the frequency range $(-1/2, +1/2)$. A region $\mathscr{W} \subseteq (-1/2, 1/2)$ consisting of I disjoint intervals $\mathscr{B}_i = (v_{i1}, v_{i2})$, $i \in \{1, \ldots, I\}$ can be defined as

$$\mathscr{W} = \bigcup_{i=1}^{I} \mathscr{B}_i = \mathscr{B}_1 \cup \mathscr{B}_2 \cup \ldots \cup \mathscr{B}_I , \tag{10}$$

with $v_{11} \leq v_{12} \leq \ldots \leq v_{I1} \leq v_{I2}$, see [1, Fig. 1].

The sequences $\{u_i[m, \mathscr{W}]\}$, $i \in \{0, \ldots, M-1\}$ band-limited to the region $\mathscr{W}$ and with *most concentrated* energy in the interval $\mathscr{I}_M$ are the solutions to

$$\sum_{\ell=0}^{M-1} C[\ell - m, \mathscr{W}]u_i[\ell, \mathscr{W}] = \lambda_i(\mathscr{W})u_i[m, \mathscr{W}], \quad m \in \mathbb{Z} \tag{11}$$

where

$$C[k, \mathscr{W}] = \int_{\mathscr{W}} \mathrm{e}^{\mathrm{j}2\pi k v}\mathrm{d}v . \tag{12}$$

Note that $C[k, \mathscr{W}]$ is proportional to the covariance function of a process exhibiting a constant spectrum with support $\mathscr{W}$. For more details please refer to [1].

The ME band-limited prediction of a time-variant channel for any $m \in \mathbb{Z}$ can be expressed as [1]

$$\hat{h}[m] = \boldsymbol{f}[m, \mathscr{W}]^{\mathrm{T}}\hat{\boldsymbol{\gamma}} = \sum_{i=0}^{D(\mathscr{W})-1} \hat{\gamma}_i u_i[m, \mathscr{W}], \tag{13}$$

where $\boldsymbol{f}[m, \mathscr{W}] = [u_0[m, \mathscr{W}], \ldots, u_{D(\mathscr{W})-1}[m, \mathscr{W}]]^{\mathrm{T}}$.

4. SUBSPACE DEFINITION AND DYNAMIC SELECTION

In practical systems information about the Doppler bandwidth must be obtained from channel observations. We define a finite number of hypotheses about the actual Doppler

Figure 1: The alpine measurement scenario.

bandwidth. Each hypothesis is represented by a subspace spanned by time-concentrated and band-limited sequences. The orthogonal basis vectors spanning each subspace are calculated once and then stored. A subspace selection method based on a probabilistic bound on the reconstruction error z (7) is used to select the subspace with the smallest reconstruction error based on the observation of a single data block. This subspace is used for ME band-limited prediction.

4.1 Subspace Definition

We define the maximum Doppler bandwidth

$$v_{\mathrm{Dmax}} = \frac{v_{\max} f_{\mathrm{C}} T_{\mathrm{S}}}{c_0} \qquad (14)$$

as system parameter given by the maximum (supported) user velocity $v_{\max}$. Furthermore, we define a set of Q subspaces with spectral support

$$\mathscr{W}_q = \left(-\frac{q}{Q}\, v_{\mathrm{Dmax}}, +\frac{q}{Q}\, v_{\mathrm{Dmax}}\right) \qquad (15)$$

for $q \in \{1, \ldots, Q\}$ as shown in [1, Fig. 3].

In mobile communication channels, fading processes frequently arise whose spectral support is the union of disjoint intervals. Hence we define an additional set of subspaces by partitioning the region $(-v_{\mathrm{Dmax}}, v_{\mathrm{Dmax}})$ into Q' spectral bins with equal length as depicted in [1, Fig. 4].

The spectral bin $i \in \{1, \ldots, Q'\}$ spans the interval

$$\mathscr{B}_i = \left[-v_{\mathrm{Dmax}} + (i-1)\frac{v_{\mathrm{Dmax}}}{Q'}, -v_{\mathrm{Dmax}} + i\frac{v_{\mathrm{Dmax}}}{Q'}\right]. \quad (16)$$

Using all possible binary combinations of $\mathscr{B}_i$ we can define $2^{Q'}-1$ band-limiting regions $\mathscr{W}'_{q'}$, $q' \in \{1, \ldots, 2^{Q'}-1\}$.

We combine the set of symmetric subspace $\boldsymbol{U}_q$ with $Q = 10$ and the set of asymmetric subspaces $\boldsymbol{U}'_{q'}$, $q' \in \{1, \ldots, 2^{Q'}-1\}$ with $Q' = 4$ leaving out duplicates.

4.2 Subspace Selection

In [7] an information theoretic subspace selection scheme is proposed. This method uses the observable data error

$$x_q = \frac{1}{M}\|\boldsymbol{y} - \boldsymbol{U}_q \boldsymbol{U}_q^{\mathrm{H}} \boldsymbol{y}\|^2 \qquad (17)$$

to obtain an upper bound $\overline{z_q}(x_q)$ on the reconstruction error

$$z_q = \frac{1}{M}\|\boldsymbol{h} - \hat{\boldsymbol{h}}_q\|^2 \le \overline{z_q}(x_q) \qquad (18)$$

which cannot be observed directly. For the subspace selection $\boldsymbol{h}$ is considered deterministic. The results in [7] are derived for real valued signals. They are adapted for complex valued signals and noise in [1].

The upper bound on the reconstruction error is used to select the appropriate subspace q spanned by the columns of $\boldsymbol{U}_q$,

$$\hat{q} = \underset{q}{\operatorname{argmin}}\, \overline{z_q}(x_q). \qquad (19)$$

The chosen subspace $\boldsymbol{U}_{\hat{q}}$ and the associated sequences $\{u_i[m, \mathscr{W}_q]\}$ are used for ME band-limited prediction [1].

5. VEHICULAR CHANNEL MEASUREMENTS

To validate the prediction algorithm we use outdoor vehicular channel measurements carried out in the alpine Drautal valley in Austria. The basic set-up of the Vienna MIMO Testbed [8] is as follows:

- A base station is set up at one side of the Drautal valley right next to already existing base stations. Exactly every 500 ms it transmits a frame with the following parameters:
  - 100 ms duration
  - 4-quadrature amplitude modulated (QAM) single carrier signal (511 training symbols and $S = 1000$ data symbols), root-raiced-cosine (RRC) filtered with a roll-off factor of 0.5
  - 15 kHz bandwidth[1], resulting in $T_{\mathrm{S}} = 66.7$ μs.
  - $f_{\mathrm{C}} = 2.5$ GHz center frequency (the wavelength is approx. 12 cm)
  - 37 dBm TX power

  We employ a Kathrein 800 10543 base station antenna [9] with $+45°$ polarization, half-power beam width $58°/6.2°$ and down tilt $6°$.

- The corresponding receiver is placed in a "VW-Sprinter" van that follows a route through the valley. Four receive antennas were placed in front of the passenger seat as depicted in Figure 1. For the analysis in this paper only one antenna is used.

Prior to the actual measurement, the TX and RX-unit were synchronized relative to each other (see [10] for more details). This initial synchronization was then maintained throughout the whole measurement to ensure perfect timing and frequency synchronization of the received frame (see Figure 2).

---

[1]chosen similar to the orthogonal frequency division multiplexing (OFDM) subcarrier bandwidth in UMTS long term evolution (LTE)
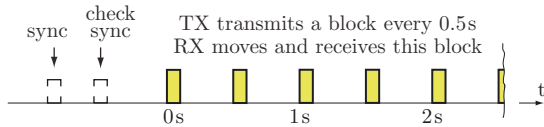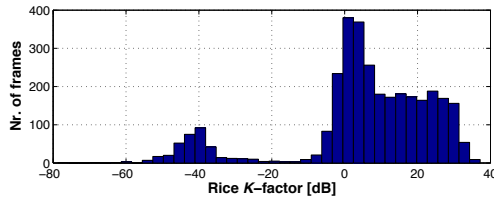
Figure 2: Timing diagram.

Figure 3: Histogram of Rice K-factor (in dB) for all measured frames.

During the actual measurement, the receiver captured the frames transmitted by the base-station and stores them on a hard-disk. These stored complex baseband-data samples are the input to all off-line evaluations carried out later.

6. POST-PROCESSING

For post-processing the received signal baseband samples are RRC filtered and synchronized in time by correlating with the training symbol sequence.

During the measurement drive with a duration of approximately half an hour a total number of $F = 3171$ frames were received. The propagation condition varied from line-of-sight (LOS) on a rural road to non-LOS within villages. In Figure 3 we plot a histogram showing the histogram of the Rice K-factor in dB. For the Rice K-factor estimation we used the method of moments [11] as initial guess for a least squares fit of the Rice probability density function (pdf). The Kolmogorov-Smirnov goodness of fit [12, pp. 392–394] is depicted in Figure 4. Hence, the largest distance between the Rice cumulative distribution function (cdf) and the empirical cdf is smaller than 0.1 for 90% of all measurement frames.

The histogram of SNR is depicted in Figure 5. The SNR of 95% of all snapshots is above 25 dB. Due to the high SNR for all frames we can treat the obtained channel sample as perfect channel knowledge $h_f[m]$ where $0 \leq f \leq F - 1$ and $0 \leq m \leq S - 1$. The frame index is denoted by f.

Finally, the velocity histogram is shown in Figure 6. The velocity per frame is obtained from the collected GPS data
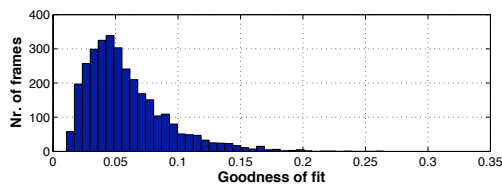
Figure 4: Histogram of Kolmogorov-Smirnov goodness of fit for Rice pdf for all measured frames.
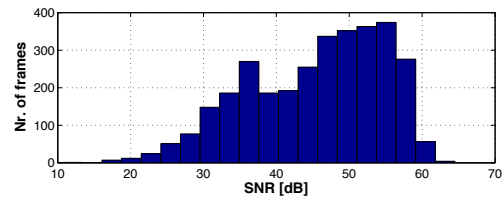
Figure 5: Histogram of SNR for all measured frames.
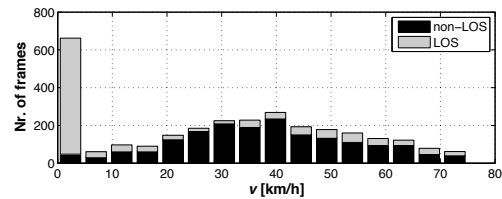
Figure 6: Histogram of velocity for measured LOS frames ($K_f \leq 10$) and non-LOS frames ($K_f > 10$).

collected during the measurement. We show the number of frames per velocity bin with non-LOS conditions for $K_f \leq 10$ (black) and LOS conditions with $K_f > 10$ (light gray). We take all snapshots into account with a velocity $v \leq 80$ km/h. This is done to ensure a sufficiently large set of frames per evaluated velocity bin for later statistical evaluations. For easier comparison with [1] we keep $v_{\max} = 100$ km/h.

Each frame is normalized such that $\mathsf{E}\{|h_f[m]|^2\} = 1$. Finally, we add complex white Gaussian noise noise $n_f[m] \sim \mathcal{N}(0, \sigma_n^2)$ with $\sigma_n^2 = 0.1$ resulting in a SNR $= 10$ dB obtaining noisy channel observations $y_f[m]$ according to (1) with defined properties.

7. SIMULATION RESULTS

We are interested to investigate the performance of ME band-limited prediction with dynamic subspace selection in realistic channel conditions.

We need to adapt the results from [1] to the symbol duration $T_S = 66.67 \mu s$ of our vehicular measurements. In [1] a symbol duration of $20.57 \mu s$ is used. We keep the assumption that the predictor is able to observe the channel at most for the duration of two wavelengths at a velocity of $v_{\max} = 100$ km/h resulting in a block length of $M = 128$. We will analyze two prediction horizons, namely $\ell \in \{8, 24\}$ (equivalent to $\{\lambda/8, 3\lambda/8\}$ at $v_{\max}$.).

As base-line performance we use Monte-Carlo simulation with Clarke's channel model [13]. The Clarke model with $P = 30$ scatterers is representative for non-LOS situations with rich scattering. These results are compared with the one for noisy channel observations $y_f[m]$ obtained from vehicular channel measurements. We will distinguish two cases, namely the quasi non-LOS case characterized by $K_f \leq 10$ and the LOS case with $K_f > 10$.

In Figure 7 we plot MSE$[M - 1 + \ell]$ versus the normalized Doppler bandwidth ν_D for a velocity range $0 \leq v \leq 80$ km/h. The predictor performance with measured channels is slightly worse in the non-LOS case (especially for small velocities) compared to Clarke's model. In the LOS case
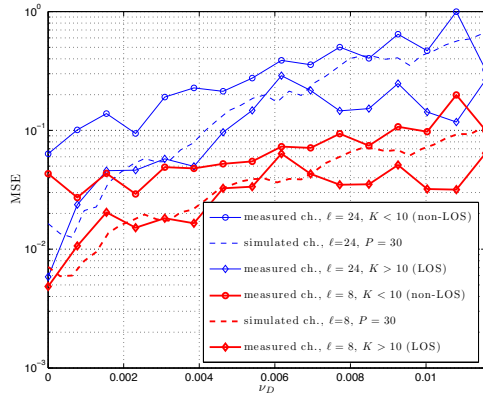
Figure 7: Mean square prediction error versus normalized Doppler bandwidth. We compare the prediction performance for measured vehicular channels with the one for the numeric Clarke channel model. Two prediction horizons $\ell \in \{8, 24\}$ are evaluated (equivalent to $\{\lambda/8, 3\lambda/8\}$ at $v_{\max}$).

the performance is better than the one obtained with Clarke's model. We emphasize that this result clearly shows the robustness of ME band-limited prediction with dynamic subspace selection. No outlier removal is required (compared to the results in [3]).

8. CONCLUSIONS

In this paper we validated the minimum-energy (ME) band-limited prediction method [1] comparing performance results for vehicular channel measurements with the one obtained for the numeric Clarke channel model with $P = 30$ paths. This comparison is important because e.g. channel prediction based on sinusoidal modelling [3] shows poor performance for a small percentage of measured channel realizations, thus requiring outlier removal.

We demonstrate the robustness of ME band-limited prediction for LOS and non-LOS scenarios for a large number of measured vehicular channel realizations. No outlier removal was required. For non-LOS scenarios the predictor performs slightly worse than for Clarke's channel model measured in terms of the mean square prediction error at a prediction horizon of $\lambda/8$ and $3\lambda/8$. For LOS scenarios the ME energy band-limited predictor is able to take advantage of the reduced number of propagation paths and shows better performance than for Clarke's model.

9. ACKNOWLEDGEMENT

REFERENCES

[1] T. Zemen, C. F. Mecklenbräuker, B. H. Fleury, and F. Kaltenberger, "Minimum-energy band-limited predictor with dynamic subspace selection for time-variant flat-fading channels," *IEEE Trans. Signal Processing*, vol. 55, no. 9, pp. 4535–4548, Sept. 2007.

[2] D. Slepian, "Prolate spheroidal wave functions, Fourier analysis, and uncertainty - V: The discrete case," *The Bell System Technical Journal*, vol. 57, no. 5, pp. 1371–1430, May-June 1978.

[3] M. Chen, T. Ekman, and M. Viberg, "New approaches for channel prediction based on sinusoidal modeling," *EURASIP J. Appl. Signal Process.*, vol. 2007, no. 1, pp. 1–13, 2007.

[4] M. Chen and M. Viberg, "Long-range channel prediction based on nonstationary parametric modeling," *IEEE Trans. Signal Processing*, vol. 57, no. 2, pp. 622–634, Feb. 2009.

[5] T. Zemen, C. F. Mecklenbräuker, J. Wehinger, and R. R. Müller, "Iterative joint time-variant channel estimation and multi-user detection for MC-CDMA," *IEEE Trans. Wireless Commun.*, vol. 5, no. 6, June 2006.

[6] T. Zemen and C. F. Mecklenbräuker, "Time-variant channel estimation using discrete prolate spheroidal sequences," *IEEE Trans. Signal Processing*, vol. 53, no. 9, pp. 3597–3607, September 2005.

[7] S. Beheshti and M. A. Dahleh, "A new information-theoretic approach to signal denoising and best basis selection," *IEEE Trans. Signal Processing*, vol. 53, no. 10, pp. 3613–3624, October 2005.

[8] S. Caban, C. Mehlführer, R. Langwieser, A. L. Scholz, and M. Rupp, "Vienna MIMO testbed," *EURASIP Journal on Applied Signal Processing*, vol. 2006, Article ID 54868, 2006.

[9] Kathrein, *Technical Specification Kathrein Antenna Type No. 800 10543*. [Online]. Available: http://www.kathrein-scala.com/catalog/80010543.pdf

[10] S. Caban, C. Mehlführer, G. Lechner, and M. Rupp, "'Testbedding' MIMO HSDPA and WiMAX," in *Proc. IEEE Vehicular Technology Conference (VTC 2009 Fall)*, Anchorage, AK, USA, Sep. 2009, submitted.

[11] L. J. Greenstein, D. G. Michelson, and V. Erceg, "Moment-method estimation of the Ricean K-factor," *IEEE Trans. Commun.*, vol. 3, no. 6, pp. 175–176, June 1999.

[12] I. M. Chakravarti, R. G. Laha, and J. Roy, *Handbook of methods of applied statistics*, ser. Wiley series in probability and mathematical statistics. John Wiley and Sons, 1967, vol. I.

[13] R. H. Clarke, "A statistical theory of mobile-radio reception," *Bell System Technical Journal*, p. 957, July-August 1968.

Iterative Time-Variant Channel Estimation for 802.11p Using Generalized Discrete Prolate Spheroidal Sequences

Thomas Zemen, *Senior Member, IEEE*, Laura Bernadó, *Student Member, IEEE*,
Nicolai Czink, *Member, IEEE*, and Andreas F. Molisch, *Fellow, IEEE*

Abstract—This paper deals with channel estimation for orthogonal frequency-division multiplexing (OFDM) in time-variant wireless propagation channels. We particularly consider the challenges of the IEEE 802.11p standard, which is the worldwide dominant system for vehicular communications. For historic reasons, 802.11p uses a pilot pattern that is identical to the pattern used in 802.11a, which was initially designed for the estimation of indoor channels with little or no time variations. Therefore, this pilot pattern violates the sampling theorem for channels with both large delay spread and large Doppler spread, as often occurs in vehicular communications. To remedy this problem, we design a robust iterative channel estimator based on a 2-D subspace spanned by generalized discrete prolate spheroidal sequences. Due to the tight subspace design, the iterative receiver is able to converge to the same bit error rate (BER) as a receiver with perfect channel knowledge. Furthermore, we propose a backward compatible modification of the 802.11p pilot pattern such that the number of iterations sufficient for convergence can be reduced by a factor of 2–3, strongly reducing implementation complexity.

Index Terms—Generalized discrete prolate spheroidal sequences, IEEE 802.11p, intelligent transportation system, time-variant channel estimation, wireless vehicular communications.

I. INTRODUCTION

WIRELESS communications for vehicle-to-vehicle or vehicle-to-infrastructure scenarios has many important applications, including collision avoidance, reduction of traffic congestion, wrong-way driving warning, as well as enabling e-mobility [1], and thus has drawn great attention over the past few years. An international standard, i.e., wireless access in vehicular environments [2], has been developed. Its physical layer is based on the 802.11p standard [3]. It is the main candidate for implementation by major car manufacturers and

is supported by various programs, in particular in the European Union and Japan.

A main challenge of vehicular communications is the rapidly changing radio propagation conditions. Many measurement campaigns have demonstrated high Doppler and delay spreads and even nonstationarities of the channel statistics (see [1] and [4] for an overview and further references). Consequently, robust channel estimation is particularly important, but also particularly difficult, in such an environment.

The challenges are exacerbated by the design of training signals in the 802.11p standard. To exploit existing chip designs and economies of scale, this standard is virtually identical to the well-known IEEE 802.11a/g (WiFi) standard. However, while the training signal design works well for environments where WiFi is normally operating in (i.e., indoor environments with little or no mobility), it does not work in conjunction with standard channel estimation techniques in many vehicular propagation channels, namely, those that have large delay and Doppler spreads.

To combat difficulties in time-variant wireless channels, we can exploit the fact that the time-variant frequency-selective impulse responses of the channels are restricted to low-dimensional subspaces. Further improvements can be achieved by iterations between channel estimation and symbol decisions.

Related Literature: A number of publications investigate the performance of 802.11p [1], [5]–[7] in a realistic vehicular channel with both large delay and Doppler spreads, demonstrating the need for improved algorithms. Parallel to the present work, [8] shows an improved orthogonal frequency-division multiplexing (OFDM) symbol-wise decision-directed channel estimation method that does not need a standard modification but is limited to frame error rates (FERs) in the order of 10^{-1}. In [9], OFDM symbol-wise decision together with smoothing in the frequency domain and antenna diversity is investigated. In [10], a modified physical layer in the form of time-domain differential modulation is proposed to remove the need for time-variant channel estimation. The insertion of additional pilot symbols is advocated in a nonbackward compatible fashion in [11] and [12].

However, it turns out that it is difficult to reach an FER below 10^{-1} in vehicular channels with the 802.11p pilot pattern. Hence, low-complexity robust frame-based channel estimation methods must be investigated such that the correlation of the

fading process can jointly be exploited in time and frequency. At the same time, the algorithm must also be robust toward the nonstationary nature of the vehicular communication channel.

A number of existing papers deal with channel estimation in time-variant channels based on subspaces. In [13], a low-dimensional subspace spanned by discrete prolate spheroidal (DPS) sequences [14] is used. The subspace is designed according to the given maximum normalized Doppler shift $\nu_{\mathrm{Dmax}} = v_{\max} f_C T_S/c_0$, which is determined by the maximum velocity $v_{\max}$, the carrier frequency f_C, the speed of light c_0, and the symbol duration T_S. The square channel estimation bias obtained with the Slepian basis expansion is more than a magnitude smaller compared with the Fourier basis expansion (i.e., a truncated discrete Fourier transform) [15].

While [13] estimates the Slepian basis expansion coefficients individually for every subcarrier in an OFDM system, further improvements can be obtained by exploiting the correlation between the individual subcarriers in the frequency domain. For this purpose, a truncated Fourier transform was used in [16]. However, this approach is optimal only for sample-spaced path delays. For more realistic real-valued path delays, Edfors *et al.* [17] exploited the correlation in the frequency domain by using the singular value decomposition (SVD) of the channel covariance matrix, which is assumed to be known. In [18], the SVD was calculated in an adaptive manner using an estimate of the covariance matrix. In [19] and [20], a 2-D Wiener filter is employed for time and frequency selective channel estimations.

Iterative channel estimation, i.e., alternate payload data estimation and channel estimation, has been discussed in a number of papers (see, e.g., [21]–[26]). The 2-D Wiener filter is employed for iterative channel estimation in [27]. In [27], a reduced-complexity SVD-based low-rank approximation [28], [29] is shown as well.

In [30], two successive Slepian subspace projections are used for time-variant frequency-selective channel estimation. This allows exploiting the correlation in the time and frequency domain without the need to estimate the channel covariance function and to perform an SVD. A 2-D projection on a fixed Slepian subspace is further explored in [31]. However, the subspace in the frequency domain is chosen twice as large as necessary (cf. [31, paragraph after eq. (2)]).

Contributions of This Paper:
1) We further tighten the 2-D subspace of [31] by using generalized DPS sequences [32] that allow for a generalized nonsymmetric (and even discontiguous) band limit in the time and frequency domains. With a tight subspace, we can further reduce the channel estimation mean square error (MSE).
2) We validate the time-variant channel estimator using a geometry-based stochastic channel model (GSCM) in an 802.11p-compliant link-level simulation [33]. The channel model is obtained from vehicular channel measurements [34].
3) We show that, with a tight subspace design, near-optimal channel estimation can still be obtained iteratively in

an 802.11p compliant system, despite the aforementioned deficiencies of the training signal design in this standard.
4) Finally, we propose a transparent backward-compatible extension to the 802.11p standard allowing for reduced-complexity channel estimation. This is achieved by adding an additional OFDM pilot symbol to the end of the otherwise standard compliant frame and by utilizing one of the reserved header bits.

Notation: We denote a scalar by a, a column vector by $\boldsymbol{a}$, and its ith element with $a[i]$. Similarly, we denote a matrix by $\boldsymbol{A}$ and its (i, ℓ)th element by $[\boldsymbol{A}]_{i,\ell}$. The transpose of $\boldsymbol{A}$ is given by $\boldsymbol{A}^{\mathrm{T}}$ and its conjugate transpose by $\boldsymbol{A}^{\mathrm{H}}$. A diagonal matrix with elements $a[i]$ is written as $\mathrm{diag}(\boldsymbol{a})$ and the $Q \times Q$ identity matrix as $\boldsymbol{I}_Q$. The absolute value of a is denoted by $|a|$ and its complex conjugate by a^*. The largest (smallest) integer that is lower (greater) than or equal to $a \in \mathbb{R}$ is denoted by $\lfloor a \rfloor$ ($\lceil a \rceil$). We denote the set of all integers by $\mathbb{Z}$, the set of real numbers by $\mathbb{R}$, and the set of complex numbers by $\mathbb{C}$.

Organization of This Paper: The OFDM signal model is presented in Section II. In Section III, we introduce the GSCM used to simulate the time-variant impulse response of a vehicular communication channel. For channel estimation at the receiver side, a subspace channel model based on generalized DPS sequences is presented in Section IV and the corresponding iterative estimator in Section V. In Section VI, the 802.11p pilot pattern and our proposed enhancement are discussed. The numeric simulation results are shown in Section VII together with a discussion of the iterative receiver complexity. We draw conclusions in Section VIII.

II. SIGNAL MODEL

We consider the equalization and detection problem for an OFDM link [35], [36]. The OFDM system utilizes N subcarriers and a cyclic prefix with length G. The transmission is frame oriented with frame length M and utilizes a bandwidth B and the sampling rate at the receiver side $1/T_C = B$. The OFDM symbol duration is given by $T_S = (N + G)T_C$.

Each frame contains $S = |\mathcal{S}|$ coded data symbols $b[m, q]$ $\forall [m, q] \in \mathcal{S}$, where $m \in \mathcal{I}_M = \{0, \dots, M-1\}$ denotes the discrete time at rate $1/T_S$, $q \in \mathcal{I}_N$ denotes the subcarrier index with frequency spacing $1/(T_C N)$, and $\mathcal{S}$ denotes the 2-D data symbol position index set in the time–frequency plane, respectively. For $[m, q] \notin \mathcal{S}$, we define $b[m, q] = 0$.

A binary information sequence $\chi[m'']$ of length $2SR_C$ is convolutionally encoded with code rate R_C, resulting in a sequence of code bits $c[m']$ (see Fig. 1). After interleaving and quadrature phase-shift keying (QPSK) modulation with Gray labeling, the data symbols are mapped on the OFDM time–frequency grid as

$$b[\mathcal{S}_s] = \frac{1}{\sqrt{2}} \left(c[2s] + jc[2s+1] \right) \qquad \forall s \in \mathcal{I}_S \qquad (1)$$

where $\mathcal{S}_s$ denotes the sth element $[m_s, q_s]$ of the set $\mathcal{S}$ in the OFDM time–frequency grid.
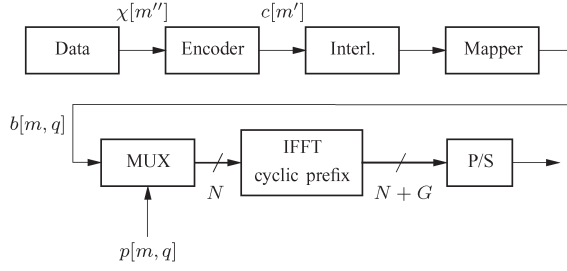
Fig. 1. Model of the OFDM transmitter.

In each frame, $J = |\mathcal{P}|$ pilot symbols $p[m,q] \; \forall \; [m,q] \in \mathcal{P}$ are transmitted, where $\mathcal{P}$ denotes the pilot symbol position index. For $[m,q] \notin \mathcal{P}$, we define $p[m,q] = 0$. The two sets $\mathcal{P}$ and $\mathcal{S}$ are nonoverlapping. The pilot symbols $p[m,q]$ are added, giving

$$d[m,q] = b[m,q] + p[m,q]. \qquad (2)$$

Subsequently, an N-point inverse discrete Fourier transform is carried out, and a cyclic prefix of length G is inserted. An OFDM symbol, including the cyclic prefix, has length $N + G$ samples.

The time-variant frequency response

$$g(t,f) = g_{\mathrm{Tx}}(f) g_{\mathrm{Ph}}(t,f)_{\mathrm{Rx}}(f) \qquad (3)$$

contains the effects of the physical (nonband-limited) channel $g_{\mathrm{Ph}}(t,f)$ as well as the band-limiting filter at the transmitter side $g_{\mathrm{Tx}}(f)$ and the receiver side $g_{\mathrm{Rx}}(f)$, respectively. The sampled time-variant frequency response, which is used for channel simulation, is defined as

$$g'[n,q] := g\left(nT_C, \varphi(q)/(NT_C)\right). \qquad (4)$$

The function $\varphi(q) = ((q + N/2 \bmod N) - N/2)$ maps the subcarrier index $q \in \{0, \ldots, N-1\}$ into the discrete frequency index $\varphi = \{0, \ldots, N/2 - 1, -N/2, \ldots, -1\}$.

Generally, in an OFDM system, intercarrier interference is caused by a time-variant channel impulse response. However, if the normalized Doppler bandwidth ν_D stays below a fraction $\epsilon = 5 \cdot 10^{-1}$ of the normalized subcarrier bandwidth

$$\frac{\nu_D N}{N + G} < \epsilon \qquad (5)$$

the intercarrier interference is small enough to be neglected for processing at the receiver side [37]–[39].

This condition is well fulfilled for IEEE 802.11p systems up to a velocity of about 1440 km/h to 400 m/s. Hence, we are able to define the sampled time-variant channel as $g[m,q] := g(m(N+G)T_C, \varphi(q)/(NT_C)) = g'[m(N+G), q]$, temporally sampled at rate $(N+G)/T_C$ for processing at the receive side. We can do this since the intercarrier interference is expected to have only a minor impact on the receiver performance. For the channel simulation, we use $g'[n,q]$ sampled at rate $1/T_C$; hence, all intercarrier interference effects are fully present in the received signal.

The received signal after cyclic prefix removal and discrete Fourier transform is

$$y[m,q] = g[m,q]d[m,q] + z[m,q] \qquad (6)$$

where circularly symmetric complex white Gaussian noise with zero mean and covariance σ_z^2 is denoted by $z[m,q]$. The output of a minimum MSE (MMSE) equalizer

$$\hat{d}[m,q] = \frac{y[m,q]\hat{g}[m,q]^*}{\sigma_z^2 + |\hat{g}[m,q]|^2} \qquad (7)$$

is used as input to a Bahl–Cocke–Jelinek–Raviv (BCJR) decoder [40] after demapping and deinterleaving. In (7), we denote by $\hat{g}[m,q]$ the channel estimate at time index m and subcarrier index q.

III. GEOMETRY-BASED STOCHASTIC MODEL FOR WIRELESS WAVE PROPAGATION

The time-variant frequency response

$$g(t,f) = g_{\mathrm{Tx}}(f) \underbrace{\left(\sum_{\ell=0}^{P-1} \eta_\ell(t) e^{-j2\pi\tau_\ell(t)f}\right)}_{g_{\mathrm{Ph}}(t,f)} g_{\mathrm{Rx}}(f) \qquad (8)$$

can be described as the superposition of P individual paths, given P is sufficiently large. Each path is characterized by the complex time-variant weighting coefficient $\eta_\ell(t)$ and its real-valued time-variant delay $\tau_\ell(t)$.

We can approximate the nonstationary fading process as wide-sense stationary for the duration of a single OFDM frame $m \in \mathcal{I}_M$ and $q \in \mathcal{I}_N$ [41], [42]. Hence, we model the time-variant path delay as $\tau_\ell(t) = \tau_\ell(0) - f_\ell t/f_C$ for the duration of MT_S, where f_ℓ denotes the Doppler shift of path ℓ. With this assumption and using (4), we obtain

$$g'[n,q] = g_{\mathrm{Tx}}[q]_{\mathrm{Rx}}[q] \underbrace{\sum_{\ell=0}^{P-1} \eta_\ell e^{-j2\pi\theta_\ell\varphi(q)} e^{j2\pi\nu_\ell n/(N+G)}}_{g_{\mathrm{Ph}}[n,q]} \qquad (9)$$

where $\nu_\ell = f_\ell T_S$ denotes the normalized Doppler shift, and $\theta_\ell = \tau_\ell(0)/(NT_C)$ denotes the normalized path delay, respectively. The geometry-based wireless wave propagation model (9) is the basic foundation for the accurate emulation of vehicular wireless wave propagation properties. It was validated for modeling wireless communication channels for cellular [43]–[45] as well as vehicular communication systems [34].

As shown in previous investigations [34], [36], the channel response in vehicular environments consists of the sum of contributions coming from different reflecting objects, each one with strongly different statistical properties. The most important contributions stem from the following: the line-of-sight (LOS) path between transmitter and receiver; discrete objects, either mobile (MD) or static (SD), producing reflections with a larger time delay; diffuse scattering (D) coming from

reflections on side walls of the road. Therefore, we can rewrite $g_{\text{Ph}}[n, q]$ as

$$
\begin{aligned}
g_{\text{Ph}}[n, q] = {} & \eta_0^{(\text{LOS})}[n] e^{-\mathrm{j}2\pi\theta_0^{(\text{LOS})}\varphi(q)} e^{\mathrm{j}2\pi\nu_0^{(\text{LOS})}n/(N+G)} \\
& + \sum_{\ell=1}^{N_{\text{SD}}} \eta_\ell^{(\text{SD})}[n] e^{-\mathrm{j}2\pi\theta_\ell^{(\text{SD})}\varphi(q)} e^{\mathrm{j}2\pi\nu_\ell^{(\text{SD})}n/(N+G)} \\
& + \sum_{\ell=1}^{N_{\text{MD}}} \eta_\ell^{(\text{MD})}[n] e^{-\mathrm{j}2\pi\theta_\ell^{(\text{MD})}\varphi(q)} e^{\mathrm{j}2\pi\nu_\ell^{(\text{MD})}n/(N+G)} \\
& + \sum_{\ell=1}^{N_{\text{D}}} \eta_\ell^{(\text{D})}[n] e^{-\mathrm{j}2\pi\theta_\ell^{(\text{D})}\varphi(q)} e^{\mathrm{j}2\pi\nu_\ell^{(\text{D})}n/(N+G)} \quad (10)
\end{aligned}
$$

where N_{SD}, N_{MD}, and N_{D} denote the number of scattering objects (SD, MD, and D) (cf. [34, eq. (9)]). The detailed parameterization of (10) will be discussed in Section VII-B2.

IV. GENERALIZED DISCRETE PROLATE SPEROIDAL SUBSPACE CHANNEL MODEL

We consider an OFDM system transmitting data frames over a time-variant frequency-selective channel. Pilot symbols are interleaved with data symbols in the time–frequency plane. Hence, we can observe the time-variant and frequency-selective channel for a certain region in time and frequency during the transmission of a single frame.

For channel estimation, we are interested to represent the channel in time and frequency by a low dimensional subspace such that a low-complexity reduced-rank (robust) Wiener filter [29] can be employed. For channel estimation, we are interested to design a subspace that minimizes the MSE. In general, this requires knowledge of the second-order statistics. The eigenvectors of the covariance matrix, i.e., the Karhunen–Loéve expansion [47], are the optimal basis functions spanning the subspace (see [17] for treatment in the frequency-domain approach and [32, Sec. III-C] for the time-domain approach, respectively). However, vehicular communication channels show local stationarity only, i.e., their second-order statistics can change rapidly. Hence, estimation of second-order statistics in frame-based communication systems is either difficult or impossible.

In Section IV-A, we introduce the concept of generalized DPS sequences, and we motivate and explain their application for a 2-D subspace model for time-variant frequency-selective channels in Section IV-B.

A. Generalized DPS Sequences

The subspace U spanned by time-limited snapshots of a band-limited (flat) fading process has an essential dimension given by the time–bandwidth product [32]

$$
D'(\mathcal{W}, M) = \lceil |\mathcal{W}| M \rceil + 1 \quad (11)
$$

where the interval

$$
\mathcal{W} = \bigcup_{i=1}^{I} \mathcal{B}_i = \mathcal{B}_1 \cup \mathcal{B}_2 \cup \ldots \cup \mathcal{B}_I \quad (12)
$$

defines the band limit [32, eq. (16)] potentially consisting of I disjoint intervals. Each interval is defined as $\mathcal{B}_i = (\nu_{i1}, \nu_{i2})$, $i \in \{1, \ldots, I\}$, with $\nu_{11} \leq \nu_{12} \leq \ldots \leq \nu_{I1} \leq \nu_{I2}$. The Lebesgue measure of $\mathcal{W}$ reads

$$
|\mathcal{W}| = \sum_{i=1}^{I} (\nu_{i2} - \nu_{i1}). \quad (13)
$$

The same subspace U is also spanned by generalized DPS sequences $\{u_i[m, \mathcal{W}, M]\}$, $i \in \{0, \ldots, M-1\}\}$, time limited to $m \in \mathcal{I}_M$. The generalized DPS sequences are band limited to the region $\mathcal{W}$, and their energy is most concentrated in the interval $\mathcal{I}_M$ (see [32, Def. 2]). They are the solutions to

$$
\sum_{\ell=0}^{M-1} C[\ell - m, \mathcal{W}] u_i[\ell, \mathcal{W}, M] = \lambda_i(\mathcal{W}, M) u_i[m, \mathcal{W}, M] \quad (14)
$$

for $m \in \mathbb{Z}$, where

$$
C[k, \mathcal{W}] = \int_{\mathcal{W}} e^{\mathrm{j}2\pi k\nu} \mathrm{d}\nu \quad (15)
$$

$$
\lambda_i(\mathcal{W}, M) = \frac{\sum\limits_{m=0}^{M-1} |u_i[m, \mathcal{W}, M]|^2}{\sum\limits_{m=-\infty}^{\infty} |u_i[m, \mathcal{W}, M]|^2} \quad (16)
$$

denotes the ith ordered eigenvalue also representing the energy concentration of $u_i[m, \mathcal{W}, M]$ within $\mathcal{I}_M$.

Note that $C[k, \mathcal{W}]$ is proportional to the covariance function of a process exhibiting a constant spectrum with support $\mathcal{W}$. Equation (15) evaluates to

$$
C[k, \mathcal{W}] = \frac{1}{\mathrm{j}2\pi k} \sum_{i=1}^{I} \left(e^{\mathrm{j}2\pi k\nu_{i2}} - e^{\mathrm{j}2\pi k\nu_{i1}} \right) \quad (17)
$$

if the band-limiting region $\mathcal{W}$ consists of I disjoint intervals.

B. Two-Dimensional Generalized DPS Channel Model

For a highly oversampled fading process $|\mathcal{W}| \ll 1$, the essential subspace dimension $D'(\mathcal{W}, M) \ll M$. This is the typical situation for modern high-rate communication systems. Due to the small degrees of freedom, the detailed shape of the power spectral density becomes less important for the estimation error. Hence, the support of the power spectral density is the crucial parameter for subspace design [13], [32] only. A similar reasoning was used for a robust Wiener filter design in [19] and [48].

Motivated by the structure of (9), we will represent $g[m, q]$ using a 2-D subspace model

$$
\begin{aligned}
g[m, q] \approx {} & \sum_{i=0}^{D_t - 1} \sum_{k=0}^{D_f - 1} u_i[m, \mathcal{W}_t, M] \\
& \cdot u_k\left[\varphi(q) + \frac{N}{2}, \mathcal{W}_f, N\right] \psi_{i,k} \quad (18)
\end{aligned}
$$
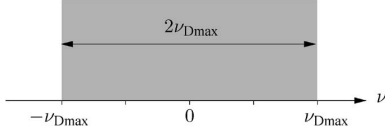
Fig. 2. Symmetric time-domain subspace $\mathcal{W}_t = [-\nu_{\mathrm{Dmax}}, \nu_{\mathrm{Dmax}}]$.
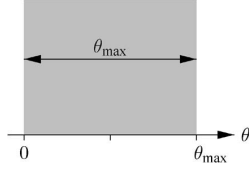
Fig. 3. Asymmetric frequency-domain subspace $\mathcal{W}_f = [0, \theta_{\max}]$.

where $\{u_i[m, \mathcal{W}_t, M], m \in \mathcal{I}_M, i \in \mathcal{I}_{D_t}\}$ spans the time-domain subspace, and $\{u_k[q, \mathcal{W}_f, N], q \in \mathcal{I}_N, k \in \mathcal{I}_{D_f}\}$ spans the frequency-domain subspace [30]. The generalized DPS coefficients are denoted by $\psi_{i,k}$.

The time-domain subspace $\{u_i[m, \mathcal{W}_t, M], m \in \mathcal{I}_M, i \in \mathcal{I}_{D_t}\}$ models a sequence in time, i.e., the channel coefficients $g[m, q]$ for a single subcarrier q and a finite time period $m \in \mathcal{I}_M$. The time-domain subspace is parameterized by the maximum support of the Doppler power spectral density $\mathcal{W}_t = [-\nu_{\mathrm{Dmax}}, \nu_{\mathrm{Dmax}}]$ (see Fig. 2).

Similarly, the frequency-domain subspace $\{u_k[q, \mathcal{W}_f, N], q \in \mathcal{I}_N, k \in \mathcal{I}_{D_f}\}$ models $g[m, q]$ for a single OFDM symbol m and a finite frequency interval $q \in \mathcal{I}_N$. The frequency-domain subspace is parameterized by the maximum support of the power delay profile $\mathcal{W}_f = [0, \theta_{\max}]$, where $\theta_{\max} = \tau_{\max}/(NT_C)$, and $\tau_{\max}$ is the maximum excess delay (see Fig. 3).

The subspace dimensions $D_t(\mathcal{W}_t, M)$ and $D_f(\mathcal{W}_f, N)$ minimizing the MSE for a given SNR can be expressed as [32], [49]

$$D(\mathcal{W}, M) = \arg \min_{\mathcal{D} \in \{1, \ldots, M\}} \left(\frac{1}{|\mathcal{W}|M} \sum_{i=\mathcal{D}}^{M-1} \lambda_i(\mathcal{W}, M) + \frac{\mathcal{D}}{M} \sigma_n^2 \right).$$
(19)

V. ITERATIVE CHANNEL ESTIMATION

After inserting the subspace channel model (18) into the signal model (6), we obtain

$$y[m, q] = \left(\sum_{i=0}^{D_t-1} \sum_{k=0}^{D_f-1} u_i[m, \mathcal{W}_t, M] \right.$$

$$\left. \cdot u_k \left[\varphi(q) + \frac{N}{2}, \mathcal{W}_f, N \right] \psi_{i,k} \right) d[m, q] + z[m, q]. \quad (20)$$

Using the generalized DPS sequences, our channel estimation problem is reduced to estimating the coefficients $\psi_{i,k}$. Note that $D_t D_f \ll NM$.

For the purpose of estimating the generalized DPS coefficients $\psi_{i,k}$, we rewrite (20) in matrix vector notation as follows.

We collect the coefficient $\psi_{i,k}$ in the vector

$$\boldsymbol{\psi} = [\boldsymbol{\psi}_0^{\mathrm{T}}, \ldots, \boldsymbol{\psi}_{D_t-1}^{\mathrm{T}}]^{\mathrm{T}} \quad (21)$$

where

$$\boldsymbol{\psi}_i = [\psi_{i,0}, \ldots, \psi_{i,D_f-1}]^{\mathrm{T}}. \quad (22)$$

We collect the received data values $y[m, q]$ for all m and q in one vector

$$\mathbf{y} = [y[0, 0], \ldots, y[0, N-1], y[1, 0], \ldots, y[1, N-1]$$
$$\ldots, y[M-1, 0], \ldots, y[M-1, N-1]]^{\mathrm{T}}. \quad (23)$$

Similarly, we define vector $\boldsymbol{d}$ containing the data values $d[m, q]$ and the noise vector $\boldsymbol{z}$ containing the noise values $z[m, q]$.

We define the vector

$$\mathbf{f}[m, \mathcal{W}_t, M] = [u_0[m, \mathcal{W}_t, M], \ldots, u_{D_t-1}[m, \mathcal{W}_t, M]]^{\mathrm{T}} \quad (24)$$

containing the elements of the generalized DPS basis functions for a given time index m.

Finally, we define the $MN \times D_t D_f$ matrix

$$\boldsymbol{\mathcal{D}} = \mathbf{D} \begin{bmatrix} \mathbf{f}[0, \mathcal{W}_t, M]^{\mathrm{T}} \otimes \mathbf{f}\left[\varphi(0) + \frac{N}{2}, \mathcal{W}_f, N\right]^{\mathrm{T}} \\ \vdots \\ \mathbf{f}[M-1, \mathcal{W}_t, M]^{\mathrm{T}} \otimes \mathbf{f}\left[\varphi(0) + \frac{N}{2}, \mathcal{W}_f, N\right]^{\mathrm{T}} \\ \vdots \\ \vdots \\ \mathbf{f}[0, \mathcal{W}_t, M]^{\mathrm{T}} \otimes \mathbf{f}\left[\varphi(N-1) + \frac{N}{2}, \mathcal{W}_f, N\right]^{\mathrm{T}} \\ \vdots \\ \mathbf{f}[M-1, \mathcal{W}_t, M]^{\mathrm{T}} \otimes \mathbf{f}\left[\varphi(N-1) + \frac{N}{2}, \mathcal{W}_f, N\right]^{\mathrm{T}} \end{bmatrix}$$
(25)

where $\boldsymbol{D} = \mathrm{diag}(\boldsymbol{d})$, allowing us to write the signal model to estimate the generalized DPS coefficient vector $\boldsymbol{\psi}$ as

$$\mathbf{y} = \boldsymbol{\mathcal{D}} \boldsymbol{\psi} + \mathbf{z}. \quad (26)$$

We use the soft-symbol feedback from the BCJR decoder [40] to enhance the channel estimates iteratively. In the first iteration, only the pilots are used. We define $\tilde{\boldsymbol{\mathcal{D}}}$ similar to (25), where we substitute $d[m, q]$ collected in $\boldsymbol{d}$ with

$$\tilde{d}[m, q] = \tilde{b}[m, q] + p[m, q] \quad (27)$$

containing the soft symbol feedback $\tilde{b}[m, q]$.

The soft symbols $\tilde{b}[m, q]$ are defined according to

$$\tilde{b}[\mathcal{S}_s] = \mathbb{E}_b^{(\mathrm{APP})} \{b[\mathcal{S}_s]\} \quad (28)$$

$$= \frac{1}{\sqrt{2}} \left(\mathbb{E}_c^{(\mathrm{APP})} \{c[2s]\} + \mathrm{j} \, \mathbb{E}_c^{(\mathrm{APP})} \{c[2s+1]\} \right) \quad (29)$$

for $s \in \mathcal{I}_S$, where

$$\mathbb{E}_c^{(\mathrm{APP})} \{c[m']\} = 2\Pr^{(\mathrm{APP})} \{c[m'] = +1 | \hat{c}[m']\} - 1 \quad (30)$$

117

calculates the expectation over the alphabet of c, which is $\{-1, +1\}$. By $\mathrm{Pr}^{(\mathrm{APP})}$, we denote the *a posteriori* probability (APP) for the code symbol being $+1$ if $\hat{c}[m']$ is observed, where $\hat{c}[m']$ is obtained from the equalizer output $\hat{d}[m, q]$ after demapping and deinterleaving [24] (see also Fig. 5).

The linear MMSE estimator for the generalized DPS coefficients ψ can be expressed as

$$\hat{\psi} = \left(\tilde{\mathcal{D}}^{\mathrm{H}} \mathbf{\Delta}^{-1} \tilde{\mathcal{D}} + \mathcal{C}_{\psi}^{-1} \right)^{-1} \tilde{\mathcal{D}}^{\mathrm{H}} \mathbf{\Delta}^{-1} \mathbf{y} \qquad (31)$$

following the derivation in [24, eq. (30)–(39)], where

$$\mathcal{C}_{\psi} = \frac{1}{|\mathcal{W}_t \| \mathcal{W}_f|} \mathrm{diag}\left(\boldsymbol{\lambda}(\mathcal{W}_t, M) \otimes \boldsymbol{\lambda}(\mathcal{W}_f, N) \right) \quad (32)$$

$$\boldsymbol{\lambda}(\mathcal{W}_t, M) = [\lambda_0(\mathcal{W}_t, M), \ldots, \lambda_{D_t}(\mathcal{W}_t, M)]^{\mathrm{T}} \qquad (33)$$

and

$$
\begin{aligned}
[\mathbf{\Delta}]_{m+Mq, m+Mq} = {} & \sigma_z^2 + \frac{1}{|\mathcal{W}_t \| \mathcal{W}_f|} \\
& \cdot \sum_{k=0}^{D_t-1} \sum_{i=0}^{D_f-1} \lambda_i(\mathcal{W}_t, M) \lambda_k(\mathcal{W}_f, N) \\
& \cdot |u_i[m, \mathcal{W}_t, M] u_k[\varphi(q) + N/2, \mathcal{W}_f, N]|^2 \\
& \cdot \left(1 - \left| \tilde{d}[m, q] \right|^2 \right).
\end{aligned} \qquad (34)
$$

VI. PILOT PATTERN DESIGN

In time-variant channels, the channel coefficients change between OFDM symbols within a frame, which needs to be tracked by the channel estimator. This is particularly true for vehicular settings, where high Doppler spreads of the channel are to be expected. In these cases, the pilot structure plays a significant role on how well these changes can be tracked by a channel estimator.

As discussed in [1], the pilot placement in the time–frequency grid in general needs to fulfill the sampling theorem. The maximum excess delay $\tau_{\max}$ determines how dense pilot symbols must be transmitted in the frequency domain. Hence, the maximum pilot spacing Δ_f (number of subcarriers) will satisfy

$$\Delta_f \leq \frac{N}{\tau_{\max} B}. \qquad (35)$$

The Doppler spread determines how dense pilot symbols must be placed in time. The maximum spacing Δ_t (number of OFDM symbols) will satisfy

$$\Delta_t \leq \frac{B}{2 f_D (N + G)}. \qquad (36)$$

Optimal pilot placement is discussed in [50] and [51].

A. Standard IEEE 802.11p Pilot Pattern

The pilot pattern of the IEEE 802.11 OFDM frame [3], [52] is shown in Fig. 4. After the so-called "short preamble" (not shown) for coarse timing estimation, the "long preamble"
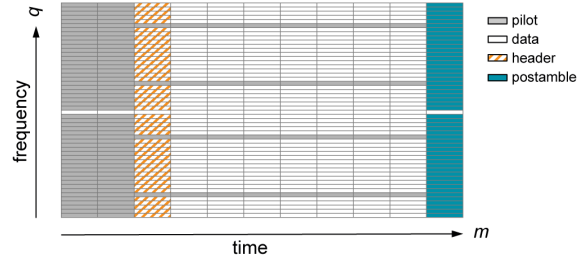
Fig. 4. Pilot pattern in an 802.11 OFDM frame extended by the proposed transparent postamble.

consists of two OFDM symbols containing pilot symbols only. Additionally, four subcarriers contain pilots throughout the whole OFDM frame. This pilot structure is usually termed a "block-comb" structure. It is particularly suited for quasi-static channels, where the block pilots are used for an initial channel estimate, whereas the comb pilots will ensure tracking of the phase for carrier frequency offset compensation.

Using the bound (35), we can see that for a time-variant channel having an impulse response with $\tau_{\max} > 490$ ns, the 802.11p pilot pattern will cause degradation of the channel estimates due to aliasing.

For iterative receiver structures as discussed in this paper, the bounds (35) and (36) can be relaxed since the fed back soft symbols are used as additional pilot information. However, if (35) and (36) are strongly violated, the number of iterations until convergence increases or the iterative receiver convergence stops early [53]. In Section VII, we provide numeric simulation results further detailing the effect of the 802.11p pilot pattern on iterative channel estimation in vehicular channels.

B. Improved Pilot Pattern

The increased number of iterations needed due to the 802.11p pilot pattern that violates (35) and (36) leads to high computational complexity for hardware design. For this reason, we advocate to use an improved pilot symbol pattern by appending another OFDM pilot symbol as postamble to the OFDM frame, as indicated in Fig. 4. The existence of this postamble is announced in the "reserved" bit of the header structure [3].

It is known that this choice is still suboptimal for channel tracking [50], [51]. However, the advantage of this choice is that this pilot pattern is backwards compatible with the established standard, as follows.

1) New receivers check the value of the "reserved" bit in the header. When set, the postamble is used for improved channel estimation.
2) Conventional receivers ignore the "reserved" bit but obtain the number of OFDM symbols in a frame from the "length" field of the header. By that, they are simply ignoring the postamble.

With the postamble, the maximum excess delay is now determined by the cyclic prefix

$$\tau_{\max} < G/B \qquad (37)$$
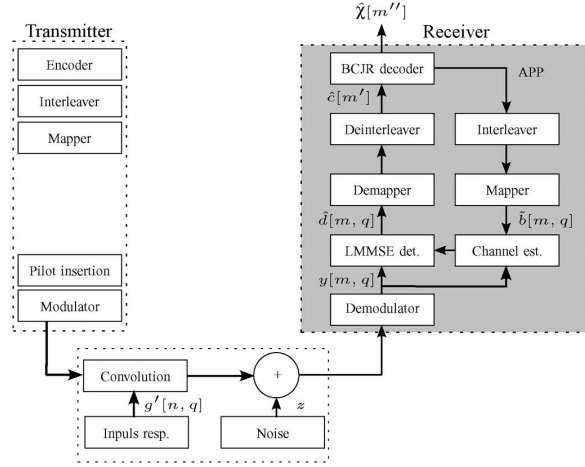
Fig. 5.   Schematic structure of the 802.11p link-level simulator with iterative channel estimation.

and the maximum Doppler bandwidth depends on the frame length M

$$f_{\mathrm{Dmax}} < B / \left(2M(N+G) \right) . \tag{38}$$

VII. NUMERIC SIMULATION RESULTS

In this section, we present numerical simulation results obtained with an 802.11p-compliant link-level simulation.

A. IEEE 802.11p Link-Level Simulator

An 802.11p [3] compliant link-level simulator implemented in MATLAB is used to evaluate the iterative time-variant channel estimator. The building blocks of the simulator are depicted in Fig. 5, showing the transmitter, channel model, and receiver with iterative channel estimation.

The 802.11p standard uses a system bandwidth $B = 10$ MHz, and the cyclic prefix has length $G = 16$ samples, corresponding to a maximum tolerable excess delay of 1.6 μs (or 480 m propagation distance). Of the $N = 64$ subcarriers, only 52 are utilized for data transmission to provide upper and lower guard bands. We assume a carrier frequency of $f_C = 5.9$ GHz.

The 802.11p standard supports eight different coding and modulation schemes that allow for data rate adaptation ranging from 3 to 27 Mb/s [1, Sec. III-B]. In this paper, we present results using coding and modulation scheme 3 at 6 Mb/s. This scheme uses QPSK (with symbol mapper rate $R_{\mathrm{S}} = 2$) and a convolutional code with constraint length 7 and code rate $R_C = 1/2$.

We present simulation results for two different types of channel models for a vehicle driving at $v = 100$ km/h ≈ 28 m/s ≈ 62 mi/h communicating with a fixed infrastructure access point (vehicle-to-infrastructure):

1) A Rayleigh fading channel with an exponentially decaying power delay profile with root mean square (RMS) de-

lay spread $\tau_{\mathrm{RMS}} = 0.4$ μs and a Clarke Doppler spectrum [54] for each tap modeling a non-LOS (NLOS) scenario (e.g., the LOS to the infrastructure access point is blocked by another vehicle). This model is similar to the "RTV-Expressway" tap delay line model described in [55].

2) A GSCM [34] implementing a vehicle-to-infrastructure scenario shown in [1, Fig. 18] that allows to model the nonstationary properties of the vehicle-to-infrastructure link with a dominant LOS propagation path (e.g., the access point is mounted on an elevated position on a motorway gantry).

Both channel models are implemented using fourfold oversampling. The bit error rate (BER) results will be shown versus E_b/N_0, where E_b denotes the energy per bit, and N_0 denotes the noise power spectral density. Hence, we calculate the variance of the additive symmetric complex white Gaussian noise according to

$$\frac{1}{\sigma_z^2} = \frac{E_b}{N_0} R_S R_C \frac{N}{N+G}$$
$$\cdot \frac{M'}{M' + M_{\mathrm{Pr}} + M_{\mathrm{H}} + M_{\mathrm{Po}}} \frac{N_{\mathrm{Da}}}{N_{\mathrm{Da}} + N_{\mathrm{Pi}}} \tag{39}$$

where M', M_{Pr}, M_{H}, and M_{Po} are the numbers of OFDM symbols contained in the data, preamble, header, and postamble fields, respectively. The number of data subcarriers is denoted by N_{Da} and the number of pilot subcarriers by N_{Pi}. For all simulations, $N_{\mathrm{Da}} = 48$, $N_{\mathrm{Pi}} = 4$, $M_{\mathrm{Pr}} = 2$, $M_{\mathrm{H}} = 1$, and $M_{\mathrm{Po}} \in \{0,1\}$, depending on the presence of the postamble pilot OFDM symbol. This corrects for the additional transmit energy used for the cyclic prefix, pilots, and header information. The generated channel impulse responses are normalized[1] to have average energy 1. Expressed by the time-variant frequency response, it reads

$$\mathbb{E}_m \left\{ \sum_{q=0}^{N-1} |g[m,q]|^2 \right\} = N \tag{40}$$

due to Parcevals's theorem. The transmitter sends a frame containing $\{200, 400, 800\}$ bytes (B), which corresponds to a total frame length of $M = \{37, 71, 137\}$ OFDM symbols without postamble and $M = \{38, 72, 138\}$ with postamble, respectively. The presented results are averaged over 500 channel realizations for the NLOS scenario and over 1000 channel realization for the LOS scenario, respectively.

For the parameters of 802.11p and $M = 37$, (37) and (38) provide the following bounds: $\tau_{\max} < 1.6$ μs, and $f_D < 1.6$ kHz (300 km/h). These are sufficient for most vehicular scenarios.

B. Simulation Results

We will compare our simulations results with the baseline performance shown in [1] for the exponentially decaying power delay profile and Clarke's Doppler spectrum in NLOS
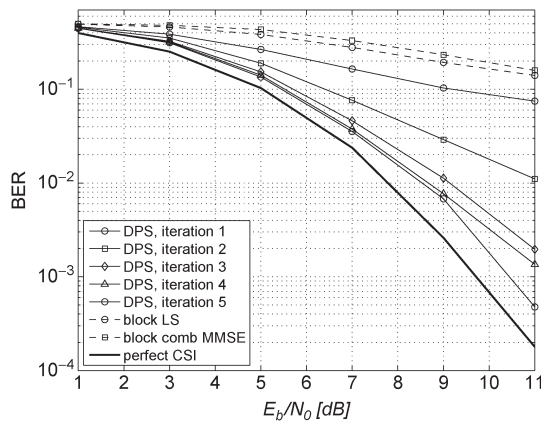
Fig. 6. BER versus E_b/N_0 for iteration $\{1, \ldots, 5\}$ for a frame length $M = 37$ and full 802.11p compliant (no postamble). The vehicles move at $v = 100$ km/h, and the channel model uses a Clarke Doppler profile for each channel tap. The power delay profile is exponentially decaying with RMS delay spread of 0.4 μs modeling a Rayleigh fading NLOS scenario.
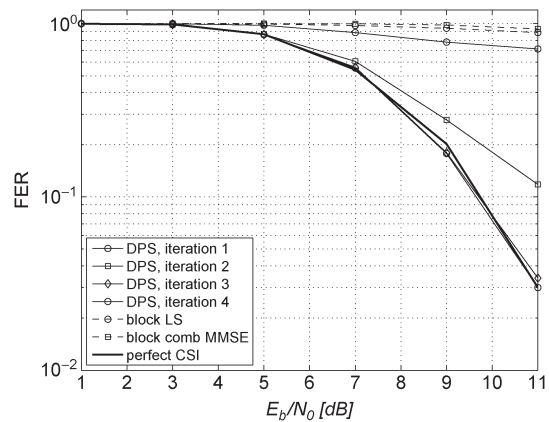
Fig. 7. FER versus E_b/N_0 for iteration $\{1, \ldots, 4\}$ for a frame length $M = 37$ and full 802.11p compliant (no postamble). The vehicles move at $v = 100$ km/h, and the channel model uses a Clarke Doppler profile for each channel tap. The power delay profile is exponentially decaying with RMS delay spread of 0.4 μs modeling a Rayleigh fading NLOS scenario.

situations as well as for the nonstationary model with strong LOS component.

In both cases, a noniterative least-square or linear MMSE estimator was used in [1] to demonstrate the current performance of common-of-the-shelf chip sets. A bit error floor at 10^{-1} for the NLOS case and at 10^{-4} for the LOS case at an $E_b/N_0 > 20$ dB was found in [1] due to the bad match of the 802.11p pilot pattern to a time-variant vehicular channel. A similar result is also reported in [56].

In the following, we will present numeric simulation results demonstrating the improved performance of the iterative receiver developed in this paper and the benefit of the modified backward compatible pilot pattern.

1) Vehicular NLOS Scenario: Fig. 6 shows the BER versus E_b/N_0 using the 802.11p compliant pilot pattern for channel estimation. The solid line without markers shows the BER with perfect channel state information (CSI) at the receiver side. The line with the circle markers shows the BER performance after the first iteration. Hence, a receiver without iterative channel estimation shows poor performance with a BER of about 10^{-1} at $E_b/N_0 = 11$ dB. Additionally, we show the baseline performance from [1] for the following: 1) the block least square estimator (block LS) where only the first two pilot symbols are used for channel estimation and 2) the block comb MMSE estimator where the four comb pilot subcarriers are employed to estimate the channel covariance function used then for MMSE channel estimation.

For a practical communication system, the FER is of high importance. In Fig. 7, we show the FER for the same scenario as in Fig. 6. Clearly, most frames can be received without error, and only a small number of frames contain multiple errors. Hence, the bit errors occur in bursts due to the time- and frequency-selective channel.

When the receiver makes reuse of the already decoded bits and their associated APPs, by running the receiver algorithm iteratively, the FER decreases and approaches the one for perfect CSI. We obtain FERs below 10^{-1} from the third iteration on,

with the FER curve converging to that of perfect CSI after four iterations.

Nevertheless, the price we have to pay at the receiver side for this improvement is an increased complexity of the hardware implementation[2] (see Section VII-C for more details). To reduce this complexity, we evaluate our proposal to add an extra dedicated OFDM pilot symbol at the end of the frame, described previously as transparent postamble. This results in a strongly improved channel estimate already after the first iteration, as depicted in Fig. 8. An FER below 10^{-1} is obtained for $E_b/N_0 > 10.5$ dB with a distance of about 0.8 dB to the FER with perfect CSI. Convergence to the FER curve with perfect CSI is achieved already after the second iteration. Hence, the transparent postamble allows for a complexity reduction by a factor of 2 in the NLOS case analyzed in Figs. 7 and 8.

In Fig. 9, we plot the FER as a function of the number of iterations at the receiver for different frame sizes at a fixed $E_b/N_0 = 11$ dB. Circular markers depict results with the transparent postamble, the square markers are used for the ones without postamble, and the lines without markers show the FER obtained with perfect CSI. Different line styles are used to denote the length of the frame.

As expected, with increasing number of iterations, the FER converges toward the one with perfect CSI. The slope of the curves with transparent postamble is steeper than without postamble, indicating higher convergence speed. More precisely, the transparent postamble allows for a complexity reduction of at least a factor of 2 to reach an FER below 10^{-1} with a maximum number of two iterations for a frame size of 400 and 200 B. We reach an FER close to 10^{-1} after four iterations for 800 B frame size.

2) Vehicular LOS Scenario: The investigated scenario consists of a highway with two lanes in each direction, with a width

---

[2]For every iteration of the receiver, the chip area needs to be increased by an additional BCJR decoder, as well as frame storage, channel estimation, and data detection logic to allow for a continuous pipelined operation.
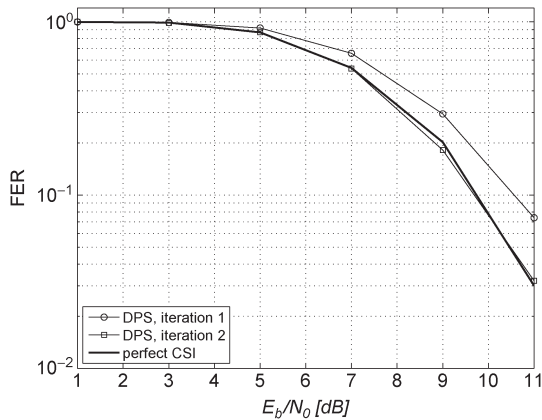
Fig. 8. FER versus E_b/N_0 for the first two iterations for a frame length of $M = 37$, with backward compatible transparent postamble. The vehicles move at $v = 100$ km/h, and the channel model uses a Clarke Doppler profile for each channel tap. The power delay profile is exponentially decaying with RMS delay spread of 0.4 μs.
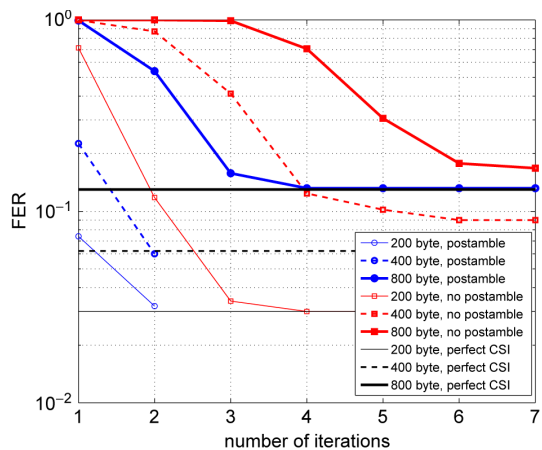
Fig. 9. FER versus number of iterations at an $E_b/N_0 = 11$ dB for varying frame size of $\{200, 400, 800\}$ B. The vehicles move at $v = 100$ km/h, and the channel model uses a Clarke Doppler profile for each channel tap. The power delay profile is exponentially decaying with RMS delay spread of 0.4 μs.

of 4 m/lane. The transmitter is at a fixed position in the middle of the road at $x = 0$, which represents a road side unit, and the receiver in the onboard unit is moving on the outer lane with a velocity of 100 km/h (see [1, Fig. 18]).

We use a GSCM [34] with a parameterization for this specific vehicle-to-infrastructure scenario [57]. The parameterization in [34] was obtained from vehicle-to-vehicle measurements; however, since they describe the geometry of the surroundings, the parameters are only changed slightly for the vehicle-to-infrastructure scenario (see [57]). In Table I, we list the modifications of the parameterization relative to [34, Tab. I] for the different scattering objects in terms of the reference power G_0 and the pathloss exponent n.

The analysis of the BER is performed over 1000 generated channel realizations and at different x coordinates of the receiver $x \in \{50, 100, 200\}$ m. Other cars are also driving in both directions with a mean speed of 100 km/h ≈ 28 m/s and

Parameters	LOS	MD	SD	D
G_0 [dB]	-20	-80+24n	-80+24n	50
n	1.8	$\mathcal{U}[0,3.5]$	$\mathcal{U}[0,3.5]$	6.4
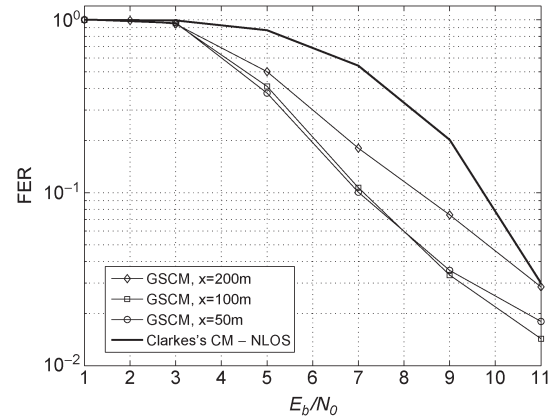
Fig. 10. FER with perfect CSI for different receiver coordinate $x = \{50, 100, 200\}$ m for the GSCM and NLOS. The frame length $M = 37$ contains 200 B.

standard deviation of 20 km/h ≈ 5.5 m/s. A band of objects producing diffuse scattering is placed beside the road (on both sides) with a width of 5 m.

For the investigation presented in this paper, we evaluate the FER versus E_b/N_0 for different positions x. Due to the strongly varying delay spread, Doppler spread, and Rician K-factor, the available diversity in the channel changes with x. To provide a baseline performance, we plot the FER with perfect CSI for all positions x in Fig. 10. The solid line in Fig. 10 depicts the FER for the NLOS Rayleigh fading scenario with exponentially decaying power delay profile and Clarke Doppler spectrum. Clearly, for the scenarios with strong LOS component, the diversity varies with x, and the NLOS channel provides highest diversity. However, for $E_b/N_0 < 11$ dB, the LOS scenario allows for smaller FERs.

Finally, in Fig. 11 we plot the FER versus the number of iterations for the LOS scenarios with receiver positions $x \in \{50, 100, 200\}$ m at a fixed $E_b/N_0 = 11$ dB. Again, we can demonstrate that the transparent postamble allows for a faster convergence of the iterative receiver with a complexity reduction of a factor of 2, reaching an FER smaller than 10^{-1} after one iteration.

For the presented simulation results, we use channel impulse responses normalized to unit average energy [see (40)]. However, in a practical receiver, the additive noise power stays constant and the signal energy will vary with x. The measured received energy over x is shown, e.g., in [46, Fig. 3], with a path loss exponent of $n = 1.8$. Hence, if we assume that we have $E_b/N_0 = 13$ dB when the receiver is at coordinate $x = 50$ m, the actual E_b/N_0 for the other distances is going to decrease, as indicated in Fig. 12. Therefore, the FER achieved is going to increase not only due to the fact that the channel properties
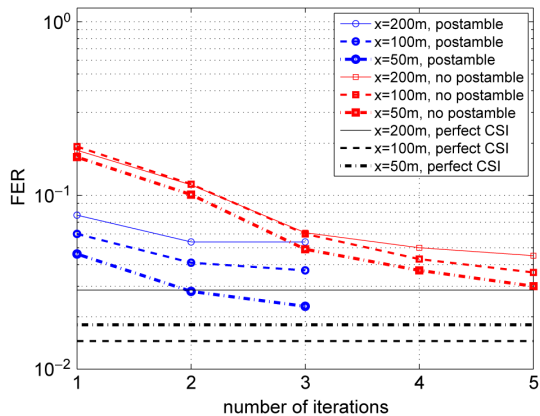
Fig. 11. FER versus number of iterations at $E_b/N_0 = 11$ dB for varying receiver coordinates $x = \{50, 100, 200\}$ m. The vehicles move at $v = 100$ km/h, and a GSCM [34] is used that allows to model the nonstationary properties of the vehicle-to-infrastructure link with a dominant LOS propagation path.
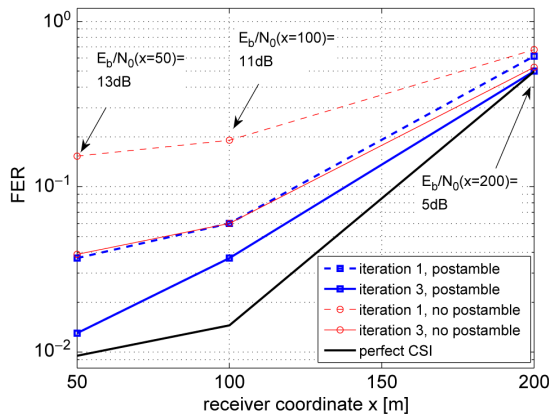
Fig. 12. FER versus receiver coordinate x for a given $E_b/N_0 = 13$ dB at distance $x = 50$ m.

vary with x but because E_b/N_0 is going to be different as well, depending on the distance. Noteworthy here again is that the FER obtained after the first iteration using the postamble is similar to the FER after three iterations without postamble.

C. Complexity

The new iterative algorithm presented in this paper together with the transparent postamble allows to operate 802.11p system in time-variant NLOS scenarios with an FER below 10^{-1}. Due to the legacy pilot pattern, a 2-D filter must be employed to achieve convergence.

The complexity of the iterative channel estimator is determined by three factors:

1) We employ a reduced rank 2-D linear MMSE filter (31), i.e., a reduced rank Wiener filter that allows to reduce the complexity compared with a normal Wiener filter [20] by utilizing only the dominant subspace. The complexity C_{RR} of the reduced rank filter (31) in terms of floating point operations [58] is determined by the dimension of

matrix $\tilde{\mathcal{D}} \in \mathbb{C}^{MN \times D_t D_f}$, as explained in [25, eq. (4)], resulting in

$$C_{\mathrm{RR}} \approx 8MN(D_t D_f)^2 + \frac{8}{3}(D_t D_f)^3. \qquad (41)$$

The full linear MMSE filter would require $C_{\mathrm{LMMSE}} \approx 32/3(MN)^3$. For a 200 B frame at $E_b/N_0 = 16$ dB, the frame consists of $M = 38$ OFDM symbols and subspace dimensions $D_t = 2$ and $D_f = 19$. Hence, the complexity reduction relative to the 2-D Wiener filter is $C_{\mathrm{LMMSE}}/C_{\mathrm{RR}} = 1.5 \cdot 10^{11}/2.8 \cdot 10^7 = 5.4 \cdot 10^3$. A further complexity reduction of the reduced rank Wiener filter (31) is possible by utilizing the Krylov subspace method (see [25] for more details).

2) The dominant factor in the computational complexity of the iterative channel estimator is by far the BCJR decoder. An efficient max. logMAP implementation [59] in C consumes more than 85% of CPU time in the numerical simulations of the iterative receiver. However, a BCJR decoder is currently state of the art for turbo decoding in Universal Mobile Telecommunications Systems (UMTS) and Long-Term Evolution (LTE) receivers, and efficient max. logMAP VLSI implementations are readily available (see [59]).

3) As shown by the simulation results, two to three iterations are sufficient for most relevant scenarios. For the concrete chip set implementation, this means that the structure depicted in Fig. 5 in the gray box needs to be replicated I times, where I is the maximum number of iterations. This will allow a pipelined operation of the iterative algorithms.

VIII. CONCLUSION

We have presented an iterative reduced-rank channel estimator for vehicular time-variant channels based on generalized DPS sequences. This iterative algorithm allows convergence to the same BER and FER as with perfect CSI even when using the pilot pattern of the IEEE 802.11p standard. The 802.11p pilot pattern violates the sampling theorem for vehicular channels because it is identical to the one used in IEEE 802.11a, which was designed for indoor scenarios. To reduce the number of iterations and the complexity of the hardware implementation, we propose a backward-compatible pilot pattern modification by adding a postamble. This modified pilot pattern allows for a complexity reduction by a factor of 2–3. We present numerical simulation results using a tap delay line model and a GSCM, representing a Rayleigh fading NLOS situation and a strongly nonstationary LOS situation, respectively. For both scenarios, the robust performance was demonstrated to reach an FER below 10^{-1} after a maximum of three iterations with the added transparent postamble.

REFERENCES

[1] C. F. Mecklenbräuker, A. F. Molisch, J. Karedal, F. Tufvesson, A. Paier, L. Bernadó, T. Zemen, O. Klemp, and N. Czink, "Vehicular channel characterization and its implications for wireless system design and performance," *Proc. IEEE*, vol. 99, no. 7, pp. 1189–1212, Jul. 2011.

[2] *IEEE Trial-Use Standard for Wireless Access in Vehicular Environments (WAVE)—Resource Manager*, IEEE Std. 1609.1-2006.

[3] *IEEE P802.11p: Part 11: Wireless LAN Medium Access Control (MAC) and Physical Layer (PHY) Specifications: Amendment 6: Wireless Access in Vehicular Environments*, IEEE Std. 802.11p-2010.

[4] A. F. Molisch, F. Tufvesson, J. Karedal, and C. F. Mecklenbräuker, "A survey on vehicle-to-vehicle propagation channels," *IEEE Wireless Commun.*, vol. 16, no. 6, pp. 12–22, Dec. 2009.

[5] A. Paier, R. Tresch, A. Alonso, D. Smely, P. Meckel, Y. Zhou, and N. Czink, "Average downstream performance of measured IEEE 802.11p infrastructure-to-vehicle links," in *Proc. IEEE ICC*, Cape Town, South Africa, May 23–27, 2010, pp. 1–5.

[6] L. Cheng, B. Henty, R. Cooper, D. Stancil, and F. Bai, "A measurement study of time-scaled 802.11 a waveforms over the mobile-to-mobile vehicular channel at 5.9 GHz," *IEEE Commun. Mag.*, vol. 46, no. 5, pp. 84–91, May 2008.

[7] J. Fernandez, D. Stancil, and F. Bai, "Dynamic channel equalization for IEEE 802.11p waveforms in the vehicle-to-vehicle channel," in *Proc. 48th Annu. Allerton Conf. Commun., Control, Comput.*, Sep. 29–Oct. 1, 2010, pp. 542–551.

[8] J. Fernandez, K. Borries, L. Cheng, V. Bhagavatula, D. Stancil, and F. Bai, "Performance of the 802.11p physical layer in vehicle-to-vehicle environments," *IEEE Trans. Veh. Technol.*, vol. 61, no. 1, pp. 3–14, Jan. 2012.

[9] A. Bourdoux, H. Cappelle, and A. Dejonghe, "Channel tracking for fast time-varying channels in IEEE802.11p systems," in *Proc. GLOBECOM*, Houston, TX, Dec. 2011, pp. 1–6.

[10] Y. Zhang, I. L. Tan, C. Chun, K. Laberteaux, and A. Bahai, "A differential OFDM approach to coherence time mitigation in DSRC," in *Proc. 5th ACM Int. Workshop Veh. Internetw.*, 2008, pp. 1–6.

[11] W. Cho, S. I. Kim, H. kyun Choi, H. S. Oh, and D. Y. Kwak, "Performance evaluation of V2V/V2I communications: The effect of midamble insertion," in *Proc. 1st Int. Conf. Wireless Commun., Veh. Technol., Inf. Theory Aerosp. Electron. Syst. Technol.*, May 2009, pp. 793–797.

[12] S. Sibecas, C. Corral, S. Emami, G. Stratis, and G. Rasor, "Pseudo-pilot OFDM scheme for 802.11a and R/A in DSRC applications," in *Proc. 58th IEEE VTC—Fall*, Oct. 2003, vol. 2, pp. 1234–1237.

[13] T. Zemen and C. F. Mecklenbräuker, "Time-variant channel estimation using discrete prolate spheroidal sequences," *IEEE Trans. Signal Process.*, vol. 53, no. 9, pp. 3597–3607, Sep. 2005.

[14] D. Slepian, "Prolate spheroidal wave functions, Fourier analysis, and uncertainty—V: The discrete case," *Bell Syst. Tech. J.*, vol. 57, no. 5, pp. 1371–1430, May/Jun. 1978.

[15] A. M. Sayeed, A. Sendonaris, and B. Aazhang, "Multiuser detection in fast-fading multipath environment," *IEEE J. Sel. Areas Commun.*, vol. 16, no. 9, pp. 1691–1701, Dec. 1998.

[16] D. Schafhuber, G. Matz, and F. Hlawatsch, "Adaptive Wiener filters for time-varying channel estimation in wireless OFDM systems," in *Proc. IEEE ICASSP*, Apr. 2003, vol. 4, pp. 688–691.

[17] O. Edfors, M. Sandell, J.-J. van de Beek, S. K. Wilson, and P. O. Börjesson, "OFDM channel estimation by singular value decomposition," *IEEE Trans. Commun.*, vol. 46, no. 7, pp. 931–939, Jul. 1998.

[18] J. Du and Y. G. Li, "D-BLAST OFDM with channel estimation," *EURASIP J. Appl. Signal Process.*, vol. 5, pp. 605–612, 2004.

[19] S. Kaiser, *Multi-Carrier CDMA Mobile Radio Systems—Analysis and Optimization of Detection, Decoding, and Channel Estimation*. Düsseldorf, Germany: VDI Verlag GmbH, 1998, ser. Fortschritts-Berichte VDI Reihe.

[20] S. Kaiser and P. Hoeher, "Performance of multi-carrier CDMA systems with channel estimation in two dimensions," in *Proc. 8th IEEE PIMRC*, Helsinki, Finland, Sep. 1997, vol. 1, pp. 115–119.

[21] A. Lampe and J. Huber, "Iterative interference cancellation for DS-CDMA systems with high system loads using reliability-dependent feedback," *IEEE Trans. Veh. Technol.*, vol. 51, no. 3, pp. 445–452, May 2002.

[22] G. Caire, R. R. Müller, and T. Tanaka, "Iterative multiuser joint decoding: Optimal power allocation and low-complexity implementation," *IEEE Trans. Inf. Theory*, vol. 50, no. 9, pp. 1950–1973, Sep. 2004.

[23] J. Wehinger and C. F. Mecklenbräuker, "Iterative CDMA multiuser receiver with soft decision-directed channel estimation," *IEEE Trans. Signal Process.*, vol. 54, no. 10, pp. 3922–3934, Oct. 2006.

[24] T. Zemen, C. F. Mecklenbräuker, J. Wehinger, and R. R. Müller, "Iterative joint time-variant channel estimation and multi-user detection for MC-CDMA," *IEEE Trans. Wireless Commun.*, vol. 5, no. 6, pp. 1469–1478, Jun. 2006.

[25] C. Dumard and T. Zemen, "Low-complexity MIMO multiuser receiver: A joint antenna detection scheme for time-varying channels," *IEEE Trans. Signal Process.*, vol. 56, no. 7, pp. 2931–2940, Jul. 2008.

[26] B. Hu, I. Land, L. Rasmussen, R. Piton, and B. Fleury, "A divergence minimization approach to joint multiuser decoding for coded CDMA," *IEEE J. Sel. Areas Commun.*, vol. 26, no. 3, pp. 432–445, Apr. 2008.

[27] S. Y. Park, Y. G. Kim, and C. G. Kang, "Iterative receiver for joint detection and channel estimation in OFDM systems under mobile radio channels," *IEEE Trans. Veh. Technol.*, vol. 53, no. 2, pp. 450–460, Mar. 2004.

[28] L. L. Scharf, *Statistical Signal Processing: Detection, Estimation, and Time Series Analysis.* Reading, MA: Addison-Wesley, 1991.

[29] F. A. Dietrich and W. Utschik, "Pilot-assisted channel estimation based on second-order statistics," *IEEE Trans. Signal Process.*, vol. 53, no. 3, pp. 1178–1193, Mar. 2005.

[30] T. Zemen, H. Hofstetter, and G. Steinböck, "Successive Slepian subspace projection in time and frequency for time-variant channel estimation," in *Proc. 14th IST IST SUMMIT*, Dresden, Germany, Jun. 2005.

[31] P. S. Rossi and R. R. Müller, "Slepian-based two-dimensional estimation of time-frequency variant MIMO-OFDM channels," *IEEE Signal Process. Lett.*, vol. 15, pp. 21–24, Jan. 2008.

[32] T. Zemen, C. F. Mecklenbräuker, B. H. Fleury, and F. Kaltenberger, "Minimum-energy band-limited predictor with dynamic subspace selection for time-variant flat-fading channels," *IEEE Trans. Signal Process.*, vol. 55, no. 9, pp. 4534–4548, Sep. 2007.

[33] L. Bernadó, N. Czink, T. Zemen, and P. Belanovic, "Physical layer simulation results for IEEE 802.11p using vehicular non-stationary channel model," in *Proc. IEEE ICC*, Cape Town, South Africa, May 2010, pp. 1–5.

[34] J. Karedal, F. Tufvesson, N. Czink, A. Paier, C. Dumard, T. Zemen, C. F. Mecklenbräuker, and A. F. Molisch, "A geometry-based stochastic MIMO model for vehicle-to-vehicle communications," *IEEE Trans. Wireless Commun.*, vol. 8, no. 7, pp. 3646–3657, Jul. 2009.

[35] S. B. Weinstein and P. M. Ebert, "Data transmission by frequency-division multiplexing using the discrete Fourier transform," *IEEE Trans. Commun.*, vol. COM-19, no. 5, pp. 628–634, Oct. 1971.

[36] Z. Wang and G. B. Giannakis, "Wireless multicarrier communications," *IEEE Signal Process. Mag.*, vol. 17, no. 3, pp. 29–48, May 2000.

[37] Y. G. Li and L. J. Cimini, "Bounds on the interchannel interference of OFDM in time-varying impairments," *IEEE Trans. Commun.*, vol. 49, no. 3, pp. 401–404, Mar. 2001.

[38] G. Faria, J. A. Henriksson, E. Stare, and P. Talmola, "DVB-H: Digital broadcast services to handheld devices," *Proc. IEEE*, vol. 94, no. 1, pp. 194–209, Jan. 2006.

[39] T. Luo, Z. Wen, J. Li, and H.-H. Chen, "Saturation throughput analysis of WAVE networks in Doppler spread scenarios," *IET Commun.*, vol. 4, no. 7, pp. 817–825, Apr. 2010.

[40] L. R. Bahl, J. Cocke, F. Jelinek, and J. Raviv, "Optimal decoding of linear codes for minimizing symbol error rate," *IEEE Trans. Inf. Theory*, vol. IT-20, no. 2, pp. 284–287, Mar. 1974.

[41] A. Paier, T. Zemen, L. Bernadó, G. Matz, J. Karedal, N. Czink, C. Dumard, F. Tufvesson, A. F. Molisch, and C. F. Mecklenbräuker, "Non-WSSUS vehicular channel characterization in highway and urban scenarios at 5.2 GHz using the local scattering function," in *Proc. WSA*, Darmstadt, Germany, Feb. 2008, pp. 9–15.

[42] O. Renaudin, V.-M. Kolmonen, P. Vainikainen, and C. Oestges, "Non-stationary narrowband MIMO inter-vehicle channel characterization in the 5-GHz band," *IEEE Trans. Veh. Technol.*, vol. 59, no. 4, pp. 2007–2015, May 2010.

[43] H. Hofstetter, "Characterization of the wireless MIMO channel," Ph.D. dissertation, Vienna Univ. Technol., Vienna, Austria, Sep. 2006.

[44] A. F. Molisch, "A generic channel model for MIMO wireless propagation channels in macro- and microcells," *IEEE Trans. Signal Process.*, vol. 52, no. 1, pp. 61–71, Jan. 2004.

[45] N. Czink, T. Zemen, J.-P. Nuutinen, J. Ylitalo, and E. Bonek, "A time-variant MIMO channel model directly parametrised from measurements," *EURASIP J. Wireless Commun. Netw.*, vol. 2009, p. 4, Feb. 2009.

[46] A. Paier, J. Karedal, N. Czink, C. Dumard, T. Zemen, F. Tufvesson, A. F. Molisch, and C. F. Mecklenbräuker, "Characterization of vehicle-to-vehicle radio channels from measurements at 5.2 GHz," *Wireless Pers. Commun.*, vol. 50, no. 1, pp. 19–32, Jul. 2009.

[47] A. Papoulis, *Probability, Random Variables and Stochastic Processes.* Singapore: McGraw-Hill, 1991.

123

[48] J. Berkmann, C. Carbonelli, F. Dietrich, C. Drewes, and W. Xu, "On 3G LTE terminal implementation—Standard, algorithms, complexities and challenges," in *Proc. IWCMC*, Aug. 2008, pp. 970–975.

[49] L. L. Scharf and D. W. Tufts, "Rank reduction for modeling stationary signals," *IEEE Trans. Acoust., Speech, Signal Process.*, vol. ASSP-35, no. 3, pp. 350–355, Mar. 1987.

[50] L. Tong, B. Sadler, and M. Dong, "Pilot-assisted wireless transmissions: General model, design criteria, and signal processing," *IEEE Signal Process. Mag.*, vol. 21, no. 6, pp. 12–25, Nov. 2004.

[51] R. Mersereau, "The processing of hexagonally sampled two-dimensional signals," *Proc. IEEE*, vol. 67, no. 6, pp. 930–949, Jun. 1979.

[52] *Supplement to IEEE Standard for Information Technology-Telecommunications and Information Exchange Between Systems—Local and Metropolitan Area Networks—Specific Requirements. Part 11: Wireless LAN Medium Access Control (MAC) and Physical Layer (PHY) Specifications: High-Speed Physical Layer in the 5 GHz Band*, IEEE Std. 802.11a-1999.

[53] S. ten Brink, "Convergence of iterative decoding," *Electron. Lett.*, vol. 35, no. 10, pp. 806–808, May 1999.

[54] R. H. Clarke, "A statistical theory of mobile-radio reception," *Bell Syst. Tech. J.*, vol. 47, pp. 957–1000, Jul./Aug. 1968.

[55] G. Acosta-Marum and M. A. Ingram, "Six time- and frequency-selective empirical channel models for vehicular wireless LANs," *IEEE Veh. Technol. Mag.*, vol. 2, no. 4, pp. 4–11, Dec. 2007.

[56] I. Ivan, P. Besnier, M. Crussiere, M. Drissi, L. Le Danvic, M. Huard, and E. Lardjane, "Physical layer performance analysis of V2V communications in high velocity context," in *Proc. 9th ITST*, Oct. 2009, pp. 409–414.

[57] A. Paier, J. Karedal, N. Czink, H. Hofstetter, C. Dumard, T. Zemen, F. Tufvesson, and A. Molisch, "First results from car-to-car and car-to-infrastructure radio channel measurements at 5.2 GHz," in *Proc. 18th IEEE PIMRC*, Athens, Greece, Sep. 2007, pp. 224–228.

[58] G. H. Golub and C. F. V. Loan, *Matrix Computations*, 3rd ed. Baltimore, MD: The Johns Hopkins Univ. Press, 1996.

[59] L. Sabeti, M. Ahmadi, and K. Tepe, "Low-complexity BCJR decoder for turbo decoders and its VLSI implementation in 0.18-μm CMOS," in *Proc. 62nd IEEE VTC—Fall*, Sep. 2005, vol. 2, pp. 912–916.

Laura Bernadó (S'09) received the M.Sc. degree from the Technical University of Catalonia, Barcelona, Spain. She is currently working toward the doctoral degree with the Vienna University of Technology, Vienna, Austria.

She is currently a Researcher in safety-related vehicular communications projects with the Telecommunications Research Center Vienna (FTW), Vienna. Her Master's thesis was written while with the Radio Communications Department, Royal Institute of Technology, Stockholm, Sweden. Her research interests are the modeling of fast time-varying fading processes and, particularly, characterization of nonstationarity for vehicular channels.

Nicolai Czink (S'04–M'08) received the Dipl.-Ing. (M.S.) degree in 2004 and the Dr.techn. (Ph.D.) degree in 2007 (with distinction) from the Vienna University of Technology, Vienna, Austria.

After his Ph.D., he joined Stanford University, Stanford, CA, as a Postdoctoral Researcher on an Erwin Schrödinger Fellowship of the FWF Austrian Science Fund. After that, he became a Senior Researcher with the FTW Telecommunications Research Center Vienna, where he works on channel modeling, cooperative communications, and intelligent transportation systems.

Dr. Czink's thesis received an award from the Austrian Electrotechnical Association.

Thomas Zemen (S'03–M'05–SM'10) received the Dipl.-Ing. degree (with distinction) in electrical engineering from the Vienna University of Technology, Vienna, Austria, in 1998 and the doctoral degree (with distinction) in 2004.

From 1998 to 2003, he was a Hardware Engineer and Project Manager with the Radio Communication Devices Department, Siemens Austria. Since October 2003, he has been with FTW Forschungszentrum Telekommunikation Wien, Vienna, where he has been leading the Department of "Signal and Information Processing" since 2008. He is the speaker of the national research network for "Signal and Information Processing in Science and Engineering" funded by the Austrian Science Fund (FWF). His research interests include vehicular channel measurements and modeling, time-variant channel estimation, orthogonal frequency-division multiplexing, iterative multiple-input–multiple-output receiver structures, cooperative communication systems, and interference management. He teaches as External Lecturer with the Vienna University of Technology and serves as Editor for the IEEE TRANSACTIONS ON WIRELESS COMMUNICATIONS. He is the author or coauthor of four book chapters and more than 80 journal papers and conference communications.

Andreas F. Molisch (S'89–M'95–SM'00–F'05) received the Dipl. Ing., Ph.D., and habilitation degrees from the Technical University of Vienna, Vienna, Austria, in 1990, 1994, and 1999, respectively.

He subsequently was with AT&T (Bell) Laboratories Research (USA); Lund University, Lund, Sweden, and Mitsubishi Electric Research Labs (USA). He is now a Professor of electrical engineering with the University of Southern California, Los Angeles. His current research interests are the measurement and modeling of mobile radio channels, ultra-wideband communications and localization, cooperative communications, multiple-input–multiple-output systems, and wireless systems for healthcare. He has authored, coauthored, or edited four books (among them the textbook *Wireless Communications*, Wiley-IEEE Press), 14 book chapters, more than 130 journal papers, and numerous conference contributions, as well as more than 70 patents and 60 standards contributions.

Dr. Molisch has been an Editor of a number of journals and special issues, General Chair, Tecnical Program Committee Chair, or Symposium Chair of multiple international conferences, as well as Chairman of various international standardization groups. He is a Fellow of the IET, an IEEE Distinguished Lecturer, and a member of the Austrian Academy of Sciences. He has received numerous awards, most recently the 2011 James Evans Avant-Garde award of the IEEE Vehicular Technology Society and the Donald Fink Prize of the IEEE.

4 Low Complexity Multi-User Detection

[Article 10]   C. Dumard and T. Zemen, "Low-complexity MIMO multiuser receiver: A joint antenna detection scheme for time-varying channels," *IEEE Transactions on Signal Processing*, vol. 56, no. 7, pp. 2931-2940, July 2008.

[Article 11]   C. Dumard and T. Zemen, "Subspace-based sphere decoder for MC-CDMA in time-varying MIMO channels," in *18th IEEE International Symposium on Personal, Indoor and Mobile Radio Communications (PIMRC)*, Athens, Greece, Sept. 3-7, 2007.

[Article 12]   C. Dumard, J. Jalden and T. Zemen, "Soft sphere decoder for an iterative receiver in time-varying MIMO channels," in *16th European Signal Processing Conference (EUSIPCO)*, Lausanne, Switzerland, Aug. 25-29, 2008, invited.

Low-Complexity MIMO Multiuser Receiver: A Joint Antenna Detection Scheme for Time-Varying Channels

Charlotte Dumard, *Student Member, IEEE*, and Thomas Zemen, *Member, IEEE*

Abstract—**This paper deals with the uplink of a wireless multiple-input multiple-output (MIMO) communication system based on multicarrier (MC) code division multiple access (CDMA). We focus on time-varying channels for users moving at vehicular speeds. The optimal maximum *a posteriori* (MAP) receiver for such a system is prohibitively complex and can be approximated using iterative linear minimum mean-square error (LMMSE) multiuser detection and parallel interference cancellation (PIC). For time-varying channels, two LMMSE filters for channel estimation and multiuser detection need to be computed at every time instant, making implementation in a real-time system difficult. We develop a novel low-complexity receiver that exploits the multiple antenna structure of the system and performs joint iterative multiuser detection and channel estimation. Our receiver algorithms are based on the Krylov subspace method, which solves a linear system with low complexity, trading accuracy for efficiency. The computational complexity of the channel estimator can be reduced by one order of magnitude. For multiuser detection, a PIC scheme in the *user space*, i.e., after the matched filter, allows simultaneous detection of all users as well as drastic computational complexity reduction by more than one order of magnitude.**

Index Terms—**Joint antenna detection, Krylov subspace method, low-complexity receiver, multiple-input multiple-output (MIMO), orthogonal frequency-division multiplexing (OFDM), time-varying channel.**

I. INTRODUCTION

THIS paper deals with the uplink of a wireless multiple-input multiple-output (MIMO) communication system for users at vehicular speeds. The communication system is based on multicarrier (MC) code-division multiple access (CDMA). Receiver algorithms for such a system require high computational complexity due to the linear minimum mean-square error (LMMSE) filters employed for multiuser detection and channel estimation [1]–[3]. We develop a novel low-complexity receiver based on the Krylov subspace method.

The Krylov subspace method [4]–[7] allows to solve a linear system with low complexity by trading accuracy for efficiency. It has long been used in signal processing, e.g., for beamforming

[8], [9] or detection [10], [11], where a computational complexity reduction is shown.

In [10], universal weights are computed, based on the self-averaging properties of random matrices modeling the channel. The *a priori* random eigenvalues of the channel matrix can be described by averaging over sufficiently large samples. The eigenvalue distribution of the channel matrix converges to a deterministic distribution when its dimensions grow to infinity. Universal weights are thus computed independently of the received signal. However, the authors in [10] do not take into account an iterative scheme using interference cancellation. In such a case, the projection computations are not common to all users anymore, and no computational complexity reduction can be achieved this way.

In [11], the authors use the Lanczos algorithm to approximate the Wiener filter in an iterative receiver for a *single-user* single-input multiple-output (SIMO) system. Their iterative scheme uses an adjusted mean of the signal based on *a priori* information to cancel the multipath interference. The computational complexity using the Lanczos algorithm in [11] scales quadratic with the length of the observation vector.

We aim at developing an efficient low-complexity iterative receiver for a multiuser MIMO system in time-varying channels, that scales linear in the number of users and the length of the observation vector. At the receiver side, we consider an algorithm performing iterative multiuser detection with parallel interference cancellation (PIC) and time-varying channel estimation jointly. For PIC and channel estimation, soft-symbols are used that are supplied by a soft-input soft-output decoder based on the BCJR algorithm [12]. Channel estimation is performed using LMMSE filtering and can be implemented with low-complexity using the Krylov subspace method.

PIC can be implemented in two basic configurations. In the first configuration, the other users interference is subtracted directly from the received chip vector, thus operating in chip space. A second configuration employs matched filtering first and then subtracts the other users interference, thus operating in user space. This model has been introduced in [13] and allows joint detection of all users. The two PIC configurations are mathematically nearly equivalent if an exact linear MMSE filter is employed. However, when using a low complexity implementation based on the Krylov subspace method, the two setups lead to large complexity differences.

In MIMO CDMA channels, joint antenna detection schemes are shown to outperform individual antenna detection schemes [14]. However, such systems are computationally expensive.

We develop a method to implement such a receiver with low-complexity.

Contributions of the Paper:
- First, we develop a reduced-rank low-complexity channel estimation method for a time-varying MIMO MU uplink based on the Krylov subspace method.
- Second, we implement a joint antenna detector for an MC-CDMA MIMO receiver, using parallel interference cancelation in *chip space*. This approach does not allow complexity reduction but parallelization of the computations into as many branches as transmit antennas. The latency time can thus be reduced by a factor that is proportional to the number of users in case of a fully loaded system.
- Finally, we develop a new model for joint antenna detection with PIC in *user space*. This approach allows saving more than one order of magnitude of complexity with only minor performance losses.

Notation: We denote by $\boldsymbol{a}$ a column vector with ith element $a[i]$. Similarly, $\boldsymbol{A}$ is a matrix with i, ℓth element $[\boldsymbol{A}]_{i,\ell}$. A diagonal matrix with entries $a[i]$ is denoted $\mathrm{diag}(\boldsymbol{a})$. The $Q \times Q$ identity matrix and $Q \times 1$ zero vector are denoted by $\boldsymbol{I}_Q$ and $\boldsymbol{0}_Q$ respectively. We denote the real and conjugate transpose with $^{\mathrm{T}}$ and $^{\mathrm{H}}$ respectively. The largest (respectively smallest) integer, lower (resp. greater) or equal than $a \in \mathbb{R}$ is represented by $\lfloor a \rfloor$ (resp. $\lceil a \rceil$). The ℓ_2-norm is denoted through $\|\boldsymbol{a}\|$. The expectation of a variable is denoted through $\mathsf{E}\{\cdot\}$. The $N_T(k-1)+t$th elementary vector of size KN_T for $k \in \{1, \ldots, K\}$ and $t \in \{1, \ldots, N_T\}$ is represented by $\boldsymbol{e}_{(k,t)}$.

Organization of the Paper: The Krylov subspace method is briefly recalled and details on the computational complexity are given in Section II. The system model is developed in Section III. The low-complexity implementation of the multiple antenna receiver using the Krylov subspace method is described in Section IV. Simulation results as well as complexity comparison are presented in Section V. Section VI summarizes the main results and concludes this work.

II. COMPLEXITY OF THE KRYLOV SUBSPACE METHODS

The main results of this paper are based on the Krylov subspace method which we shortly recall in this section. The complete description of the algorithm can be found in [4]–[7] and more specifically for our use in [15].

Considering a linear system $\boldsymbol{Ax} = \boldsymbol{a}$, where $\boldsymbol{A}$ is a known invertible matrix of size $Q \times Q$ and $\boldsymbol{a}$ a known vector of length Q, the Krylov subspace based algorithms compute iteratively (s increasing) an approximation of the solution $\boldsymbol{x}$, starting from an initial guess $\boldsymbol{x}_0$ and using projections on Krylov subspaces of dimension s. The final step S is referred to as the number of iterations in the algorithm or as the dimension of the Krylov subspace on which we project $\boldsymbol{a} - \boldsymbol{Ax}_0$.

Using the algorithm which is recalled in Table I, we can now discuss on the computational complexity using the Krylov subspace method for an LMMSE filter. Let us here define a *flop* as a floating-point operation, as given in [16]. A *flop* is either an addition, substraction, multiplication, division or square root operation in the *real* domain. Thus, one complex multiplication (CM) requires four real multiplications and two additions, leading to

TABLE I
KRYLOV SUBSPACE-BASED ALGORITHM FOR A HERMITIAN MATRIX

	Steps	Complexity in *flop*s using (1)
1	input $\boldsymbol{A}$, $\boldsymbol{a}$, $\boldsymbol{x}_0$, S	$2a(4b-1)$ for $\boldsymbol{a} = \boldsymbol{Mv}$
2	$\tilde{\boldsymbol{a}} = \boldsymbol{a} - \boldsymbol{Ax}_0$	$16ab + 8a + 4b$
3	$\boldsymbol{v}_1 = \tilde{\boldsymbol{a}}/\|\tilde{\boldsymbol{a}}\|$	$10a - 1$
4	$\boldsymbol{u} = \boldsymbol{Av}_1$	$16ab + 6a + 4b$
5	$\alpha = \boldsymbol{v}_1^{\mathrm{H}}\boldsymbol{u}$	$8a - 2$
6	$c_{\mathrm{first}} = c_{\mathrm{last}} = 1/\alpha$	1
7	$\boldsymbol{w} = \boldsymbol{u} - \alpha\boldsymbol{v}_1$	$8a$
8	for $s = 2, \ldots, S$	
9	$\quad \beta = \|\boldsymbol{w}\|$	$8a - 1$
10	$\quad \boldsymbol{v}_s = \boldsymbol{w}/\beta$	$2a$
11	$\quad \boldsymbol{u} = \boldsymbol{Av}_s$	$16ab + 6a + 4b$
12	$\quad \alpha = \boldsymbol{v}_s^{\mathrm{H}}\boldsymbol{u}$	$8a - 2$
13	$\quad \gamma = \alpha - \beta^2 c_{\mathrm{last}}[s-1]$	$2a + 2$
14	$\quad \boldsymbol{c} = \gamma^{-1} \left[-\beta\boldsymbol{c}_{\mathrm{last}}^{\mathrm{T}}, 1 \right]^{\mathrm{T}}$	$6(s+1)$
15	$\quad \boldsymbol{c}_{\mathrm{first}} = \begin{bmatrix} \boldsymbol{c}_{\mathrm{first}}^{\mathrm{T}}, 0 \end{bmatrix}^{\mathrm{T}} - c_{\mathrm{last}}[1]_* \beta\boldsymbol{c}$	$8(s+1)$
16	$\quad \boldsymbol{c}_{\mathrm{last}} = \boldsymbol{c}$	
17	$\quad \boldsymbol{w} = \boldsymbol{u} - \alpha\boldsymbol{v}_s - \beta\boldsymbol{v}_{s-1}$	$8a$
18	end	
19	$\boldsymbol{V}_S = [\boldsymbol{v}_1, \ldots, \boldsymbol{v}_S]$	
20	output $\boldsymbol{x}_S = \|\tilde{\boldsymbol{a}}\|\boldsymbol{V}_S\boldsymbol{c}_{\mathrm{first}} + \boldsymbol{x}_0$	$2a(4S+1)$

6 flops. Similarly, one complex addition (CA) corresponds to 2 flops.

The general structure of an LMMSE filter can be written as [17]

$$\boldsymbol{f} = \underbrace{\left(\boldsymbol{D}_1 + \boldsymbol{MD}_2\boldsymbol{M}^{\mathrm{H}}\right)^{-1}}_{\boldsymbol{A}}\boldsymbol{Mv} \qquad (1)$$

where $\boldsymbol{M} \in \mathbb{C}^{a \times b}$, $\boldsymbol{v} \in \mathbb{C}^b$, and $\boldsymbol{D}_1 \in \mathbb{C}^{a \times a}$ and $\boldsymbol{D}_2 \in \mathbb{C}^{b \times b}$ are diagonal.

Computing $\boldsymbol{f}$ in (1) directly requires the following operations:
- computation of $\boldsymbol{A} = \boldsymbol{D}_1 + \boldsymbol{MD}_2\boldsymbol{M}^{\mathrm{H}}$, i.e., $ab\mathrm{CM} + a^2(b\mathrm{CM} + (b-1)\mathrm{CA}) + a\mathrm{CA} = 8a^2b + 6ab - 2a^2 + 2a$ flops;
- inversion of $\boldsymbol{A}$, i.e., $(1/3)a(a-1)(8a-1)$ flops (see Appendix A for details);
- computation of $\boldsymbol{A}^{-1}\boldsymbol{a}$ with $\boldsymbol{a} = \boldsymbol{Mv}$, i.e., $4a(2a + 2b - 1)$ flops.

This leads to the approximate computational complexity

$$C_{\mathrm{LMMSE}}^1 \approx 8a^2 \left(\frac{a}{3} + b\right) \text{ flops.} \qquad (2)$$

Using the Krylov approximation, the main computations required to approximate $\boldsymbol{f}$ are as follows:
- the product $\boldsymbol{Av}_s = \boldsymbol{D}_1\boldsymbol{v}_s + \boldsymbol{M}(\boldsymbol{D}_2(\boldsymbol{M}^{\mathrm{H}}\boldsymbol{v}_s))$ for $s \in \{1, \ldots, S\}$, in lines 4 and 11 of the algorithm in Table I, as well as $\boldsymbol{Ax}_0$ on line 2, i.e., $(16ab + 6a + 4b)(S+1)$ flops;
- two inner products for S steps, in lines 3, 5 and lines 9 and 12, i.e., $2(8a - 2)S$ flops.

The computational complexity of each step is detailed in Table I. Adding all these steps, the total computational complexity using the Krylov subspace method becomes after approximation

$$C_{\mathrm{K}}^1 \approx (16ab + 42a)(S+1) + 8ab \text{ flops.} \qquad (3)$$

If $a \geq b$, the computational complexity can be reduced by first applying the matrix inversion lemma [6]

to (1). Detailed computations in Appendix B lead to $\boldsymbol{f} = \boldsymbol{D}_1^{-1}\boldsymbol{M}(\alpha\boldsymbol{I}_b + \boldsymbol{D}_2\boldsymbol{M}^{\mathrm{H}}\boldsymbol{D}_1^{-1}\boldsymbol{M})^{-1}\boldsymbol{v}$. Similar computational complexity expressions as (2) and (3) can be obtained for the new LMMSE filter and its Krylov approximation

$$C_{\mathrm{LMMSE}}^2 \approx 8b^2\left(\frac{b}{3} + a\right) \text{ flops}$$
$$C_{\mathrm{K}}^2 \approx (8ab + 14b + 12a)(2S + 3) + 12b \text{ flops}. \quad (4)$$

Finally, we obtain for the general case

$$C_{\mathrm{LMMSE}} \approx 8ab\min\{a, b\} + \frac{8}{3}\min\{a, b\}^3 \text{ flops}$$
$$\begin{aligned} C_{\mathrm{K}} &\approx 8ab(2S + 3) \\ &+ 14(S + 1)\min\{3a, 2(a + b)\} \text{ flops}. \end{aligned} \quad (5)$$

If a and b are high enough, as it will be the case in our application, the second term in C_{K} might be ignored, leading to $C_{\mathrm{K}} \approx 8ab(2S + 3)$.

In this approximation, a and b are interchangeable, so we can set $\min\{a, b\} = a$ without loss of generality. The exact LMMSE filter has a complexity of order $\mathcal{O}(8a^2((a/3) + b))$ and the ratio $\gamma = C_{\mathrm{K}}/C_{\mathrm{LMMSE}}$ is of order

$$\mathcal{O}\left(\frac{2S + 3}{a\left(\frac{a}{3b} + 1\right)}\right) \leq \mathcal{O}\left(\frac{2S + 3}{a}\right). \quad (6)$$

Assuming $S \ll a$, the computational complexity reduction by the Krylov subspace method is substantial.

III. SYSTEM MODEL

We consider the uplink of an MC-CDMA system. At the same time $K \geq 1$ users having each $N_T \geq 1$ antennas transmit to a receiver with $N_R \geq 1$ antennas. Hence, we have a MIMO multiuser (MU) system. In this section, we detail the model used for the multiple antenna transmitter and receiver.

A. Multiple Antenna Transmitter

Each user $k \in \{1, \ldots, K\}$ has $N_T \geq 1$ transmit antennas. The MC-CDMA uplink transmission is based on orthogonal frequency division multiplexing (OFDM) with N subcarriers, where N is also the spreading factor. We consider the transmission of N_T data blocks per user, each data block consists of $M - J$ OFDM data symbols and J pilot symbols. From the receiver point of view, the KN_T transmit antennas behave like KN_T independent virtual users. Thus, and for clarity, we will refer to the transmit antenna t of user k as transmit antenna or virtual user (k, t). Each transmit antenna $(k, t) \in \{1, \ldots, K\} \times \{1, \ldots, N_T\}$ transmits symbols $b_{(k,t)}[m]$ with symbol rate $1/T_{\mathrm{S}}$, where m denotes the discrete time index and T_{S} the symbol duration. Each symbol $b_{(k,t)}[m]$ is spread by a random spreading sequence $\boldsymbol{s}_{(k,t)} \in \mathbb{C}^N$ with independent identically distributed elements chosen from the set $\{\pm 1 \pm \mathrm{j}\}/\sqrt{2N}$. The data symbols $b_{(k,t)}[m]$ result from the binary information sequence $\chi_k[m'']$ of length $2(M - J)R_C$ by convolutional encoding with code rate R_C, random interleaving
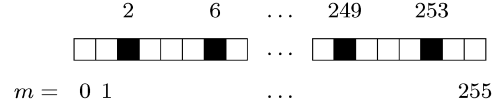
Fig. 1. Pilot placement for $J = 60$ pilots among $M = 256$ symbols.

and quadrature phase shift keying (QPSK) modulation with Gray labeling.

The $M - J$ data symbols are distributed over a block of length M fulfilling

$$\begin{aligned} b_{(k,t)}[m] &\in \{\pm 1 \pm \mathrm{j}\}/\sqrt{2} \quad \text{for} \quad m \notin \mathcal{P} \\ b_{(k,t)}[m] &= 0 \quad \text{for} \quad m \in \mathcal{P} \end{aligned} \quad (7)$$

allowing for pilot symbol insertion. The pilot placement is defined through the index set

$$\mathcal{P} = \left\{\left\lfloor i\frac{M}{J} + \frac{M}{2J}\right\rfloor \Big| i \in \{0, \ldots, J - 1\}\right\}. \quad (8)$$

Fig. 1 gives an illustration of the pilot placement.

We use joint encoding [18], [19] for all N_T antennas of one user: the N_T data blocks of one user are jointly encoded, interleaved and mapped. Then the $N_T(M - J)$ coded symbols are split into N_T coded symbol blocks that are independently spread to be transmitted over their corresponding antenna.

After spreading, the pilot symbols $\boldsymbol{p}_{(k,t)}[m] \in \mathbb{C}^N$ are added

$$\boldsymbol{d}_{(k,t)}[m] = \boldsymbol{s}_{(k,t)}b_{(k,t)}[m] + \boldsymbol{p}_{(k,t)}[m]. \quad (9)$$

For $m \in \mathcal{P}$ and $q \in \{0, \ldots, N - 1\}$, the elements $p_{(k,t)}[m, q]$ of the pilot symbol vector $\boldsymbol{p}_{(k,t)}[m]$ are randomly chosen from the QPSK symbol set $\{\pm 1 \pm \mathrm{j}\}/\sqrt{2N}$. Otherwise $\boldsymbol{p}_{(k,t)}[m] = \boldsymbol{0}_N$ for $m \notin \mathcal{P}$.

At each transmit antenna an N-point inverse discrete Fourier transform (DFT) is performed and a cyclic prefix of length G is inserted. A single OFDM symbol together with the cyclic prefix has length $P = N + G$ chips. After parallel to serial conversion the chip stream with chip rate $1/T_{\mathrm{C}} = P/T_{\mathrm{S}}$ is transmitted over a time-varying multipath fading channel with L resolvable paths.

The transmission of KN_T symbols at time instant m is done over K independent $N_T \times N_R$ MIMO channels. These KN_TN_R channels are assumed uncorrelated. Thus, the receiver treats the KN_T antennas in the same way as if they were KN_T independent users having one transmit antenna each.

B. Multiple Antenna Receiver

The iterative receiver performing channel estimation and multiuser detection is shown in Fig. 2. The receiver is equipped with $N_R \geq 1$ receive antennas. At each receive antenna $r \in \{1, \ldots, N_R\}$, the signals of all KN_T transmit antennas add up.

Each of the N_R receivers performs cyclic prefix removal and a DFT on its own received signal. After these two operations,

129
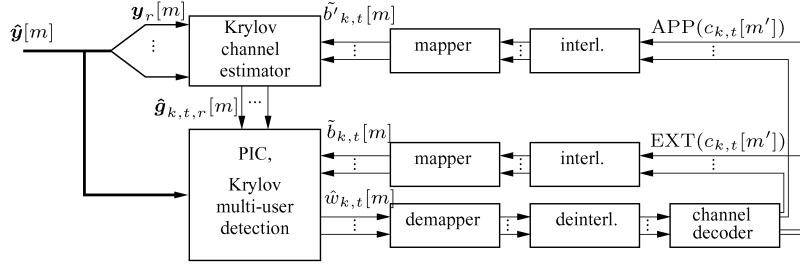
Fig. 2.   Iterative MC-CDMA receiver.

the received signal at receive antenna r for subcarrier q and time instant m is given by

$$y_r[m,q] = \sum_{k=1}^{K}\sum_{t=1}^{N_T} g_{(k,t),r}[m,q]d_{(k,t)}[m,q] + z_r[m,q] \quad (10)$$

where $d_{(k,t)}[m,q]$ is the qth element of $\boldsymbol{d}_{(k,t)}[m]$ defined in (9) and complex additive white Gaussian noise with zero mean and covariance σ_z^2 is denoted by $z_r[m,q]$. The time-varying frequency response between transmit antenna (k,t) and receive antenna r for discrete time-index m and subcarrier q is denoted by $g_{(k,t),r}[m,q]$, for $q \in \{0, \ldots, N-1\}$, $m \in \{0, \ldots, M-1\}$.

In vector notation, (10) becomes

$$\boldsymbol{y}_r[m] = \sum_{k=1}^{K}\sum_{t=1}^{N_T} \mathrm{diag}\left(\boldsymbol{g}_{(k,t),r}[m]\right)$$
$$\times \left(\boldsymbol{s}_{(k,t)}b_{(k,t)}[m] + \boldsymbol{p}_{(k,t)}[m]\right) + \boldsymbol{z}_r[m] \quad (11)$$

where $\boldsymbol{z}_r[m] = [z_r[m,0], \ldots, z_r[m,N-1]]^{\mathrm{T}}$ and $\boldsymbol{y}_r[m] = [y_r[m,0], \ldots, y_r[m,N-1]]^{\mathrm{T}}$.

All time-varying channels $\boldsymbol{g}_{(k,t),r}$ are assumed uncorrelated. Hence, receive antenna r can perform channel estimation independently from the other receive antennas without loss of information. We define $\hat{\boldsymbol{g}}_{(k,t),r}[m]$ as the channel estimate at discrete time m of the time-varying channel $\boldsymbol{g}_{(k,t),r}$ and the effective spreading sequence for transmit antenna (k,t) at time m as

$$\tilde{\boldsymbol{s}}_{(k,t),r}[m] = \mathrm{diag}\left(\hat{\boldsymbol{g}}_{(k,t),r}[m]\right)\boldsymbol{s}_{(k,t)} \in \mathbb{C}^N. \quad (12)$$

Unless necessary, we will omit the time-index m for clarity sake. The time-varying effective spreading matrix containing the KN_T spreading sequences at receive antenna r is given by

$$\tilde{\boldsymbol{S}}_r = [\underbrace{\tilde{\boldsymbol{s}}_{(1,1),r}, \ldots, \tilde{\boldsymbol{s}}_{(1,N_T),r}}_{\text{user } 1}, \ldots, \tilde{\boldsymbol{s}}_{(k,t),r}, \ldots,$$
$$\underbrace{\tilde{\boldsymbol{s}}_{(K,1),r}, \ldots, \tilde{\boldsymbol{s}}_{(K,N_T),r}}_{\text{user } K}]. \quad (13)$$

Using these definitions the signal received at antenna r given in (11) writes for $m \notin \mathcal{P}$

$$\boldsymbol{y}_r = \tilde{\boldsymbol{S}}_r \boldsymbol{b} + \boldsymbol{z}_r \quad (14)$$

where $\boldsymbol{b}$ contains the data symbols for the KN_T virtual users. To take maximal advantage of the multiantenna structure of the

receiver we perform joint antenna detection [14], [19]. Here all N_R received signals are processed jointly. We define

$$\hat{\boldsymbol{y}} = [\boldsymbol{y}_1^{\mathrm{T}}, \ldots, \boldsymbol{y}_{N_R}^{\mathrm{T}}]^{\mathrm{T}} \in \mathbb{C}^{NN_R} \quad (15)$$

containing the N_R received vectors. Similarly, we define the effective spreading matrix

$$\hat{\boldsymbol{S}} = [\tilde{\boldsymbol{S}}_1^{\mathrm{T}}, \ldots, \tilde{\boldsymbol{S}}_{N_R}^{\mathrm{T}}]^{\mathrm{T}} \in \mathbb{C}^{NN_R \times KN_T}. \quad (16)$$

The column $N_T(k-1)+t$ of $\hat{\boldsymbol{S}}$, denoted through $\hat{\boldsymbol{s}}_{(k,t)}$, corresponds to the joint effective spreading sequence of user (k,t) and contains the N_R effective spreading sequences of this user

$$\hat{\boldsymbol{s}}_{(k,t)} = [\tilde{\boldsymbol{s}}_{(k,t),1}^{\mathrm{T}}, \ldots, \tilde{\boldsymbol{s}}_{(k,t),N_R}^{\mathrm{T}}]^{\mathrm{T}}. \quad (17)$$

Similarly, we also define the noise vector with covariance matrix $\sigma_z^2 \boldsymbol{I}_{NN_R}$

$$\hat{\boldsymbol{z}} = [\boldsymbol{z}_1^{\mathrm{T}}, \ldots, \boldsymbol{z}_{N_R}^{\mathrm{T}}]^{\mathrm{T}} \in \mathbb{C}^{NN_R}. \quad (18)$$

Using these notations, the joint received vector can be written as

$$\hat{\boldsymbol{y}} = \hat{\boldsymbol{S}}\boldsymbol{b} + \hat{\boldsymbol{z}}. \quad (19)$$

IV. Low Complexity Implementation of the Receiver

The optimal maximum *a posteriori* (MAP) detector [20] for (14) or (19) is prohibitively complex. The MAP detector can be approximated using an iterative linear receiver with parallel interference cancelation (PIC). We perform PIC using the soft symbol estimates $\tilde{b}_{(k,t)}$. These are computed from the extrinsic probabilities supplied by the decoding stage (see Fig. 2)

$$\tilde{b}_{(k,t)}[m] = \frac{1}{\sqrt{2}}\left(2\mathrm{EXT}\left(c_{(k,t)}[2m]\right) - 1\right)$$
$$+ \mathrm{j}\frac{1}{\sqrt{2}}\left(2\mathrm{EXT}\left(c_{(k,t)}[2m+1]\right) - 1\right). \quad (20)$$

We define the error covariance matrix of the soft symbols $\tilde{\boldsymbol{b}}[m] = [\tilde{b}_{(1,1)}[m], \ldots, \tilde{b}_{(k,t)}[m], \ldots, \tilde{b}_{(K,N_T)}[m]]^{\mathrm{T}}$

$$\boldsymbol{V} = \mathsf{E}\left\{(\boldsymbol{b} - \tilde{\boldsymbol{b}})(\boldsymbol{b} - \tilde{\boldsymbol{b}})^{\mathrm{H}}\right\} \quad (21)$$

130

with constant diagonal elements $[\boldsymbol{V}]_{k,t} = \mathsf{E}\{1 - |\tilde{b}_{(k,t)}|^2\}$. The elements of $\boldsymbol{b}$ and $\tilde{\boldsymbol{b}}$ are supposed to be independent and the off diagonal elements of $\boldsymbol{V}$ are assumed to be zero.

The goal of this paper is to combine the Krylov subspace method with an appropriate iterative receiver structure to minimize the computational complexity. More details follow in Section IV-A for time-varying channel estimation and in Sections IV-B and IV-C for MU-MIMO detection.

A. Iterative Time-Varying Channel Estimation

The performance of the iterative receiver depends on the channel estimates for the time-varying frequency response $\boldsymbol{g}_{(k,t),r}[m]$ since the effective spreading sequence $\tilde{\boldsymbol{s}}_{(k,t),r}$ directly depends on the actual channel realization.

The maximum variation in time of the wireless channel is upper bounded by the maximum normalized one-sided Doppler bandwidth

$$\nu_{\mathrm{Dmax}} = \frac{v_{\max} f_C}{c_0} T_{\mathrm{S}} \qquad (22)$$

where $v_{\max}$ is the maximum (supported) velocity, T_{S} is the OFDM symbol duration, f_C is the carrier frequency and c_0 the speed of light. Time-limited snapshots of the bandlimited fading process span a subspace with very small dimensionality. The same subspace is spanned by discrete prolate spheroidal (DPS) sequences [21]. The DPS sequences $\{u_i[m]\}$ are defined as [22]

$$\lambda_i u_i[m] = \sum_{\ell=0}^{M-1} \frac{\sin(2\pi\nu_{\mathrm{Dmax}}(\ell-m))}{\pi(\ell-m)} u_i[\ell]. \qquad (23)$$

The sequences $\{u_i[m]\}$ are doubly orthogonal over the infinite set $\{-\infty,\dots,\infty\}$ and the finite set $\mathcal{I}_M = \{0,\dots,M-1\}$, bandlimited by ν_{Dmax} and maximally energy concentrated on $\mathcal{I}_M$.

We are interested in describing the time-varying frequency selective channel $\boldsymbol{g}_{r,(k,t)}$ for the duration of a single data block $\mathcal{I}_M$. For $m \in \mathcal{I}_M$, we model the time-varying channel $\boldsymbol{g}_{r,(k,t)}[m]$ using the Slepian basis expansion [21]. The Slepian basis functions $\boldsymbol{u}_i = [u_i[0],\dots,u_i[M-1]]^{\mathrm{T}}$ for $i \in \{0,\dots,D-1\}$ are the time-limited DPS sequences. The eigenvalue λ_i are ordered such that $\lambda_1 > \lambda_2 \dots > \lambda_M$.

The time-varying channel $\boldsymbol{g}_{r,(k,t)}[m] \in \mathbb{C}^N$ is projected onto the subspace spanned by the first D Slepian sequences and is approximated as

$$g_{(k,t),r}[m,q] \approx \tilde{g}_{(k,t),r}[m,q] = \sum_{i=0}^{D-1} u_i[m]\psi_{(k,t),r}[i,q] \qquad (24)$$

for $m \in \mathcal{I}_M$ and $q \in \{0,\dots,N-1\}$. The dimension D of this basis expansion fulfills $\lceil 2\nu_{\mathrm{Dmax}}M \rceil + 1 \leq D \ll M - 1$. For practical mobile communication systems, $D \leq 5$ for $M = 256$, see [21]. Substituting the basis expansion (24) for the time-varying subcarrier coefficients $g_{(k,t),r}[m,q]$ into the system model (10) we obtain

$$y_r[m,q] = \sum_{k=1}^{K}\sum_{t=1}^{N_T}\sum_{i=0}^{D-1} u_i[m]\psi_{(k,t),r}[i,q]d_{(k,t)}[m,q] + z_r[m,q] \qquad (25)$$

where $d_{(k,t)}[m,q]$ are the elements of $\boldsymbol{d}_{(k,t)}[m]$ defined in (9).

For channel estimation, J pilot symbols in (9) are known. The remaining $M - J$ symbols are not known. We replace them by soft symbols that are calculated from the *a posteriori* probabilities (APP) obtained in the previous iteration from the BCJR decoder output. The soft symbols are computed as

$$\tilde{b}'_{(k,t)}[m] = \frac{1}{\sqrt{2}}\left(2\mathrm{APP}\left(c_{(k,t)}[2m]\right) - 1\right)$$
$$+ \mathrm{j}\frac{1}{\sqrt{2}}\left(2\mathrm{APP}\left(c_{(k,t)}[2m+1]\right) - 1\right). \qquad (26)$$

This enables us to obtain refined channel estimates if the soft symbols get more reliable from iteration to iteration.

The KN_TN_R channels are assumed uncorrelated, thus channel estimation can be performed for every receive antenna independently, without loss of information. For clarity, we drop the subscript r in the following.

At each receive antenna, the subcarrier coefficients $\psi_{(k,t)}[i,q]$ can be obtained jointly for all KN_T virtual users but individually for every subcarrier q. We define the vectors

$$\boldsymbol{\psi}_{q,d} = [\psi_{(1,1)}[d,q],\dots,\psi_{(1,N_T)}[d,q],\dots,$$
$$\psi_{(K,1)}[d,q],\dots,\psi_{(K,N_T)}[d,q]]^{\mathrm{T}} \in \mathbb{C}^{KN_T} \qquad (27)$$

for $d \in \{0,\dots,D-1\}$ and

$$\boldsymbol{\phi}_q = \left[\boldsymbol{\psi}_{q,0}^{\mathrm{T}},\dots,\boldsymbol{\psi}_{q,D-1}^{\mathrm{T}}\right]^{\mathrm{T}} \in \mathbb{C}^{KN_TD} \qquad (28)$$

containing the basis expansion coefficients of all KN_T virtual users for subcarrier q. The received symbol sequence of each single data block on subcarrier q is given by

$$\boldsymbol{y}_q = [y[0,q],\dots,y[M-1,q]]^{\mathrm{T}} \in \mathbb{C}^M. \qquad (29)$$

Using these definitions we write

$$\boldsymbol{y}_q = \tilde{\boldsymbol{\mathcal{D}}}_q\boldsymbol{\phi}_q + \boldsymbol{z}_q \qquad (30)$$

where

$$\tilde{\boldsymbol{\mathcal{D}}}_q = \left[\mathrm{diag}(\boldsymbol{u}_0)\tilde{\boldsymbol{D}}_q,\dots,\mathrm{diag}(\boldsymbol{u}_{D-1})\tilde{\boldsymbol{D}}_q\right] \in \mathbb{C}^{M\times KN_TD}. \qquad (31)$$

The matrix $\tilde{\boldsymbol{D}}_q \in \mathbb{C}^{M\times KN_T}$ contains all the transmitted symbols at all time instants $m \in \mathcal{I}_M$ on subcarrier q

$$\tilde{\boldsymbol{D}}_q = \begin{bmatrix} \tilde{d}'_{(1,1)}[0,q] & \dots & \tilde{d}'_{(K,N_T)}[0,q] \\ \vdots & \ddots & \vdots \\ \tilde{d}'_{(1,1)}[M-1,q] & \dots & \tilde{d}'_{(K,N_T)}[M-1,q] \end{bmatrix} \qquad (32)$$

Here, $\tilde{d}'_{(k,t)}[m,q] = s_{(k,t)}[q]\tilde{b}'_{(k,t)}[m] + p_{(k,t)}[m,q]$ are computed using the APP provided by the decoding stage (26).

The LMMSE estimator can be expressed as [1]–[3]

$$\hat{\boldsymbol{\phi}}_q = \left(\tilde{\boldsymbol{\mathcal{D}}}_q^{\mathrm{H}}\boldsymbol{\Delta}^{-1}\tilde{\boldsymbol{\mathcal{D}}}_q + \boldsymbol{\mathcal{C}}_\phi^{-1}\right)^{-1}\tilde{\boldsymbol{\mathcal{D}}}_q^{\mathrm{H}}\boldsymbol{\Delta}^{-1}\boldsymbol{y}_q. \qquad (33)$$

where $\boldsymbol{\Delta} \triangleq \boldsymbol{\Lambda} + \sigma_z^2\boldsymbol{I}_M \in \mathbb{C}^{M\times M}$ and the elements of the diagonal matrix $\boldsymbol{\Lambda} \in \mathbb{C}^{M\times M}$ are defined as

$$\boldsymbol{\Lambda}_{mm} = \frac{1}{\nu_{\mathrm{Dmax}}}\sum_{k=1}^{K}\sum_{t=1}^{N_T}\sum_{i=0}^{D-1}\frac{1}{N}\lambda_i u_i^2[m]\left(1 - \left|\tilde{b}'_{(k,t)}[m]\right|^2\right). \qquad (34)$$

The diagonal covariance matrix $\boldsymbol{\mathcal{C}}_\phi$ for $\boldsymbol{\phi_q}$ is given by

$$\boldsymbol{\mathcal{C}}_\phi = \frac{1}{2\nu_{\mathrm{Dmax}}}\mathrm{diag}\left([\lambda_0,\dots,\lambda_{D-1}]\right) \otimes \boldsymbol{I}_{KN_T} \qquad (35)$$

131

where $\otimes$ denotes the Kronecker matrix product. We note that $\boldsymbol{\mathcal{C}}_\phi$ does not depend on the subcarrier q.

After estimating $\boldsymbol{\phi}_q$ and using (27) and (28), an estimate for the time-varying frequency response is given by

$$\hat{g}'_{(k,t)}[m, q] = \sum_{i=0}^{D-1} u_i[m]\hat{\psi}_{(k,t)}[i, q]. \tag{36}$$

Further noise suppression is achieved if we exploit the correlation between the subcarriers

$$\hat{\boldsymbol{g}}_{(k,t)}[m] = \boldsymbol{F}_{N \times L} \boldsymbol{F}^{\mathrm{H}}_{N \times L} \hat{\boldsymbol{g}}'_{(k,t)}[m], \tag{37}$$

where $[\boldsymbol{F}_{N \times L}]_{i,\ell} = 1/\sqrt{N}\mathrm{e}^{-\mathrm{j}2\pi i\ell/N}$ for $(i, \ell) \in \{0, \dots, N-1\} \times \{0, \dots, L-1\}$.

For the projection (37), a different set of DPS sequences could be used as well in the frequency domain [23]. However, using DPS sequences in the frequency domain leads to a small reduction in BER only. Hence, we choose the low complexity DFT implementation.

Given $\boldsymbol{D}_1 = \boldsymbol{\mathcal{C}}_\phi$, $\boldsymbol{D}_2 = \boldsymbol{\Delta}^{-1}$, $\boldsymbol{M} = \tilde{\boldsymbol{\mathcal{D}}}^{\mathrm{H}}_q$, $\boldsymbol{v} = \boldsymbol{\Delta}^{-1}\boldsymbol{y}$, $a = KN_T D$ and $b = M$, we can use the model in Section II. With the parameters used in our simulations, $b \leq a$. Here the approximation is computed individually for each subcarrier q but jointly for all virtual users (k, t). We are able to use the results (5) for the computational complexity. Channel estimation is done at each receive antenna, thus a factor N_R appears, leading to the expressions of the complexity per subcarrier

$$C_{\mathrm{LMMSE}} \approx 8N_R M^2 \left(\frac{M}{3} + KN_T D \right)$$
$$C_{\mathrm{K}} \approx 8MKN_T DN_R(2S + 3). \tag{38}$$

The ratio $\gamma = C_{\mathrm{K}}/C_{\mathrm{LMMSE}}$ is of order $\mathcal{O}(2(S + 3)/M)$. Depending on the Krylov subspace dimension S, considerable computational complexity reduction can be achieved.

B. PIC in Chip Space

In this section, we briefly recall iterative multiuser detection based on PIC in chip space [2], [19] and describe its implementation using the Krylov subspace method. After parallel interference cancelation for user (k, t), the received signal (19) becomes

$$\breve{\boldsymbol{y}}_{(k,t)} = \hat{\boldsymbol{y}} - \hat{\boldsymbol{S}}\tilde{\boldsymbol{b}} + \hat{\boldsymbol{s}}_{(k,t)}\tilde{b}_{(k,t)}$$
$$= \hat{\boldsymbol{S}}(\boldsymbol{b} - \tilde{\boldsymbol{b}}) + \hat{\boldsymbol{s}}_{(k,t)}\tilde{b}_{(k,t)} + \hat{\boldsymbol{z}}. \tag{39}$$

The corresponding unbiased LMMSE filter [17] is

$$\hat{\boldsymbol{f}}^{\mathrm{H}}_{(k,t)} = \frac{\hat{\boldsymbol{s}}^{\mathrm{H}}_{(k,t)} \left(\sigma_z^2 \boldsymbol{I}_{NN_R} + \hat{\boldsymbol{S}}\boldsymbol{V}\hat{\boldsymbol{S}}^{\mathrm{H}} \right)^{-1}}{\hat{\boldsymbol{s}}^{\mathrm{H}}_{(k,t)} \left(\sigma_z^2 \boldsymbol{I}_{NN_R} + \hat{\boldsymbol{S}}\boldsymbol{V}\hat{\boldsymbol{S}}^{\mathrm{H}} \right)^{-1} \hat{\boldsymbol{s}}_{(k,t)}} \tag{40}$$

and the estimate of $b_{(k,t)}$ is given by $\hat{w}_{(k,t)} = \hat{\boldsymbol{f}}^{\mathrm{H}}_{(k,t)}\breve{\boldsymbol{y}}_{(k,t)}$. These $KN_T M$ estimates are then demapped, deinterleaved and decoded using a BCJR decoder [12].

Given $\boldsymbol{D}_1 = \sigma_z^2 \boldsymbol{I}_{NN_R}$, $\boldsymbol{D}_2 = \boldsymbol{V}$, $\boldsymbol{M} = \hat{\boldsymbol{S}}$, $\boldsymbol{v} = \boldsymbol{e}_{(k,t)}$, $a = NN_R$ and $b = KN_T$, we can use the model in Section II

to obtain expressions for the computational complexity. We assume a non overloaded system, thus $b \leq a$. In this situation, each virtual user (k, t) requires its own filter, while the KN_T filters (40) have a common matrix inverse. However, an approximation algorithm such as the Krylov subspace method has to be performed *per (virtual) user*. This adds a multiplicative factor KN_T in the global computational complexity using the Krylov subspace method, leading to

$$C_{\mathrm{LMMSE}} \approx 8(KN_T)^2 \left(NN_R + \frac{KN_T}{3} \right)$$
$$C_{\mathrm{K}} \approx 8NN_R(KN_T)^2(2S + 3). \tag{41}$$

For a nonoverloaded system (i.e., $KN_T \leq NN_R$), the ratio

$$\gamma = \frac{C_{\mathrm{K}}}{C_{\mathrm{LMMSE}}} = \frac{2S + 3}{1 + \frac{KN_T}{3NN_R}} \tag{42}$$

satisfies $3/4(2S+3) \leq \gamma \leq 2S+3$. Thus, γ is of order $\mathcal{O}(2S+3)$. The complexity reduction expected by using the Krylov subspace method is neutralized by the multiplicative factor KN_T and no computational complexity is achieved. However parallelization of the computations in KN_T branches is possible [19], allowing dividing latency time by a factor $KN_T/(2S+3)$.

C. PIC in User Space

We want to define an LMMSE filter that allows joint detection of all users using only one filter in order to solve the complexity problem mentioned above in Section IV-B.

We apply a matched filter on the received signal (19), without loss of information [20]

$$\boldsymbol{x} = \hat{\boldsymbol{S}}^{\mathrm{H}}\hat{\boldsymbol{y}} = \hat{\boldsymbol{S}}^{\mathrm{H}}\hat{\boldsymbol{S}}\boldsymbol{b} + \hat{\boldsymbol{S}}^{\mathrm{H}}\hat{\boldsymbol{z}}. \tag{43}$$

Performing interference cancelation for user (k, t) in a mathematically exactly identical way as in (39) writes

$$\hat{\boldsymbol{x}}_{(k,t)} = \hat{\boldsymbol{S}}^{\mathrm{H}}\hat{\boldsymbol{y}} - \hat{\boldsymbol{S}}^{\mathrm{H}}\hat{\boldsymbol{S}}\tilde{\boldsymbol{b}} + \hat{\boldsymbol{S}}^{\mathrm{H}}\hat{\boldsymbol{s}}_{(k,t)}\tilde{b}_{(k,t)}. \tag{44}$$

In this equation, the element $\hat{x}_{(k,t)} = \boldsymbol{e}^{\mathrm{T}}_{(k,t)}\hat{\boldsymbol{x}}_{(k,t)}$ contains most information on the specific user (k, t). In all other elements of $\hat{\boldsymbol{x}}_{(k,t)}$, the information about user (k, t) consists of interference which is mostly canceled using PIC. From now on, we set these correcting terms to zero. This way the received signal after PIC for user (k, t) becomes

$$\hat{x}_{(k,t)} = x_{(k,t)} - \hat{\boldsymbol{s}}^{\mathrm{H}}_{(k,t)}\hat{\boldsymbol{S}}\tilde{\boldsymbol{b}} + \hat{\boldsymbol{s}}^{\mathrm{H}}_{(k,t)}\hat{\boldsymbol{s}}_{(k,t)}\tilde{b}_{(k,t)}. \tag{45}$$

Combining these KN_T expressions in a matrix form leads to

$$\hat{\boldsymbol{x}} = \hat{\boldsymbol{S}}^{\mathrm{H}}\hat{\boldsymbol{y}} - (\hat{\boldsymbol{S}}^{\mathrm{H}}\hat{\boldsymbol{S}} - \hat{\boldsymbol{D}})\tilde{\boldsymbol{b}} \tag{46}$$

where $\hat{\boldsymbol{D}} \in \mathbb{C}^{KN_T \times KN_T}$ is defined as the diagonal matrix with diagonal elements of the covariance matrix $\hat{\boldsymbol{R}} = \hat{\boldsymbol{S}}^{\mathrm{H}}\hat{\boldsymbol{S}}$, $[\hat{\boldsymbol{D}}]_{i,i} = [\hat{\boldsymbol{R}}]_{i,i}$ for $i \in \{1, \dots, KN_T\}$.

Performing PIC in user space as described in (46) allows joint detection of all users *using one filter only*. It is expected that some information will get lost since we have set some terms to zero, and as a consequence performance will slightly degrade.

The LMMSE filter for PIC in user space $\hat{F}$ defined by $\hat{F}^{\mathrm{H}} = \arg\min_{F} \mathsf{E}\{\|\boldsymbol{F}^{\mathrm{H}}\hat{x} - \boldsymbol{b}\|^2\}$ can be expressed as

$$\hat{F}^{\mathrm{H}} = (V\hat{R} - V\hat{D} + \hat{D})\left(\hat{R}V\hat{R} + \sigma_z^2\hat{R} + \hat{D}(I_{KN_T} - V)\hat{D}\right)^{-1}. \tag{47}$$

The proof of (47) can be found in Appendix C. Estimates $\hat{w}_{(k,t)}$ of the transmitted symbols $b_{(k,t)}$ are then given in $\hat{w} = \hat{F}^{\mathrm{H}}\hat{x}$. The KN_TM estimates are demapped, deinterleaved and decoded by a BCJR decoder.

Although the LMMSE filter in this case is more complex than the one in chip space, the product $\boldsymbol{F}^{\mathrm{H}}\hat{x}$ needs to be computed only once to detect all users simultaneously. Thus, the use of the Krylov subspace method allows a considerable computational complexity reduction, as we will show now.

Applying the Krylov method to the LMMSE filter (47), we need to define

$$\boldsymbol{A} = \hat{R}V\hat{R} + \sigma_z^2\hat{R} + \hat{D}(I_{KN_T} - V)\hat{D} \in \mathbb{C}^{KN_T \times KN_T},$$
$$\boldsymbol{a} = \hat{x} = \hat{S}^{\mathrm{H}}\hat{y} - (\hat{S}^{\mathrm{H}}\hat{S} - \hat{D})\tilde{b} \in \mathbb{C}^{KN_T}. \tag{48}$$

In this case $\boldsymbol{A}$ slightly differs from the model in Section II. However, replacing the complexity of the computation of $\boldsymbol{a}$, $\boldsymbol{A}$ and the multiplication of $\boldsymbol{A}$ with a vector, the following expressions are obtained

$$C_{\mathrm{LMMSE}} \approx 8(KN_T)^2\left(NN_R + \frac{4}{3}KN_T\right)$$
$$C_{\mathrm{K}} \approx 48KN_TN_RS + 72KNN_RN_T. \tag{49}$$

Note that in this case, no simple expression can be obtained for the filter (47) using a matrix inversion lemma, thus an eventual computational complexity reduction can not be achieved this way. Assuming KN_T and NN_R are of the same order, (49) cannot be simplified in an obvious manner. However the ratio

$$\gamma = \frac{C_{\mathrm{K}}}{C_{\mathrm{LMMSE}}} = \frac{6S + 9}{KN_T\left(1 + \frac{4KN_T}{3NN_R}\right)} \tag{50}$$

is of order $\mathcal{O}((6S + 9)/KN_T)$. Hence, and depending on the Krylov subspace dimension S, considerable computational complexity reduction can be achieved.

V. SIMULATION RESULTS

A. Simulation Setup

We use the same simulation setup as in [1], [2]. The realizations of the time-varying frequency-selective channel $h_{(k,t),r}[n,\ell]$, sampled at the chip rate $1/T_\mathrm{C}$, are generated using an exponentially decaying power delay profile

$$\eta^2[\ell] = e^{-\frac{\ell}{4}}/\sum_{\ell'=0}^{L-1}e^{-\frac{\ell'}{4}} \tag{51}$$

with root mean-square delay spread $T_\mathrm{D} = 4T_\mathrm{C} = 1\,\mu s$ for a chip rate of $1/T_\mathrm{C} = 3.84 \cdot 10^6\,\mathrm{s}^{-1}$ [24]. We assume $L = 15$ resolvable paths. The autocorrelation for every channel tap is given by the classical Clarke spectrum [25]. The system operates at carrier frequency $f_C = 2\,\mathrm{GHz}$ and $K = 32$ users move with velocity $v = 70\,\mathrm{kmh}^{-1}$. These gives a Doppler bandwidth of $B_\mathrm{D} = 126\,\mathrm{Hz}$. We use $N_T = 4$ transmit antennas per user
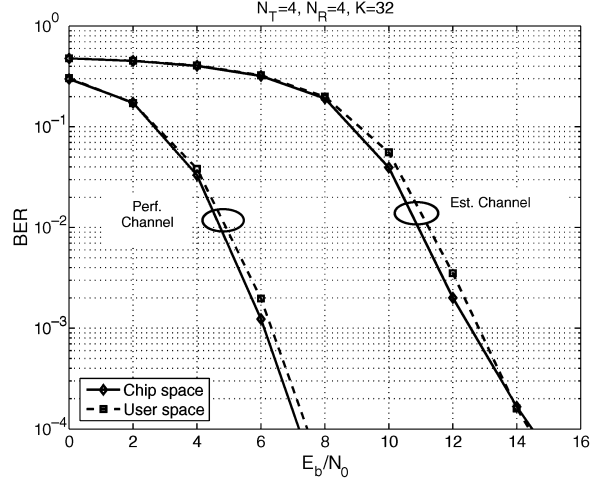
Fig. 3. **Detection Methods Comparison:** BER versus SNR after receiver iteration 4 for $K = 32$ users. We compare the performance of joint antenna detection with PIC in chip space (denoted "Chip") and in user space (denoted "User").

and $N_R = 4$ receive antennas at the base station. The number of subcarriers is $N = 64$ and the OFDM symbol with cyclic prefix has length $P = G + N = 79$. The data block consists of $M = 256$ OFDM symbols including $J = 60$ pilot symbols. The system is designed for $v_{\max} = 102.5\,\mathrm{kmh}^{-1}$ which results in a dimension $D = 3$ for the Slepian basis expansion. The MIMO channel taps are normalized so that

$$\mathsf{E}\left\{\sum_{r=1}^{N_R}\sum_{t=1}^{N_T}\sum_{\ell=0}^{L-1}|h_{(k,t),r}[n,\ell]|^2\right\} = 1 \tag{52}$$

in order to analyze the diversity gain of the receiver only. No antenna gain is present due to this normalization.

For data transmission, a convolutional, nonsystematic, non-recursive, four state, rate $R_C = 1/2$ code with code generators [101] and [111], see [26], denoted in octal notation $(5, 7)_8$, is used. All illustrated results are obtained by averaging over 100 independent channel realizations. The QPSK symbol energy is normalized to 1 and we define the signal-to-noise ratio (SNR)

$$E_b/N_0 = \frac{1}{2R_C\sigma_z^2}\frac{P}{N}\frac{M}{M - J} \tag{53}$$

taking into account the loss due to coding, pilots and cyclic prefix. The noise variance σ_z^2 is assumed to be known at the receiver.

B. Discussion of the Results

Simulations are performed in three steps. Firstly, we compare PIC in chip and in user space in terms of bit-error-rate (BER) versus SNR. All filters are exact LMMSE filters, and the receiver performs four iterations. In Fig. 3, we see that when PIC is performed in the user space, a slight increase in BER can be observed.

Second, we focus on the joint antenna detector with PIC in user space: at this point, the channel is either assumed to be perfectly known or that LMMSE channel estimates are used. The multiuser detector utilizes the Krylov subspace method.

133
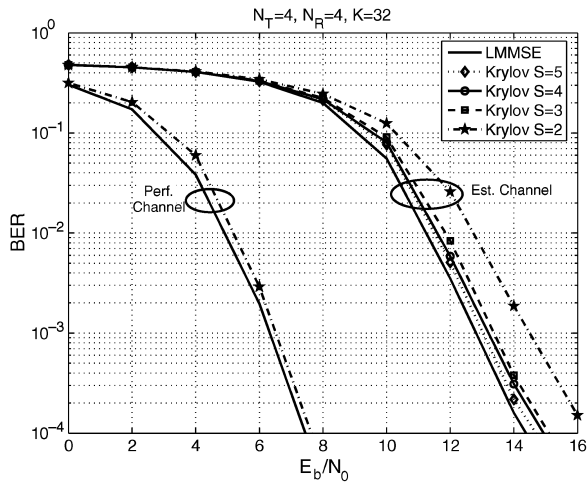
Fig. 4. **Performance of the Krylov subspace method for joint antenna detection with PIC in user space:** BER versus SNR after receiver iteration 4 for $K = 32$ users. The channel is either assumed perfectly known at the receiver or we use LMMSE estimates. We vary the Krylov subspace dimension S for multiuser detection.
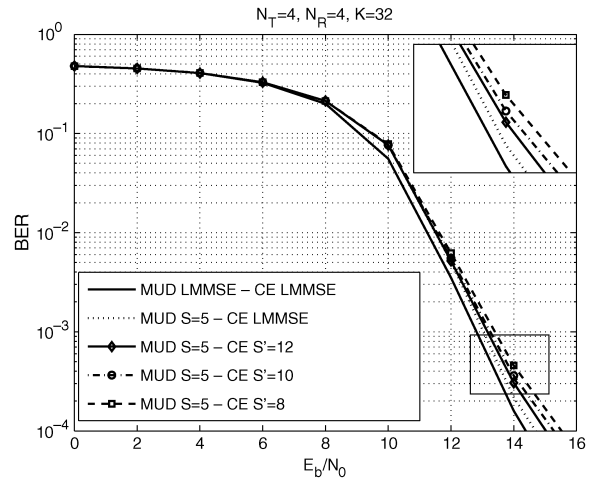
Fig. 5. **Performance of the double Krylov subspace method:** BER versus SNR after receiver iteration 4 for $K = 32$ users. Joint antenna detection is performed after PIC in user space. Both multiuser detection (MUD) and channel estimation (CE) are performed using the Krylov subspace method, and we vary the Krylov subspace dimension S' for channel estimation. For multiuser detection, $S = 5$ is kept constant.

Fig. 4 shows the BER curves for varying Krylov subspace dimension S. As lower bound we plot the BER curve with the exact LMMSE filter for multiuser detection. When the channel is perfectly known, $S = 2$ is sufficient to reach LMMSE multiuser detection performance. When LMMSE channel estimates are used, some loss in performance appears, and a higher subspace dimension is required ($S = 5$ leads to a loss of approximatively 0.25 dB). The expected computational complexity reduction involved allows trading accuracy for efficiency.

At the final step, we keep $S = 5$ constant for joint antenna detection with PIC in user space, and vary the Krylov subspace dimension S' for channel estimation. Results are shown in Fig. 5. Again, a slight loss is inevitable but a trade-off has to be made between computation complexity and performance. A dimension $S' = 12$ is sufficient for channel estimation, introducing a loss of about 0.5 dB compared to the double LMMSE receiver.

Knowing these results, we now compare the computational complexity quantities. We plot the computational complexity in Fig. 6 for $S = 5$, $S' = 12$ as obtained from the simulations. Exact LMMSE computation and its approximation using the Krylov subspace method are compared.

The following observations can be made from these results.

- The use of the Krylov subspace method for channel estimation with $S' = 12$ allows a complexity reduction of about one order of magnitude.
- For PIC in chip space, the use of the Krylov approximation induces an increase in complexity of about one order of magnitude. However, it allows parallelization of the computations in KN_T branches, reducing processing delay with a factor $KN_T/(2S + 3) \approx 19, 7$.
- Using PIC in user space allows joint detection of all users using only one filter. Applying the Krylov subspace method leads to computational complexity reduction by more than one order of magnitude for multiuser detection.
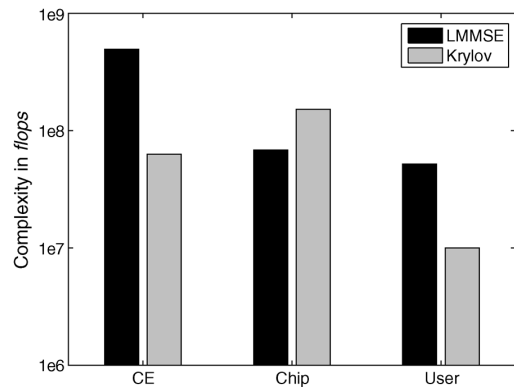
Fig. 6. Computational complexity: We show Krylov (left) and LMMSE (right) implementations, per receiver iteration. Parameters are $S' = 12$ for channel estimation (denoted "CE"), $S = 5$ for multiuser detection using joint antenna detection with PIC in chip space (denoted "Chip") or in user space (denoted "User"). $K = 32$, $N_T = N_R = 4$, $M = 256$, $J = 60$ and $D = 3$.

This complexity reduction comes at the cost of a slight increase of BER (about 0.5 dB).

VI. CONCLUSION

We have presented a low-complexity receiver performing joint antenna detection. Trading accuracy for efficiency, we approximate the two LMMSE filters for joint time-varying channel estimation and multiuser detection using the Krylov subspace method. Combined with interference cancelation in the user space, our new method allows drastic computational complexity reduction of one order of magnitude at the channel estimator as well as at the multiuser detector, compared to a system using exact LMMSE filters. Using the Krylov subspace

TABLE II
GAUSSIAN ELIMINATION FOR $\boldsymbol{A}$ OF SIZE $Q \times Q$

1	for $q = 1 : Q - 1$
2	$\boldsymbol{A}(q+1:Q,q) = \boldsymbol{A}(q+1:Q)/[\boldsymbol{A}]_{q,q}$
3	$\boldsymbol{A}(q+1:Q,q+1:Q) = \quad \boldsymbol{A}(q+1:Q,q+1:Q)$
	$\qquad\qquad -\boldsymbol{A}(q+1:Q)\boldsymbol{A}(Q,q+1)$
4	end

methods implies a slight loss in performance which is negligible compared to the gain in computational complexity.

APPENDIX A
INVERSION OF A COMPLEX MATRIX USING GAUSSIAN ELIMINATION [16]

The Gaussian elimination algorithm [16] to invert a matrix $\boldsymbol{A}$ of size $Q \times Q$ is given in Table II.

For each step q, $Q - q$ multiplications are needed at line 2 and $(Q-q)^2$ multiplications as well as $(Q-q)^2$ additions at line 3. This leads to the total computational complexity in a complex case (recalling one complex multiplication corresponds to 6 flops and one complex addition requires 2 flops):

$$
\begin{aligned}
C_{\mathrm{GE}} &= \sum_{q=1}^{Q-1} \left(2(Q-q) + 8(Q-q)^2 \right) \\
&= \sum_{q=1}^{Q-1} \left(2q + 8q^2 \right) \\
&= \frac{1}{3} Q(Q-1)(8Q-1).
\end{aligned}
\tag{54}
$$

APPENDIX B
MATRIX INVERSION LEMMA FOR EQUATION (1)

Using the matrix inversion lemma in [6], we can write

$$
\begin{aligned}
(\boldsymbol{D}_1 + \boldsymbol{M}\boldsymbol{D}_2\boldsymbol{M}^{\mathrm{H}})^{-1} &= \boldsymbol{D}_1^{-1} - \boldsymbol{D}_1^{-1}\boldsymbol{M} \\
&\times \left(\boldsymbol{D}_2^{-1} + \boldsymbol{M}^{\mathrm{H}}\boldsymbol{D}_1^{-1}\boldsymbol{M} \right)^{-1} \boldsymbol{M}^{\mathrm{H}}\boldsymbol{D}_1^{-1}
\end{aligned}
\tag{55}
$$

leading to

$$
\begin{aligned}
(\boldsymbol{D}_1 &+ \boldsymbol{M}\boldsymbol{D}_2\boldsymbol{M}^{\mathrm{H}})^{-1}\boldsymbol{M} \\
&= \boldsymbol{D}_1^{-1}\boldsymbol{M} - \boldsymbol{D}_1^{-1}\boldsymbol{M} \left(\boldsymbol{D}_2^{-1} + \boldsymbol{M}^{\mathrm{H}}\boldsymbol{D}_1^{-1}\boldsymbol{M} \right)^{-1} \boldsymbol{M}^{\mathrm{H}}\boldsymbol{D}_1^{-1}\boldsymbol{M} \\
&= \boldsymbol{D}_1^{-1}\boldsymbol{M} \left(\boldsymbol{I}_b - \left(\boldsymbol{D}_2^{-1} + \boldsymbol{M}^{\mathrm{H}}\boldsymbol{D}_1^{-1}\boldsymbol{M} \right)^{-1} \boldsymbol{M}^{\mathrm{H}}\boldsymbol{D}_1^{-1}\boldsymbol{M} \right) \\
&= \boldsymbol{D}_1^{-1}\boldsymbol{M} \left(\boldsymbol{D}_2^{-1} + \boldsymbol{M}^{\mathrm{H}}\boldsymbol{D}_1^{-1}\boldsymbol{M} \right)^{-1} \boldsymbol{D}_2^{-1} \\
&= \boldsymbol{D}_1^{-1}\boldsymbol{M} \left(\boldsymbol{I}_b + \boldsymbol{D}_2\boldsymbol{M}^{\mathrm{H}}\boldsymbol{D}_1^{-1}\boldsymbol{M} \right)^{-1}.
\end{aligned}
\tag{56}
$$

Finally, we obtain

$$
(\boldsymbol{D}_1 + \boldsymbol{M}\boldsymbol{D}_2\boldsymbol{M}^{\mathrm{H}})^{-1}\boldsymbol{M} = \boldsymbol{D}_1^{-1}\boldsymbol{M} \left(\boldsymbol{I}_b + \boldsymbol{D}_2\boldsymbol{M}^{\mathrm{H}}\boldsymbol{D}_1^{-1}\boldsymbol{M} \right)^{-1}.
\tag{57}
$$

APPENDIX C
DERIVATION OF THE LMMSE FILTER (47)

We need to determine $\hat{\boldsymbol{F}}$ such as

$$
\hat{\boldsymbol{F}}^{\mathrm{H}} = \arg\min_{\hat{\boldsymbol{F}}} \mathsf{E}\left\{ \|\hat{\boldsymbol{F}}^{\mathrm{H}}\hat{\boldsymbol{x}} - \boldsymbol{b}\|^2 \right\}
\tag{58}
$$

where $\hat{\boldsymbol{x}} = \tilde{\boldsymbol{S}}^{\mathrm{H}}\hat{\boldsymbol{y}} - (\hat{\boldsymbol{S}}^{\mathrm{H}}\hat{\boldsymbol{S}} - \hat{\boldsymbol{D}})\tilde{\boldsymbol{b}}$. We can write

$$
\begin{aligned}
\|\hat{\boldsymbol{F}}^{\mathrm{H}}&\hat{\boldsymbol{x}} - \boldsymbol{b}\|^2 \\
&= \mathrm{tr}\left\{ (\hat{\boldsymbol{F}}^{\mathrm{H}}\hat{\boldsymbol{x}} - \boldsymbol{b})(\hat{\boldsymbol{x}}^{\mathrm{H}}\hat{\boldsymbol{F}} - \boldsymbol{b}^{\mathrm{H}}) \right\} \\
&= \mathrm{tr}\left\{ \underbrace{\hat{\boldsymbol{F}}^{\mathrm{H}}\hat{\boldsymbol{x}}\hat{\boldsymbol{x}}^{\mathrm{H}}\hat{\boldsymbol{F}}}_{(a)} - \underbrace{\boldsymbol{b}\hat{\boldsymbol{x}}^{\mathrm{H}}\hat{\boldsymbol{F}}}_{(b)} - \underbrace{\hat{\boldsymbol{F}}^{\mathrm{H}}\hat{\boldsymbol{x}}\boldsymbol{b}^{\mathrm{H}}}_{(b)^{\mathrm{H}}} + \underbrace{\boldsymbol{b}\boldsymbol{b}^{\mathrm{H}}}_{(c)} \right\}
\end{aligned}
\tag{59}
$$

where $\mathrm{tr}\{\cdot\}$ designs the trace of a matrix. We analyze separately the elements (a), (b), and (c) of the previous equation. We recall that $\mathsf{E}\{\tilde{\boldsymbol{b}}\boldsymbol{b}^{\mathrm{H}}\} = \mathsf{E}\{\boldsymbol{b}\tilde{\boldsymbol{b}}^{\mathrm{H}}\} = \mathsf{E}\{\tilde{\boldsymbol{b}}\tilde{\boldsymbol{b}}^{\mathrm{H}}\} = \boldsymbol{I}_{KN_T} - \boldsymbol{V}$ and $\hat{\boldsymbol{R}} = \hat{\boldsymbol{S}}^{\mathrm{H}}\hat{\boldsymbol{S}}$.

$$
(c) \qquad \mathsf{E}\{\boldsymbol{b}\boldsymbol{b}^{\mathrm{H}}\} = \boldsymbol{I}_{KN_T}
$$

$$
\begin{aligned}
(b) \qquad \boldsymbol{b}\hat{\boldsymbol{x}}^{\mathrm{H}}\hat{\boldsymbol{F}} &= \boldsymbol{b}\left(\hat{\boldsymbol{y}}^{\mathrm{H}}\hat{\boldsymbol{S}} - \tilde{\boldsymbol{b}}^{\mathrm{H}}(\hat{\boldsymbol{R}} - \hat{\boldsymbol{D}}) \right)\hat{\boldsymbol{F}} \\
&= \boldsymbol{b}\left(\boldsymbol{b}^{\mathrm{H}}\hat{\boldsymbol{R}} + \boldsymbol{z}^{\mathrm{H}}\hat{\boldsymbol{S}} - \tilde{\boldsymbol{b}}^{\mathrm{H}}(\hat{\boldsymbol{R}} - \hat{\boldsymbol{D}}) \right)\hat{\boldsymbol{F}} \\
\mathsf{E}\{\boldsymbol{b}\hat{\boldsymbol{x}}^{\mathrm{H}}\hat{\boldsymbol{F}}\} &= (\boldsymbol{V}\hat{\boldsymbol{R}} - \boldsymbol{V}\hat{\boldsymbol{D}} + \hat{\boldsymbol{D}})\hat{\boldsymbol{F}} = \boldsymbol{M}_1\hat{\boldsymbol{F}}
\end{aligned}
$$

$$
\begin{aligned}
(a) \qquad \hat{\boldsymbol{F}}^{\mathrm{H}}\hat{\boldsymbol{x}}\hat{\boldsymbol{x}}^{\mathrm{H}}\hat{\boldsymbol{F}} &= \hat{\boldsymbol{F}}^{\mathrm{H}}\Big(\hat{\boldsymbol{S}}^{\mathrm{H}}\hat{\boldsymbol{y}}\hat{\boldsymbol{y}}^{\mathrm{H}}\hat{\boldsymbol{S}} + (\hat{\boldsymbol{R}} - \hat{\boldsymbol{D}})\tilde{\boldsymbol{b}}\tilde{\boldsymbol{b}}^{\mathrm{H}}(\hat{\boldsymbol{R}} - \hat{\boldsymbol{D}}) \\
&\quad - (\hat{\boldsymbol{R}} - \hat{\boldsymbol{D}})\tilde{\boldsymbol{b}}\hat{\boldsymbol{y}}^{\mathrm{H}}\hat{\boldsymbol{S}} - \hat{\boldsymbol{S}}^{\mathrm{H}}\hat{\boldsymbol{y}}\tilde{\boldsymbol{b}}^{\mathrm{H}}(\hat{\boldsymbol{R}} - \hat{\boldsymbol{D}}) \Big)\hat{\boldsymbol{F}}.
\end{aligned}
\tag{60}
$$

Taking now the expectation of (a), and knowing that

$$
\begin{aligned}
\mathsf{E}\{\hat{\boldsymbol{y}}\hat{\boldsymbol{y}}^{\mathrm{H}}\} &= \mathsf{E}\left\{ (\hat{\boldsymbol{S}}\boldsymbol{b} + \boldsymbol{z})(\boldsymbol{b}^{\mathrm{H}}\hat{\boldsymbol{S}}^{\mathrm{H}} + \boldsymbol{z}^{\mathrm{H}}) \right\} \\
&= \hat{\boldsymbol{S}}\hat{\boldsymbol{S}}^{\mathrm{H}} + \sigma_z^2\boldsymbol{I}_N \\
\mathsf{E}\{\hat{\boldsymbol{y}}\tilde{\boldsymbol{b}}^{\mathrm{H}}\} &= \mathsf{E}\left\{ (\hat{\boldsymbol{S}}\boldsymbol{b} + \boldsymbol{z})\tilde{\boldsymbol{b}}^{\mathrm{H}} \right\} = \hat{\boldsymbol{S}}\left(\boldsymbol{I}_{KN_T} - \boldsymbol{V} \right)
\end{aligned}
\tag{61}
$$

we obtain

$$
\begin{aligned}
\mathsf{E}\{\hat{\boldsymbol{F}}^{\mathrm{H}}\hat{\boldsymbol{x}}\hat{\boldsymbol{x}}^{\mathrm{H}}\hat{\boldsymbol{F}}\} &= \hat{\boldsymbol{F}}^{\mathrm{H}}\left(\hat{\boldsymbol{R}}\boldsymbol{V}\hat{\boldsymbol{R}} + \sigma_z^2\hat{\boldsymbol{R}} + \hat{\boldsymbol{D}}\left(\boldsymbol{I}_{KN_T} - \boldsymbol{V} \right)\hat{\boldsymbol{D}} \right)\hat{\boldsymbol{F}} \\
&= \hat{\boldsymbol{F}}^{\mathrm{H}}\boldsymbol{M}_2\hat{\boldsymbol{F}}.
\end{aligned}
\tag{62}
$$

Combining (a), (b), and (c), the expectation of (59) becomes

$$
\begin{aligned}
\mathsf{E}\left\{ \|\hat{\boldsymbol{F}}^{\mathrm{H}}\hat{\boldsymbol{x}} - \boldsymbol{b}\|^2 \right\} \\
= \mathrm{tr}\left\{ \boldsymbol{I}_{KN_T} - \hat{\boldsymbol{F}}^{\mathrm{H}}\boldsymbol{M}_1^{\mathrm{H}} - \boldsymbol{M}_1\hat{\boldsymbol{F}} + \hat{\boldsymbol{F}}^{\mathrm{H}}\boldsymbol{M}_2\hat{\boldsymbol{F}} \right\}.
\end{aligned}
\tag{63}
$$

The matrix $\boldsymbol{M}_2$ is hermitian and invertible, thus we can write

$$
\begin{aligned}
\mathsf{E}\left\{ \|\hat{\boldsymbol{F}}^{\mathrm{H}}\hat{\boldsymbol{x}} - \boldsymbol{b}\|^2 \right\} = \mathrm{tr}\Big\{ \boldsymbol{I}_{KN_T} - \boldsymbol{M}_1\boldsymbol{M}_2^{-1}\boldsymbol{M}_1^{\mathrm{H}} \\
+ \left(\hat{\boldsymbol{F}} - \boldsymbol{M}_2^{-1}\boldsymbol{M}_1^{\mathrm{H}} \right)^{\mathrm{H}}\boldsymbol{M}_2\left(\hat{\boldsymbol{F}} - \boldsymbol{M}_2^{-1}\boldsymbol{M}_1^{\mathrm{H}} \right) \Big\}.
\end{aligned}
\tag{64}
$$

This expression is minimized when $\hat{\boldsymbol{F}} - \boldsymbol{M}_2^{-1}\boldsymbol{M}_1^{\mathrm{H}} = \boldsymbol{0}$, leading to $\hat{\boldsymbol{F}} = \boldsymbol{M}_2^{-1}\boldsymbol{M}_1^{\mathrm{H}}$ and

$$
\hat{\boldsymbol{F}}^{\mathrm{H}} = (\boldsymbol{V}\hat{\boldsymbol{R}} - \boldsymbol{V}\hat{\boldsymbol{D}} + \hat{\boldsymbol{D}})\left(\hat{\boldsymbol{R}}\boldsymbol{V}\hat{\boldsymbol{R}} + \sigma_z^2\hat{\boldsymbol{R}} + \hat{\boldsymbol{D}}\left(\boldsymbol{I}_{KN_T} - \boldsymbol{V} \right)\hat{\boldsymbol{D}} \right)^{-1}.
\tag{65}
$$

135

REFERENCES

[1] C. F. Mecklenbräuker, J. Wehinger, T. Zemen, H. Artés, and F. Hlawatsch, "Multiuser MIMO channel equalization," in *Smart Antennas—State-of-the-Art*, ser. EURASIP Book Series on Signal Processing and Communications, T. Kaiser, A. Bourdoux, H. Boche, J. R. Fonollosa, J. B. Andersen, and W. Utschick, Eds. New York: Hindawi, 2006, ch. 1.4, pp. 53–76.

[2] T. Zemen, C. F. Mecklenbräuker, J. Wehinger, and R. R. Müller, "Iterative joint time-variant channel estimation and multi-user detection for MC-CDMA," *IEEE Trans. Wireless Commun.*, vol. 5, no. 6, pp. 1469–1478, Jun. 2006.

[3] T. Zemen, "OFDM multi-user communication over time-variant channels," Ph.D. dissertation, Vienna Univ. of Technology, Vienna, Austria, Jul. 2004.

[4] H. van der Vorst, *Iterative Krylov Methods for Large Linear Systems*. Cambridge, U.K.: Cambridge Univ. Press, 2003.

[5] Y. Saad, *Iterative Methods for Sparse Linear Systems*, 2nd ed. Philadelphia, PA: SIAM, 2003.

[6] T. K. Moon and W. Stirling, *Mathematical Methods and Algorithms*. Englewood Cliffs, NJ: Prentice-Hall, 2000.

[7] T. Kailath and A. H. Sayed, *Fast Reliable Algorithms for Matrices With Structure*. Philadelphia, PA: SIAM, 1999.

[8] B. Kecicioglu and M. Torlak, "Reduced rank beamforming methods for SDMA/OFDM communications," in *Proc. 38th Asilomar Conf. Signals, Systems, Computers*, Jul. 12, 2004, vol. 2, pp. 1973–1977.

[9] I. P. Kirsteins and G. Hongya, "Performance analysis of Krylov space adaptive beamformers," in *Proc. IEEE Workshop Sensor Array Multichannel Signal*, Jul. 12, 2006, vol. 3, pp. 16–20.

[10] L. Cottatellucci, R. Müller, and M. Debbah, "Linear detectors for multiuser systems with correlated spatial diversity," presented at the 14th Eur. Signal Processing Conf. (EUSIPCO), Florence, Italy, Sep. 2006.

[11] G. Dietl and W. Utschick, "Complexity reduction of iterative receivers using low-rank equalization," *IEEE Trans. Signal Process.*, vol. 55, no. 3, pp. 1035–1046, Mar. 2007.

[12] L. R. Bahl, J. Cocke, F. Jelinek, and J. Raviv, "Optimal decoding of linear codes for minimizing symbol error rate," *IEEE Trans. Inf. Theory*, vol. 20, no. 2, pp. 284–287, Mar. 1974.

[13] M. Honig, G. Woodward, and Y. Sun, "Adaptive iterative multiuser decision feedback detection," *IEEE Trans. Wireless Commun.*, vol. 3, no. 2, pp. 477–485, Mar. 2004.

[14] S. Hanly and D. Tse, "Resource pooling and effective bandwidths in CDMA networks with multiuser receivers and spatial diversity," *IEEE Trans. Inf. Theory*, vol. 47, no. 4, pp. 1328–1351, May 2001.

[15] C. Dumard, F. Kaltenberger, and K. Freudenthaler, "Low-cost LMMSE equalizer based on Krylov subspace methods for HSDPA," *IEEE Trans. Wireless Commun.*, vol. 6, no. 5, pp. 1610–1614, May 2007.

[16] G. H. Golub and C. F. V. Loan, *Matrix Computations*, 3rd ed. Baltimore, MD: The Johns Hopkins Univ. Press, 1996.

[17] J. Wehinger, "Iterative multi-user receivers for CDMA Systems," Ph.D. dissertation, Vienna Univ. of Technology, Vienna, Austria, Jul. 2005.

[18] P. W. Wolniansky, G. J. Foschini, G. D. Golden, and R. A. Valenzuela, "V—BLAST: An architecture for achieving very high data rates over rich-scattering wireless channels," presented at the Int. Symp. Signals, Systems, and Electronics (ISSSE), Pisa, Italy, 1998.

[19] C. Dumard and T. Zemen, "Krylov subspace method based low-complexity MIMO multi-user receiver for time-variant channels," presented at the 17th IEEE Int. Symp. Personal, Indoor, Mobile Radio Communication (PIMRC), Helsinki, Finland, Sep. 2006.

[20] S. Verdú, *Multiuser Detection*. New York: Cambridge Univ. Press, 1998.

[21] T. Zemen and C. F. Mecklenbräuker, "Time-variant channel estimation using discrete prolate spheroidal sequences," *IEEE Trans. Signal Process.*, vol. 53, no. 9, pp. 3597–3607, Sep. 2005.

[22] D. Slepian, "Prolate spheroidal wave functions, Fourier analysis, and uncertainty—V: The discrete case," *Bell Syst. Tech. J.*, vol. 57, no. 5, pp. 1371–1430, May–June 1978.

[23] T. Zemen, H. Hofstetter, and G. Steinböck, "Successive Slepian subspace projection in time and frequency for time-variant channel estimation," presented at the 14th IST Mobile Wireless Communication Summit (IST SUMMIT), Dresden, Germany, Jun. 19–22, 2005.

[24] L. M. Correia, *Wireless Flexible Personalised Communications*. New York: Wiley, 2001.

[25] R. H. Clarke, "A statistical theory of mobile-radio reception," *Bell Syst. Tech. J.*, vol. 47, pp. 957–1000, Jul./Aug. 1968.

[26] L. Hanzo, T. H. Liew, and B. L. Yeap, *Turbo Coding, Turbo Equalization and Space-Time Coding for Transmission Over Fading Channels*. New York: Wiley, 2002.

Charlotte Dumard (S'05) was born in Paris, France. She received a double Master's of Science degree from the Royal Institute of Technology (KTH), Stockholm, Sweden, and the École Supérieure d'Électricité (Supélec), Gif-sur-Yvette, France, both in 2002. Since February 2006, she has been working towards the Ph.D. degree at the Vienna University of Technology, Vienna, Austria.

Since September 2004, she has been with the Telecommunications Research Center Vienna (ftw.), working as a Junior Researcher on the project Future Mobile Communications Systems—Mathematical Modeling, Analysis, and Algorithms for Multi Antenna Systems, which is funded by the Vienna Science and Technology Fund (Wiener Wissenschafts-, Forschungs- und Technologiefonds, WWTF). Her research interest are low-complexity transceiver design in time-varying MIMO channels as well as distributed signal processing.

Thomas Zemen (S'03–M'05) was born in Mödling, Austria. He received the Dipl.-Ing. degree (with distinction) in electrical engineering and the doctoral degree (with distinction), both from the Vienna University of Technology, Vienna, Austria, in 1998 and 2004, respectively.

He joined Siemens Austria in 1998, where he worked as a Hardware Engineer and Project Manager for the Radio Communication Devices Department. He engaged in the development of a vehicular GSM telephone system for a German car manufacturer. From October 2001 to September 2003, he was delegated by Siemens Austria as a Researcher to the Mobile Communications Group at the Telecommunications Research Center Vienna (ftw.). Since October 2003, he has been with the Telecommunications Research Center Vienna, working as researcher in the strategic I0 project. His research interests include orthogonal frequency division multiplexing (OFDM), multiuser detection, time-variant channel estimation, iterative MIMO receiver structures, and distributed signal processing. Since May 2005, he has led the project Future Mobile Communications Systems—Mathematical Modeling, Analysis, and Algorithms for Multi Antenna Systems, which is funded by the Vienna Science and Technology Fund (Wiener Wissenschafts-, Forschungs- und Technologiefonds, WWTF). He teaches MIMO Communications as an external Lecturer at the Vienna University of Technology.

SUBSPACE-BASED SPHERE DECODER FOR MC-CDMA IN TIME-VARYING MIMO CHANNELS

Charlotte Dumard and Thomas Zemen [*]

ftw. Forschungzentrum Telekommunikation Wien

Donau-City-Strasse 1/3, A-1220 Vienna, Austria

Email: dumard@ftw.at

ABSTRACT

We focus on sphere decoding for the uplink of a multi-carrier (MC) code division multiple access (CDMA) system based on orthogonal frequency division multiplexing (OFDM). The users move at vehicular speed, hence the multiple-input multiple-output (MIMO) channel from each user to the base-station is time-varying. The receiver at the base-station performs iterative multi-user (MU) detection using parallel interference cancelation followed by a sphere decoder. Such a MU-MIMO detector is less complex and more robust to channel estimation errors than a linear minimum mean square error (LMMSE) filter as was shown by the authors recently.

However, for time-varying channels the complexity of the sphere decoder is still high, due to a QR-factorization for each symbol. In this paper we develop a novel implementation of the sphere decoder to reduce complexity. Time-limited snapshots of a bandlimited fading process span a subspace with very small dimensionality. The same subspace is spanned by prolate spheroidal sequences. Exploiting this specific structure we develop a new sphere decoding algorithm for time-varying channels that achieves considerable computational complexity reduction compared to a classical sphere decoder.

I. INTRODUCTION

We consider the uplink of a multi-carrier (MC) code-division multiple access (CDMA) system based on orthogonal frequency division multiplexing (OFDM) with N subcarriers. Each user $k \in \{1, \ldots, K\}$ has T transmit antennas and the base-station is equipped with R receive antennas. The receiver performs iterative parallel interference cancellation (PIC), channel estimation and multi-user (MU) detection jointly [1]. For multi-user detection a sphere-decoder is employed.

We show in [1] that sphere decoding is more robust to channel estimation errors than a linear minimum mean square error (LMMSE) filter. Furthermore, the computational complexity is reduced as well. However, for time-varying channels the complexity of the sphere decoder is still high since a QR-factorization is needed for each received data symbol.

Contribution of the Paper: We model the time-varying channel using a subspace representation. This model allows developing a novel implementation of the sphere decoder for time-varying channels that exploits the structure of the time-varying channel. Our new algorithm allows considerable computational complexity reduction.

Notation: We denote a column vector by $\boldsymbol{a}$ and its i-th element with $a[i]$. The transpose of a matrix $\boldsymbol{A}$ is given by $\boldsymbol{A}^{\mathrm{T}}$ and its conjugate transpose by $\boldsymbol{A}^{\mathrm{H}}$. A diagonal matrix with elements $a[i]$ is written as $\mathrm{diag}(\boldsymbol{a})$ and the $Q \times Q$ identity matrix as $\boldsymbol{I}_Q$. The norm of $\boldsymbol{a}$ is denoted through $\|\boldsymbol{a}\|$.

Organization of the Paper: We present the signal model in Section II. The time-variant channel model utilizing the subspace structure of a bandlimited fading process is introduced in Section III. Section IV. reviews the sphere decoding algorithm and our new subspace based sphere decoder is presented in Section V. The computational complexity is discussed in Section VI. We conclude the paper in Section VII.

II. SYSTEM MODEL

In [1] we present an iterative MU-MIMO receiver for a MC-CDMA uplink, performing PIC followed by sphere decoding. This paper builds on [1] introducing a novel implementation of the sphere decoder more suitable for time-varying channels.

A. Multi-Antenna Transmitter

Let us consider the transmitter of user $k \in \{1, \ldots, K\}$. We denote its transmit antenna $t \in \{1, \ldots, T\}$ using the indexing (k, t). $(M - J)T$ data symbols are jointly coded, interleaved, mapped to a QPSK constellation and split into T blocks of length $M - J$. Transmit antenna (k, t) sends a block of M OFDM symbols, including J distributed pilot symbols allowing for channel estimation. Data symbol $b_{(k,t)}$ is spread over all N subcarriers using a spreading sequence $\boldsymbol{s}_{(k,t)} \in \mathbb{C}^N$ with independent identically distributed elements from a QPSK constellation. Thus, transmit antenna (k, t) sends the OFDM symbols $\boldsymbol{s}_{(k,t)} b_{(k,t)}[m]$ for $m \notin \mathcal{P}$, where $\mathcal{P} \subset \{0, \ldots, M - 1\}$ is the set of pilot positions in each data block [2].

B. Iterative Multi-Antenna Receiver

The iterative receiver structure is shown in Fig. 1. The receiver is equipped with R antennas. The propagation channel from transmit antenna (k, t) to receive antenna r is characterized by the frequency response $\boldsymbol{g}_{r,(k,t)}[m] \in \mathbb{C}^N$ at time instant m with elements $g_{r,(k,t)}[m, q]$. The index $q \in \{0, \ldots, N - 1\}$ denotes the subcarrier index. The related effective spreading sequence is defined by

$$\tilde{\boldsymbol{s}}_{r,(k,t)} = \mathrm{diag}(\boldsymbol{g}_{r,(k,t)}[m])\boldsymbol{s}_{(k,t)}. \tag{1}$$

In the following, we will omit the time index m unless necessary. The contribution of transmit antenna (k, t) to the signal at receive antenna r is $\tilde{\boldsymbol{s}}_{r,(k,t)} b_{(k,t)}$. At receive antenna r, the signals from all transmit antennas of all users add up

137
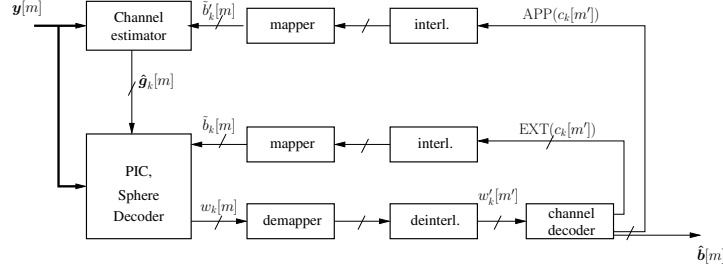
Figure 1: Iterative MC-CDMA receiver.

$$y_r = \sum_{k=1}^{K} \sum_{t=1}^{T} \tilde{s}_{r,(k,t)} b_{(k,t)} + n_r \,, \qquad (2)$$

where n_r is additive white Gaussian noise with zero mean and variance $\sigma_z^2 I_N$. This can be written in matrix notation as

$$y_r = \tilde{S}_r b + n_r \,, \qquad (3)$$

where $\tilde{S}_r = [\tilde{s}_{r,(1,1)}, \ldots, \tilde{s}_{r,(K,T)}] \in \mathbb{C}^{N \times KT}$ is the effective spreading matrix at antenna r and $b = [b_{(1,1)}, \ldots, b_{(K,T)}]^{\mathrm{T}} \in \mathbb{C}^{KT}$ contains all KT transmitted symbols.

Denoting by $y = [y_1^{\mathrm{T}}, \ldots, y_R^{\mathrm{T}}]^{\mathrm{T}}$ the vector containing the R received signals stacked upon each other, we can write

$$y = \tilde{S} b + n \,, \qquad (4)$$

where $\tilde{S} = [\tilde{S}_1^{\mathrm{T}}, \ldots, \tilde{S}_R^{\mathrm{T}}]^{\mathrm{T}} \in \mathbb{C}^{NR \times KT}$ contains all R effective spreading matrices. The complex Gaussian noise vector $n = [n_1^{\mathrm{T}}, \ldots, n_R^{\mathrm{T}}]^{\mathrm{T}}$ has zero-mean and variance $\sigma_z^2 I_{NR}$.

The contribution of user k stemming from symbols $b^{(k)} = [b_{(k,1)}, \ldots, b_{(k,T)}]^{\mathrm{T}}$ is defined as $y^{(k)} = \hat{S}^{(k)} b^{(k)} + n^{(k)}$, where

$$\hat{S}^{(k)} = \begin{bmatrix} \tilde{s}_{1,(k,1)} & \cdots & \tilde{s}_{1,(k,T)} \\ \vdots & \tilde{s}_{r,(k,t)} & \vdots \\ \tilde{s}_{R,(k,1)} & \cdots & \tilde{s}_{R,(k,T)} \end{bmatrix} \in \mathbb{C}^{NR \times T} \qquad (5)$$

contains the effective spreading sequences from all transmit antennas of user k to all receive antennas.

We perform PIC for user k by removing the contribution of users $k' \neq k$ using soft-symbol estimates

$$\tilde{y}^{(k)} = y - \sum_{k' \neq k} \hat{S}^{(k')} \tilde{b}^{(k')} \approx \hat{S}^{(k)} b^{(k)} + n^{(k)} \,. \qquad (6)$$

The soft symbols in $\tilde{b}^{(k')}$ are computed from the extrinsic probabilities supplied by the BCJR decoder [3], see [1]. We apply the sphere decoding algorithm in order to detect $b^{(k)}$, see Sec. IV. and V.

III. TIME-VARYING CHANNEL MODEL

The maximum variation in time of the wireless channel is upper bounded by the maximum normalized one-sided Doppler bandwidth $\nu_{\mathrm{Dmax}} = \frac{v_{\max} f_{\mathrm{C}}}{c_0} T_{\mathrm{S}}$, where $v_{\max}$ is the maximum (supported) velocity, T_{S} is the OFDM symbol duration, f_{C} is the carrier frequency and c_0 the speed of light. Time-limited snapshots of the bandlimited fading process span a subspace with very small dimensionality. The same subspace is spanned by discrete prolate spheroidal (DPS) sequences [2] $\{u_i[m]\}$ defined as [4]

$$\lambda_i u_i[m] = \sum_{l=0}^{M-1} \frac{\sin(2\pi \nu_{\mathrm{Dmax}}(l-m))}{\pi(l-m)} u_i[l] \,. \qquad (7)$$

We are interested in describing the time-varying frequency selective channel $g_{r,(k,t)} \in \mathbb{C}^N$ for the duration of a single data block $\mathcal{I}_M = \{0, \ldots, M-1\}$. For $m \in \mathcal{I}_M$ we write $g_{r,(k,t)}[m]$ as linear superposition of the first D DPS sequences index limited to the time interval $\mathcal{I}_M$,

$$\hat{g}_{r,(k,t)}[m] = \Gamma_{r,(k,t)} f[m] \,, \qquad (8)$$

where $f[m] = [u_1[m], \ldots, u_{D-1}[m]]^{\mathrm{T}} \in \mathbb{C}^D$ for $m \in \mathcal{I}_M$. In practical cases, D is of the order of 3 to 5 [2, 5]. Dedicated pilot symbols together with feedback soft symbols are used to estimate the coefficients in $\Gamma_{r,(k,t)} \in \mathbb{C}^{N \times D}$ as described in [2, 5, 6].

Inserting (8) in (1) we can write

$$\tilde{s}_{r,(k,t)}[m] = \mathrm{diag}(s_{(k,t)}) \Gamma_{r,(k,t)} f[m] \qquad (9)$$

and inserting (9) into (5) we obtain $\hat{S}^{(k)} = \hat{\Gamma}^{(k)} \tilde{F}[m]$, where

$$\hat{\Gamma}^{(k)} = \begin{bmatrix} \mathrm{diag}(s_{(k,1)}) \Gamma_{1,(k,1)} & \cdots & \mathrm{diag}(s_{(k,T)}) \Gamma_{1,(k,T)} \\ \vdots & \ddots & \vdots \\ \mathrm{diag}(s_{(k,1)}) \Gamma_{R,(k,1)} & \cdots & \mathrm{diag}(s_{(k,T)}) \Gamma_{R,(k,T)} \end{bmatrix}$$

and

$$\tilde{F}[m] = \begin{bmatrix} f[m] & 0 & 0 \\ 0 & \ddots & 0 \\ 0 & 0 & f[m] \end{bmatrix} \in \mathbb{C}^{DT \times T} \,. \qquad (10)$$

The received signal of user k after PIC (6) finally becomes

$$\tilde{y}^{(k)}[m] = \hat{\Gamma}^{(k)} \tilde{F}[m] b^{(k)}[m] + n^{(k)}[m] \,. \qquad (11)$$

Note that $\hat{\Gamma}^{(k)}$ is time-invariant but user dependent while $\tilde{F}[m]$ is common to all users but time-varying. This specific structure will be essential for the low complexity sphere decoder which we develop in Section V.

IV. Classical Sphere Decoder

In this section we briefly recall the classical sphere decoding algorithm for a MIMO MC-CDMA system [1]. Dropping the user index k in (6) and assuming identity of the left and rightmost terms we obtain $\tilde{\boldsymbol{y}} = \hat{\boldsymbol{S}}\boldsymbol{b} + \boldsymbol{n}$. A ML detector searches for the vector $\boldsymbol{b}$ in the discrete alphabet $\mathcal{A}^T$ that minimizes the distance $\|\tilde{\boldsymbol{y}} - \hat{\boldsymbol{S}}\boldsymbol{b}\|$, and is defined by

$$\hat{\boldsymbol{b}} = \underset{\boldsymbol{b} \in \mathcal{A}^T}{\operatorname{argmin}}\{\|\tilde{\boldsymbol{y}} - \hat{\boldsymbol{S}}\boldsymbol{b}\|^2\}. \qquad (12)$$

A sphere decoder [7,8] restrains this search to a sphere centered on $\tilde{\boldsymbol{y}}$ with radius ρ, thus focusing on the closest elements only

$$\hat{\boldsymbol{b}} = \underset{\boldsymbol{b} \in \mathcal{A}^T \| \|\tilde{\boldsymbol{y}} - \hat{\boldsymbol{S}}\boldsymbol{b}\|^2 < \rho^2}{\operatorname{argmin}} \{\|\tilde{\boldsymbol{y}} - \hat{\boldsymbol{S}}\boldsymbol{b}\|^2\}. \qquad (13)$$

This corresponds to a ML search under the so-called sphere constraint $\|\tilde{\boldsymbol{y}} - \hat{\boldsymbol{S}}\boldsymbol{b}\|^2 < \rho^2$.

Let us consider the *thin* QR factorization of the matrix $\hat{\boldsymbol{S}}$. We write $\hat{\boldsymbol{S}} = \boldsymbol{QR}$, where $\boldsymbol{Q} \in \mathbb{C}^{NR \times T}$ is a unitary matrix and $\boldsymbol{R} \in \mathbb{C}^{T \times T}$ is upper triangular. This factorization is unique [9]. Matrix $\boldsymbol{Q}$ being unitary, the sphere constraint is equivalent to $\|\boldsymbol{z} - \boldsymbol{Rb}\|^2 < \rho^2$ where $\boldsymbol{z} = \boldsymbol{Q}^H \tilde{\boldsymbol{y}}$. The error vector to be minimized is given by $\boldsymbol{\epsilon} = \boldsymbol{z} - \boldsymbol{Rb}$.

For $t \in \{1, \ldots, T\}$, we define the partial vectors $\boldsymbol{z}^{(t)} = [z[t], \ldots, z[R]]^T$ and $\boldsymbol{b}^{(t)}$ and $\boldsymbol{\epsilon}^{(t)}$ similarly. The partial upper triangular matrix $\boldsymbol{R}^{(t)} \in \mathbb{C}^{(T-t+1) \times (T-t+1)}$ is given by

$$\boldsymbol{R}^{(t)} = \begin{bmatrix} R_{t,t} & \cdots & R_{t,T} \\ 0 & \ddots & \vdots \\ 0 & 0 & R_{T,T} \end{bmatrix}. \qquad (14)$$

Matrix $\boldsymbol{R}$ being upper triangular, $\boldsymbol{\epsilon}^{(t)} = \boldsymbol{z}^{(t)} - \boldsymbol{R}^{(t)}\boldsymbol{b}^{(t)}$ can be expressed using the partial vectors and matrices only. The squared partial distance $d(t)^2 = \|\boldsymbol{\epsilon}^{(t)}\|^2 = \sum_{i=t}^{T} |\epsilon[i]|^2$ is computed for t decreasing using the iterative relation

$$d(t)^2 = d(t+1)^2 + |\epsilon[t]|^2. \qquad (15)$$

As soon as an index t is reached, such that $d(t)^2 > \rho^2$, all $\boldsymbol{b} \in \mathcal{A}^T$ having the partial $\boldsymbol{b}^{(t)} \in \mathcal{A}^{T-t+1}$ are discarded since they lie outside the sphere. The set of remaining candidates (with $d(t) \leq \rho$) at step t is denoted $\mathcal{C}_t$ and depends on the actual realization of $\boldsymbol{b}$, $\hat{\boldsymbol{S}}$ and $\boldsymbol{n}$. The T steps of the classical sphere decoder are summarized in Table 1. Although being a low-complexity implementation of a ML detector, the classical sphere decoder requires a QR factorization at every time index. This is too demanding for time-varying channels. In the next section, we use the model (11) and the time-non-dependency of the matrix $\hat{\boldsymbol{\Gamma}}^{(k)}$ to develop a low-complexity implementation.

V. Subspace-based Sphere Decoder

In this section we exploit the subspace structure of the time-varying channel to reduce the computational complexity of the

step T:	For all $b[T] \in \mathcal{A}$, compute $d(T)^2$ If $d(T)^2 \leq \rho^2$, store $b[T] \in \mathcal{C}_T$
$\vdots$	
step t:	For all $[b[t+1], \ldots, b[T]]^T \in \mathcal{C}_{t+1}$, for all $b[t] \in \mathcal{A}$, compute $d(t)^2$ from $d(t+1)^2$ using (15) or (23) If $d(t)^2 \leq \rho^2$, store $[b[t], \ldots, b[T]]^T \in \mathcal{C}_t$
$\vdots$	
step 1:	For all $[b[2], \ldots, b[T]]^T \in \mathcal{C}_2$, for all $b[1] \in \mathcal{A}$, compute $d(1)^2$ from $d(2)^2$ using (15) or (23) If $d(1)^2 \leq \rho^2$, store $[b[1], \cdots, b[T]]^T \in \mathcal{C}_1$

Table 1: The T steps of the Sphere Decoder

sphere decoder. Let us first recall the received signal after PIC (11), dropping index (k)

$$\tilde{\boldsymbol{y}}[m] = \hat{\boldsymbol{\Gamma}}\tilde{\boldsymbol{F}}[m]\boldsymbol{b}[m] + \boldsymbol{n}[m]. \qquad (16)$$

We consider the *thin* QR factorization [9] of $\hat{\boldsymbol{\Gamma}} = \boldsymbol{QR}$ where $\boldsymbol{Q} \in \mathbb{C}^{NR \times DT}$ is unitary and $\boldsymbol{R} \in \mathbb{C}^{DT \times DT}$ is upper triangular. Multiplying (16) from the left side with $\boldsymbol{Q}^H$ we obtain

$$\boldsymbol{z}[m] = \boldsymbol{Q}^H \tilde{\boldsymbol{y}}[m] = \boldsymbol{R}\tilde{\boldsymbol{F}}[m]\boldsymbol{b}[m] + \boldsymbol{Q}^H \boldsymbol{n}[m]. \qquad (17)$$

We rewrite the ML detector after QR factorization of $\hat{\boldsymbol{\Gamma}}$

$$\hat{\boldsymbol{b}} = \underset{\boldsymbol{b} \in \mathcal{A}^T}{\operatorname{argmin}}\{\|\boldsymbol{z}[m] - \boldsymbol{R}\tilde{\boldsymbol{F}}[m]\boldsymbol{b}\|^2\}. \qquad (18)$$

To make use of the block diagonal structure of $\tilde{\boldsymbol{F}}[m]$ (10), we decompose the matrix $\boldsymbol{R}$ into blocks of size $D \times D$

$$\boldsymbol{R} = \begin{bmatrix} \boldsymbol{\Delta}_{1,1} & \boldsymbol{\Delta}_{1,2} & \cdots & \boldsymbol{\Delta}_{1,T} \\ 0 & \boldsymbol{\Delta}_{2,2} & \cdots & \boldsymbol{\Delta}_{2,T} \\ \vdots & \ddots & \ddots & \vdots \\ 0 & \cdots & 0 & \boldsymbol{\Delta}_{T,T} \end{bmatrix}, \qquad (19)$$

where the matrices $\boldsymbol{\Delta}_{t,t} \in \mathbb{C}^{D \times D}$ are upper triangular and the matrices $\boldsymbol{\Delta}_{t,t'>t} \in \mathbb{C}^{D \times D}$ are full.

The sphere constraint is given by $\|\boldsymbol{z}[m] - \boldsymbol{R}\tilde{\boldsymbol{F}}[m]\boldsymbol{b}\|^2 < \rho^2$. We define the difference vector $\boldsymbol{\epsilon} = \boldsymbol{z}[m] - \boldsymbol{R}\tilde{\boldsymbol{F}}[m]\boldsymbol{b}$. For $t \in \{1, \ldots, T\}$ we write the partial vectors

$$\begin{aligned} \boldsymbol{z}^{(t)} &= [z[D(t-1)+1], \ldots, z[DT]]^T & \in \mathbb{C}^{D(T-t+1)}, \\ \boldsymbol{b}^{(t)} &= [b[t], \ldots, b[T]]^T & \in \mathbb{C}^{T-t+1}, \\ \boldsymbol{\epsilon}^{(t)} &= [\epsilon[D(t-1)+1], \ldots, \epsilon[DT]]^T & \in \mathbb{C}^{D(T-t+1)}, \end{aligned} \qquad (20)$$

and the partial matrices

$$\boldsymbol{R}^{(t)} = \begin{bmatrix} \boldsymbol{\Delta}_{t,t} & \cdots & \boldsymbol{\Delta}_{t,T} \\ 0 & \ddots & \vdots \\ 0 & 0 & \boldsymbol{\Delta}_{T,T} \end{bmatrix} \in \mathbb{C}^{D(T-t+1) \times D(T-t+1)},$$

$$\tilde{\boldsymbol{F}}^{(t)} = \begin{bmatrix} \boldsymbol{f}[m] & 0 & 0 \\ 0 & \ddots & 0 \\ 0 & 0 & \boldsymbol{f}[m] \end{bmatrix} \in \mathbb{C}^{D(T-t+1) \times (T-t+1)}. \qquad (21)$$

We also define $\hat{\boldsymbol{z}}^{(t)} = [z_{D(t-1)+1}, \ldots, z_{Dt}]^{\mathrm{T}} \in \mathbb{C}^D$ and $\hat{\boldsymbol{\Delta}}^{(t)} = [\boldsymbol{\Delta}_{t,t} \cdots \boldsymbol{\Delta}_{t,T}]^{\mathrm{T}} \in \mathbb{C}^{D \times D(T-t+1)}$.

The partial distance $d(t)$ is given by

$$
\begin{aligned}
d(t)^2 &= \|\boldsymbol{\epsilon}^{(t)}\|^2 = \|\boldsymbol{z}^{(t)} - \boldsymbol{R}^{(t)} \tilde{\boldsymbol{F}}^{(t)} \boldsymbol{b}^{(t)}\|^2 \\
&= \sum_{i=t}^{T} \|\hat{\boldsymbol{z}}^{(i)} - \hat{\boldsymbol{\Delta}}^{(i)} \tilde{\boldsymbol{F}}^{(i)} \boldsymbol{b}^{(i)}\|^2
\end{aligned}
\tag{22}
$$

$$
d(t)^2 = d(t+1)^2 + \|\hat{\boldsymbol{z}}^{(t)} - \hat{\boldsymbol{\Delta}}^{(t)} \tilde{\boldsymbol{F}}^{(t)} \boldsymbol{b}^{(t)}\|^2
\tag{23}
$$

Similarly as for the classical sphere decoder, $d(1)^2 = \|\boldsymbol{\epsilon}\|^2$ can be iteratively computed for decreasing t and starting from $d(T)^2 = \|\boldsymbol{\epsilon}^{(T)}\|^2$ using (23). The T steps of the subspace based sphere decoder are the same as for the classical sphere decoder in Table 1 with new definitions of the partial vectors, matrices and distances.

An illustration of the t-th step of the subspace based sphere decoder algorithm is given in (24) and (25).

VI. ON THE COMPUTATIONAL COMPLEXITY

We define a *flop* as a floating point operation (addition, substraction, multiplication, division or square root) in the *real* domain [9]. Thus, one complex multiplication (CM) requires 4 real multiplications and 2 additions, leading to 6 *flop*s. Similarly, one complex addition (CA) requires 2 *flop*s. We recall that q_t denotes the number of candidates in $\mathcal{C}_t$ at step t, both are random variable since they depend on the realization of $\boldsymbol{b}$, $\hat{\boldsymbol{S}}$ and $\boldsymbol{n}$. $Q = |\mathcal{A}|$ is the size of the alphabet.

A. Details of the Operations

According to the algorithm presented in Section V., for a single data block of length $M - J$ we have to perform

- one *thin* QR factorization of size $NR \times DT$, with computational complexity [9]

$$
c_{\mathrm{QR}} = 2DT \left(2(NR)^2 - DNRT + \frac{(DT)^2}{3} \right) \, flops \, ,
$$

- $M - J$ runs of the subspace based sphere decoder (SBSD) with complexity $c_{\mathrm{SBSD}}[m]$, performing the following operations per step t and time instant m:

  - computation of $\boldsymbol{v}^{(t)}[m] = \tilde{\boldsymbol{F}}^{(t)}[m] \boldsymbol{b}^{(t)}$ requiring:
    * $D(T-t)$ CM for all $\boldsymbol{b}^{(t+1)} \in \mathcal{C}_{t+1}$,
    * D CM for all $b_t \in \mathcal{A}$.
  - computation of $\hat{\boldsymbol{\Delta}}^{(t)} \boldsymbol{v}^{(t)}[m]$ requiring:
    * $D^2(T-t) - \frac{D(D-1)}{2}$ CM and $D^2(T-t) - \frac{D(D+1)}{2}$ CA for all $\boldsymbol{b}^{(t+1)} \in \mathcal{C}_{t+1}$,
    * $\frac{D(D+1)}{2}$ CM and $\frac{D(D-1)}{2}$ CA for all $b_t \in \mathcal{A}$.

This leads to the complexity at time instant m

$$
\begin{aligned}
c_{\mathrm{SBSD}}[m] = \; & 2D\left[(T-t)(4D+3) - 2D + 1\right] \sum_{i=1}^{T-1} q_{t+1}[m] \\
& + 4TDQ(D+2) \, flops \, .
\end{aligned}
\tag{26}
$$
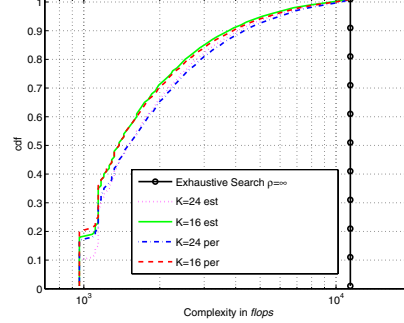
Figure 2: Cumulative distribution function (cdf) of the subspace-based sphere decoder complexity $c_{\mathrm{SBSD}}[m]$ (26). We show both cases of perfect channel knowledge (per) and channel estimation (est).

Using simulations and (26), we obtain an empirical cumulative distribution function (cdf) of the computational complexity, shown in Fig. 2. For simulations, we define the radius ρ as the distance to the zero-forcing solution

$$
\rho^2 = \left\| \tilde{\boldsymbol{y}} - \left(\hat{\boldsymbol{S}}^{\mathrm{H}} \hat{\boldsymbol{S}} \right)^{-1} \hat{\boldsymbol{S}}^{\mathrm{H}} \tilde{\boldsymbol{y}} \right\|^2 .
\tag{27}
$$

This way we avoid the sphere being empty. We also show an upper bound on the figure, which is the complexity using sphere decoding to perform exhaustive search, *i.e.* sphere decoding with infinite radius. In this case, $q_t = Q^{T-t}$ becomes deterministic.

The computational complexity for a single data block is finally given by $C_{\mathrm{SBSD}} = c_{\mathrm{QR}} + \sum_{m \notin \mathcal{P}} c_{\mathrm{SBSD}}[m]$.

B. Classical versus Subspace-Based Sphere Decoding

Mathematically, the subspace based sphere decoder presented here is equivalent to the classical sphere decoder. Using both methods, the ML solution (12) is obtained. We show the bit error rate (BER) versus SNR curves in Fig. 3 for $K \in \{16, 24, 32\}$ users. The detailed simulation setup can be found in [1]. We compare results using perfect channel knowledge and LMMSE channel estimates.

Utilizing the subspace structure of the time-varying channel enables a more efficient implementation. We compare the global computational complexity of both the classical and the subspace based sphere decoder for detection of a block of $M - J$ symbols.

With the classical sphere decoder (CSD), the following operations have to be done <u>per symbol</u> $m \notin \mathcal{P}$

- One *thin* QR factorization of size $NR \times T$,

$$
c_{\mathrm{QR}} = 2T \left(2(NR)^2 - NRT + \frac{T^2}{3} \right) \, flops \, ,
\tag{28}
$$

- one sphere decoder iteration with complexity

$$
c_{\mathrm{CSD}}[m] = 4(2T - 2t + 1) \sum_{t=1}^{T-1} q_{t+1}[m] + 4T(4Q+1) \, flops \, .
$$

$$d(1)^2 = \left\| \begin{bmatrix} z_1 \\ \vdots \\ \boxed{\begin{matrix} z_{D(t-1)+1} \\ \vdots \\ z_{Dt} \end{matrix}} \\ \vdots \\ z_{DT} \end{bmatrix} - \begin{bmatrix} \boldsymbol{\Delta}_{1,1} & \boldsymbol{\Delta}_{1,2} & \cdots & \cdots & \boldsymbol{\Delta}_{1,T} \\ \vdots & \ddots & & & \vdots \\ \mathbf{0} & \ddots & \boxed{\begin{matrix} \boldsymbol{\Delta}_{t,t} & \cdots & \boldsymbol{\Delta}_{t,T} \end{matrix}} \\ \vdots & \ddots & \ddots & \ddots & \vdots \\ \mathbf{0} & \cdots & \cdots & \mathbf{0} & \boldsymbol{\Delta}_{T,T} \end{bmatrix} \begin{bmatrix} \boldsymbol{f}[m] & \mathbf{0} & \cdots & \cdots & \mathbf{0} \\ \vdots & \ddots & & & \vdots \\ \mathbf{0} & & \boxed{\boldsymbol{f}[m]} & \cdots & \mathbf{0} \\ \vdots & & \ddots & \ddots & \vdots \\ \mathbf{0} & \cdots & & \mathbf{0} & \boldsymbol{f}[m] \end{bmatrix} \begin{bmatrix} b_1 \\ \vdots \\ \boxed{\begin{matrix} b_t \\ \vdots \\ b_T \end{matrix}} \end{bmatrix} \right\|^2 \tag{24}$$

$$d(t)^2 = d(t+1)^2 + \left\| \underbrace{\begin{bmatrix} z_{D(t-1)+1} \\ \vdots \\ z_{Dt} \end{bmatrix}}_{\hat{\boldsymbol{z}}^{(t)}} - \underbrace{\begin{bmatrix} \boldsymbol{\Delta}_{t,t} & \cdots & \boldsymbol{\Delta}_{t,T} \end{bmatrix}}_{\hat{\boldsymbol{\Delta}}^{(t)}} \underbrace{\begin{bmatrix} \boldsymbol{f}[m] & \mathbf{0} & \mathbf{0} \\ \mathbf{0} & \ddots & \mathbf{0} \\ \mathbf{0} & \mathbf{0} & \boldsymbol{f}[m] \end{bmatrix}}_{\tilde{\boldsymbol{F}}^{(t)}[m]} \underbrace{\begin{bmatrix} b_t \\ \vdots \\ b_T \end{bmatrix}}_{\boldsymbol{b}^{(t)}} \right\|^2 \tag{25}$$
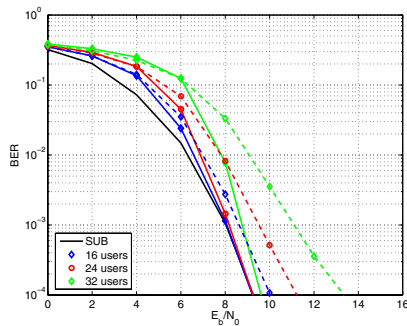

Figure 3: BER vs. SNR for subspace based sphere decoding, with $K \in \{16, 24, 32\}$ users and perfectly known channel (solid lines) or LMMSE channel estimates (dashed lines). We also show the single user bound (SUB).

Figure 4: Cumulative distribution function (cdf) of the random computational complexity for a complete data block using classical (CSD) or subspace-based (SBSD) sphere decoding, as well as the upper bound using exhaustive search. We also show the complexity for LMMSE detection.

Thus the complete complexity over the block of size $M - J$ is
$$C_{CSD} = (M - J) \cdot c_{QR} + \sum_{m \notin \mathcal{P}} c_{CSD}[m].$$

Fig. 4 shows a comparison of the computational complexity cdf using the empirical number of candidates q_t from the simulations. We show the computational complexity for the classical and the subspace based sphere decoder. Results are given using the empirical distribution and the upper bound over the whole set $\mathcal{A}^T$ (with $\rho = \infty$) is shown for comparison. Computational complexity is reduced by more than one order of magnitude when using the subspace based sphere decoder. For comparison we also show the computational complexity of LMMSE detection of a block of length $M - J$ [1].

VII. CONCLUSIONS

We have presented a novel implementation of a sphere decoder. We make use of the basis expansion channel model to develop a low-complexity sphere decoder specially suitable for time-varying channels. This method allows considerable computational complexity reduction.

REFERENCES

[1] C. Dumard and T. Zemen, "Sphere decoder for a MIMO multi-user MC-CDMA uplink in time-varying channels," in *Proc. 17th IEEE International Conference on Communications (ICC)*, Glasgow, Scotland, June 2007.

[2] T. Zemen and C. F. Mecklenbräuker, "Time-variant channel estimation using discrete prolate spheroidal sequences," *IEEE Trans. Signal Processing*, vol. 53, no. 9, pp. 3597–3607, September 2005.

[3] L. R. Bahl, J. Cocke, F. Jelinek, and J. Raviv, "Optimal decoding of linear codes for minimizing symbol error rate," *IEEE Trans. Inform. Theory*, vol. 20, no. 2, pp. 284–287, Mar. 1974.

[4] D. Slepian, "Prolate spheroidal wave functions, Fourier analysis, and uncertainty - V: The discrete case," *The Bell System Technical Journal*, vol. 57, no. 5, pp. 1371–1430, May-June 1978.

[5] T. Zemen, C. F. Mecklenbräuker, J. Wehinger, and R. R. Müller, "Iterative joint time-variant channel estimation and multi-user detection for MC-CDMA," *IEEE Trans. Wireless Commun.*, vol. 5, no. 6, pp. 1469–1478, June 2006.

[6] C. F. Mecklenbräuker, J. Wehinger, T. Zemen, H. Artés, and F. Hlawatsch, "Multiuser MIMO channel equalization," in *Smart Antennas — State-of-the-Art*, ser. EURASIP Book Series on Signal Processing and Communications, T. Kaiser, A. Bourdoux, H. Boche, J. R. Fonollosa, J. B. Andersen, and W. Utschick, Eds. New York (NY), USA: Hindawi, 2006, ch. 1.4, pp. 53–76.

[7] U. Fincke and M. Pohst, "Improved methods for calculating vectors of short length in a lattice, including a complex analysis," *Mathematics of Computation*, vol. 44, no. 169-170, pp. 463–471, April 1985.

[8] A. Burg, M. Borgmann, M. Wenk, M. Zellweger, W. Fichtner, and H. Bölcskei, "VLSI implementation of MIMO detection using the sphere decoding algorithm," *IEEE J. Solid-State Circuits*, vol. 40, no. 7, pp. 1566 – 1577, July 2005.

[9] G. H. Golub and C. F. V. Loan, *Matrix Computations*, 3rd ed. Baltimore (MD), USA: Johns Hopkins University Press, 1996.

SOFT SPHERE DECODER FOR AN ITERATIVE RECEIVER IN TIME-VARYING MIMO CHANNELS

Charlotte Dumard[1], Joakim Jaldén[2] and Thomas Zemen[1]

[1] ftw. Forschungszentrum Telekommunikation Wien, Donau City Str. 1/3, A-1220 Vienna, Austria
{dumard, zemen}@ftw.at

[2] Vienna University of Technology, Guhausstr. 25-29 // 389, A-1040 Vienna, Austria
joakim.jalden@nt.tuwien.ac.at

ABSTRACT

Iterative multi-user detection based on linear minimum mean square error (LMMSE) filtering in time-variant MIMO systems involves high computational complexity. Sphere decoding after an initial interference cancellation step allows for substantial complexity reduction if the sphere decoder exploits the reduced rank time-variant channel subspace. However, a performance loss in terms of bit error rate (BER) versus signal to noise ratio (SNR) is incurred mainly due to the hard decision supplied by the sphere decoder. Building on past work of the authors we demonstrate in this paper that a soft output max-log sphere decoder can exploit the reduced rank time-variant channel subspace as well. We show that the proposed sphere decoder solution provides a computationally more efficient approach, with maintained quality in terms of bit error rate compared to an iterative LMMSE multi-user detector.

1. INTRODUCTION

We focus on the uplink of a MC-CDMA system based on orthogonal frequency division multiplexing (OFDM). The users move at vehicular speed, hence the MIMO channel from each user to the base-station is time-varying. The receiver at the base-station performs iterative multi-user (MU) detection using parallel interference cancellation (PIC) followed by a sphere decoder implemented on a per user basis. In [1], hard outputs of the sphere decoder are used. This method has been shown to be less complex than a linear minimum mean square error filter that would detect all users jointly. However, the hard sphere decoder, assuming perfect PIC, does not take residual interference into account and induces a substantial performance loss.

In this paper we replace the hard sphere decoder by a soft sphere decoder. The computation of log-likelihood ratios (LLR) lead to an increase of the complexity compared to hard sphere decoding. Still, the complexity remains about one order of magnitude below the linear minimum mean square error (LMMSE) filter complexity.

Contribution of the paper: We develop a soft sphere decoder, using the complexity efficient subspace based implementation of a sphere decoder developed in [1] in order to compute the LLR, based on a method presented in [2]. The soft sphere decoder complexity is one order of magnitude higher than for hard sphere decoding and one order of magnitude lower than for LMMSE. The use of soft outputs allows reaching LMMSE performance.

Notation: We denote a column vector with elements a_i by $\boldsymbol{a}$. The transpose of a matrix $\boldsymbol{A}$ is given by $\boldsymbol{A}^{\mathrm{T}}$ and its conjugate transpose by $\boldsymbol{A}^{\mathrm{H}}$. A diagonal matrix with elements a_i is written as $\mathrm{diag}(\boldsymbol{a})$ and the $Q \times Q$ identity matrix as $\boldsymbol{I}_Q$. The norm of $\boldsymbol{a}$ is denoted $\|\boldsymbol{a}\|$.

Organization of the Paper: We describe the system model and iterative receiver with parallel interference cancelation in Sec. 2. The soft sphere decoder is presented in Sec. 3. Simulations results are shown in Sec. 4. Comments on the computational complexity are given in Sec. 5 and conclusions are drawn afterwards.

2. SYSTEM MODEL

In [1] we present a complexity efficient implementation of the sphere decoder in an iterative MU-MIMO receiver for a MC-CDMA uplink, based on the structure of the time-varying channel model. This paper builds on [1], using its implementation of a sphere decoder to compute the LLR with lower complexity.

2.1 Multi-Antenna Transmitter

Let us consider the transmitter of user $k \in \{1, \ldots, K\}$. We denote its transmit antenna $t \in \{1, \ldots, T\}$ by (k,t). $(M - J)T$ data symbols are jointly coded, interleaved, mapped to a QPSK constellation and split into T blocks of length $M - J$. Transmit antenna (k,t) sends a block of M OFDM symbols, including J distributed pilot symbols allowing for channel estimation. Data symbol $b_{(k,t)}[m]$ is spread over all N subcarriers using a spreading sequence $\boldsymbol{s}_{(k,t)} \in \mathbb{C}^N$ with i.i.d. elements from a QPSK constellation. Thus, transmit antenna (k,t) sends the OFDM symbols $\boldsymbol{s}_{(k,t)}b_{(k,t)}[m]$ for $m \notin \mathcal{P}$, where $\mathcal{P}$ is the set of pilot positions in each data block [3].

2.2 Time-Varying Channel Model

The iterative receiver structure is shown in Fig. 1. The receiver is equipped with R antennas. The propagation channel from transmit antenna (k,t) to receive antenna r is characterized by the frequency response $\boldsymbol{g}_{r,(k,t)}[m] \in \mathbb{C}^N$ at time instant m with elements $g_{r,(k,t)}[m,q]$. The index $q \in \{0, \ldots, N-1\}$ denotes the subcarrier index. The related effective spreading sequence is defined by

$$\tilde{\boldsymbol{s}}_{r,(k,t)}[m] = \mathrm{diag}(\boldsymbol{s}_{(k,t)})\boldsymbol{g}_{r,(k,t)}[m]. \tag{1}$$

The maximum variation in time of the wireless channel is upper bounded by the maximum normalized one-sided Doppler bandwidth $\nu_{\mathrm{Dmax}} = \frac{v_{\max}f_{\mathrm{C}}}{c_0}T_{\mathrm{S}}$, where $v_{\max}$ is the maximum (supported) velocity, T_{S} is the OFDM symbol duration, f_{C} is the carrier frequency and c_0 the speed of light. Time-limited snapshots of the bandlimited fading process span a subspace with very small dimensionality. The same subspace is spanned by discrete prolate spheroidal (DPS) sequences [3] $\{u_i[m]\}$ defined as in [4].

We are interested in describing the time-varying frequency selective channel $\boldsymbol{g}_{r,(k,t)} \in \mathbb{C}^N$ for the duration of
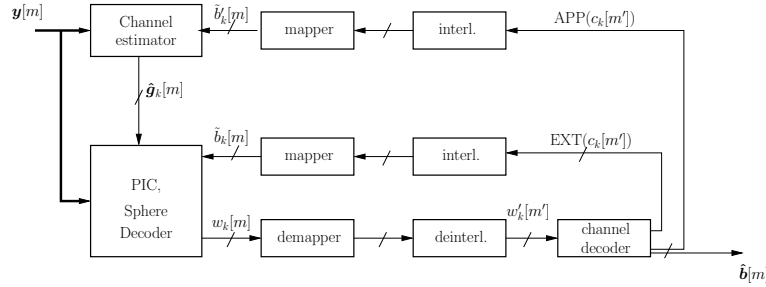
143

Figure 1: Iterative MC-CDMA receiver.

a single data block $\mathcal{I}_M = \{0, \ldots, M-1\}$. For $m \in \mathcal{I}_M$ we write $\boldsymbol{g}_{r,(k,t)}[m]$ as linear superposition of the first D DPS sequences, index limited to the time interval $\mathcal{I}_M$,

$$\tilde{\boldsymbol{g}}_{r,(k,t)}[m] = \boldsymbol{\Gamma}_{r,(k,t)} \boldsymbol{f}[m], \tag{2}$$

where $\boldsymbol{f}[m] = [u_0[m], \ldots, u_{D-1}[m]]^{\mathrm{T}} \in \mathbb{C}^D$ for $m \in \mathcal{I}_M$. In practical cases, D is of the order of 3 to 5 [3]. Dedicated pilot symbols together with feedback soft symbols are used to estimate the coefficients in $\boldsymbol{\Gamma}_{r,(k,t)} \in \mathbb{C}^{N \times D}$, see [3].

Inserting (2) in (1) and after summation of the signals from all transmit antennas of all users, we obtain the signal at antenna r

$$\boldsymbol{y}_r[m] = \sum_{k=1}^{K} \sum_{t=1}^{T} \mathrm{diag}(\boldsymbol{s}_{(k,t)}) \boldsymbol{\Gamma}_{r,(k,t)} \boldsymbol{f}[m] b_{(k,t)}[m] + \boldsymbol{n}_r[m],$$

where $\boldsymbol{n}_r$ is additive white Gaussian noise (AWGN) with zero mean and variance $\sigma^2 \boldsymbol{I}_N$. Denoting by $\boldsymbol{y}[m] = [\boldsymbol{y}_1[m]^{\mathrm{T}}, \ldots, \boldsymbol{y}_R[m]^{\mathrm{T}}]^{\mathrm{T}}$ the stacked vector containing the R received signals, we can write

$$\boldsymbol{y}[m] = \boldsymbol{\Gamma} \boldsymbol{F}[m] \boldsymbol{b}[m] + \boldsymbol{n}[m],$$

where $\boldsymbol{\Gamma} = [\boldsymbol{\Gamma}_1 \cdots \boldsymbol{\Gamma}_K]$ and

$$\boldsymbol{\Gamma}_k = \begin{bmatrix} \mathrm{diag}(\boldsymbol{s}_{(k,1)})\boldsymbol{\Gamma}_{1,(k,1)} & \cdots & \mathrm{diag}(\boldsymbol{s}_{(k,T)})\boldsymbol{\Gamma}_{1,(k,T)} \\ \vdots & \ddots & \vdots \\ \mathrm{diag}(\boldsymbol{s}_{(k,1)})\boldsymbol{\Gamma}_{R,(k,1)} & \cdots & \mathrm{diag}(\boldsymbol{s}_{(k,T)})\boldsymbol{\Gamma}_{R,(k,T)} \end{bmatrix}$$

are time-independent. The matrix

$$\boldsymbol{F}[m] = \begin{bmatrix} \boldsymbol{f}[m] & \boldsymbol{0} & \boldsymbol{0} \\ \boldsymbol{0} & \ddots & \boldsymbol{0} \\ \boldsymbol{0} & \boldsymbol{0} & \boldsymbol{f}[m] \end{bmatrix} \in \mathbb{R}^{DKT \times KT},$$

contains the time-varying basis expansion, $\boldsymbol{b}[m] = [b_{(1,1)}[m], \ldots, b_{(K,T)}[m]]^{\mathrm{T}} \in \mathbb{C}^{KT}$ contains all KT transmitted symbols and $\boldsymbol{n}$ is AWGN with zero mean and variance $\sigma^2 \boldsymbol{I}_{NR}$.

The contribution of user k stemming from symbols $\boldsymbol{b}_k[m] = [b_{(k,1)}[m], \ldots, b_{(k,T)}[m]]^{\mathrm{T}}$ is defined as

$$\boldsymbol{y}_k[m] = \boldsymbol{\Gamma}_k \boldsymbol{F}_0[m] \boldsymbol{b}_k[m] + \boldsymbol{n}_k[m],$$

where $\boldsymbol{n}_k[m]$ is AWGN with zero mean and variance $\sigma^2 \boldsymbol{I}_{NR}$ and $\boldsymbol{F}_0[m]$ contains the first DT rows and T columns of $\boldsymbol{F}[m]$.

2.3 Parallel Interference Cancelation

We perform PIC for user k by removing the contribution of users $k' \neq k$ using soft-symbol estimates [5]

$$\begin{aligned} \tilde{\boldsymbol{y}}_k[m] &= \boldsymbol{y}[m] - \sum_{k' \neq k} \boldsymbol{\Gamma}_{k'} \boldsymbol{F}_0[m] \tilde{\boldsymbol{b}}_{k'}[m] \\ &\approx \boldsymbol{\Gamma}_k \boldsymbol{F}_0[m] \boldsymbol{b}_k[m] + \boldsymbol{n}_k[m]. \end{aligned} \tag{3}$$

The soft symbols in $\tilde{\boldsymbol{b}}_{k'}$ are computed from the extrinsic probabilities supplied by the BCJR decoder [6], from the previous iteration of the receiver.

3. SOFT SPHERE DECODING

For simplification, we omit the user index k in the following. For computational complexity reasons, sphere decoding is performed on a per user basis. Admittedly, under the assumption that all channels are independent and uncorrelated, the grouping of transmit antennas based on their physical co-location is not a prerequisite and any partitioning would do. However, for intuitive reasons we prefer the user basis partitioning.

3.1 Conversion Imaginary to Real Space

So far all elements are complex valued. The transmitted symbols $\boldsymbol{b}$ stem from a QPSK symbol alphabet $\mathcal{A} \in \{\frac{\pm 1 \pm 1}{\sqrt{2}}\}$. However, the soft sphere decoder requires computations of log-likelihood ratios, which is somewhat simpler to perform in the real domain.

In order to convert the signal model into the real domain, we define the subscripts (r) and (i) respectively denoting the real and imaginary part of a complex, vector or matrix. Furthermore, we scale the input vector such that we consider entries for $\hat{\boldsymbol{b}}$ in $\{\pm 1\}$ only. We denote (time index m is omitted in these definitions)

$$\hat{\boldsymbol{b}} = \sqrt{2} \begin{bmatrix} \boldsymbol{b}^{(r)} \\ \boldsymbol{b}^{(i)} \end{bmatrix}, \quad \hat{\boldsymbol{y}} = \begin{bmatrix} \tilde{\boldsymbol{y}}^{(r)} \\ \tilde{\boldsymbol{y}}^{(i)} \end{bmatrix}, \quad \hat{\boldsymbol{n}} = \begin{bmatrix} \boldsymbol{n}^{(r)} \\ \boldsymbol{n}^{(i)} \end{bmatrix},$$

$$\hat{\boldsymbol{\Gamma}} = \begin{bmatrix} \boldsymbol{\Gamma}^{(r)} & -\boldsymbol{\Gamma}^{(i)} \\ \boldsymbol{\Gamma}^{(i)} & \boldsymbol{\Gamma}^{(r)} \end{bmatrix} \quad \text{and} \quad \hat{\boldsymbol{F}} = \begin{bmatrix} \boldsymbol{F}_0 & \boldsymbol{0} \\ \boldsymbol{0} & \boldsymbol{F}_0 \end{bmatrix}.$$

Then the system model (3) can be rewritten as

$$\hat{\boldsymbol{y}}[m] = \frac{1}{\sqrt{2}} \hat{\boldsymbol{\Gamma}} \hat{\boldsymbol{F}}[m] \hat{\boldsymbol{b}}[m] + \hat{\boldsymbol{n}}[m]. \tag{4}$$

Using the channel model (4), the maximum likelihood equation writes

$$\hat{\boldsymbol{b}}_{\mathrm{ML}}[m] = \underset{\boldsymbol{b}}{\mathrm{argmin}} \, \|\hat{\boldsymbol{y}}[m] - \frac{1}{\sqrt{2}} \hat{\boldsymbol{\Gamma}} \hat{\boldsymbol{F}}[m] \hat{\boldsymbol{b}}[m]\|^2$$

which becomes after QR-decomposition of $\hat{\boldsymbol{\Gamma}} = \hat{\boldsymbol{Q}}_\Gamma \hat{\boldsymbol{R}}_\Gamma$

$$\hat{\boldsymbol{b}}_{\mathrm{ML}}[m] = \underset{\boldsymbol{b}}{\operatorname{argmin}} \, \|\hat{\boldsymbol{z}}[m] - \hat{\boldsymbol{R}}_\Gamma \hat{\boldsymbol{F}}[m]\hat{\boldsymbol{b}}[m]\|^2 \,, \qquad (5)$$

where $\hat{\boldsymbol{z}}[m] = \sqrt{2}\hat{\boldsymbol{Q}}_\Gamma^{\mathrm{T}}\hat{\boldsymbol{y}}[m]$, $\hat{\boldsymbol{Q}}_\Gamma$ is unitary and $\hat{\boldsymbol{R}}_\Gamma$ is square upper triangular.

In [1], we developed a suitable implementation to solve (5), taking the block structure of the basis expansion matrix $\boldsymbol{F}[m]$ into account. Although proven less complex than LMMSE, this method introduces a substantial loss in performance. This loss is partly due to the fact that the hard sphere decoder assumes perfect interference cancelation and thus does not take residual interference into account. An additional loss is due to the fact that the BCJR decoder receives hard inputs.

To solve this problem, it is necessary to compute soft symbols to feed the BCJR decoder. The authors in [2] present a method to compute the LLR using sphere decoding to reduce the complexity. We will recall the method in the following, and apply our subspace based implementation, that is more suitable for time-varying channels.

3.2 Definition of the Log-Likelihood Ratios

Let us denote by $\lambda_{\mathrm{PRIOR}}(b_t)$, $\lambda_{\mathrm{POST}}(b_t)$ and $\lambda_{\mathrm{EXT}}(b_t)$ the *a priori*, *a posteriori* and *extrinsic* probabilities of $b_t = \hat{b}(t)$, respectively. For each $t \in \{1, \ldots, 2T\}$, these are given by

$$
\begin{aligned}
\lambda_{\mathrm{PRIOR}}(b_t) &= \ln\left(\frac{p(b_t = +1)}{p(b_t = -1)}\right), \\
\lambda_{\mathrm{POST}}(b_t) &= \ln\left(\frac{p(b_t = +1|\hat{\boldsymbol{z}})}{p(b_t = -1|\hat{\boldsymbol{z}})}\right) \quad \text{and} \\
\lambda_{\mathrm{EXT}}(b_t) &= \lambda_{\mathrm{POST}}(b_t) - \lambda_{\mathrm{PRIOR}}(b_t).
\end{aligned} \qquad (6)
$$

3.3 Explicit Computation of Extrinsic Probabilities

Let $\mathbb{B}_t^+$ and $\mathbb{B}_t^-$ be the subsets of $\{-1, +1\}^{2T}$ such that $b_t = +1$ or $b_t = -1$, respectively. We have

$$
\begin{aligned}
p(b_t = \pm 1|\hat{\boldsymbol{z}}) &= \sum_{\hat{\boldsymbol{b}} \in \mathbb{B}_t^\pm} p(\hat{\boldsymbol{b}}|\hat{\boldsymbol{z}}) = \sum_{\hat{\boldsymbol{b}} \in \mathbb{B}_t^\pm} p(\hat{\boldsymbol{z}}|\hat{\boldsymbol{b}}) \cdot p(\hat{\boldsymbol{b}})/p(\hat{\boldsymbol{z}}) \\
&= p(b_t = \pm 1)/p(\hat{\boldsymbol{z}}) \sum_{\hat{\boldsymbol{b}} \in \mathbb{B}_t^\pm} p(\hat{\boldsymbol{z}}|\hat{\boldsymbol{b}}) \prod_{t' \neq t} p(b_{t'})
\end{aligned}
$$

leading to

$$\lambda_{\mathrm{POST}}(b_t) = \lambda_{\mathrm{PRIOR}}(b_t) + \ln\left(\frac{\sum_{\hat{\boldsymbol{b}} \in \mathbb{B}_t^+} p(\hat{\boldsymbol{z}}|\hat{\boldsymbol{b}}) \cdot \prod_{t' \neq t} p(b_{t'})}{\sum_{\hat{\boldsymbol{b}} \in \mathbb{B}_t^-} p(\hat{\boldsymbol{z}}|\hat{\boldsymbol{b}}) \cdot \prod_{t' \neq t} p(b_{t'})}\right).$$

We also know

$$
\begin{aligned}
p(b_{t'} = \pm 1) &= \frac{\exp\left(\pm\lambda_{\mathrm{PRIOR}}(b_{t'})\right)}{1 + \exp\left(\pm\lambda_{\mathrm{PRIOR}}(b_{t'})\right)} \\
&= \underbrace{\frac{\exp\left(-\lambda_{\mathrm{PRIOR}}(b_{t'})/2\right)}{1 + \exp\left(-\lambda_{\mathrm{PRIOR}}(b_{t'})\right)}}_{A_{t'}} \cdot \exp\left(\pm\frac{\lambda_{\mathrm{PRIOR}}(b_{t'})}{2}\right) \\
&= A_{t'} \exp\left(b_{t'}\frac{\lambda_{\mathrm{PRIOR}}(b_{t'})}{2}\right).
\end{aligned}
$$

and thus

$$
\begin{aligned}
\prod_{t' \neq t} p(b_{t'}) &= \underbrace{\left(\prod_{t' \neq t} A_{t'}\right)}_{\mathcal{A}_t} \cdot \exp\left(\sum_{t' \neq t} \frac{b_{t'}\lambda_{\mathrm{PRIOR}}(b_{t'})}{2}\right) \\
&= \mathcal{A}_t \exp\left(\frac{\boldsymbol{b}_t^{\mathrm{T}}\boldsymbol{\lambda}_{\mathrm{PRIOR},t}}{2}\right)
\end{aligned}
$$

where $\boldsymbol{b}_t$ contains $\hat{\boldsymbol{b}}$ except b_t and $\boldsymbol{\lambda}_{\mathrm{PRIOR},t}$ contains the *a priori* probabilities of the elements of $\boldsymbol{b}_t$. Finally, after simplification, we obtain

$$\lambda_{\mathrm{EXT}}(b_t) = \ln\left(\frac{\sum_{\hat{\boldsymbol{b}} \in \mathbb{B}_t^+} p(\hat{\boldsymbol{z}}|\hat{\boldsymbol{b}}) \cdot \exp\left(\frac{\boldsymbol{b}_t^{\mathrm{T}}\boldsymbol{\lambda}_{\mathrm{PRIOR},t}}{2}\right)}{\sum_{\hat{\boldsymbol{b}} \in \mathbb{B}_t^-} p(\hat{\boldsymbol{z}}|\hat{\boldsymbol{b}}) \cdot \exp\left(\frac{\boldsymbol{b}_t^{\mathrm{T}}\boldsymbol{\lambda}_{\mathrm{PRIOR},t}}{2}\right)}\right).$$

Knowing $\boldsymbol{b}_t^{\mathrm{T}}\boldsymbol{\lambda}_{\mathrm{PRIOR},t} = \hat{\boldsymbol{b}}^{\mathrm{T}}\boldsymbol{\lambda}_{\mathrm{PRIOR}} - b_t\lambda_{\mathrm{PRIOR}}(b_t)$ and $p(\hat{\boldsymbol{z}}|\hat{\boldsymbol{b}}) \propto \exp\left(-\frac{1}{\sigma^2}\|\hat{\boldsymbol{z}} - \hat{\boldsymbol{R}}_\Gamma \hat{\boldsymbol{F}}\hat{\boldsymbol{b}}\|^2\right)$, and using the max-log approximation [7] the extrinsic probability becomes

$$
\begin{aligned}
\lambda_{\mathrm{EXT}}(b_t) \approx \quad & \max_{\hat{\boldsymbol{b}} \in \mathbb{B}_t^+}\left(-\tfrac{1}{\sigma^2}\|\hat{\boldsymbol{z}} - \hat{\boldsymbol{R}}_\Gamma \hat{\boldsymbol{F}}\hat{\boldsymbol{b}}\|^2 + \frac{\hat{\boldsymbol{b}}^{\mathrm{T}}\boldsymbol{\lambda}_{\mathrm{PRIOR}}}{2}\right) \\
& - \max_{\hat{\boldsymbol{b}} \in \mathbb{B}_t^-}\left(-\tfrac{1}{\sigma^2}\|\hat{\boldsymbol{z}} - \hat{\boldsymbol{R}}_\Gamma \hat{\boldsymbol{F}}\hat{\boldsymbol{b}}\|^2 + \frac{\hat{\boldsymbol{b}}^{\mathrm{T}}\boldsymbol{\lambda}_{\mathrm{PRIOR}}}{2}\right) \\
& - \lambda_{\mathrm{PRIOR}}(b_t).
\end{aligned}
$$

To maximize the two expressions above, it is useful to find a vector $\boldsymbol{\Lambda}$ satisfying $4(\hat{\boldsymbol{R}}_\Gamma\hat{\boldsymbol{F}})^{\mathrm{T}}\boldsymbol{\Lambda} = \sigma^2\boldsymbol{\lambda}_{\mathrm{PRIOR}}$. This allows writing

$$
\begin{aligned}
\max &\left\{-\tfrac{1}{\sigma^2}\|\hat{\boldsymbol{z}} - \hat{\boldsymbol{R}}_\Gamma \hat{\boldsymbol{F}}\hat{\boldsymbol{b}}\|^2 + \frac{\hat{\boldsymbol{b}}^{\mathrm{T}}\boldsymbol{\lambda}_{\mathrm{PRIOR}}}{2}\right\} \\
&= \max\left\{-\tfrac{1}{\sigma^2}\|\hat{\boldsymbol{z}} - \hat{\boldsymbol{R}}_\Gamma \hat{\boldsymbol{F}}\hat{\boldsymbol{b}}\|^2 + 2\frac{\left(\hat{\boldsymbol{R}}_\Gamma \hat{\boldsymbol{F}}\hat{\boldsymbol{b}}\right)^{\mathrm{T}}\boldsymbol{\Lambda}}{\sigma^2}\right\} \\
&= -\tfrac{1}{\sigma^2}\min\|\hat{\boldsymbol{z}} + \boldsymbol{\Lambda} - \hat{\boldsymbol{R}}_\Gamma \hat{\boldsymbol{F}}\hat{\boldsymbol{b}}\|^2 + \mathrm{c}\,,
\end{aligned}
$$

where c is not dependent on $\hat{\boldsymbol{b}}$. For instance, it can be easily checked that the vector $\boldsymbol{\Lambda}$ defined as $\boldsymbol{\Lambda} = \frac{\sigma^2}{2u_{D-1}}[0, \ldots, 0, \lambda_{\mathrm{PRIOR}}(1), \ldots, 0, \ldots, 0, \lambda_{\mathrm{PRIOR}}(T)]^{\mathrm{T}} \in \mathbb{R}^{2TD}$ is a valid solution.

Let us now define $\boldsymbol{b}_{\mathrm{SD}}$ the ML solution of the equation $\operatorname{argmin}\|\hat{\boldsymbol{z}} + \boldsymbol{\Lambda} - \hat{\boldsymbol{R}}_\Gamma \hat{\boldsymbol{F}}\hat{\boldsymbol{b}}\|^2$, and s the sign of its t−th element $b_{\mathrm{SD}}(t)$. The *extrinsic* probability is simplified to

$$
\begin{aligned}
\lambda_{\mathrm{EXT}}(b_t) = \quad & -\frac{b_{\mathrm{SD}}(t)}{\sigma^2}\|\hat{\boldsymbol{z}} + \boldsymbol{\Lambda} - \hat{\boldsymbol{R}}_\Gamma \hat{\boldsymbol{F}}\boldsymbol{b}_{\mathrm{SD}}\|^2 \\
& + \frac{b_{\mathrm{SD}}(t)}{\sigma^2}\min_{\boldsymbol{b} \in \mathbb{B}_t^{-s}}\|\hat{\boldsymbol{z}} + \boldsymbol{\Lambda} - \hat{\boldsymbol{R}}_\Gamma \hat{\boldsymbol{F}}\boldsymbol{b}\|^2 \\
& - \lambda_{\mathrm{PRIOR}}(b_t),.
\end{aligned}
$$

Denoting $\boldsymbol{b}_{\mathrm{SD},t}$ the solution of $\underset{\boldsymbol{b} \in \mathbb{B}_t^{-s}}{\operatorname{argmin}}\|\hat{\boldsymbol{z}} + \boldsymbol{\Lambda} - \hat{\boldsymbol{R}}_\Gamma \hat{\boldsymbol{F}}\boldsymbol{b}\|^2$, we obtain

$$
\begin{aligned}
\lambda_{\mathrm{EXT}}(b_t) = \quad & -\frac{b_{\mathrm{SD}}(t)}{\sigma^2}\|\hat{\boldsymbol{z}} + \boldsymbol{\Lambda} - \hat{\boldsymbol{R}}_\Gamma \hat{\boldsymbol{F}}\boldsymbol{b}_{\mathrm{SD}}\|^2 \\
& + \frac{b_{\mathrm{SD}}(t)}{\sigma^2}\|\hat{\boldsymbol{z}} + \boldsymbol{\Lambda} - \hat{\boldsymbol{R}}_\Gamma \hat{\boldsymbol{F}}\boldsymbol{b}_{\mathrm{SD},t}\|^2 \\
& - \lambda_{\mathrm{PRIOR}}(b_t),.
\end{aligned} \qquad (7)
$$

The $4T+1$ vectors $\boldsymbol{b}_{\mathrm{SD}}$ and $\boldsymbol{b}_{\mathrm{SD},t}$ can be computed using hard sphere decoding, $\boldsymbol{\lambda}_{\mathrm{PRIOR}}$ is given by the soft inputs from the iterative receiver.

3.4 Iterative Receiver with Subspace-based Sphere Decoder

We use the subspace-based implementation of the sphere decoder that has been presented and detailed in [1]. To summarize, this implementation making use of the subspace structure and the channel model presented in Sec. 2 allows saving complexity by performing only one QR-decomposition
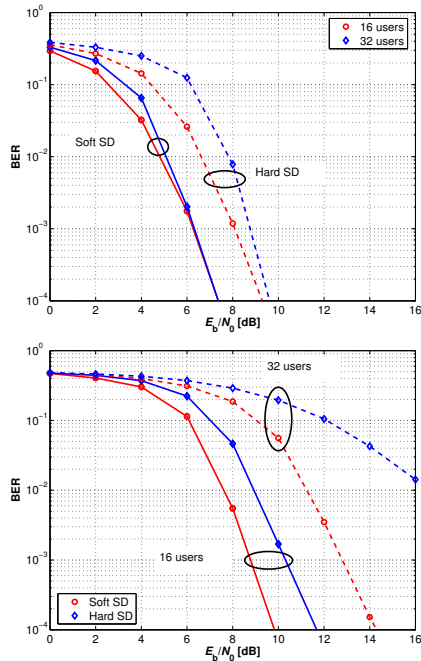
Figure 2: **Hard vs Soft Sphere Decoder:** BER versus SNR after 4 receiver iteration for $K \in \{16, 32\}$ users. The channel is perfectly known (top) or estimated (bottom).
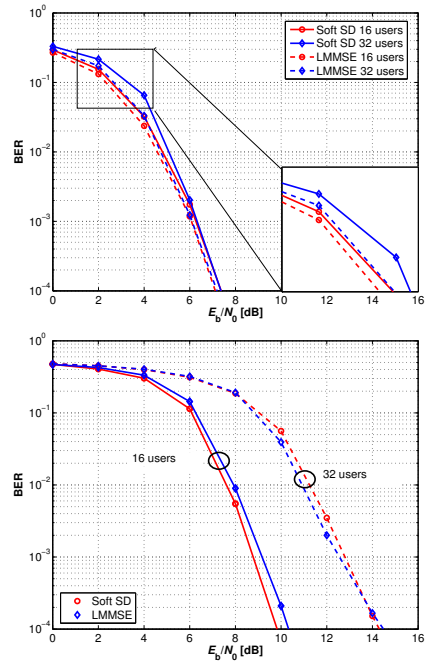

Figure 3: **Soft Sphere Decoder vs LMMSE** BER versus SNR after 4 receiver iterations for $K \in \{16, 32\}$ users. The channel is perfectly known (top) or estimated (bottom) at the receiver.

valid for a whole data block (see (5)) instead of one per data symbol. This implies modifications of the sphere decoder algorithm into a block structured sphere decoder. The details can be found in [1]. Note that the algorithm in [1] performs hard-sphere decoding and is used to compute the $4T + 1$ vectors $\boldsymbol{b}_{\mathrm{SD}}$ and $\boldsymbol{b}_{\mathrm{SD},t} \in \{1, \ldots, 2T\}$ needed for the log-likelihood ratios in (7).

The soft outputs of the sphere decoder $\boldsymbol{\lambda}_{\mathrm{PRIOR}}$ are sent to a BCJR decoder [6], which provides *extrinsic* and *a posteriori* probabilities on the data bits. Both are fed back for the next receiver iteration (see Figure 1). The *a posteriori* probabilities are used for channel estimation (see [3]). The *a priori* probabilities needed as soft input for the sphere decoder are computed using $\boldsymbol{\lambda}_{\mathrm{PRIOR}} = \boldsymbol{\lambda}_{\mathrm{POST}} - \boldsymbol{\lambda}_{\mathrm{EXT}}$, see (6)

4. SIMULATION RESULTS

The realizations of the time-varying frequency-selective channel are generated using an exponentially decaying power delay profile with root mean square delay spread $T_{\mathrm{D}} = 4T_{\mathrm{C}} = 1\mu\mathrm{s}$ for a chip rate of $1/T_{\mathrm{C}} = 3.84 \cdot 10^6\,\mathrm{s}^{-1}$ [8]. We assume $L = 15$ resolvable paths. The autocorrelation for every channel tap is given by the classical Clarke spectrum [9]. The system operates at carrier frequency $f_C = 2\,\mathrm{GHz}$ and the users move with velocity $v = 70\mathrm{kmh}^{-1}$. These gives a Doppler bandwidth of $B_{\mathrm{D}} = 126\mathrm{Hz}$. We use $T = R = 4$ transmit and receive antennas and $N = 64$ subcarriers. A data block consists of $M = 256$ OFDM symbols including $J = 60$ pilot symbols. The system is designed for $v_{\max} = 102.5\,\mathrm{kmh}^{-1}$ which results in a dimension $D = 3$ for the Slepian basis expansion. The MIMO channel taps are normalized in order to analyze the diversity gain of the receiver only. No antenna gain is present due to this normalization.

For data transmission, a convolutional, non-systematic, non-recursive, 4 state, rate $R_C = 1/2$ code with code genera-

tors $(5, 7)_8$, is used. All illustrated results are obtained by averaging over 100 independent channel realizations. We define the signal-to-noise ratio $E_b/N_0 = PM/\left(2R_C\sigma^2 N(M - J)\right)$, taking into account the loss due to coding, pilots and cyclic prefix. The noise variance σ^2 is assumed to be known at the receiver.

The following simulations have been performed:

• **Hard Sphere Decoder vs Soft Sphere Decoder** A comparison of the performance of soft and hard sphere decoders is shown in Fig. 2. Using soft input soft output sphere decoder allows at least 2dB gain over hard sphere decoding.

• **Soft Sphere Decoder vs LMMSE** We compare the performance of the soft sphere decoder on a per user basis to the performance of a LMMSE equalizer detecting jointly all users in Fig. 3. Both detection methods perform similar.

5. ON THE COMPUTATIONAL COMPLEXITY

We define a *flop* as a floating point operation (addition, substraction, multiplication, division or square root) in the *real* domain [10]. Thus, one complex multiplication (CM) requires 4 real multiplications and 2 additions, leading to 6 *flop*s. Similarly, one complex addition (CA) requires 2 *flop*s. We denote by $q_t \leq Q^{(T-t+1)}$ the number of candidates after the step t of the sphere decoder (see [1] for details). q_t is a random variable since it depends on the realization of $\boldsymbol{b}$, $\hat{\boldsymbol{S}}$ and $\boldsymbol{n}$. $Q = |\mathcal{A}|$ is the size of the alphabet.

5.1 Hard Sphere Decoder

As given in [1], the computational complexity for a block of length $M - J$ using hard sphere decoding requires:

• one *thin* complex QR factorization of size $NR \times DT$, with

computational complexity [10]

$$c_{\mathrm{QR}} = 8(DT)^2 \left(NR - \frac{DT}{3} \right) \, flops \,,$$

- $M - J$ runs of the hard sphere decoder with complexity

$$c_{\mathrm{hard}}[m] = \quad 2D \sum_{t=1}^{T-1} \left[(T-t)(4D+3) - 2D + 1 \right] q_{t+1}[m] \\ + 4(T-1)DQ(D+2) \, flops \,.$$

An upper bound of this expression can be computed using $q_t = Q^{(T-t+1)}$, which corresponds to the case where all combinations remain valid candidate at all steps. This is equivalent to an exhaustive search using the sphere decoder implementation and an infinite radius:

$$c_{\mathrm{hard}}[m] \leq \quad 2D(4D+3) \sum_{t=1}^{T-1} t Q^t - 2D(2D-1) \sum_{t=1}^{T-1} Q^t \\ + 4(T-1)DQ(D+2) \, flops \,. \quad (8)$$

The computational complexity for a single data block can be upper bounded using (8) and $C_{\mathrm{hard}} = c_{\mathrm{QR}} + \sum_{m \notin \mathcal{P}} c_{\mathrm{hard}}[m]$.

5.2 Soft Sphere Decoder

Computations are very similar except that they are done in the real domain. Thus dimension are multiplied by a factor 2. However, we have now real multiplications and additions, equivalent to one *flop* each. Furthermore, the alphabet size is reduced to $Q/2$. The computations required are:

- one *thin* real QR factorization of size $2NR \times 2DT$, with computational complexity [10]

$$c_{\mathrm{QR}} = 8(DT)^2 \left(NR - \frac{2DT}{3} \right) \, flops \,,$$

- $(M-J)(4T+1)$ runs of the subspace based sphere decoder with complexity

$$c_{\mathrm{soft}}[m] = \quad D \sum_{t=1}^{2T-1} \left[(2T-t)(2D+1) - D \right] q_{t+1}[m] \\ + (2T-1)DQ(D+1)/2 \, flops \,.$$

As previously, an upper bound of this expression can be computed using $q_t = \left(\frac{Q}{2} \right)^{(2T-t+1)}$:

$$c_{\mathrm{soft}}[m] \leq \quad D(2D+1) \sum_{t=1}^{2T-1} t \left(\frac{Q}{2} \right)^t - D \sum_{t=1}^{2T-1} \left(\frac{Q}{2} \right)^t \\ + (2T-1)DQ(D+1)/2 \, flops \,. \quad (9)$$

The complexity for a single data block can be upper bounded using (9) and $C_{\mathrm{soft}} = c_{\mathrm{QR}} + (4T+1) \sum_{m \notin \mathcal{P}} c_{\mathrm{soft}}[m]$.

5.3 Comparison of the computational complexity

In Fig. 4 we show upper bounds of the iterative receiver complexity over a block of size $M - J$ using, respectively, hard sphere decoder, soft sphere decoder and linear minimum mean square error (LMMSE), see for example [11] for details. We can see that the soft sphere decoder is about one order of magnitude more complex than the hard sphere decoder and one order of magnitude less complex than LMMSE detection.

6. CONCLUSIONS

We have presented a subspace based implementation of a soft sphere decoder, making use of the basis expansion channel model.
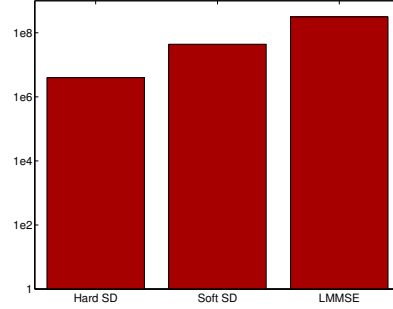

Figure 4: **Upper bound for the complexity per user:** we show the maximum computational complexity using hard sphere decoding as in [1], soft sphere decoding or LMMSE.

This allows for complexity reduction when the channels are time-varying. The use of soft outputs is a compromise between complexity and performance. The soft sphere decoder performs close to the LMMSE filter, while saving one order of magnitude of complexity.

REFERENCES

[1] C. Dumard and T. Zemen, "Subspace based sphere decoder for MC-CDMA in time-varying MIMO channels," in *Proc. 18th IEEE PIMRC*, Athens, Greece, September 2007.

[2] R. Wang and G. B. Giannakis, "Approaching MIMO channel capacity with reduced-complexity soft sphere decoding," in *Proc. Wireless Communications and Networking Conference (WCNC)*, Atlanta, Georgia, USA, March 2004.

[3] T. Zemen and C. F. Mecklenbräuker, "Time-variant channel estimation using discrete prolate spheroidal sequences," *IEEE Trans. Signal Processing*, vol. 53, no. 9, pp. 3597–3607, September 2005.

[4] D. Slepian, "Prolate spheroidal wave functions, Fourier analysis, and uncertainty - V: The discrete case," *The Bell System Technical Journal*, vol. 57, no. 5, pp. 1371–1430, May-June 1978.

[5] J. Wehinger, "Iterative multi-user receivers for CDMA systems," Ph.D. dissertation, Vienna University of Technology, Vienna, Austria, July 2005.

[6] L. R. Bahl, J. Cocke, F. Jelinek, and J. Raviv, "Optimal decoding of linear codes for minimizing symbol error rate," *IEEE Trans. Inform. Theory*, vol. 20, no. 2, pp. 284–287, Mar. 1974.

[7] B. M. Hochwald and S. ten Brink, "Achieving near-capacity on a multiple-antenna channel," *IEEE Trans. Commun.*, vol. 51, no. 3, pp. 389–399, march 2003.

[8] L. M. Correia, *Wireless Flexible Personalised Communications*. Wiley, 2001.

[9] R. H. Clarke, "A statistical theory of mobile-radio reception," *The Bell System Technical Journal*, vol. 47, pp. 957–1000, July/August 1968.

[10] G. H. Golub and C. F. V. Loan, *Matrix Computations*, 3rd ed. Baltimore (MD), USA: Johns Hopkins University Press, 1996.

[11] C. Dumard and T. Zemen, "Low-complexity MIMO multi-user receiver: A joint antenna detecion scheme for time-varying channels," *IEEE Trans. Signal Processing*, 2008, in print.

5 Utilization of Cooperation and Selection Diversity

[Article 13] P. Castiglione, M. Nicoli, S. Savazzi and T. Zemen, "Cooperative regions for coded cooperation over time-varying fading channels," in *International ITG/IEEE Workshop on Smart Antennas (WSA 2009)*, Berlin, Germany, February 16-19, 2009.

[Article 14] H. A. Saleh, A. F. Molisch, T. Zemen, S. D. Blostein, and N. B. Mehta, "Receive antenna selection for time-varying channels using discrete prolate spheroidal sequences," in *IEEE Transaction on Wireless Communications*, 2012, to be published.

Cooperative Regions For Coded Cooperation Over Time-Varying Fading Channels

P. Castiglione[1], M. Nicoli[2], S. Savazzi[2] and Thomas Zemen[1]

[1] Forschungszentrum Telekommunikation Wien, Donau-City-Strasse 1, A-1220 Vienna, Austria

[2] Dip. di Elettronica e Informazione, Politecnico di Milano, Piazza L. da Vinci 32, I-20133 Milano, Italy

e-mail: {castiglione, thomas.zemen}@ftw.at, {nicoli,savazzi}@elet.polimi.it

Abstract—The performance analysis of coded cooperation has been mainly focused on two extreme cases of channel variability, i.e. the block-fading (BF) and the fast-fading (FF) model. In more practical propagation environments the fading correlation across time depends on the level of user mobility. This paper analyzes the effects of time-selective fading on the performance of coded cooperation by providing an analytical framework for the error rate evaluation as a function of the mobility degree of the mobile station (MS) and of the quality of the inter-MS channel. The purpose is to evaluate the conditions on the propagation settings where the additional exploitation of spatial diversity (when time-diversity is available) provided by cooperative transmission is able to enhance substantially the performance of the non-cooperative transmission. We show that coded cooperation can outperform the non-cooperative (coded and bit-interleaved) transmission only up to a certain degree of mobility. The *cooperative region* is defined as the collection of mobility settings for which coded cooperation can be regarded as a competitive strategy compared to non-cooperative transmission. Contrary to what has been previously shown for BF channels, we demonstrate that the inter-MS channel quality plays a key role in the definition of the cooperative region.

I. Introduction

Cooperative communication [1] was originally motivated as a method to bring *spatial diversity* gain in networks of single antenna terminals through redundant transmissions from multiple mobile stations (MSs). The integration of the user cooperation idea with channel coding was then proposed in [2] to further improve the cooperative link performance. Forward error correcting (FEC) codes are used by two or more mobile stations that cooperate by transmitting to the base station (BS) incremental redundancy for the partners. This approach was shown to provide significant performance enhancements, compared to conventional non-cooperative transmission, primarily in networks with fixed or nomadic terminals: in such a situation *time diversity* cannot be exploited, while spatial diversity is beneficial as it reduces the fading impairments.

In the literature the performance analysis of coded cooperation has been mainly focused on two extreme cases of channel variability, i.e. the block-fading (BF) and the fast-fading (FF) model. However, more practical propagation environments, e.g. in vehicular networks, experience fading variations across time with a degree of correlation depending on the level of MS mobility. In these cases, temporal diversity can be exploited to improve the link reliability by the joint use of channel coding and bit-interleaved modulation [3]. Hence, it is crucial to investigate to what extent the additional exploitation of
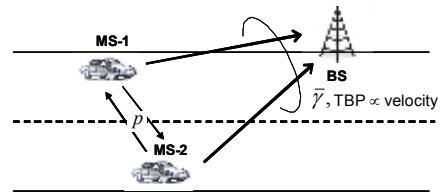

Fig. 1. System setting: the average signal-to-noise ratio (SNR) $\bar{\gamma}$ and the time-bandwidth product (TBP) of the uplink channels; the block error probability p of the inter-MS channels.

spatial diversity through collaborative transmission is able to provide substantial performance enhancements compared to non-cooperative transmission.

The contribution of this paper is twofold. Firstly, the effects of MS mobility on the performance of coded cooperation are analyzed by providing an analytical framework for the error rate evaluation as a function of the degree of fading variations. The variation degree is here measured in terms of the time-bandwidth product (TPB), that is the product of the codeword duration (for bit interleaved coded modulation) and the Doppler bandwidth. Our performance analysis is carried out in closed form and extends the results obtained by simulations in [4]. The analysis takes into account the reliability of the communication link between the cooperating MSs, by considering the block error probability p over the inter-MS link as a penalty factor that limits the cooperation performance (an overview of the system setting is shown in Fig. 1).

The above analysis is then used to evaluate the performance gain provided by coded cooperation with respect to a non-cooperative system for varying degree of MS mobility and for different channel state conditions. We show that coded cooperation can outperform the non-cooperative (coded and bit-interleaved) transmission only up to a certain degree of mobility. Beyond this limiting threshold, the temporal diversity gain, which is made available by channel coding and bit-interleaving, dominates the performances, while the spatial diversity gain offered by collaborative transmissions provides only marginal improvements. Analytical and numerical results show that the mobility degree threshold, beyond which coded cooperation is no more advantageous, decreases with the
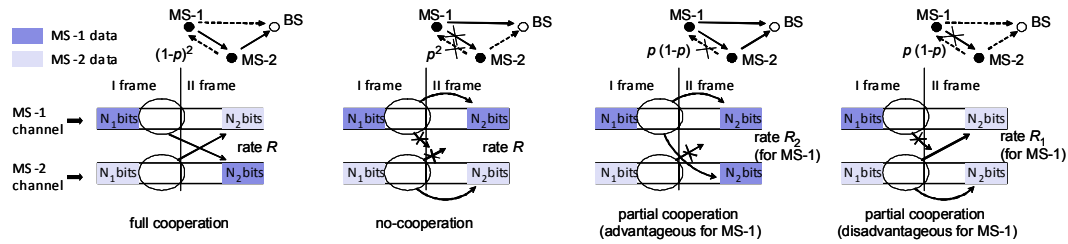
Fig. 2. Possible configurations of the coded cooperation scheme.

quality of the inter-MS channel and strongly depends on the quality of the relayed links (the uplink signal-to-noise ratio $\bar{\gamma}$ - SNR) from the cooperating MSs towards the common BS. To better highlight these results, we evaluate the *cooperative region* [5] as the collection of mobility and channel settings for which coded cooperation can be regarded as a competitive option compared to non-cooperative transmission.

The paper is organized as follows. In Section II we give a brief description of the system and the channel model. Section III presents the derivation of the analytical upperbound on the bit error rate (BER). We derive the statistical distribution of the SNR at the decision variable (here referred to as *effective SNR*) [6], based on the knowledge of the fading channel autocorrelation over the transmitted data block (a similar approach has been used for performance evaluation in frequency-selective OFDM systems [7], [8]). Section IV contains both numerical and analytical results, for the validation of the analytical BER and the investigation of the MSs' mobility effects on coded cooperation. Conclusions are drawn in Section V.

II. SYSTEM MODEL

We consider the transmission of rate-R coded data from two mobile stations, MS-1 and MS-2, towards a common BS through two orthogonal channels by frequency division multiple access (FDMA). The two channels are assumed to be subject to *independent* time-selective (due to MS mobility) frequency-flat fading. Coded cooperation is carried out according to the scheme introduced in [2], by sending portions of each MS data over the two independent channels so that a diversity gain is provided, as briefly summarized below. Each MS encodes its data block of K information bits by means of a rate-compatible punctured convolutional (RCPC) code [9] that yields an overall codeword of $N = K/R$ bits. This codeword is divided through puncturing into two sub-codewords of length N_1 and N_2, with $N = N_1 + N_2$: the first subset is the punctured codeword of rate $R_1 = K/N_1$, the second one is the set of removed parity bits. The sub-codewords are then transmitted into two subsequent time frames. In the first frame each MS broadcasts the first sub-codeword, that is received by the cooperating partner and the BS. If the partner successfully decodes the first sub-codeword (this is determined by a cyclic redundancy check - CRC - code or any other error detection code), then it will compute and

transmit the N_2 additional parity bits in the second frame. At the BS this incremental redundancy is used for de-puncturing the rate-R_1 codeword received in the first frame, thus obtaining the initial rate-R codeword. Hence, the level of cooperation is quantified by $\alpha = \frac{N_2}{N}$. If the partner cannot successfully decode the MS' first-frame data, it will transmit its own N_2 code bits during the second frame. The latter rule avoids error propagation: each MS is forced to stop cooperating if the inter-MS transmission fails due to various possible reasons related to the inter-MS channel conditions (e.g. a deep fade, channel estimation and/or synchronization errors, etc.). Notice that even if the MSs are close and no obstacle stands on their line of sight (e.g. two vehicles running adjacently on the motorway), the media access control (MAC) protocol at one MS could anyhow decide to stop the ongoing cooperation with the partner.

Characterizing the different causes of no cooperation goes beyond the scope of the present work. Here we assume that no cooperation occurs only due to a block error event in the inter-MS transmission, with block error probability p being the same for both MSs. Furthermore, we assume, as worst case, that the inter-MS channels are independent (which is true in FDMA). Under these assumptions, four different configurations of coded cooperation can occur [2] with probability depending on the inter-MS block error rate p, as specified below (see also Fig. 2)[1]:

- *Full cooperation* ($\Theta = 1$). Both MSs successfully decode each other during the first frame and can transmit the partner's code bits during the second frame. Probability: $\Pr(\Theta = 1) = (1 - p)^2$.
- *No-cooperation* ($\Theta = 2$). Both MSs fail to decode the partner's first frame and transmit their own code bits during the second frame. Probability: $\Pr(\Theta = 2) = p^2$.
- *Partial cooperation - advantageous for MS-1* ($\Theta = 3$). MS-1 cannot decode MS-2's data during the first frame, while MS-2 successfully decodes MS-1's data. During the second frame both MSs transmit the N_2 parity bits for MS-1. Probability: $\Pr(\Theta = 3) = p(1 - p)$.
- *Partial cooperation - disadvantageous for MS-1* ($\Theta = 4$). The same as the previous case, with switched MSs.

---

[1]To simplify the reasoning, the cases of partial cooperation are described from the point of view of MS-1, while MS-2 is the partner.
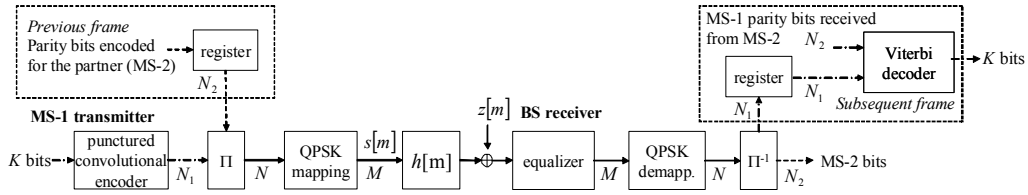
Fig. 3. Uplink system model for MS-1 successfully cooperating with MS-2.

Probability: $\Pr(\Theta = 4) = \Pr(\Theta = 3) = p(1 - p)$.

Notice that the transmission of one codeword is temporally concatenated with the transmission of the previous one (see Fig. 2). Therefore, splitting the codeword transmission into two frames does not generally modify the overall code rate R, apart from the case of partial cooperation in which the code-rate raises to R_1 for the disadvantaged MS and lowers to $R_2 = K/(N + N_2)$ for the advantaged MS.

The complete system model is depicted in Fig. 3 for each MS-BS link (only the case $\Theta = 1$ is represented for simplicity). Bit-interleaved quadrature phase shift keying (QPSK) modulation is assumed [11] with symbol rate $1/T_{\mathrm{S}}$. The baseband-equivalent discrete-time signal transmitted by MS-i, with $i \in \{1, 2\}$, is $s_i[m] = \sqrt{E_{\mathrm{S}}} q_i[m]$, $m = 1, \ldots, M$, where $M = N/2$ is the number of symbols per frame, E_{S} is the transmitted energy per symbol, and $q_i[m] = (\pm 1 \pm j)/\sqrt{2}$ is the QPSK symbol at time mT_{S}. The corresponding signal received at the BS is then

$$y_i[m] = h_i[m]s_i[m] + z[m], \tag{1}$$

where $z[m] \sim \mathcal{CN}(0, \sigma_n^2)$ denotes the complex additive white Gaussian noise (AWGN) at all receivers, with variance σ_n^2. The time-variant Rayleigh-fading channel for the link between MS-i and the BS is $h_i[m] \sim \mathcal{CN}(0, \Omega_i)$ with variance Ω_i. The fading process is assumed to be wide-sense stationary (up to the second-order statistics) with Clarke's auto-correlation function given by [10]

$$R_i[k] = \mathrm{E}\{h_i[m]h_i^*[m + k]\} = \Omega_i J_0(2\pi k\nu_{\mathrm{D}i}), \tag{2}$$

where J_0 is the zeroth-order Bessel function of the first kind, $\nu_{\mathrm{D}i}$ is the one-sided normalized Doppler bandwidth $\nu_{\mathrm{D}i} = \frac{v_i f_{\mathrm{C}}}{c_0} T_{\mathrm{S}}$, v_i is the MS-i velocity, f_{C} the carrier frequency and c_0 the speed of light. The parameter $\nu_{\mathrm{D}i}$ is a measure of the temporal variability of the channel. A more meaningful parameter for coded transmissions is the time-bandwidth product, here defined as

$$\mathrm{TBP}_i = 2M\nu_{\mathrm{D}i}, \tag{3}$$

where $2M$ is the temporal duration of the codeword expressed in symbol times (two frames), i.e. the time interval in which the interleaved code can exploit the temporal diversity. By definition (3), TBP represents the velocity of MS-i in terms of number of wavelengths travelled during the transmission of two frames.

According to the Rayleigh fading assumption, the instantaneous SNR, defined as

$$\gamma_i[m] = |h_i[m]|^2 \frac{E_{\mathrm{S}}}{\sigma_n^2}, \tag{4}$$

exhibits an exponential distribution with mean $\overline{\gamma_i} = \Omega_i \frac{E_s}{\sigma_n^2}$ [6].

At the receiver side, coherent equalization is carried out using perfect knowledge for the channel $h_i[m]$, followed by de-mapping, de-interleaving and decoding, as illustrated in Fig. 3.

III. Performance Analysis

In the following, the derivation of the analytical upperbound on the average BER is presented. We first assume that the MSs are always cooperating, as for an error-free inter-MS channel with $p = 0$ (Sect. III-A). Then in Sect. III-B the analysis is extended to include the other cases of coded cooperation.

A. Analysis for ideal (error-free) inter-MS channel

According to the union bound approach [11], the average bit error probability, for the full cooperation case ($\Theta = 1$), P_b at the Viterbi decoder output is:

$$P_{\mathrm{b}} \leq \frac{1}{k} \sum_{d \geq d_{\mathrm{free}}} \sum_{\mathbf{c} \in \mathcal{E}(d)} \beta(\mathbf{c})P(\mathbf{c}), \tag{5}$$

where k is the number of input bits for each branch of the convolutional code trellis, d_{free} is the free distance, $\mathcal{E}(d)$ is the set of error events $\mathbf{c}$ at a certain Hamming distance d, $\beta(\mathbf{c})$ is the Hamming weight of the input sequence corresponding to $\mathbf{c}$ and $P(\mathbf{c})$ is the average pairwise error probability (PEP). The average PEP $P(\mathbf{c})$ is the probability of detecting the codeword $\mathbf{c}$ instead of the transmitted all-zero codeword.

Let $\mathcal{T}_{\mathbf{c}} = \{\tau_{\mathbf{c},1}, \ldots, \tau_{\mathbf{c},d}\}$ be the set of time instants associated with the d error bits in $\mathbf{c}$, and $\tilde{\mathbf{h}} = \sqrt{E_s}[h(\tau_{\mathbf{c},1}) \cdots h(\tau_{\mathbf{c},d})]^{\mathrm{T}}/\sigma_{\mathrm{n}}$ be the vector that gathers the corresponding channel gains scaled by $\sqrt{E_s}/\sigma_{\mathrm{n}}$. The average PEP $P(\mathbf{c})$ can be calculated as [3]:

$$P(\mathbf{c}) = \int_0^\infty Q\left(\sqrt{2\gamma_{\mathrm{eff}}}\right) p\left(\gamma_{\mathrm{eff}}\right) d\gamma_{\mathrm{eff}}, \tag{6}$$

where γ_{eff} (effective SNR) is the sum of the SNR variates that are experienced over the time instants $\mathcal{T}_{\mathbf{c}}$ [7], or, equivalently, the sum of the squared magnitudes of the vector $\tilde{\mathbf{h}}$'s entries:

$$\gamma_{\mathrm{eff}} = \sum_{k \in \mathcal{T}_{\mathbf{c}}} \gamma(k) = \left\| \tilde{\mathbf{h}} \right\|^2. \tag{7}$$
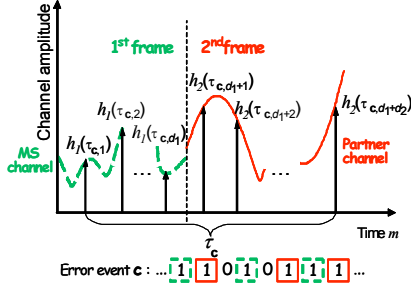
153

Fig. 4. Example of the correlated fading observed along the error event in the case of full cooperation ($\Theta = 1$).

Its probability density function (pdf), $p(\gamma_{\text{eff}})$, clearly depends on the correlation of the channel gains contained in $\tilde{\mathbf{h}}$. We observe that $\tilde{\mathbf{h}}$ is a zero-mean complex Gaussian random vector, $\tilde{\mathbf{h}} \sim \mathcal{CN}(\mathbf{0}, \mathbf{R_c})$, with covariance $\mathbf{R_c} = \mathrm{E}[\tilde{\mathbf{h}} \cdot \tilde{\mathbf{h}}^{\mathrm{H}}]$ whose entries are samples of the auto-correlation function (2). The distribution of the effective SNR is here derived based on the knowledge of the correlation matrix $\mathbf{R_c}$, by extending the approach in [8] to the cooperative scenario with time-selective fading channels.

Recalling that the codeword is partitioned into two frames due to the coded cooperation scheme, it should be observed that, for the case of full cooperation ($\Theta = 1$), the d error bits in $\mathbf{c}$ are split into two groups of bits coming from the MS's and the partner's uplink channels (see Fig. 4). Let us consider for instance the codeword of MS-1, the time instants associated with the first and the second groups are here indicated as $\mathcal{T}_{\mathbf{c};1}$ (d_1 elements) and $\mathcal{T}_{\mathbf{c};2}$ (d_2 elements), respectively, with $\mathcal{T}_{\mathbf{c}} = \mathcal{T}_{\mathbf{c};1} \bigcup \mathcal{T}_{\mathbf{c};2}$. Accordingly, the channel vector is $\tilde{\mathbf{h}} = [\tilde{\mathbf{h}}_{1,d_1}^{\mathrm{T}}, \tilde{\mathbf{h}}_{2,d_2}^{\mathrm{T}}]^{\mathrm{T}}$, where $\tilde{\mathbf{h}}_{1,d_1} = \sqrt{E_{\mathrm{s}}} [h_1(\tau_{\mathbf{c},1}) \cdots h_1(\tau_{\mathbf{c},d_1})]^{\mathrm{T}} / \sigma_{\mathrm{n}}$ and $\tilde{\mathbf{h}}_{2,d_2} = \sqrt{E_{\mathrm{s}}} [h_2(\tau_{\mathbf{c},d_1+1}) \cdots h_2(\tau_{\mathbf{c},d_1+d_2})]^{\mathrm{T}} / \sigma_{\mathrm{n}}$ gather the channel coefficients for, respectively, the MS-1 and MS-2 uplink channels, at time instants $\mathcal{T}_{\mathbf{c};1}$ and $\mathcal{T}_{\mathbf{c};2}$. In order to derive the effective SNR's statistical distribution, we introduce the eigenvalue decomposition (EVD) of the covariance matrices of the two channel vectors:

$$[\mathbf{R_c}_{,1}]_{d_1 \times d_1} = \mathrm{E}[\tilde{\mathbf{h}}_{1,d_1} \cdot \tilde{\mathbf{h}}_{1,d_1}^{\mathrm{H}}] = \mathbf{U}_1 \mathbf{\Lambda}_1 \mathbf{U}_1^{\mathrm{H}}, \quad (8)$$

$$[\mathbf{R_c}_{,2}]_{d_2 \times d_2} = \mathrm{E}[\tilde{\mathbf{h}}_{2,d_2} \cdot \tilde{\mathbf{h}}_{2,d_2}^{\mathrm{H}}] = \mathbf{U}_2 \mathbf{\Lambda}_2 \mathbf{U}_2^{\mathrm{H}}. \quad (9)$$

The matrices $\mathbf{\Lambda}_1 = \mathrm{diag}[\lambda_{1,1}, \ldots, \lambda_{1,r_1}]$ and $\mathbf{\Lambda}_2 = \mathrm{diag}[\lambda_{1,1}, \ldots, \lambda_{1,r_2}]$ contain the non-zero eigenvalues, with $r_1 = \mathrm{rank}[\mathbf{R_c}_{,1}]_{d_1 \times d_1} \leq d_1$ and $r_2 = \mathrm{rank}[\mathbf{R_c}_{,2}]_{d_2 \times d_2} \leq d_2$. $\mathbf{U}_1$ and $\mathbf{U}_2$ gather the corresponding eigenvectors. We recall that the two MSs' channels are assumed to be independent, hence it is $\mathrm{E}[\tilde{\mathbf{h}}_{1,d_1} \cdot \tilde{\mathbf{h}}_{2,d_2}^{\mathrm{H}}] = \mathbf{0}$ and the correlation matrix can

be written as

$$\mathbf{R_c} = \begin{bmatrix} [\mathbf{R_c}_{,1}]_{d_1 \times d_1} & \mathbf{0} \\ \mathbf{0} & [\mathbf{R_c}_{,2}]_{d_2 \times d_2} \end{bmatrix} \quad (10)$$

$$= \underbrace{\begin{bmatrix} \mathbf{U}_1 & \mathbf{0} \\ \mathbf{0} & \mathbf{U}_2 \end{bmatrix}}_{\mathbf{U}} \underbrace{\begin{bmatrix} \mathbf{\Lambda}_1 & \mathbf{0} \\ \mathbf{0} & \mathbf{\Lambda}_2 \end{bmatrix}}_{\mathbf{\Lambda}} \underbrace{\begin{bmatrix} \mathbf{U}_1 & \mathbf{0} \\ \mathbf{0} & \mathbf{U}_2 \end{bmatrix}^{\mathrm{H}}}_{\mathbf{U}^{\mathrm{H}}},$$

where $\mathbf{\Lambda} = \mathrm{diag}[\lambda_{1,1}, \ldots, \lambda_{1,r_1}, \lambda_{2,1}, \ldots, \lambda_{2,r_2}]$ collects the eigenvalues of $\mathbf{R_c}$ and $\mathbf{U}$ the corresponding eigenvectors. Notice that it is $r = \mathrm{rank}[\mathbf{R_c}] = r_1 + r_2$.

Using the EVD (10), the effective SNR can now be rewritten as $\gamma_{\text{eff}} = \|\mathbf{b}\|^2 = \sum_{i=1}^{r} b_i^2$, in terms of the projection of the channel onto the r-dimensional column-space of $\mathbf{R_c}$: $\mathbf{b} = \mathbf{U}^{\mathrm{H}} \tilde{\mathbf{h}} = [b_1 \cdots b_r]^{\mathrm{T}}$. Notice that $\mathbf{b} \sim \mathcal{CN}(\mathbf{0}, \mathbf{\Lambda})$, thus the effective SNR is the sum of r independent exponentially distributed variates having as mean values the eigenvalues of $\mathbf{R_c}$. It follows that the pdf of γ_{eff} exhibits the moment-generating function (MGF) [6], [12] :

$$\mathbf{M}_{\gamma_{\text{eff}}}(s) = \prod_{i=1}^{r_1} \frac{1}{1 - \lambda_{1,i}s} \prod_{j=1}^{r_2} \frac{1}{1 - \lambda_{2,j}s}. \quad (11)$$

The integral over γ_{eff} in (6) can now be derived using the alternate integral form of the Q-function [13] and the well known MGF method [12]. We get the average PEP

$$P(\mathbf{c}) = \frac{1}{\pi} \int_0^{\frac{\pi}{2}} \prod_{i=1}^{r_1} \left(1 + \frac{\lambda_{1,i}}{\sin^2 \vartheta}\right)^{-1} \prod_{j=1}^{r_2} \left(1 + \frac{\lambda_{2,j}}{\sin^2 \vartheta}\right)^{-1} d\vartheta \quad (12)$$

$$\leq \frac{1}{2} \prod_{i=1}^{r_1} \frac{1}{1 + \lambda_{1,i}} \prod_{j=1}^{r_2} \frac{1}{1 + \lambda_{2,j}}, \quad (13)$$

upperbounded in (13) using $\sin^2 \vartheta \leq 1$.

We observe that each MS interleaves its own bits and the parity bits computed for the other MS before mapping them into symbols. It follows that the $d = d_1 + d_2$ non-zero bits of the error event $\mathbf{c}$ can appear within the two time frames in several possible configurations, each corresponding to a different shift of $\mathbf{c}$ at the input of the Viterbi decoder. To get an upperbound, we will select for each error event $\mathbf{c}$ the most probable configuration among all these possible shifts by finding the one that maximizes (12).

B. Extension to imperfect inter-MS channel

In Sect. III-A, the average BER performance (for MS-1) has been analyzed only for the full cooperation case ($\Theta = 1$). The average BER over all the possible cooperation configurations $\Theta = \{1, 2, 3, 4\}$ can be evaluated as:

$$P_{\mathrm{b}} \leq \frac{1}{k} \sum_{d \geq d_{\text{free}}} \sum_{\mathbf{c} \in \mathcal{E}(d)} \beta(\mathbf{c}) \left[\sum_{\Theta=1}^{4} \mathrm{Pr}(\Theta) P(\mathbf{c} | \Theta)\right]. \quad (14)$$

The conditioned PEP $P(\mathbf{c} | \Theta = 1)$ for the full cooperation case is evaluated as in (12) - (13) based on the eigenvalue decomposition of the matrix (10). For the other cases $\Theta =$
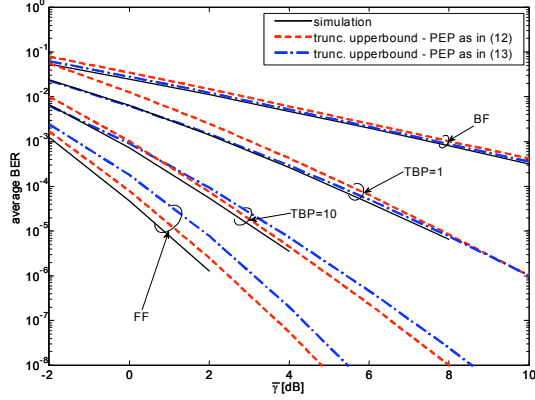
Fig. 5. Performance of full cooperation ($\Theta = 1$). Code-rate $R = 1/4$.
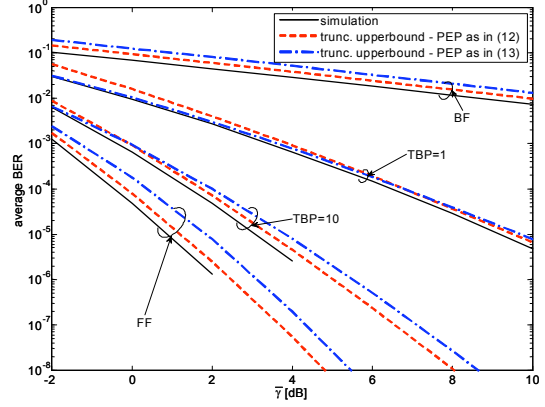

Fig. 6. Performance of no-cooperation ($\Theta = 2$). Code-rate $R = 1/4$.

$\{2, 3, 4\}$, the conditioned PEP can be obtained similarly using the eigenvalues of the following matrices:

$$\mathbf{R_c}(\Theta = 2) = \begin{bmatrix} [\mathbf{R_{c}},1]_{d_1 \times d_1} & [\mathbf{R_{c}},1]_{d_1 \times d_2} \\ \left[[\mathbf{R_{c}},1]_{d_1 \times d_2}\right]^{\mathrm{H}} & [\mathbf{R_{c}},1]_{d_2 \times d_2} \end{bmatrix}, \quad (15)$$

$$\mathbf{R_c}(\Theta = 3) = \begin{bmatrix} \mathbf{R_c}(\Theta = 2) & \mathbf{0} \\ \mathbf{0} & \mathbf{0} \end{bmatrix} + \begin{bmatrix} \mathbf{0} & \mathbf{0} \\ \mathbf{0} & [\mathbf{R_{c}},2]_{d_2 \times d_2} \end{bmatrix}, \quad (16)$$

$$\mathbf{R_c}(\Theta = 4) = [\mathbf{R_{c}},1]_{d_1 \times d_1}, \quad (17)$$

where $[\mathbf{R_{c}},1]_{d_2 \times d_2} = E[\tilde{\mathbf{h}}_{1,d_2} \tilde{\mathbf{h}}_{1,d_2}^{\mathrm{H}}]$ is the auto-correlation of the MS-1 uplink channel gains associated to the d_2 second-frame error bits: $\tilde{\mathbf{h}}_{1,d_2} = \sqrt{E_s} [h_1(\tau_{\mathbf{c},d_1+1}) \cdots h_1(\tau_{\mathbf{c},d_1+d_2})]^{\mathrm{T}} / \sigma_{\mathrm{n}}$. The matrix $[\mathbf{R_{c}},1]_{d_1 \times d_2} = E[\tilde{\mathbf{h}}_{1,d_1} \tilde{\mathbf{h}}_{1,d_2}^{\mathrm{H}}]$ denotes the cross-correlation between $\tilde{\mathbf{h}}_{1,d_1}$ and $\tilde{\mathbf{h}}_{1,d_2}$. Notice that the sum in (16) is due to the assumption that the two sets of N_2 bits received from MS-1 and MS-2 during the second frame are optimally combined at the receiver using a maximum ratio combiner (MRC).

IV. SIMULATION RESULTS

In this Section we provide both numerical and analytical results on the performance of coded cooperation. The numerical results are obtained by Monte-Carlo simulations, BER results are obtained by averaging over a large number of frames. In Sect. IV-A, we validate the exact derivation (12) and the upperbound (13) on the average PEP by evaluating the average BER performance of coded cooperation for ideal inter-MS channel ($\Theta = 1$). Next, by removing the assumption of error-free inter-MS channel, more insight is given on the conditions for which coded cooperation can be regarded as competitive in terms of performance compared to non-cooperative (direct) transmission (Sect. IV-B): the cooperative regions for coded cooperation over time-varying channels are defined through examples.

A. Performance limits of coded cooperation

The results presented here refer to the case of ideal inter-MS channel, the best case for coded cooperation. The aim is to show the mobility conditions for which coded cooperation gains significantly. We employ a rate $R = 1/4$ RCPC mother-code [9], with octal generators (23, 35, 27, 33) and free distance $d_{\mathrm{free}} = 15$. The mother-code is punctured, obtaining a rate $R_1 = 1/2$ sub-codeword for the first frame transmission ($\alpha = 50\%$). A soft-input hard-output Viterbi decoder is implemented at the receiver-side [11] and the error events $\mathbf{c}$ are found via computer-enumeration. The coded-block length is $N = 512$ bits, resulting in $M = 256$ QPSK symbols. Before symbol mapping, the coded bits are interleaved by a block bit-interleaver, which writes the input codeword row by row in a (128×4) matrix, and then reads it column by column. The two MSs transmit on independent time-varying flat-fading channels with average SNR $\bar{\gamma}_i$ and time-bandwidth product TBP_i, with $i \in \{1, 2\}$. In Fig. 5, 6 and 7 the fading statistics are the same for both uplink channels, i.e. $\bar{\gamma} = \bar{\gamma}_i$ and $\mathrm{TBP} = \mathrm{TBP}_i$, which is almost true if the two MSs are moving at the same speed and are close to each other with respect to the location of the BS. The Clarke's model is implemented as in [14], [15, App. A].

In Fig. 5 and 6, the average BER performance of cooperative and non-cooperative systems is plotted versus the average SNR $\bar{\gamma}$ for different values of TBP. A vehicle-to-vehicle communication system is considered with carrier frequency $f_{\mathrm{C}} = 5.2$GHz. The symbol duration is set to $T_{\mathrm{S}} = 10\mu\mathrm{s}$, this ensure that the channel' spectrum is flat[2]. The time-bandwidth product TBP is chosen as performance metric to assess the degree of temporal variability of the channel (compared to the length of the codeword), as an example, when the MSs exhibit velocities up to $v = 160$km/h, the time-bandwidth product TBP goes proportionally up to 4. The analytical BER

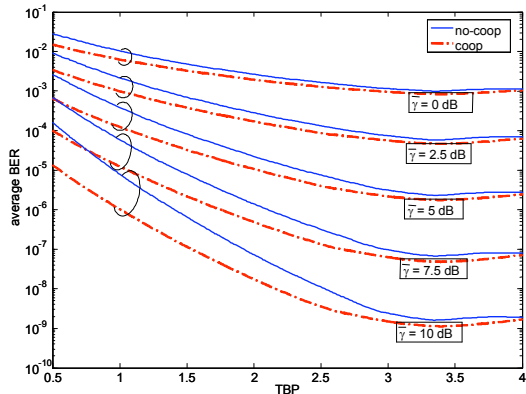[2]Recent channel measurements presented in [16] show that the delay spread at $f_{\mathrm{C}} = 5.2$GHz is around 1μs.

Fig. 7. Full cooperation ($\Theta = 1$) and no-cooperation ($\Theta = 2$) performance comparison. Code-rate $R = 1/4$.

Fig. 8. Performance of MS-1 for asymmetric uplink channel conditions: MS-1 moves with $TBP_1 = 1$ and $\bar{\gamma}_1 = 10$dB; MS-2 moves at different velocities with varying $\bar{\gamma}_2$. Full coded cooperation and no-cooperation are compared. Code-rate $R = 1/4$.

Fig. 9. Performance of the four cases of coded cooperation at $\bar{\gamma} = 7.5$dB: truncated bounds and simulation results. Partial cooperation is adavantageous or disadvantageous from the point of view of one MS. Code-rate $R = 1/3$.

bounds are computed by truncating the first summation in (5) at $d = 23$, or at values that are smaller but sufficient to upper bound the simulation results. The average PEP is computed both according to (12) and (13), (for the latter we truncate (5) at $d_{\text{free}} = 15$). We observe that the performance for increasing TBP moves to the one obtained for FF.

In Fig. 7 the bounds on the average BER are plotted versus the TBP. Coded cooperation and no-cooperation are compared at different average SNR values $\bar{\gamma}$. Up to TBP ≈ 3 ($v = 120$km/h), the performance gain of coded cooperation increases with increasing average SNR. At higher velocities the gain is almost negligible, which means that benefits of coded cooperation vanish for TBP $\gtrsim 3$.

We analyze now the case where the uplink channels are unbalanced (thus showing different values of average SNR and/or velocity). In Fig. 8 MS-1 moves at $TBP_1 = 1$ and transmits on a channel with average SNR $\bar{\gamma}_1 = 10$dB. On the other hand, average SNR for MS-2 varies from 5dB to 10dB, and time-bandwidth product $TBP_2 = \{0, 0.5, 1\}$. The performance results suggest that coded cooperation outperforms remarkably no-cooperation only if the MSs are moving approximately at the same speed. The larger is the difference between MSs' velocities, the less advantageous it is for the fastest MS to cooperate. This result can be useful in case partner selection can be allowed [4].

We argue that the conclusions drawn in this Section are valid for every good RCPC code, because the diversity gain is carried by the cooperation scheme (space-diversity) and the bit-interleaving (time-diversity), independently from the specific code.

B. Cooperative regions

We now consider the more realistic case of imperfect inter-MS channel. We also adopt a RCPC code with higher rate than the one in Sect. IV-A to allow for a reasonable simulation complexity. The adopted RCPC mother-code, with octal
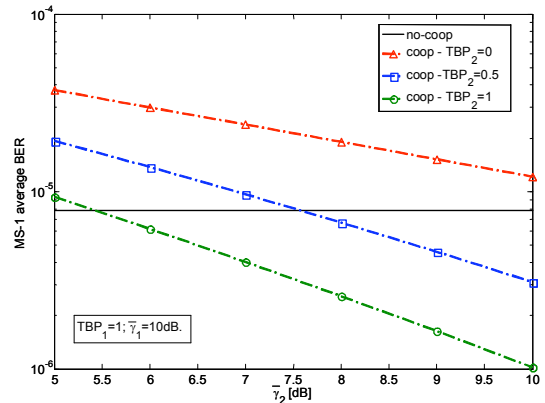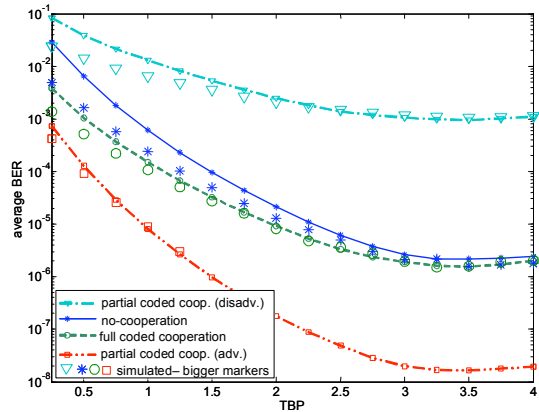
generators (15, 17, 13), has rate $R = 1/3$ and free distance $d_{\text{free}} = 10$. The coded-block length is $N = 384$ bits, resulting in $M = 192$ QPSK symbols. The punctured code has rate $R_1 = 1/2$, with code-length $N_1 = \frac{2N}{3}$ ($\alpha \simeq 33\%$). The coded bits are interleaved by a block bit-interleaver (96×4). Average BER performance for the four cases of coded cooperation (see Sect. II) are depicted in Fig. 9 for an average SNR of both uplink channels $\bar{\gamma} = 7.5$dB and varying degree of temporal variability TBP. In accordance with the results in Sect. IV-A, the coded cooperation (for the case $\Theta = 1$) does not provide any significant gain with respect to non-cooperative case for TBP ≥ 3. The upperbound (5), with PEP computed as in (12) and error event autocorrelation matrices according to (10) and (15) - (17), are truncated at $d = 14$,

Fig. 10. Performance of coded cooperation at different inter-MS block error probability p compared to no-cooperation at $\bar{\gamma} = 7.5$dB. Code-rate $R = 1/3$.

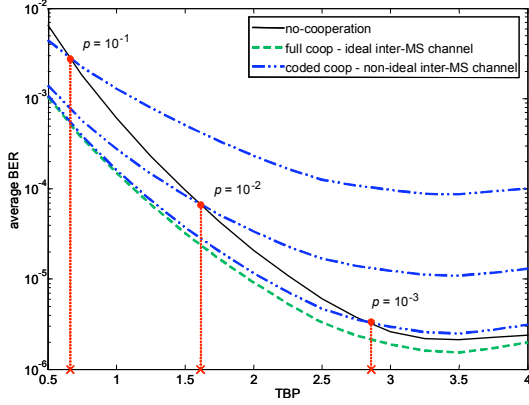Fig. 11. *Cooperative regions* for coded cooperation at different $\bar{\gamma}$. Coded cooperation outperforms no-cooperation in the region below the analytical boundary. Code-rate $R = 1/3$.

Fig. 12. *Cooperative regions* for MS-1. Uplink channels are both at $\bar{\gamma} = 10$dB, but MS-2 velocity is β times smaller than MS-1 velocity. Code-rate $R = 1/3$.

or at smaller values, in order to get tighter bounds for the subsequent analysis. These bounds are weighted as in (14) for different values of the inter-MS block error probability p and compared to no-cooperation in Fig. 10. As far as the mobility degree becomes large enough, the average BER performance of coded cooperation with non-ideal inter-MS channel is increasingly dominated by the worst case partial cooperation ($\Theta = 4$), as expected. The comparison between cooperative and non-cooperative transmission in terms of BER performances shows that the mobility degree threshold (cross markers in Fig. 10), beyond which coded cooperation is no more advantageous, decreases with decreasing quality of the inter-MS channel. For instance, coded cooperation with inter-MS block error probability $p = 10^{-3}$ is advantageous only up to TBP $\simeq 2.5$ for the considered code and channel settings. Furthermore, analytical and numerical results reveal that this threshold strongly depends on the quality of the relayed links ($\bar{\gamma}$).

The *cooperative region* is the collection of mobility (TBPs) and channel ($\bar{\gamma}$, p) settings for which coded cooperation is beneficial in providing enhanced average BER performance with respect to the non-cooperative case. The cooperative regions are illustrated as shaded areas delimited by solid lines in Fig. 11. For different values of the average SNR $\bar{\gamma}$, shaded areas contain the collection of values (TBP, p) for which coded cooperation provides superior performances compared to non-cooperative transmission. Interestingly, we observe that, for $\bar{\gamma} < 10$dB, the cooperative region spans the entire TBP range considered: the most promising opportunities to exploit the benefits of coded cooperation (in time-varying fading) arise for those applications where energy efficiency (for low SNR) is a key issue. Reasonably, the cooperative region size increases (decreases) with decreasing (increasing) average SNR $\bar{\gamma}$. In Fig. 12, the cooperative region for MS-1 is depicted by assuming the uplink channels with average SNR $\bar{\gamma} = 10$dB,
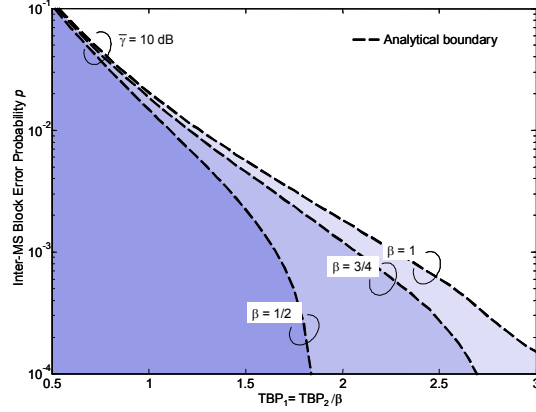
while the degree of mobility of MS-2 is lower compared to MS-1 as $\text{TBP}_2 = \beta \times \text{TBP}_1$ with $\beta < 1$. As expected from the analysis in Sect. IV-A, the cooperative region for MS-1 becomes smaller if the partner moves at lower velocities ($\text{TBP}_2 < \text{TBP}_1$).

V. CONCLUSIONS

We have provided an analytical method to evaluate the average BER performance of coded cooperation over time-varying flat fading channels. The key idea lies in recognizing the algebraic structure of the fading channel autocorrelation matrix associated to the decision variable. The theoretical results have been corroborated and validated by simulation results. The present work has focused on a generic single-carrier transmission system with narrowband channels, but

the methodology can be transposed to broadband frequency-selective OFDM systems taking into account the correlation of the fading channel over the subcarriers. The analysis has at first encompassed the widest range of temporal variability of the fading process, from the BF to the FF model. However, the temporal variability strictly depends on the velocity of the mobile stations, which is necessarily limited. This physical limitation has been taken into account by circumscribing the performance evaluations to a more realistic range of temporal variability of the channel.

Analytical results, validated by simulations, have shown that coded cooperation, in the best case of error-free inter-MS channel, outperforms significantly a comparable non-cooperative transmission only up to a certain degree of mobility, approximately when the time-bandwidth product $\text{TBP} \lesssim 3$ (corresponding to the speed $v = 120\text{km/h}$ in a system with carrier frequency $f_C = 5.2\text{GHz}$, symbol duration $T_S = 10\mu s$ and code block length $M = 256$ symbols). Beyond this limit, coded cooperation and non-cooperative transmissions perform similarly, since the gain offered by the time diversity is now dominant.

We have also investigated how the MSs' speed difference and the degradation of the inter-MS channel quality affect the BER performance. As expected, the larger is the speed difference the less advantageous it is to cooperate for the fastest MS. However, it has been shown that, for the MS moving at twice the velocity of the partner, coded cooperation improves significantly the performance with respect to no-cooperation up to $\text{TBP} \simeq 1.5$ ($v = 60\text{km/h}$). Furthermore, the increase of the inter-MS block error probability has been proven to be a penalty factor for coded cooperation performance. For instance, coded cooperation in symmetric uplink channels' conditions performs better than no-cooperation at $\text{TBP} = 2.5$, average SNR $\bar{\gamma} = 10\text{dB}$ and inter-MS block error probability $p = 10^{-4}$, while performing worse as the inter-MS block error probability raises to $p = 10^{-3}$. The *cooperative region* have been derived in order to provide more insight to the analysis by defining the mobility and channel settings for which coded cooperation provides better performance than no-cooperation. The proposed approach can be used in network design in order to define algorithms for the selection of the cooperating MSs and the optimization of the cooperation level [4].

We believe that the present work contributes to build the base for future evaluations of coded cooperation in real mobile communication systems, with the support of detailed channel and mobility models.

ACKNOWLEDGEMENTS

REFERENCES

[1] J. N. Laneman, D. N. C. Tse and G. W. Wornell, "Cooperative diversity in wireless networks: efficient protocols and outage behavior," *IEEE Trans. Inform. Theory*, vol.50, pp.3062-3080, Dec. 2004.

[2] T. E. Hunter and A. Nosratinia, "Cooperation diversity through coding," in *Proc. IEEE ISIT*, July 2002, p. 220.

[3] D. Tse and P. Viswanath, *Fundamentals of Wireless Communication*, Cambridge University Press, 2005.

[4] S. Valentin and H. Karl, "Effect of user mobility in coded cooperative systems with joint partner and cooperation level selection," in *Proc. IEEE WCNC*, March 2007, pp. 896-901.

[5] Z. Lin, E. Erkip, A. Stefanov, "Cooperative regions and partner choice in coded cooperative systems," *IEEE Trans. Commun.*, vol. 54, pp. 1323-1334, Jul. 2006.

[6] J. Proakis, *Digital Communications*, 4th Ed., McGraw Hill, 2001.

[7] K.Witrisal, Y.Kim, R.Prasad, "A novel approach for performance evaluation of OFDM with error correction coding and interleaving," in *Proc. IEEE VTC Fall*, Sep. 1999, Vol. 1, pp. 294-299.

[8] D. Molteni, M. Nicoli, R. Bosisio, L. Sampietro, "Performance analysis of multiantenna WiMax systems over frequency-selective fading channels," in *Proc. IEEE PIMRC*, Athens, Sep. 2007.

[9] J. Hagenauer, "Rate-compatible punctured convolutional codes (RCPC codes) and their applications," *IEEE Trans. Commun.*, vol. 38, pp. 389-400, Nov. 1988.

[10] R. H. Clarke, "A statistical theory of mobile-radio reception," *Bell Syst.Tech. J.*, p. 957, Jul.–Aug. 1968.

[11] S. Lin and J. D. Costello, *Error Control Coding - Fundamentals and Application*, Prentice-Hall, 2003.

[12] M.K. Simon, M.S. Alouini, *Digital communications over fading channels: a unified approach to performance analysis*, Wiley, 2000.

[13] J. W. Craig, "A new, simple, and exact result for calculating the probability of error for two-dimensional signal costellations," in *Proc. IEEE MILCOM*, Nov. 1991, vol. 2, pp. 571-575.

[14] Y. R. Zheng and C. Xiao, "Simulation models with correct statistical properties for Rayleigh fading channels," *IEEE Trans. Commun.*, vol. 51, no. 6, pp. 920-928, June 2003.

[15] T. Zemen and C. F. Mecklenbräuker, "Time-variant channel estimation using discrete prolate spheroidal sequences," *IEEE Trans. Signal Processing*, vol. 53, no. 9, pp. 3597-3607, Sep. 2005.

[16] A. Paier et al, "Non-WSSUS vehicular channel characterization in highway and urban scenarios at 5.2 GHz using the local scattering function," in *Proc. IEEE WSA*, Darmstadt, Germany, Feb. 2008.

Receive Antenna Selection For Time-Varying Channels Using Discrete Prolate Spheroidal Sequences

Hassan A. Abou Saleh, *Student Member, IEEE,* Andreas F. Molisch, *Fellow, IEEE,* Thomas Zemen, *Senior Member, IEEE,* Steven D. Blostein, *Senior Member, IEEE,* and Neelesh B. Mehta, *Senior Member, IEEE*

Abstract—Receive antenna selection (AS) has been shown to maintain the diversity benefits of multiple antennas while potentially reducing hardware costs. However, the promised diversity gains of receive AS depend on the assumptions of perfect channel knowledge at the receiver and slowly time-varying fading. By explicitly accounting for practical constraints imposed by the next-generation wireless standards such as training, packetization and antenna switching time, we propose a single receive AS method for time-varying fading channels. The method exploits the low training overhead and accuracy possible from the use of discrete prolate spheroidal (DPS) sequences based reduced rank subspace projection techniques. It only requires knowledge of the Doppler bandwidth, and does not require detailed correlation knowledge. Closed-form expressions for the channel prediction and estimation error as well as symbol error probability (SEP) of M-ary phase-shift keying (MPSK) for symbol-by-symbol receive AS are also derived. It is shown that the proposed AS scheme, after accounting for the practical limitations mentioned above, outperforms the ideal conventional single-input single-output (SISO) system with perfect CSI and no AS at the receiver and AS with conventional estimation based on complex exponential basis functions.

I. INTRODUCTION

To accommodate the rate and reliability requirements set by forthcoming applications such as wireless broadband access and mobile television, next-generation wireless standards such as IEEE 802.11n [1] and long term evolution (LTE) of the third generation partnership project (3GPP) [2] have adopted multiple-input multiple-output (MIMO) technology, orthogonal frequency division multiplexing (OFDM) and/or orthogonal frequency division multiple access (OFDMA) as signalling formats over the physical channel. Further, AS at the transmitter and/or receiver has been standardized, e.g., in IEEE 802.11n, or is being standardized [3].

Antenna selection may be used to reduce hardware complexity at the transmitter and/or receiver of a wireless system. In AS, only a subset of the antenna elements (AEs) is connected to a limited number of radio-frequency (RF) chains based on the current channel fades. This potentially retains the advantages of multiple antennas, despite using fewer of the expensive RF chains that are comprised of low-noise amplifiers (LNAs), mixers, and oscillators [4], [5]. We focus here on the practical single receive AS scenario because it retains most of the diversity benefits of multiple antennas while minimizing hardware complexity. As will be shown, performance evaluation of even the single AS problem is very challenging.

There are a number of existing studies on both optimal and suboptimal AS algorithms [6], [7] as well as on the capacity, diversity, and diversity-multiplexing (D-M) performance of AS [8]–[13]. However, to date, far fewer studies exist that deal with the practical issues of pilot-based training and AS implementation. A media-access-control (MAC) based AS training and calibration protocol, in which the AEs are trained using packets transmitted in burst mode is proposed in [14] for slowly time-varying environments. The protocol in [14] is adopted in the IEEE 802.11n standard for high-throughput wireless local area networks (WLANs).

In the above references, perfect channel knowledge is assumed. However, the mobile communication environment exhibits a randomly time-varying channel due to the mobility of users and reflections from multiple scatterers. This implies that channel state information (CSI) gets rapidly outdated, limiting the accuracy of the channel knowledge at the receiver. The impact of erroneous CSI on the performance of a space-time coded AS system in Rayleigh fading is studied in [15]. The performance of maximal ratio transmission (MRT) and transmit antenna selection with space-time block coding (TAS/STBC) in MIMO systems with both CSI feedback delay and channel estimation error is analyzed in [16]. An analytical framework to evaluate the symbol error probability (SEP) performance for diversity systems in which a subset of the available diversity branches are selected and combined over flat Rayleigh fading with imperfect channel knowledge is developed in [17]. Receive AS for space-time-frequency (STF) coded MIMO-OFDM systems with imperfect channel estimation is studied in [18]. The effects of feedback delay and channel estimation errors on the performance of a MIMO system employing AS at the transmitter and maximal ratio

combining (MRC) at the receiver is studied in [19]. In [19], it is shown that channel estimation errors result in a fixed signal-to-noise ratio (SNR) loss while feedback delay alters the diversity order.

Motivated by the fact that AE channel gain estimates are outdated by different amounts in time-varying channels, a single-antenna selection rule is proposed in [20] which minimizes the SEP of M-ary PSK (MPSK)/MQAM by linearly weighting the channel estimates before selection. In [20], it is shown that the optimal weights are proportional to the temporal channel correlation coefficients of the antennas. The general case of selecting more than one antenna and the problem of *training voids* have been recently treated in [21]. However, it is worth mentioning that only channel gain estimates obtained during the *AS training phase* are used in the selection and decoding mechanisms in [20] and [21] since channel gain estimates over the *data transmission phase* are not available, which incurs a loss in SNR. We also note that the weighted selection criterion used in [20] and [21] requires temporal correlation knowledge.

The above observations motivate investigation into practical training-based AS algorithms for time-varying channels which use channel knowledge in the data transmission phase in the selection and decoding processes by utilizing channel prediction. It is important to highlight that the optimal Wiener predictor utilizes detailed covariance knowledge, which is difficult to obtain due to bursty transmission, or over the short time interval in which the channel is wide-sense stationary in vehicular scenarios [22]. This motivates the use of the recently-proposed low-complexity Slepian basis expansion channel estimator [23] and channel predictor [22] to obtain reliable CSI at the receiver. This Slepian basis expansion estimator/predictor uses discrete prolate spheroidal (DPS) sequences as basis functions which enables low-complexity reduced-rank channel estimation/prediction. Furthermore, in contrast to many linear estimation/prediction techniques that require detailed autocorrelation knowledge, it requires only knowledge of the Doppler bandwidth. In [23], the Slepian basis expansion channel estimator is used to estimate the time-varying channel for each subcarrier of a multiuser multi-carrier code division multiple access (MC-CDMA) system. It is shown that with a pilot-to-packet length ratio of only 2%, the bit error rate (BER) of the system approaches that of a system with perfect CSI. It is shown in [22] that for a prediction horizon of one eighth of a wavelength, the Slepian basis expansion channel predictor outperforms the classical predictor that uses complex exponentials as the basis. We note that the complex exponential predictor utilizes the exact Doppler frequencies of each propagation path of the channel. For a prediction horizon of three eighths of a wavelength, the performance of the Slepian basis expansion channel predictor is shown to be very close to that of the optimal Wiener predictor.

In this paper, we propose and analyze the performance of a training-based single receive AS system in time-varying channels that uses the Slepian basis expansion predictor and estimator. The paper's contributions are summarized as follows:

- A method for accurately estimating/predicting time-

varying frequency-flat channels, which utilizes projections onto a subspace spanned by orthonormal DPS sequences [22], [23], is extended to AS.
- Closed-form expressions are provided for the channel prediction and estimation error as well as the SEP of MPSK with receive AS, and verified with Monte Carlo simulation results.
- Extensive simulation results are presented to compare the performance of the proposed AS method with ideal conventional single-input single-output (SISO) systems with perfect CSI but no AS at the receiver and AS based on prediction/estimation techniques that are based on complex exponential basis functions.

The paper is organized as follows: the detailed system model is described in Sec. II, and the Slepian basis expansion predictor and estimator are then introduced in Sec. III. The training-based receive AS method is described in Sec. IV. The SEP is analyzed in Sec. V. Analytical and simulation results are discussed in Sec. VI. Our conclusions follow in Sec. VII. Detailed mathematical derivations are provided in the Appendix.

II. SYSTEM MODEL

Consider the downlink of a cellular radio system consisting of a single-antenna base station (BS) transmitting to a K-antenna element (AE) mobile station (MS) equipped with only one RF chain as depicted in Fig. 1. A micro-electromechanical system (MEMS) based antenna switch connects the selected AE to the RF chain; such switches provide sufficient switching speeds while keeping the insertion loss in the order of 0.1 dB, which is negligible.

Each AS cycle consists of an *AS training phase* followed by a *data transmission phase*, as illustrated in Fig. 2. We first introduce DPS sequences which are used to predict/estimate the time-varying channel over the data transmission phase as shown in Sec. III, and then describe the AS training and data transmission phases.

A. Discrete Prolate Spheroidal (DPS) Sequences

The orthogonal DPS sequences are simultaneously band-limited to the frequency range $\mathcal{W} = (-\nu_{\max}, +\nu_{\max})$ and energy-concentrated in the time interval $\mathcal{I}_{\mathrm{bl}} = \{0, 1, \ldots, M' - 1\}$, where the normalized one-sided Doppler bandwidth $\nu_{\max}$ is given by

$$\nu_{\max} \triangleq \frac{v_{\max} f_{\mathrm{c}}}{c} T_{\mathrm{s}} \ll \frac{1}{2} \tag{1}$$

where $v_{\max}$ is the radial component of the user velocity, f_{c} is the carrier frequency, and c is the speed of light. The M' DPS sequences $\{u_i[m] \mid m \in \mathbb{Z}\}_{i=0}^{M'-1}$ are defined as the real solutions to the following system of linear equations [23]

$$\sum_{l=0}^{M'-1} C[l-m]\, u_i[l] = \lambda_i\, u_i[m], \qquad m \in \mathbb{Z},\ i \in \mathcal{I}_{\mathrm{bl}} \tag{2}$$

where
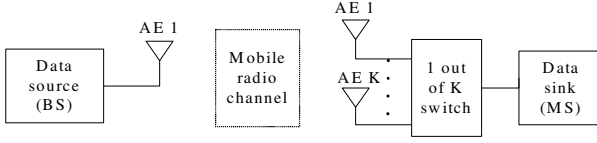
$$C[l-m] = \frac{\sin(2\pi\nu_{\max}(l-m))}{\pi(l-m)}. \tag{3}$$

Fig. 1. Antenna selection system model.

Fig. 2. Antenna selection cycle consists of AS training and data transmission phases. (AE 1 is selected, $K = 2$, $L = 2$, $L' = 2$, and $T_\text{p} = 2\,T_\text{s}$).

The eigenvalues $\{\lambda_i\}_{i=0}^{M'-1}$ decay exponentially for $i \geq D'$, where the essential subspace dimension D' is given by [23]

$$D' = \lceil 2\,\nu_\text{max}\,M' \rceil + 1 \qquad (4)$$

and $\lceil x \rceil$ denotes the smallest integer greater than or equal to x.

As mentioned earlier, the DPS sequences $\{u_i\,[m] \mid m \in \mathbb{Z}\}_{i=0}^{M'-1}$ are orthogonal. Further, even the restrictions of the DPS sequences on $\mathcal{I}_\text{bl}$, i.e., $\{u_i\,[m] \mid m \in \mathcal{I}_\text{bl}\}_{i=0}^{M'-1}$, are orthonormal [23], and, thus, form a set of M'-length basis vectors $\{\boldsymbol{u}_i\}_{i=0}^{M'-1}$. Based on (2), the length-M' basis vectors $\{\boldsymbol{u}_i\}_{i=0}^{M'-1}$ are, thus, the eigenvectors of the $M' \times M'$ matrix $\boldsymbol{C}$ [23]

$$\boldsymbol{C}\,\boldsymbol{u}_i = \lambda_i\,\boldsymbol{u}_i \qquad (5)$$

where $M' \times 1$ basis vector $\boldsymbol{u}_i \triangleq \left[u_i\,[0], u_i\,[1], \ldots, u_i\,[M'-1]\right]^T$ with $(\cdot)^T$ denoting the transpose. The entries of $\boldsymbol{C}$ are formed from (3) as $[\boldsymbol{C}]_{l,m} = C\,[l-m]$ for $l,\,m \in \mathcal{I}_\text{bl}$. As shown in Sec. III-A, the DPS sequences time-limited to $\mathcal{I}_\text{bl}$, which form an orthonormal set of basis functions $\{\boldsymbol{u}_i\}_{i=0}^{M'-1}$, can be used to estimate the time-varying channel over $\mathcal{I}_\text{bl}$.

B. AS Training Phase

In each *AS training phase*, the BS transmits $L \geq 2$ training symbols sequentially in time to each antenna. We note here that more than one pilot symbol is needed in order to employ AS in time-varying channels to improve channel prediction. Pilot symbols are used to estimate the predictor's basis expansion coefficients as discussed in Sec. III. We also note that the 3GPP-LTE standard uses two training symbols within a 1 ms duration to improve channel estimation. The duration between consecutive pilots for AE k and AE $k+1$ is $T_\text{p} \triangleq \alpha\,T_\text{s}$, where T_s is the symbol duration and $\alpha \geq 2$. Two consecutive AS training pilots transmitted for each AE are thus separated in time by a duration of $T_\text{t} \triangleq K\,T_\text{p} = \alpha\,K\,T_\text{s}$. The pilot and data symbol duration T_s is assumed to be much longer than the delay spread and much shorter than the coherence time of the channel, i.e., the channel is frequency-flat time-varying. The data symbols are drawn with equal probability from an MPSK constellation of average energy $E_\text{s} = 1$.

Let m index discrete time with sampling rate $R_\text{s} \triangleq \frac{1}{T_\text{s}}$. The channel gain $h_k\,[m]$ is estimated from the AS training pilot symbol $p_k\,[m]$ that is received by AE k at time $m \in T_\text{tr}^k$. The received signal is

$$y_k\,[m] = h_k\,[m]\,p_k\,[m] + n_k\,[m], \qquad 1 \leq k \leq K,\ m \in T_\text{tr}^k \qquad (6)$$
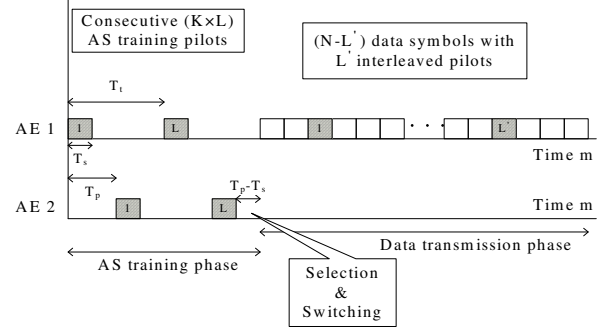
where

$$T_\text{tr}^k \triangleq \{\alpha\,[(k-1) + K\,(\ell-1)]\}, \qquad 1 \leq \ell \leq L \qquad (7)$$

denotes the set of time indices when the L AS training pilots are received by AE k, $h_k\,[m]$ is the sampled time-varying channel gain, and $n_k\,[m]$ is additive white Gaussian noise (AWGN) with variance N_0 and is independent of $h_k\,[m]$. Based on (6), channel gain estimates $\left\{\tilde{h}_k\,[m] \mid m \in T_\text{tr}^k\right\}$ for AE k can be expressed as

$$\begin{aligned}\tilde{h}_k\,[m] &= y_k\,[m]\,p_k^*\,[m] \\ &\triangleq h_k\,[m] + e_k^\text{n}\,[m], \quad 1 \leq k \leq K,\ m \in T_\text{tr}^k\end{aligned} \qquad (8)$$

where $(\cdot)^*$ denotes complex conjugate and $e_k^\text{n}\,[m] \triangleq n_k\,[m]\,p_k^*\,[m]$ is the channel estimation error resulting from the AWGN. From (7) and accounting for the additional selection and switching time of duration $T_\text{p} - T_\text{s}$, it follows that the *AS training phase* spans the discrete time interval $\mathcal{I}_\text{tr} = \{0, 1, \ldots, M-1\}$, where $M = \alpha\,K\,L$.

Using the noisy channel estimates $\left\{\tilde{h}_k\,[m] \mid m \in T_\text{tr}^k\right\}$, the receiver performs minimum-energy (ME) band-limited channel prediction [22] for each antenna over the *data transmission phase* time interval $\mathcal{I}_\text{dt} = \{M, M+1, \ldots, M+N-1\}$. Denote the predicted channel gains by $\left\{\hat{h}_k^\text{SP}\,[m] \mid m \in \mathcal{I}_\text{dt}\right\}$, where the superscript $(\cdot)^\text{SP}$ indicates Slepian prediction [22]. The MS selects its receive antenna according to a certain criterion, and then switches its RF chain accordingly.

Depending on the AS switching time, either per-packet or symbol-by-symbol AS can be used. For example, solid-state switches achieve switching times on the order of hundreds of nanoseconds, which is less than typical cyclic prefixes, and thus enable the switching of antennas between symbols. Thus, different symbols of a packet may be received by their most suitable AEs as the channel varies with time. However, these switches have attenuations on the order of 1 to 3 dB. In contrast, MEMS switches have attenuations on the order of 0.1 to 0.3 dB, but achieve switching times on the order of microseconds, and thus typically enable only per-packet switching. We note as the AS switching times and attenuations decrease, symbol-by-symbol switching may become viable in

futuristic systems. Furthermore, similar to 802.11n, per-packet switching can be enabled by modifications of the MAC layer, while per-symbol switching requires changes to the physical-layer standard. Therefore, both symbol-by-symbol and per-packet switching are relevant, and are both considered in our analysis. We denote by $\hat{\imath}$ the index of the selected antenna, with $(\hat{\cdot})$ indicating that the selection is based on (imperfect) prediction and/or estimation.

C. Data Transmission Phase

In each *data transmission phase* the BS sends out a length-N data packet, which consists of $N - L'$ data symbols and L' interleaved post-selection pilot symbols. The symbol locations in the packet that carry the pilots are given by [23]

$$\mathcal{P} \triangleq \left\{ \left\lfloor (\ell' - 1) \frac{N}{L'} + \frac{N}{2L'} \right\rfloor \mid 1 \leq \ell' \leq L' \right\} \quad (9)$$

where $\lfloor x \rfloor$ denotes the largest integer not greater than x. After selection, the pilots are received by AE $\hat{\imath}$ at times $m \in T_{\text{dt}}$, where

$$T_{\text{dt}} \triangleq \left\{ M - 1 + \left\lfloor (\ell' - 1) \frac{N}{L'} + \frac{N}{2L'} \right\rfloor \mid 1 \leq \ell' \leq L' \right\} \quad (10)$$

and $M = \alpha K L$. Thus, in total, $L_{\text{tot}} \triangleq L + L'$ pilot symbols are received by AE $\hat{\imath}$ at times $m \in T_{\text{tot}}^{\hat{\imath}}$, where

$$T_{\text{tot}}^{\hat{\imath}} = T_{\text{tr}}^{\hat{\imath}} \cup T_{\text{dt}} \quad (11)$$

with $T_{\text{tr}}^{\hat{\imath}}$ and T_{dt} given in (7) and (10), respectively. From these L_{tot} pilots, refined channel gain estimates $\left\{ \hat{h}_{\hat{\imath}}^{\text{SE}} [m] \mid m \in \mathcal{I}_{\text{dt}} \right\}$ of the selected AE $\hat{\imath}$ are obtained using the Slepian basis expansion channel estimator [23] and used to decode data. The received signal at AE $\hat{\imath}$ can be expressed as

$$y_{\hat{\imath}} [m] = h_{\hat{\imath}} [m] \, s [m] + n_{\hat{\imath}} [m], \qquad m \in \mathcal{I}_{\text{dt}} \quad (12)$$

where the transmitted symbol $s[m]$ is given by

$$s [m] = \begin{cases} d [m], & m \in \mathcal{I}_{\text{dt}} \backslash T_{\text{dt}} \\ p [m], & m \in T_{\text{dt}} \end{cases} . \quad (13)$$

Here, $d[m]$ and $p[m]$ denote the transmitted data and post-selection pilot symbols, respectively.

III. REDUCED-RANK CHANNEL ESTIMATION AND MINIMUM-ENERGY BAND-LIMITED PREDICTION

A. Reduced-Rank Channel Estimation

To enable estimation of a time-varying channel for a length-M' block of data transmission, $M' - J$ data symbols and J interleaved pilot symbols are transmitted in a pattern specified by index set $\mathcal{J}$.

The aforementioned DPS sequences time-limited to $\mathcal{I}_{\text{bl}} = \{0, 1, \ldots, M' - 1\}$ are used to estimate the time-varying channel over time interval $\mathcal{I}_{\text{bl}}$. The basis expansion estimator approximates the $M' \times 1$ true channel vector $\boldsymbol{h} \triangleq \left[h[0], h[1], \ldots, h[M'-1] \right]^T$ in terms of a linear combination $\hat{\boldsymbol{h}}^{\text{SE}}$ of D length-M' basis vectors $\{\boldsymbol{u}_i\}_{i=0}^{D-1}$ as [22]

$$\boldsymbol{h} \approx \hat{\boldsymbol{h}}^{\text{SE}} = \boldsymbol{U} \, \hat{\boldsymbol{\gamma}} = \sum_{i=0}^{D-1} \hat{\gamma}_i \, \boldsymbol{u}_i \quad (14)$$

where $\boldsymbol{U} \triangleq \left[\boldsymbol{u}_0, \ldots, \boldsymbol{u}_{D-1} \right]$ is an $M' \times D$ matrix, $\boldsymbol{u}_i \triangleq \left[u_i[0], u_i[1], \ldots, u_i[M'-1] \right]^T$, and D is the optimal sub-space dimension which minimizes the mean-square-error (MSE) in the above approximation. It is given by

$$D = \underset{d \in \{1, \ldots, J\}}{\text{argmin}} \left(\frac{1}{2 \, \nu_{\max} \, J} \sum_{i=d}^{J-1} \lambda_i + \frac{d}{J} N_0 \right) \quad (15)$$

where $\eta \triangleq \frac{E_s}{N_0}$ is the average SNR. In (15), the eigenvalues are assumed to be ranked as $\lambda_0 \geq \lambda_1 \geq \ldots \geq \lambda_{J-1}$. The $D \times 1$ vector $\hat{\boldsymbol{\gamma}} \triangleq \left[\hat{\gamma}_0, \hat{\gamma}_1, \ldots, \hat{\gamma}_{D-1} \right]^T$ contains the basis expansion coefficients. It is estimated using the J interleaved pilot symbols $\{p[l] \mid l \in \mathcal{J}\}$, received at times $l \in \mathcal{J}$, via [23]

$$\hat{\boldsymbol{\gamma}} = \boldsymbol{G}^{-1} \sum_{l \in \mathcal{J}} y[l] \, p^*[l] \, \boldsymbol{f}^*[l] \quad (16)$$

where $y[l]$ is the received signal, the $D \times 1$ vector $\boldsymbol{f}[l]$ is defined as $\left[u_0[l], \ldots, u_{D-1}[l] \right]^T$, and $\boldsymbol{G}$ is a $D \times D$ matrix given by

$$\boldsymbol{G} = \sum_{l \in \mathcal{J}} \boldsymbol{f}[l] \, \boldsymbol{f}^\dagger[l] \quad (17)$$

where $(\cdot)^\dagger$ denotes Hermitian transpose.

B. Minimum-Energy Band-Limited Channel Prediction

The ME band-limited predictor uses the extension of the DPS sequences that are time-limited to $\mathcal{I}_{\text{bl}}$ as the basis vectors. They are calculated by [22]

$$u_i [m] = \frac{1}{\lambda_i} \sum_{l=0}^{M'-1} C[l - m] \, u_i[l], \qquad m \in \mathbb{Z} \setminus \mathcal{I}_{\text{bl}}. \quad (18)$$

The ME band-limited prediction of a time-varying frequency-flat channel can be expressed as [22]

$$\hat{h}^{\text{SP}} [m] = \boldsymbol{f}^T [m] \, \hat{\boldsymbol{\gamma}} = \sum_{i=0}^{D-1} \hat{\gamma}_i \, u_i [m], \qquad m \in \mathbb{Z} \setminus \mathcal{I}_{\text{bl}} \quad (19)$$

where $\boldsymbol{f}[m] = [u_0[m], \ldots, u_{D-1}[m]]^T$.

IV. DOWNLINK RECEIVE ANTENNA SELECTION ALGORITHM

We propose the following training-based "one out of K" receive AS algorithm for time-varying channels for per-packet switching:

1) Following an AS request, each AE is trained using $L \geq 2$ pilot symbols. The spacing between consecutive AS training pilots transmitted for each AE is $T_t = \alpha K T_s$. To keep the *AS training phase* as short as possible, α is chosen as

$$\alpha = \left\lceil \frac{T_{\text{sw}}}{T_s} \right\rceil + 1 \quad (20)$$

where T_{sw} is the antenna switching time.

2) On receiving these AS training pilots, the receiver then:

   a) Obtains the preliminary channel gain estimates $\left\{ \tilde{h}_k [m] \mid m \in T_{\text{tr}}^k \right\}_{k=1}^K$ using (8).

b) Performs channel prediction for each AE over the data time interval $\mathcal{I}_{\mathrm{dt}}$ via (19)

$$\hat{h}_k^{\mathrm{SP}}[m] = \boldsymbol{f}^T[m]\,\hat{\boldsymbol{\gamma}}_k = \sum_{i=0}^{D-1} \hat{\gamma}_{k,i}\,u_i[m] \quad (21)$$

where $1 \le k \le K$, $m \in \mathcal{I}_{\mathrm{dt}}$, and D is calculated from (15) (with L replacing J). Slepian prediction sequences $\{u_i[m] \mid m \in \mathcal{I}_{\mathrm{dt}}\}_{i=0}^{D-1}$ are calculated from (18), and $\hat{\boldsymbol{\gamma}}_k \triangleq \left[\hat{\gamma}_{k,0}, \hat{\gamma}_{k,1}, \ldots, \hat{\gamma}_{k,D-1}\right]^T$ is of size $D \times 1$ and contains the basis expansion coefficients for AE k which are estimated via (16) $\left(\text{with } T_{\mathrm{tr}}^k \text{ replacing } \mathcal{J}\right)$.

c) Selects its receive AE $\hat{\imath}$ which maximizes the post-processing SNR over the data time interval $\mathcal{I}_{\mathrm{dt}}$, which consists of N symbol durations, as

$$\hat{\imath} = \underset{1 \le k \le K}{\arg\max} \sum_{m=M}^{M+N-1} \left|\hat{h}_k^{\mathrm{SP}}[m]\right|^2. \quad (22)$$

3) The single-antenna BS then sends out a length-N data packet which consists of $N - L'$ data symbols plus L' post-selection pilot symbols interleaved according to (9). Using the $L_{\mathrm{tot}} = L + L'$ pilots, refined channel gain estimates $\left\{\hat{h}_{\hat{\imath}}^{\mathrm{SE}}[m] \mid m \in \mathcal{I}_{\mathrm{dt}}\right\}$ are obtained by

$$\hat{\boldsymbol{h}}_{\hat{\imath}}^{\mathrm{SE}} = \boldsymbol{U}'\,\hat{\boldsymbol{\gamma}}_{\hat{\imath}} = \sum_{i=0}^{D-1} \hat{\gamma}_{\hat{\imath},i}\,\boldsymbol{u}_i' \quad (23)$$

where the $N \times 1$ vector $\hat{\boldsymbol{h}}_{\hat{\imath}}^{\mathrm{SE}} \triangleq \left[\hat{h}_{\hat{\imath}}^{\mathrm{SE}}[M], \hat{h}_{\hat{\imath}}^{\mathrm{SE}}[M+1], \ldots, \hat{h}_{\hat{\imath}}^{\mathrm{SE}}[M+N-1]\right]^T$, D is obtained from (15) (with L_{tot} replacing J), the $D \times 1$ vector $\hat{\boldsymbol{\gamma}}_{\hat{\imath}} \triangleq \left[\hat{\gamma}_{\hat{\imath},0}, \ldots, \hat{\gamma}_{\hat{\imath},D-1}\right]^T$ contains AE $\hat{\imath}$ basis expansion coefficients which are estimated using (16) (with $T_{\mathrm{tot}}^{\hat{\imath}}$ replacing $\mathcal{J}$), $\boldsymbol{U}' \triangleq \left[\boldsymbol{u}_0', \ldots, \boldsymbol{u}_{D-1}'\right]$ is the $N \times D$ *submatrix* of the *complete* $(M+N) \times D$ DPS sequences matrix $\boldsymbol{U}$. The vector $\boldsymbol{u}_i' \triangleq \left[u_i[M], u_i[M+1], \ldots, u_i[M+N-1]\right]^T$ is of size $N \times 1$.

We note that while other selection criteria may alternatively be used [20]; we consider the maximum total post-processing SNR criterion in (22).

Remark: In symbol-by-symbol AS, for each symbol an AE is selected. Since different AEs might be selected during the data transmission phase $\mathcal{I}_{\mathrm{dt}}$, L' pilots should be sent to each AE in the data transmission phase so that refined channel gain estimates can be obtained for each AE. Thus, the number of pilots is now KL'. Note that we still have $\mathcal{I}_{\mathrm{dt}} = \{M, M+1, \ldots, M+N-1\}$ since the switching time is less than the symbol duration. The above algorithm is converted into a symbol-by-symbol receive AS algorithm as follows: (i) In Step 2(c) the receiver then selects its receive AE, $\hat{\imath}_m$, for the data symbol at time m according to

$$\hat{\imath}_m = \underset{1 \le k \le K}{\arg\max} \left|\hat{h}_k^{\mathrm{SP}}[m]\right|^2. \quad (24)$$

To denote this alternative AS strategy, symbol index m has been added to $\hat{\imath}$ in (24). (ii) In Step 3 the BS sends out a

length-N data packet which consists of $N - KL'$ data symbols plus KL' pilots for the K AEs. Note that no AS is employed during the transmission of the KL' pilots. Thus, in total, $L_{\mathrm{tot}} = L + L'$ pilot symbols are received by each AE. From these L_{tot} pilots, refined channel gain estimates $\left\{\hat{h}_{\hat{\imath}_m}^{\mathrm{SE}}[m] \mid m \in \mathcal{I}_{\mathrm{dt}}\right\}$ are obtained using the Slepian basis estimator and used to decode data. To reduce overhead L' can be set to 1.

V. Symbol Error Probability (SEP) Analysis

In this section, we analyze the proposed receive AS algorithm from Section IV as well as the symbol-by-symbol receive AS, to evaluate the SEP of MPSK in time-varying channels.

A. Prediction and Estimation CSI Models

To derive closed-form expressions for the variances of the predicted/estimated channel gains and prediction/estimation errors, we first define the CSI uncertainty model for Slepian basis expansion estimation as

$$\hat{h}_k^{\mathrm{SE}}[m] = h_k[m] + e_k^{\mathrm{SE}}[m], \qquad 1 \le k \le K, \ m \in \mathcal{I}_{\mathrm{dt}} \quad (25)$$

where $\hat{h}_k^{\mathrm{SE}}[m]$ is the estimated channel gain, $h_k[m]$ is the true channel gain, and $e_k^{\mathrm{SE}}[m]$ is the estimation error. We assume the variables $h_k[m]$ and $e_k^{\mathrm{SE}}[m]$ are uncorrelated. The true channel gain $h_k[m]$ is modeled as a zero-mean circularly symmetric complex Gaussian random variable (RV) with unit-variance. The true channel gain is correlated over time. From (25), the variance of the channel gain estimate $\hat{h}_k^{\mathrm{SE}}[m]$ can be expressed as

$$\sigma_{\hat{h}_k^{\mathrm{SE}}}^2[m] = \sigma_{h_k}^2[m] + \sigma_{e_k^{\mathrm{SE}}}^2[m] = 1 + \mathrm{MSE}_k^{\mathrm{SE}}[m] \quad (26)$$

where $\mathrm{MSE}_k^{\mathrm{SE}}[m]$ is the MSE per sample for the Slepian basis expansion estimator of AE k.

The MSE per sample of the Slepian basis expansion estimator for AE k takes the form [22]

$$\mathrm{MSE}_k^{\mathrm{SE}}[m] = \left(\mathrm{bias}_k^{\mathrm{SE}}[m]\right)^2 + \mathrm{var}_k^{\mathrm{SE}}[m] \quad (27)$$

where $\mathrm{bias}_k^{\mathrm{SE}}[m]$ and $\mathrm{var}_k^{\mathrm{SE}}[m]$ are the bias and variance terms, respectively. In (27), the squared bias term can be expressed as [22]

$$\left(\mathrm{bias}_k^{\mathrm{SE}}[m]\right)^2 = \int_{-\frac{1}{2}}^{+\frac{1}{2}} E_k^{\mathrm{SE}}[m,\nu]\,S_h(\nu)\,\mathrm{d}\nu \quad (28)$$

where $S_h(\nu)$ is the power spectral density (PSD) of the time-varying channel $\{h[m]\}$, and $E_k^{\mathrm{SE}}[m,\nu]$ is the instantaneous error characteristic given by

$$E_k^{\mathrm{SE}}[m,\nu] = \left|1 - G_k^{\mathrm{SE}}[m,\nu]\right|^2. \quad (29)$$

Here, the instantaneous amplitude frequency response $G_k^{\mathrm{SE}}[m,\nu]$ is given by

$$G_k^{\mathrm{SE}}[m,\nu] = \boldsymbol{f}^T[m]\,\boldsymbol{G}_k^{-1} \sum_{l \in T_{\mathrm{tot}}^k} \boldsymbol{f}^*[l]\,\exp\left(-j2\pi\nu(m-l)\right). \quad (30)$$

In (27), $\text{var}_k^{\text{SE}}[m]$ can be well approximated by [23]

$$\text{var}_k^{\text{SE}}[m] \approx N_0 \, \boldsymbol{f}^\dagger [m] \, \boldsymbol{G}_k^{-1} \, \boldsymbol{f}[m]. \qquad (31)$$

The CSI model for the Slepian basis expansion predictor can be obtained from (25)–(31) by replacing superscript $(\cdot)^{\text{SE}}$ by $(\cdot)^{\text{SP}}$ and T_{tot}^k by T_{tr}^k in (30).

B. SEP Analysis

1) SEP of Per-Packet Basis Selection: We now analyze the SEP of an MPSK symbol received at time m of a system which employs the per-packet basis receive AS algorithm in Sec. IV. Note that the predicted channel gains $\left\{ \hat{h}_k^{\text{SP}}[m] \mid m \in \mathcal{I}_{\text{dt}} \right\}_{k=1}^K$ are used to select AE $\hat{\imath}$ to receive the length-N data packet, while the estimated channel gain $\hat{h}_{\hat{\imath}}^{\text{SE}}[m]$ is used to decode the received symbol at time m. The maximum-likelihood (ML) soft estimate for the symbol received by AE $\hat{\imath}$ at time m can be expressed as

$$
\begin{aligned}
r_{\hat{\imath}}[m] &= \left(\hat{h}_{\hat{\imath}}^{\text{SE}}[m] \right)^* y_{\hat{\imath}}[m] \\
&= \left| \hat{h}_{\hat{\imath}}^{\text{SE}}[m] \right|^2 d[m] - \left(\hat{h}_{\hat{\imath}}^{\text{SE}}[m] \right)^* d[m] \, e_{\hat{\imath}}^{\text{SE}}[m] \\
&\quad + \left(\hat{h}_{\hat{\imath}}^{\text{SE}}[m] \right)^* n_{\hat{\imath}}[m]
\end{aligned} \qquad (32)
$$

where the last equality follows from substitution of (12), (13), and (25). Conditioned on $\hat{h}_{\hat{\imath}}^{\text{SE}}[m]$ and $d[m]$, $r_{\hat{\imath}}[m]$ in (32) is a complex Gaussian RV whose conditional mean $\mu_{r_{\hat{\imath}}}[m]$ and variance $\sigma_{r_{\hat{\imath}}}^2[m]$, as shown in the Appendix, are given by

$$
\begin{aligned}
\mu_{r_{\hat{\imath}}}[m] &\triangleq \mathbb{E}\left\{ r_{\hat{\imath}}[m] \mid \hat{h}_{\hat{\imath}}^{\text{SE}}[m], d[m] \right\} \\
&= \left| \hat{h}_{\hat{\imath}}^{\text{SE}}[m] \right|^2 d[m] \, \zeta_{\hat{\imath}}^{\text{SE}}[m]
\end{aligned} \qquad (33)
$$

$$
\begin{aligned}
\sigma_{r_{\hat{\imath}}}^2[m] &\triangleq \text{var}\left\{ r_{\hat{\imath}}[m] \mid \hat{h}_{\hat{\imath}}^{\text{SE}}[m], d[m] \right\} \\
&= \left| \hat{h}_{\hat{\imath}}^{\text{SE}}[m] \right|^2 |d[m]|^2 \left(1 - \zeta_{\hat{\imath}}^{\text{SE}}[m] \right) \\
&\quad + N_0 \left| \hat{h}_{\hat{\imath}}^{\text{SE}}[m] \right|^2
\end{aligned} \qquad (34)
$$

where $\mathbb{E}\{\cdot\}$ and $\text{var}\{\cdot\}$ denote statistical expectation and variance, respectively. $\zeta_{\hat{\imath}}^{\text{SE}}[m] \triangleq \frac{1}{1+\sigma_{e^{\text{SE}}}^2[m]} = \frac{1}{1+\text{MSE}_{\hat{\imath}}^{\text{SE}}[m]}$, and the other symbols are defined in (13) and (26).

Conditioned on $\left\{ \left\{ \hat{h}_k^{\text{SP}}[m] \right\}_{m=M}^{M+N-1} \right\}_{k=1}^K$, $\hat{\imath}$, and $\hat{h}_{\hat{\imath}}^{\text{SE}}[m]$, the SEP of an MPSK symbol received at time m $\text{SEP}_m \left(\left\{ \left\{ \hat{h}_k^{\text{SP}}[m] \right\}_{m=M}^{M+N-1} \right\}_{k=1}^K, \hat{\imath}, \hat{h}_{\hat{\imath}}^{\text{SE}}[m] \right)$, which is denoted by $\text{SEP}_m(\varkappa)$, is [20], [24]

$$
\begin{aligned}
\text{SEP}_m(\varkappa) &= \frac{1}{\pi} \int_0^{\frac{\text{M}-1}{\text{M}}\pi} \exp\left(\frac{-|\mu_{r_{\hat{\imath}}}[m]|^2 \sin^2\left(\frac{\pi}{\text{M}}\right)}{\sigma_{r_{\hat{\imath}}}^2[m] \sin^2(\theta)} \right) d\theta \\
&= \frac{1}{\pi} \int_0^{\frac{\text{M}-1}{\text{M}}\pi} \exp\left(\frac{-\left| \hat{h}_{\hat{\imath}}^{\text{SE}}[m] \right|^2 b_{\hat{\imath}}^{\text{SE}}[m]}{\sin^2(\theta)} \right) d\theta
\end{aligned} \qquad (35)
$$

where $b_k^{\text{SE}}[m] \triangleq \frac{\left(\zeta_k^{\text{SE}}[m] \right)^2 \sin^2\left(\frac{\pi}{\text{M}}\right)}{\left(1 - \zeta_k^{\text{SE}}[m] \right) + \frac{1}{\eta}}$ and the last equality follows from substitution of (33) and (34). Note that the SEP expression above depends only $\hat{\imath}$ and $\hat{h}_{\hat{\imath}}^{\text{SE}}[m]$. We shall, therefore, denote (35) by $\text{SEP}_m \left(\hat{\imath}, \hat{h}_{\hat{\imath}}^{\text{SE}}[m] \right)$ henceforth.

Now averaging over the index $\hat{\imath}$ to get $\text{SEP}_m \left(\left\{ \left\{ \hat{h}_k^{\text{SP}}[m] \right\}_{m=M}^{M+N-1} \right\}_{k=1}^K, \left\{ \hat{h}_k^{\text{SE}}[m] \right\}_{k=1}^K \right)$, which is denoted by $\text{SEP}_m(\Xi)$, yields

$$
\begin{aligned}
\text{SEP}_m(\Xi) &= \sum_{k=1}^K \Pr\left(\hat{\imath} = k \,\middle|\, \left\{ \left\{ \hat{h}_k^{\text{SP}}[m] \right\}_{m=M}^{M+N-1} \right\}_{k=1}^K \right) \\
&\quad \times \text{SEP}_m \left(\hat{\imath} = k, \hat{h}_{\hat{\imath}}^{\text{SE}}[m] \right) \\
&= \frac{1}{\pi} \sum_{k=1}^K \left(\prod_{\substack{l=1 \\ l \neq k}}^K \Pr\left(\sum_{m=M}^{M+N-1} \left| \hat{h}_l^{\text{SP}}[m] \right|^2 < \right. \right. \\
&\qquad \left. \sum_{m=M}^{M+N-1} \left| \hat{h}_k^{\text{SP}}[m] \right|^2 \,\middle|\, \right. \\
&\qquad \left. \left. \left\{ \left\{ \hat{h}_k^{\text{SP}}[m] \right\}_{m=M}^{M+N-1} \right\}_{k=1}^K \right) \right) \\
&\quad \times \int_0^{\frac{\text{M}-1}{\text{M}}\pi} \exp\left(\frac{-\left| \hat{h}_k^{\text{SE}}[m] \right|^2 b_k^{\text{SE}}[m]}{\sin^2(\theta)} \right) d\theta.
\end{aligned} \qquad (36)
$$

After averaging over fading (i.e., Ξ), the SEP as a function of the SNR per branch $\eta = \frac{E_s}{N_0}$ is

$$
\begin{aligned}
\text{SEP}_m(\eta) &= \frac{1}{\pi} \sum_{k=1}^K \int_0^{\frac{\text{M}-1}{\text{M}}\pi} \int_0^\infty \int_0^\infty \exp\left(\frac{-x' b_k^{\text{SE}}[m]}{\sin^2(\theta)} \right) \\
&\quad \times f_{X_k', Y_k'}(x', y') \prod_{\substack{l=1 \\ l \neq k}}^K F_{Y_l'}(y') \, dx' \, dy' \, d\theta
\end{aligned} \qquad (37)
$$

where $f_{X_k', Y_k'}(x', y')$ is the joint probability distribution of the exponentially distributed RV $X_k' \triangleq \left| \hat{h}_k^{\text{SE}}[m] \right|^2$ and RV $Y_k' \triangleq \sum_{m=M}^{M+N-1} \left| \hat{h}_k^{\text{SP}}[m] \right|^2$. Thus, Y_k' is the sum of correlated exponentially distributed RVs, and $F_{Y_k'}(y')$ denotes its cumulative distribution function (CDF). Deriving a closed-form expression for $\text{SEP}_m(\eta)$ in (37) is analytically intractable since closed-form expressions for $f_{X_k', Y_k'}(x', y')$ and $F_{Y_k'}(y')$ do not exist. Therefore, Monte Carlo averaging techniques [25] are used to evaluate the fading-averaged SEP $\text{SEP}_m(\eta)$ from $\text{SEP}_m(\Xi)$.

We now derive the SEP of MPSK for a system that performs receive AS on a symbol-by-symbol basis. As shown in the next section, symbol-by-symbol AS is analytically tractable and provides insights for per-packet AS.

2) Symbol-By-Symbol AS SEP For MPSK: Receive AS is on an instantaneous symbol-by-symbol basis according to (24) with the channel gain estimate $\hat{h}_{\hat{\imath}_m}^{\text{SE}}[m]$ used to decode the MPSK symbol received at time m.

Theorem 1 The SEP of an MPSK symbol received at time m in a time-varying channel for a system with one transmit and K receive antennas employing selection criterion (24) with channel gain estimate $\hat{h}_{l_m}^{\mathrm{SE}}[m]$ to decode an MPSK symbol received at time m is given by

$$
\begin{aligned}
SEP'_m(\eta) \;=\; & \frac{1}{\pi}\sum_{k=1}^{K}\sum_{r=0}^{K-1}\sum_{\substack{l_0,\ldots,l_r=1\\ l_0=1,\,l_1\neq\ldots\neq l_r\neq k}}^{K}\frac{(-1)^r}{r!\left(4\sigma_{k,c_1}^2[m]\right)}\\
& \times \frac{1}{\sigma_{k,c_2}^2[m]\left(1-\left[\rho_{k,c_1c_2}^2[m]+\rho_{k,c_1s_2}^2[m]\right]\right)}\\
& \int_0^{\frac{M-1}{M}\pi}\int_0^{\infty}\int_0^{\infty}\exp\left(\frac{-x\,b_k^{SE}[m]}{\sin^2(\theta)}\right.\\
& -y\sum_{j=1}^{r}\zeta_{l_j}^{SP}[m]-\left[\frac{x}{\sigma_{k,c_1}^2[m]}+\frac{y}{\sigma_{k,c_2}^2[m]}\right]\\
& \times\frac{1}{2\left(1-\left[\rho_{k,c_1c_2}^2[m]+\rho_{k,c_1s_2}^2[m]\right]\right)}\Bigg)\\
& \times I_0\left(\frac{\sqrt{\rho_{k,c_1c_2}^2[m]+\rho_{k,c_1s_2}^2[m]}}{\left(1-\left[\rho_{k,c_1c_2}^2[m]+\rho_{k,c_1s_2}^2[m]\right]\right)}\right.\\
& \left.\times\frac{\sqrt{xy}}{\sigma_{k,c_1}[m]\,\sigma_{k,c_2}[m]}\right)\,\mathrm{d}x\,\mathrm{d}y\,\mathrm{d}\theta \qquad (38)
\end{aligned}
$$

where the notation $\displaystyle\sum_{\substack{l_0,\ldots,l_r=1\\ l_0=1,\,l_1\neq\ldots\neq l_r\neq k}}^{K}$ compactly denotes

$$
\sum_{l_0=1}^{1}\sum_{\substack{l_1=1\\(l_1\neq k)}}^{K}\sum_{\substack{l_2=1\\(l_2\neq k,l_2\neq l_1)}}^{K}\cdots\sum_{\substack{l_r=1\\(l_r\neq k,\,l_r\neq l_1,\ldots,l_r\neq l_{r-1})}}^{K}\,,\quad \zeta_{l_j}^{SP}[m]\;\triangleq
$$

$\frac{1}{\sigma_{\hat{h}_{l_j}^{SP}}^2[m]}=\frac{1}{1+\sigma_{e_{l_j}^{SP}}^2[m]}=\frac{1}{1+\mathrm{MSE}_{l_j}^{SP}}$, $b_k^{SE}[m]\triangleq\frac{\left(\zeta_k^{SE}[m]\right)^2\sin^2\left(\frac{\pi}{M}\right)}{\left(1-\zeta_k^{SE}[m]\right)+\frac{1}{\eta}}$, and $I_0(\cdot)$ is the zeroth-order modified Bessel function of the first kind. In (38), $\rho_{k,c_1c_2}[m]$ and $\rho_{k,c_1s_2}[m]$ denote the correlation coefficients of $(X_{k,c_1}[m],X_{k,c_2}[m])$ and $(X_{k,c_1}[m],X_{k,s_2}[m])$, respectively, where $X_k\triangleq\left|\hat{h}_k^{SE}[m]\right|^2=X_{k,c_1}[m]+jX_{k,s_1}[m]$ and $Y_k\triangleq\left|\hat{h}_k^{SP}[m]\right|^2=X_{k,c_2}[m]+jX_{k,s_2}[m]$, and $(X_{k,c_1}[m],X_{k,s_1}[m])$ and $(X_{k,c_2}[m],X_{k,s_2}[m])$ are i.i.d. zero-mean Gaussian RVs with variances $\sigma_{k,c_1}^2[m]=\sigma_{k,s_1}^2[m]$ and $\sigma_{k,c_2}^2[m]=\sigma_{k,s_2}^2[m]$, respectively.

Proof: The proof is given in the Appendix. ∎

VI. SIMULATIONS

We now present numerical results to gain further insight into the previous analysis and study performance over time-varying channels. In the sequel, a system with one transmit and one receive antenna is denoted as 1×1, while a system with one transmit and K receive antennas out of which only one is selected is denoted as $1\times(1,K)$. Unless otherwise stated, a $1\times(1,K)$ system is simulated with the following parameters: (i) symbol duration $T_s=20.57\,\mu\mathrm{s}$ chosen according to [23], (ii) packet size $N=40$ symbols, (iii) packet duration of
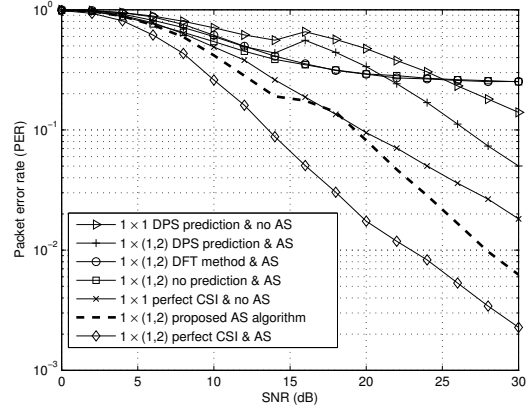

Fig. 3. PER performance of the proposed AS algorithm for a $1\times(1,2)$ system. (4PSK, data packet length $N=40$, training pilots $L=2$, post-selection pilots $L'=2$, and $T_p=3\,T_s$).

0.8228 ms, (iv) user velocity $v_{\max}=100\,\mathrm{km/h}=27.8\,\mathrm{m/s}$, (v) carrier frequency $f_c=2\,\mathrm{GHz}$, (vi) normalized Doppler bandwidth $\nu_{\max}=3.8\times10^{-3}$, (vii) symmetric spectral support $\mathcal{W}=(-\nu_{\max},\nu_{\max})$, (viii) MPSK modulation with Gray labeling, and (ix) channel gains generated assuming plane-wave propagation [26], i.e.,

$$
h[m]=\sum_{p=0}^{P-1}a_p\,\exp(j2\pi\nu_p m) \qquad (39)
$$

where the number of propagation paths is set to $P=30$, the normalized Doppler shift per path $\nu_p=\nu_{\max}\cos\alpha_p$, where path angles α_p are uniformly distributed over $[-\pi\ \pi)$, the path weights are $a_p=\frac{1}{\sqrt{P}}\exp(j\psi_p)$, and ψ_p is uniformly distributed over $[-\pi\ \pi)$. We note that the random path parameters a_p and ν_p are assumed to be constant over an AS cycle time interval $\mathcal{I}_{\mathrm{cycle}}=\{0,1,\ldots,M+N-1\}$ but change independently from cycle to cycle. The covariance function of $\{h[m]\}$ converges to $R_h[\Delta m]=J_0(2\pi\nu_{\max}\Delta m)$ for $P\to\infty$, where $J_0(\cdot)$ is the zeroth order Bessel function of the first kind [22]. The channel model in (39) is also suitable for the evaluation of channel prediction algorithms [22].

Figs. 3 and 4 show the PER of the proposed receive AS algorithm as a function of average SNR for $1\times(1,2)$ and $1\times(1,4)$ systems, respectively. For comparison, we also show the PER performance of (i) a 1×1 system with perfect CSI and no AS, (ii) a 1×1 system employing Slepian basis expansion channel prediction and no AS, (iii) $1\times(1,2)$ and $1\times(1,4)$ systems employing discrete Fourier transform (DFT) basis expansion channel prediction and AS according to the maximum total post-processing SNR selection criterion, as in (22). DFT channel estimation is used for data decoding, (iv) $1\times(1,2)$ and $1\times(1,4)$ systems employing AS without channel prediction. We note that the antenna with the highest channel gain estimate $\tilde{h}_k[m]$ in (8) is selected since no channel prediction is used, (v) $1\times(1,2)$ and $1\times(1,4)$ systems employing Slepian channel prediction and AS according to (22), with the
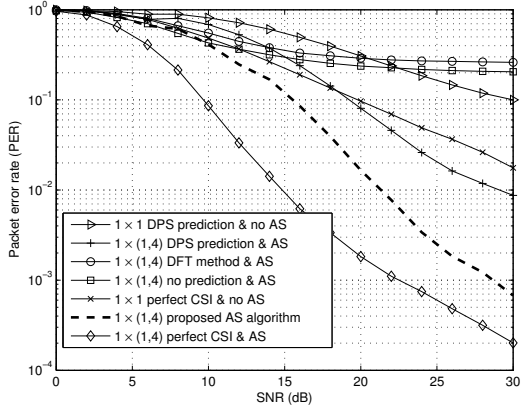
Fig. 4. PER performance of the proposed AS algorithm for a $1 \times (1,4)$ system. (4PSK, data packet length $N = 40$, training pilots $L = 2$, post-selection pilots $L' = 2$, and $T_p = 3\,T_s$).
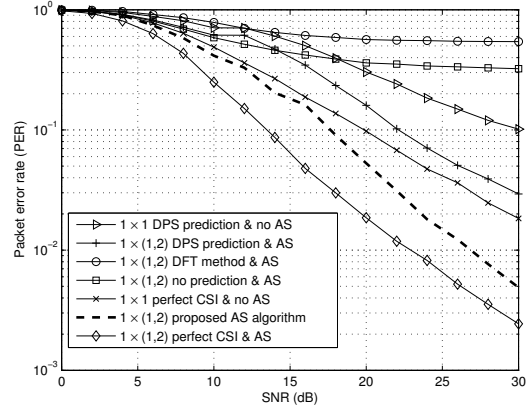

Fig. 5. PER performance of the proposed AS algorithm for a $1 \times (1,2)$ system. (4PSK, data packet length $N = 40$, training pilots $L = 3$, post-selection pilots $L' = 2$, and $T_p = 3\,T_s$).

predicted channel gains $\left\{ \hat{h}_k^{\text{SP}}[m] \mid m \in \mathcal{I}_{\text{dt}} \right\}$ used not only for selection but also data decoding, (vi) $1 \times (1,2)$ and $1 \times (1,4)$ systems employing the AS algorithm proposed in Sec. IV. Now the predicted channel gains are used for AE selection, while the refined channel gain estimates $\left\{ \hat{h}_{\hat{i}}^{\text{SE}}[m] \mid m \in \mathcal{I}_{\text{dt}} \right\}$ are used for decoding, and (vii) $1 \times (1,2)$ and $1 \times (1,4)$ systems with perfect CSI and employing AS according to (22) $\left(\text{with } h_k[m] \text{ replacing } \hat{h}_k^{\text{SP}}[m] \right)$. Inspection of Figs. 3 and 4 reveal that the $1 \times (1,2)$ and $1 \times (1,4)$ systems employing the proposed AS algorithm achieve SNR performance gains in excess of 3 dB and 9 dB over the 1×1 system with perfect CSI and no AS, respectively, at a PER equal to 10^{-2}. To highlight the importance of channel estimation, the performance of the same proposed $1 \times (1,2)$ and $1 \times (1,4)$ systems are about 5 dB and 6 dB worse than $1 \times (1,2)$ and $1 \times (1,4)$ systems employing AS with perfect CSI at the same PER of 10^{-2}, respectively. Also, error-floors exist at moderate to high SNR for the $1 \times (1,2)$ and $1 \times (1,4)$ systems employing AS either with DFT basis expansion or without channel prediction. In contrast, no error-floors arise with Slepian basis expansion.

Fig. 5 shows the PER of the proposed receive AS algorithm for a $1 \times (1,2)$ system with $L = 3$ AS training pilots rather than $L = 2$ as in Fig. 3. Comparison of Figs. 3 and 5 confirms an SNR performance gain of about 1 dB at a PER $= 10^{-2}$ due to the addition of one AS training pilot.

The analytical and simulation results for the sample mean of the Slepian estimator and predictor for AE k denoted by $\text{MSE}_{k,N}^{\text{SE}} \triangleq \frac{1}{N} \sum_{m=M}^{M+N-1} \text{MSE}_k^{\text{SE}}[m]$ and $\text{MSE}_{k,N}^{\text{SP}} \triangleq \frac{1}{N} \sum_{m=M}^{M+N-1} \text{MSE}_k^{\text{SP}}[m]$, respectively, are depicted in Fig. 6. The sample mean is plotted for a $1 \times (1,2)$ system with a packet length $N = 15$, $L = 2$ training pilot symbols, $L' = 2$ post-selection pilot symbols, and $T_p = 5\,T_s$. That is, AS training symbols for AE 1 and AE 2 are received at time indices $T_{\text{tr}}^1 = \{0, 10\}$ and $T_{\text{tr}}^2 = \{5, 15\}$, respectively. To evaluate
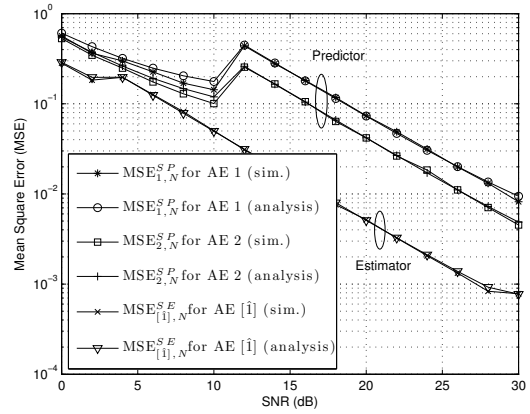
Fig. 6. Sample mean MSE_N of the basis expansion predictor and estimator for a $1 \times (1,2)$ system. (Prediction/Estimation horizon $N = 15$, training pilots $L = 2$, post-selection pilots $L' = 2$, and $T_p = 5\,T_s$).

the MSE per sample $\text{MSE}_k^{\text{SE}}[m]$ and $\text{MSE}_k^{\text{SP}}[m]$, given in Sec. V-A, we use Clarke's spectrum:

$$ S_h(\nu) = \begin{cases} \dfrac{1}{\pi \nu_{\max} \sqrt{1 - \left(\frac{\nu}{\nu_{\max}} \right)^2}} & |\nu| < \nu_{\max}, \\ 0 & \text{otherwise.} \end{cases} \tag{40} $$

It can be observed that: (i) there is a very good match between the analytical and simulation results, (ii) the sample mean of the estimator is less than the sample mean of the predictor, (iii) the sample mean $\text{MSE}_{2,N}^{\text{SP}}$ of AE 2 is slightly less than the sample mean $\text{MSE}_{1,N}^{\text{SP}}$ of AE 1. This is expected since the AS training pilots for AE 2 are received closer in time to the prediction horizon $\mathcal{I}_{\text{dt}} = \{20, 21, \dots, 34\}$ than the AS training symbols for AE 1, and (iv) there are upward transitions in the estimation and prediction MSE curves which occur in the $2-4$ and $10-12$ dB ranges, respectively, which are the result of
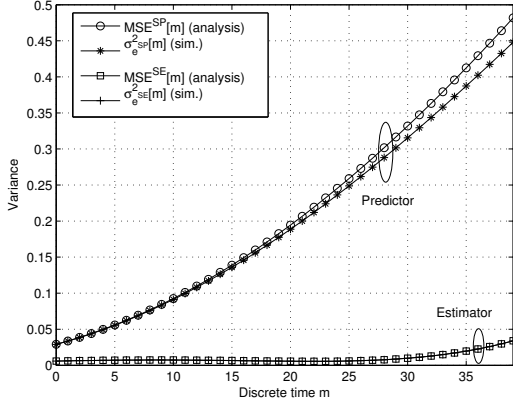
Fig. 7. Comparison of the simulated and calculated expressions for the basis expansion error variance for a 1×1 system at an average SNR $\eta = 20$ dB. (Prediction/Estimation horizon $N = 40$, training pilots $L = 2$, post-selection pilots $L' = 2$, and $T_p = 5\,T_s$).

Fig. 8. SEP for the 20-*th* 4PSK data symbol as a function of the average SNR for a $1 \times (1,2)$ system. (Data packet length $N = 40$, training pilots $L = 2$, post-selection pilots $L' = 2$, and $T_p = 5T_s$).

Fig. 9. SEP for the first 4PSK data symbol as a function of the average SNR for a $1 \times (1,2)$ system. (Data packet length $N = 40$, training pilots $L = 2$, post-selection pilots $L' = 2$, and $T_p = 5T_s$).

an increase of the subspace dimension D in (15). In addition, they indicate that D is suboptimal in these intervals.

Fig. 7 compares the simulated and analytically obtained variances of the estimation and prediction errors in Sec. V-A. It can be observed that: (i) these variances are close to each other, and (ii) not surprisingly, the MSE per sample of the predicted $\mathrm{MSE}^{\mathrm{SP}}[m]$, in contrast to the MSE per sample of the estimated $\mathrm{MSE}^{\mathrm{SE}}[m]$, increases with the prediction horizon, which is consistent with the behavior of typical prediction algorithms.

Fig. 8 shows the SEP of the 20-*th* 4PSK symbol as a function of average SNR for $1 \times (1,2)$ systems employing the proposed receive AS algorithm and the symbol-by-symbol instantaneous receive AS scheme, which is analyzed in *Theorem 1*. It can be observed that the curves are close to each other. Since the SEP behaviour might be slightly different for the $N = 40$ different symbols of the data packet, we plot the SEP for the first 4PSK symbol in Fig. 9. A gap can be observed between the curves at moderate to high SNRs since channel prediction for the first symbol is much better than channel prediction for the 20-*th* symbol, which clearly affects the selection decision and, thus, the SEP. Similarly, there is a slight upward shift of the proposed AS scheme's SEP curve in Fig. 9, due to the fact that the first symbol is located far from the post-selection pilots $\mathcal{P} = \{11, 31\}$. We also observe from Figs. 8 and 9 and from other simulations (not included) that the SEP of the first few symbols in a packet for a system which uses symbol-by-symbol instantaneous receive AS is lower than that of the AS algorithm proposed in Sec. IV, while the SEPs of remaining symbols are close to one another.

VII. Conclusions

The downlink of a cellular radio system consisting of a single-antenna base station transmitting to a K-antenna mobile station is considered, where only one receive antenna is selected. B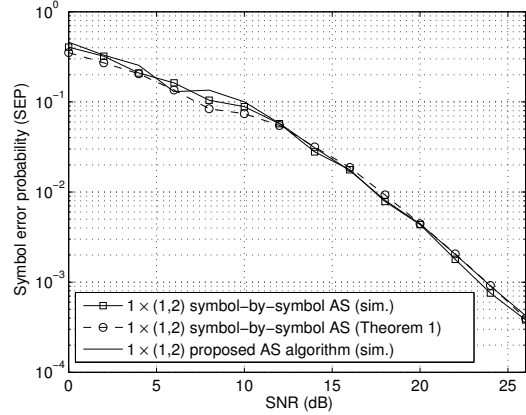y explicitly accounting for practical constraints imposed by next-generation wireless standards such as training and packet reception for antenna selection (AS), a single receive AS method is proposed for time-varying channels using the low-complexity Slepian basis expansion channel predictor and estimator. Closed-form expressions are derived for the channel prediction and estimation error as well as the SEP of MPSK with receive AS. It is shown that, in spite of the aforementioned realistic limitations, the proposed AS scheme outperforms ideal conventional SISO systems with perfect channel knowledge and no AS at the receiver and conventional complex basis based estimation. Although the focus was on single carrier communication over time-varying frequency-flat channels, the proposed AS scheme may be extendible to OFDM systems. The extension to the case where subsets of more than one receive antenna are selected in time-varying frequency-selective channels remains as an important topic for
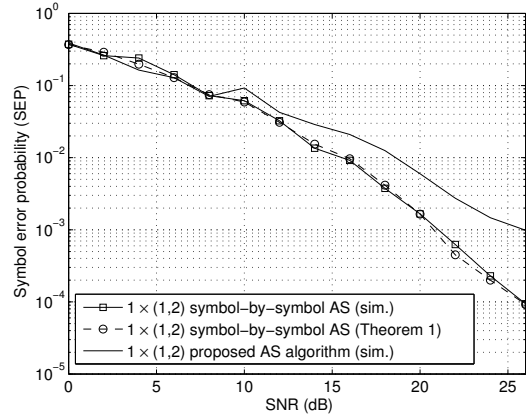
future research.

APPENDIX

A. Derivation of the Conditional Mean and Variance

If A and B are zero-mean jointly complex Gaussian, then [20], [21]

$$\mathbb{E}\left\{A \,\middle|\, B\right\} = \mathbb{E}\left\{A B^*\right\} \left(\mathbb{E}\left\{B B^*\right\}\right)^{-1} B \qquad (41)$$

$$\mathrm{var}\left\{A \,\middle|\, B\right\} = \mathrm{var}\left\{A\right\} - \mathbb{E}\left\{A B^*\right\} \left(\mathbb{E}\left\{B B^*\right\}\right)^{-1} \mathbb{E}\left\{B A^*\right\}. \qquad (42)$$

From (41), it follows that $\mathbb{E}\left\{e_{\hat{\imath}}^{\mathrm{SE}}[m] \,\middle|\, \hat{h}_{\hat{\imath}}^{\mathrm{SE}}[m]\right\} = \frac{\sigma_{e_{\hat{\imath}}^{\mathrm{SE}}[m]}^2}{1+\sigma_{e_{\hat{\imath}}^{\mathrm{SE}}[m]}^2} \hat{h}_{\hat{\imath}}^{\mathrm{SE}}[m]$ and $\mathbb{E}\left\{n_{\hat{\imath}}[m] \,\middle|\, \hat{h}_{\hat{\imath}}^{\mathrm{SE}}[m]\right\} = 0$. Substituting and simplifying yields the desired conditional mean result in (33). Similarly, from (42) we get that $\mathrm{var}\left\{e_{\hat{\imath}}^{\mathrm{SE}}[m] \,\middle|\, \hat{h}_{\hat{\imath}}^{\mathrm{SE}}[m]\right\} = \frac{\sigma_{e_{\hat{\imath}}^{\mathrm{SE}}[m]}^2}{1+\sigma_{e_{\hat{\imath}}^{\mathrm{SE}}[m]}^2}$ and $\mathrm{var}\left\{n_{\hat{\imath}}[m] \,\middle|\, \hat{h}_{\hat{\imath}}^{\mathrm{SE}}[m]\right\} = N_0$. Substituting and simplifying yields the conditional variance result in (34).

B. Proof of Theorem 1

From (32), the ML soft estimate for the symbol received by AE $\hat{\imath}_m$ at time m can be modified to

$$r_{\hat{\imath}_m}[m] = \left|\hat{h}_{\hat{\imath}_m}^{\mathrm{SE}}[m]\right|^2 d[m] - \left(\hat{h}_{\hat{\imath}_m}^{\mathrm{SE}}[m]\right)^* d[m]\, e_{\hat{\imath}_m}^{\mathrm{SE}}[m]$$
$$+ \left(\hat{h}_{\hat{\imath}_m}^{\mathrm{SE}}[m]\right)^* n_{\hat{\imath}_m}[m]. \qquad (43)$$

Conditioned on $\hat{h}_{\hat{\imath}_m}^{\mathrm{SE}}[m]$ and $d[m]$, $r_{\hat{\imath}_m}[m]$ in (43) is a complex Gaussian RV whose conditional mean $\mu_{r_{\hat{\imath}_m}}[m]$ and variance $\sigma_{r_{\hat{\imath}_m}}^2[m]$ are given by

$$\mu_{r_{\hat{\imath}_m}}[m] = \left|\hat{h}_{\hat{\imath}_m}^{\mathrm{SE}}[m]\right|^2 d[m]\, \zeta_{\hat{\imath}_m}^{\mathrm{SE}}[m] \qquad (44)$$

$$\sigma_{r_{\hat{\imath}_m}}^2[m] = \left|\hat{h}_{\hat{\imath}_m}^{\mathrm{SE}}[m]\right|^2 |d[m]|^2 \left(1 - \zeta_{\hat{\imath}_m}^{\mathrm{SE}}[m]\right)$$
$$+ N_0 \left|\hat{h}_{\hat{\imath}_m}^{\mathrm{SE}}[m]\right|^2 \qquad (45)$$

where $\zeta_{\hat{\imath}_m}^{\mathrm{SE}}[m] \triangleq \frac{1}{1+\sigma_{e_{\hat{\imath}_m}^{\mathrm{SE}}}^2[m]} = \frac{1}{1+\mathrm{MSE}_{\hat{\imath}_m}^{\mathrm{SE}}[m]}$.

Conditioned on $\left\{\hat{h}_k^{\mathrm{SP}}[m]\right\}_{k=1}^K$, $\hat{\imath}_m$, and $\hat{h}_{\hat{\imath}_m}^{\mathrm{SE}}[m]$, the SEP of an MPSK symbol received at time m $\mathrm{SEP}'_m\left(\left\{\hat{h}_k^{\mathrm{SP}}[m]\right\}_{k=1}^K, \hat{\imath}_m, \hat{h}_{\hat{\imath}_m}^{\mathrm{SE}}[m]\right)$, which is denoted by $\mathrm{SEP}'_m(\varkappa)$, is [20]

$$\mathrm{SEP}'_m(\varkappa) = \frac{1}{\pi}\int_0^{\frac{\mathsf{M}-1}{\mathsf{M}}\pi} \exp\left(\frac{-\left|\mu_{r_{\hat{\imath}_m}}[m]\right|^2 \sin^2\left(\frac{\pi}{\mathsf{M}}\right)}{\sigma_{r_{\hat{\imath}_m}}^2[m]\, \sin^2(\theta)}\right) \mathrm{d}\theta$$
$$= \frac{1}{\pi}\int_0^{\frac{\mathsf{M}-1}{\mathsf{M}}\pi} \exp\left(\frac{-\left|\hat{h}_{\hat{\imath}_m}^{\mathrm{SE}}[m]\right|^2 b_{\hat{\imath}_m}^{\mathrm{SE}}[m]}{\sin^2(\theta)}\right) \mathrm{d}\theta \qquad (46)$$

where $b_k^{\mathrm{SE}}[m] \triangleq \frac{\left(\zeta_k^{\mathrm{SE}}[m]\right)^2 \sin^2\left(\frac{\pi}{\mathsf{M}}\right)}{\left(1-\zeta_k^{\mathrm{SE}}[m]\right)+\frac{1}{\eta}}$, and the last equality follows from substituting (44) and (45). Note that the SEP

expression above depends only on $\hat{\imath}_m$ and $\hat{h}_{\hat{\imath}_m}^{\mathrm{SE}}[m]$. Therefore, we shall denote it by $\mathrm{SEP}'_m\left(\hat{\imath}_m, \hat{h}_{\hat{\imath}_m}^{\mathrm{SE}}[m]\right)$ henceforth.

Now averaging over the index $\hat{\imath}_m$ to get $\mathrm{SEP}'_m\left(\left\{\hat{h}_k^{\mathrm{SP}}[m]\right\}_{k=1}^K, \left\{\hat{h}_k^{\mathrm{SE}}[m]\right\}_{k=1}^K\right)$, denoted for brevity by $\mathrm{SEP}'_m(\Xi)$, yields

$$\mathrm{SEP}'_m(\Xi) = \sum_{k=1}^K \mathrm{Pr}\left(\hat{\imath}_m = k \,\middle|\, \left\{\hat{h}_k^{\mathrm{SP}}[m]\right\}_{k=1}^K\right)$$
$$\times \mathrm{SEP}'_m\left(\hat{\imath}_m = k, \hat{h}_{\hat{\imath}_m}^{\mathrm{SE}}[m]\right)$$
$$= \frac{1}{\pi}\sum_{k=1}^K \left(\prod_{\substack{l=1\\l\neq k}}^K \mathrm{Pr}\left(\left|\hat{h}_l^{\mathrm{SP}}[m]\right|^2 < \left|\hat{h}_k^{\mathrm{SP}}[m]\right|^2 \,\middle|\, \left\{\hat{h}_k^{\mathrm{SP}}[m]\right\}_{k=1}^K\right)\right)$$
$$\times \int_0^{\frac{\mathsf{M}-1}{\mathsf{M}}\pi} \exp\left(\frac{-\left|\hat{h}_k^{\mathrm{SE}}[m]\right|^2 b_k^{\mathrm{SE}}[m]}{\sin^2(\theta)}\right) \mathrm{d}\theta. \qquad (47)$$

The expression for the SEP, when averaging over fading (i.e., Ξ), becomes

$$\mathrm{SEP}'_m(\eta) = \frac{1}{\pi}\sum_{k=1}^K \int_0^{\frac{\mathsf{M}-1}{\mathsf{M}}\pi} \int_0^\infty \int_0^\infty \exp\left(\frac{-x\, b_k^{\mathrm{SE}}[m]}{\sin^2(\theta)}\right)$$
$$\times f_{X_k, Y_k}(x, y) \prod_{\substack{l=1\\l\neq k}}^K F_{Y_l}(y)\, \mathrm{d}x \mathrm{d}y \mathrm{d}\theta \qquad (48)$$

where $f_{X_k, Y_k}(x, y)$ is the joint PDF of the two correlated exponentially distributed RVs $X_k \triangleq \left|\hat{h}_k^{\mathrm{SE}}[m]\right|^2 = X_{k,c_1}[m] + jX_{k,s_1}[m]$ and $Y_k \triangleq \left|\hat{h}_k^{\mathrm{SP}}[m]\right|^2 = X_{k,c_2}[m] + jX_{k,s_2}[m]$ given by [27]

$$f_{X_k, Y_k}(x, y) = \frac{1}{4\,\sigma_{k,c_1}^2[m]\,\sigma_{k,c_2}^2[m]}$$
$$\times \frac{1}{\left(1 - \left[\rho_{k,c_1c_2}^2[m] + \rho_{k,c_1s_2}^2[m]\right]\right)}$$
$$\times \exp\left(\left[\frac{x}{\sigma_{k,c_1}^2[m]} + \frac{y}{\sigma_{k,c_2}^2[m]}\right]\right.$$
$$\times \frac{-1}{2\left(1 - \left[\rho_{k,c_1c_2}^2[m] + \rho_{k,c_1s_2}^2[m]\right]\right)}\right)$$
$$\times I_0\left(\frac{\sqrt{\rho_{k,c_1c_2}^2[m] + \rho_{k,c_1s_2}^2[m]}}{\left(1 - \left[\rho_{k,c_1c_2}^2[m] + \rho_{k,c_1s_2}^2[m]\right]\right)}\right.$$
$$\times \frac{\sqrt{xy}}{\sigma_{k,c_1}[m]\,\sigma_{k,c_2}[m]}\right) \qquad (49)$$

where $x, y \geq 0$, $I_0(\cdot)$ is the zeroth-order modified Bessel function of the first kind, $(X_{k,c_1}[m], X_{k,s_2}[m])$

and $\left(X_{k,c_2}\left[m\right], X_{k,s_2}\left[m\right]\right)$ are i.i.d. zero-mean Gaussian RVs with variances $\sigma_{k,c_1}^2\left[m\right] = \sigma_{k,s_1}^2\left[m\right]$ and $\sigma_{k,c_2}^2\left[m\right] = \sigma_{k,s_2}^2\left[m\right]$, respectively. $\rho_{k,c_1c_2}\left[m\right]$ and $\rho_{k,c_1s_2}\left[m\right]$ are the correlation coefficients of $\left(X_{k,c_1}\left[m\right], X_{k,c_2}\left[m\right]\right)$ and $\left(X_{k,c_1}\left[m\right], X_{k,s_2}\left[m\right]\right)$, respectively, and lie in $(-1,1)$.

In (48), $F_{Y_l}\left(y\right)$ is the CDF of the exponentially distributed RV $Y_l \triangleq \left|\hat{h}_l^{\text{SP}}\left[m\right]\right|^2$, and is given by

$$F_{Y_l}\left(y\right) = \begin{cases} 1 - \exp\left(-\zeta_l^{\text{SP}}\left[m\right]y\right), & y \geq 0 \\ 0, & y < 0 \end{cases} \qquad (50)$$

where the rate parameter is $\zeta_l^{\text{SP}}\left[m\right] \triangleq \frac{1}{1+\sigma_{e_l^{\text{SP}}}^2\left[m\right]} = \frac{1}{1+\text{MSE}_l^{\text{SP}}\left[m\right]}$.

Substituting (50) and (49) into (48) yields

$$\begin{aligned}
\text{SEP}_m'\left(\eta\right) &= \frac{1}{\pi}\sum_{k=1}^K \int_0^{\frac{M-1}{M}\pi} \int_0^\infty \int_0^\infty \exp\left(\frac{-x\,b_k^{\text{SE}}\left[m\right]}{\sin^2\left(\theta\right)}\right) \\
&\quad \times f_{X_k,Y_k}\left(x,y\right) \\
&\quad \times \prod_{\substack{l=1 \\ l\neq k}}^K \left(1 - \exp\left(-\zeta_l^{\text{SP}}\left[m\right]y\right)\right)\,\mathrm{d}x\,\mathrm{d}y\,\mathrm{d}\theta \\
&= \frac{1}{\pi}\sum_{k=1}^K \sum_{r=0}^{K-1} \sum_{\substack{l_0,\dots,l_r=1 \\ l_0=1,\,l_1\neq\dots\neq l_r\neq k}}^K \frac{(-1)^r}{r!\left(4\sigma_{k,c_1}^2\left[m\right]\right)} \\
&\quad \times \frac{1}{\sigma_{k,c_2}^2\left[m\right]\left(1-\left[\rho_{k,c_1c_2}^2\left[m\right]+\rho_{k,c_1s_2}^2\left[m\right]\right]\right)} \\
&\quad \int_0^{\frac{M-1}{M}\pi}\int_0^\infty\int_0^\infty \exp\left(\frac{-x\,b_k^{\text{SE}}\left[m\right]}{\sin^2\left(\theta\right)}\right. \\
&\quad \left. -y\sum_{j=1}^r \zeta_{l_j}^{\text{SP}}\left[m\right] - \left[\frac{x}{\sigma_{k,c_1}^2\left[m\right]}+\frac{y}{\sigma_{k,c_2}^2\left[m\right]}\right]\right. \\
&\quad \left.\times\frac{1}{2\left(1-\left[\rho_{k,c_1c_2}^2\left[m\right]+\rho_{k,c_1s_2}^2\left[m\right]\right]\right)}\right) \\
&\quad \times I_0\left(\frac{\sqrt{\rho_{k,c_1c_2}^2\left[m\right]+\rho_{k,c_1s_2}^2\left[m\right]}}{\left(1-\left[\rho_{k,c_1c_2}^2\left[m\right]+\rho_{k,c_1s_2}^2\left[m\right]\right]\right)}\right. \\
&\quad \left.\times\frac{\sqrt{xy}}{\sigma_{k,c_1}\left[m\right]\sigma_{k,c_2}\left[m\right]}\right)\,\mathrm{d}x\,\mathrm{d}y\,\mathrm{d}\theta \qquad (51)
\end{aligned}$$

where the identity $\prod_{\substack{l=1 \\ l\neq k}}^K \left(1 - \exp\left(-\zeta_l^{\text{SP}}\left[m\right]y\right)\right) = \sum_{r=0}^{K-1}\frac{(-1)^r}{r!}\sum_{\substack{l_0,\dots,l_r=1 \\ l_0=1,\,l_1\neq\dots\neq l_r\neq k}}^K \exp\left(-y\sum_{j=1}^r \zeta_{l_j}^{\text{SP}}\left[m\right]\right)$ is used in the last equality [20].

References

[1] "Draft amendment to wireless LAN media access control (MAC) and physical layer (PHY) specifications: enhancements for higher throughput," Tech. Rep. P802.11n/D0.04, IEEE, Mar. 2006.

[2] "Technical specification group radio access network; evolved universal terrestrial radio access (E-UTRA); physical layer procedures (release 8)," Tech. Rep. 36.211 (v8.3.0), 3rd Generation Partnership Project (3GPP), 2008.

[3] N. B. Mehta, A. F. Molisch, J. Zhang, and E. Bala, "Antenna selection training in MIMO-OFDM/OFDMA cellular systems," in *Proc. IEEE CAMSAP*, 2007.

[4] A. F. Molisch and M. Z. Win, "MIMO systems with antenna selection," *IEEE Microw. Mag.*, vol. 5, pp. 46–56, Mar. 2004.

[5] S. Sanayei and A. Nosratinia, "Antenna selection in MIMO systems," *IEEE Commun. Mag.*, vol. 42, pp. 68–73, Oct. 2004.

[6] D. A. Gore and A. Paulraj, "MIMO antenna subset selection with space-time coding," *IEEE Trans. Signal Process.*, vol. 50, pp. 2580–2588, Oct. 2002.

[7] H. Mehrpouyan, S. D. Blostein, and E. C. Y. Tam, "Random antenna selection & antenna swapping combined with OSTBCs," in *Proc. IEEE ISSSE*, 2007.

[8] M. Z. Win and J. H. Winters, "Virtual branch analysis of symbol error probability for hybrid selection/maximal-ratio combining in Rayleigh fading," *IEEE Trans. Commun.*, vol. 49, pp. 1926–1934, Nov. 2001.

[9] A. Ghrayeb and T. M. Duman, "Performance analysis of MIMO systems with antenna selection over quasi-static fading channels," *IEEE Trans. Veh. Technol.*, vol. 52, pp. 281–288, Mar. 2003.

[10] A. F. Molisch, M. Z. Win, Y.-S. Choi, and J. H. Winters, "Capacity of MIMO systems with antenna selection," *IEEE Trans. Wireless Commun.*, vol. 4, pp. 1759–1772, Jul. 2005.

[11] Z. Chen, J. Yuan, and B. Vucetic, "Analysis of transmit antenna selection/maximal-ratio combining in Rayleigh fading channels," *IEEE Trans. Veh. Technol.*, vol. 54, pp. 1312–1321, Jul. 2005.

[12] Z. Xu, S. Sfar, and R. S. Blum, "Analysis of MIMO systems with receive antenna selection in spatially correlated Rayleigh fading channels," *IEEE Trans. Veh. Technol.*, vol. 58, pp. 251–262, Jan. 2009.

[13] Y. Jiang and M. K. Varanasi, "The RF-chain limited MIMO system–part I: Optimum diversity-multiplexing tradeoff," *IEEE Trans. Wireless Commun.*, vol. 8, pp. 5238–5247, Oct. 2009.

[14] H. Zhang, A. F. Molisch, and J. Zhang, "Applying antenna selection in WLANs for achieving broadband multimedia communications," *IEEE Trans. Broadcast.*, vol. 52, pp. 475–482, Dec. 2006.

[15] W. Xie, S. Liu, D. Yoon, and J.-W. Chong, "Impacts of Gaussian error and Doppler spread on the performance of MIMO systems with antenna selection," in *Proc. WiCOM*, 2006.

[16] S. Han and C. Yang, "Performance analysis of MRT and transmit antenna selection with feedback delay and channel estimation error," in *Proc. IEEE WCNC*, 2007, pp. 1135–1139.

[17] W. M. Gifford, M. Z. Win, and M. Chiani, "Antenna subset diversity with non-ideal channel estimation," *IEEE Trans. Wireless Commun.*, vol. 7, pp. 1527–1539, May 2008.

[18] A. B. Narasimhamurthy and C. Tepedelenlioglu, "Antenna selection for MIMO-OFDM systems with channel estimation error," *IEEE Trans. Veh. Technol.*, vol. 58, pp. 2269–2278, Jun. 2009.

[19] T. R. Ramya and S. Bhashyam, "Using delayed feedback for antenna selection in MIMO systems," *IEEE Trans. Wireless Commun.*, vol. 8, pp. 6059–6067, Dec. 2009.

[20] V. Kristem, N. B. Mehta, and A. F. Molisch, "Optimal receive antenna selection in time-varying fading channels with practical training constraints," *IEEE Trans. Commun.*, vol. 58, pp. 2023–2034, Jul. 2010.

[21] ——, "Training and voids in receive antenna subset selection in time-varying channels," *IEEE Trans. Wireless Commun.*, vol. 10, pp. 1992–2003, Jun. 2011.

[22] T. Zemen, C. F. Mecklenbräuker, F. Kaltenberger, and B. H. Fleury, "Minimum-energy band-limited predictor with dynamic subspace selection for time-variant flat-fading channels," *IEEE Trans. Signal Process.*, vol. 55, pp. 4534–4548, Sep. 2007.

[23] T. Zemen and C. F. Mecklenbräuker, "Time-variant channel estimation using discrete prolate spheroidal sequences," *IEEE Trans. Signal Process.*, vol. 53, pp. 3597–3607, Sep. 2005.

[24] M.-S. Alouini and A. Goldsmith, "A unified approach for calculating error rates of linearly modulated signals over generalized fading channels," *IEEE Trans. Commun.*, vol. 47, pp. 1324–1334, Sep. 1999.

[25] G. S. Fishman, *Monte Carlo: Concepts, Algorithms, and Applications.*, 1st ed. Springer, 1996.

[26] R. H. Clarke, "A statistical theory of mobile-radio reception," *Bell Syst. Tech. J.*, vol. 47, pp. 957–1000, Jul.-Aug. 1968.

[27] R. K. Mallik, "On multivariate Rayleigh and exponential distributions," *IEEE Trans. Inf. Theory*, vol. 49, pp. 1499–1515, Jun. 2003.
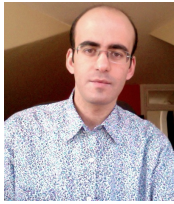
Hassan A. Abou Saleh is currently pursuing his doctoral studies in electrical engineering at the Information Processing & Communications Laboratory (IPCL) at Queen's University, Kingston, Canada. He has been awarded a Natural Sciences and Engineering Research Council of Canada (NSERC) Postgraduate Scholarship (2009–2012). His areas of concentration are in wireless cutting-edge technologies and multiple antenna systems.

Andreas F. Molisch (S'89-M'95-SM'00-F'05) received the Dipl. Ing., Ph.D., and habilitation degrees from the Technical University of Vienna, Vienna, Austria, in 1990, 1994, and 1999, respectively. He subsequently was with AT&T (Bell) Laboratories Research (USA); Lund University, Lund, Sweden, and Mitsubishi Electric Research Labs (USA). He is now a Professor of electrical engineering with the University of Southern California, Los Angeles.

His current research interests are the measurement and modeling of mobile radio channels, ultra-wideband communications and localization, cooperative communications, multiple-inputmultiple-output systems, and wireless systems for healthcare. He has authored, coauthored, or edited four books (among them the textbook Wireless Communications, Wiley-IEEE Press), 14 book chapters, some 140 journal papers, and numerous conference contributions, as well as more than 70 patents and 60 standards contributions.

Dr. Molisch has been an Editor of a number of journals and special issues, General Chair, Technical Program Committee Chair, or Symposium Chair of multiple international conferences, as well as Chairman of various international standardization groups. He is a Fellow of the IET, an IEEE Distinguished Lecturer, and a member of the Austrian Academy of Sciences. He has received numerous awards, most recently the 2011 James Evans Avant-Garde award of the IEEE Vehicular Technology Society, the Donald Fink Prize of the IEEE, and the Eric Sumner Award of the IEEE.

Thomas Zemen (S'03-M'05-SM'10) was born in Mdling, Austria. He received the Dipl.-Ing. degree (with distinction) in electrical engineering from Vienna University of Technology in 1998 and the doctoral degree (with distinction) in 2004. From 1998 to 2003 he worked as hardware engineer and project manager for the radio communication devices department at Siemens Austria. Since October 2003 Thomas Zemen has been with FTW Forschungszentrum Telekommunikation Wien, he leads the department "Signal and Information Processing" since 2008. He is the speaker of the national research network for "Signal and Information Processing in Science and Engineering" funded by the Austrian Science Fund (FWF). His research interests include vehicular channel measurements and modelling, time-variant channel estimation, orthogonal frequency division multiplexing (OFDM), iterative multiple-input multiple-output (MIMO) receiver structures, cooperative communication systems and interference management. Dr. Zemen teaches as external lecturer at Vienna University of Technology and serves as editor for the IEEE Transactions on Wireless Communications. He is the author or co-author of three books chapters and more than 80 journal papers and conference communications.

Steven D. Blostein (SM'83, M'88, SM'96) received his B.S. degree in Electrical Engineering from Cornell University, Ithaca, NY, in 1983, and the M.S. and Ph.D. degrees in Electrical and Computer Engineering from the University of Illinois, Urbana-Champaign, in 1985 and 1988, respectively. He has been on the faculty in the Department of Electrical and Computer Engineering Queen's University since 1988 and currently holds the position of Professor. From 2004-2009 he was Department Head. He has also been a consultant to industry and government in the areas of image compression, target tracking, radar imaging and wireless communications. He spent sabbatical leaves at Lockheed Martin Electronic Systems, McGill University and at Communications Research Centre in Ottawa. His current interests lie in the application of signal processing to problems in wireless communications systems, including synchronization, cooperative and network MIMO, and cross-layer optimization for multimedia transmission. He has been a member of the Samsung 4G Wireless Forum as well as an invited distinguished speaker. He served as Chair of IEEE Kingston Section (1994), Chair of the Biennial Symposium on Communications (2000,2006,2008), Associate Editor for IEEE Transactions on Image Processing (1996-2000), and Publications Chair for IEEE ICASSP 2004, and an Editor of IEEE Transactions on Wireless Communications (2007-present). He has also served on Technical Program Committees for IEEE Communications Society conferences for many years. He is a registered Professional Engineer in Ontario and a Senior Member of IEEE.

Neelesh B. Mehta (S'98-M'01-SM'06) received his Bachelor of Technology degree in electronics and communications engineering from the Indian Institute of Technology (IIT), Madras in 1996, and his M.S. and Ph.D. degrees in electrical engineering from the California Institute of Technology, Pasadena, CA, USA in 1997 and 2001, respectively. He is now an Associate Professor in the Dept. of Electrical Communication Eng., Indian Institute of Science (IISc), Bangalore, India. Prior to joining IISc in 2007, he was a research scientist from in the Wireless Systems Research Group in AT&T Laboratories, Middletown, NJ, USA from 2001 to 2002, Broadcom Corp., Matawan, NJ, USA from 2002 to 2003, and Mitsubishi Electric Research Laboratories (MERL), Cambridge, MA, USA from 2003 to 2007.

His research includes work on link adaptation, multiple access protocols, WCDMA downlinks, cellular systems, MIMO and antenna selection, energy harvesting networks, and cooperative communications. He was also actively involved in the Radio Access Network (RAN1) standardization activities in 3GPP from 2003 to 2007. He has served on several TPCs. He was a TPC co-chair for the WISARD 2010 and 2011 workshops and tracks in NCC 2011, SPCOM 2010, VTC 2009 (Fall), and Chinacom 2008. He will serve as a TPC co-chair of the Wireless Communications Symposium of ICC 2013. He has co-authored 30 IEEE journal papers, 55 conference papers, and 3 book chapters, and is a co-inventor in 16 issued US patents. He was an Editor of the IEEE TRANSACTIONS ON WIRELESS COMMUNICATIONS from 2008 to 2011. He is now an Editor of IEEE WIRELESS COMMUNICATIONS LETTERS. He is currently serving as Director of Conference Publications in the Board of Governors of the IEEE Communications Society. He is also an executive committee member of the IEEE Bangalore Section and the Bangalore Chapter of the IEEE Signal Processing Society.

Bibliography

[1] "IEEE P802.11p: Part 11: Wireless LAN Medium Access Control (MAC) and Physical Layer (PHY) Specifications: Amendment 6: Wireless Access in Vehicular Environments," July 2010.

[2] "IEEE trial-use standard for wireless access in vehicular environments (WAVE) - resource manager," *IEEE Std 1609.1-2006*, pp. c1 – 63, 2006.

[3] 3GPP, "Third Generation Partnership Project (3GPP)." [Online]. Available: http://www.3gpp.org/

[4] ——, "Technical specification group radio access network; evolved universal terrestrial radio access (E-UTRA); physical channels and modulation (Tech. Spec. 36.211 V10.2.0)," June 2011.

[5] G. Acosta, K. Tokuda, and M. A. Ingram, "Measured joint Doppler-delay power profiles for vehicle-to-vehicle communications at 2.4 GHz," in *IEEE Global Telecommunications Conference (GLOBECOM)*, vol. 6, Dallas, Texas, December 2004, pp. 3818–3817.

[6] G. Acosta and M. A. Ingram, "Model development for the wideband vehicle-to-vehicle 2.4 GHz channel," in *IEEE Wireless Communications and Networking Conference (WCNC)*, vol. 3, Las Vegas (NV), USA, April 2006, pp. 1283–1288.

[7] G. Acosta-Marum and M. A. Ingram, "Doubly selective vehicle-to-vehicle channel measurements and modeling at 5.9 GHz," in *Wireless Personal Multimedia Communications (WPMC)*, San Diego, California, USA, September 2006.

[8] S. Alamouti, "A simple transmitter diversity sceme for wireless communications," *IEEE Journal on Selected Areas in Communications*, vol. 16, no. 8, pp. 1451–1458, Oct. 1998.

[9] G. Athanasiadou, A. Nix, and J. McGeehan, "A microcellular ray-tracing propagation model and evaluation of its narrow-band and wide-band predictions," *IEEE Journal on Selected Areas in Communications*, vol. 18, no. 3, pp. 322 –335, March 2000.

[10] J. Bach Andersen, J. Jensen, S. H. Jensen, and F. Frederiksen, "Prediction of future fading based on past measurements," in *50th IEEE Vehicular Technology Conference (VTC)*, vol. 1, Amsterdam, Netherlands, September 1999, pp. 151 – 155.

[11] L. R. Bahl, J. Cocke, F. Jelinek, and J. Raviv, "Optimal decoding of linear codes for minimizing symbol error rate," *IEEE Transactions on Information Theory*, vol. 20, no. 2, pp. 284–287, March 1974.

[12] S. Beheshti and M. A. Dahleh, "A new information-theoretic approach to signal denoising and best basis selection," *IEEE Transactions on Signal Processing*, vol. 53, no. 10, pp. 3613–3624, October 2005.

[13] P. A. Bello, "Characterization of randomly time-variant linear channels," *IEEE Transsactions on Communication Systems*, vol. CS-11, no. 4, pp. 360–393, December 1963.

[14] L. Bernadó, N. Czink, T. Zemen, A. Paier, F. Tufvesson, C. F. Mecklenbräuker, and A. F. Molisch, "Vehicular channels," in *LTE Advanced and Beyond Wireless Networks: Channel Modeling and Propagation*, G. de la Roche, A. Alayón, and B. Allen, Eds.   John Wiley and Sons, 2012.

[15] A. Burg, M. Borgmann, M. Wenk, M. Zellwegera, W. Fichtner, and H. Bölcskei, "VLSI implementation of MIMO detection using the sphere decoding algorithm," *IEEE Journal of Solid-State Circuits*, vol. 40, no. 7, pp. 1566–1577, July 2005.

[16] M. Chen, T. Ekman, and M. Viberg, "New approaches for channel prediction based on sinusoidal modeling," *EURASIP Journal on Applied Signal Processing*, vol. 2007, no. 1, pp. 1–13, 2007.

[17] M. Chen and M. Viberg, "Long-range channel prediction based on nonstationary parametric modeling," *IEEE Transactions on Signal Processing*, vol. 57, no. 2, pp. 622–634, February 2009.

[18] M. Chen, M. Viberg, and T. Ekman, "Two new approaches to channel prediction based on sinusoidal modelling," in *13th Workshop on Statistical Signal Processing (SSP)*, Bordeaux, France, July 2005.

[19] Z. Chen, J. Yuan, and B. Vucetic, "Analysis of transmit antenna selection/maximal-ratio combining in rayleigh fading channels," *IEEE Transactions on Vehicular Technology*, vol. 54, no. 4, pp. 1312–1321, July 2005.

[20] L. Cheng, B. Henty, R. Cooper, D. Stancil, and F. Bai, "Multi-path propagation measurements for vehicular networks at 5.9 GHz," in *IEEE Wireless Communincations and Networking Conference (WCNC)*, Las Vegas (NV), USA, April 2008, pp. 1239–1244.

[21] L. Cheng, B. Henty, D. Stancil, F. Bai, and P. Mudalige, "Mobile vehicle-to-vehicle narrow-band channel measurement and characterization of the 5.9 GHz dedicated short range communication (DSRC) frequency band," *IEEE Journal on Selected Areas in Communications*, vol. 25, no. 8, pp. 1501–1516, October 2007.

[22] R. H. Clarke, "A statistical theory of mobile-radio reception," *Bell System Technical Journal*, p. 957, July-August 1968.

[23] L. Correia, Ed., *Mobile Broadband Multimedia Networks.* San Diego, Calif, USA: Academic Press, 2006.

[24] L. Cottatellucci, R. R. Müller, and M. Debbah, "Linear detectors for multiuser systems with correlated spatial diversity," in *14th European Signal Processing Conference (EUSIPCO)*, Florence, Italy, September 2006.

[25] N. Czink, F. Kaltenberger, Y. Zhou, L. Bernadó, T. Zemen, and X. Yin, "Low-complexity geometry-based modeling of diffuse scattering," in *European Conference on Antennas and Propagation (EuCAP)*, Barcelona, Spain, April 2010.

[26] N. Czink, T. Zemen, L. Bernadó, and A. Molisch, "Channel estimation in an OFDM transmission system," *Patent application No. 10450186.1 - 1237*, 2011.

[27] V. Degli-Esposti, F. Fuschini, E. M. Vitucci, and G. Falciasecca, "Measurement and modelling of scattering from buildings," *IEEE Transactions on Antennas and Propagation*, vol. 55, no. 1, pp. 143 –153, January 2007.

[28] S. Dharanipragada and K. S. Arun, "Bandlimited extrapolation using time-bandwidth dimension," *IEEE Transactions on Signal Processing*, vol. 45, no. 12, pp. 2951–2966, December 1997.

[29] G. Dietl and W. Utschick, "Complexity reduction of iterative receivers using low-rank equalization," *IEEE Transactions on Signal Processing*, vol. 55, no. 3, pp. 1035 –1046, March 2007.

[30] F. A. Dietrich and W. Utschik, "Pilot-assisted channel estimation based on second-order statistics," *IEEE Transactions on Signal Processing*, vol. 53, no. 3, pp. 1178–1193, March 2005.

[31] M. Dong, L. Tong, and B. M. Sadler, "Optimal insertion of pilot symbols for transmissions over time-varying flat fading channels," *IEEE Transactions on Signal Processing*, vol. 52, no. 5, pp. 1403–1418, May 2004.

[32] J. Du and Y. G. Li, "D-BLAST OFDM with channel estimation," *EURASIP Journal on Applied Signal Processing*, vol. 5, pp. 605–612, May 2004.

[33] C. Dumard, "Low-complexity iterative receiver for multi-user OFDM systems in time-varying MIMO channels," Ph.D. dissertation, Vienna University of Technology, Vienna, Austria, April 2009.

[34] C. Dumard, J. Jaldén, and T. Zemen, "Multi-user MIMO receiver processing for time-varying channels," in *Wireless Communications over Rapidly Time-Varying Channels*, F. Hlawatsch and G. Matz, Eds. Academic Press, 2011.

[35] C. Dumard, F. Kaltenberger, and K. Freudenthaler, "Low-cost equalizer based on Krylov subspace methods for HSDPA," *IEEE Transactions on Wireless Communications*, vol. 6, no. 5, pp. 1610–1614, May 2007.

[36] A. Edelman and N. Rao, "Random matrix theory," *Acta Numerica*, vol. 14, no. 233-297, p. 139, 2005.

[37] O. Edfors, M. Sandell, J.-J. van de Beek, S. K. Wilson, and P. O. Börjesson, "OFDM channel estimation by singular value decomposition," *IEEE Transactions on Communications*, vol. 46, no. 7, pp. 931–939, July 1998.

[38] P. Eggers, T. Brown, K. Olesen, and G. Pedersen, "Assessment of capacity support and scattering in experimental high speed vehicle to vehicle MIMO links," in *65th IEEE Vehicular Technology Conference (VTC)*, Dublin, Ireland, April 2007, pp. 466–470.

[39] T. Ekman, "Prediction of mobile radio channels - modeling and design," Ph.D. dissertation, Uppsala University, Uppsala, Sweden, 2002.

[40] ETSI TR 102 638, "Intelligent transport sytems (ITS); vehicular communications; basic set of applications; definitions," V1.1.1, June 2009.

[41] E. Failli, "Digital land mobile communications: COST 207," European Union, Tech. Rep., 1989.

[42] U. Fincke and M. Pohst, "Improved methods for calculating vectors of short length in a lattice, including a complex analysis," *Mathematics of Computation*, vol. 44, no. 169-170, pp. 463–471, April 1985.

[43] B. H. Fleury, M. Tschudin, R. Heddergott, D. Dalhaus, and K. I. Pedersen, "Channel parameter estimation in mobile radio environments using the SAGE algorithm," *IEEE Journal on Selected Areas in Communications*, vol. 17, no. 3, pp. 434–450, March 1999.

[44] T. Fügen, S. Knorzer, M. Landmann, R. Thomä, and W. Wiesbeck, "A 3-D ray tracing model for macrocell urban environments and its verification with measurements," in *Second European Conference on Antennas and Propagation (EuCAP)*, Edinburgh, United Kingdom, November 2007.

[45] G. D. Galdo, N. Czink, and M. Haardt, "Cluster spatial localization from high-resolution parameter estimation," in *IEEE/ITG Workshop on Smart Antennas*, Ulm, Germany, March 2006.

[46] A. Ghosh, R. Ratasuk, B. Mondal, N. Mangalvedhe, and T. Thomas, "LTE-advanced: next-generation wireless broadband technology," *IEEE Wireless Communications Magazine*, vol. 17, no. 3, pp. 10–22, June 2010.

[47] A. Ghrayeb and T. Duman, "Performance analysis of mimo systems with antenna selection over quasi-static fading channels," *IEEE Transactions on Vehicular Technology*, vol. 52, no. 2, pp. 281–288, March 2003.

[48] K. Gomadam, V. R. Cadambe, and S. A. Jafar, "Approaching the capacity of wireless networks through distributed interference alignment," in *IEEE Global Communications Conference (GLOBECOM)*, New Orleans (LA), USA, December 2008.

[49] A. Gore and A. Paulraj, "MIMO antenna subset selection with space-time coding," *IEEE Transactions on Signal Processing*, vol. 50, pp. 2580–2588, October 2002.

[50] F. Hlawatsch and G. Matz, Eds., *Wireless Communications over Rapidly Time-Varying Channels*. Academic Press, 2011.

[51] H. Hofstetter, "Characterization of the wireless MIMO channel," Ph.D. dissertation, Vienna University of Technology, Vienna, Austria, September 2006.

[52] M. Honig, G. Woodward, and Y. Sun, "Adaptive iterative multiuser decision feedback detection," *IEEE Transactions on Wireless Communications*, vol. 3, no. 2, pp. 477–485, March 2004.

[53] B. Hu, I. Land, L. Rasmussen, R. Piton, and B. Fleury, "A divergence minimization approach to joint multiuser decoding for coded CDMA," *Selected Areas in Communications, IEEE Journal on*, vol. 26, no. 3, pp. 432–445, April 2008.

[54] T. E. Hunter and A. Nosratinia, "Cooperation diversity through coding," in *IEEE International Symposium on Information Theory*, July 2002, p. 220.

[55] ITU, "Guidlines for evalutation of radio transmission technologies for IMT-2000," International Telecommunications Union (ITU)," Recommendation ITU-R M.1225, 1997.

[56] S. A. Jafar, *Interference Alignment: A New Look at Signal Dimensions in a Communication Network*, ser. Foundations and Trends in Communications and Information Theory. Now Publishers, 2011, vol. 7, no. 1.

[57] A. K. Jain and S. Ranganath, "Extrapolation algorithms for discrete signals with application in spectral estimation," *IEEE Transactions on Acoustics, Speech, and Signal Processing*, vol. ASSP-29, no. 4, pp. 830–845, August 1981.

[58] W. Jakes, *Microwave Mobile Communications*. New York, USA: John Wiley & Sons, 1974.

[59] Y. Jiang and M. Varanasi, "The RF-chain limited MIMO system-part I: Optimum diversity-multiplexing tradeoff," *IEEE Transactions on Wireless Communications*, vol. 8, no. 10, pp. 5238–5247, 2009.

[60] T. Kailath and A. H. Sayed, *Fast Reliable Algorithms for Matrices with Structure.* SIAM, 1999.

[61] S. Kaiser, *Multi-Carrier CDMA Mobile Radio Systems - Analysis and Optimization of Detection, Decoding, and Channel Estimation*, ser. Fortschritts-Berichte VDI Reihe. Düsseldorf, Germany: VDI Verlag GmbH, 1998, vol. 10, no. 531.

[62] S. Kaiser and P. Hoeher, "Performance of multi-carrier CDMA systems with channel estimation in two dimensions," in *8th IEEE International Symposium on Personal, Indoor and Mobile Radio Communications (PIMRC)*, vol. 1, Helsinki, Finnland, September 1997, pp. 115–119.

[63] J. Karedal, "Measurement-based modeling of wireless propagation channels - MIMO and UWB," Ph.D. dissertation, Lund University, Lund, Sweden, 2009.

[64] J. Karedal, F. Tufvesson, N. Czink, A. Paier, C. Dumard, T. Zemen, C. F. Mecklenbräuker, and A. F. Molisch, "A geometry-based stochastic MIMO model for vehicle-to-vehicle communications," *IEEE Transactions on Wireless Communications*, vol. 8, no. 7, pp. 3646–3657, July 2009.

[65] S. Kay, *Fundamentals of Statistical Signal Processing: Estimation Theory.* Upper Saddle River (NJ), USA: Prentice-Hall, 1993.

[66] V. Kristem, N. Mehta, and A. Molisch, "Training and voids in receive antenna subset selection in time-varying channels," *IEEE Transactions on Wireless Communications*, vol. 10, no. 6, pp. 1992–2003, June 2011.

[67] ——, "Optimal receive antenna selection in time-varying fading channels with practical training constraints," *IEEE Transactions on Communications*, vol. 58, no. 7, pp. 2023–2034, July 2010.

[68] V. Kühn, *Wireless Communications over MIMO Channels.* New York: John Wiley & Sons, 2006.

[69] P. Kyösti, J. Meinilä, L. Hentilä, X. Zhao, T. Jämsä, C. Schneider, M. Narandzić, M. Milojević, A. Hong, J. Ylitalo, V.-M. Holappa, M. Alatossava, R. Bultitude, Y. de Jong, and T. Rautiainen, "WINNER II channel models (d1.1.2v1.1)," European Commission, http://www.ist-winner.org, September 2007.

[70] J. N. Laneman, D. N. C. Tse, and G. W. Wornell, "Cooperative diversity in wireless networks: Efficient protocols and outage behavior," *IEEE Transactions on Information Theory*, vol. 50, no. 12, pp. 3062–3080, December 2004.

[71] G. Leus, S. Zhou, and G. B. Giannakis, "Orthogonal multiple access over time- and frequency-selective channels," *IEEE Transactions on Information Theory*, vol. 49, no. 8, pp. 1942–1950, August 2003.

[72] Z. Lin, E. Erkip, and A. Stefanov, "Cooperative regions and partner choice in coded cooperative systems," *IEEE Transactions on Communications*, vol. 54, no. 7, pp. 1323–1334, July 2006.

[73] R. J. Lyman, "Optimal mean-square prediction of the mobile-radio fading envelope," *IEEE Transactions on Signal Processing*, vol. 51, no. 3, pp. 819–824, March 2003.

[74] R. J. Lyman and W. W. Edmonson, "The prediction of bandlimited processes with flat spectral densities," *IEEE Transactions on Signal Processing*, vol. 49, no. 7, pp. 1564–1569, July 2001.

[75] R. J. Lyman, W. W. Edmonson, S. McCullough, and M. Rao, "The predictability of continuous-time, bandlimited processes," *IEEE Transactions on Signal Processing*, vol. 48, no. 2, pp. 311–316, February 2000.

[76] F. Mani and C. Oestges, "Ray-tracing evaluation of diffuse scattering in an outdoor scenario," in *5th European Conference on Antennas and Propagation (EUCAP)*, Rome, Italy, April 2011, pp. 3439–3443.

[77] D. Matolak, I. Sen, W. Xiong, and N. Yaskoff, "5 GHz wireless channel characterization for vehicle to vehicle communications," in *IEEE Military Communications Conference*, vol. 5, Atlantic City, New Jersey, USA, October 2005, pp. 3016–3022.

[78] G. Matz, A. Molisch, F. Hlawatsch, M. Steinbauer, and I. Gaspard, "On the systematic measurement errors of correlative mobile radio channel sounders," *IEEE Transactions on Communications*, vol. 50, no. 5, pp. 808–821, May 2002.

[79] G. Matz, "Doubly underspread non-WSSUS channels: Analysis and estimation of channel statistics," in *4th IEEE Workshop on Signal Processing Advances in Wireless Communications (SPAWC)*, Rome, Italy, June 2003, pp. 190–194.

[80] ——, "On non-WSSUS wireless fading channels," *IEEE Transactions on Wireless Communications*, vol. 4, no. 5, pp. 2465–2478, September 2005.

[81] J. Maurer, T. Fügen, T. Schäfer, and W. Wiesbeck, "A new inter-vehicle communications (IVC) channel model," in *IEEE 60th Vehicular Technology Conference (VTC)*, vol. 1, Los Angeles, CA, USA, September 2004, pp. 9–13.

[82] J. Maurer, T. Fügen, and W. Wiesbeck, "Narrow-band measurement and analysis of the inter-vehicle transmission channel at 5.2 GHz," in *55th Vehicular Technology Conference (VTC)*, Brimingham, AL, USA, May 2002, pp. 1274–1278.

[83] J. Maurer, "Strahlenoptisches Kanalmodell für die Fahrzeug-Fahrzeug Funkkommunikation," Ph.D. dissertation, Universität Karlsruhe, Karlsruhe, Germany, July 2005.

[84] C. F. Mecklenbräuker, A. F. Molisch, J. Karedal, F. Tufvesson, A. Paier, L. Bernadó, T. Zemen, O. Klemp, and N. Czink, "Vehicular channel characterization and its implications for wireless system design and performance," *Proceedings of the IEEE*, vol. 99, no. 7, pp. 1189–1212, July 2011.

[85] C. F. Mecklenbräuker, J. Wehinger, T. Zemen, H. Artés, and F. Hlawatsch, "Multiuser MIMO channel equalization," in *Smart Antennas — State-of-the-Art*, ser. EURASIP Book Series on Signal Processing and Communications, T. Kaiser, A. Bourdoux, H. Boche, J. R. Fonollosa, J. B. Andersen, and W. Utschick, Eds. New York (NY), USA: Hindawi, 2006, ch. 1.4, pp. 53–76.

[86] N. Mehta, A. F. Molisch, J. Zhang, and E. Bala, "Antenna selection training in MIMO-OFDM/OFDMA cellular systems," in *2nd IEEE International Workshop on Computational Advances in Multi-Sensor Adaptive Processing (CAMPSAP)*, St. Thomas, VI, USA, December 2007, pp. 113–116.

[87] A. F. Molisch, F. Tufvesson, J. Karedal, and C. F. Mecklenbräuker, "A survey on vehicle-to-vehicle propagation channels," *IEEE Wireless Communications Magazine*, vol. 16, no. 6, pp. 12–22, December 2009.

[88] A. F. Molisch, M. Z. Win, Y. S. Choi, and J. H. Winters, "Capacity of MIMO systems with antenna selection," *IEEE Transactions on Wireless Communications*, vol. 4, no. 4, pp. 1759–1772, July 2005.

[89] A. F. Molisch, *Wireless Communications*. John Wiley & Sons, 2005.

[90] ——, "A generic channel model for MIMO wireless propagation channels in macro- and microcells," *IEEE Transactions on Signal Processing*, vol. 52, no. 1, pp. 61–71, January 2004.

[91] A. F. Molisch and M. Z. Win, "MIMO systems with antenna selection," *IEEE Microwave Magazine*, vol. 5, no. 1, pp. 46–56, March 2004.

[92] T. K. Moon and W. C. Stirling, *Mathematical methods and algorithms for signal processing*. Upper Saddle River (NJ), USA: Prentice Hall, 2000.

[93] M. Morelli and U. Mengali, "A comparison of pilot-aided channel estimation methods for OFDM systems," *IEEE Transactions on Signal Processing*, vol. 49, no. 12, pp. 3065 –3073, December 2001.

[94] A. Paier, J. Karedal, N. Czink, H. Hofstetter, C. Dumard, T. Zemen, F. Tufvesson, and A. Molisch, "First results from car-to-car and car-to-infrastructure radio channel measurements at 5.2 GHz," in *18th IEEE International Symposium on Personal, Indoor and Mobile Radio Communications (PIMRC)*, Athens, Greece, September 2007.

[95] A. Paier, J. Karedal, N. Czink, H. Hofstetter, C. Dumard, T. Zemen, F. Tufvesson, A. Molisch, and C. F. Mecklenbräuker, "Car-to-car radio channel measurements at 5 GHz: Pathloss, power-delay profile, and delay-Doppler spectrum," in *IEEE International Symposium on Wireless Communication Systems (ISWCS)*, Trondheim, Norway, October 2007.

[96] A. Paier, L. Bernadó, J. Karedal, O. Klemp, and A. Kwoczek, "Overview of vehicle-to-vehicle radio channel measurements for collision avoidance applications," in *IEEE 71st Vehicular Technology Conference (VTC)*, Taipei, Taiwan, May 2010.

[97] P. Paschalidis, K. Mahler, A. Kortke, M. Wisotzki, M. Peter, and W. Keusgen, "2 x 2 MIMO measurements of the wideband car-to-car channel at 5.7 GHz on urban street intersections," in *IEEE Vehicular Technology Conference (VTC)*, San Francisco (CA), USA, September 2011.

[98] P. Paschalidis, M. Wisotzki, A. Kortke, W. Keusgen, and M. Peter, "A wideband channel sounder for car-to-car radio channel measurements at 5.7 GHz and results for an urban scenario," in *68th IEEE Vehicular Technology Conference (VTC)*, Calgary, Canada, September 2008.

[99] A. Paulraj, R. Nabar, and D. Gore, *Introduction to Space-Time Wireless Communications*. Cambridge University Press, 2003.

[100] G. F. Pedersen, J. B. Andersen, P. C. F. Eggers, J. O. Nielsen, H. Ebert, T. Brown, A. Yamamoto, T. Hayashi, and K. Ogawa, "Small terminal MIMO channels with user interaction," in *2nd European Conference on Antennas and Propagation (EuCAP)*, Edinburgh, United Kingdom, November 2007.

[101] D. B. Percival and A. T. Walden, *Spectral Analysis for Physical Applications*. Cambridge University Press, 1963.

[102] J. G. Proakis, *Digital Communications*, 4th ed. New York, USA: McGraw-Hill, 2000.

[103] O. Renaudin, V.-M. Kolmonen, P. Vainikainen, and C. Oestges, "Non-stationary narrowband MIMO inter-vehicle channel characterization in the 5-GHz band," *IEEE Transactions on Vehicular Technology*, vol. 59, no. 4, pp. 2007 –2015, May 2010.

[104] P. S. Rossi and R. R. Müller, "Slepian-based two-dimensional estimation of time-frequency variant MIMO-OFDM channels," *IEEE Signal Processing Letters*, vol. 15, pp. 21–24, January 2008.

[105] Y. Saad, *Iterative Methods for Sparse Linear Systems*, 2nd ed. SIAM, 2003.

[106] A. Saleh and R. Valenzuela, "A statistical model for indoor multipath propagation," *IEEE Journal on Selected Areas in Communications*, vol. 5, no. 2, pp. 128 – 137, February 1987.

[107] S. Sanayei and A. Nosratinia, "Antenna selection in MIMO systems," *IEEE Communications Magazine*, vol. 42, pp. 68–73, October 2004.

[108] M. Sawahashi, Y. Kishiyama, A. Morimoto, D. Nishikawa, and M. Tanno, "Coordinated multipoint transmission/reception techniques for LTE-advanced," *IEEE Wireless Communications Magazine*, vol. 17, no. 3, pp. 26 –34, June 2010.

[109] A. M. Sayeed, A. Sendonaris, and B. Aazhang, "Multiuser detection in fast-fading multipath environment," *IEEE Journal on Selected Areas in Communications*, vol. 16, no. 9, pp. 1691–1701, December 1998.

[110] D. Schafhuber, G. Matz, and F. Hlawatsch, "Adaptive Wiener filters for time-varying channel estimation in wireless OFDM systems," in *IEEE International Conference on Acoustics, Speech, and Signal Processing (ICASSP)*, vol. 4, Hong Kong, China, April 2003, pp. 688–691.

[111] L. L. Scharf, *Statistical Signal Processing: Detection, Estimation, and Time Series Analysis*. Reading (MA), USA: Addison-Wesley Publishing Company, Inc., 1991.

[112] S. Semmelrodt, "Methoden zur prädiktiven Kanalschätzung für adaptive Übertragunstechniken im Mobilfunk," Ph.D. dissertation, Kassel University, 2003.

[113] A. Sendonaris, E. Erkip, and B. Aazhang, "User cooperation diversity - part I: System description," *IEEE Transactions on Communications*, vol. 51, no. 11, pp. 1927–1938, November 2003.

[114] ——, "User cooperation diversity - part II: Implementation aspects and performance analysis," *IEEE Transactions on Communications*, vol. 51, no. 11, pp. 1939 – 1948, November 2003.

[115] D.-S. Shiu, G. Foschini, M. Gans, and J. Kahn, "Fading correlation and its effect on the capacity of multielement antenna systems," *IEEE Transactions on Communications*, vol. 48, no. 3, pp. 502–513, 2000.

[116] M. Šimko, C. Mehlführer, T. Zemen, and M. Rupp, "Inter-carrier interference estimation in MIMO OFDM systems with arbitrary pilot structure," in *73rd IEEE Vehicular Technology Conference (VTC-Spring)*, Budapest, Hungary, May 2011.

[117] D. Slepian, "Prolate spheroidal wave functions, Fourier analysis, and uncertainty - V: The discrete case," *The Bell System Technical Journal*, vol. 57, no. 5, pp. 1371–1430, May-June 1978.

[118] D. Slepian and H. O. Pollak, "Prolate spheroidal wave functions, Fourier analysis, and uncertainty - I," *The Bell System Technical Journal*, vol. 40, no. 1, pp. 43–64, January 1961.

[119] I. E. Telatar, "Capacity of multi-antenna Gaussian channels," AT&T Bell Laboratories, Murray Hill, NJ, USA, Tech. Rep. BL0112170-950615-07TM, June 1995.

[120] ——, "Capacity of multi-antenna Gaussian channels," *European Transactions on Telecommunications*, vol. 10, no. 6, pp. 585–595, 1999.

[121] R. Thomä, D. Hampicke, A. Richter, G. Sommerkorn, A. Schneider, U. Trautwein, and W. Wirnitzer, "Identification of time-variant directional mobile radio channels," *IEEE Transactions on Instrumentation and Measurement*, vol. 49, no. 2, pp. 357 – 364, April 2000.

[122] D. J. Thomson, "Spectrum estimation and harmonic analysis," *Proceedings of the IEEE*, vol. 70, no. 9, pp. 1055 – 1096, September 1982.

[123] S. Valentin and H. Karl, "Effect of user mobility in coded cooperative systems with joint partner and cooperation level selection," in *IEEE Wireless Communications and Networking Conference (WCNC)*, Hong Kong, China, March 2007, pp. 896–901.

[124] H. van der Vorst, *Iterative Krylov Methods for Large Linear Systems*. Cambridge University Press, 2003.

[125] S. Verdú, *Multiuser Detection*. New York, USA: Cambridge University Press, 1998.

[126] I. Viering, *Analysis of Second Order Statistics for Improved Channel Estimation in Wireless Communications*, ser. Fortschritts-Berichte VDI Reihe. Düsseldorf, Germany: VDI Verlag GmbH, 2003, no. 733.

[127] Z. Wang and G. B. Giannakis, "Wireless multicarrier communications," *IEEE Signal Processing Magazine*, vol. 17, no. 3, pp. 29–48, May 2000.

[128] J. Wehinger, "Iterative multi-user receivers for CDMA systems," Ph.D. dissertation, Vienna University of Technology, Vienna, Austria, July 2005.

[129] W. Weichselberger, M. Herdin, H. Özcelik, and E. Bonek, "A stochastic MIMO channel model with joint correlation of both link ends," *IEEE Transactions on Wireless Communications*, vol. 5, no. 1, pp. 90–100, January 2006.

[130] S. B. Weinstein and P. M. Ebert, "Data transmission by frequency-divison multiplexing using the discrete Fourier transform," *IEEE Transactions on Communications*, vol. 19, no. 5, pp. 628–634, October 1971.

[131] M. Z. Win and J. H. Winters, "Virtual branch analysis of symbol error probability for hybrid selection/maximal-ratio combining in rayleigh fading," *IEEE Transactions on Communications*, vol. 49, no. 11, pp. 1926–1934, November 2001.

[132] S. Wyne, A. F. Molisch, P. Almers, G. Eriksson, J. Karedal, and F. Tufvesson, "Outdoor-to-indoor office MIMO measurements and analysis at 5.2 GHz," *IEEE Transactions on Vehicular Technology*, vol. 57, no. 3, pp. 1374–1386, May 2008.

[133] T. Zemen, N. Czink, L. Bernadó, and C. Vogel, "Funkkommunikation für intelligente Verkehrssysteme — Status und Ausblick," *E&I Elektrotechnik und Informationstechnik*, no. 7-8, pp. 276–281, July/August 2011, invited survey paper.

[134] T. Zemen, H. Hofstetter, and G. Steinböck, "Successive Slepian subspace projection in time and frequency for time-variant channel estimation," in *14th IST Mobile and Wireless Communication Summit (IST SUMMIT)*, Dresden, Germany, June 2005.

[135] T. Zemen and C. F. Mecklenbräuker, "Time-variant channel estimation using discrete prolate spheroidal sequences," *IEEE Transactions on Signal Processing*, vol. 53, no. 9, pp. 3597–3607, September 2005.

[136] T. Zemen, C. F. Mecklenbräuker, J. Wehinger, and R. R. Müller, "Iterative joint time-variant channel estimation and multi-user detection for MC-CDMA," *IEEE Transactions on Wireless Communications*, vol. 5, no. 6, pp. 1469–1478, June 2006.

[137] T. Zemen and A. F. Molisch, "Adaptive reduced-rank estimation of non-stationary time-variant channels using subspace selection," *IEEE Transactions on Vehicular Technology*, vol. 61, no. 9, pp. 4042–4056, November 2012.

[138] H. Zhang, A. F. Molisch, and J. Zhang, "Applying antenna selection in WLANs for achieving broadband multimedia communications," *IEEE Transactions on Broadcasting*, vol. 52, no. 4, pp. 475–482, December 2006.

[139] Y. R. Zheng and C. Xiao, "Simulation models with correct statistical properties for Rayleigh fading channels," *IEEE Transactions on Communications*, vol. 51, no. 6, pp. 920–928, June 2003.